30 JUNE 1967

LMSC-A874728
CODE Y-87-67-1

A Study of LIQUID PROPELLANT BEHAVIOR DURING PERIODS OF VARYING ACCELERATIONS

FINAL REPORT

PREPARED UNDER CONTRACT NO. NAS 9-5174

For The
NATIONAL
AERONAUTICS
AND SPACE
ADMINISTRATION
MANNED SPACECRAFT CENTER
HOUSTON, TEXAS

LOCKHEED MISSILES & SPACE COMPANY
A GROUP DIVISION OF LOCKHEED AIRCRAFT CORPORATION
SUNNYVALE, CALIFORNIA

30 JUNE 1967

LMSC-A874728
CODE Y-87-67-1

A Study of LIQUID PROPELLANT BEHAVIOR DURING PERIODS OF VARYING ACCELERATIONS

FINAL REPORT

PREPARED UNDER CONTRACT NO. NAS 9-5174

Prepared by

M. P. HOLLISTER
H. M. SATTERLEE
H. COHAN

For The
NATIONAL
AERONAUTICS
AND SPACE
ADMINISTRATION
MANNED SPACECRAFT CENTER
HOUSTON, TEXAS

LOCKHEED MISSILES & SPACE COMPANY
A GROUP DIVISION OF LOCKHEED AIRCRAFT CORPORATION
SUNNYVALE, CALIFORNIA

PREFACE

This report is submitted by Lockheed Missiles and Space Co. to the National Aeronautics and Space Administration -- Manned Spacecraft Center in partial fulfillment of contract number NAS 9-5174. This is the complete technical report on the analytical and experimental study of liquid propellant behavior carried out under this contract. Specific substudies within the study include:

Small amplitude lateral sloshing -- the quasi-steady state analytical treatment of sloshing.

Large amplitude lateral motions -- an anlysis of such motions as a boundary/initial value problem.

Transient lateral motions following engine shutdown -- an analysis related to the one just preceding.

Damping provided by ring and screen type baffles -- an analysis to extend the results of earlier work to tank geometries of practical interest.

An experiment to verify sloshing frequencies for small amounts of liquid in a hemispherically bottomed cylindrical tank and to verify calculated response to impulsive perturbations.

An experiment to determine the response of laterally sloshing liquid to the sudden reduction in body forces as when engine cutoff occurs.

An experiment to determine the effect of interface curvature (as when the axial Bond number is low) on the damping afforded by ring baffles.

Large amplitude axisymmetric slosh and analysis of liquid motions in response to axial accelerations.

An analysis of the liquid response to axisymmetric structural vibrations of a propellant tank.

An experimental investigation of the reorientation flow or response to an axial acceleration in clean tanks and in a baffled tank. This investigation also included an examination of the effect of an impulsive acceleration.

An experiment to examine the geysering or rebound that results from a reorientation flow.

An experimental investigation of ullage gas entrainment resulting from a reorientation flow.

In addition to the basic investigations required by the study, the material developed as well as other available material was applied to the prediction of liquid behavior in:

The Apollo Service Propulsion System (SPS)

The Lunar Module Ascent and Descent Propulsion Systems

The SPS passive liquid retention system during an earth orbital mission in which the SPS is propelled backwards by the Lunar Module

Other reports submitted under this contract include:

"A Study of Liquid Propellant Behavior During Periods of Varying Acceleration -- Summary Report" -- LMSC/A874729.

"The Literature of Low-g Propellant Behavior" -- LMSC/A874730

"Low-g Liquid Propellant Behavior -- An Engineering Handbook" -- LMSC/A874731

The authors of this report are grateful for the help of the following persons who gave of themselves during the course of this study in leading the many substudies in the project.

Richard M. Cima
George E. Crane
Edward E. Ferrin
Bob D. Neff
Lawrence M. Perko
James G. Seebold
Robert M. Vernon
Coleman Waller
Phineas S. Woods

Test Engineer W. V. Moore, photographer M. Oberto, and the photographers under R. M. Betty provided essential support for the test work.

J. W. Baxter, C. F. Merlet, and H. M. Kindsvater contributed key managerial support. The help and patience of M. Tucker and H. P. Kerfoot were invaluable in assisting the progress of the project.

Professor Dayton D. Wittke of the University of Nebraska provided valuable help in analysis work as well as the basic design of the steady-state ullage gas entrainment experiment described in this report.

CONTENTS

ILLUSTRATIONS

TABLES

Section 1
INTRODUCTION

Until the last few years the field of low gravity fluid mechanics was a curious mixture of classical theory, severely limited experimental work and semi-technical conjecture.

Although basic work on capillary dominated phenomena had been done early in the 19th century, the application to physical situations was related to very small vessels and to geometries of little practical value. The advent of space flight soon presented technology with a host of novel problems related to the behavior of fluids in very low gravity environments, when capillary forces become as important as, or more important than, the conventional body forces, such as gravitational acceleration.

In a rocket powered space vehicle on orbit or in transfer to another planet or the moon, residual propellants may migrate to the forward ends of the tanks due to the very small accelerations imposed on the vehicle by the slight but sensible drag forces present. It is necessary to assure the position of liquid rocket propellants at the tank drains (engine feed lines) to enable the engines to be restarted in space after a period of time in a "weightless" condition. (The terms "weightless" and "low" or "zero gravity" all refer to the condition in which the sum of steady forces acting between the tank and liquid is equal or nearly equal to zero). Early solutions to this positioning problem utilized ullage positioning rockets -- small solid

propellant motors which, upon ignition, provide sufficient thrust to the rocket vehicle to result in an acceleration which will properly reorient the liquid propellants from the worst possible position in their tanks. This solution is positive, provided the timing is correct, but it is also heavy (solid rockets subtract from payload), unreliable (timing sequences and multiple firing commands are required), and impractical for multiple restarts.

The concept of passive retention systems, making use of capillary phenomena, came under investigation. The primary requirement imposed on passive retention systems is to retain sufficient propellant at the tank drain to assure complete ignition.

The requirement for propellant reorientation underscores another problem area of low gravity fluid dynamics. Regardless of the method used to orient the propellants prior to engine ignition, it is necessary to know the reorientation behavior of liquids in typical rocket vehicle tanks when the engine ignites and the main bodies of propellants are "bottomed". Although some theory existed, scaled experiments had to await the development of apparatus which could provide meaningful experimental conditions. These conditions include the capability to place a partially liquid-filled model tank in zero gravity condition briefly, then to accelerate the tank so as to reorient the liquid mass from one end of the tank to the other. During these experiments, some method of data taking is required.

Another difficult problem is presented by liquid sloshing in a partially filled tank in low g. Again, some body of theory existed, and some simple

experiments had been performed. Nevertheless, much was still unknown of the effect of low gravity on slosh dynamics. The forces exerted on a tank by the sloshing liquid could exert important influences on a space vehicle's attitude control system. The effects of baffles had to be explored, and consideration given to the interaction between baffles, passive retention system hardware, and liquid reorientation.

A number of similar problems, all complicated by the virtual elimination of the major body force of conventional fluid mechanics, gravitational acceleration, required examination by theoretical or experimental means, or both.

There are essentially only three tools with which to carry out such experiments. They are, space vehicles in orbit, aircraft flown on a zero gravity flight path, and drop towers. The space vehicle provides unlimited experiment times, but at extremely high cost and difficulty of data retrieval; the aircraft provides a maximum of about 30 seconds of zero g time, but initial liquid conditions induced by preliminary maneuvers may be chaotic, and air movements in the cabin add uncertain small forces to the experiment; the drop tower provides opportunity for controlled pre-low g conditions, but is severely limited in time, usually the order of 1 to 4 seconds.

Lockheed Missiles and Space Company was fortunate to be selected to conduct the present project, whose main purpose was to furnish engineering information for the management of liquid propellants in space vehicles. In order to meet the requirements, much of the work was more complex and difficult than had been attempted before in this field. Some of the experiments, particularly, achieved a level of sophistication and concommittant complexity not

previously attempted in a drop tower.

The description and results of this project are presented in the following sections of this report. It will be seen that the primary purpose of the project has been achieved; to develop engineering tools for the solution of the problems of managing liquid propellants and other liquids in spacecraft. In some cases specific answers have been provided. In other instances, the work done has not resulted in definite positive information, but has provided the insight to allow intelligent engineering around the problem, while establishing its order of importance more clearly than was previously known.

Some discussion of the organization of this report, as well as the others required by the contract, is in order. The report is divided into five sections plus one appendix. Following sections discuss analyses carried out under the study, the experiments performed and the general results which have been developed in this work. In the last section, these results are used to analyze the behavior of liquids in the Apollo Spacecraft Propulsion System and both Lunar Module stages. The appendix comprises the special report submitted to NASA MSC in support of the liquid behavior experiments carried by the Gemini XI spacecraft.

The scope of the work carried out in this study is large enough that it is impractical to unify the notation used. Care has been taken to make each subsection of the report stand by itself notationwise.

References are made in this report to other literature. The bibliography prepared under the study, entitled "The Literature of Low-g Liquid Propellant

Behavior", published under separate cover, includes essentially all pertinent literature items available.

The general results of this study have been incorporated into an "Engineering Handbook for Low-g Liquid Propellant Behavior", also published under separate cover. In this work, a sincere attempt was made to gather all of the pertinent material from the literature with emphasis on the needs of spacecraft propulsion system designers.

Two computer codes were developed for the analysis of specific problems. Descriptions of these codes have been published under separate cover.

Section 2

ANALYSIS

The major purpose of this Project has been to develop information about the behavior of liquids in rocket propellant tanks under conditions to be met in spaceflight. It is also required that this information is to be correlated so as to enable ready calculation of liquid behavior in tanks of any size under any level of acceleration. One of the best ways of assuring that engineering calculations can be performed for a variety of conditions is to obtain the information required by analysis. Through analysis, the problem at hand can be reduced to a suitable physical idealization which hopefully will yield to techniques of mathematical analysis. If this can be accomplished, the behavior of the idealization, at least, can be computed for any condition for which the idealization is adequate. Experimentation, then, is reduced to the role of verifying the validity of the idealization and the establishment of a range of applicability for the results of analysis.

Analysis has proved to be a very important tool in the study of liquid behavior in rocket propellant tanks. In the first place, many of the operating conditions envisioned in the operation of space vehicles have been impossible of experimental simulation. Analysis has had to fill the gap where experimental evidence was not available. Secondly, what experimentation has been possible has proven to be relatively expensive and time consuming because of the equipment needed (drop towers and aircraft). Analysis has been invaluable in providing guidance for experiments so that wasted motion can be

voided.

Analytical work carried out in this Project can be placed in several categories. The first includes that analytical work making use of the classical approach and methods of applied mathematics. The reorientation of liquids in rocket tanks subjected to settling impulses resulting in large amplitude axial liquid motion were studied this way, as were large amplitude lateral liquid motions. The same techniques were used in the detailed analysis of small amplitude lateral sloshing and the small amplitude axial motion of liquid resulting from the post engine shutdown relaxation of the tank shell. In these problems, the liquid has been assumed inviscid and incompressible and its motion irrotational. These assumptions, of course, greatly simplified the problem statement as well as the method of solution. Unfortunately, the numerical solution of this type of problem is most often far from easy.

Analysis was also applied to prediction of the behavior of baffles in propellant tanks. Here, the motion of the liquid is far from ideal especially in the vicinity of the baffles. However, some of the results of the small amplitude lateral sloshing problem could be applied to a straightforward estimate of damping afforded by baffles.

Assuming that the first portion of the axial reorientation of liquid under the action of a settling thrust can be suitably attacked by assuming ideal liquid behavior, later portions of the overall settling of the liquid is certainly much too chaotic to allow use of classical techniques. Analysis should be limited to the assumption of quasi-steady state behavior. Application of simple continuity, momentum, and kinetic energy relations enabled

development of some information where the exact formulation obviously cannot be solved.

Lastly, simple analysis of the hydrostatic behavior of liquids when restrained by the capillary forces in screens or perforated plates enables design of devices for retention of liquid propellants around the tank drain, thereby eliminating or reducing the need for settling rockets.

This section treats first the analysis of large amplitude liquid motions, both axisymmetric and asymmetric; then briefly reviews the rather conventional analysis of lateral sloshing under low-g conditions. After that the results of simple analysis of the later portions of the axial reorientation of liquids during settling is discussed. The analysis of the behavior of baffles in cylindrical tanks with hemispherical bottom is then described. The last analysis presented is that of the response of liquid to the post engine shutdown relaxation of its tank.

ANALYSIS OF LARGE AMPLITUDE LIQUID BEHAVIOR - It is important, first of all, to define the type of fluid motion that can be determined by this analysis. The scope is actually quite broad. The analysis described here applies to both symmetric and asymmetric motions; large and small amplitude motions; motions with zero and non-zero initial velocity. The main type of motion that does not fall within the scope of this analysis is surface tension dominated motion (e.g., the transition of a high-g flat initial shape into a hemispherical surface shape in a low-g field). This can best be summarized by saying that the accelerations must be relatively large (Bond numbers greater than ten in magnitude) and/or the liquid velocity must be relatively large. Several examples depicting the results of the analysis are discussed later in the results subsection. The comparison of experimental and analytical results is also discussed in a section of this report along with a review of all the results of the Project.

Problem Formulation - Let $\vec{v}(r,\theta,z,t)$ be the velocity of a point (r,θ,z) in the fluid at time t. It is assumed that the flow is irrotational, i.e., that $\nabla \times \vec{V} = 0$ so that there exists a velocity potential $\varphi(r,\theta,z,t)$ such that $\vec{V} = \nabla \varphi$. The geometry is indicated in Figure 2-1. Since the flow is assumed incompressible, the equation of continuity implies that $\nabla \cdot \vec{V} = 0$ and hence the velocity potential satisfies Laplace's equation interior to the

fluid,

$$\varphi_{rr} + \frac{1}{r}\varphi_r + \frac{1}{r^2}\varphi_{\theta\theta} + \varphi_{zz} = 0 \qquad (2.1)$$

for $t > 0$, $G(r,z) < 0, 0 < z < f(r,\theta,t)$ and $0 \leq \theta < 2\pi$ where $G(r,z) = 0$ is the equation of the container and where $z - f(r,\theta,t) = 0$ is the equation of the free surface. The normal derivative is assumed to be zero on the fluid boundaries, i.e., for

$$\left.\frac{\partial \varphi}{\partial n}\right|_{G(r,z)=0} = \left.\frac{\varphi_r G_r + \varphi_z G_z}{\left(G_r^2 + G_z^2\right)^{1/2}}\right|_{G(r,z)=0} = 0 \qquad (2.2)$$

where, as was previously indicated, $G(r,z)=0$ is the equation of the fixed boundary, i.e., the axisymmetric container. For example, for a flat bottomed container as shown in Figure 2-1

$$G(r,z) = \begin{cases} r - r_o & \text{for } 0 \leq z \leq f(r_o, \theta, t) \\ -z & \text{for } 0 \leq r \leq r_o \end{cases}$$

and

$$\left.\frac{\partial \varphi}{\partial n}\right|_{G=0} = \begin{cases} \varphi_r(r_o, \theta, z, t) = 0 & \text{for } 0 \leq z \leq f(r_o, \theta, t) \\ \varphi_z(r, \theta, 0, t) = 0 & \text{for } 0 \leq r \leq r_o \end{cases}$$

and for $0 \leq \theta \leq 2\pi$ and $t \geq 0$.

The free surface boundary condition which follows from a first integral of

Euler's equation for invisid flow* is known as Bernoulli's equation. It can be written in the form

$$\left.\begin{aligned} &\varphi_t(r,\theta,z,t)\Big|_{z=f(r,\theta,t)} = \Phi(r,\theta,t) \\ &\Phi(r,\theta,t) = \frac{1}{1+\beta}\left[\alpha_1(t)\, r\cos\theta + \alpha_3(t)(f-H)\right] \\ &\quad -\frac{1}{2}\left[\nabla\varphi(r,\theta,f,t)\right]^2 + \frac{\beta}{1+\beta}\,\nabla\cdot\left[\frac{\nabla f}{\sqrt{1+|\nabla f|^2}}\right] \end{aligned}\right\} \qquad (2.3)$$

and where f = f(r,θ, t) describes the free surface. In equation (2.3), H is the volumetric average height and the dimensionless parameter

$$\beta = \frac{\sigma}{\rho r_o^2 g} = \frac{1}{B}$$

where B is the axial Bond number. The last term in equation (2.3) is the expression for the mean curvature of the free surface, i.e., the surface tension term. It can be written out as

$$\nabla\cdot\left[\frac{\nabla f}{\sqrt{1+|\nabla f|^2}}\right] = \frac{1}{r}\frac{\partial}{\partial r}\left[\frac{r f_r}{\sqrt{1+f_r^2+\frac{1}{r^2}f_\theta^2}}\right] + \frac{1}{r^2}\frac{\partial}{\partial\theta}\left[\frac{f_\theta}{\sqrt{1+f_r^2+\frac{1}{r^2}f_\theta^2}}\right] \qquad (2.4)$$

The coordinates in (2.1)-(2.3) have been normalized by dividing distances by r_o, time by $\left[r_o/g\,(1+\beta)\right]^{1/2}$ and the velocity potential by $\left[r_o^3 g\,(1+\beta)\right]^{1/2}$ Laplace's equation (2.1) and the boundary conditions (2.2) remain invariant

*Landau, L.D. and Lifshitz, E.M., Fluid Mechanics, Pergamon Press, New York, 1959, p 3.

under this normalization. The constants r_o and g can be any distance and acceleration; however, in practice r_o is conveniently taken as the radius of the cylinder (in the case of a cylindrical container) and g is taken as the magnitude of the maximum acceleration on the container. $(\alpha_1(t)g, 0, \alpha_3(t)g)$ is the actual acceleration on the container. Note that the acceleration vector has been assumed to lie in a plane through the axis of the axisymmetric container.

Associated with the boundary condition (2.3) is the boundary condition at the liquid-vapor-solid interface which geometrically requires the contact angle, ψ_o, to be maintained constant. It is expressed by the vector equation

$$-\frac{\nabla G \cdot \nabla G_1}{|\nabla G||\nabla G_1|} = \cos\psi_o \qquad \begin{matrix} t \geq 0 \\ 0 \leq \theta \leq 2\pi \end{matrix} \tag{2.5}$$

where as before $G(r,z) = 0$ describes the axisymmetric container surface and where $G_1(r,z,\theta,t) = z - f(r,\theta,t) = 0$ describes the free surface. For example, if the container is a cylinder of radius one (in normalized coordinates), this condition reduces to

$$\frac{f_r(1,\theta,t)}{\left(1 + f_r^2(1,\theta,t) + f_\theta^2(1,\theta,t)\right)^{1/2}} = \cos\psi_o \tag{2.6}$$

for $t \geq 0,\ 0 \leq \theta \leq 2\pi$

The remaining equation, which together with (2.3) relates the motion of the surface to the potential, follows from

$$\vec{v} = \frac{d\vec{r}}{dt}$$

where $\vec{r}(t)$ is a point in the fluid corresponding to (r,θ,z) and t has been introduced as a parameter. This equation for points on the surface $z=f(r,\theta,t)$ can be written in component form as:

$$\frac{dr}{dt} = \phi_r \,, \quad r\frac{d\theta}{dt} = \frac{1}{r}\phi_\theta \,, \quad \frac{df}{dt} = \phi_z$$

Using the fact that the total derivative

$$\frac{df}{dt} = f_t + f_r \frac{dr}{dt} + f_\theta \frac{d\theta}{dt}$$

these equations can be combined into the single first order partial differential equation, the kinematic equation,

$$f_t = \phi_z - \phi_r f_r - \frac{1}{r^2}\phi_\theta f_\theta \tag{2.7}$$

on $z=f(r,\theta,t)$, for $0<r<1$, $0\le\theta\le 2\pi$, $t\ge 0$.

The remaining information necessary to complete the description of the mathematical model are the initial conditions at t = 0. These conditions can be given in the form of an initial free surface shape

$$f(r,\theta,0) = f_0(r,\theta) \tag{2.8}$$

together with the velocity of the free surface

$$\begin{aligned} u(r,\theta) &= \phi_r\,(r,\theta,f_0(r,\theta),0) \\ v(r,\theta) &= \frac{1}{r}\phi_\theta\,(r,\theta,f_0(r,\theta),0) \\ w(r,\theta) &= \phi_z\,(r,\theta,f_0(r,\theta),0) \end{aligned} \tag{2.9}$$

for $0 \le r \le 1$, $0 \le \theta \le 2\pi$ or alternatively the initial free surface shape, $f_0(r,\theta)$, together with the velocity potential

$$\varphi(r,\theta,z,0) = \varphi_0(r,\theta,z) \tag{2.10}$$

for $G(r,z) \le 0$, $0 \le z \le f_0(r,\theta)$, $0 \le \theta \le 2\pi$.

Laplace's equation (2.1) together with the boundary conditions (2.2), (2.3), (2.5) and (2.7) and the initial conditions (2.8) and (2.9) or (2.10) define the free surface boundary problem to be solved.

METHOD OF SOLUTION - The method used to approximate the solution to the problem posed in the preceding section is described in this section. In brief, the velocity potential is represented in the form of a series

$$\varphi(r,\theta,z,t) = \sum_n C_n(t)\,\Psi_n(r,\theta,z) \tag{2.11}$$

where the functions $\Psi_n(r,\theta,z)$ satisfy Laplace's equation (2.1) (and possibly some of the boundary conditions, e.g., (2.2)). The time dependent coefficients $C_n(t)$ are determined numerically by an orthonormalizing computation in order to satisfy those boundary conditions (2.2), (2.3), (2.5), and (2.7) which are not satisfied by $\Psi_n(r,\theta,z)$.

Separation of Variables (Flat Bottomed Cylindrical Container)

An elementary flow chart for this method is shown in Figure 2-2. For a flat bottomed cylindrical container, the velocity potential satisfying (2.1) and (2.2) has the representation, determined by separation of variables,

$$\varphi(r,\theta,z,t) = \sum_{m,n} C_n^{(m)}(t)\,J_m(\lambda_n^{(m)} r)\cos m\theta\,\frac{\cosh(\lambda_n^{(m)} z)}{\cosh(\lambda_n^{(m)} H)} \tag{2.12}$$

where $J_m'(\lambda_n^{(m)}) = 0$ determines the numbers $\lambda_n^{(m)}$, $n, m = 1, 2, \cdots$. The time variation of the velocity potential $\varphi(r,\theta,z,t)$ (i.e., of the coefficients $c_n^{(m)}(t)$) is determined by requiring that the representation (2.12) satisfy the boundary condition (2.3); i.e., that

$$\sum_{n,m} \frac{dc_n^{(m)}}{dt}(t)\, F_n^{(m)}(r,\theta,t) = \dot{f}(r,\theta,t) \tag{2.13}$$

where

$$F_n^{(m)}(r,\theta,t) = J_m(\lambda_n^{(m)} r)\cos m\theta\, \frac{\cosh[\lambda_n^{(m)} f(r,\theta,t)]}{\cosh(\lambda_n^{(m)} H)}$$

This can be satisfied approximately by determining the coefficients $c_n^{(m)}(t)$ numerically by some orthonormalizing computation (cf. Davis and Rabinowitz,* for a general description of orthonormalizing methods). The method developed to determine the first few coefficients $c_n^{(0)}(t)$, $n = 1, \cdots N_0$ and $c_n^{(1)}(t)$, $n = 1, \cdots N_1$ is outlined below. Basically, it amounts to following the motion of the free surface on the two planes $\theta = 0, \pi$ and $\theta = \pm \frac{\pi}{2}$ (plus neighboring planes in order to compute the mean curvature on these two planes; e.g., in order to compute the mean curvature on the $\theta = \pi/2$ plane, it is necessary to carry along points on the neighboring planes $\theta = \pi/2 \pm \Delta\theta$). The derivatives $\frac{dc_n^{(0)}}{dt}(t)$ are determined from Bernoulli's equation on the $\pi/2$ plane; i.e., from

$$\sum_{n=1}^{N_0} \frac{dc_n^{(0)}}{dt}(t)\, F_n^{(0)}(r, \tfrac{\pi}{2}, t) = \dot{f}(r, \tfrac{\pi}{2}, t)$$

by the orthonormalization technique used in the symmetric case following

*Davis, P.J., Rabinowitz, P., "Advances in Orthonormalizing Computation", appears in Advances in Computers, V. 2, Academic Press, N.Y., 1961.

Moore and Perko.* The functions $\Phi(r,\theta,t)$ and $F_n^{(m)}(r,\theta,t)$ are defined in (2.3) and (2.13) respectively. Having determined the derivatives $\frac{dc_n^{(0)}}{dt}(t)$, the derivatives $\frac{dc_n^{(1)}}{dt}(t)$ are then determined from Bernoulli's equation on the $(0,\pi)$ plane, i.e., from

$$\sum_{n=1}^{N_1} \frac{dc_n^{(1)}}{dt}(t)\, F_n^{(1)}(r,\tfrac{0}{\pi},t) = \Phi(r,\tfrac{0}{\pi},t) - \sum_{n=1}^{N_0} \frac{dc_n^{(0)}}{dt}(t) F_n^{(0)}(r,\tfrac{0}{\pi},t)$$

The effect of the higher harmonics, i.e., of non-zero $C_n^{(2)'}$, $C_n^{(3)'}$ .... , in the above equations for $C_n^{(0)'}$ and $C_n^{(1)'}$ has been neglected. It was originally proposed that the higher harmonic coefficients $C_n^{(2)'}$, $C_n^{(3)'}$, ... could be determined from Bernoulli's equation on various other planes combined with a successive approximation technique for correcting the first approximations for the $C_n^{(0)'}$, $C_n^{(1)'}$; however, the successive approximation scheme could not be made to converge. The accurate determination of the higher harmonics can be effected by an orthonormalizing computation over the entire free surface. This would exceed the drum storage of the computer available at Lockheed.

The predicted coefficients at t+Δt are given by $C_n^{(m)}(t+\Delta t) = C_n^{(m)}(t) + \frac{dc_n^{(m)}}{dt}(t)\,\Delta t$ for $m=0,1$. The predicted surface shape at t+Δt follows from the kinematic equation (2.7) for a fixed r-mesh

$$\begin{aligned} f(r,\theta,t+\Delta t) &= f(r,\theta,t) + f_t(r,\theta,t)\,\Delta t \\ &= f(r,\theta,t) + \left[\varphi_z - f_r \varphi_r - \tfrac{1}{r^2}\varphi_\theta f_\theta\right](r,\theta,t)\,\Delta t \end{aligned} \qquad (2.14)$$

*Moore, R. E. and Perko, L. M., "Inviscid Fluid Flow in an Accelerating Cylindrical Container", J. Fluid Mech., V. 22, June 1965, pp. 305-320.

Having computed the predicted coefficients and surface shape, one then proceeds to the correction step of the modified Euler method to move ahead one increment of time. The time dependent coefficients $C_n^{(o)}(t)$, $n=1,\dots N_o$ and $C_n^{(1)}(t)$, $n=1,\dots N_1$ and the motion of the free surface $f(r,\theta,t)$ (based on the fundamental and first harmonic of the velocity potential) are determined in this way. The computation scheme is outlined in figure 2-2.

The above description was for a fixed r-mesh; if f_r becomes unbounded, it is necessary to use a variable r-mesh i.e., to follow the r-characteristics as

$$r(t+\Delta t) = r(t) + \phi_r(\dots, t)\,\Delta t$$

$$f(r(t+\Delta t), \theta, t+\Delta t) = f(r(t), \theta, t) + \left[\phi_z - f_r \phi_r - \frac{1}{r^2}\phi_\theta f_\theta\right](\dots,t)\Delta t$$

in the predictor step.

The mean curvature of the surface $f(r,\theta,t)$, i.e., the surface tension term in Bernoulli's equation, is computed by finite differencing based on the values of $f(r,\theta,t)$, $f(r\pm\Delta r,\theta,t)$, $f(r,\theta\pm\Delta\theta,t)$ and $f(r\pm\Delta r,\theta\pm\Delta\theta,t)$. The boundary condition (2.6) is incorporated into the surface tension computation at the wall; i.e., it is used in the finite differencing in order to compute the mean curvature at the wall. The effect of incorporating this boundary condition into the computation is to maintain the contact angle very nearly constant. An explicit example of this effect (figures 2-4 and 2-5) is discussed in this section of the report under results.

Harmonic Polynomials - A second representation of the form (2.10) was attempted in order to overcome some of the difficulties encountered in the separation of variables approach, particularly, the instability which developed in the

computation. The representation (2.11) was assumed in the form of an expansion in terms of harmonic polynomials

$$\varphi(r,\theta,z,t) = \sum_{n,m} C_n^{(m)}(t)\, \psi_n^{(m)}(r,\theta)$$

where the polynomials

$$\psi_n^{(m)}(r,\theta) = \sum_{j+k+l=n} (-1)^{k+l} \frac{z^j (r/2)^{m+2k} (m\theta)^{2l}}{j!\; k!\; (m+k)!\; (2l)!}$$

satisfy Laplace's equation (2.1). This approach also has the advantage that it is more suitable for application to containers of arbitrary shape (e.g. hemispherical bottomed tanks). The coefficients $C_n^{(m)}(t)$ must now, however, be chosen to satisfy the zero normal derivative boundary condition on the container wall (2.2) as well as Bernoulli's equation (2.3) on the free surface. This leads to a more complicated computational problem. The method in brief is to first obtain the predicted potential function $\varphi(r,\theta,z,t+\Delta t)$ on the surface from a knowledge of the derivative at time t

$$\left.\frac{d\varphi}{dt}(r,\theta,z,t)\right|_{z=f(r,\theta,t)} = \left.\frac{\partial\varphi}{\partial t}(r,\theta,z,t)\right|_{z=f(r,\theta,t)} + \left.(\nabla\varphi)^2(r,\theta,z,t)\right|_{z=f(r,\theta,t)}$$

where φ_t is obtained from Bernoulli's equation and the velocities $(\nabla\varphi)^2$ are known at time t. In this way, a mixed boundary value problem is obtained for the potential φ at time $t+\Delta t$. The predicted coefficients $C_n^{(m)}(t+\Delta t)$ are then obtained by an orthonormalizing computation over the entire free sur-

face and container surface. The computation scheme is outlined in Figure 2-3. This has actually been implemented on the computer for the symmetric case (in which case the orthonormalization is over a curve, not a surface, and the computer storage is not exceeded) and meaningful results have been obtained. However, there is still a good deal of work that needs to be done in perfecting this approach.

A few of the details of this approach when applied to the symmetric case will be pointed out. First of all, only the harmonic polynomials $\psi_n^{(o)}(r, z)$ need be used. These polynomials have the following form:

$$\psi_0^{(o)}(r, z) = 1$$

$$\psi_1^{(o)}(r, z) = z$$

$$\psi_2^{(o)}(r, z) = \frac{1}{2!}\left(z^2 - r^2/2\right)$$

$$\psi_3^{(o)}(r, z) = \frac{1}{3!}\left(z^3 - \frac{3}{2} r^2 z\right)$$

$$\vdots$$

$$\psi_n^{(o)}(r, z) = \sum_{k=0}^{\left[\frac{n}{2}\right]} \frac{(-1)^k \, z^{n-2k} \, \left(\frac{r}{2}\right)^{2k}}{(n-2k)! \quad (k!)^2}$$

The velocity potential in the symmetric case has the following representation

$$\phi(r, z, t) = \sum_n C_n^{(o)}(t) \, \psi_n^{(o)}(r, z)$$

The coefficients, $C_n^{(o)}(t)$, as functions of time are determined by an orthonormalizing computation. The orthonormalization which has been discussed above did not work well in this case. An orthogonalizing computation in which the polynomials were orthogonalized in a different order than they are

listed above had to be used (cf. Householder* and also Bussinger & Golub) .** The surface motion based on the $C_n^{(o)}(t)$ then follows from the kinematic equation (2.7) as is indicated in Figure 2-3.

The surface tension in this approach is computed by finite differencing as was described for the previous program, the constant contact angle boundary condition (2.6) again being used to compute the surface tension at the wall.

Non-Zero Initial Velocity - Many practical problems arise in which the liquid is initially in motion. Starting the computations with non-zero initial velocity can be achieved in two ways, 1) by specifying the velocities on the initial surface, $u(r,\Theta)$, $v(r,\Theta)$, $w(r,\Theta)$, $0 \le r \le 1$, or 2) by specifying one or more of the $C_n^{(m)}(o) \neq 0$ (e.g. $C_1^{(1)}(o) \neq 0$ and the other coefficients, initially zero, would start the motion with a velocity corresponding to the velocity of a pure first mode slosh, cf. Figure 2-15a, b, c). The former of these two methods will be discussed in this section since it is not evident what the initial coefficients $C_n^{(m)}(o)$ should be, given the initial velocity on the free-surface. The $C_n^{(m)}(o)$ are determined by an orthonormalizing computation as follows. Suppose that

$$\varphi(r,z,\Theta,o)\Big|_{z=f(r,\Theta)} = \sum_{n,m} C_n^{(m)}(o)\, F_n^{(m)}(r,\Theta,o)$$

where the $F_n^{(m)}(r,\Theta,t)$ are defined as in (2.13). The problem is then to determine the $C_n^{(m)}(o)$ to satisfy

---

*Householder, A. S., "Unitary Triangularization of a Nonsymmetric Matrix", J. Assoc. Comp. Mach., 5, 339-342, 1958.

**Bussinger, P., Golub, G., "Linear Least Squares Solutions by Householder Transformations", Numerische Math., 7, p. 269 ff (1965).

$$\sum_{m,n} \lambda_n^{(m)} C_n^{(m)}(o) \; \vec{F}_n^{(m)}(r,\theta) = \vec{V}(r,\theta)$$

where

$$F_n^{(m)}(r,\theta) = \frac{1}{\cosh(\lambda_n^{(m)} H)} \begin{pmatrix} J_m'(\lambda_n^{(m)} r)\cosh\left[\lambda_n^{(m)} f_o(r,\theta)\right]\cos m\theta \\ \frac{-m}{\lambda_n^{(m)}} J_m(\lambda_n^{(m)} r)\cosh\left[\lambda_n^{(m)} f_o(r,\theta)\right]\sin m\theta \\ J_m(\lambda_n^{(m)} r)\sinh\left[\lambda_n^{(m)} f_o(r,\theta)\right]\cos m\theta \end{pmatrix}$$

and

$$\vec{V}(r,\theta) = \begin{pmatrix} u(r,\theta) \\ v(r,\theta) \\ w(r,\theta) \end{pmatrix}$$

This is accomplished by orthonormalizing the set of functions $\vec{F}_n^{(m)}(r,\theta)$ with respect to the inner product

$$\left(\vec{F}_n^{(m)}, \vec{F}_\ell^{(k)}\right) = \frac{1}{2\pi} \int_0^{2\pi} \int_0^1 \vec{F}_n^{(m)}(r,\theta) \cdot \vec{F}_\ell^{(k)}(r,\theta) \; r \, dr \, d\theta$$

the dot denoting the usual vector inner product.

This has only been implemented in the axisymmetric case which suffices for all of the programs completed to date; i.e., only the following two equations

need to be solved, first for $C_n^{(o)}(o)$ and then for $C_n^{(1)}(o)$:

$$\sum_n C_n^{(o)}(o)\,\lambda_n^{(o)}\,\vec{F}_n^{(o)}(r,\tfrac{\pi}{2}) = \vec{V}(r,\tfrac{\pi}{2})$$

and

$$\sum_n C_n^{(1)}(o)\,\lambda_n^{(1)}\,\vec{F}_n^{(1)}(r,\tfrac{o}{\pi}) = \vec{V}(r,\tfrac{o}{\pi}) - \sum_n C_n^{(o)}(o)\,\lambda_n^{(o)}\,\vec{F}_n^{(o)}(r,\tfrac{o}{\pi})$$

The orthonormalization described above worked very well to determine the coefficients from the given velocity data. It was found that by reading in coefficients $C_n^{(o)}(o)$, $n = 1, \ldots, 7$ computing velocities $u(r,\theta,o)$ and $w(r,\theta,o)$ (and $v(r,\theta,o)$ for the asymmetric case) and then using the technique described on page 2-10 to recompute the coefficients $C_n^{(o)}(o)$, $n = 1,\ldots,7$ that the computed coefficients agreed with the original coefficients to within an accuracy of $0(10^{-7})$.

RESULTS - The relative success of the methods described in the preceding material in determining the solution to the problem formulated in the problem formulation subsection (i.e., in determining the irrotational motion of an inviscid incompressible fluid) is discussed here. Numerical results obtained principally from the separation of variables method are presented together with a method of velocity extrapolation for bypassing the numerical instability that arises in the computation. The result of the velocity extrapolation which describes a very large amplitude motion over a long period of time is compared with experimental results.

Relative Success of the Method - The separation of variables method described previously has been, as a whole, quite successful in determining large amplitude symmetric and asymmetric motions. The major difficulty with all of the methods (aside from not being able to compute the higher harmonic coefficients without going to a surface orthonormalization) occurs in reorientation type problems or in very large amplitude sloshing problems. This difficulty amounts to the development of an instability (usually in the form of an unbounded oscillation) in the velocity of the fluid surface near the high point on the surface. This causes surface "splashing" in the computation. This behavior is considered a numerical instability although it has the appearance of the well known Taylor instability*. This limits the time interval over which the computation can be carried out in reorientation studies to about 50% of that of interest (or possibly to 30% for long narrow tanks).

Several possible causes of this instability were investigated in an effort to overcome this difficulty. The basic causes that were investigated are:

1) The convergence of the series expansion (2.12)
2) The nature of the functions in the expansion of the velocity potential (2.12)
3) The modified Euler scheme
4) Numerical round-off errors

Since the results of the computation using more and more terms in the series (beyond some sufficiently large number roughly of the order of 10), were es-

*Taylor, G.I., Proc. Roy. Soc., Ser. A., V. 201, pp. 192 ff.

sentially identical, convergence difficulties with the series (2.12) were discounted as a possible cause of the instability.

It seemed that the most probable cause of the instability lies in the nature of the functions used in the expansion (2.12) (i.e., the cosh ($\lambda_n z$) terms grow exponentially with z). The harmonic polynomial computation method described earlier was developed to test this thesis. The results, however, have been inconclusive since the computations based on this method also become unstable. (Somewhat earlier in fact, but as was pointed out, this approach still bears investigation.)

The stability of the modified Euler scheme was tested by computing with smaller and smaller time steps. Identical results were obtained for all sufficiently small time steps (roughly less than 0.05). Also, a fourth order Adams extrapolation and interpolation scheme* was incorporated into the computation in order to introduce added stability into the time sequence computation. This also failed to enable the computation to proceed for a longer time.

Finally, in an effort to check out the effect of numerical round off errors on the stability of the computation, the entire (symmetric) code was converted to double precision.

This had little or no effect on the stability. The instability appeared at almost exactly the same time point as it had in the single-precision code.

*Davis, P.J., Polonsky, I., "Numerical Interpolation, Differentiation and Integration", appears in Handbook of Mathematical Functions, N.B.S., Appl. Math. Series 55, June 1964.

To summarize, of the various effects investigated, only computing with a different set of functions in the series expansion had any significant effect on the time at which, or manner in which, the instability occurred.

In a more positive vein, it was found that a wide variety of symmetric sloshing (oscillations) and asymmetric (transverse) sloshing types of motions could be computed over extended time periods. It was also found that large amplitude symmetric and asymmetric reorientation types of motion could be computed up to the point at which the instability developed and that these motions could be extended beyond the instability by extrapolating the velocities (and that the extended motion was still in good agreement with experimental results). These results are reported in the next section.

Numerical Results - The numerical results will be described following their temporal development starting with symmetric sloshing (or oscillation) and reorientation and ending with asymmetric (or transverse) sloshing and reorientation. Plots of those results which require discussion along with experimental results are presented in Section 4 of this report.

1. Symmetric Sloshing ($\alpha_1 = 0, \alpha_3 < 0$)

   This type of motion is only very briefly discussed in order to illustrate a type of motion to which the separation of variables method is particularly well adapted. One case is illustrated. Figure 2-4 illustrates one complete cycle of an oscillatory motion in which a 15° contact angle is maintained. Figure 2-5 shows the surface shape after one complete cycle. It almost exactly agrees with the initial shape. Figure 2-6 shows the vertical velocity profile $w(r, t)$

for the motion of Figure 2-5 (actually $w(r,t)$ is shown for r = 0 and r = 1. The velocities $w(r,t)$ for $0<r<1$ lie in between these two curves). The Bond number for the run shown in Fig. 2-5 is $B=\frac{1}{\beta}=10$. With a larger Bond number, e.g. B = 100, a central crown shaped splash was found to develop.

2. Symmetric Reorientation ($\alpha_1 = 0$, $\alpha_3 > 0$)

This type of motion serves to illustrate the instability which develops in the velocities near the wall. This instability manifests itself in the development of "breakers" near the wall. This is illustrated in Figures 2-7 and 2-8. Figure 2-7 shows a reorientation motion for the case of an initially spherical surface shape with 45° contact angle and $\beta = 0$. The development of the "breakers" at the wall for this case is shown in detail in Figure 2-7. Figure 2-9 shows that surface tension does have a smoothing effect; however, this case also becomes unstable. Figure 2-10 shows the vertical velocity profile for a case computed for $\psi_o = 45°$ as well as the case in Figure 2-7. Also shown in Figure 2-10 is the velocity extrapolation based on the formulae

$$w(r,t) = w(r,t_o) + \frac{\partial w(r,t_o)}{\partial t}(t-t_o) + \frac{\partial^2 w(r,t_o)}{\partial t^2}\frac{(t-t_o)^2}{2}K$$

and

$$u(r,t) = u(r,t_o) + \frac{\partial u(r,t_o)}{\partial t}(t-t_o) + \frac{\partial^2 u(r,t_o)}{\partial t^2}\frac{(t-t_o)^2}{2}K$$

The upper dashed curve in Figure 2-10 for the $\psi_o = 45°$ case corresponds to the case $t_o = 0.7$ and $K = 0.21$. The vertical velocity near the center grows too fast in this particular extrapolation. The velocity at the center should be approaching the asymptote $\omega = .46$ (the velocity of a bubble rising in an infinite fluid) as is shown by the lower dashed extrapolation curve for the $\psi_o = 45°$ case in Figure 2-10. This is approximately what the actual computed vertical velocity at the center appears to be doing for small t. What should probably be done is to start the velocity extrapolation at the wall sooner than the extrapolation at the center for this type of motion.

Figure 2-10 also shows the vertical velocity profile for a 15° contact angle case picked to correspond more closely to the experimental results. In this case the value of k was not properly chosen to give proper behavior for large t. The results of this extrapolation are shown in Figure 2-11. Figure 4-13 in Section 4 shows the approximate quantitative agreement of these results with the experimental results for the initial part of the extrapolation (for later times the extrapolated velocity at the center is again too large).

It should be emphasized that in Figure 2-10 the velocity at the wall is very close to a straight line with slope (i.e., acceleration) equal to 1.0. The experimental results discussed later indicate a straight line velocity (i.e., constant acceleration) with slope equal to approximately 0.7 (in normalized coordinates). It is evident that viscosity has a definite effect on this velocity.

Figure 2-12 shows the vertical velocity profile for the computation based on the harmonic polynomials described previously. Direct comparison of these results with the corresponding results of Figure 2-10 shows good agreement up to a point, roughly for $0 \leq t \leq 0.5$ Again an instability is seen to develop in the vertical velocity at (and near) the wall. The dashed lines depict the correct behavior expected in this case.

3. Asymmetric Sloshing ($\alpha_1 \neq 0$, $\alpha_3 \leqq 0$)

Large amplitude asymmetric sloshing from a flat initial shape is shown in Figure 2-13. Note that the slosh is all in one direction since $\alpha_1(t) = +1$ for all $t \geq 0$. Note also that surface splashing takes place on the high part of the surface. This instability could again be bypassed by velocity extrapolation. This case could also be considered as the beginning of a reorientation to a plane surface with a meniscus at the wall, the plane being perpendicular to the 45° line through the origin.

A bonafide sloshing is shown in Figure 2-14 a - n. This is the case where an impulse is applied from the right and the fluid sloshes first to the right and then to the left. It was found that exactly this same behavior took place for a wide range of impulses with $\int_0^\infty \alpha_1(t)\, dt = 0.2$. In a similar run with $\alpha_3(t) = -2.0$ for $0 \leq t \leq 1.5$ and $\alpha_3(t) = 0$ for $t > 1.5$ (1.5 is when the maximum kinetic energy is approximately attained), the same initial motion took place; however, a splash developed on the slosh to the left. The arrows in-

dicate how the wave progresses with time. Another type of lateral sloshing is shown in Figure 2-15 a-c. This sloshing was generated by setting $C_1^{(1)}(o) = 0.1$ in the velocity potential and therefore corresponds to what is initially pure first mode lateral sloshing. Note that the nonlinear nature of the problem causes this to deviate from pure first mode sloshing as is evidenced by the node moving to the right in Figure 2-15 a,b. Note that the method of velocity extrapolation has been used in Figure 2-15 c, to bypass the surface splashing that occurs in Figure 2-15 b. Figure 2-16 a-d, shows a similar motion ($\alpha_1 = -1$, $\beta = 0.0$ in this case), the surface shape being shown in an isometric projection.

4. Asymmetric Reorientation ($\alpha_1 \neq o$, $\alpha_3 > o$)

Figure 2-17 shows an example of asymmetric reorientation with $\beta = 0$. Figure 2-18 shows the same case with $\beta = 0.05$. It is observed that the constant contact angle boundary condition is being maintained over most of the motion in Figure 2-18. Surface splashing occurs in both cases. This could again be bypassed by velocity extrapolation. This will not be elaborated on since most of the concepts discussed above apply as well here. A comparison between results of analysis and experiments is given in Figure 4-14.

THE EFFECT OF BAFFLES ON REORIENTATION FLOW

Currently many propellant tanks contain internal ring stiffeners or slosh baffles that are attached to the inner wall and protrude radially into the tank. These structural members can have a marked influence on the character of a reorientation flow. It is the purpose here to analyze this effect insofar as possible and set down some considerations relating to this aspect of reorientation. It is instructive to consider for the moment a cylinder open at both ends so that the gas pressure remains unchanged during the flow. We will also limit our considerations to solid ring baffles or stiffeners in order to simplify the analysis.

As shown in Figure 2-20 liquid encountering a baffle as it flows in a thin sheet down the cylindrical surface will be turned and forced toward the center of the tank. When this symmetrical flow impinges upon itself at the center, the flow will be turned again so that the liquid flows as a jet along the axis of the cylinder. A portion of the liquid will proceed in each direction. The amount moving in each direction depends upon the acceleration, fluid flow velocity and system dimensions. A sketch is shown of the anticipated flow with the nomenclature which applies.

If the thickness of the liquid sheet is sufficiently large compared to the baffle size, it is known that the sheet simply flows over the baffle and the breakaway from the wall does not occur. The critical conditions for breakaway in terms of sheet thickness and baffle width are not presently known.

The angle through which the liquid sheet is turned by the baffle will depend upon the size and shape of the baffle. For a baffle mounted perpendicular to

the wall, the initial change in direction should be 90° provided the sheet thickness is not too great relative to the baffle dimensions. The corner will quickly fill with liquid and some type of apparent ramp will effectively exist and the resulting angle of deflection will be less than 90° with a separated flow and vortex in the corner.

After leaving the baffle the liquid will be acted upon by the local acceleration which will produce a bending of the liquid stream prior to its impingement on itself. The angle of deflection at the wall is φ and the angle of impingement is θ. As the sheet progresses toward the tank center the circumferential distance decreases causing an increase in the sheet thickness t_d approximately as follows:

$$t_d = t_s \frac{r_o}{r}$$

Since an acceleration field is present the two jets of liquid resulting from impingement at the axis will be effected. The flow in the direction of the acceleration diminishes as a function of its position in the axial direction while the jet flow in the opposite direction thicknes as a function of its position.

The classical problem of impingement of a jet on an inclined plate is used here to gain some information as to the sizes of the two axial jets. No energy loss at impact is considered and change in elevation is neglected. Thus, the velocity of the jet is unchanged in magnitude by the impact. Only the direction is changed.

$$v_1 = v_2 = v_i$$

From the classical problem

$$Q_1 = \frac{Q_d}{2}\left[1 + \cos\theta\right]$$

$$Q_2 = \frac{Q_d}{2}\left[1 - \cos\theta\right]$$

where Q_1, Q_2 and Q_d are the volume flow rates given by

$$Q_1 = \pi r_1^2 v_1$$

$$Q_2 = \pi r_2^2 v_2$$

$$Q_d = Q_s = 2\pi r_o t_s v_s$$

Substituting and rearranging

$$\left(\frac{r_1}{r_o}\right)^2 = \frac{t_s}{r_o}\left[1 + \cos\theta\right]\frac{v_s}{v_i}$$

$$\left(\frac{r_2}{r_o}\right)^2 = \frac{t_s}{r_o}\left[1 - \cos\theta\right]\frac{v_s}{v_i}$$

Since the sheet thickness t_s and baffle width, b, are small compared to the tank radius, r_o, the axial and radial distance over which the sheet flow deflection takes place is also small. The momentum loss in the deflection process is also small compared to the flow energy. Thus it is reasonable to state that no change in velocity magnitude occurs during the deflection or

$$|v_s| = |v_d|$$

At the present time a relation between v_d and v_i is not known, however, in cognizance of the other assumptions, it seems reasonable to take

$$v_s \approx v_i$$

$$\left(\frac{r_1}{r_o}\right)^2 = \frac{t_s}{r_s}\left[1 + \cos\Theta\right] \tag{2.15}$$

$$\left(\frac{r_2}{r_o}\right)^2 = \frac{t_s}{r_s}\left[1 - \cos\Theta\right] \tag{2.16}$$

Sample calculations using 2.15 and 2.16 are given below

Θ	$\frac{t_s}{r_o}$	$\frac{r_1}{r_o}$	$\frac{r_2}{r_o}$
30°	0.050	0.306	0.082
	0.100	0.432	0.117
45°	0.050	0.293	0.121
	0.100	0.414	0.171
60°	0.050	0.294	0.158
	0.100	0.388	0.224

The assumption that the impingement velocity $\vec{v}_i$ is equal to the deflected velocity at the baffle is dependent on velocity of the wall sheet, acceleration level and tank radius. The velocity at (or near) the wall, v_d , may be written in its component form. The radial and axial components at the wall are

$$v_{r_d} = v_d \sin\phi$$

$$v_{z_d} = v_d \cos\phi$$

The time, τ_d , required for the fluid to traverse the distance from the wall to the point of impingement is given by

$$\tau_d = \frac{r_o}{v_{r_d}}$$

For more detailed consideration r_o would be replaced by the distance from the baffle to the actual point of impingement which is less than r_o.

During the time, τ_d , the radial component of velocity will not change, however, the axial component will change due to the fact that the fluid is experiencing acceleration in the axial direction. Thus, at the center

$$v_{r_i} = v_{r_d} = v_d \sin\varphi$$

$$v_{z_i} = v_{z_d} + a\tau_d = v_d \cos\varphi + \frac{a r_o}{v_d \sin\varphi}$$

With this knowledge of the components both the magnitude of the velocity at the tank center, v_i , and the impingement angle, θ, can be determined

$$v_i = \sqrt{v_{r_i}^2 + v_{z_i}^2} = \left[v_d^2 + 2a r_o \cot\varphi + \frac{a r_o^2}{v_d^2 \sin^2\varphi} \right] \qquad (2.17)$$

$$\Theta = \tan^{-1} \frac{v_{r_i}}{v_{z_i}} = \tan^{-1} \left[\frac{\tan\varphi}{1 + \frac{2 a r_o}{v_d^2 \sin 2\varphi}} \right] \qquad (2.18)$$

Of course, it is necessary to know ϕ before 2.17 and 2.18 can be evaluated.

The effect of the acceleration will be to increase velocity, v_1, and decrease velocity v_2. If the jets are assumed axially symmetric, the radii can be calculated as a function of the distance from a reference point, Z=0, at the point where the two jets form. The positive Z direction corresponds to the direction in which the acceleration is applied and v_{1_o} and v_{2_o} give the corresponding liquid velocities at the reference point. Applying the laws of motion and the continuity relation

$$v_1^2(z) = v_{1_o}^2 + 2az$$

$$v_2^2(z) = v_{2_o} + 2az$$

$$Q_1 = \pi r_1^2(z)\, v_1(z) = \pi r_{1_o}^2\, v_{2_o}$$

$$Q_2 = \pi r_2^2(z)\, v_2(z) = \pi r_{2_o}^2\, v_{2_o}$$

Combining and solving

$$r_1^2(z) = r_{1_o}^2 \frac{v_{2_o}}{\left[v_{1_o}^2 + 2az\right]^{1/2}}$$

$$r_2^2(z) = r_{2_o}^2 \frac{v_{2_o}}{\left[v_{2_o}^2 + 2az\right]^{1/2}}$$

The maximum distance in the -Z direction which would result in the liquid being brought to rest can easily be calculated and is

$$z = \frac{v_{2_o}^2}{2a}$$

After stoppage the liquid will accelerate in the +Z direction and the flow will become complicated.

The general flow behavior discussed above is changed somewhat when considered in the context of a partially filled propellant tank. In this case the gas and liquid volumes are of course constant. Also the liquid velocities are dependent on the tank length and radius.

The position of the baffle relative to the liquid wave front at the start of the reorientation maneuver determines the magnitude of φ and the sheet thickness, t_s. The wall sheet is thickest near the liquid initial position. As mentioned above the angle through which the sheet is deflected, φ , is largely dependent on the ratio, b/t and the angle that the baffle makes with the wall, α . The thickness, t, is a function of distance, s, downstream of the initial liquid wave front position. Thus for rapid flow

$$\varphi = f\left(\frac{b}{t}, \alpha, \frac{s}{r_o}\right)$$

The above functional dependence is not known at this time. The problem is discussed in Rouse * but not analyzed.

Another consideration occurs when the deflected flow impinges at the tank center as shown in Figure 2-21a. This divides the pressurant gas into two parts as shown and the flow problem is changed. Gas cannot for the moment enter region 1 to displace the liquid flow along the wall. The gas bubble "1" continues to rise and the wall flow now "fills in" behind the bubble

*Rouse, H., "Fluid Mechanics for Hydraulic Engineers", Dover 1938, pp 301-307

thickening the web of liquid spanning the tank. Similarly the liquid flow rate into region 2 is cut off. A certain portion of the propellant, say that below the dotted line a, will be pinched off and continue to the tank bottom as shown in Figure 2-21b leaving a relatively flat liquid gas interface spanning the tank at the baffle. The stability limit for this configuration is greater than that for the original interface position where the liquid-gas-tank contact point is free to move. In the latter the Bond number stability limit is approximately 0.8. With the propellant suspended between the ring baffles a stuck edge condition is possible which results in an interface Bond number stability limit of 14.7. Reorientation at low B_R ($B_R \leq 10$) could be temporarily interrupted as the result of the above described activity.

In any event the time required to completely settle the propellants will be increased because the interface in Figure 2-21c must fail again allowing the remaining pressurant gas "2" to pass the baffle and join the gas volume 1.

SMALL AMPLITUDE LATERAL SLOSHING ANALYSIS - The oscillation of bodies of liquids has been of interest to scientists and mathematicians for over one-hundred years. In the recent past, this subject has been of special importance to the designers of rocket propelled space vehicles because liquids comprise a large percentage of the total mass. The oscillation of liquids in rocket propellant tanks imposes reaction forces on the tank walls which are important in the design of guidance, control, and propulsion systems. This problem has been thoroughly studied and there now exists much literature about sloshing under conditions when surface tension is not important. The bulk of currently available analysis of sloshing is limited to small amplitude analysis and has until recently avoided complications arising from surface tension effects such as the curvature of the equilibrium surface. Up to date examples of conventional sloshing literature include the work of Abramson*.

The technical objective of this study was to extend calculation of linear sloshing to cases where the effective gravitational acceleration acting on the liquid is so small that surface tension effects become important.

Specific objectives of this study include (a) determination of natural frequencies of liquids in cylindrical tanks with hemispherical bottoms as affected by the level of steady axial acceleration, surface tension and density properties of the liquid, and the volume of liquid in the tank; and (b) determination of the response of liquids to lateral perturbing accelerations.

*Abramson, N.H. (ed) The Dynamic Behavior of Liquids in Moving Containers, NASA SP-106, 1966.

The linear analysis used here does not treat large amplitude effects; results must be cautiously interpreted for finite amplitude. It has been shown that the resonant sloshing frequency of a liquid of moderate viscosity is acceptably close to the first normal mode sloshing frequency obtained from inviscid analysis, even in small scale experiments. Hence, viscosity is neglected. It is also assumed that surface tension, density, and wetting properties are constant and do not vary dynamically.

Analysis for this study uses a frame of reference fixed to the container. This is shown in Figure 2-22. A space vehicle acted upon by a lateral perturbing force will be translated laterally and rotated relative to an external fixed coordinate system. The liquid contained in the tank will not be directly acted upon by the lateral force but, rather, indirectly acted upon by the moving walls of the tank. From an analytic viewpoint, it is more convenient to consider the tank fixed. When a transformation is effected from the fixed coordinate system to the coordinate system moving with the tank, the liquid can be considered as being influenced directly by lateral perturbing accelerations relative to a tank fixed with respect to the moving coordinate system.

Problem Formulation - The purpose of this section is to detail the derivation of the boundary conditions peculiar to this problem. It is assumed here that the liquid is incompressible, inviscid, and that it behaves irrotationally. This allows application of the nonsteady state Bernoulli equation to

the free-surface (using subscript to denote partial differentiation)

$$\frac{p}{\rho} + \frac{1}{2}\left|\underline{\nabla}\,\varphi - \underline{\Omega}\times\bar{\underline{R}}\right|^2 + g_\alpha(\bar{f}+\bar{h}) - g_\tau\,\bar{r}\cos\theta + \varphi_{\bar{t}}$$

$$+\frac{1}{2}(\underline{\Omega}\cdot\bar{\underline{R}})^2 - \frac{1}{2}\left|\underline{\Omega}\right|^2\left|\bar{\underline{R}}\right|^2 = F(\bar{t}) \qquad (2.19)$$

where g_α and g_τ are axial and lateral accelerations and φ is the velocity potential defined by the three orthogonal fluid velocities.

$$\left.\begin{aligned} \bar{u} &= \varphi_{\bar{r}}\ , \\ \bar{v} &= \frac{1}{\bar{r}}\varphi_\theta\ , \text{ and} \\ \bar{w} &= \varphi_{\bar{z}}\ . \end{aligned}\right\} \qquad (2.20)$$

Most of the symbols here are defined in Figure (2-22). Additionally, $\bar{\underline{\Omega}}$ is the angular velocity of the tank fixed coordinate system and $\bar{\underline{R}}$ is the radius vector from the origin of the same system. Bars over symbols denote dimensional quantities.

The choice of the function of time on the right hand side of this equation is arbitrary and, for convenience, is set equal to p_o/ρ, the static liquid pressure at the center of the equilibrium meniscus divided by the liquid density. The liquid pressure at the interface is related to the gas pressure through the surface-tension and the mean curvature of the free-surface by means of the equation

$$p_g - p = 2\sigma H = \sigma \left\{ \frac{1}{\bar{r}} \frac{\partial}{\partial \bar{r}} \left[\frac{\bar{r}\bar{s}_{\bar{r}}}{\left(1+\bar{s}_{\bar{r}}^2+\frac{1}{\bar{r}^2}\bar{s}_\theta^2\right)^{1/2}} \right] + \frac{1}{\bar{r}^2} \frac{\partial}{\partial \theta} \left[\frac{\bar{s}_\theta}{\left(1+\bar{s}_{\bar{r}}^2+\frac{1}{\bar{r}^2}\bar{s}_\theta^2\right)^{1/2}} \right] \right\} \quad (2.21)$$

Substitution of this relation and p_o/ρ for $F(\bar{t})$ into equation (2.19) results in

$$\frac{\sigma}{\rho} 2H - \frac{1}{2}\left|\nabla \varphi - \underline{\Omega}\times\bar{\underline{R}}\right|^2 - g_\alpha(\bar{f}+\bar{h}) + g_\tau \bar{r}\cos\theta - \varphi_{\bar{t}}$$

$$- \frac{1}{2}\left(\underline{\Omega}\cdot\bar{\underline{R}}\right)^2 - \frac{1}{2}|\underline{\Omega}|^2|\bar{\underline{R}}|^2 = \frac{p_g - p_o}{\rho} \quad (2.22)$$

The kinematic condition is derived as follows. Consider $\bar{s} = \bar{s}(\bar{r},\theta,\bar{t})$. The total derivative of $\bar{s}$ with respect to time is written

$$\frac{d\bar{s}}{d\bar{t}} = \bar{s}_{\bar{t}} + \bar{s}_{\bar{r}} \frac{d\bar{r}}{d\bar{t}} + \frac{1}{\bar{r}^2} \bar{s}_\theta \frac{d\theta}{d\bar{t}}$$

Use of the definition of the velocity potential results in the following familiar form for the kinematic condition

$$\bar{s}_{\bar{t}} = \varphi_{\bar{z}} - \varphi_{\bar{r}} \bar{s}_{\bar{r}} - \frac{1}{\bar{r}^2} \varphi_\theta \bar{s}_\theta \quad (2.23)$$

The non linearities of the problem appear in the free-surface boundary conditions, Equations (2.22) and (2.23). These can be linearized by assuming

that the free-surface is the sum of an axisymmetric equilibrium surface $\bar{f}$ and a small time-varying perturbation $\bar{h}$,

$$\bar{s}(r, \theta, \bar{t}) = \bar{f}(\bar{r}) + \bar{h}(\bar{r}, \theta \bar{t}) \tag{2.24}$$

Substituting this into Equation (2.22) and neglecting the $O(\bar{h}^2)$ terms (all angular velocity terms are of this order) yields

$$\frac{\sigma}{\rho}\left\{\frac{1}{\bar{r}}\frac{\partial}{\partial \bar{r}}\frac{\bar{r}\bar{f}_{\bar{r}}}{(1+\bar{f}_{\bar{r}}^2)^{1/2}} + \frac{1}{\bar{r}}\frac{\partial}{\partial \bar{r}}\frac{\bar{r}\bar{h}_{\bar{r}}}{(1+\bar{f}_{\bar{r}}^2)^{3/2}} + \frac{1}{\bar{r}^2}\frac{\bar{h}_{\theta\theta}}{(1+\bar{f}_{\bar{r}}^2)^{1/2}}\right\}$$

$$-g_\alpha \bar{f} - g_\alpha \bar{h} + g_\tau \bar{r}\cos\theta - \ddot{\varphi}_{\bar{t}} - \frac{p_g - p_o}{\rho} = 0$$

The first, fourth, and last terms sum to zero; they form the equation of the equilibrium surface

$$\frac{\sigma}{\rho}\frac{1}{\bar{r}}\frac{d}{d\bar{r}}\frac{\bar{r}\bar{f}_{\bar{r}}}{(1+\bar{f}_{\bar{r}}^2)^{1/2}} - g_\alpha \bar{f} - \frac{p_g - p_o}{\rho} = 0 \tag{2.25}$$

With these deleted, the linearized free-surface condition becomes

$$\frac{\sigma}{\rho}\left\{\frac{1}{\bar{r}}\frac{\partial}{\partial \bar{r}}\frac{\bar{r}\bar{h}_{\bar{r}}}{(1+\bar{f}_{\bar{r}}^2)^{3/2}} + \frac{1}{\bar{r}^2}\frac{\bar{h}_{\theta\theta}}{(1+\bar{f}_{\bar{r}}^2)^{1/2}}\right\} - g_\alpha \bar{h}$$

$$+ g_\tau \bar{r}\cos\theta - \ddot{\varphi}_t = 0 \tag{2.26}$$

Substituting Equation (2.24) into Equation (2.23) and linearizing gives the kinematic condition in the form

$$\bar{h}_{\bar{t}} = \Phi_{\bar{z}} - \Phi_{\bar{r}} \frac{d\bar{f}}{d\bar{r}} \tag{2.27}$$

Formulation of the problem is completed by nondimensionalization with the use of the following definitions

$$\left.\begin{aligned} r = \frac{\bar{r}}{r_o}\,, \quad z = \frac{\bar{z}}{r_o}\,, \quad s = \frac{\bar{s}}{r_o}\,, \quad f = \frac{\bar{f}}{r_o}\,, \quad h = \frac{\bar{h}}{r_o}\,, \quad \omega = \frac{\bar{\omega}}{r_o} \\ t = \bar{t}\left((1+B_\alpha)\frac{\sigma}{\rho r_o^3}\right)^{1/2}\,, \quad \Phi = \frac{\Phi}{\left((1+B_\alpha)\frac{\sigma r_o}{\rho}\right)^{1/2}}\,, \\ B_\alpha = \frac{\rho g_\alpha r_o^2}{\sigma}\,, \qquad B_\tau = \frac{\rho g_\tau r_o^2}{\sigma} \end{aligned}\right\} \tag{2.28}$$

Introducing Equations (2.28) yields the complete problem statement for the problem

$$\Phi_{rr} + \frac{1}{r}\Phi_r + \frac{1}{r^2}\Phi_{\theta\theta} + \Phi_{zz} = 0 \quad \text{in } D, \tag{2.29}$$

$$\Phi_n = 0 \quad \text{on } W, \tag{2.30}$$

$$\frac{1}{r}\frac{\partial}{\partial r}\frac{r h_r}{\sqrt{1+f_r^2}^3} + \frac{1}{r^2}\frac{h_{\theta\theta}}{\sqrt{1+f_r^2}} - B_\alpha h + B_\tau r\cos\theta - (1+B_\alpha)\Phi_t = 0 \quad \text{on } f, \tag{2.31}$$

$$h_t = \Phi_z - f_r \Phi_r \quad \text{on} \quad f, \tag{2.32}$$

and $h_r = 0$ at $r = r_w$ if $r_w = 1$,

or

$$h_r = \left(1 + f_r^2\right)^{1/2} \left[\left(1 - r_w^2\right)^{1/2} \cos\theta + r_w \sin\theta\right] \frac{h}{r_w} \text{ at } r = r_w \tag{2.33}$$

if $r_w = 1$

Equation (2.33) is the constant contact angle condition in the cylindrical and hemispherical portions of the tank. In these the equilibrium surface defined by the following equation and boundary conditions

$$\frac{1}{r} \frac{d}{dr} \frac{r f_r}{\sqrt{1 + f_r^2}} - B_\alpha f - \lambda = 0, \tag{2.34}$$

$$\frac{df}{dr} = 0 \qquad r = 0,$$

and

$$\frac{df}{dr} = \left(1 + f_r^2\right)^{1/2} \left[r_w \cos\theta - \left(1 - r_w^2\right)^{1/2} \sin\theta\right] \text{ at } r = r_w \tag{2.35}$$

Here λ is a parameter related to the pressure difference across the vertex of the equilibrium surface located at the origin and r_w is r at the tank wall.

In the foregoing, it is assumed that $B_\alpha \geq 0$. Oscillation can take place for $B_\alpha < 0$, but only for small values of $|B_\alpha|$ beyond which the surface becomes unstable. That region is not considered in this study.

The problem posed by Equations (2.29) through (2.33) is a linear boundary value problem. Equation (2.31) is inhomogenous. This dictates that the solution must be obtained in two parts. The problem is first made homogeneous by setting B_τ to zero and solving the normal mode problem.

The result of this is a set of eigenfunctions which is then used in a Fourier series expansion to obtain the response to transverse perturbing accelerations.

Normal Mode Problem - Let the periodic time dependence and the angular dependence of Φ and h for the kth normal mode be

$$\Phi = \Phi_k (r, z) \cos\Theta \cos\omega_k t$$

$$h = h_k (r) \cos\Theta \sin\omega_k t$$

When these expressions are substituted into Equation (2.31) with $B_\tau = 0$ and Equation (2.32) there follows

$$\left.\begin{aligned} &(1 + B_\alpha)\omega_k \Phi_k - B_\alpha h_k + \frac{1}{r}\frac{\partial}{\partial r}\frac{r h_{k_r}}{(1+f_r^2)^{3/2}} - \frac{1}{r^2}\frac{h_k}{(1+f_r^2)^{1/2}} = 0 \qquad (2.36)\\ &\omega_k h_k = \Phi_{k_z} - f_r \Phi_{k_r} = (1 + f_r^2)^{1/2} \Phi_{k_n} \qquad (2.37)\end{aligned}\right\} z = f(r)$$

The boundary conditions on h_k and Φ_k are the one on h in Equation (2.37) and

$$h_k(0) = 0, \quad \Phi_{k_n} = 0 \text{ on } \underline{w}, \text{ and } \Phi_k(0, z) = 0 \qquad (2.38)$$

Solution of this problem yields a set of eigenfunctions $\{\Phi_k\}$, eigenvalues $\{\omega_k^2\}$, and eigenmodes $\{h_k\}$. The method used in this study to obtain these quantities is detailed in the next part of this report.

Response to Perturbing Accelerations - The proper way of determining response to lateral perturbing accelerations is to expand the velocity potential for the perturbed liquid in a Fourier series of eigenfunctions of the normal mode

problem. This process is detailed in NASA CR-54700 prepared under contract NAS 3-7119 for the Lewis Research Center. Many engineering calculations can be adequately treated by use of an equivalent mechanical oscillator. The normal mode calculations can be used to compute parameters of an equivalent mechanical analog with which approximate dynamic computations can be made with somewhat less effort. The theoretical basis for this is outlined below.

The pressure in a liquid which is sloshing in a container can be computed from a knowledge of the velocity potential using the nonsteady state Bernoulli equation (Equation (2.19) and the relation for the pressure difference across the free surface (Equation (2.21)). It may be shown that the pressure within the liquid consistent with the limitations of the linearization of the lateral sloshing problem is given by

$$\frac{p}{\rho} = \frac{p_g}{\rho} + g_\alpha \bar{f} - \frac{\sigma}{\rho} \frac{1}{\bar{r}} \frac{\partial}{\partial \bar{r}} \frac{\bar{r} \bar{f}_{\bar{r}}}{\left(1 + \bar{f}_{\bar{r}}^2\right)^{1/2}} - g_\alpha \bar{z} - \frac{\partial \varphi}{\partial \bar{t}} \qquad (2.39)$$

The first four terms on the right in this equation represent the contributions due to surface tension and gravitational body forces, second and fourth are merely the hydrostatic head, and the third appears only if surface tension effects are considered. The last term in thie equation is the contribution due to sloshing of the liquid. The first four terms will contribute nothing to lateral forces on the tank since they represent the static equilibrium balance only.

Equation (2.39) can be used to determine the lateral force acting on the tank due to k th normal mode sloshing from the velocity potential $\Phi_k(r,z) \cos\theta \cos \omega_k t$. Using the notation of Figure 2-22, the lateral force due to the k-th mode is given by

$$\int_0^{2\pi} \int_{\bar{\xi}=0}^{\bar{\xi}=\bar{\xi}_0} \rho \sin\beta \cos\theta \, \bar{r}_t \, d\bar{\xi} \, d\theta$$

and its maximal value is

$$\bar{F}_x = \pi \bar{\omega}_k \int_0^{\bar{\xi}_0} \rho \Phi_k (\bar{r}_t, \bar{z}_t) \, \bar{r}_t \sin\beta \, d\bar{\xi} \tag{2.40}$$

The expression, obtained in a similar fashion, for the maximum moment of the lateral forces generated by the k-th normal mode is

$$\bar{M}_y = \pi \bar{\omega}_k \int_0^{\bar{\xi}_0} \rho \Phi_k (\bar{r}_t, \bar{z}_t) \, \bar{r}_t \, z_t \sin\beta \, d\bar{\xi} \tag{2.41}$$

The ratio of $\bar{M}_y$ to $\bar{F}_x$ is, of course, the point of action, $\bar{Z}$, of a single force on the axis which can be substituted for the integral of the lateral component of pressure forces acting on the tank.

The quantities just calculated can be related to parameters of an equivalent spring-mass oscillator as follows. The maximum force imposed by an oscillator and the maximum potential energy stored are defined by

$$\bar{F}_x = \bar{\kappa} \bar{x}$$

and (2.42)

$$\bar{V} = \frac{\bar{\kappa}}{2} \bar{x}^2$$

where $\bar{\kappa}$ is the equivalent spring and x is the maximum displacement. Elimination of the parameter x results in a formula for the spring constant as a function of the maximum lateral force and potential energy stored in the

system

$$\bar{\kappa} = \frac{\bar{F}_x^2}{2\bar{V}} \tag{2.43}$$

This constant can be calculated by use of the integral

$$\bar{V} = \frac{\pi\rho}{2}\int_0^{\bar{r}_w} \Phi_k(\bar{r},\bar{z})\frac{\partial}{\partial n}\Phi_k(\bar{r},\bar{z})(1+\bar{f}_{\bar{r}}^2)^{1/2}\,\bar{r}\,d\bar{r} \tag{2.44}$$

taken over a meridian of the equilibrium free surface.

The magnitude of the mass to be substituted for the liquid sloshing in the k-th mode is obtained by dividing the spring constant by the square of the appropriate frequency.

$$\bar{m} = \frac{\bar{F}_x^2}{2\bar{\omega}_k^2\bar{V}}$$

For convenience in making calculations, these expressions can be non-dimensionalized with the use of Equation (2.28). The mechanical analog parameters equivalent to k-th normal mode sloshing are as follows:

Maximum lateral force:

$$F_x = \frac{\bar{F}_x}{\sigma r_o} = \pi(1+B_\alpha)\omega_k\int_0^{\xi_o}\Phi_k(r_t,z_t)\,r_t\sin\beta\,d\xi \tag{2.46}$$

Maximum moment:

$$M_y = \frac{\bar{M}_y}{\sigma r_o^2} = \pi(1+B_\alpha)\omega_k\int_0^{\xi_o}\Phi_k(r_t,z_t)\,r_t\,z_t\sin\beta\,d\xi \tag{2.47}$$

Lateral force action point:

$$Z = \frac{\bar{z}}{r_o} = \frac{M_y}{F_x} \tag{2.48}$$

Equivalent spring constant:

$$K = \frac{\kappa}{\sigma} = \frac{\pi(1+B_\alpha)\omega_k^2\left[\int_0^{\xi_o} \Phi_k(r_t, z_t)\, r_t \sin\beta \, d\xi\right]^2}{V} \tag{2.49}$$

Equivalent sloshing mass:

$$m = \frac{\bar{m}}{\rho r_o^3} = \frac{\pi\left[\int_0^{\xi_o} \Phi_k(r_t, z_t)\, r_t \sin\beta \, d\xi\right]}{V} \tag{2.50}$$

where V is given by

$$V = \int_0^{r_w} \Phi_k(r, z)\, \frac{\partial \Phi_k(r,z)}{\partial n} (1+f_r^2)^{1/2}\, r\, dr$$

the integral being taken over a meridian of the equilibrium free-surface.

The quantities Z, k and m are homogeneous in Φ_k and therefore independent of the amplitude of the eigenfunction; however, F_x and M_y depend linearly upon the amplitude. From these facts, the displacement history of an equivalent mechanical analog of kth mode sloshing can be computed as the solution of a dynamics problem that is much simpler than determining the motion of the liquid. The procedure is to compute an equivalent spring constant and sloshing mass from Equations (2.49) and (2.50). These can be used in the simple, spring-mass dynamical model shown in Figure 2-22 and the excursion x produced by a lateral perturbing acceleration computed. The maximum value of x can be inserted into the first of Equations (2.42) to establish the maximum lateral

force. This can be used to determine the wall rise height h_{k_w} corresponding to F_x by multiplying the integrals for F_x and M_y by the constant

$$\frac{\omega_k \bar{h}_{k_w}}{r_o \psi_k}$$

with

$$\psi_k = \left[(1+f_r^2)^{1/2} \frac{\partial \Phi_k}{\partial n} \right]_{\substack{z=f(r) \\ r=r_w}}$$

Consequently, $\bar{h}_{k_w}$ can be determined from

$$\frac{\bar{F}_x}{\sigma \bar{h}_{k_w}} = \frac{\pi(1+B_\alpha)\omega_k^2}{\psi_k} \int_0^{\xi_o} \Phi_k(r_t, z_t) r_t \sin\beta \, d\xi \qquad (2.51)$$

The corresponding moment and action point are determined from

$$\frac{\bar{M}_y}{\sigma r_o \bar{h}_{k_w}} = \frac{\pi(1+B_\alpha)\omega_k^2}{\psi_k} \int_0^{\xi_o} \Phi_k(r_t, z_t) r_t z_t \sin\beta \, d\xi \qquad (2.52)$$

and Equation (2.48).

Several schemes were briefly considered for obtaining numerical solutions to the problem. Among these one involves construction of the velocity potential as a series of the product-type solutions obtained by separating variables in Laplace's equation. Boundary conditions are satisfied by a least-squares collocation method---that is, the boundary conditions are applied at a

number of points on the boundary larger than the number of terms in the series used; and the set of equations thus obtained is solved in the least-squares sense. Alternatively, finite-difference techniques offer more promise of accuracy, particularly when the contact angle is small. Other investigators have experienced numerical difficulties in obtaining satisfactory convergence for the series expansion in the same type of problem. Further, the use of an irregular-triangular, finite-difference mesh offers significant advantages. First, the mesh is space-filling; no difficulties are encountered in applying boundary conditions at places where the boundary intersects mesh lines. Second, the mesh can be constructed so as to facilitate obtaining accurate representation of the boundary conditions. A typical computing mesh obtained in the course of calculations is given in Figure 2-23.

The first normal mode eigenvalues are presented in Figure 4-1 in Section 4. Higher eigenvalues are given in Table 4-I. The equivalent mechanical analog parameters are given in Figures 4-4 and 4-5.

BAFFLE ANALYSIS STUDY

Introduction - A spacecraft in a low gravity environment may experience attitude control procedures which can induce low frequency liquid sloshing motions of the propellants. Such sloshing, unless damped, can result in disturbing forces on the vehicle and consequent further requirement for attitude control. Baffles have a major influence on the rate of slosh damping.

The material which follows presents an analytical approach to the damping problem followed by incorporation of the analytical method into two mathematical models to predict damping factors. Specific applications are presented to the Apollo SPS and LM propellant tanks.

Certain restrictions in the scope of the analysis are necessary in order to make them capable of solution and still applicable to the SPS and LM spacecraft tankage. They are:

1. A linearized mathematical approach was taken in developing the potential flow functions used to describe sloshing motions in the tanks. Hence, the results of this slosh damping study are most applicable to low amplitude sloshing.

2. Only axisymmetric liquid tanks were considered, of spherical geometry or cylindrical with hemispherical ends.

3. The baffles were restricted to straight cross-sectioned, axisymmetric types of two classifications: 1) ring baffles attached to the tank wall, and 2) full circular screen baffles.

4. Under any stable Bond number value, the equilibrium free surface of the liquid is assumed to be flat and perpendicular to the coincident tank axis and acceleration vector. Hence, this slosh damping analysis is most applicable to a higher Bond number, flat interface configuration, or a low Bond number configuration with a wall contact angle which will yield a flat equilibrium surface.

5. This analytical model includes only a single baffle under the liquid surface, and this baffle must be fully submerged with respect to the equi-

librium free surface as well as during the sloshing motions in order for the computed slosh damping factors to be applicable. As the slosh damping effects of individual baffles are independent in this derivation, the slosh damping factors of two or more baffles in a tank are additive.

6. Only first mode lateral antisymmetric sloshing was considered as this represents the most important mode in spacecraft tanks.

The method of analysis is similar to that developed by Miles*. Potential flow function $\emptyset$ is developed to describe first mode lateral sloshing in a clean tank, assuming inviscid, incompressible and irrotational flow of liquid in an unbaffled tank of the same geometry. The differential equations which describe this motion are usually linearized and are solved either in closed form or by an approximate method using a digital computer. These solutions of the function $\emptyset$ are made to satisfy boundary conditions at the tank wall and at the liquid free surface. The work of Satterlee and Reynolds** employs a closed form mathematical solution of $\emptyset$ to describe sloshing in a cylindrical tank whereas Rattayya*** uses an approximate variational principle to determine the function $\emptyset$ for both spheroidal and ellipsoidal tanks.

The frequency of the free surface sloshing modes may be computed from the potential function solution $\emptyset$. The first mode of lateral sloshing usually contains the major slosh energy and creates the largest disturbing forces and

*J. W. Miles, "Ring Damping of Free Surface Oscillations in a Circular Tank" Journal of Applied Mechanics, Vol. 25, Number 2, June 1958, pp. 274-276.

**H. M. Satterlee and W. C. Reynolds, "The Dynamics of the Free Liquid Surface in Cylindrical Containers Under Strong Capillary and Weak Gravity Conditions", Dept. of Mechanical Engineering, Report LG-2, Stanford University, Stanford, California, 1964.

***J. V. Rattayya, "Sloshing of Liquids in Axisymmetric Ellipsoidal Tanks", AIAA Second Aerospace Sciences Meeting, AIAA Paper No. 65-114, New York, N. Y., January 25-27, 1965.

torques; it is therefore of primary interest. The frequency is usually expressed in the dimensionless form $\lambda = \omega^2 R/g$, where ω is slosh frequency in radians per second, R the tank radius and g the tank axial acceleration. The dimensionless frequency λ is a function of the tank fill level h and the Bond number, $Bo = gR^2/\beta$, where β , the kinematic surface tension, is the ratio of surface tension to density of the liquid.

Potential flow velocities within the liquid due to first mode sloshing are computed by taking the gradient of the potential function at the location of interest, $\vec{U} = -\nabla\phi$. For axisymmetric baffled tanks as considered here the potential function ϕ is expressed in terms of a cylindrical coordinate system (r, θ, z) , from which the components of the velocity factor $\vec{U}$ may be easily computed.

Thus the liquid velocity components define the vector velocity $\vec{U}(r, \theta, z, t)$ within the tank and may be computed at any location and time within the liquid region. Using the computed velocities the forces exerted on the baffles may be determined by employing experimentally derived drag coefficients. The methods of predicting these forces are described below for the ring baffle and the porous plate screen baffle.

The drag coefficients for flat plates in oscillating liquid flows are presented in Keulegan and Carpenter*, Figure 13. The flat plate drag coefficient C_D is correlated against a period parameter $P = U_m T/D$, where U_m is

*G. H. Keulegan and L. H. Carpenter, "Forces on Cylinders and Plates in an Oscillating Fluid", Journal of Research of the National Bureau of Standards Volume 60, number 5, May 1958.

the maximum sloshing velocity perpendicular to the plate, T is the period of a sloshing cycle, and D is the width of the flat plate. Although the data presented result from a plate in an oscillating flow field well away from any wall, this data can be applied to ring baffles attached to the tank walls. The ring baffle attached to the wall may be considered to be one half of a full baffle that extends through the wall. The maximum component of the liquid velocity at the wall and baffle U_w that is perpendicular to the baffle surface $U_{w\perp}$ will be considered as the maximum sloshing velocity U_m. The period T is simply $T = 2\pi/\omega$. The width of this real plus imaginary baffle assumed to be centered at the wall would be twice the baffle width 2W which is equivalent to D. Therefore, the ring baffle attached to the wall would have a period parameter P defined as $P = U_{w\perp}(2\pi/\omega)/2W = \pi U_{w\perp}/\omega W$ which is equivalent to $P = \frac{U_m T}{D}$ in Figure 13 of Keulegan and Carpenter. According to Miles the Keulegan and Carpenter drag coefficient may be related to P by $C_D = 15.0/P^{1/2}$ in the range $2 < P < 20$. This representation of C_D versus P can be extended over the range $0 < P < 20$, by observing that it fits the C_D versus P data of Figure 13, Keulegan and Carpenter. For values of P in the range $20 < P < \infty$, the data presented is best correlated by $C_D = 1.98 + 53.10\ P^{-1.22}$, which yields the correct value $C_D = 1.98$ as $P \rightarrow \infty$ and matches perfectly with the previous correlation at P = 20. Therefore, for ring baffles attached to the tank walls, the following correlations for the drag coefficient can be used:

$$C_D = 15.0\ P^{-1/2} \qquad \text{for } 0 < P < 20,$$

$$C_D = 1.98 + 53.10\ P^{-1.22} \qquad \text{for } 20 < P < \infty$$

where $P = \pi U_{w\perp} / \omega W$.

The drag coefficient for full circular baffles employing either screens or porous plates are estimated based on Hoerner*. For screens or perforated plates, which normally have a porosity ρ less than 0.5, where the porosity ρ is the ratio of open area to total area, the drag coefficient C_D is a function of the porosity ρ only. In the case of a screen or grid of round rods or wires, the drag coefficient is $\left(\frac{1-\rho}{\rho}\right)^2$. In the case of sharp edged srips or grids, and also sharp edged holes drilled in plates, the drag coefficient is $\left(\frac{1.5-\rho}{\rho}\right)^2$. For screens, grids, or porous plates with $\rho > 0.5$, the drag coefficient is a more complex function of the drag coefficients of the elements as well as the porosity. Neglecting the high porosity, $\rho > 0.5$, baffle elements for this application of full circular porous baffles, the drag coefficients of screens or porous plate can be estimated from;

$C_D = \left(\frac{1-\rho}{\rho}\right)^2$ for screens or porous plates with rounded openings,

$C_D = \left(\frac{1.5-\rho}{\rho}\right)^2$ for grids or porous plates with sharp edged openings,

where the porosity $\rho < 0.5$.

With the drag coefficients defined for both ring baffles attached to the tank wall and full circular porous or screen baffles, it is now possible to calculate the force acting on the baffle. From the definition of the drag coefficient, $C_D = \frac{F}{\frac{1}{2}\rho_L U^2 A}$, the force dF exerted on an elemental area dA of the baffle can be estimated using the liquid velocity perpendicular to the baffle area, $U_\perp$.

*S. F. Hoerner, Fluid-Dynamic Drag, Published by Author, Midland Park, New Jersey, 1958, ch. 3, sect. 9.

$$dF = C_D \cdot \tfrac{1}{2} \rho_L U_\perp^2 dA.$$

The force F acting on a baffle area A may be determined by integrating the above equation over the desired baffle area.

The rate of energy decrement $\frac{dE}{dt}$ caused by the baffle on the sloshing motion can now be computed using Miles' method. Over an elemental area, dA, the rate of energy decrement is $\frac{dE}{dt} = -|U_\perp| \cdot dF$, the negative product of the perpendicular velocity $U_\perp$ and the elemental force dF. Over the entire baffle area A, the rate of energy decrement is

$$\frac{dE}{dt} = -\frac{1}{2} \rho_L \iint_A C_D |U_\perp^3| \cdot dA$$

which is a function of time. For the average rate of energy decrement over one slosh cycle $\overline{\frac{dE}{dt}}$, the time dependent rate of energy decrement $\frac{dE}{dt}$ is averaged over one slosh cycle.

$$\overline{\frac{dE}{dt}} = \frac{\omega}{2\pi} \int_0^{\frac{2\pi}{\omega}} \left(\frac{dE}{dt}\right) \cdot dt$$

The total slosh energy E of the sloshing liquid in the tank can be calculated by determining the maximum slosh kinetic energy T_{MAX} as the liquid sloshing surface passes through the equilibrium free surface where the potential energy is zero. Hence, this slosh energy is equivalent to the maximum kinetic energy which can be expressed in terms of the potential function ϕ.

$$E = T_{MAX} = \frac{\rho_L}{2} \cdot \iint_S \phi \cdot \frac{\partial \phi}{\partial z} \cdot dS$$

where S is the equilibrium free surface at z = 0.

The logarithmic decrement δ_ℓ of the sloshing due to the baffle damping is defined

$$\delta_\ell = -\frac{\pi}{\omega E} \cdot \frac{\overline{dE}}{dt}$$

In a like manner, the damping ratio ν, which is the logarithmic decrement δ_ℓ divided by 2π, is given by the equation

$$\nu = \frac{\delta_\ell}{2\pi} = -\frac{1}{2\omega E} \frac{\overline{dE}}{dt}$$

Slosh Damping Factor Analysis - The slosh damping factors have been determined for two tank geometries of interest to the Apollo CSM and LM propellant tanks. One is a cylindrical tank with hemispherical bottom, and the other is spherical. Both of these tank types may have ring baffles attached to the walls, or full circular screen or porous baffles. Slosh damping analyses were made for each of these geometries in dimensionless form.

For the cylindrical tank with hemispherical bottom shown in Figure 2-24a the potential flow function ϕ was derived from that developed for a cylindrical tank with a flat bottom. However, the moment existing at the bottom of the cylindrical section was matched to the moment of inertia of a hemispherical section, resulting in a Bessel function velocity distribution at the bottom of the cylindrical section and about the sloshing axis of the hemisphere. Hence, by modifying the boundary condition at the bottom of the cylindrical tank section, an approximate potential function ϕ was obtained for a cylindrical tank with a hemispherical bottom.

$$\phi^* = \frac{\phi \rho_L^{1/2}}{\sigma_T^{1/2} R^{1/2}} = \psi \cos\theta \cos\tau$$

where $\tau = \omega t$

$$\psi = J_1(k\rho)(A^* \cosh k\sigma + B^* \sinh k\sigma)$$

$$\rho = r/R, \quad \sigma = z/R, \quad \zeta_o^* = \zeta_o/R, \quad L^* = L/R, \quad Bo = \rho_L g R^2/\sigma_T$$

$$A^* = \frac{\zeta_o^*}{k^{1/2} J_1(k)} \left[(Bo + k^2) \frac{(4kK + 3J_2(k) \tanh kL^*)}{(4kK \tanh kL^* + 3J_2(k))} \right]^{1/2}$$

$$B^* = \frac{\zeta_o^*}{k^{1/2} J_1(k)} \left[(Bo + k^2) \frac{(4kK \tanh kL^* + 3J_2(k))}{(4kK + 3J_2(k) \tanh kL^*)} \right]^{1/2}$$

$k = 1.84118$, $K = 0.2469096$, $J_1(k) = 0.58187$, $J_2(k) = 0.315937$

The sloshing frequency ω is expressed in two dimensionless parameters.

$$\Omega = \frac{\omega^2 \rho_L R^3}{\sigma_T} = k(Bo + k^2) \cdot \frac{(4kK \tanh kL^* + 3J_2(k))}{(4kK + 3J_2(k) \tanh kL^*)}$$

$$\lambda = \frac{\omega^2 R}{g} = \frac{\Omega}{Bo}$$

The rate of energy decrement $\overline{\frac{dE}{dt}}$ is expressed nondimensionally as

$$\left(\overline{\frac{dE}{dt}}\right) = \frac{\overline{\frac{dE}{dt}}}{\rho_L g^{3/2} R^{7/2}} = -\frac{2}{3\pi} \sqrt{1 + C_k^2} \cdot I_1 \cdot I_2$$

where C_k = slope of the baffle.

$$I_1 = 4\int_0^{\pi/2} C_D \cos^3\Theta \, d\Theta$$

$$I_2 = \int_{\rho_1}^{\rho_2} \left| \sin^3\delta \left[\left(\frac{\partial\psi}{\partial\rho}\right)^2 + \left(\frac{\partial\psi}{\partial\rho}\right)^2 \right]^{3/2} \right| \rho \, d\rho$$

where for I_2:

$$\sigma = \sigma_A + C_k\rho \quad \text{for } \rho_1 < \rho < \rho_2$$

$\delta = (\gamma - \beta)$ = angle that U makes with baffle cross-section

$$\gamma = \tan^{-1}\left(\frac{w}{u}\right) = \tan^{-1}\left(\frac{\frac{\partial\psi}{\partial\sigma}}{\frac{\partial\psi}{\partial\rho}}\right) = \text{angle that U makes with horizontal}$$

$\beta = \tan^{-1}(C_k)$ = angle that baffle makes with the horizontal.

The total sloshing energy E is expressed nondimensionally as

$$E^* = \frac{E}{\rho_L g R^4} = \frac{\pi}{2} \cdot I_3$$

where $I_3 = \int_0^{\rho_0} \psi \cdot \frac{\partial\psi}{\partial\sigma} \cdot \rho \, d\rho$

where for I_3: $\sigma = 0$ for $0 < \rho < \rho_o$

The slosh damping factors are then defined.

For the logarithmic decrement:

$$\delta_e = \frac{-\pi}{\Omega^{1/2} E^*} \cdot \left(\frac{\overline{dE}}{dt}\right)^*$$

For the damping ratio:

$$\nu = \frac{\delta_e}{2\pi}$$

The above equations represent the results of the slosh damping analysis performed for a cylindrical tank with a hemispherical bottom, employing straight cross-sectioned, axisymmetric baffled.

For the spherical tank geometry shown in Figure 2 the potential flow function developed by Rattayya was used to represent the potential flow sloshing in a spherical tank. This potential flow function ϕ is solved using variational methods on a digital computer and results in an approximate potential function ϕ which can be expressed nondimensionally as:

$$\phi^* = \frac{\phi}{\alpha_1} = \psi(\rho, \sigma) \cos\Theta \sin\tau$$

where

$$\rho = r/R, \quad \sigma = z/R, \quad \tau = \omega t$$

$$\psi(\rho,\sigma) = \sum_{m=1}^{12} \left(\frac{\alpha_m}{\alpha_1}\right) \psi_m(\rho,\sigma)$$

The functions $\psi_m(\rho,\sigma)$ defined by Rattayya are:

$$\psi_1 = \rho$$

$$\psi_2 = \rho\sigma$$

$$\psi_3 = \rho\sigma^2 - 1/4\,\rho^3$$

$$\psi_4 = \rho\sigma^3 - 3/4\,\rho^3\sigma$$

$$\psi_5 = \rho\sigma^4 - 3/2\,\rho^3\sigma^2 + 1/8\,\rho^5$$

$$\psi_6 = \rho\sigma^5 - 5/2\,\rho^3\sigma^3 + 5/8\,\rho^5\sigma$$

$$\psi_7 = \rho\sigma^6 - 15/4\,\rho^3\sigma^4 + 15/8\,\rho^5\sigma^2 - 5/64\,\rho^7$$

$$\psi_8 = \rho\sigma^7 - 21/4\,\rho^3\sigma^5 + 35/8\,\rho^5\sigma^3 - 35/64\,\rho^7\sigma$$

$$\psi_9 = \rho\sigma^8 - 7\rho^3\sigma^6 + 35/4\,\rho^5\sigma^4 - 35/16\,\rho^7\sigma^2 + 7/128\,\rho^9$$

$$\psi_{10} = \rho\sigma^9 - 9\rho^3\sigma^7 + 63/4\,\rho^5\sigma^5 - 105/16\,\rho^7\sigma^3 + 63/128\,\rho^9\sigma$$

$$\psi_{11} = \rho\sigma^{10} - 45/4\,\rho^3\sigma^8 + 105/4\,\rho^5\sigma^6 - 525/32\,\rho^7\sigma^4 + 315/128\,\rho^9\sigma^2 - 21/512\,\rho^{11}$$

$$\psi_{12} = \rho\sigma^{11} - 55/4\,\rho^3\sigma^9 + 165/4\,\rho^5\sigma^7 - 1155/32\,\rho^7\sigma^5 + 1155/128\,\rho^9\sigma^3 - 231/512\,\rho^{11}\sigma$$

The coefficients (α_m/α_1) are functions of the tank fill level h^* and the Bond number $Bo = \rho_L g R^2/\sigma_T$, and are computed by means of a digital computer program.

The sloshing frequency ω in the spherical tank geometry is related to the dimensionless parameter $\lambda = \omega^2 R/g$. The value of λ is the first eigenvalue obtained from the eigenvalue matrix by determining the first several roots of the characteristic determinant.

The rate of energy decrement due to sloshing $\overline{\frac{dE}{dt}}$ may be expressed as

$$\left(\overline{\frac{dE}{dt}}\right)^* = \frac{\left(\overline{\frac{dE}{dt}}\right)}{\left(\frac{\alpha_1^3 \rho_L}{R}\right)} = -\frac{16}{9\pi} \cdot C_D \sqrt{1+k^2} \cdot I_1$$

where k = slope of the baffle cross-section.

$$I_1 = \int_{\rho_1}^{\rho_2} \left| \sin^3 \delta \left[\left(\frac{\partial \psi}{\partial \rho}\right)^2 + \left(\frac{\partial \psi}{\partial \sigma}\right)^2 \right]^{3/2} \right| \rho \, d\rho$$

where for I_1: $\sigma = \sigma_A + k\rho$ for $\rho_1 < \rho < \rho_2$

$\delta = (\gamma - \beta)$ = angle that velocity U makes with baffle cross-section

$\gamma = \tan^{-1}\left(\frac{w}{u}\right) = \tan^{-1}\left(\frac{\frac{\partial \psi}{\partial \sigma}}{\frac{\partial \psi}{\partial \rho}}\right)$ = angle velocity U makes with horizontal

$\beta = \tan^{-1}(k)$ = angle that baffle cross-section makes with the horizontal.

Total energy of slosh E expressed in dimensionless form.

$$E^* = \frac{E}{\rho_L \alpha_1^2 R} = \frac{\pi}{2} \int_0^{\rho_o} \psi \cdot \frac{\partial \psi}{\partial \sigma} \cdot \rho \, d\rho$$

where $\sigma = 0$ for $0 < \rho < \rho_o$

The slosh damping factors result from the following expressions:

For logarithmic decrement:

$$\delta_\ell = -\pi \frac{\alpha^*}{E^*} \cdot \left(\frac{dE}{dt}\right)^*$$

where

$$\alpha^* = \frac{\alpha_1}{\omega R^2} = \frac{\gamma_o^*}{\left.\frac{\partial \psi}{\partial \sigma}\right|_{\substack{\rho=\rho_o \\ \sigma=0}}} \quad , \text{ and } \quad \gamma_o^* = \gamma_o / R$$

For the damping ratio:

$$\nu = \delta_\ell / 2\pi$$

The slosh damping analysis presented above applies to spherical tanks with straight cross-sectioned, axisymmetric baffles. The above analysis requires a digital computer solution to define the potential function ϕ. For a spherical tank, it is not possible to solve the sloshing potential function in a closed mathematical form, so the approximate potential flow function ϕ presented above was used in the spherical tank slosh damping analysis.

Results and Conclusions - The analyses described in the previous section were programmed for digital computer solutions and were then checked against experimentally determined damping factors and analytical solutions for similar geometries available in the literature. The damping factors obtained from both the cylindrical tank with hemispherical bottom model and the spherical model show good agreement with the damping factors appearing in the literature*. Somewhat surprisingly, the cylindrical tank with hemispherical bottom analysis yields reasonable values of the damping factor for low values of L^* (dimensionless cylindrical fill height) where the validity of this model could be questioned. For the spherical model, using Rattayya's variational approximation for the potential function $\emptyset$ the eigenvalue solutions to the potential function matrix are sometimes unstable for either high or low spherical fill levels, and no valid solution is obtained. Although this unstable feature of the potential function program is present, a method of examining the validity of the potential function is used to assure that valid damping factors are obtained.

The results of the initial calculations of damping factors for representative tanks and baffles indicate an unexpected result. If the geometry, fill level h^*, and sloshing amplitude ζ_o^* are held constant, then the logarithmic decrement δ_ℓ of damping is found to be independent of the tank Bond number. The damping for a single cycle was found to be constant as the Bond number ranges from $0 < Bo < \infty$. As the Bond number increases, the sloshing

*NASA SP 106, The Dynamic Behavior of Liquids in Moving Containers, H. N. Abramson ed. 1966

frequency increases, but the logarithmic decrement of the slosh damping remains constant. In this case, the sloshing amplitude will decrease by the same amount in the same number of cycles independent of the Bond number which exists during the damping, and the frequency of the sloshing during this damping process. Examination of the mathematics indicates that the Bond number dependence completely disappears from the slosh damping factors formulated as in this study.

With the slosh damping factors independent of Bond number, then all liquid properties are removed from this slosh damping analysis based upon an equilibrium free surface that is flat. For this analysis, the slosh damping factors for all liquids in geometrically similar tanks and baffle models would have equal values. The slosh damping factors presented here are only functions of baffle and tank geometries, and of the slosh wave amplitude, $\mathcal{P}_o^*$. Only the sloshing frequency ω is a function of Bond number, and hence of the acceleration level g and the liquid-gas properties.

A general baffle study of both the full circular screen (or porous plate) baffles and the ring baffles attached to the wall was then made using the damping analysis of a cylindrical tank with hemispherical bottom which applies to Figure 2-24, as the basis for this study. Slosh damping analyses were then made with baffles of various designs and depth located in the cylindrical section of the tank with various fill levels. The object of this general baffle study was to find parameters that would help correlate the slosh damping parameters with respect to the many baffle and tank fill parameters that could be varied.

For the full screen or porous plate baffles, the logarithmic decrement δ_ℓ of slosh damping is a function of 5 parameters for the tank geometry shown in Figure 2-24.

$$\delta_\ell = f\,(C_D,\ \gamma_o^*,\ d^*,\ L^* \text{ or } h^*,\ \beta).$$

For the screen or porous plate baffle, the drag coefficient C_D is a function of porosity φ of the baffle, so that C_D is a constant. The analysis for this type of baffle shows that δ_ℓ is a linear function of C_D and γ_o^*, the dimensionless slosh amplitude. The term $\delta_\ell / C_D\ \gamma_o^*$ would then appear to be a good correlating parameter. Results are plotted in Figure 4-8 in Section 4 versus dimensionless baffle depth d^* and as a function of tank fill level in the cylindrical section L^*, for horizontally flat full screened baffles, $\beta = 0$. This plot shows that for $L^* \geq 2.0$, no effect of the tank bottom is seen in the term $\delta_\ell / C_D\ \gamma_o^*$ for any value of d^*. The shape of these curves are similar for all values of L^*.

For conical full screened baffles in the range $-30° < \beta < +30°$, the data was found to correlate as in Figure 4-9. If the damping ratio defined as $(\delta_\ell / C_D\ \gamma_o^*)/(\delta_\ell / C_D\ \gamma_o^*)_{\beta=0}$ is plotted against the angle of the baffle with respect to the horizontal, the correlation appears to hold for all values of d^* and probably L^*, although this data was plotted for $L^*=2.0$. From the baffle angle β, the damping ratio can be found from Figure 4-9. Figures 4-8 and 4-9 represent a rather complete correlation of the slosh damping data for full circular and conical screen or porous plate baffles in the tank geometry shown in Figure 2-24.

The slosh damping factors for ring baffles attached to the cylindrical wall of Figure 2-24 were next studied in the hope of finding similar correlating parameters as before. In this case, the logarithmic decrement δ_ℓ of the slosh damping is a function of the following variables.

$$\delta_\ell = f(C_D,\ \gamma_o^*,\ d^*,\ L^* \text{ or } h^*,\ \beta\ ,\ W^*)$$

In this case, for the ring baffles, W^* is the dimensionless baffle width, and C_D is not constant but varies around the baffle and is a function of the period parameter P, which is a function of virtually all of the other parameters in brackets on the right hand side of the equation. No parameters have been found to satisfactorily correlate the logarithmic decrement, especially in the face of baffle geometry variations. Figures 4-10, 4-11, and 4-12 however, give the calculated performance of ring baffle slosh damping for the tank geometry of Figure 2-24.

In Figure 4-10, the log decrement δ_ℓ is plotted versus dimensionless baffle depth with L^* as a parameter and with the following values fixed; $W^* = 0.10$, $\beta = 0°$, and $\gamma_o^* = 0.10$. This curve is similar to Figure 4-8, and shows the same characteristics in δ_ℓ for $L^* \geq 2.0$. In Figure 4-11, the log decrement δ_ℓ is plotted versus dimensionless baffle width W^* with dimensionless baffle depth d^* as a parameter, and with fixed values of $L^* = 2.0$, $\beta = 0°$, and $\gamma_o^* = 0.10$. The logarithmic decrement is seen to increase rapidly with increase in baffle width W^*, especially near the surface where d^* is small. This slosh damping model should, in accordance with the earlier work (c.f. Miles), be restricted to rather short width baffles of $W^* \leq 0.3$, especially near the liquid surface.

In Figure 4-12, the logarithmic decrement ration, $\delta_2 / (\delta_2)_{\beta=0}$, is plotted versus the baffle angle with the projected horizontal width of baffle, W^* cos β , as a parameter, and with $L^* = 2.00$ and $\gamma_o^* = 0.10$ fixed as constants. From Figure 4-12, the log decrement ratio can be found for a value of β and projected width W^* cos β . Then from Figure 4-11, with the W^* equal to the projected width and the same value of baffle depth d^*, the log decrement of the horizontal baffle $(\delta_2)_{\beta=0}$ is found. With this and the log decrement ratio from Figure 4-12, the logarithmic decrement of the sloping baffle can be computed.

Although strong correlating parameters do not appear to exist for the general ring baffle, a correlating parameter has been developed for a fixed geometry ring baffle, and this will be presented in the following section on Apollo SPS and LM baffle studies.

An application of the slosh damping analysis techniques developed in this study was then made to the Apollo SPS and LM tank baffles. The Apollo SPS fuel and oxidizer tanks are similar in design with full conical porous plate baffles located in the lower hemisphere of the tank, as shown in Figure 2-25. The relative locations of these conical baffles vary slightly between the fuel and oxidizer tank. A cylindrical propellant retention tank exists at the center of the conical baffles, and extends through them down to the base of the tank. To determine the slosh damping performance of these baffles, full conical baffles were assumed because the perpendicular velocity to the baffle at the center of the cone is small, so that the region of the baffle intercepted by the containment sump would have little influence on the value

of the predicted slosh damping factor, thereby justifying, at least in part, neglecting the effect of the center body.

Based upon our slosh damping analyses, the logarithmic decrement δ_ℓ of slosh damping was computed as a function of drag coefficient C_D, slosh amplitude γ_o^*, and tank fill level from the bottom, h^*. This data is presented in Figure 2-26 for both the fuel and oxidizer tank, with upper and lower baffles. In this figure, the normalized logarithmic decrement of damping ($\delta_\ell / C_D \gamma_o^*$) is plotted against the dimensionless liquid depth h^* in the tank. Then for either the oxidizer or fuel tank loaded to a liquid depth h^*, the drag coefficient C_D of the porous plate can be estimated from its porosity ρ. Then, with the sloshing amplitude γ_o^* decided upon, the logarithmic decrement δ_ℓ can be computed from Figure 2-26 for one or both of the conical porous plate baffles at the bottom of the Apollo SPS tanks.

In the LM ascent and descent tanks, a series of ring baffles has been proposed to afford slosh damping of the propellants. These baffles, although not directly attached to the wall, are close enough to the wall to be considered ring baffles attached to the tank wall. These horizontal baffles, $\beta = 0°$, have a dimensionless width W^* in the range $0.07 < W^* < 0.12$. The configuration of these proposed baffles in the LM descent and ascent tanks are shown in Figures 2-27 and 2-29, respectively.

Using the slosh damping analyses developed in this study, the slosh damping factors were computed for these baffles individually as a function of dimensionless slosh amplitude γ_o^* and dimensionless liquid depth h^* in the tank.

Because of the fixed geometry of any one baffle, as only the two parameters $\mathcal{Y}_o^*$ and h^* are varied, it was possible to correlate the logarithmic decrement δ_ℓ of the slosh damping in a useful manner. The correlations of the slosh damping factors for the four ring baffles in both the LM descent and ascent tanks are presented in Figures 2-28 and 2-30, respectively.

Both Figures 2-28 and 2-30 have the slosh damping factor δ_ℓ expressed as the logarithmic decrement ratio $\delta_\ell / C_{D\ MIN}\ \mathcal{Y}_o^*$. Because the drag coefficient C_D varies around the baffle because of different values of the period parameter P, the minimum value of the drag coefficient was chosen as the correlating parameter. This minimum value $C_{D\ MIN}$ occurs on the baffle where the period parameter has a maximum value, P_{MAX}. Since P_{MAX} is proportional to the slosh amplitude $\mathcal{Y}_o^*$, a period parameter ratio $P_{MAX}/\ \mathcal{Y}_o^*$ is also presented as a correlating parameter. Hence, in Figures 2-28 and 2-30 both the period parameter ratio $P_{MAX}/\ \mathcal{Y}_o^*$ and the logarithmic decrement ratio $\delta_\ell / C_{D\ MIN}\ \mathcal{Y}_o^*$ are plotted versus the dimensionless liquid depth in the tanks, h^*.

The manner in which these graphs are used to compute the logarithmic decrement of the sloshing follows in a straight forward manner. With a liquid level h^* fixed, the period parameter ratio $P_{MAX}/\ \mathcal{Y}_o^*$ value is now read from the graph (dashed line). With the sloshing amplitude $\mathcal{Y}_o^*$ chosen, the value of the maximum period parameter P_{MAX} is now computed. For ring baffles attached to the wall, we have assumed the following relationships between the drag coefficient C_D and the period parameter P.

$$C_D = 15.0\ P^{-1/2} \text{ for } 0 < P < 20.$$

$$C_D = 1.98 + 53.10\ P^{-1.22} \text{ for } 20 < P < \infty .$$

The value of $C_{D\ MIN}$ may be calculated from the above relationships by substituting P_{MAX} for P. From the value of the logarithmic decrement ratio $\delta_\ell / C_{D\ MIN}\ \gamma_o^*$ taken from the graph (solid line) at the same value of h^*, the logarithmic decrement δ_ℓ can now be computed with $C_{D\ MIN}$ and γ_o^* known.

Using this procedure, the slosh damping factor δ_ℓ can be computed for any fill level h^* in either the LM descent or ascent tanks. Usually, only the baffle located directly below the liquid surface contributes substantially to the slosh damping, but in some locations the second closest baffle to the free surface contributes also. In this case, the logarithmic decrement of each baffle can be added independently to obtain the logarithmic decrement resulting from two or more baffles providing substantial damping.

ANALYSIS OF LIQUID PROPELLANT RESPONSE TO POST ENGINE SHUTDOWN STRUCTURAL RELAXATION

Fluid behavior following engine shut-down is of considerable interest in vehicles having re-startable engines; for example, the Agena or the Apollo Service Module. It is even more important in vehicles which have forward tank vents and which must vent just following engine shut-down. Attention is focused here on the motion imparted to the free surface of fluid in a partially filled tank by sudden structural relaxation of the tank walls following thrust cut-off.

In formulating a method of approach, one important fact should be recognized. The potential and kinetic energy contained in the oscillating free surface, according to Gossard*, make up a small part of the total energy originally stored in the walls of the container and in the contained moving liquid. As a consequence, the motion of the container walls is very nearly independent of the motions of the free surface and in fact may be prescribed without incurring significant error. Accordingly, the container walls are represented as a simple oscillator in the analysis which follows. The source of damping in the oscillator is assumed to be structural damping only. Viscous fluid damping is ignored.

Some simplification is achieved by restricting tank geometry to flat-bottomed cylinders of circular cross-section. In practice, the tank bottom is more

*Gossard, Myron L., "Axisymmetric Dynamic Response of Liquid-Filled Hemispherical, Thin-Walled, Elastic Tanks", AIAA Symposium on Structural Dynamics and Aeroelasticity, Boston, Mass., Aug. 30 through Sept. 1, 1965, Proceedings p. 177.

often in the shape of a hemisphere or ellipsoid of revolution. However, it is shown that the contribution of bottom motion to motion of the free surface is quite small except for fluid depths $a/d < 2$. Hence, the shape of the bottom is not important so long as the depth of the fluid is sufficient to allow sidewall motion to dominate the response of the free surface.

The procedure to be followed is divided into six consecutive steps: namely,

1) Formulation of series solution to the boundary conditions of the fluid mass.
2) Calculation of oscillator frequencies using membrane theory and the Rayleigh method.
3) Combining steps (1) and (2) to obtain free surface displacements.
4) Mathematical representation of thrust decay in typical vehicles.
5) Response of free surface to instantaneous change in thrust; Duhamel response to ramp change in thrust.
6) Combine steps (3), (4) and (5) with application to Agena and Apollo Service Module.

Detailed algebraic manipulations are presented in various sections of the Appendix but for clarity are omitted in the Analysis which follows.

Analysis - Formulation of Series Solution - The velocity potential satisfying all boundary conditions may be expressed as the sum of three Fourier series each of which is chosen to satisfy part of the boundary conditions.

$$\varphi(r,z,t) = \sum_{n=1}^{\infty} a_n(t)\, J_o(k_n r) \cosh k_n (l-z) + \sum_{n=1}^{\infty} b_n(t)\, J_o(l_n r) \sinh(l_n z) + \sum_{n=1}^{\infty} C_n(t)\, I_o(m_n r) \sin(m_n z)$$

This is illustrated in Figure 2-31.

The kinematic constraints at the bottom and along the wall of the container are prescribed by known velocities at these boundaries. Thus,

$$w(r,t) = \varphi_{2_z}(r,-\ell,t) = \sum_{n=1}^{\infty} b_n(t)\, J_0(\ell_n r)\, \ell_n \cosh(-\ell_n \ell) \qquad (2.53)$$

$$\frac{d}{dr} J_0(\ell_n a) = 0$$

where

$$u(z,t) = \varphi_{3_r}(a,z,t) = \sum_{n=1}^{\infty} c_n(t)\, m_n I_0'(m_n a) \sin(m_n z) \qquad (2.54)$$

where

$$m_n = \left(\frac{2n-1}{2}\right)\frac{\pi}{\ell}$$

The orthogonal properties of the $J_0(\ell_n r)$ in Eq. (2.53) and $\sin m_n z$ in Eq. (2.54) readily provide general expressions for $b_n(t)$ and $c_n(t)$

$$b_n(t) = \frac{2\int_0^a w(r,t)\, J_0(\ell_n r)\, r\, dr}{a^2 \left[J_0(\ell_n a)\right]^2 \ell_n \cosh(-\ell_n \ell)} \qquad (2.55)$$

$$c_n(t) = \frac{-2\int_0^{-\ell} u(z,t) \sin(m_n z)\, dz}{\ell\, m_n I_0'(m_n a)} \qquad (2.56)$$

To solve for the coefficients, a_n, we make use of the dynamical constraint provided by the Bernoulli equation at the free surface. The linearized dif-

ferential equation of motion for constant gravity is

$$-\frac{\sigma}{\rho}\,\frac{1}{r}\left[\varphi_{zr} + \varphi_{zrr}\right] + \varphi_{tt} + g\,\varphi_z = 0 \tag{2.57}$$

Substituting the appropriate derivatives of

$$\varphi(r,z,t) = \sum_{n=1}^{\infty} \Big\{ a_n(t)\, J_0(k_n r) \cosh\left[k_n(l+z)\right] + b_n(t)\, J_0(l_n r) \sinh(l_n z) + c_n(t)\, I_0(m_n r) \sin(m_n z) \Big\} \text{ at } z = 0$$

into Eq. (2.57) yields

$$\sum_{n=1}^{\infty} \left\{ a_{n_{tt}}(t) \cosh(k_n l) + \left(\frac{\sigma}{\rho} k_n^3 + g k_n\right) \sinh(k_n l) \right\} J_0(k_n r) + \sum_{n=1}^{\infty} \left\{ b_n(t) \left(\frac{\sigma}{\rho} l_n^3 J_0(l_n r) + g l_n J_0(l_n r)\right)\right\} = \sum_{n=1}^{\infty} c_n(t)\, I_0(m_n r) \left(m_n^3 \frac{\sigma}{\rho} - g m_n\right) \tag{2.58}$$

Noting that for the case of $J_0(k_n r) = J_0(l_n r)$, Eq. (2.58) has the form

$$\sum_{m=1}^{\infty} c_m\, J_0(k_m r) = f(r)$$

By orthogonality $\int_0^a r\, J_0(k_p r)\, J_0(k_m r)\, dr = 0$ for $k_m \neq k_p$

Observing the required boundary conditions*

$$J_o'(k_m a) = J_o'(k_\rho a)$$

$$c_m = \frac{2\int_o^a r f(r) J_o(k_m r)\, dr}{a^2 \left[J_o(k_m a)\right]^2} \quad \text{for } 0 < r < a$$

Thus: Eq. (2.58) becomes a 2nd order ordinary differential equation for each n

$$a_{n_{tt}}(t) + \left(\frac{\sigma}{\rho} k_n^3 + g k_n\right) \tanh(k_n l)\, a_n(t)$$

$$= \frac{-b_n(t)\, k_n \left\{\frac{\sigma}{\rho} k_n^2 + g\right\}}{\cosh(k_n l)} \qquad (2.59)$$

$$+ \frac{2\int_o^a \left[\sum_{n=1}^{\infty} c_n(t) I_o(m_n r)\left(m_n^3 \frac{\sigma}{\rho} - g m_n\right)\right] r J_o(k_n r)\, dr}{a^2 \left[J_o(k_n a)\right]^2 \cosh(k_n l)}$$

Recalling that $b_n(t)$ and $c_n(t)$ refer to motions of the bottom and sides respectively, we examine a "worst case" when the two motions are moving in phase at the same frequency. In such a case, Eq. (2.59) takes the form of the equation of motion of an undamped system driven by an oscillator at a single frequency. With no damping in the system

$$a_{n_{tt}}(t) + \omega_n^2 a_n(t) = A_n \lambda \sin \lambda t \qquad (2.60)$$

*Bronwell, A., "Advanced Mathematics In Physics and Engineering", 1st Edition, McGraw-Hill Book Co., Inc., New York, 1953, pp. 81-83.

where the slosh frequency is

$$\omega_n = \left[\left(\frac{\sigma}{\rho} k_n^3 + g k_n\right) \tanh(k_n \ell)\right]^{1/2}$$

λ = Rayleigh frequency of dynamical system consisting of fluid and structure

By definition, the Raleigh frequency, λ , is established by the relation

$$\lambda^2 = \frac{T}{V} \tag{2.61}$$

where the total kinetic energy of fluid is

$$T = \tfrac{1}{2} \int_0^{-\ell} \int_0^{a} (u^2 + w^2)\, 2\pi r \rho \, dr \, dx$$

and V is the strain energy of tank walls and bottom

By this definition the potential energy of the fluid surface and the kinetic energy of the tank structure are discarded as negligible quantities. Satisfactory agreement with more elaborate analyses is demonstrated by Albert* by comparing the Raleigh frequency obtained with that of Coale and Nagano**. The constant coefficient A_n in Eq. (2.60) is a function of tank geometry, fluid depth and shape of the bulging tank which oscillates at frequency λ .

Eq. (2.60) is for a system with no damping. Before proceeding with the solution of $q_n(t)$, it is convenient to examine the driving oscillator in detail and establish the effect of structural damping as well as explicit relations for $b_n(t)$, $c_n(t)$ and A_n.

*Albert, R.S., "Transient Response of Elastic Tank Walls at Thrust Cut-off", LMSC/A799400, Structures Report SS/1086/5522, 4 March 1966.
**Coale and Nagano, "Axisymmetric Dynamics of a Cylindrical Membrane Shell Partially Filled With a Liquid", LMSC Solid Mechanics TR6-90-63-92. Sept. 1963.

The Oscillating Tank Structure - A study of the oscillating tank structure is reported by Albert*. The work is used as an integral part of the present analysis for prescribing the boundary conditions of the tank bottom and walls. The results are repeated here with coordinate system changed to agree with Fig. 2.31.

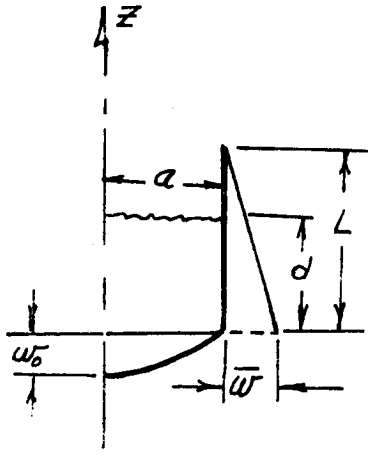

For tank walls and bottom

$$\bar{w}(z,t) = \bar{w}\left(1 - \frac{d+z}{L}\right)e^{-\alpha t}\cos\lambda t \quad (2.62)$$

$$w_o(r,t) = w_o\left[1 - \frac{5}{4}\left(\frac{r}{a}\right)^2 + \left(\frac{r}{a}\right)^4\right]e^{-\alpha t}\cos\lambda t \quad (2.63)$$

The Rayleigh frequency, λ , is shown in Fig. 2-32 as a function of fluid depth, d/L, for parametric variation of tank geometry L/a . Static deflection of the sidewall, $\bar{w}$, shown in the sketch above is given by

$$\bar{w} = \frac{\gamma a^2 d}{E h} \quad (2.64)$$

Fig.2-33 shows the deflection ratio, $\left(\frac{w_o}{\bar{w}}\right)$, (ratio of bottom deflection/side deflection) required to match side wall frequency given by Fig. 2-32. From Eq's (2.62) and (2.63), the corresponding container wall velocities are

$$u(z,t) = \bar{w}\left(1 - \frac{d+z}{L}\right)\lambda e^{-\alpha t}\left[\sin\lambda t + \left(\frac{\alpha}{\lambda}\right)\cos\lambda t\right] \quad (2.65)$$

---

*Albert, op.cit.

$$W(r,t) = w_o \lambda e^{-\alpha t}\left[1 - \frac{5}{4}\left(\frac{r}{a}\right)^2 + \left(\frac{r}{a}\right)^4\right]\left[\sin \lambda t + \left(\frac{\alpha}{\lambda}\right)\cos \lambda t\right] \quad (2.66)$$

The term involving damping ratio, $\left(\frac{\alpha}{\lambda}\right)$, is discarded since it is, for most structures, only two or three percent.

Solution of Free Surface Displacement - Eq's (2.65) and (2.66) establish the prescribed boundary conditions of the tank walls. The coefficients, $b_n(t)$ and $C_n(t)$ of the series solution for the velocity potential, φ, can now be calculated.

Substituting Eq. (2.66) in Eq. (2.55) yields

$$b_n(t) = \frac{2 w_o \lambda e^{-\alpha t} \sin \lambda t}{a^2 [J_o(k_n a)]^2 k_n \cosh(-k_n d)} \int_o^r r\left[1 - \frac{5}{4}\left(\frac{r}{a}\right)^2 + \frac{1}{4}\left(\frac{r}{a}\right)^4\right] J_o(k_n r)\, dr$$

The integral can be evaluated by a series expansion of $J_o(k_n r)$ (see Dwight*) to give

$$b_n(t) = \frac{2 w_o \lambda e^{-\alpha t} \sin \lambda t}{J_o(k_n a)\, k_n} (F_n)$$

where

$$F_n = \frac{1}{J_o(k_n a)\cosh(k_n d)} \left\{\left(\frac{11}{48}\right) - \left(\frac{k_n a}{2}\right)^2\left(\frac{1}{96}\right) + \left(\frac{k_n a}{2}\right)^4\left(\frac{17}{1920}\right) - \left(\frac{k_n a}{2}\right)^6\left(\frac{1}{1728}\right)\right\} \quad (2.67)$$

The function, F_n, is a function of fluid geometry, a/d. For values of $a/d < 2$, $\sum_{n=1}^{\infty} F_n$ becomes quite small.

*Dwight, H.B., "Tables of Integrals and other Mathematical Data", Revised Edition, The MacMillan Company, 1947. Page 178 #807.1.

Returning to Eq. (2.65) and substituting it into Eq. (2.56) yields

$$C_n(t) = 2\int_{-d}^{0} \frac{u(z,t)\sin m_n z\, dz}{d\, m_n I_o'(m_n a)}$$

$$= \frac{-2\bar{w}\lambda e^{-\alpha t}\sin\lambda t}{Ld\, m_n^3 I_o'(m_n a)}(-1)^n\left\{1-\cos\left[\left(\frac{2n-1}{2}\right)\frac{\pi L}{d}\right]\right\} \qquad (2.68)$$

$$= \frac{2\bar{w}\left(\lambda e^{-\alpha t}\sin\lambda t\right)}{m_n I_o'(m_n a)} H_n$$

where

$$H_n = -\left(\frac{d}{L}\right)\frac{(-1)^n}{\left(\frac{2n-1}{2}\right)^2\pi^2}\left\{1-\cos\left[\left(\frac{2n-1}{2}\right)\frac{\pi L}{d}\right]\right\}$$

To calculate the coefficient, A_n, in Eq. (2.60), it is expedient to consider the case for which gravity is absent. Referring to Eq. (2.59) with zero gravity we have

$$a_{n_{tt}}(t) + \left(\frac{\sigma}{\rho}\right)\left(\frac{k_n a}{a}\right)^2 k_n \tanh(k_n d)\, a_n(t)$$

$$= b_n(t)\left(\frac{\sigma}{\rho}\right)\left(\frac{k_n a}{a}\right)^2 k_n / \cosh(k_n d)$$

$$+ 2\int_0^a \left[\sum_{m=1}^{\infty} C_m(t) I_o(m_m r) m_m^3\left(\frac{\sigma}{\rho}\right)\right] r J_o(k_n r)\, dr \Big/ a^2\left[J_o(k_n a)\right]^2 \cosh(k_n d) \qquad (2.69)$$

The last term on the right hand side of Eq. (2.69) contains the subscript m instead of n since integration must be performed on a series of m terms. The result can be expressed as

$$a_{n_{tt}}(t) + \omega_n^2 \; a_n(t)$$

$$\frac{-2\bar{w}\left(\frac{\sigma}{\rho}\right)\left(\frac{k_m r}{a}\right)^2}{J_0(k_n a)\cosh(k_n d)} \left\{\left(\frac{w_0}{\bar{w}}\right) F_n + G_n\right\} \lambda e^{-\alpha t} \sin \lambda t = A_n \lambda e^{-\alpha t} \sin \lambda t \tag{2.70}$$

where

$$A_n = \frac{-2\bar{w}\left(\frac{\sigma}{\rho}\right)\left(\frac{k_n r}{a}\right)^2}{J_0(k_n a)\cosh(k_n d)} \left\{\left(\frac{w_0}{\bar{w}}\right) F_n + G_n\right\} \tag{2.71}$$

$$G_n = \frac{2\left(\frac{\sigma}{\rho}\right)}{a^2 J_0(k_n a)\cosh(k_n d)} \int_0^a \left[\sum_{m=1}^{\infty} C_m(t) I_0(m_m r)\, m_m^3\right] r J_0(k_n r)\, dr \tag{2.72}$$

and F_n is defined by Equation (2.67) and ω_n is defined as on page 2-73.

In passing it should be noted that non-zero gravity cases would result in a different function, G_n. There is no restriction on the calculation of such cases as equation (2.72) stands. However, the zero-gravity case was chosen to define ω_n and G_n because it is the only case suitable for calculating the response of the fluid surface to a step change in thrust.

Proceeding now to the solution of the differential equation for $a_n(t)$, Eq. (2.70),

$$a_n(t) = \frac{A_n \lambda}{\omega_n^2 - \alpha^2 - \lambda^2} \left\{ \left(\frac{\alpha}{\lambda}\right)\left(e^{-\alpha t} \cos \lambda t - \cos \omega_n t\right) + e^{-\alpha t} \sin \lambda t - \left(\frac{\lambda}{\omega_n}\right) \sin \omega_n t \right\} \tag{2.73}$$

Eq. (2.73) is a variation of the familiar expression for response of a 2nd order system to a forced oscillation.* Resonance, however, is not important in Eq. (2.73) since the ratio of $\left(\frac{\lambda}{\omega_n}\right)$ will run as high as 4×10^3. In the Agena tank, for example, λ is about 240 rad/sec; ω_n, is only .06 rad/sec. For all practical purposes, all terms but the last term in Eq. (2.73) may be discarded which leaves us with

$$a_n(t) = \frac{A_n}{\omega_n} \sin \omega_n t \tag{2.74}$$

Substituting Eq. (2.71) into Eq. (2.74)

$$a_n(t) = \frac{-2\bar{w}\left(\frac{\sigma}{\rho}\right)\left(\frac{k_n r}{a}\right)^2}{\omega_n J_0(k_n a) \cosh(k_n d)} \left\{ \left(\frac{w_0}{\bar{w}}\right) F_n + G_n \right\} \sin \omega_n t$$

We may now substitute $a_n(t)$, $b_n(t)$ and $c_n(t)$ into the series solution for the velocity ϕ_z at $z = 0$.

$$\phi_{z_n}(r, 0, t) = -2\bar{w}\left(\frac{J_0(k_n r)}{J_0(k_n a)}\right) \left\{ \left(\frac{w_0}{\bar{w}}\right) F_n + G_n \right\} \omega_n \sin \omega_n t$$

(cont next page)

*Timoshenko, S., "Vibration Problems in Engineering", Sec. Ed. D. VanNostrand Co., Inc., 1937. pg. 17.

$$+ 2\omega_o \left(\frac{J_o(k_n r)}{J_o(k_n a)} \right) F_n \lambda e^{-\alpha t} \sin \lambda t$$

$$+ 2\bar{\omega} \left(\frac{I_o(m_n r)}{I_o'(m_n a)} \right) H_n \lambda e^{-\alpha t} \sin \lambda t \qquad (2.75)$$

Restricting ourselves to the vicinity of the wall; $r = a$ and summing all components, n

$$\varphi_z(a,o,t) = -2\bar{\omega} \sum_{n=1}^{\infty} A_n^* \omega_n \sin \omega_n t - 2\bar{\omega} \sum_{n=1}^{\infty} B_n^* \lambda e^{-\alpha t} \sin \lambda t \qquad (2.76)$$

where:

$$A_n^* = \left(\frac{\omega_o}{\bar{\omega}} \right) F_n + G_n$$

$$B_n^* = \left(\frac{\omega_o}{\bar{\omega}} \right) F_n + \left(\frac{I_o(m_n a)}{I_o'(m_n a)} \right) H_n$$

Finally, the displacement of the free surface from its initial position (at $r = a$) is given by the relation

$$h(a,o,t) = \sum_{n=1}^{\infty} h_n(a,o,t) = \sum_{n=1}^{\infty} \int_o^t \varphi_{z_n}(a,o,t)\, dt$$

The response of the free surface to an arbitrary thrust decay function may be shown to be:

$$h(a,o,t) = h_o(a,o,o) + \int_o^t F(\tau)\, \dot{A}_\tau(t)\, d\tau \qquad (2.78)$$

where

$h_o(a,o,o)$ = initial static displacement of fluid

$F(\tau)$ = input force; i.e., thrust-decay function

$\dot{A}_\tau(t)$ = response of free surface to unit impulse

For a step change in thrust, Eq. (2.78) becomes

$$h(a,o,t)_{\text{Step}} = h_o(a,o,o) + (2\bar{w})\left(\frac{T}{W}\right)\sum_{n=1}^{\infty}\left\{A_n^*(1-\cos\omega_n t)+B_n^*\right\} \qquad (2.79)$$

For a ramp thrust input, sketched at the right.

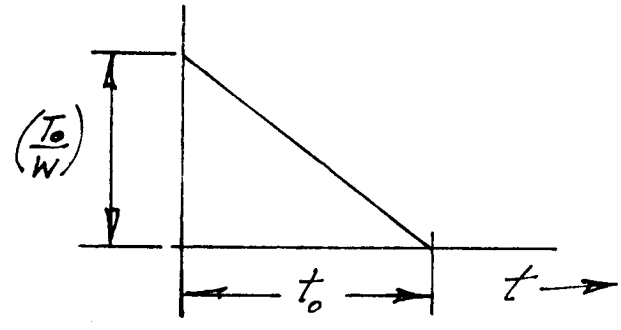

$$h(a,o,t)_{\text{ramp}} = h_o(a,o,o)+2\bar{w}\left(\frac{T_o}{W}\right)\sum_{n=1}^{\infty}\left\{\left[\frac{A_n^*\sin\omega_n t(1-\cos\omega_n t_o)}{\omega_n t_o}\right]+B_n^*\right\} \qquad (2.80)$$

where: $\left(\frac{T_o}{W}\right)$ = initial thrust/vehicle weight

$\bar{w}$ = static displacement of sidewall per unit $\left(T_o/W\right)$

Equations (2.79) and (2.80) are valid for $\tau >> t_o$ and are to be used in calculating maximum response.

Eq. (2.79) as it stands, requires the summation

$$\sum_{n=1}^{\infty} A_n^* (1 - \cos \omega_n t) + \sum_{n=1}^{\infty} B_n^*$$

to be formed. For simplicity, the sum of the n components in the first quarter wave will be approximated by the maximum value of each component summed from $n = 1$ to ∞. Which is to say, convergence of the series will be assumed sufficiently rapid so that phasing between maximum values of each component can be neglected.

Thus:

$$\sum_{n=1}^{\infty} A_n^* (1 - \cos \omega_n t) + \sum_{n=1}^{\infty} B_n^*$$

$$= 2 \sum_{n=1}^{\infty} A_n^* + \sum_{n=1}^{\infty} B_n^*$$

$$= 2\left\{\left(\frac{\omega_o}{\bar{\omega}}\right)\sum_{n=1}^{\infty} F_n + \sum_{n=1}^{\infty} G_n\right\} - \left\{\left(\frac{\omega_o}{\bar{\omega}}\right)\sum_{n=1}^{\infty} F_n - \sum_{n=1}^{\infty}\left(\frac{I_o(m_n a)}{I_o'(m_n a)}\right) H_n\right\}$$

It is convenient to express the total maximum response for a step change in thrust in the form

$$h(a,o,t)_{\text{Step}} = h_o(a,o,o) + \bar{\omega}\left(\frac{T_o}{W}\right)\left\{2\left(\frac{\omega_o}{\bar{\omega}}\right)H_B^{\omega} + 2H_S^{\omega} - \left(\frac{\omega_o}{\bar{\omega}}\right)H_B^{\lambda} + H_S^{\lambda}\right\} \qquad (2.81)$$

where the subscripts B and S represent the contributions of bottom and sidewall relaxation respectively. The superscripts ω and λ represent the functional dependence of H_B and H_λ. From this definition we have

$$\left.\begin{aligned} H_B^{\omega} &= 2\sum_{n=1}^{\infty} F_n \\ H_S^{\omega} &= 2\sum_{n=1}^{\infty} G_n \\ H_B^{\lambda} &= -2\sum_{n=1}^{\infty} F_n \\ H_S^{\lambda} &= 2\sum_{n=1}^{\infty} \left\{\frac{I_o(m_n a)}{I_o'(m_n a)}\right\} H_n \end{aligned}\right\} \qquad (2.82)$$

Equations (2.82) have been computed for a range of tank geometries, (a/L) from 0.2 to 4 and a range of liquid depths, (d/L) from 0.2 to 1.0. Results of these calculations are plotted in Figures (2.34), (2.35) and (2.36).

Some Typical Thrust Decay Data - Thrust decay curves for a number of vehicles have been examined to determine the form of the thrust transient. Either an exponential or a ramp function appears to be suitable. Of the two, however, the ramp is a more realistic representation and tends to give a higher fluid free surface response. Coale and Nagano* idealize the Agena thrust transient as a double ramp while Edwards et al** indicate that the Apollo Service Module may be represented as a single ramp for the first second after thrust cut-off down to nearly one percent of its initial thrust. The two vehicles are represented in Fig. 2-37. Typical numbers for Saturn stages are:

*Coale and Nagano op.cit.

**AEDC Memorandum from C. A. Edwards, Jr./D. L. Reid to D. L. Kors: "Shutdown Transient Impulse for Apollo Engine 23 Tested at Altitude Conditions (Tullahoma, Tenn.) Memo: 9642:0328, 28 January 1966.

	Stage	t_o
Saturn:	SIC	0.5 sec.
	SII	0.25 sec.
	SIVB	0.1 sec.

The effect of a finite time duration, t_o, for thrust decay can be shown through a straightforward analysis of the response of a simple spring-mass oscillator using Laplace transform theory to be

$$h_{m}(a,0,t)_{ramp} \approx -2\bar{\omega}\left(\frac{T}{W}\right)\left[\frac{A_m^* \sin\omega_n t\,(1-\cos\omega_n t_o)}{\omega_n t_o} + B_m^*\right] \qquad (2.83)$$

with A_n^* and B_n^* defined by Equation (2.76).

Generally, the response of the free surface to a ramp input in thrust is less than that of a step input, but this effect is not particularly significant since the term B_m^* in Eq. (2.83) is not affected by t_o. Recalling that B_m^* is associated with response due to structural oscillation and A_m^* is associated with response due to slosh frequency, ω_m, the principal effect of a finite t_o is to suppress the response of the slosh modes. The contribution of the slosh modes to the total response becomes significant compared to that of the structural modes only at low fluid depth, d/L.

Conclusions and Applications . . . - The Agena and the Apollo Service Module represent extreme variations in the initial level of thrust and the duration of thrust decay and have been chosen to illustrate the use of the preceeding results. The oxidizer tanks of each vehicle are illustrated in Figures 2-38 and 2-39.

For this example, consider the response of the fluid surface at the tank wall when subjected to a step input for the following known conditions

	Agena	Apollo SM
Initial Thrust Level: $(\frac{T_o}{W})$	6.35 g's	0.36 g's
a/L	.5	.223
d/L	.5	.5
$\bar{\omega}$ (from Eq. 2.64),	.0137 in/g	.00304 in/g
$(\lambda/\lambda_{ref.})$ from Fig. 2-32,	1.4	Estim. 1.5
$(\frac{\omega_o}{\bar{\omega}})$ from Fig. 2-33,	1.0	.9
H_B^{ω} from Fig. 2-34	+.0550	negligible
H_B^{λ} from Fig. 2-34	-.0550	negligible
H_s^{ω} from Fig. 2-35	.0056	negligible
H_s^{λ} from Fig. 2-36	1.248	2.10
static deflection, h_o (a,0,0)*	.196 in.	.00418

Substituting in Eq. (2.81)

$$h(a,o,t)_{\text{Step}} = h_o(a,o,o) + \bar{\omega}\left(\frac{T_o}{W}\right)\left\{2\left(\frac{\omega_o}{\bar{\omega}}\right)H_B^{\omega} + 2H_s^{\omega} - \left(\frac{\omega_o}{\bar{\omega}}\right)H_B^{\lambda} + H_s^{\lambda}\right\}$$

Agena: = 0.310 in.

---

*Albert, op.cit.

Apollo Service Module: = 0.0065 in.

From these calculations it is seen that the static deflection of the tank walls and bottom contribute the largest part of the total response. Moreover, the contribution of the bottom of the tank due to the dynamic terms H_B^{ω} and H_B^{λ} is very small.

The effect of size is apparent in the static deflection quantity $\bar{w}$. From Eq. (2.64), $\bar{w}$ is

$$\bar{w} = \frac{\gamma a^2 d}{E h}$$

For very large vehicles the response of the fluid surface can be expected to be somewhat larger than the above calculations, because $\bar{w}$ is proportional to the square of the tank radius. In any event, the response appears to be insignificant even for step input in thrust decay.

It is concluded that the state-of-the-art for building fuel and oxidizer tank structures in the present generation of liquid propelled spacecraft is <u>not</u> likely to cause problems of excessive fluid motion due to structural relaxation of such tanks following thrust decay.

PASSIVE LIQUID RETENTION SYSTEM ANALYSIS

Introduction - This section is concerned with the discussion and analysis of passive propellant retention systems. The fundamental theory governing the operation of such systems will be derived and discussed together with various aspects affecting the proper operation of a passive retention system. The application of this theory to vehicle design and operation is illustrated in terms of some current designs proposed or in actual use on vehicles. Each design then will be analyzed in terms of the theory and operational requirements that have been outlined.

The considerations of this section shall be limited to "passive" propellant retention systems. These are devices having no moving parts which rely for operation on a combination of container geometry and propellant capillary properties (surface tension, density and wetting characteristics) to accomplish the positioning and retention of propellant masses in the presence of upsetting body forces due to vehicle maneuvers. Thus, excluded from consideration are those propellant management systems employing bladders, bellows, pistons, ullage rockets, valves, and dielectrophoretic forces. Although for certain specific applications a positive expulsion device such as a bladder or bellows may be more desirable, in general, the above listed systems have in varying degrees the disadvantages of large system weights, higher part count (and hence lower reliability), and material compatibility problems with rocket propellants currently employed. This is particularly true when these systems are employed in large propellant tanks for booster and upper stage vehicles. With the increased understanding of the behavior of capillary systems, passive retention systems for spacecraft have become ac-

cepted as the most generally desirable means of controlling propellant location. The results of a survey of most of the techniques employed for liquid propellant control and expulsion including those active systems listed above have been reported by Bell Aerosystems Co.* The advantages and disadvantages of these systems are discussed. The reader is referred to this source for more information regarding positive expulsion techniques.

The basic function of a spacecraft propellant retention system is to position all or a part of the liquid propellant in a partially filled tank at the tank outlet and supply propellant to the propulsion system (or to another tank in the case of a resupply tanker operation). This must be accomplished in the presence of the vehicle acceleration environment during its mission. Vehicle accelerations result from such sources as attitude control thrust, aerodynamic drag, secondary propulsion systems operation, docking, crew movements, solar pressure, gravity gradients, etc. The table below lists rough order of magnitudes for these accelerations for a typical vehicle mass of approximately 20,000 lbm.

Source (Not Orbit Dependent)	a/g_o
Attitude control, RCS, etc.	10^{-3} g_o
Centripetal due to roll rates (L = 4 ft.)	10^{-6}

*Bell Aerosystems Company, "Development of Expulsion and Orientation Systems for Advanced Liquid Rocket Propulsion Systems", Tech. Doc. Rpt. No. RTD-TDR-63-1048, AF Contract No. AF04(611)-8200, July 1963.

Source (Orbit Dependent)	Sun	Earth	Moon
Aerodynamic drag	-	10^{-6}	-
Radiation pressure	10^{-9}	-	-
Centripetal due to orbital rate	$4x10^{-14}$	10^{-6}	$7x10^{-7}$
Gravity gradient	$8x10^{-5}$	$3x10^{-7}$	10^{-7}

Because of the inertia of the propellants, the vehicle accelerations result in a propellant body force tending to move the liquid mass relative to the tank. If motion is to be prevented this body force must be opposed by some other force of equal magnitude. In this case, that force is produced by the surface tension at the liquid-gas interface, often referred to as a capillary force.

Capillary Stabilized Systems

Pressure Supported Systems - Reynolds* has proposed the terms "pressure supported" and "capillary supported" to describe two classes or modes of the stabilization of liquid masses in containers against gravitational forces by the action of surface tension forces. The first of these concepts can be illustrated with aid of the diagram of a tank partially filled with liquid shown in Figure 2-40a. If the tank is accelerated in the Y direction normal to the static equilibrium liquid-gas surface with magnitude α , the entire mass of liquid tends to "fall" away from its original position to the other end of the tank much like a piston. The retention of this mass in its original position is dependent on two criterion.

*Reynolds, W. C., M. A. Saad, and H. M. Satterlee, "Capillary Hydrostatics and Hydrodynamics at Low-g", Tech. Rept. No. LG-3, Mechanical Engineering Dept., Stanford University, Stanford, California, September 1, 1964.

One is the balance of forces on the liquid in the Y direction. Thus:

$$\sum F_y = 0 \quad \text{for static Y equilibrium}$$

$$\rho_g \pi R^2 - \pi \int_0^R \rho \alpha \, h(r) \, d(r) - \rho_\ell (y)_{y=0} \pi R^2 = 0$$

$$\text{or} \quad \rho_g - \rho_\ell = \frac{1}{R^2} \int_0^R \rho \alpha \, h(r) \, d(r) \tag{2.85}$$

This criterion should be considered in cases where ρ_g approaches the propellant vapor pressure such that the permissible value of $\rho_g - \rho_\ell$ approaches zero. For storable propellant systems this is generally of secondary importance.

The remaining criterion in this case concerns the relative ability of surface tension to resist deformation of the liquid-gas interface which allows an exchange of equal volumes of liquid and gas across the original equilibrium surface. This criterion is stated in terms of the Bond number, B_o, a dimensionless ratio of body forces to surface tension forces.

$$B_o = \frac{\rho g L^2}{\sigma}$$

where ρ = liquid density

g = local acceleration normal to the equilibrium liquid surface

L = container characteristic dimension (in most cases the tank radius)

σ = propellant surface tension

In general, this criterion can be stated as follows:

$$Bo \leq \Phi_1 \quad \text{for interface stability} \tag{2.86}$$

where Φ_1 is a function of the container geometry and contact angle between the liquid and container wall, θ. The dependence of Φ_1 on container geometry for axisymmetric tanks with no internal hardware has been thoroughly discussed by Reynolds (op cit). Seebold et al* presents the results of an analysis to determine the value of Φ_1 for annular tank geometries. The dependence of Φ_1 on contact angle is rather weak. In addition, most propellants in current use wet the tank walls quite well so that θ is of the order of 15° or less, further reducing for practical purposes this dependence.

Most propellant tank geometries combine right circular cylinders with hemispherical ends. For this broad class it can be stated:

$$Bo \Big|_{STABLE} \leq 0.8 \tag{2.87}$$

with R the tank radius taken as the characteristic dimension L. This includes cylindrical tanks with a centrally located standpipe.

The liquid-gas interface in a spherical tank with no internal hardware is unconditionally stable, as is pointed out by Reynolds (op cit). That is

$$Bo \Big|_{STABLE} = 0 \tag{2.88}$$

*Seebold, J. G., M. P. Hollister, and H. M. Satterlee, "Capillary Hydrostatics in Annular Tanks", Paper No. 66-425, AIAA 4th Aerospace Sciences Meeting, Los Angeles, California, June 27-29, 1966.

For all other tank geometries involving spheriods, conical walls, etc., specific reference must be made to the literature for values of Φ_1 .

The above then are considerations related to the case where the local acceleration vector is directed from the gas toward the liquid, tank pressure supports the liquid mass and surface tension stabilizes the liquid-gas interface.

Capillary Supported Stability - In most instances, however, the net acceleration vector of a propellant tank is not directed in the manner stated above but will either have a component parallel to the liquid surface or will be directed entirely normal to the axis of symmetry of the equilibrium surface. This is illustrated in Figure 2-40a by the acceleration vector β . In this case, the stabilization of the liquid is in the capillary supported sense. The hydrostatic pressure variation across the tank diameter, $\rho\beta(2R)$, is counterbalanced by a surface tension force associated with the distortion of the interface shape.

Analysis of this mode due to its asymmetry and nonlinearity has not yielded a stability criterion. Experimentation reported by Masica*, however, indicates a Bond number stability limit of 1 for right circular cylindrical tanks with no internal hardware, thus

$$Bo\Big|_{STABLE} = \frac{\rho\beta R^2}{\sigma} \leq 1 \qquad (2.89)$$

for transverse acceleration components in clean tanks.

*Masica, W. J., D. A. Petrash, and E. W. Otto, "Hydrostatic Stability of the Liquid-Vapor Interface in a Low-Acceleration Field", NASA TN-D-2267, May 1964.

Since the locational stability of liquid masses in both of the above cases is largely governed by the stability of the liquid-gas interface which in turn is highly dependent on the characteristic container dimension, L, the technique most generally employed is to reduce this dimension. This can be accomplished with little loss in tank flow area by placing a screen grid or perforated plate surface at the liquid-gas interface position. This stabilization surface is illustrated in Figure 2-40b. For the liquid at this screen grid surface, the characteristic dimension L now becomes r which is much smaller than R, resulting in interfacial stability to much higher acceleration levels.

For the pressure supported capillary stabilized surface

$$Bo\Big|_{STABLE} = \frac{\rho \alpha r^2}{\sigma} \leq 0.8$$

in each screen or perforated plate opening where r is the effective hole radius.

Again, since in most cases all or a component of the net acceleration vector will be parallel to all or some portion of a stabilization surface, attention will be turned to the stability criterion for this case. This criterion is a form of capillary supported stability and can be illustrated by the analysis that follows.

Consider a container enclosing a mass of liquid that has a density, ρ , and surface tension, σ , against the surrounding gas. See Figure 2-41. The local acceleration, β , acts in the direction shown. On one side of the container at its extreme top and bottom a distance, h, apart are located

holes of radius r. The hole radius is small compared to the local hydrostatic pressure variation so that the liquid-gas interface can be considered spherical with radius R (i.e., hole Bond No. $\frac{\rho g r^2}{\sigma} < 0.1$). The system contact angle is indicated as θ. Writing the pressure drops across the curved liquid-gas interface at the upper and lower holes in accordance with the Laplace relation:

$$p_o - p_a = \sigma \left(\frac{1}{r_1} + \frac{1}{r_2} \right)_a = \frac{2\sigma}{R_a}$$

$$p_b - p_o = \sigma \left(\frac{1}{r_1} + \frac{1}{r_2} \right)_b = \frac{2\sigma}{R_b}$$

the hydrostatic pressure difference between holes is

$$p_b - p_a = \rho \beta h$$

combining the above yields

$$\frac{\rho \beta R_a h}{2} = 2 \left(1 - \frac{R_a}{R_b} \right) \tag{2.90}$$

From the geometry of the surface at the upper hole

$$r = R_a \cos \theta$$

Substituting this into (2.90) yields

$$\frac{\rho \beta r h}{\sigma} = 2 \left(\cos \theta + \frac{r}{R_b} \right) \tag{2.91}$$

The development of an analytical relation beyond this point is dependent on more explicit knowledge of the influence of hole geometry, contact angle, and contact angle hysteresis on the shape and size of the liquid gas interface in the containment surface holes. Rather than attempt this, all the

known parameters can be grouped on the left hand side of the equation as was done in Equation 2.91 leaving those aspects about which accurate assumptions could not be made to the right hand side as a non-dimensional constant for the particular system, a constant which can be examined experimentally. Thus, we may write:

$$\frac{\beta r h}{\sigma/\rho} \leq \Phi \qquad (2.92)$$

where $\Phi = \varphi$ (contact angle, contact angle hysteresis, containment surface geometry).

A theoretical upper limit for the value of Φ for circular holes is 4 since this represents one full bubble pressure based on hole radius at the top and one full drop pressure at the bottom based on hole radius. This amounts to an inversion of wetting between holes and is, of course, difficult to obtain in a practical situation. In this line of thinking, for a really good wetting combination ($\theta = 0$) a Φ value of 2 would indicate one "bubble pressure" based on hole radius with no aid to containment furnished by the "lower" holes. In Equation 2.92 it is understood that the distance h must be measured parallel to the direction of β and be the maximum wetted distance along this line of action.

Experiments performed at LMSC and reported by Hollister* show that Φ is a weak function of the parameters indicated in Equation 2.92 varying between 1.5 and 3.5. For the purposes of setting an unconditional stability limit

*Hollister, M. P., "Propellant Containment Utilizing Screen Mesh and Perforated Plate Surfaces", LMSC/A665481, Lockheed Missiles and Space Company, December 1964.

then, the following would apply:

$$\frac{\rho \beta r h}{\sigma} \leq 1 \qquad (2.93)$$

The above stability limit consideration was also reported by Jetter* and verified by a series of experiments.

Retention System Refill - During the operation of passive retention system, the volume within the system may become partially emptied of liquid. This can occur as the result of an acceleration exceeding one of the above stability limits allowing pressurant gas to enter the volume in exchange for the loss of liquid or by necessity and design as during an engine startup sequence. This is illustrated in Figure 2-42. Shown in (a) is a partially empty propellant tank containing a simple propellant retention device consisting of a perforated metal sheet spanning the tank above the outlet enclosing a volume bounded by the tank walls and the retention surface. The main body of propellant has been disoriented and is located at the opposite end of the tank, leaving one side of the containment surface in partial or total contact with the pressurant gas. Engine restart (Figure 2-42b) results in a withdrawal of propellant from the retention volume. As it takes a finite time for the propellants to reorient and arrive at the drain end under the resulting vehicle acceleration, α , pressurant gas is drawn into the retention volume. The main body of propellants then arrive and begin flow past the retention surface to meet the engine demand (Figure 2-42c). The gas within the retention volume must be expelled prior to the next engine start or the possibility exists that a portion of this gas will be ingested at restart causing engine malfunction.

As will be shown analytically below, once propellant is oriented so as to cover the retention surface, a portion of this pressurization gas will remain trapped with the retention volume (as in Figure 2-42d) unless provision is made in the system design to vent this gas volume.

Refill Under Engine Thrust - Consider Figure 2-43 which is a diagram of a portion of a passive propellant retention system such as might be employed at the drain. As the reorienting propellant approaches the retention system, the liquid level inside retention volume is at some distance h_i below the top of the retention system with pressurant gas above it at pressure p_o . The flow rate, ω , to the engine will be very much less than the propellant flow entering retention system region. Thus, h_i will begin to diminish as the propellant level rises. Due to the large propellant mass flux outside the retention surface, this surface will become quickly submerged. The level in the retention volume will continue to rise until the gas pressure in the retention system is p_{v_s} (see Figure 2-43),

where $$p_{v_s} = p_o + \rho \alpha (H + h_f)$$

and $$h_f = h_c + h_L$$

For h to be reduced below h_f, gas would have to be expelled past the retention surface against the capillary bubble pressure. Thus

$$h_o = \frac{\Delta p_c}{\alpha \rho}$$

This is another form of the capillary supported stability criterion.

$$\frac{\alpha \rho h_o r}{\sigma} = 2, \quad \therefore \quad h_o = \frac{2\sigma}{\alpha \rho r} \tag{2.94}$$

Flow thru the retention surface results in a pressure loss which is reflected as an additional head differential, h_L, relative to the pressure outside the surface.

Thus, $$h_L = C_L \frac{\rho V_s^2}{2 g_c} \qquad (2.95)$$

where V_s is propellant velocity in the retention surface holes

C_L a loss coefficient. In general $C_L \approx 1.2$, and

g_c is the conversion factor from mass to force units.

The above consideration illustrates the fact that pressurant gas drawn into a passive retention system is not entirely expelled when the exterior portion of retention surface becomes wet. Note particularly that retention surfaces normal to vehicle thrust axis having no value for h_f are particularly poor from this standpoint since at all points along the surface the liquid pressure in the exterior exceeds the interior trapped gas pressure.

Means for eliminating or reducing the trapped volume include venting to main ullage volume or configuring the containment surface so the volume associated with the entrapment height, h_f, is small. A conical retention surface shape is an example of the latter. These are illustrated in Figure 2-44.

Refill Under Capillary Forces - The refill considerations above apply to those conditions resulting in the submergence of a retention system by the bulk of the propellant. If the retention system is large enough or the propellant level in the tanks low enough this may not occur. If this condition results

in a portion of the retention surface becoming dry, allowing gas pressure communication between gas in the retention volume and the ullage pressurant gas; then, during a period of zero or low gravity, the retention system can refill itself under the action of surface tension forces if properly designed. This is depicted in Figure 2-45 which shows a representative-retention system placed over the tank drain and consisting of a right circular cylinder with a screen mesh connecting the base to the tank wall and closed off across the top by another screen mesh. The propellant is a good wetting combination with the tank materials (i.e., contact angle near zero). In "a" the retention system is partially full. The gas in the reservoir has pressure communication to the ullage pressurant via the screen at the top. Following a reduction of the acceleration level such as at main engine shut off, the propellant interfaces interior and exterior to retention system will assume the characteristic capillary dominated curved interface shape. From the Laplace relation we can determine the pressure change across each interface as a function of the surface curvature:

For the retention system

$$p_o - p_2 = \sigma\left(\frac{1}{r_1} + \frac{1}{r_2}\right) \approx \frac{2\sigma}{r}$$

For the tank

$$p_o - p_1 = \sigma\left(\frac{1}{R_1} + \frac{1}{R_2}\right)$$

Noting that

$$2R_1 = R - r$$

and that R_2 in this annular geometry is very large so that

$$\frac{1}{R_2} \longrightarrow 0$$

we have

$$p_0 - p_1 = 2\sigma\left(\frac{1}{R-r}\right)$$

combining the above to eliminate p_0 yields

$$p_1 - p_2 = 2\left(\frac{1}{r} - \frac{1}{R-r}\right)$$

In the absence of a vehicle acceleration, the above relation states that the propellant will flow into the retention system in response to the capillary pressure difference if

$$\frac{1}{r} > \frac{1}{R-r}$$

is in the local region of the retention system.

Considering the effect of a small axial acceleration component, α , that produces a hydrostatic pressure variation, we write

$$p_1 - p_2 = \rho\alpha(h_2 - h)$$

For complete system refill by capillary action in the presence of a positive acceleration, α ,

$$\Delta p \text{ (capillary)} \geq \Delta p \quad \text{(hydrostatic)}$$

or

$$2\sigma\left(\frac{1}{r} - \frac{1}{R-r}\right) \geq \rho\alpha(h_2 - h_1)$$

setting $(h_2-h_1)_{max.} = H$

where H is the height of the retention system, we have

$$\alpha \leq \frac{2\sigma}{\rho H}\left(\frac{1}{r} - \frac{1}{R-r}\right) \qquad (2.96)$$

for complete capillary refill.

The rate of system refill is a function of the driving forces on the liquid mass and the dissipative forces, all of which are strongly dependent on the particular system geometry. The transient process of retention system refill can be expressed in terms of a differential equation in refill height, h, derived from Newton's Second Law thus:

$$F_{Cap} + F_{Hydro} - F_{Dissip} = m(t)\,\ddot{h}(t) \qquad (2.97)$$

F_{Cap} is a function of tank and retention system geometry, system wetting characteristics and surface tension.

$$F_{Cap} = f(\sigma, \theta, R, r)$$

Acceleration induced body forces, F_{Hydro}, are dependent on the propellant density, ρ, local acceleration, α, and height differences, h.

$F_{Dissipative}$ is a function of the propellant velocity, $\dot{h}$, flow area ratios and propellant viscosity μ.

The propellant mass, m(t), engaged in the system refill will be time varying in value, being a function of h.

The comments above point out the essential aspects of retention system refill under surface tension and small body forces. Details of a particular system

design must be considered in applying these in an analysis. Siegel* presents a more detailed discussion pertaining to the transient flow characteristics of a capillary system.

Partial or Total Propellant Retention - An initial consideration in retention system design is whether it is required to control with the passive system all or a specific smaller volume of the propellants. The governing criterion in this case is the stability criterion for capillary supported systems,

$$\frac{\rho g r h}{\sigma} = 1 \text{ for unconditional stability,}$$

since upsetting accelerations other than those aligned with the thrust axis will occur and must be considered. The two alternatives are illustrated in Figure 2-46. In order to keep the gross retention system dimension "h" at a low value so that the permissible upsetting acceleration may remain large, total propellant control generally results in large retention system surface areas and weights relative to the tank weight. In this regard, total retention is not attractive for large propellant tanks, but may be acceptable for smaller tank sizes associated with attitude control or secondary propulsion systems.

The approach with partial propellant control is to retain at the tank outlet sufficient propellant to assure engine start and settling of the bulk of the propellant. This provides a minimum volumetric requirement for the retention system in order to prevent pressurant gas entering the engine feed line.

*Siegel, R., "Transient Capillary Rise in Reduced and Zero-Gravity Fields", ASME, Trans., Ser. E. J. Appl. Mech., Vol. 28, June 1961.

$$\mathcal{V}_{R.S.}\Big|_{MIN} = \mathcal{V}_{s.t.} + \mathcal{V}_{s} + \mathcal{V}_{p.t.} + \mathcal{V}_{r.f.} \qquad (2.98)$$

where
- $\mathcal{V}_{R.S.}$ = propellant volume to be retained
- $\mathcal{V}_{s.t.}$ = volume required for engine start transient
- $\mathcal{V}_{s}$ = volume required to settle bulk of propellant
- $\mathcal{V}_{p.t.}$ = volume required to provide a liquid level above the drain to prevent "pull-through" or suction dip
- $\mathcal{V}_{r.f.}$ = volume associated with any inability to completely refill the system

The above breakdown is somewhat arbitrary but provides a list of those aspects which must be considered in an analysis of a partial retention system.

The engine start transient is characterized by propellant withdrawal from the retention volume under low gravity conditions building up to rated thrust and a high acceleration condition. This volume of propellant is that necessary to fill passages downstream of valves, thrust chamber fuel or oxidizer leads, turbine flow (for pump fed engines), etc. This requirement, of course, is dependent on the particular engine system. Also, since the flow occurs initially under very low gravity conditions, the tendency for pull-through or suction dip is extreme. Thus, the tendency of the propellant surface to follow locally large velocity potential gradients in the absence of gravity potential gradients must be considered in the shape of the retention system.

Depending on such factors as tank shape, fill level, and reorientation Bond number, a finite amount of time is required for the wave front of the bulk propellant to arrive at the retention system. During this period the propellant volume V_S is withdrawn from that in the retention system.

Just prior to the start of refill of the retention system by the reorienting propellant, the propellant level in the system may be low, thus placing the interface close to the tank outlet. Under these conditions, pull-through or suction dip is possible. The volume of propellant, $V_{p.t.}$, is that which then cannot be drained or scavenged from the tank bottom, but must be provided to prevent pull-through.

Finally, due to the considerations discussed above regarding refill, it may not be possible with a particular design to completely refill the retention system following the initial engine restart with deoriented propellants and volume, $V_{r.f.}$, must be provided to prevent propellant depletion in the retention system during a subsequent start.

Applications to Vehicle Design and Operation - The discussion above presented those considerations and design criteria generally essential to the analysis and design of a passive propellant retention system. Summarized, these are:

1. Interfacial Stability, Pressure Supported:

$$\frac{\rho g R^2}{\sigma} \leq \Phi_1 \qquad 0.8 \leq \Phi \leq 2$$

for most common tank geometries and propellants

2. Interfacial Stability, Capillary Supported:

$$\frac{\rho g r h}{\sigma} \leq \Phi \qquad 1 \leq \Phi \leq 3$$

3. Retention System Refill
4. Volume Size for Partial Retention System

In this section, some vehicle designs in current use or proposed for use will be presented and analyzed in terms of the above. Many of the design details of the systems below reflect particular requirements of the vehicle, its mission, or compromises that do not originate from passive retention considerations and are not immediately obvious. It is not the purpose here to justify or criticize these details without the necessary background information. Only design aspects illustrating passive retention behavior will be considered.

Agena Retention Sump - Shown in Figure 2-47 is a diagram of the Agena SO1B Containment and Scavenging Sump (Oxidizer) currently in use on the Standard Agena upper stage. Only the oxidizer sump is shown since the fuel sump is similar and is based on the same design philosophy. Figure 2-48 shows the placement of the sumps relative to the propellant tanks and engines. The sump inlet is covered by a conical shaped containment surface with the gross dimensions shown. This surface is a stainless steel screen constructed of 0.0035" diameter wire with a mesh 84 x 84 wires per inch providing 50% open area. The screen holes are nominally 0.0084" square; thus, the "r" dimension is 0.0042". Also shown in the sump interior above the outlet duct is a disk shaped pleated screen which spans the sump diameter and a velocity control plate at the junction of the sump and the outlet duct. The pleated screen is constructed of the same material as the containment or retention screen.

The design is typical of the partial retention approach. Between the pleated screen and the retention surface the sump volume is sized to provide restart

propellants, $V_{R.S.}$. This is made possible in small vertical dimension in part by the pleated screen and velocity control plate. The basic function of these devices is to "smooth out" the velocity profile above the outlet duct and thereby delay the onset of gas pull-through (or suction dip) during the engine start transient and sump refill sequence.

Table 2-I is a summary of the expected maximum acceleration environment for the Agena in the oxidizer sump region. With the dimensions of the containment screen given above and the oxidizer properties, the stability limits for the retention surface can be determined.

For the oxidizer (IRFNA)

$$\sigma/\rho = 26.2 \ cm^3/sec^2$$

Considering the three-dimensional shape of the retention surface and the fact that the screen hole radius dimension r is much smaller than any characteristic gross dimension h for the surface, it is apparent that the governing stability limit is that associated with a capillary supported system rather than that for the pressure supported system. For this stability mode, the limiting accelerations in the vertical and transverse directions to the retention screen are calculated below.

$$\frac{\rho g r h}{\sigma} = 1$$

$h_{Vertical} = 2" = 5.08$ cm

$h_{Transverse} = 8.8" = 22.4$ cm

$$r = 4.2 \times 10^{-3}" = 10.68 \times 10^{-3} \text{ cm}$$

$$g_o = 980 \text{ cm/sec}^2$$

$$g/g_{o\ \text{Vert.}} \leq 1. \frac{26.2}{(5.08)\ (0.01068)\ 980}$$

$$\leq 0.483$$

similarly

$$g/g_{o\ \text{Transv.}} = 0.1097$$

These stability limits are in excess of any upsetting acceleration expected in flight.

Refill of the sump volume is accomplished under the main engine thrust at acceleration levels of 2 g_o or greater. These levels are larger by a factor of 5 or greater than the stability limit calculated above for g/g_o vertical. Thus, the entrapped gas that can be stabilized below the retention screen following refill is less than the 2" height of the screen. Testing under 1 g_o conditions during the sump development has borne this out.

Apollo Service Module Retention System* - A schematic diagram of the propellant retention "can" installed in the oxidizer sump tank of the Apollo Service Module is shown in Figure 2-49. The configuration of the fuel system is essentially identical. Dimensions shown are in inches. Propellant flow from the tank to the engine is as shown by the arrows. The volume beneath the umbrella screens communicate with the outer tank volume via the still-well pipe which runs the length of the tank, having six 3/8 in. diameter

* A more detailed analysis of the failure modes of this retention device has been performed as part of the study and is reported later in this report.

holes at the top on the pipe circumference.* The umbrella screens are perforated metal sheets with hole perforations 0.02" in diameter.

The propellant in this case is N_2O_4 which has the following values for surface tension and density, respectively:

$$\sigma_{N_2O_4} = 26.5 \ \text{dynes/cm}$$

$$\rho_{N_2O_4} = 1.45 \ \text{gm/cm}^3$$

With the information above the various liquid-gas interface stability limits can be calculated.

a) In the tank region above the retention sump for pressure supported stability

$$\frac{\rho \alpha R^2}{\sigma} \leq \Phi_1 \ ; \ \Phi_1 = 1.4 \text{ for } \frac{r_i}{r_o} = 0.1 \ \text{/}$$

$$\therefore \left.\frac{\alpha}{g_o}\right|_{STABLE} \leq \frac{1.4\,(26.5)}{1.45\,(25)^2\,(2.54)^3\,980} = 6.48 \times 10^{-6}$$

for capillary supported stability **

$$\frac{\rho R^2 \beta}{\sigma} \leq \Phi_1 \approx 1$$

$$\left.\frac{\beta}{g_o}\right|_{STABLE} \leq 4.62 \times 10^{-6}$$

---

* The stillwell contains a propellant level gauging system.

**Assumes that the stillwell diameter does not effect the transverse stability characteristic appreciably as given by Masica (op cit)

/ Seebold, J.G., Hollister, M.P., and Satterlee, H.M. (op cit)

b) In the tank region below the sump level for pressure supported stability

$$\frac{\rho R^2 \alpha}{\sigma} \leq \Phi_1 \qquad \Phi_1 = 1.8 \text{ for } \frac{r_i}{r_o} = 0.29$$

$$\left.\frac{\alpha}{g_o}\right|_{STABLE} \leq 8.33 \times 10^{-6}$$

c) The value for capillary supported stability to transverse accelerations in this region where the annulus radius ratio is 0.29 is not known.

d) The pressure supported stability limit in the inner annulus space surrounding the stillwell inside the retention sump (see Figure 2-49 (1)) is

$$\frac{\rho r^2 \alpha}{\sigma} \leq \Phi_1 \qquad \Phi = 1 \text{ for } \frac{r_i}{r_o} = 0.7$$

$$\left.\frac{\alpha}{g_o}\right|_{STABLE} \leq 2.4 \times 10^{-4}$$

The capillary supported stability limit for the umbrella screens is somewhat dominated by the presence of the stillwell as, effectively, a large diameter gas path into the volume below the screens. Disregarding this effect for the moment, the stability limits for umbrella screen number (2) (see Figure 2-49) are:

a) Transverse directed

$$\frac{\rho \beta d h_\beta}{2\sigma} \leq 1 \qquad h_\beta = 50'' \qquad d = 0.02''$$

$$\left.\frac{\beta}{g_o}\right|_{STABLE} \leq 5.8 \times 10^{-8}$$

b) Axial directed

$$\frac{\rho \alpha d h_\alpha}{2\sigma} \leq 1 \qquad h_\alpha = 3"$$

$$\left.\frac{\alpha}{g_o}\right|_{STABLE} \leq 9.6 \times 10^{-2}$$

The above axial stability limit is modified considerably when the effect of the stillwell is considered. For the extreme case with a tank fill level such that the retention sump and stillwell are full due to capillary pumping and contain the remaining propellant as shown in the simplified diagram of the retention system in Figure 2-50a. In this case, the gross system dimension, h, is of the order of the tank length, 165"-13" = 152".

Hence,

$$\left.\frac{\alpha}{g_o}\right|_{STABLE} \leq \frac{3}{152} \times 9.6 \times 10^{-2}$$

$$\leq 1.89 \times 10^{-2}$$

The transverse stability limit is altered also by the presence in the system of the 3/8" diameter holes. In this case

$$h = 25"$$

$$r = 3/16" = 0.475 \text{ cm}$$

Yielding

$$\left.\frac{\beta}{g_o}\right|_{STABLE} \leq 4.9 \times 10^{-4}$$

As is the case with the Agena system discussed above, the configuration is representative of the partial retention approach to propellant containment. In this case, the volume of propellant enclosed in the retention system is considerably greater than that for the Agena sump. The retention can and volume beneath the umbrella screens contain approximately 4.8% of the sump tank volume as compared to approximately 0.67% for the Agena sump (it should be noted that the percentage of total tank volume is less since there is a storage tank in series with the sump tank for each propellant). It is apparent that the volume contained in the Apollo sump then is greater than the minimum amount required to provide engine restart and, therefore, could be the result of some other requirement such as the amount of impulse propellant for the final Service Propulsion System thrust period.

Propellant flows from the tank to the outlet through a "syphon" represented by the annular passage (1) shown in Figure 2-49. When the propellant level in the tanks is approximately 3% of the tank volume, the interface will enter this annular passage. The stability limit calculated above for this passage is 2.4×10^{-4} g_o which is certainly less than that which would exist during Service Propulsion System engine thrust. Thus, the interface would not be stable, allowing pressurant gas to enter the annulus while the propellant fell back into the sump entrance region "breaking the siphon". In this manner, the propellant in this annular passage cannot be scavenged from the tank.

The relative complexity of this retention system can be partly attributed to the rather specific mission profile for the Apollo system. Once the precise sequence of events and mission requirements for a propulsive system have been set down to include acceleration levels, the designer for a passive retention system is free to incorporate features intended to exercise control at predicted situations often resulting in a more complex design.

Propellant Feed System for Ion Engine Application - An example of a total propellant control system has been proposed for use with a cesium ion rocket engine and is discussed by Barcatta, et al*. In this case, not only is propellant positioning desired but, in addition, propellant feed to a porous vaporizing surface is sought. The propellant vapors are then used in the electrical propulsion system. It should be emphasized here that the thrust levels for these propulsion systems are extremely low producing accelerations of the order of 10^{-4} g_o for a moderate vehicle mass.

Conceptually, the passive propellant control system is shown in Figure 2-51a and consists of a three dimensional porous media or "sponge" with void space size decreasing in the direction of the propellant tank outlet. In this manner, capillary pumping provides an effective accelerating force in the flow direction. A simplified relation for the acceleration on the liquid mass is derived in the reference above and states

$$\gamma = \frac{4\sigma}{a^2 \rho g_o} \frac{da}{dx}$$

*Barcatta, F.A., H. L. Daley, A. H. Firestone, A. T. Forrester, "Zero G Propellant Feed Systems for Cesium Ion Rocket Engines", AIAA, Electric Propulsion Conference, Colorado Springs, Colorado, March 11-13, 1963. AIAA No. 63027.

where: σ = interfacial tension

ρ = liquid density

g_o = standard gravity

a = effective pore diameter

$\frac{da}{dx}$ = pore size gradient = 1.0

γ = acceleration in number of g_o's on liquid

Barcatta reports tests conducted on porous steel "sponges" having extremely low density values of 5 to 10 percent of the solid material. With pore sizes of the order of 100 microns ($a \sim 10^{-2}$ cm), the media produced capillary pumping accelerations of the order of 2 g_o. Hence, for a space vehicle application where a reduction in environmental acceleration level to say 10^{-2} g_o can be expected, porous media with a 1 cm pore size can be employed and still have a tank volume that is capillary dominated. Also, with a larger allowable pore size for the low environment, a decrease in "sponge" density could be expected. Nonetheless, from the standpoint of total system weight, the use of a total propellant control system such as the above is justifiable only when the propellant tank weight is a small percentage of the total vehicle mass. Main propulsion system tankages have "densities" (tank dry weight to volume ratio) of the order of 2 lb/ft^3. For a capillary sponge with a density as low as 1% of the solid material, the tank dry weight would still be doubled using say aluminum ($\rho_{AL.}$ = 179 lb/ft^3) sponge material.

Conclusions

In this section, those aspects of passive propellant retention that are fundamental to the design, analysis and operation of such systems have been pre-

sented. The various modes by which capillary forces stabilize propellant masses against upsetting vehicle accelerations have been pointed out. Finally, the application of those principles is illustrated in terms of passive retention system designs proposed or in actual use on space vehicles.

Beyond the fundamental considerations pointed out, the particular configuration of a passive propellant retention system is highly dependent on the specific mission and vehicle system to which this technique is applied. In this respect, no particular passive retention system is the best for all applications. In view of a general desire to minimize system weight and design complexity, however, a partial retention system is more suitable than a total retention system. Furthermore, a partial retention system controlling only the minimum amount of restart propellant necessary to provide propulsion system restart and steady state operation would be recommended. This approach results in a small retention system size, making it possible to provide a design stable under a wide variety of upsetting acceleration levels as well as resulting in minimum vehicle weight increments.

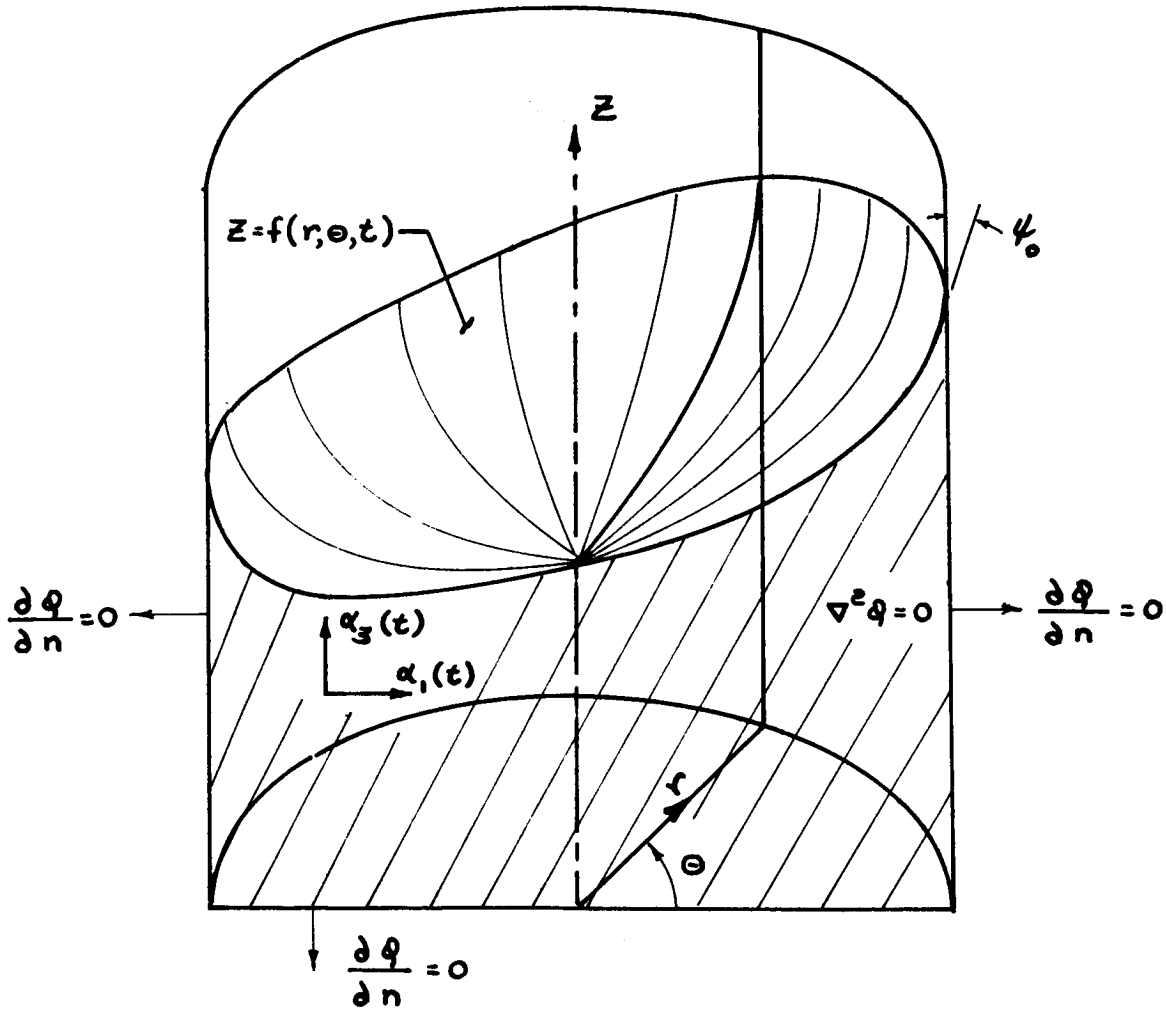

Container Geometry and Free Surface

Figure 2-1

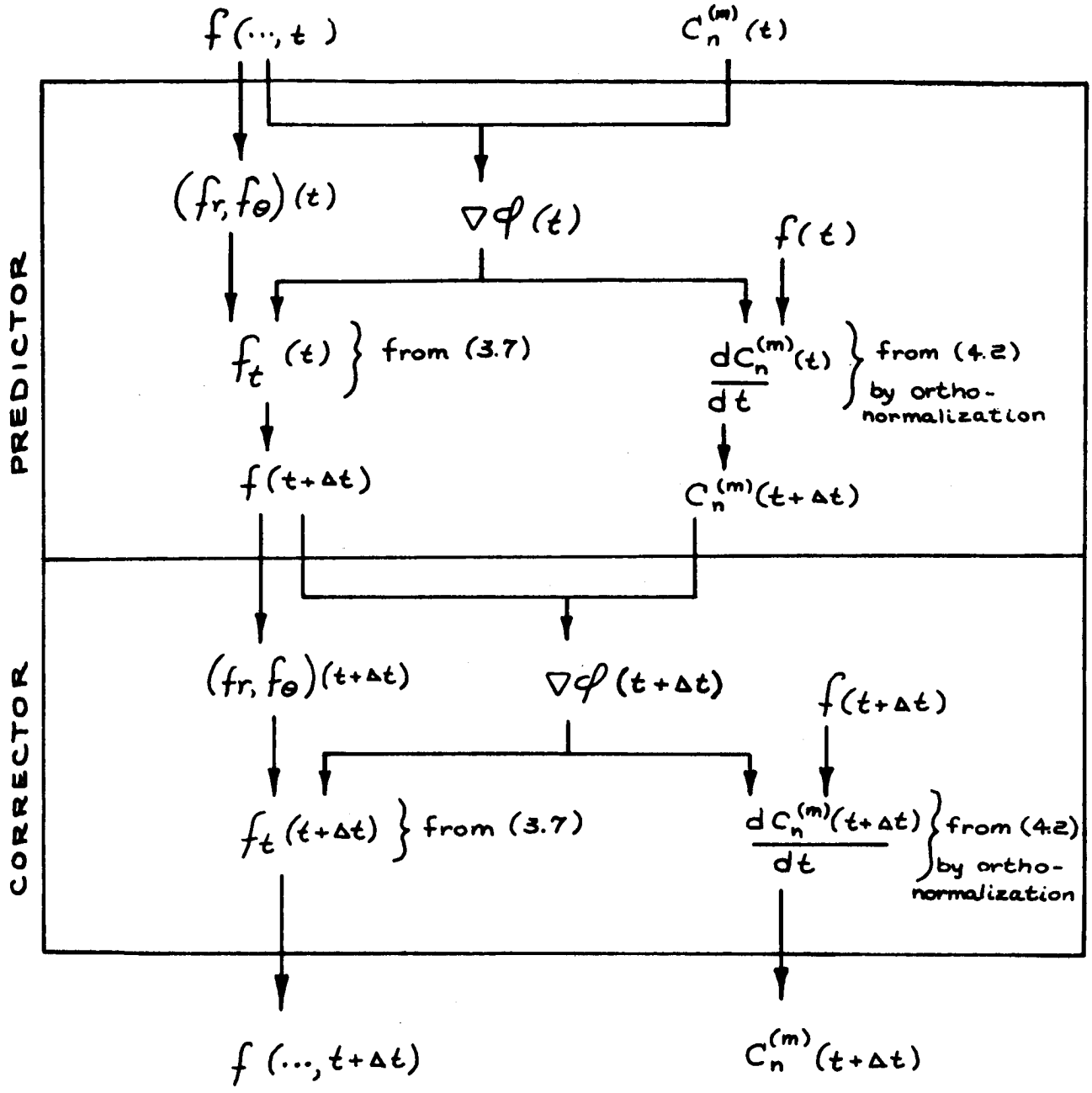

Computation Scheme for Separation of Variable Approach

Figure 2-2

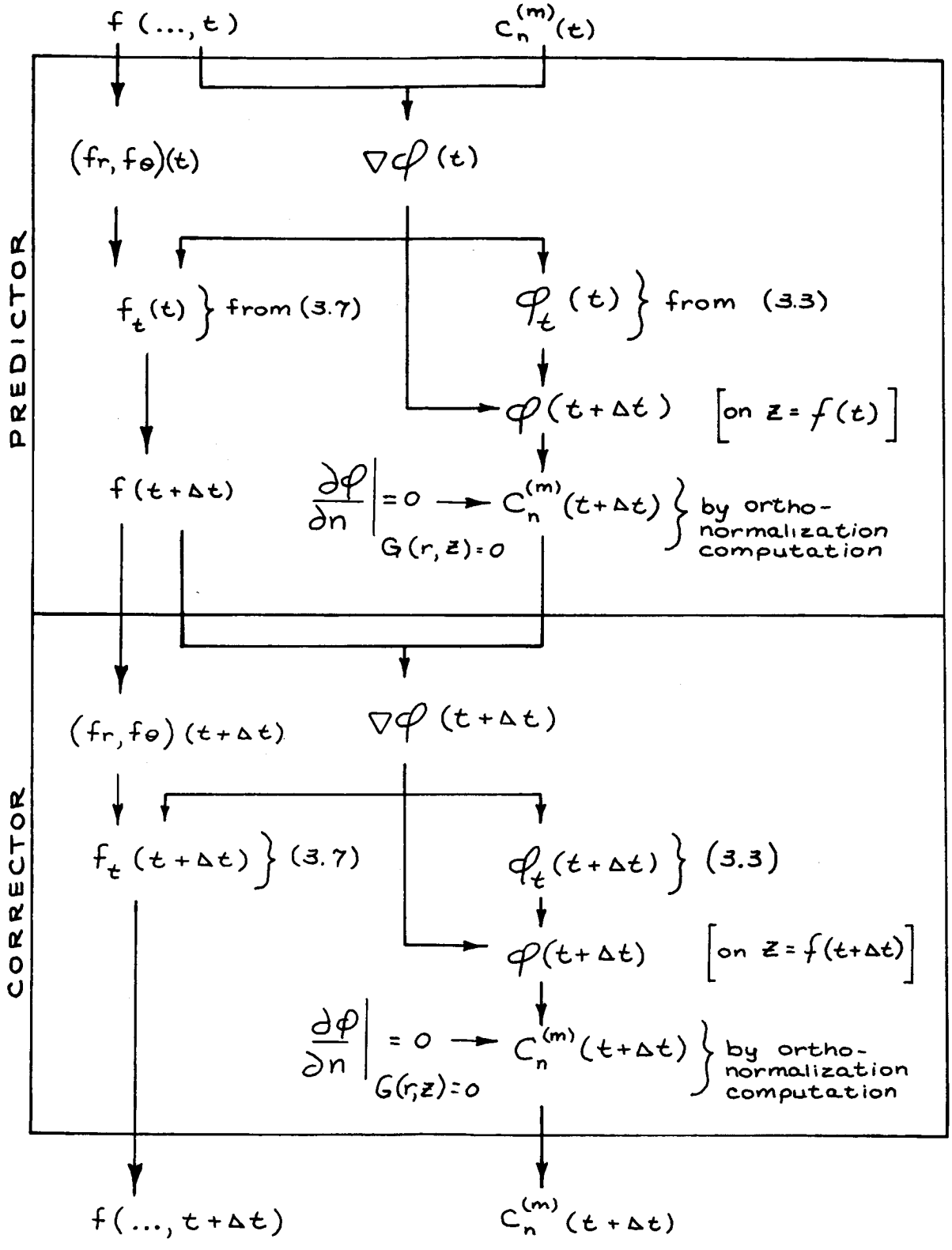

Computation Scheme for Harmonic Polynomials Approach

Figure 2-3

Note: Figures 2-4, 2-5, 2-7, 2-9, 2-11, and 2-13 thru 2-18 are digital computer plotter output.

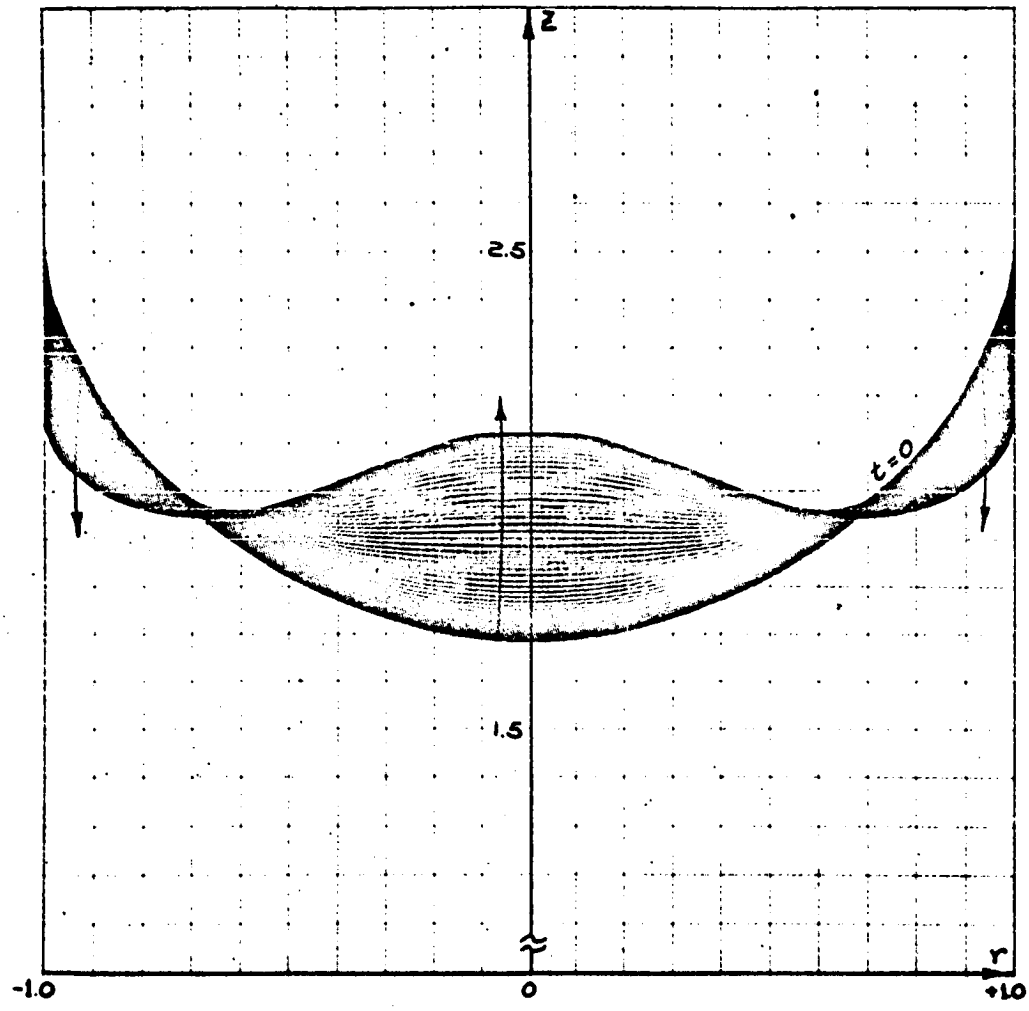

Symmetric Oscillation: Spherical Initial Shape

with H = 2.0, ψ_0 = 15°, α_3 = -1.0, β = 0.1,

Δt = 0.025, $0 \leq t \leq 2.57$.

Figure 2-4

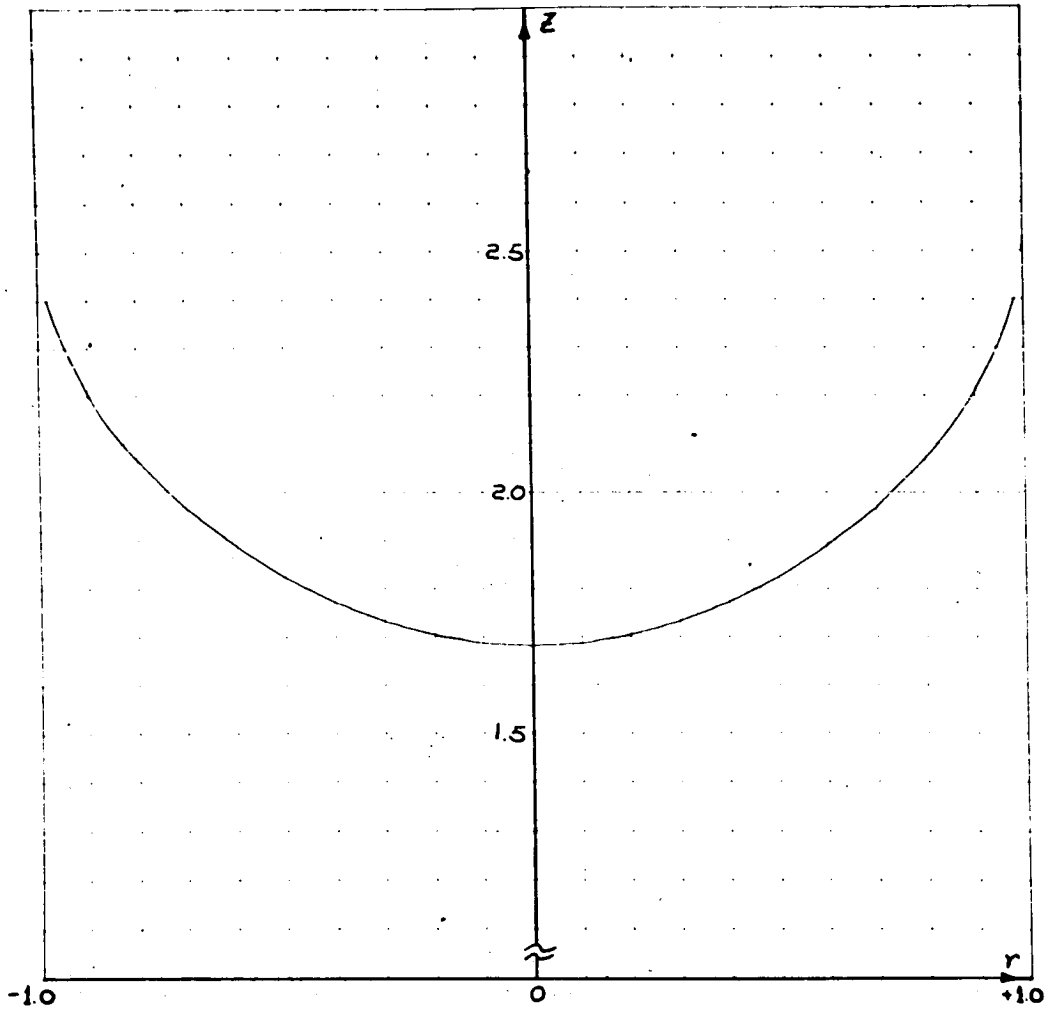

The Surface Shape for Figure 2-4 After One Cycle

Figure 2-5

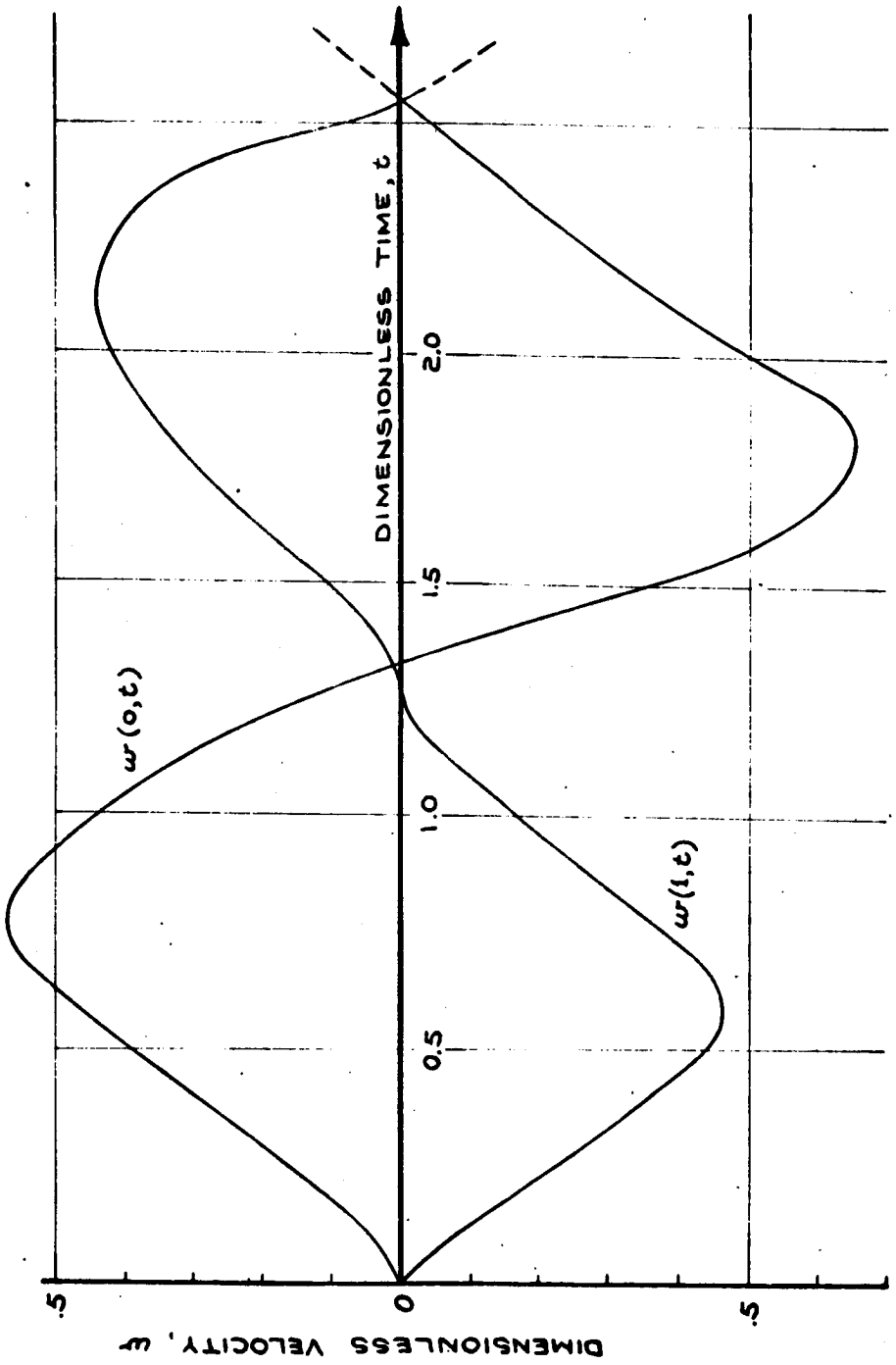

The Vertical Velocity Profile for the Motions in Figure 2-4

$\alpha = -1$, $\beta = 0.1$, $\psi_0 = 15°$

Figure 2-6

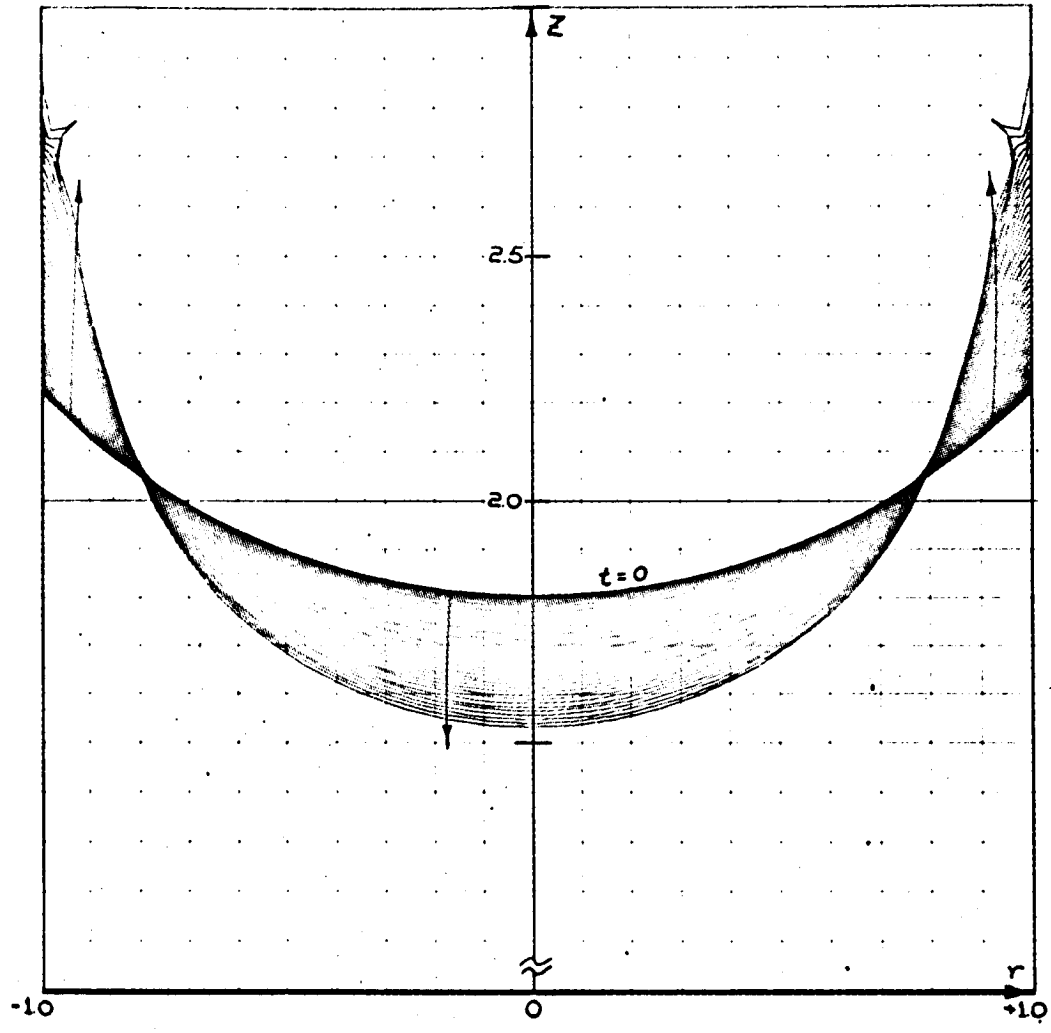

Symmetric Reorientation: Spherical Initial Shape

with $\psi_0 = 45°$, $H = 2.0$, $\alpha_3 = +1.0$, $\beta = 0$,

$\Delta t = 0.02$, $0 \leq t \leq 1.08$.

Figure 2-7

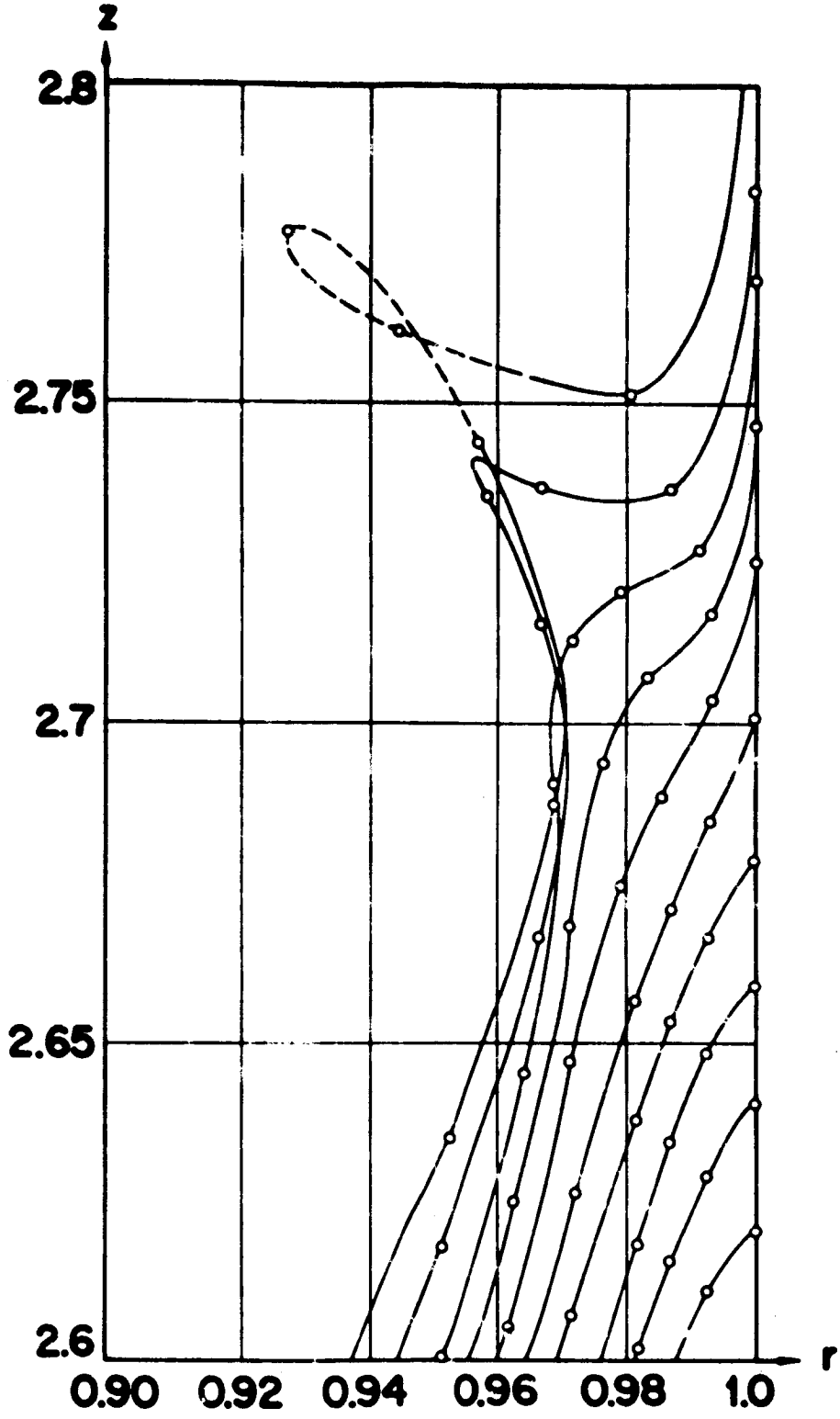

The Breakers at the Wall for the Case in Figure 2-7

Figure 2-8

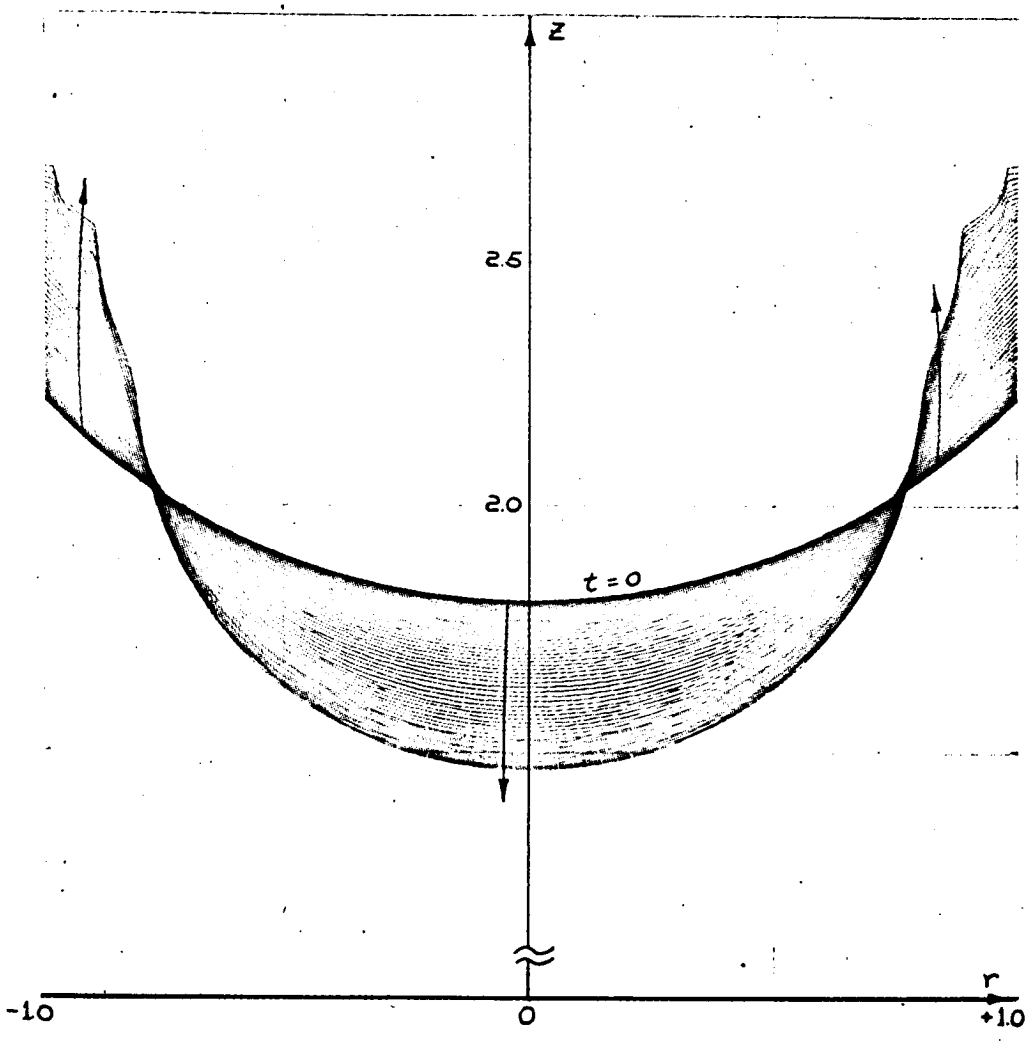

Symmetric Reorientation: Spherical Initial Shape

with ψ_o = 45°, H + 2.0, α_3 = +1.0, β = 0.05,
Δt = 0.25 (reduced by 1/2 every 25 iterations),
$0 \leq t \leq 1.2$.

Figure 2-9

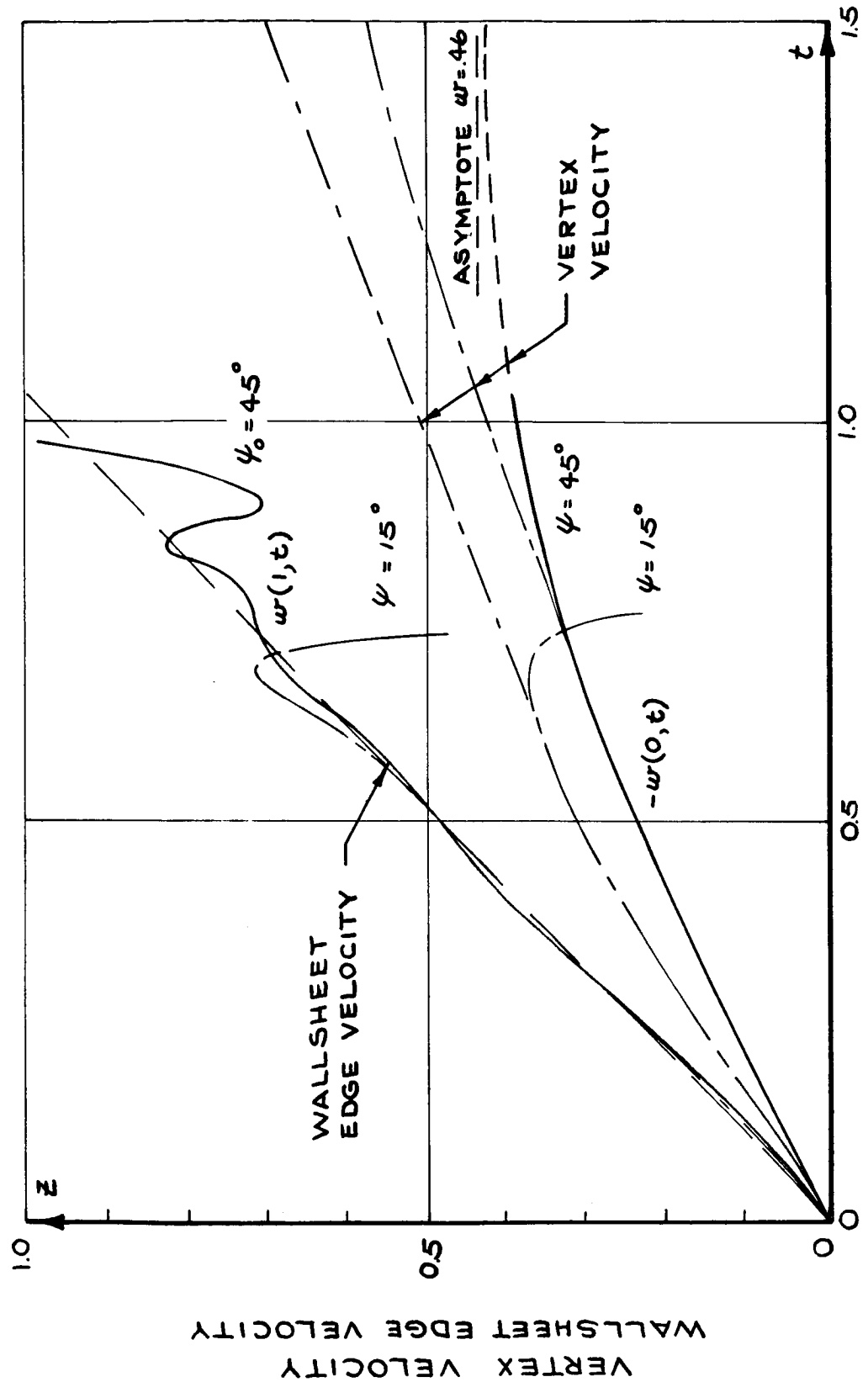

Vertical Velocity Profile for the Case of Figure 8 ($\psi_0 = 45°$) and for $\psi_0 = 15°$ ($\alpha_3 = +1, \beta = 1/260$). Dashed lines indicate velocity extrapolation.

Figure 2-10

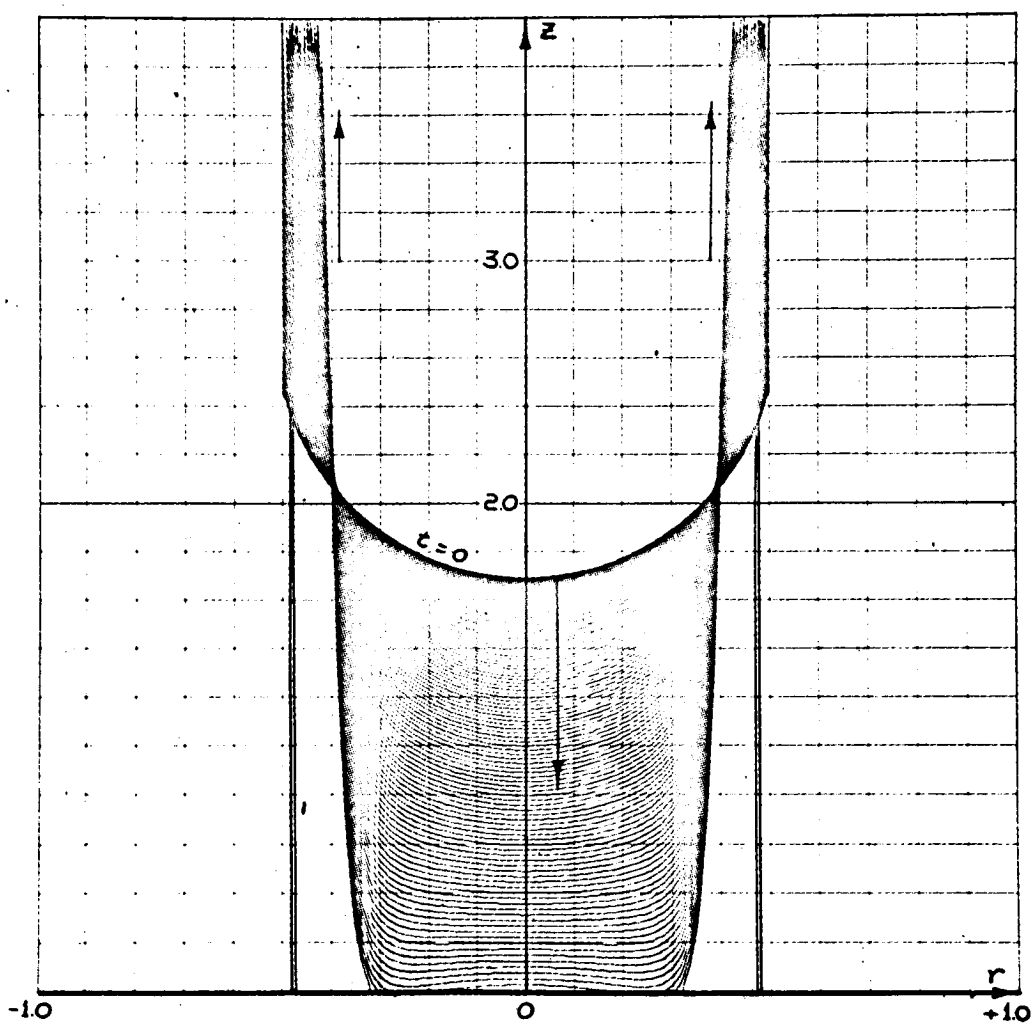

Velocity Extrapolation in Symmetric Liquid Reorientation,

$H = 2.0$, $\psi_o = 15°$, $\alpha_3 = +1.0$, $\beta = 1/260$,

$\Delta t = .025$, $0 \leq t \leq 2.85$.

Figure 2-11

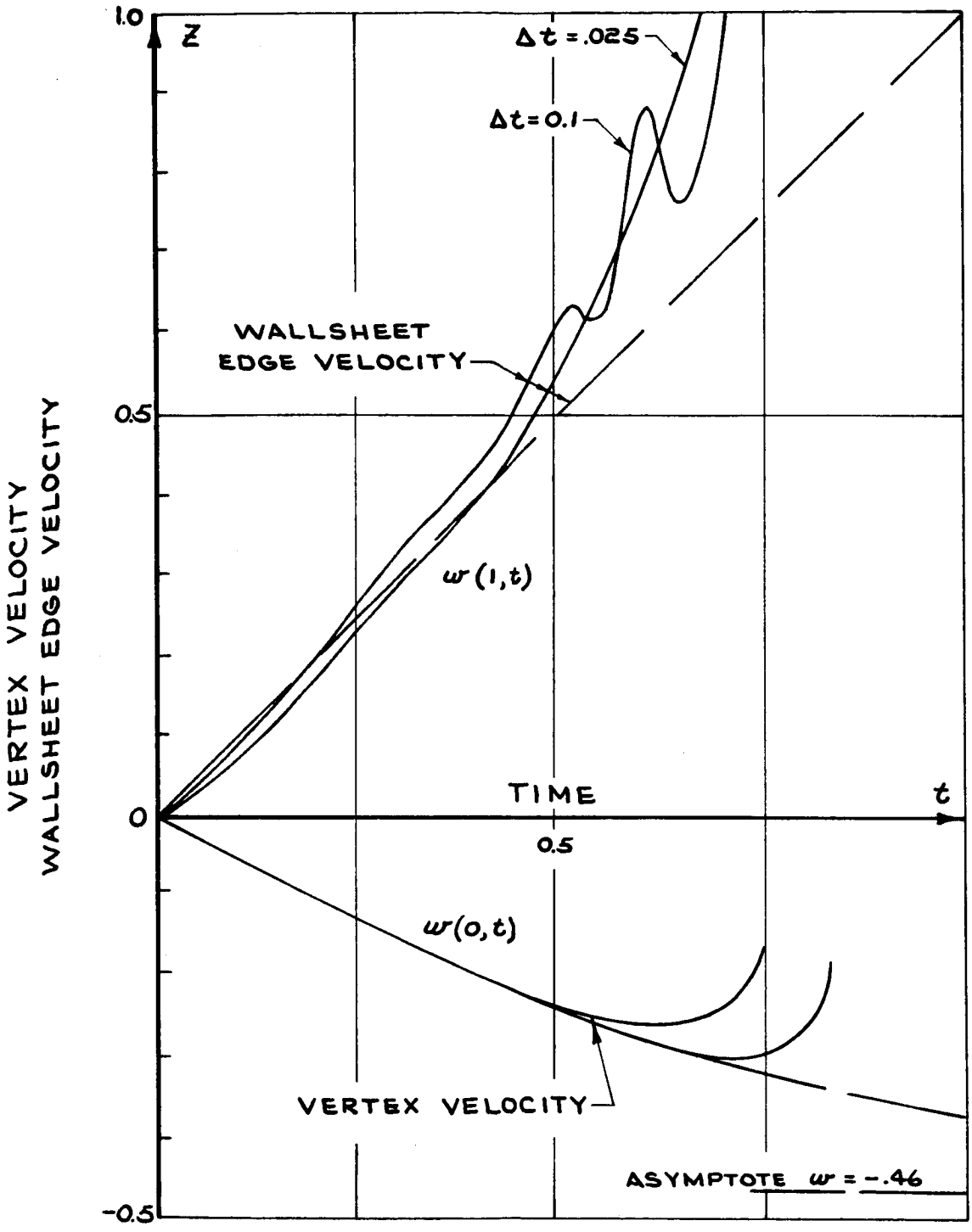

Vertical Velocity Profile Based on Harmonic Polynomials for the $\Psi_0 = 45°$ Case, $\alpha_3 = +1$, $\beta = 0$.

Figure 2-12

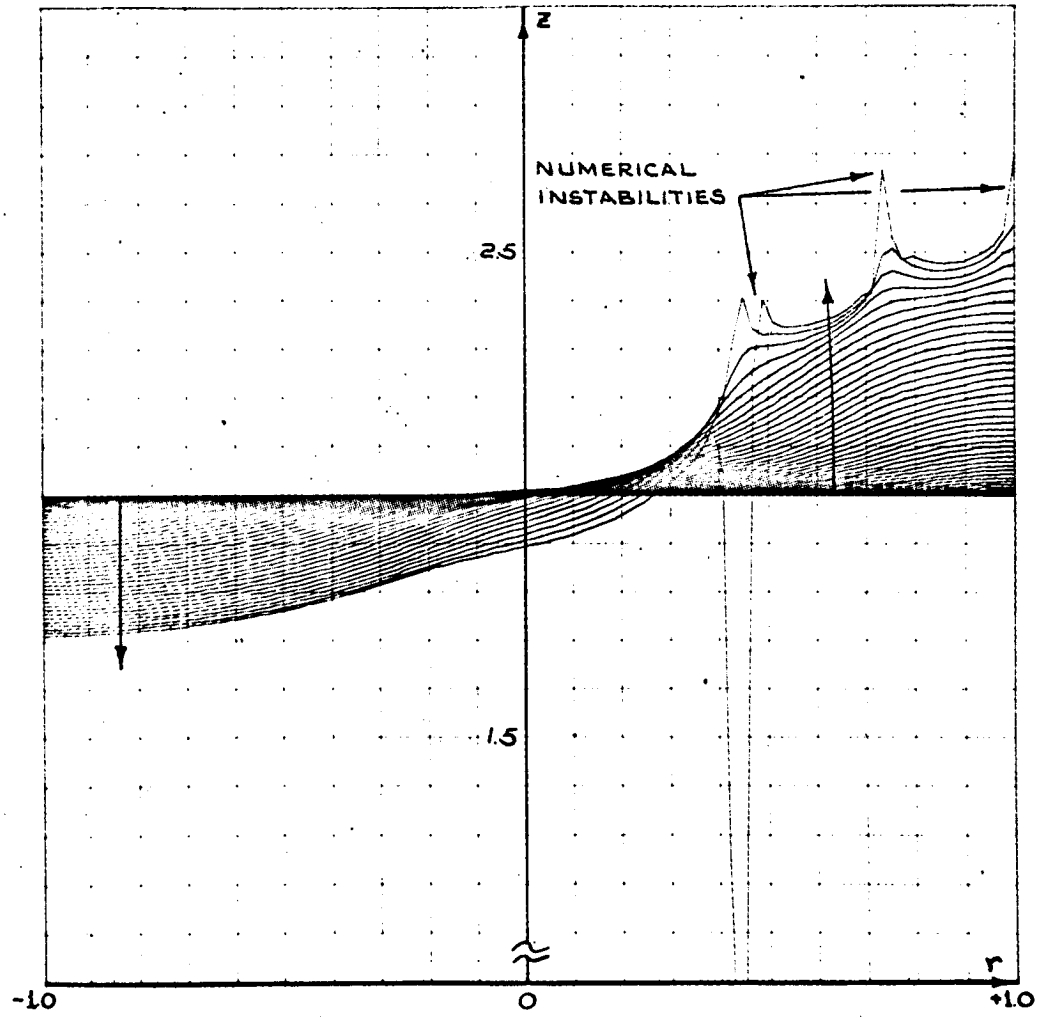

Asymmetric Sloshing from a Flat Initial Shape

$\alpha_1 = +1, \quad \alpha_3 = -1, \quad \beta = 1/B = 0.1,$

$\Delta t = 0.02$, M = 50, NO = N1 = 5 $\quad \psi_o = 90$ degrees

Figure 2-13

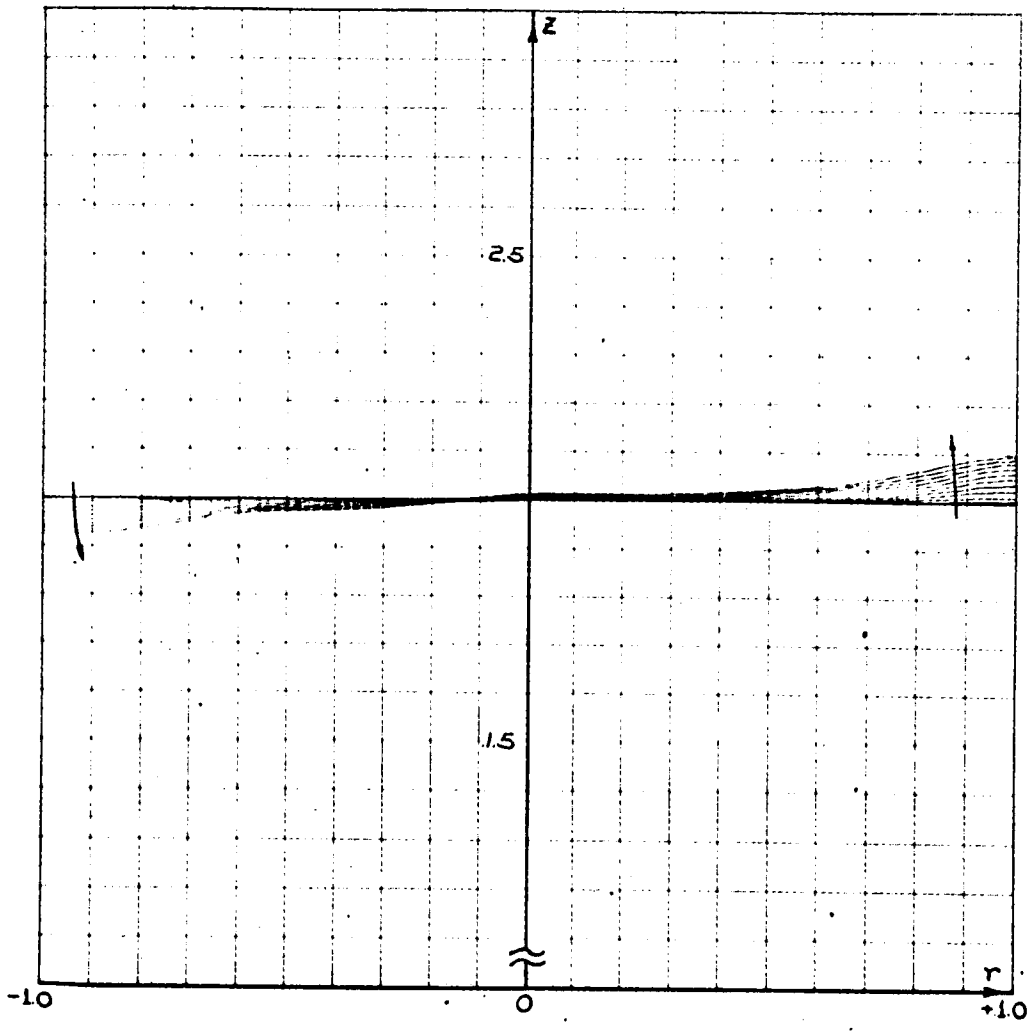

Transverse Impulsive Sloshing, $0 \leq t \leq 0.25$

$\alpha_3 = -2.0$, $\alpha_1 = +4.0$ for $t \leq 0.05$, $\alpha_1 = 0$ for $t > 0.05$
$\beta = 0.04$, $\Delta t = 0.025$
$\psi_0 = 90$ degrees

Figure 2-14a

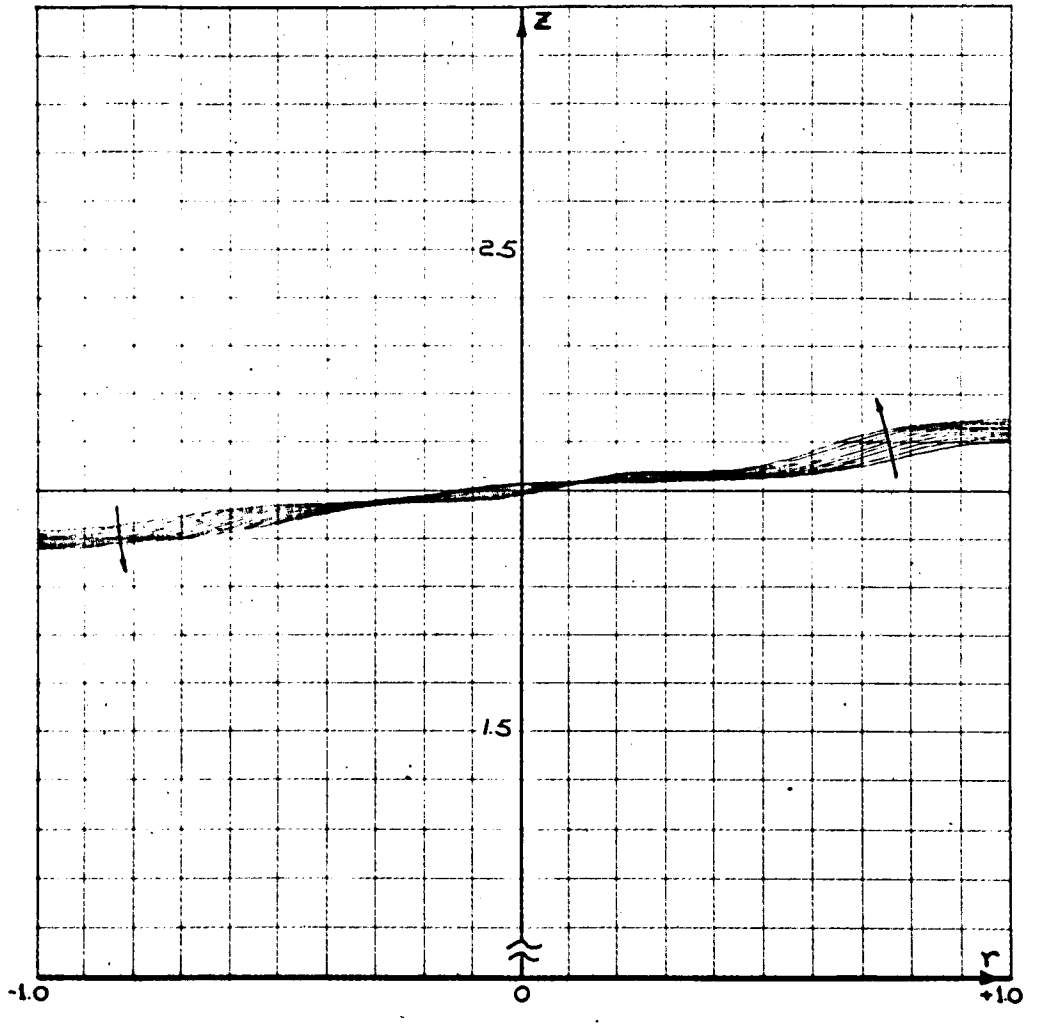

Transverse Impulsive Sloshing, $0.25 \leq t \leq 0.5$

Figure 2-14b

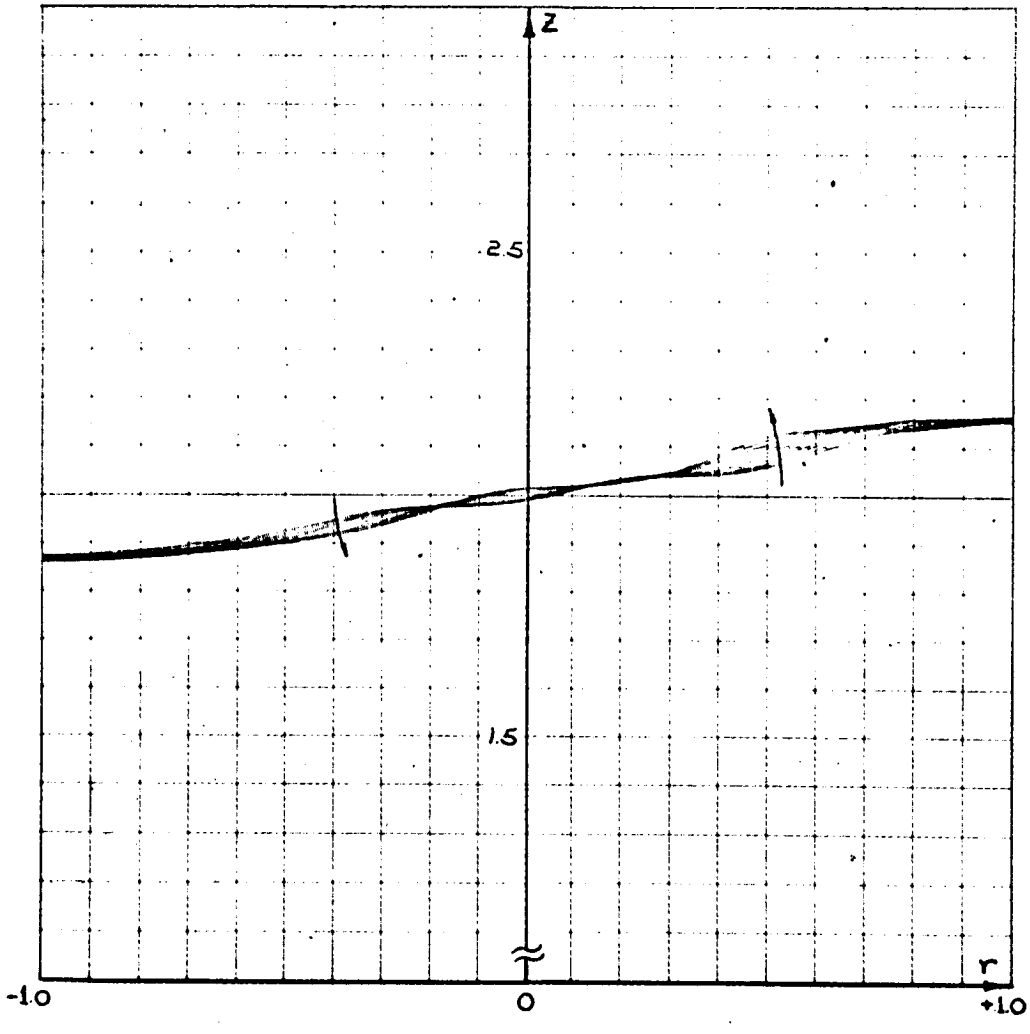

Transverse Impulsive Sloshing, $0.5 \leq t \leq 0.75$

Figure 2-14c

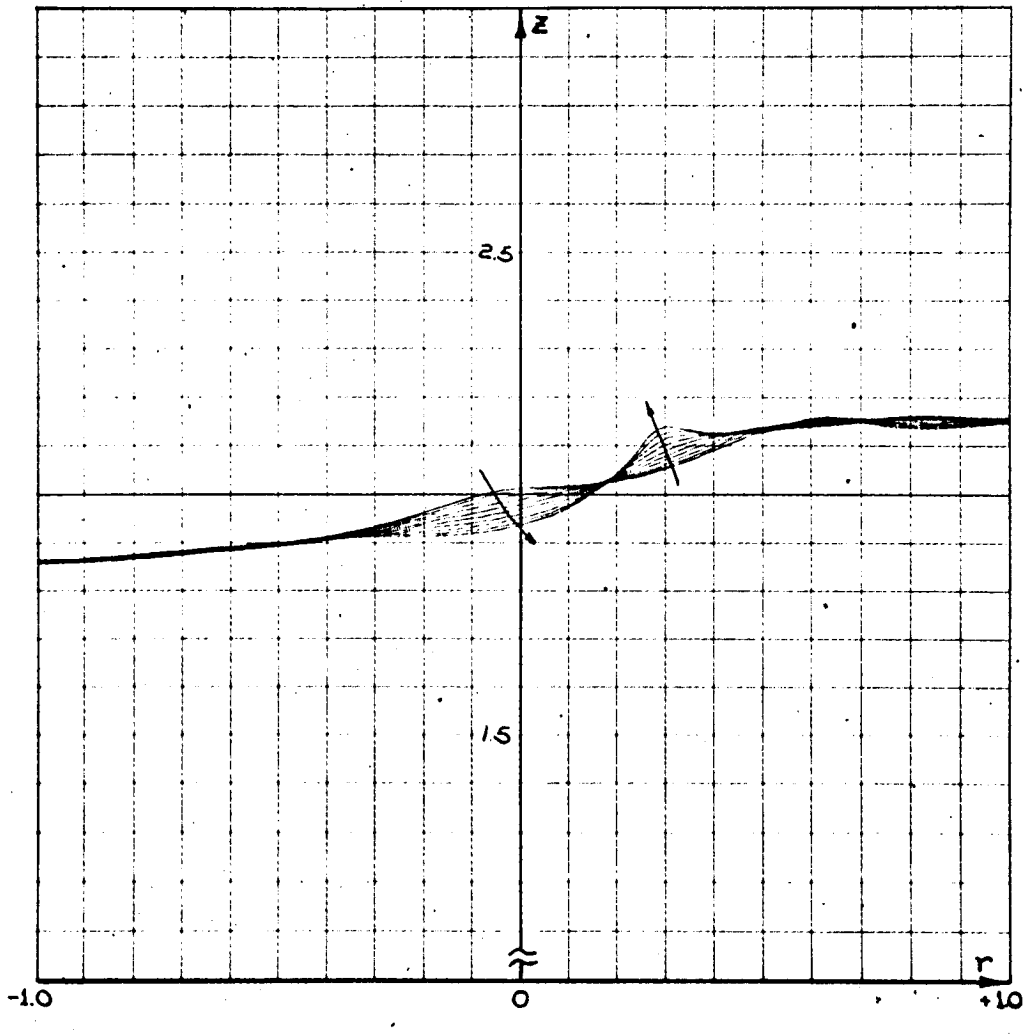

Transverse Impulsive Sloshing, $0.75 \leq t \leq 1.00$

Figure 2-14d

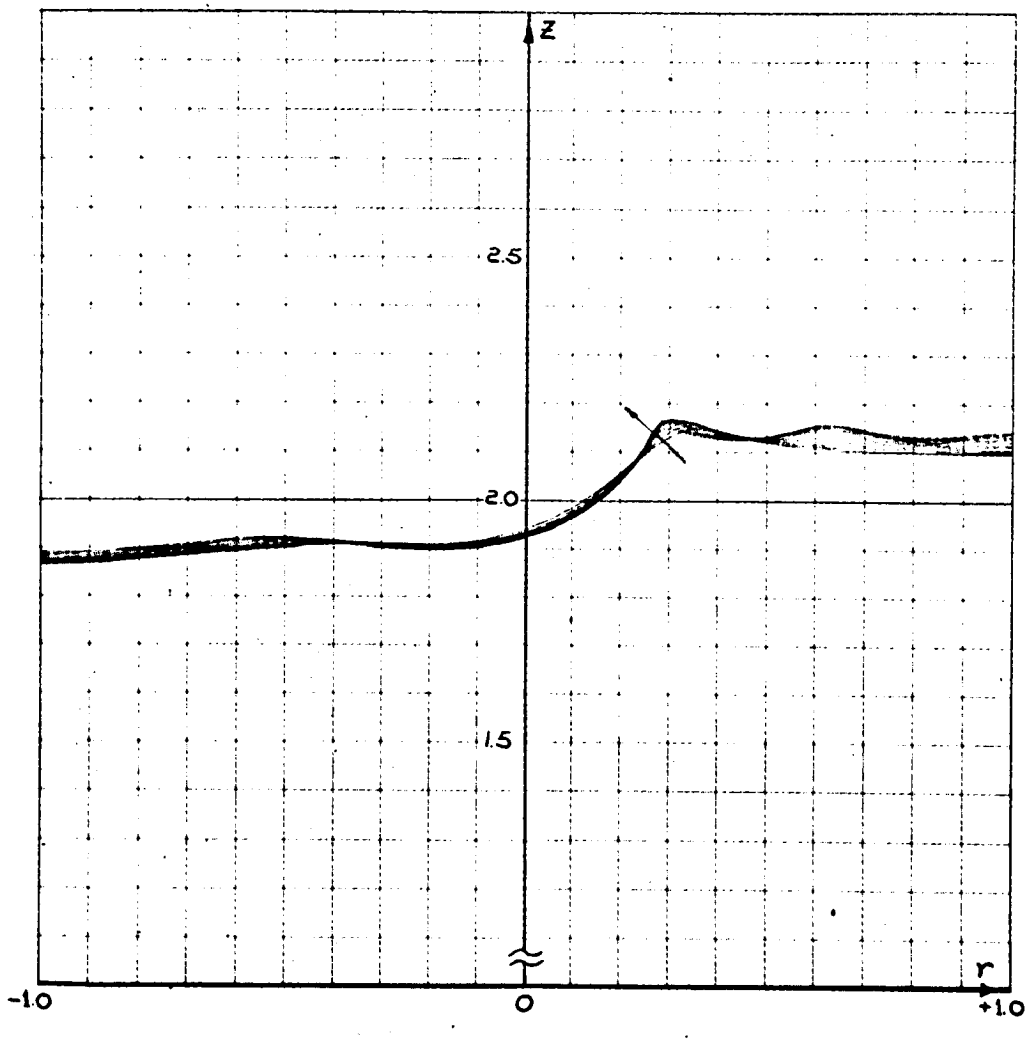

Transverse Impulsive Sloshing, $1.00 \leq t \leq 1.25$

Figure 2-14e

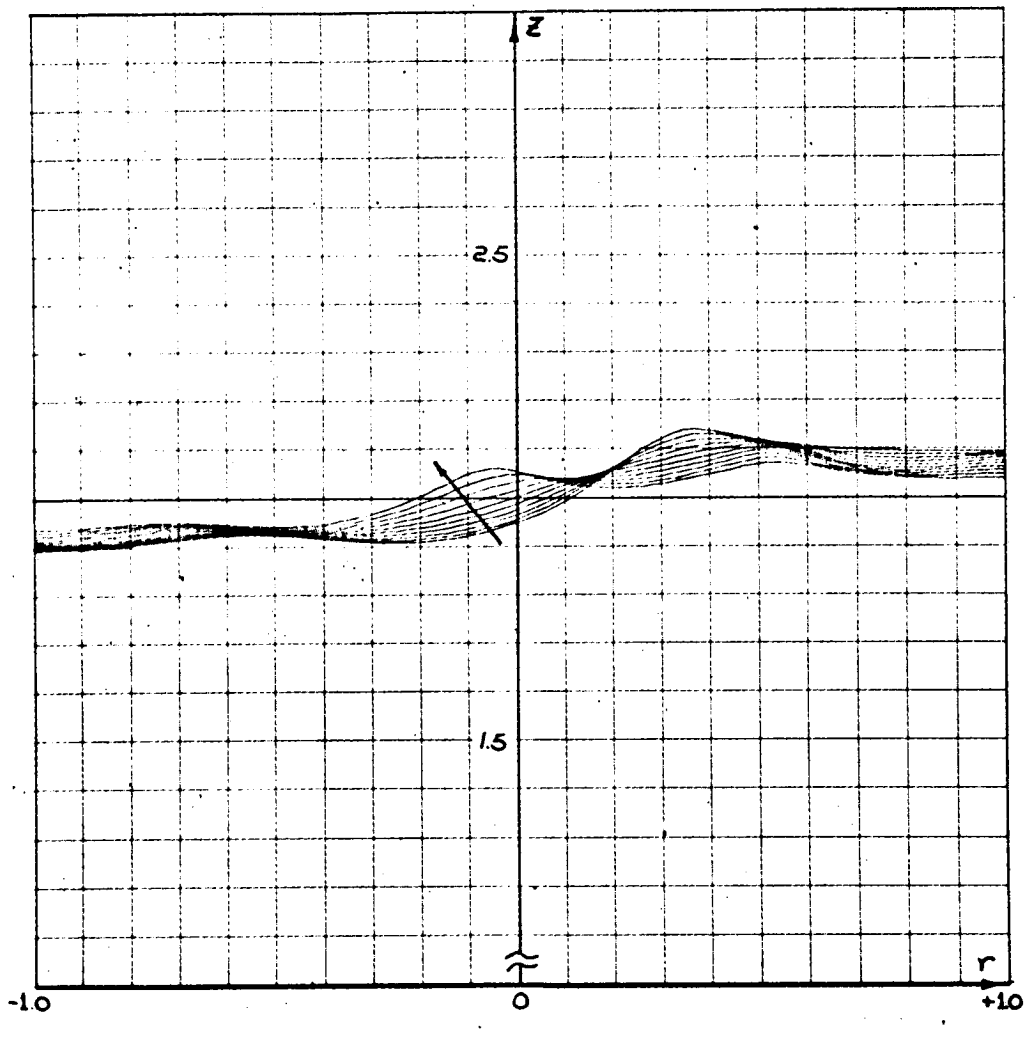

Transverse Impulsive Sloshing, $1.25 \leq t \leq 1.50$

Figure 2-14f

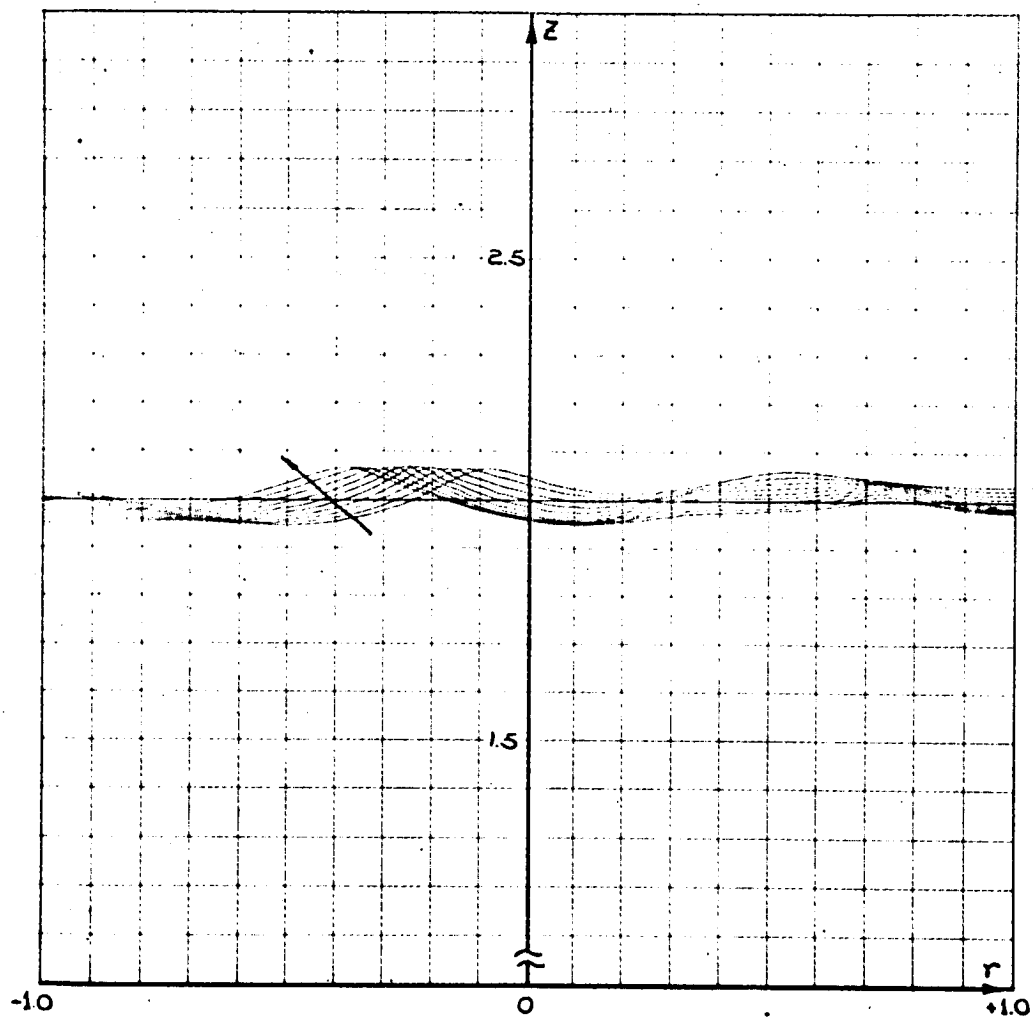

Transverse Impulsive Sloshing, $1.50 \leq t \leq 1.75$

Figure 2-14g

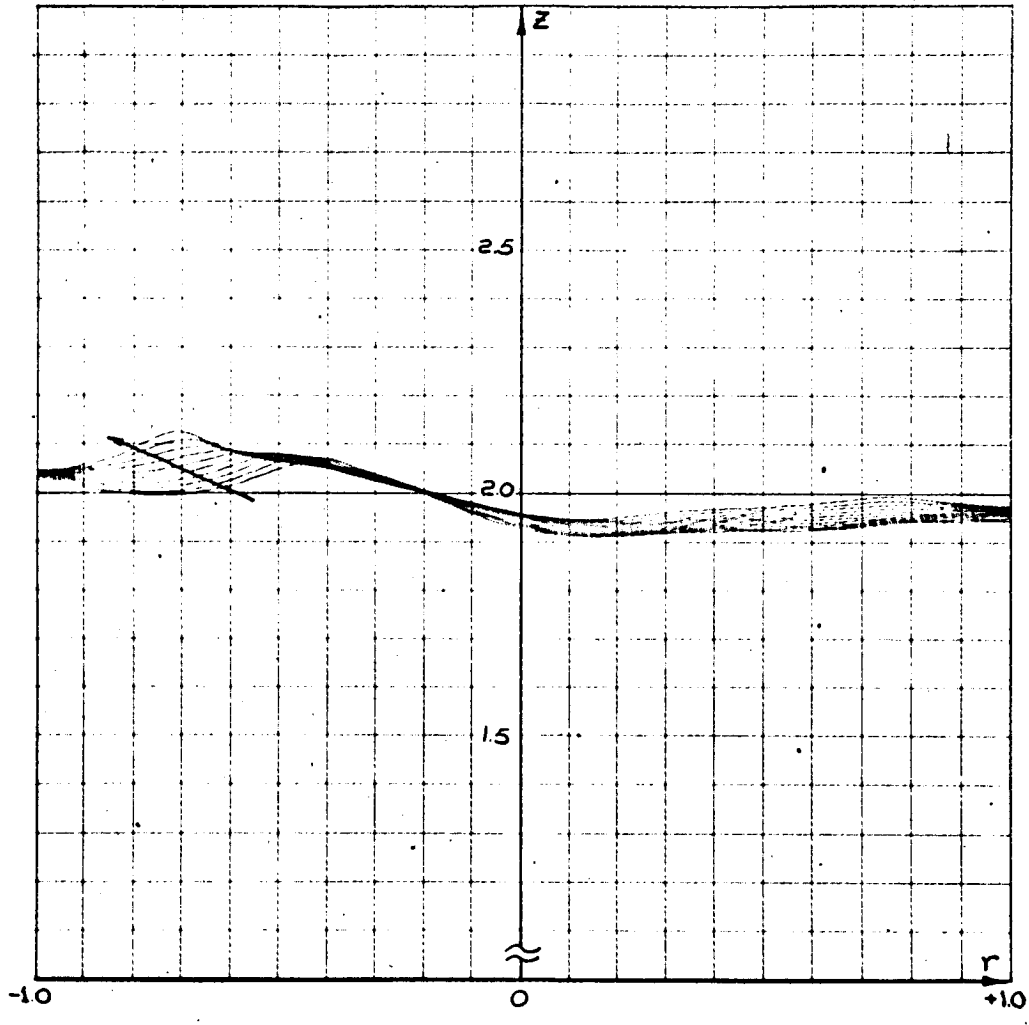

Transverse Impulsive Sloshing, $1.75 \leq t \leq 2.00$

Figure 2-14h

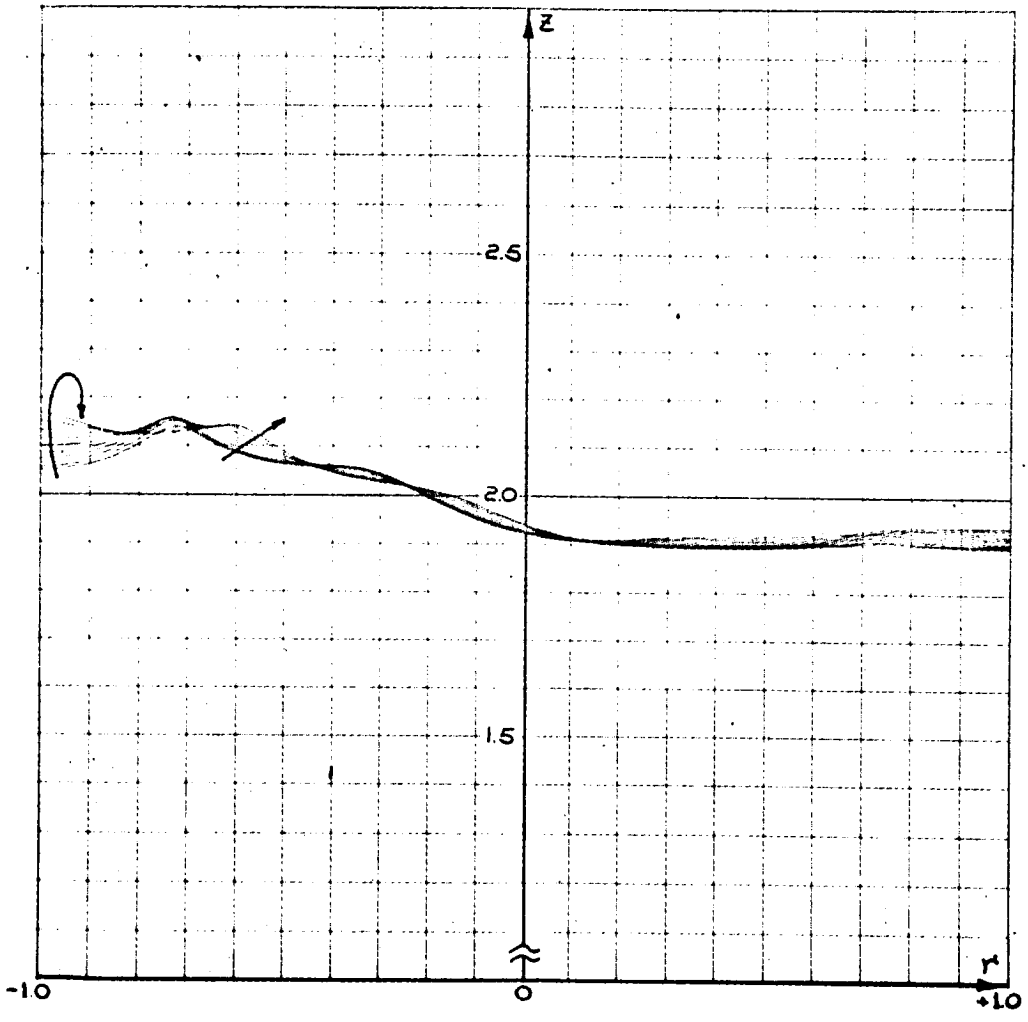

Transverse Impulsive Sloshing, $2.00 \leq t \leq 2.25$

Figure 2-14i

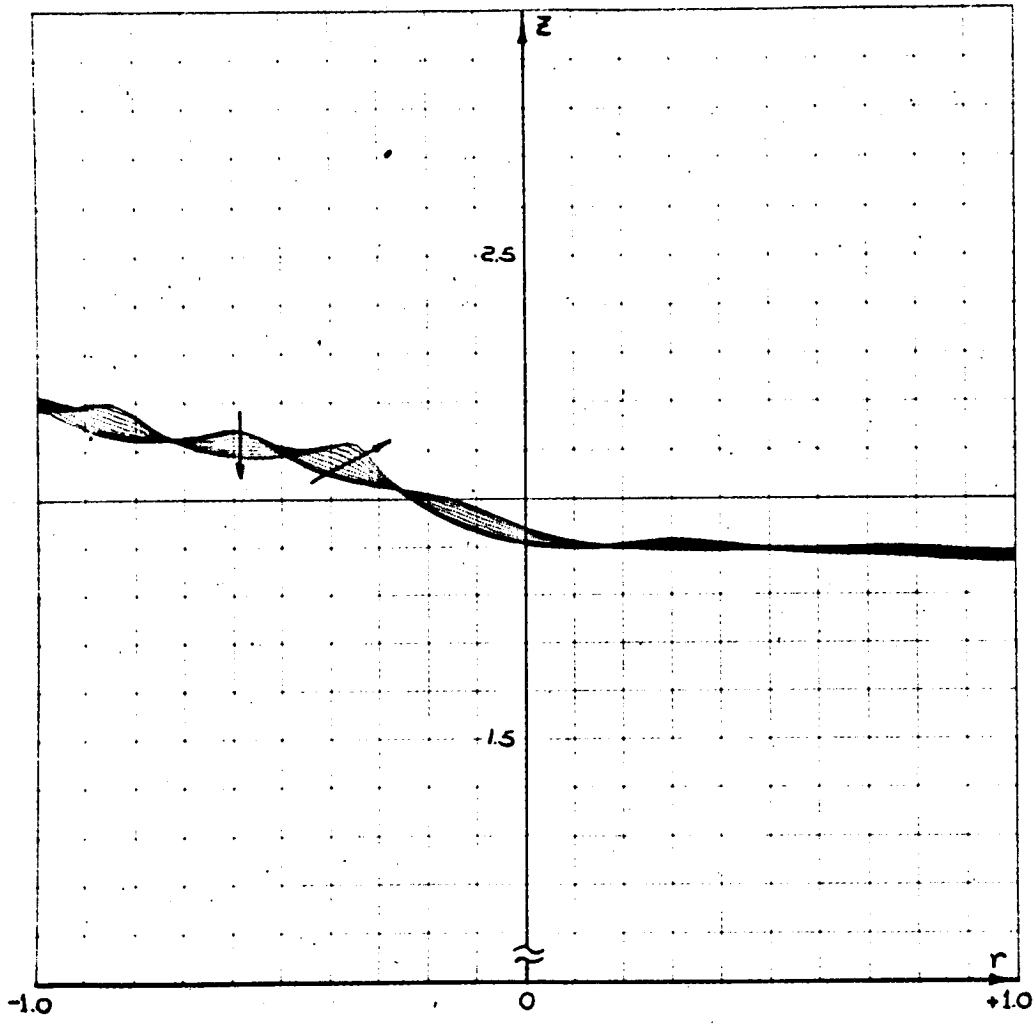

Transverse Impulsive Sloshing, $2.25 \leq t \leq 2.50$

Figure 2-14j

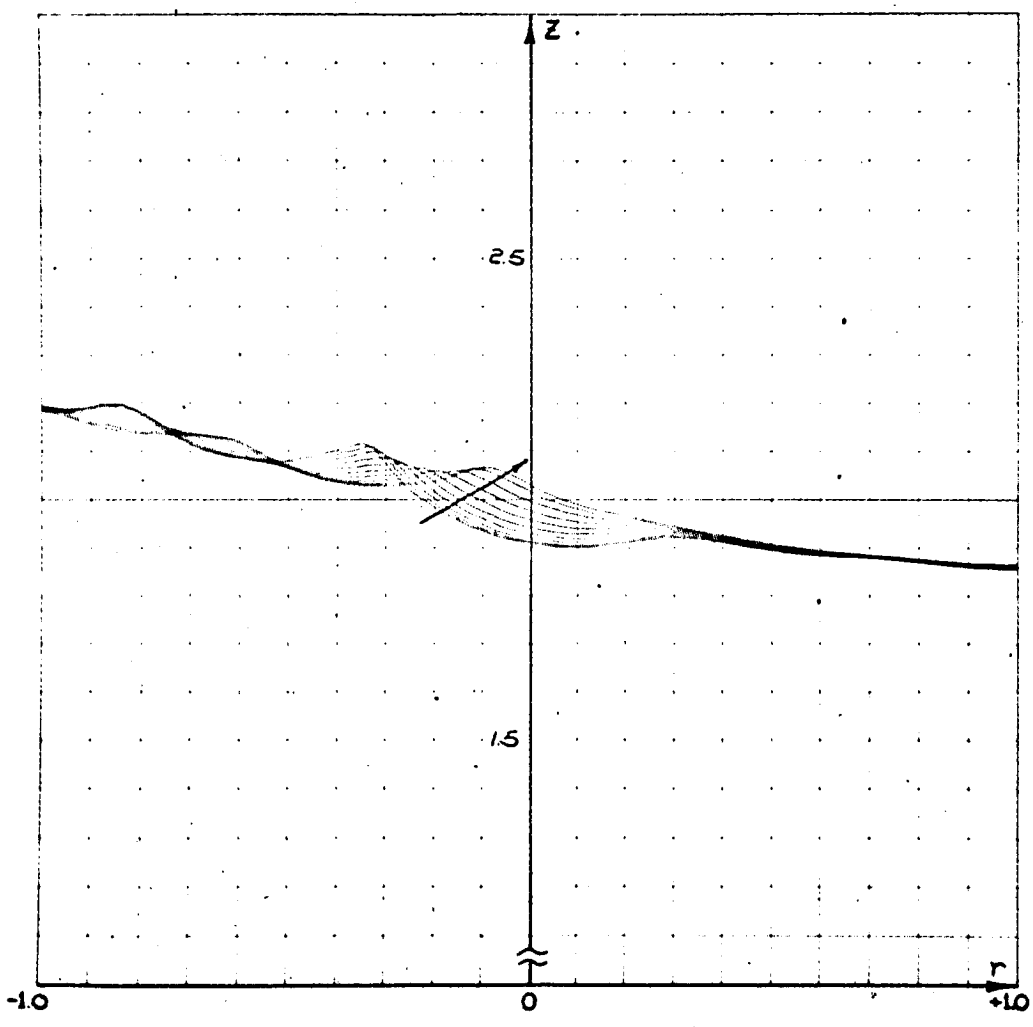

Transverse Impulsive Sloshing, $2.50 \leq t \leq 2.75$

Figure 2-14k

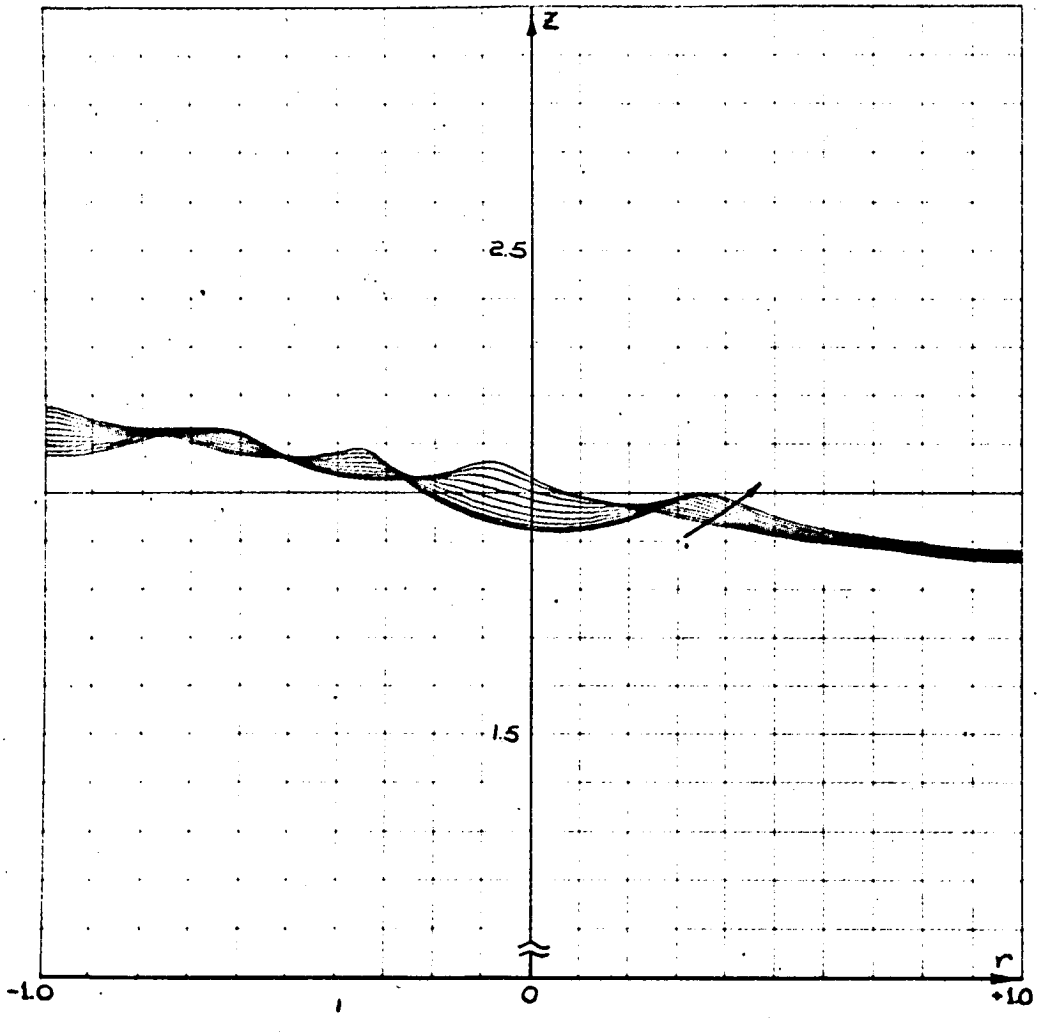

Transverse Impulsive Sloshing, $2.75 \leq t \leq 3.00$

Figure 2-14 1

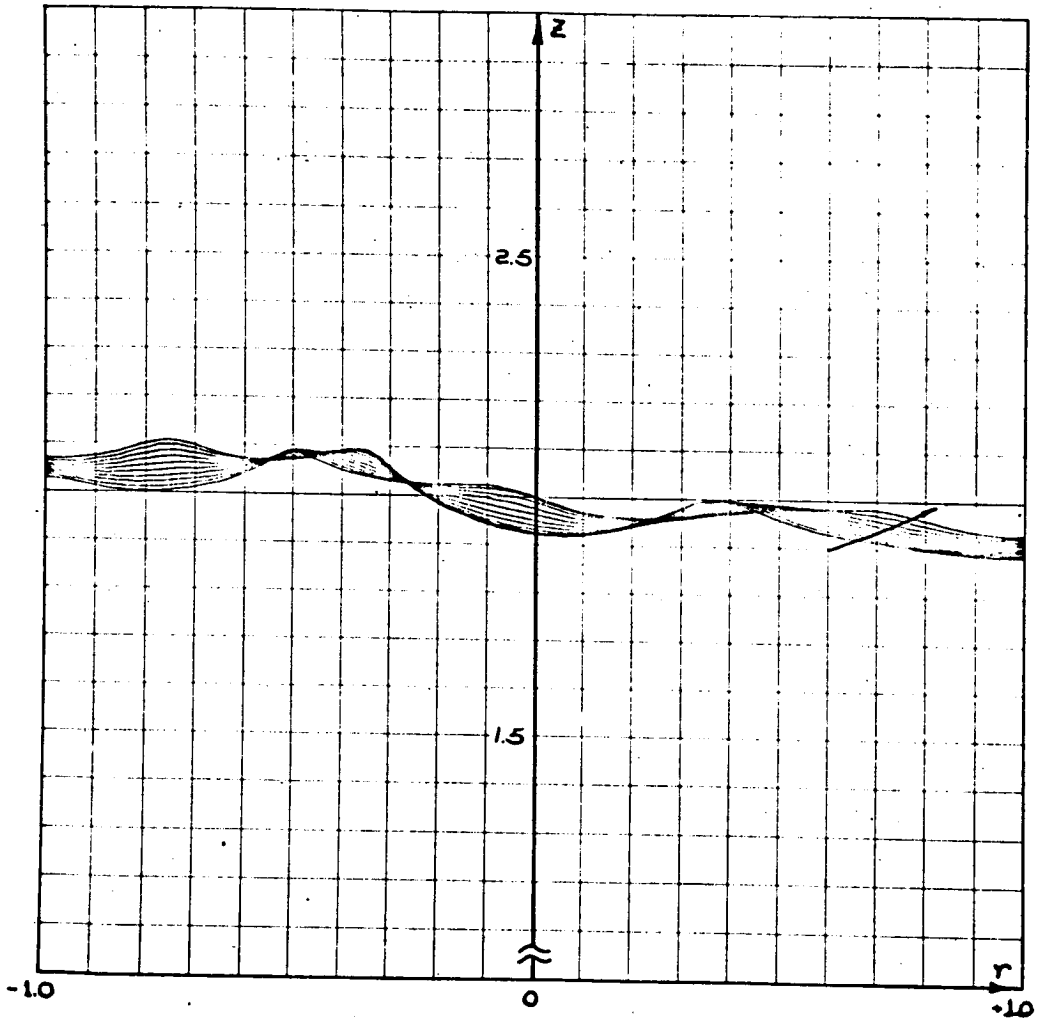

Transverse Impulsive Sloshing, $3.00 \leq t \leq 3.25$

Figure 2-14m

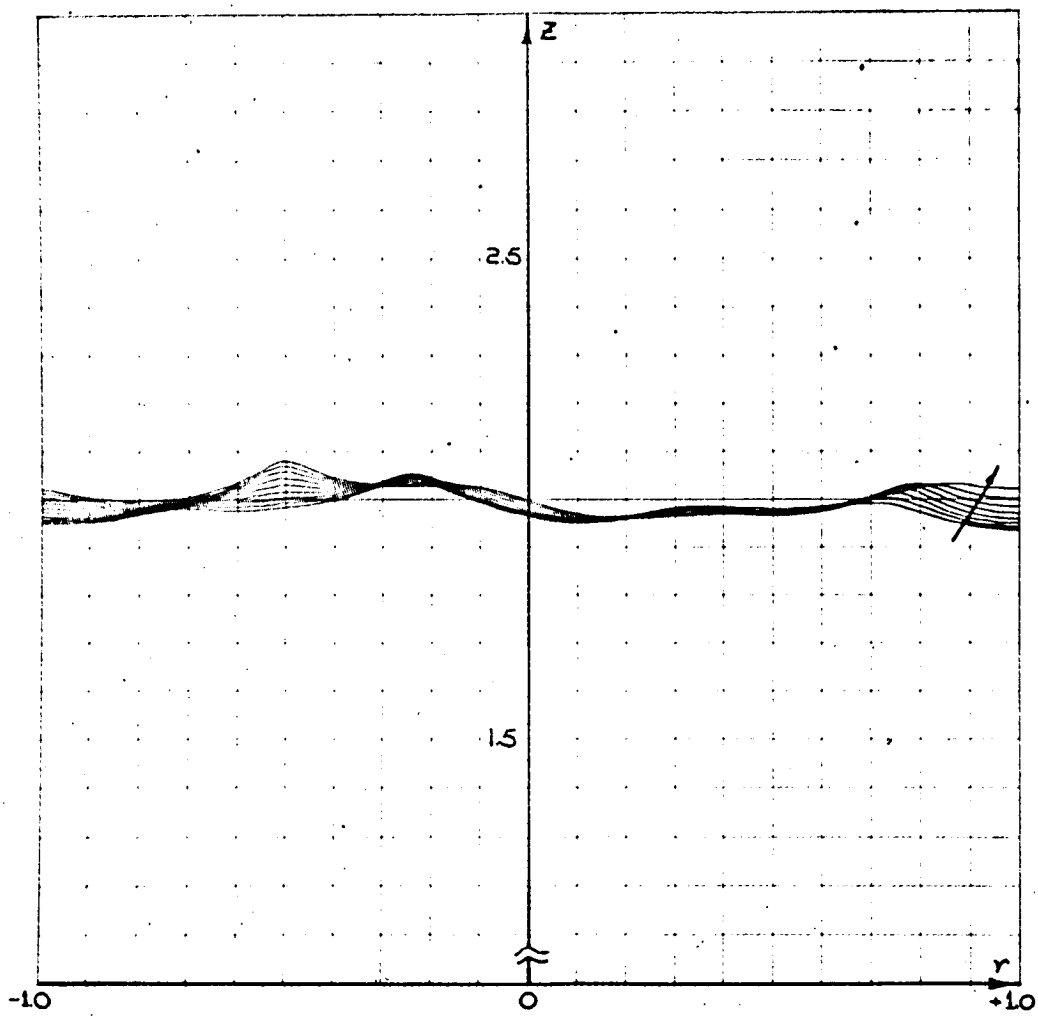

Transverse Impulsive Sloshing, $3.25 \leq t \leq 3.50$

Figure 2-14n

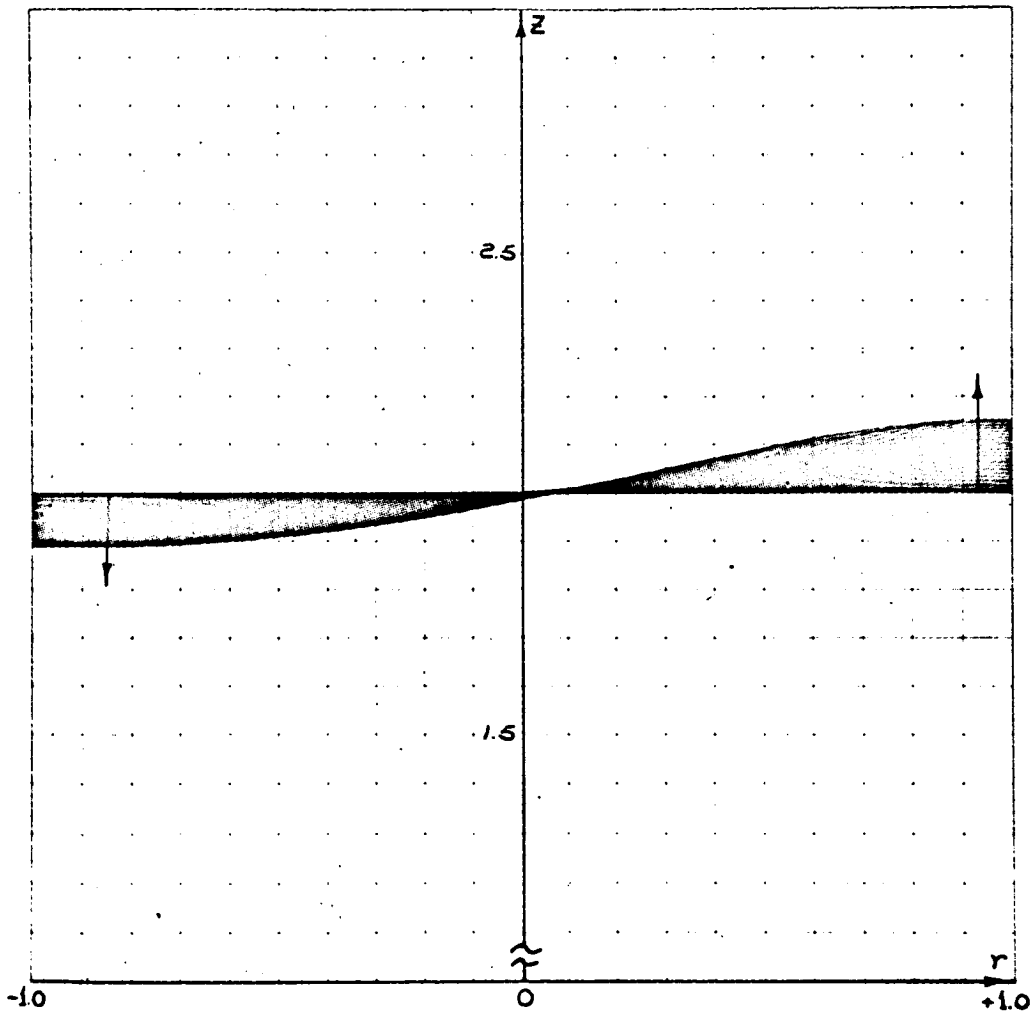

First Mode Lateral Sloshing $0 \leq t \leq 1.25$

$\alpha_1 = \alpha_3 = \beta = 0, \quad \Delta t = 0.025, \; C_1^{(1)}(0) = 0.1$

$\psi_o = 90$ degrees

Figure 2-15a

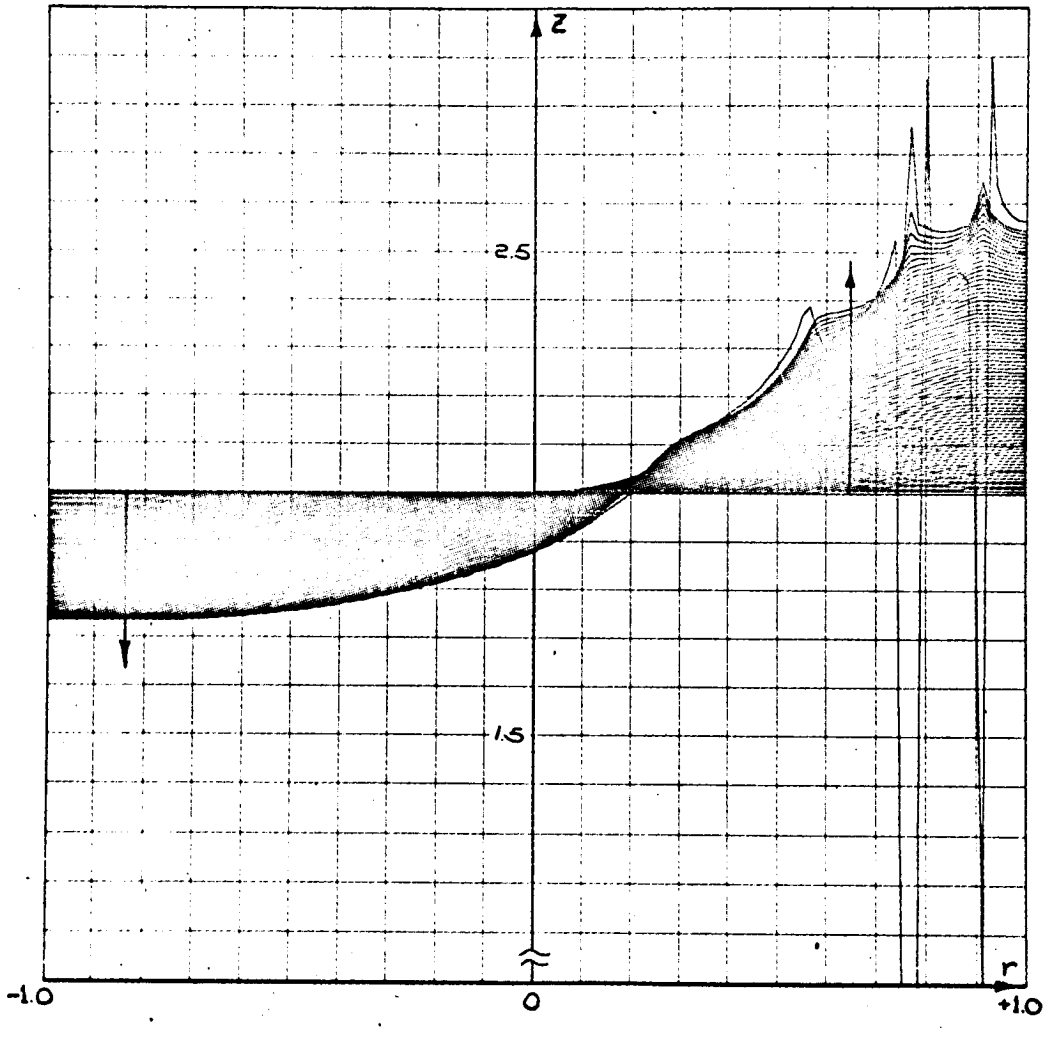

First Mode Lateral Sloshing $0 \leq t \leq 3.90$

$\alpha_1 = \alpha_3 = \beta = 0, \quad \Delta t = 0.05, \quad C_1^{(1)} = 0.1$

Figure 2-15b

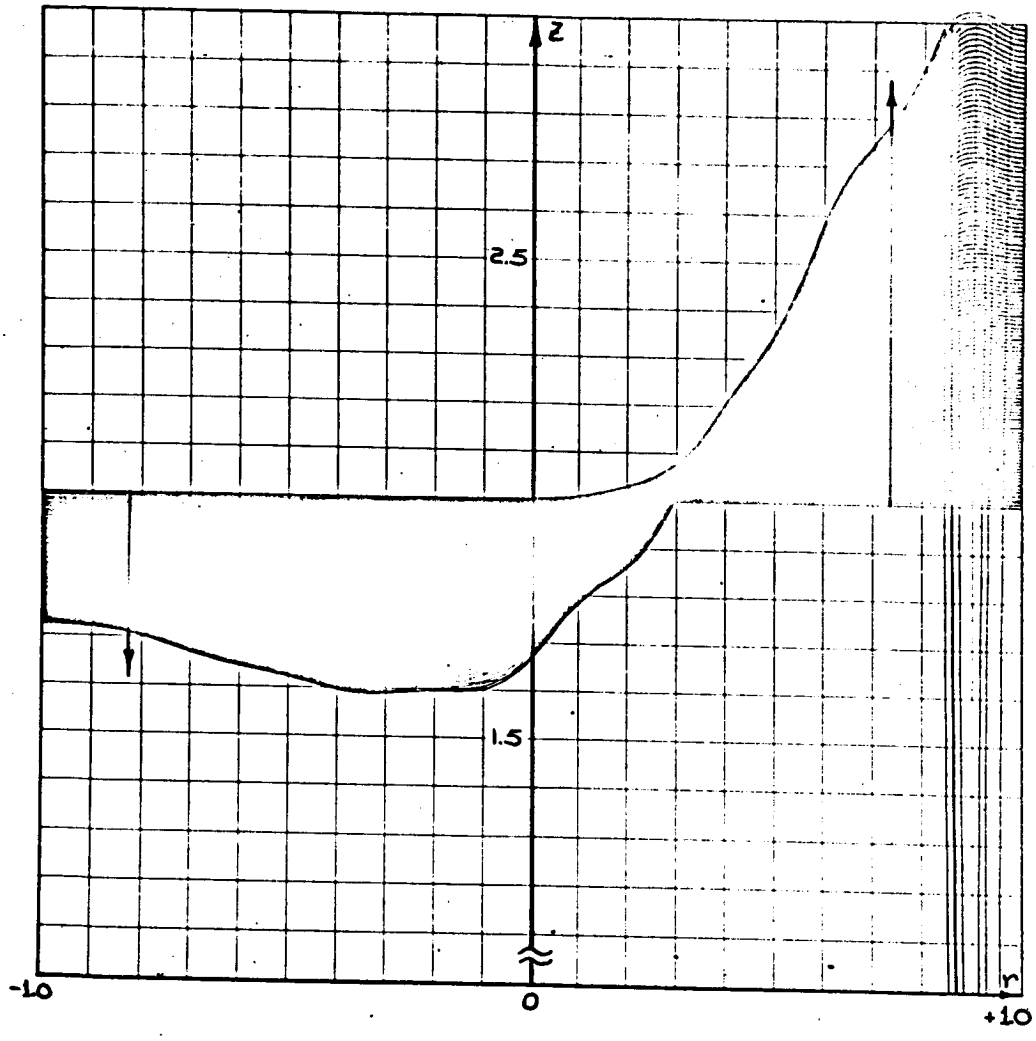

Velocity Extrapolation in First Mode Lateral Sloshing

Figure 2-15c

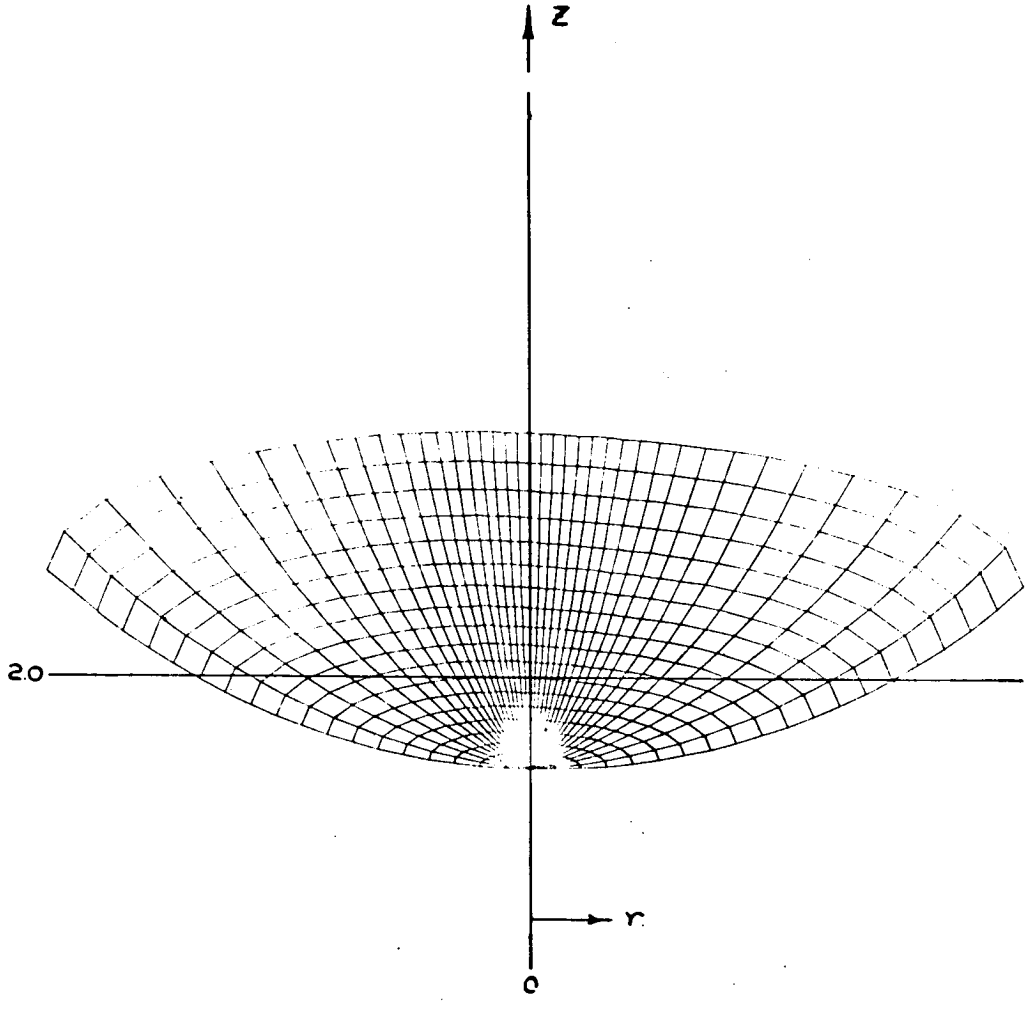

Graphical Representation of Asymmetric Surface Motion

$\alpha_1 = \alpha_3 = -1.0, \beta = 0, \quad \Delta t = 0.1, \; t = 0$

NO = N1 = 5

Figure 2-16a

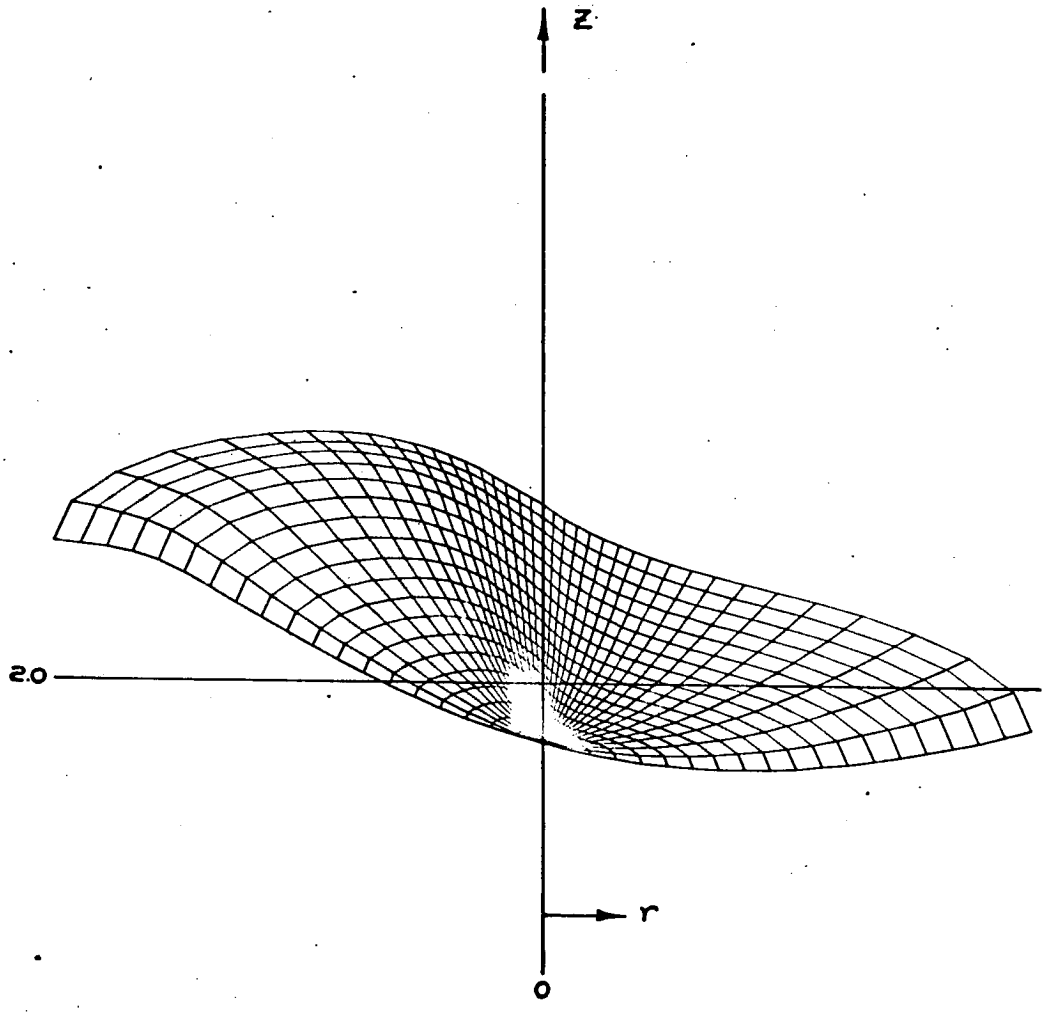

Graphical Representation of Asymmetric Surface Motion

t = 0.5

Figure 2-16b

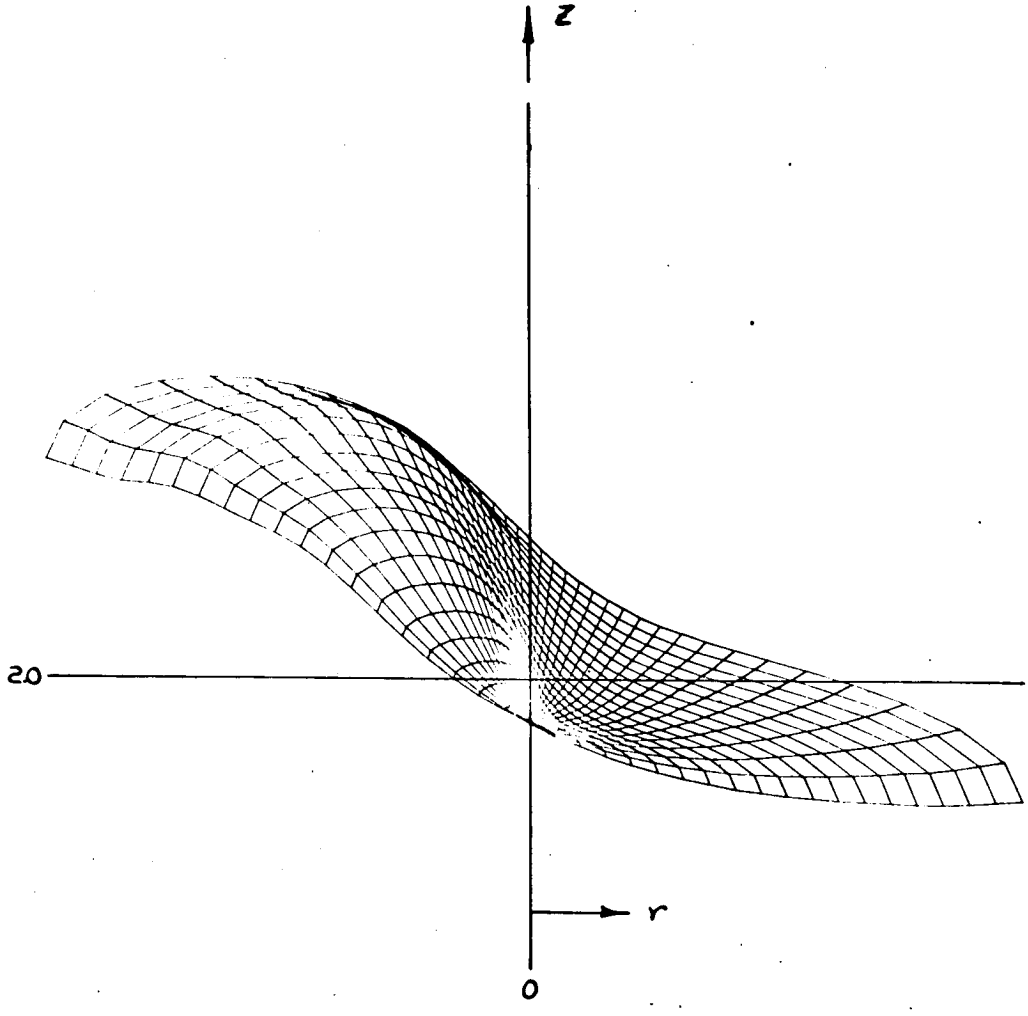

Graphical Representation of Asymmetric Surface Motion

t = 0.7

Figure 2-16c

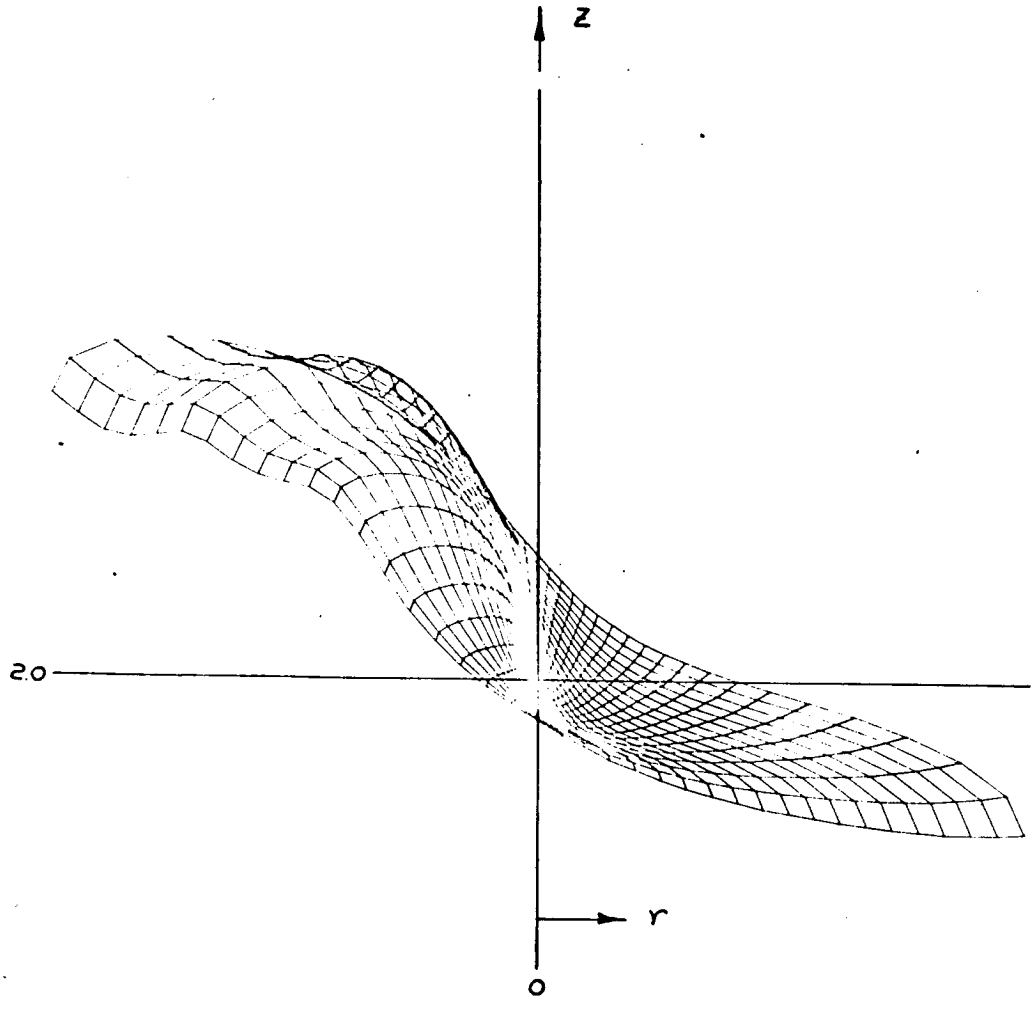

Graphical Representation of Asymmetric Surface Motion

t = 0.8

Figure 2-16d

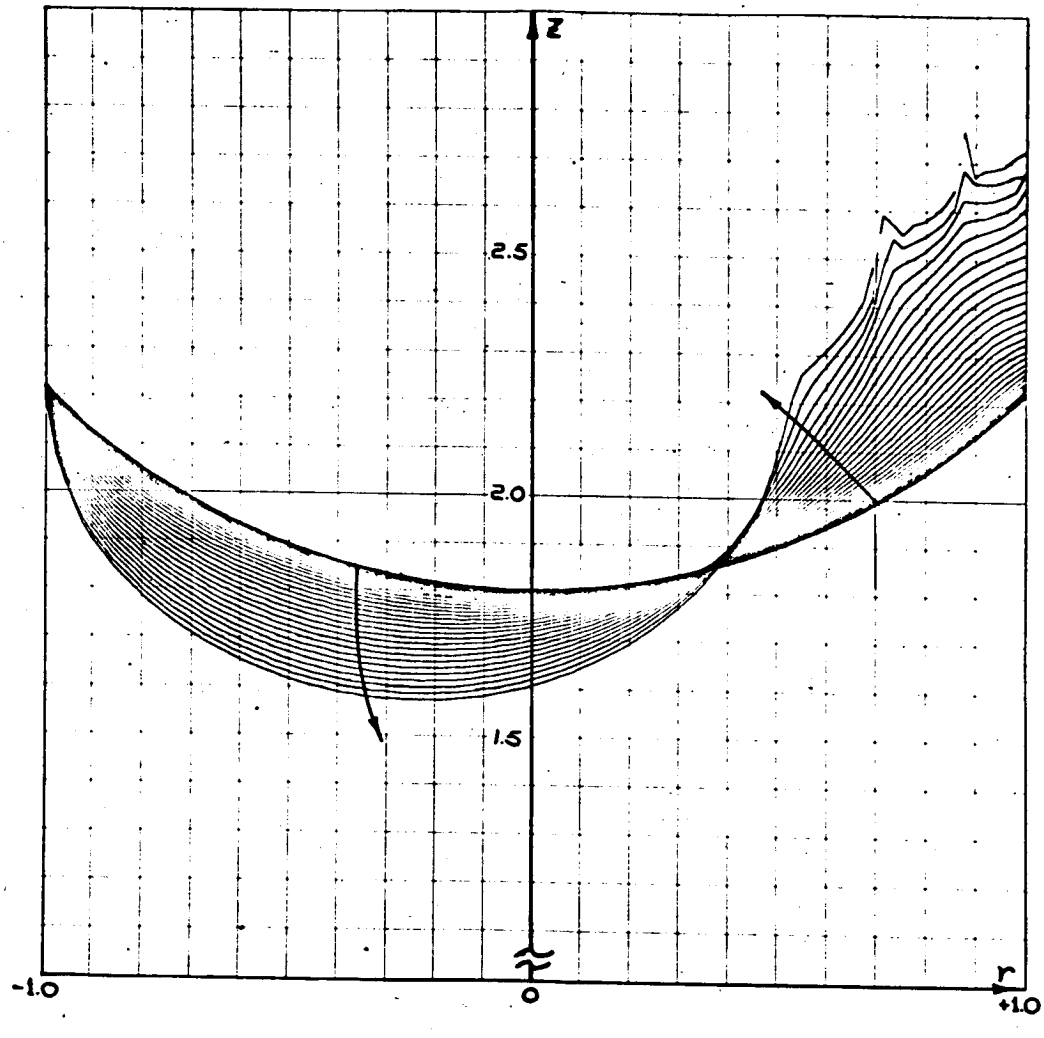

Asymmetric Liquid Reorientation (to t = 0.700)

$\alpha_1 = \alpha_3 = +1, \quad \beta = 0 \quad \Delta t = 0.025$

M = 50, N0 = N1 = 7

Figure 2-17

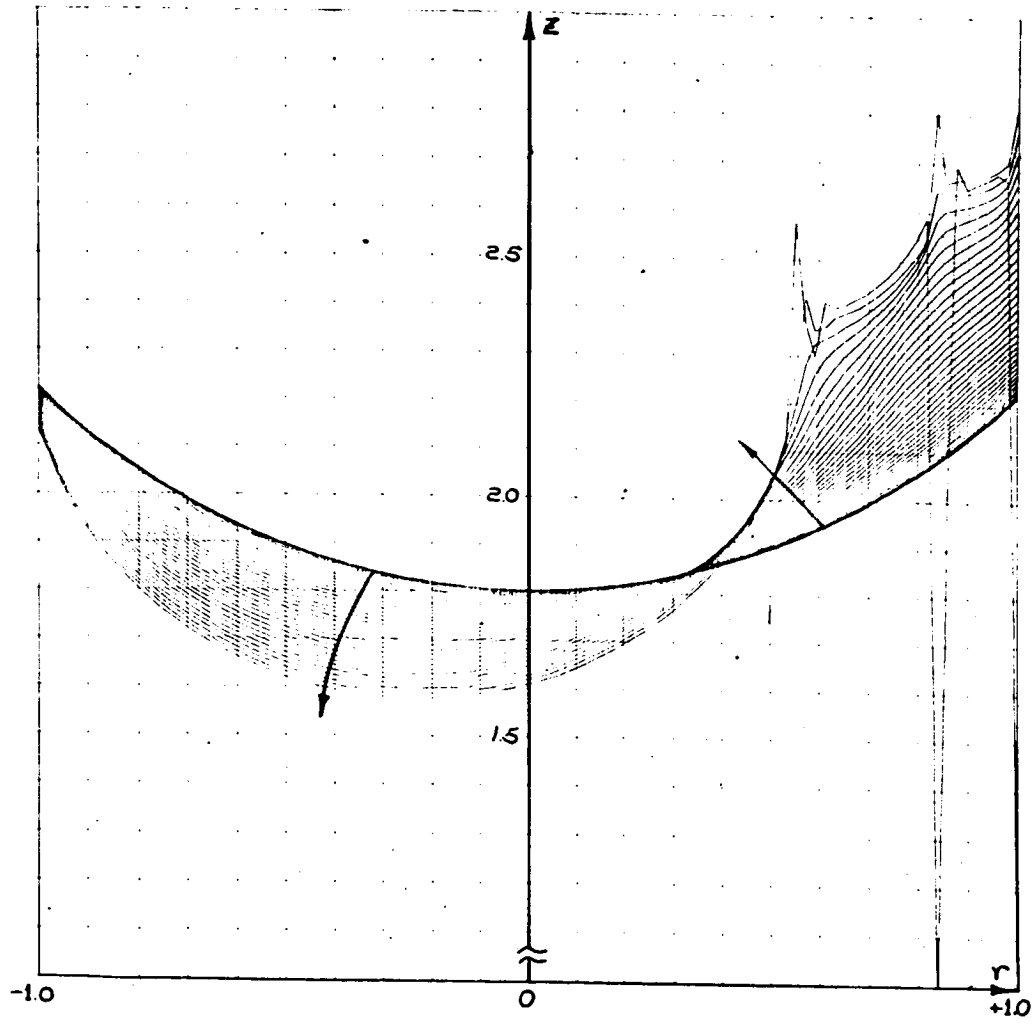

Asymmetric Reorientation (to t = 0.8)

$\alpha_1 = \alpha_3 = +1$, $\beta = 1/B = 0.05$, $\Delta t = 0.02$

M = 50, NO = N1 ± 5, $\gamma_0 = 45°$

Figure 2-18

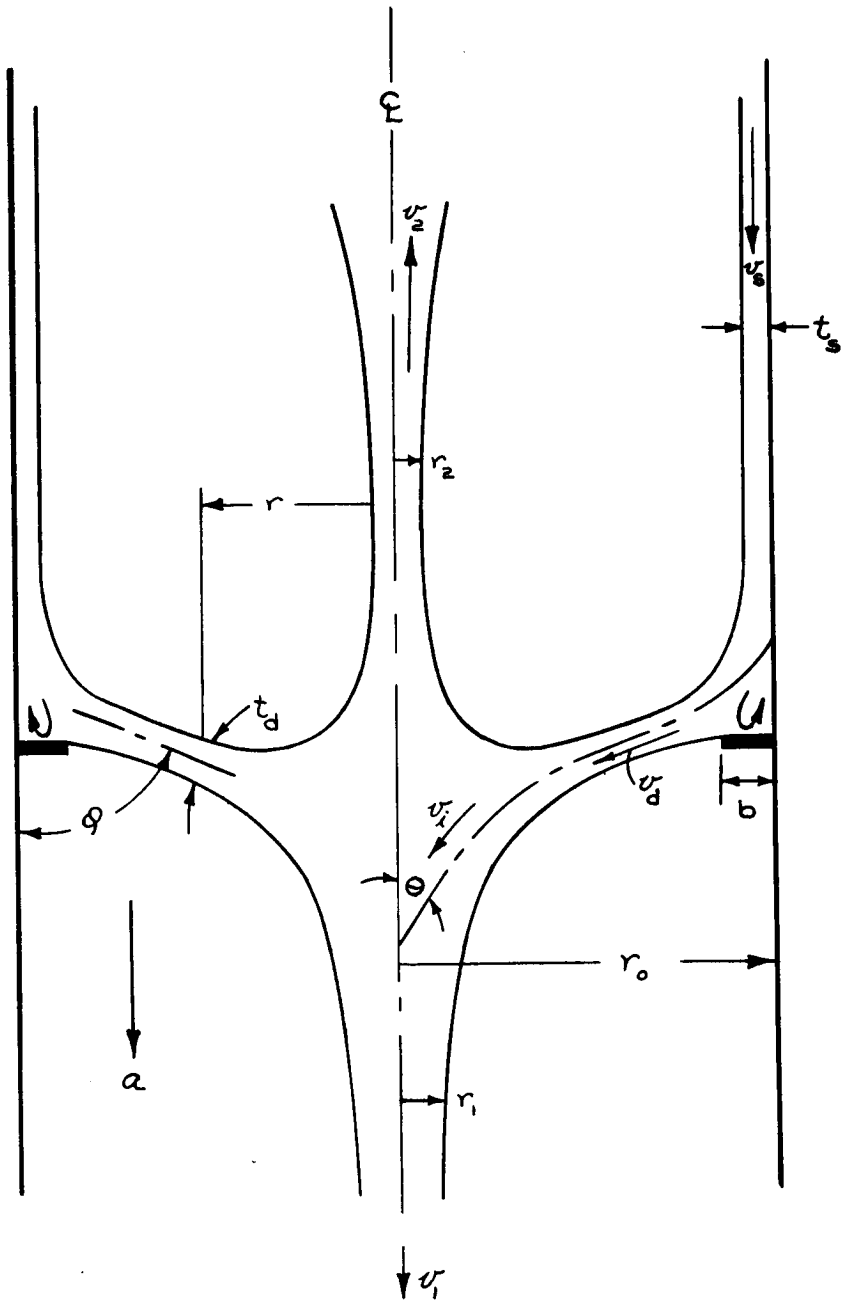

Effect of Baffles on Reorientation Flow

Figure 2-20

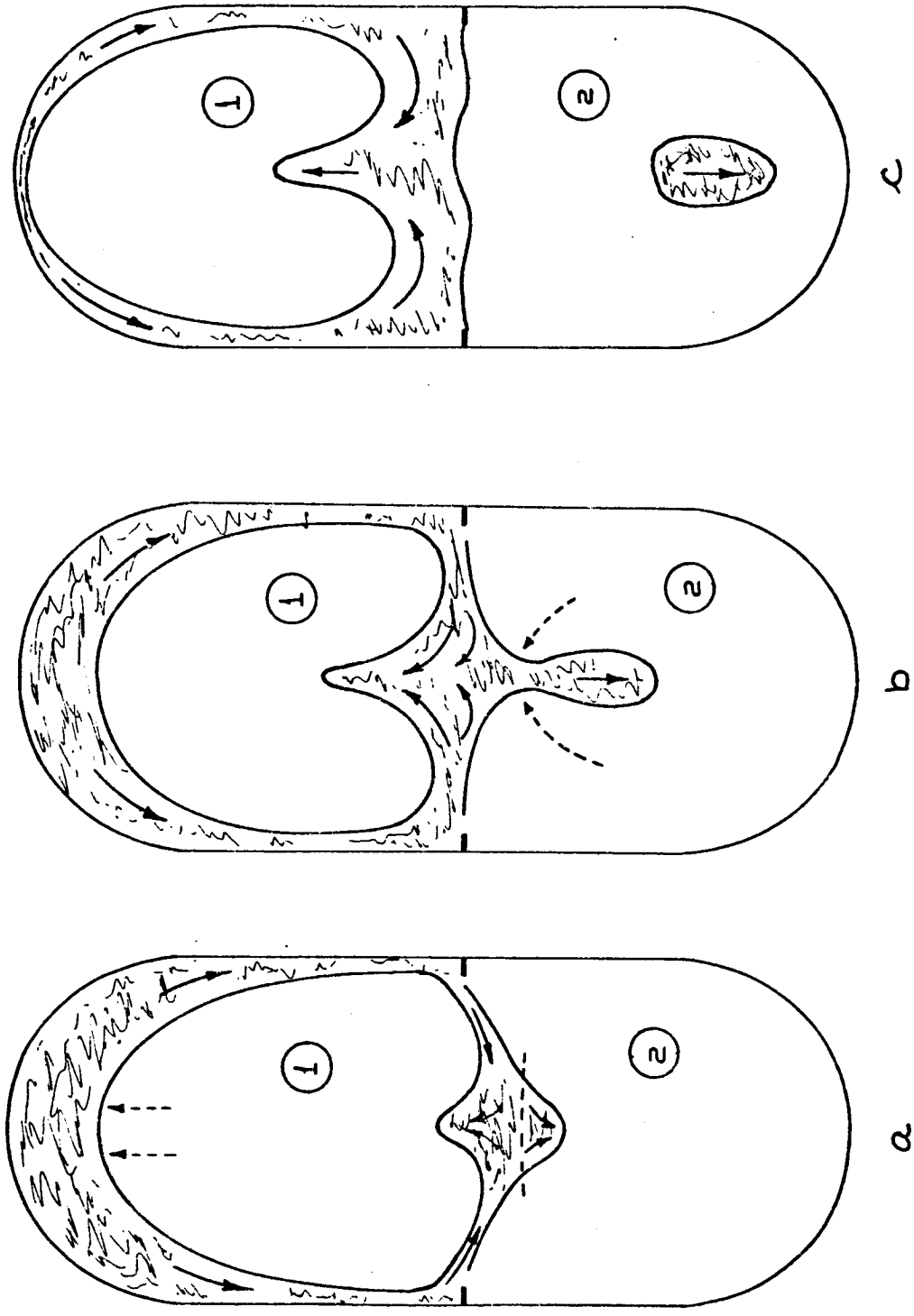

Reorientation in a Tank with Ring Baffles

Figure 2-21

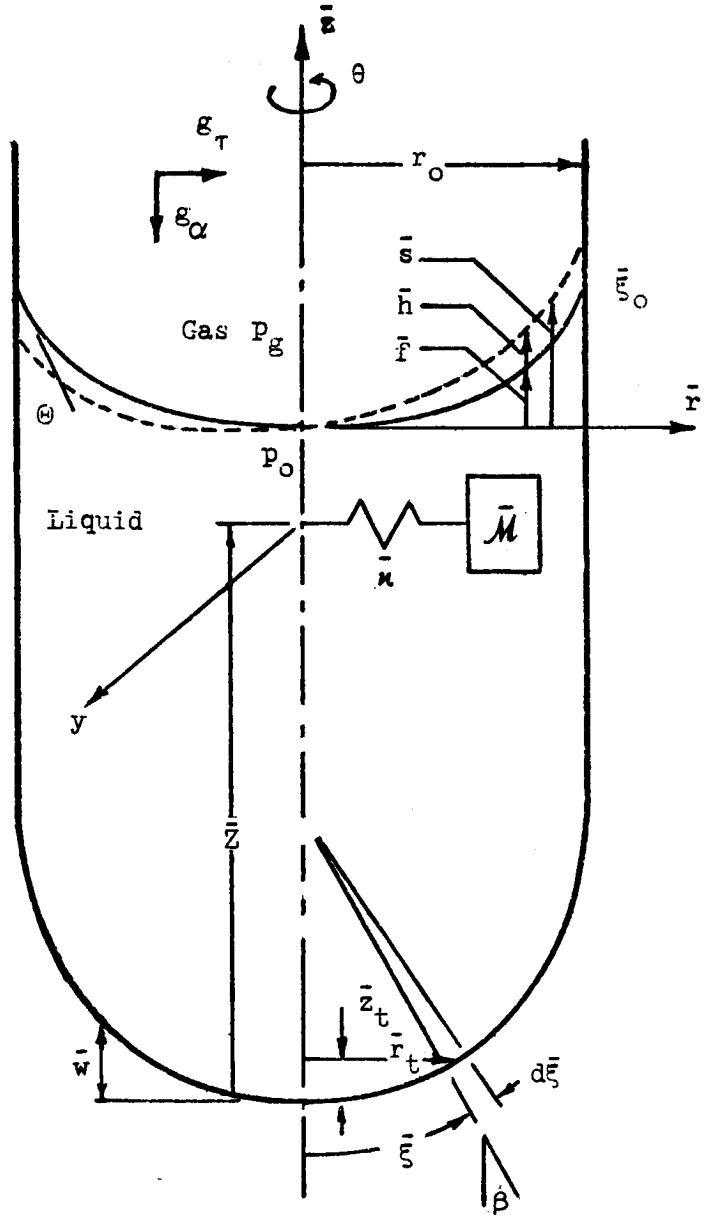

Container Geometry and Coordinate System

Figure 2-22

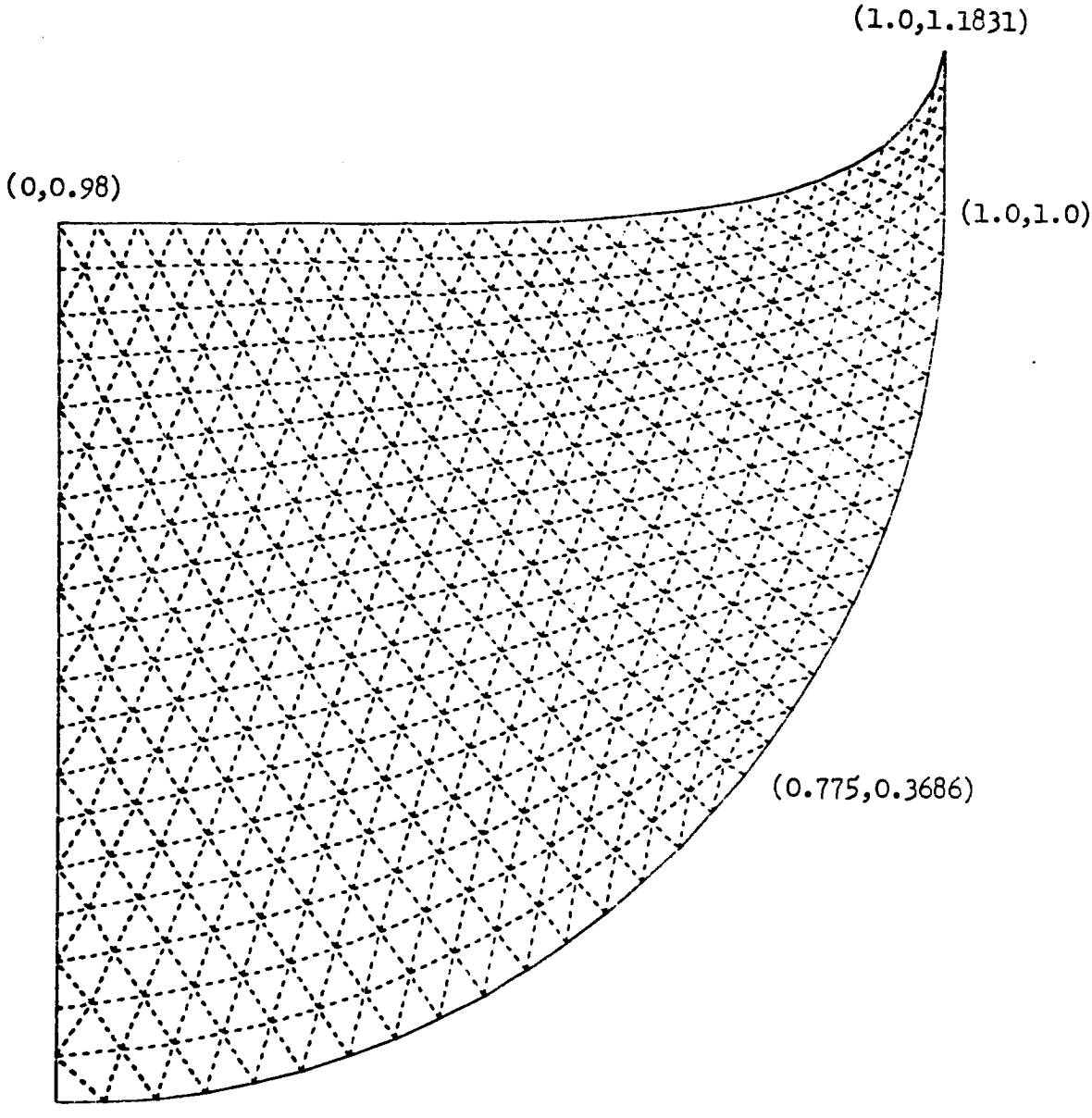

Physical Cross-Section of D
Computing Mesh for $B_\alpha = 50$, $h_o = 1, \theta = 5$ degrees
25 free-surface computing points

Figure 2-23

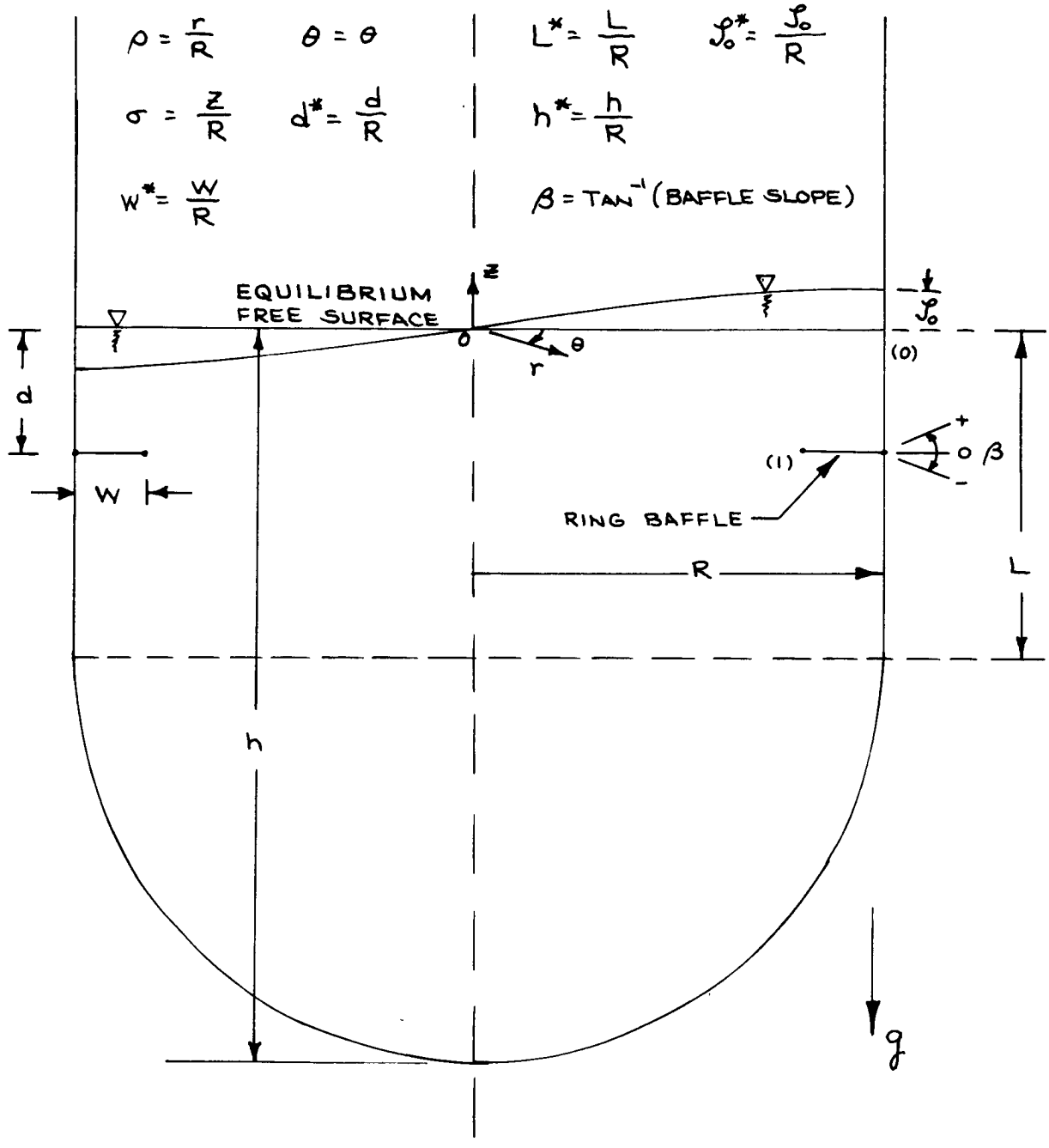

Slosh Damping Parameter Definitions

for Cylindrical Tank with Hemispherical Bottom

Figure 2-24a

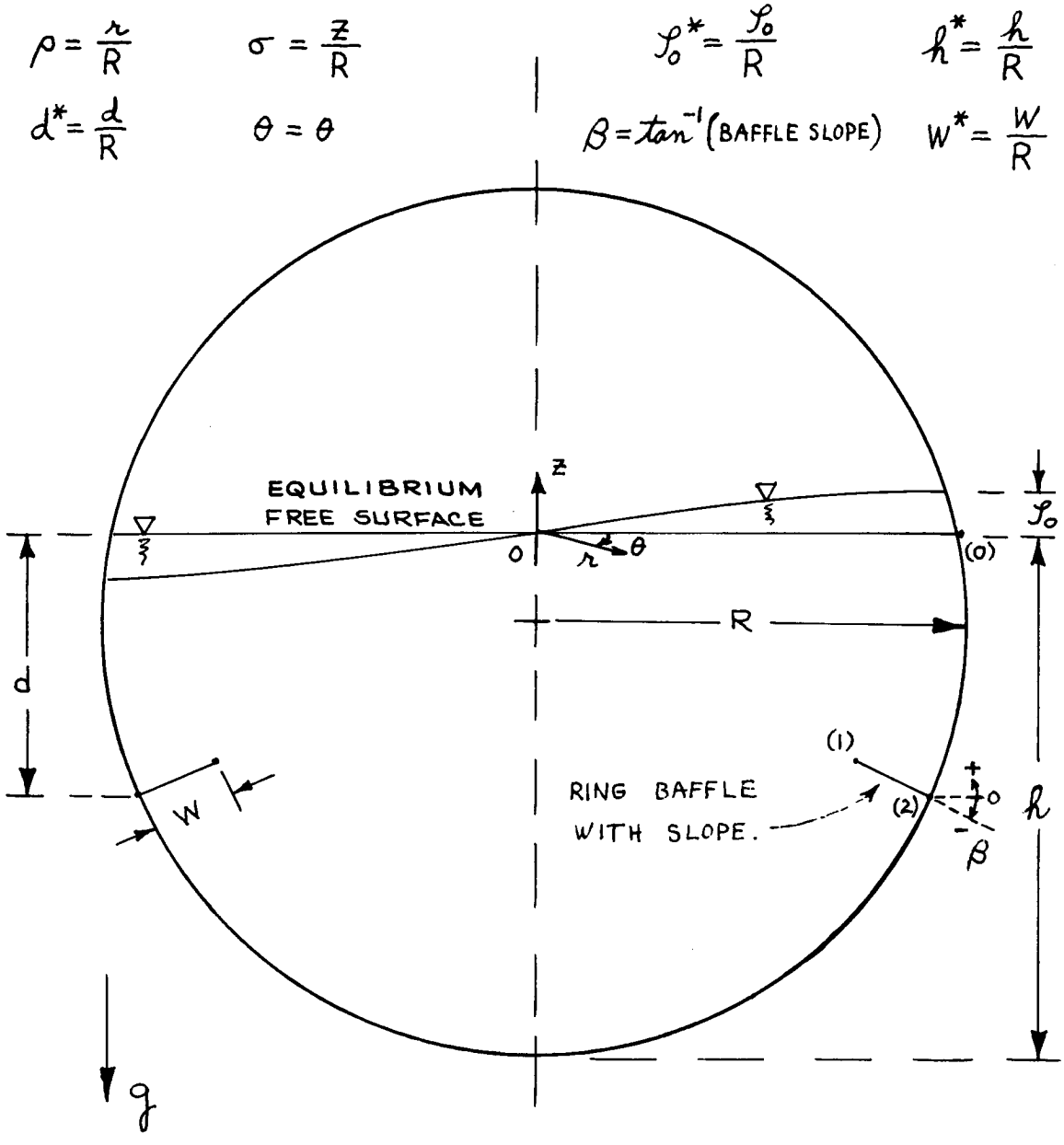

Slosh Damping Parameter Definitions

for Spherical Tank with a Ring Baffle

Figure 2-24b

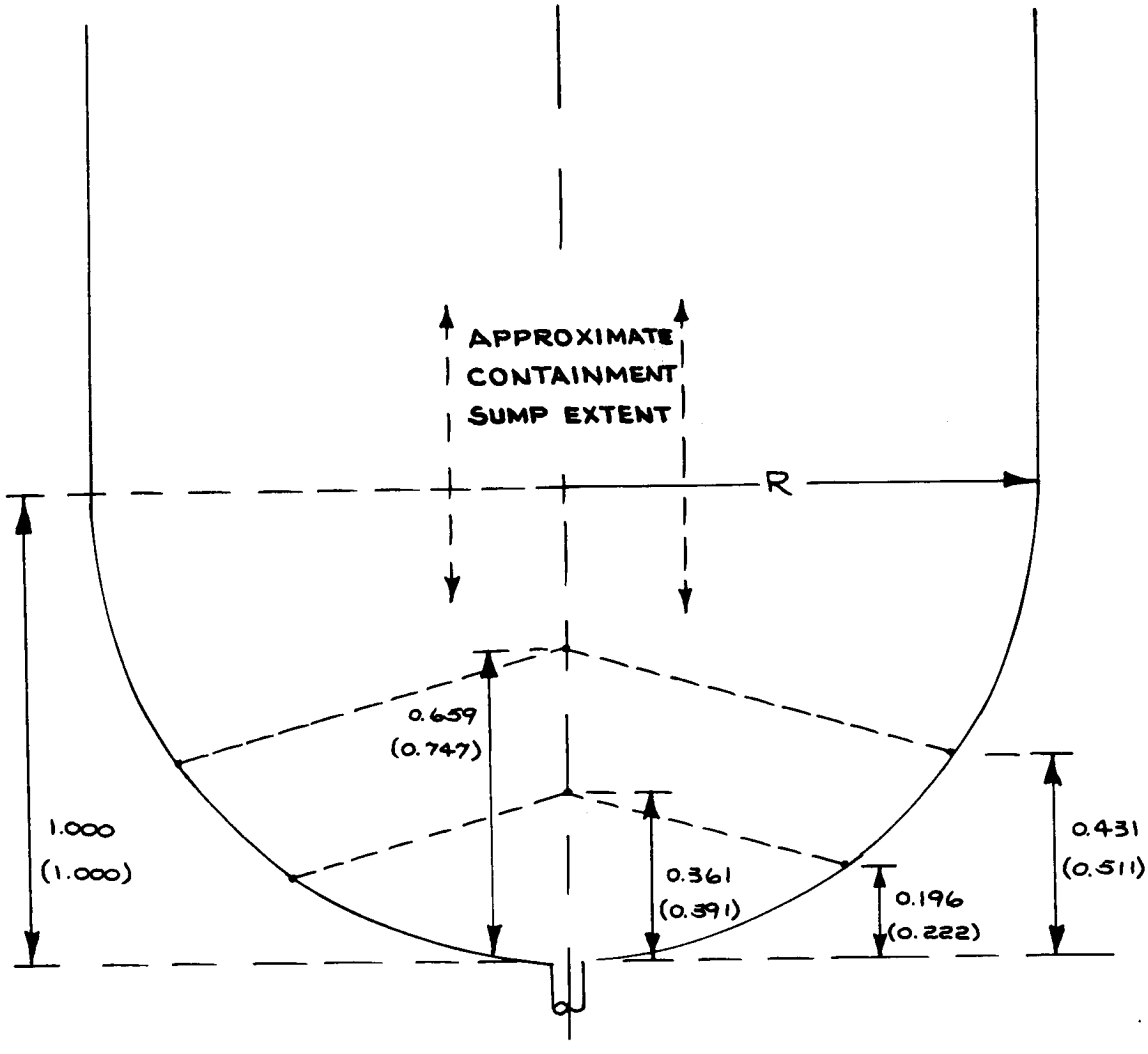

All dimensions are nondimensionalized with respect to R

Apollo Spacecraft Propulsion System

Oxidizer and Fuel Tanks Baffle Geometries

(Fuel Tank Dimensions Shown in Parenthesis)

Figure 2-25

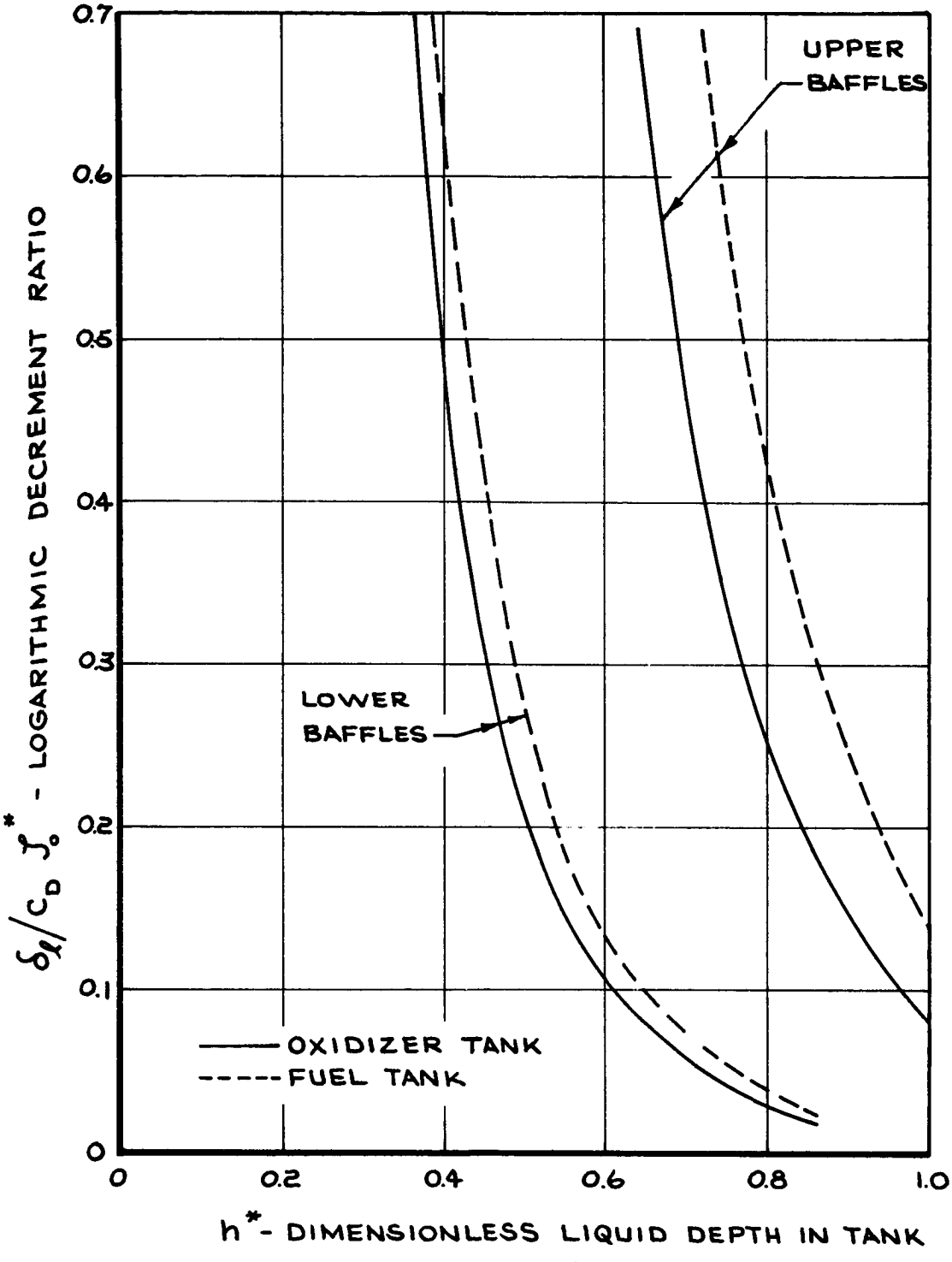

Logarithmic Decrement Vs Dimensionless Liquid Depth for the Apollo/SPS Conical Porous Plate Baffles

Figure 2-26

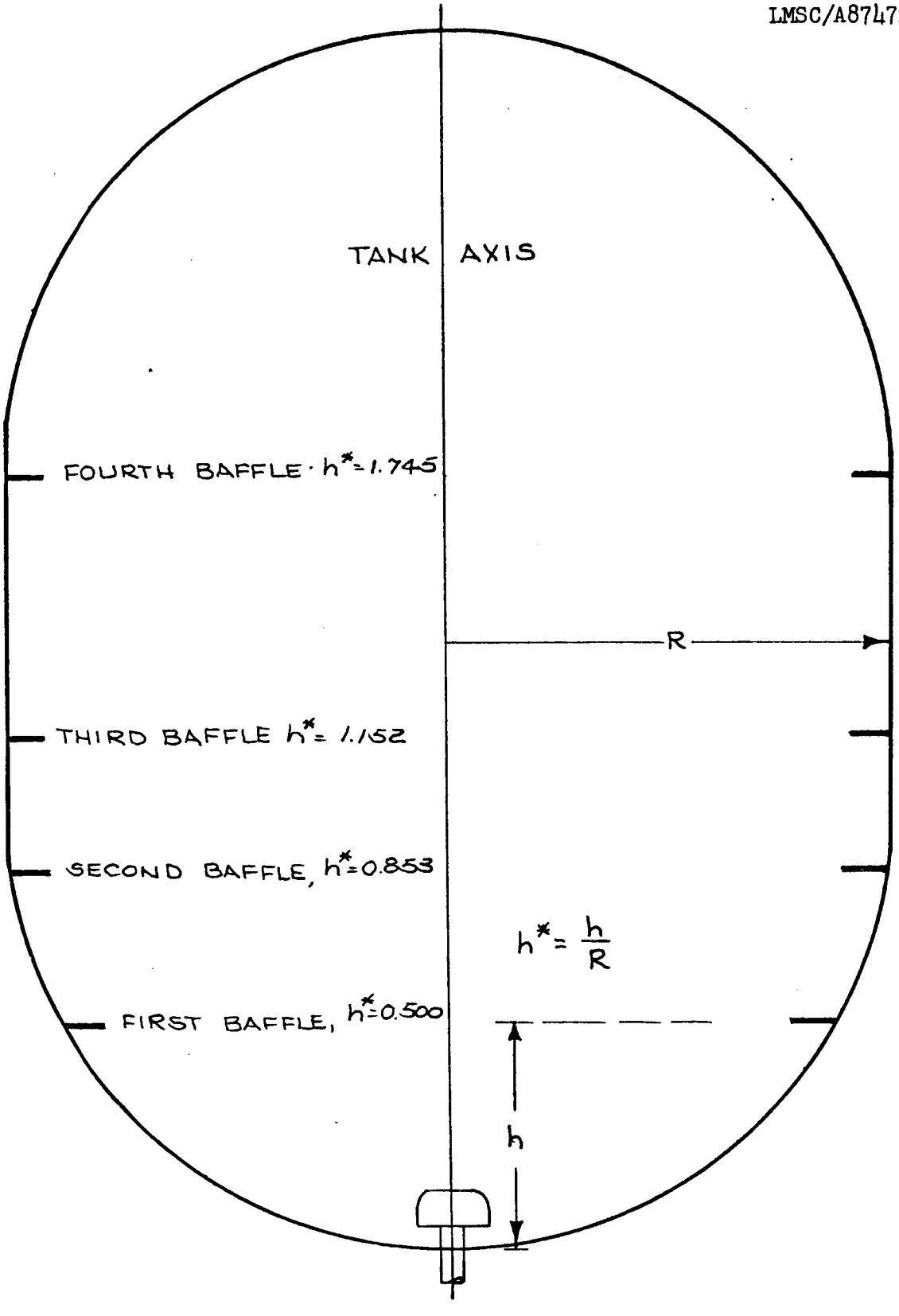

LM Descent Tanks with Proposed Ring Baffles

Figure 2-27

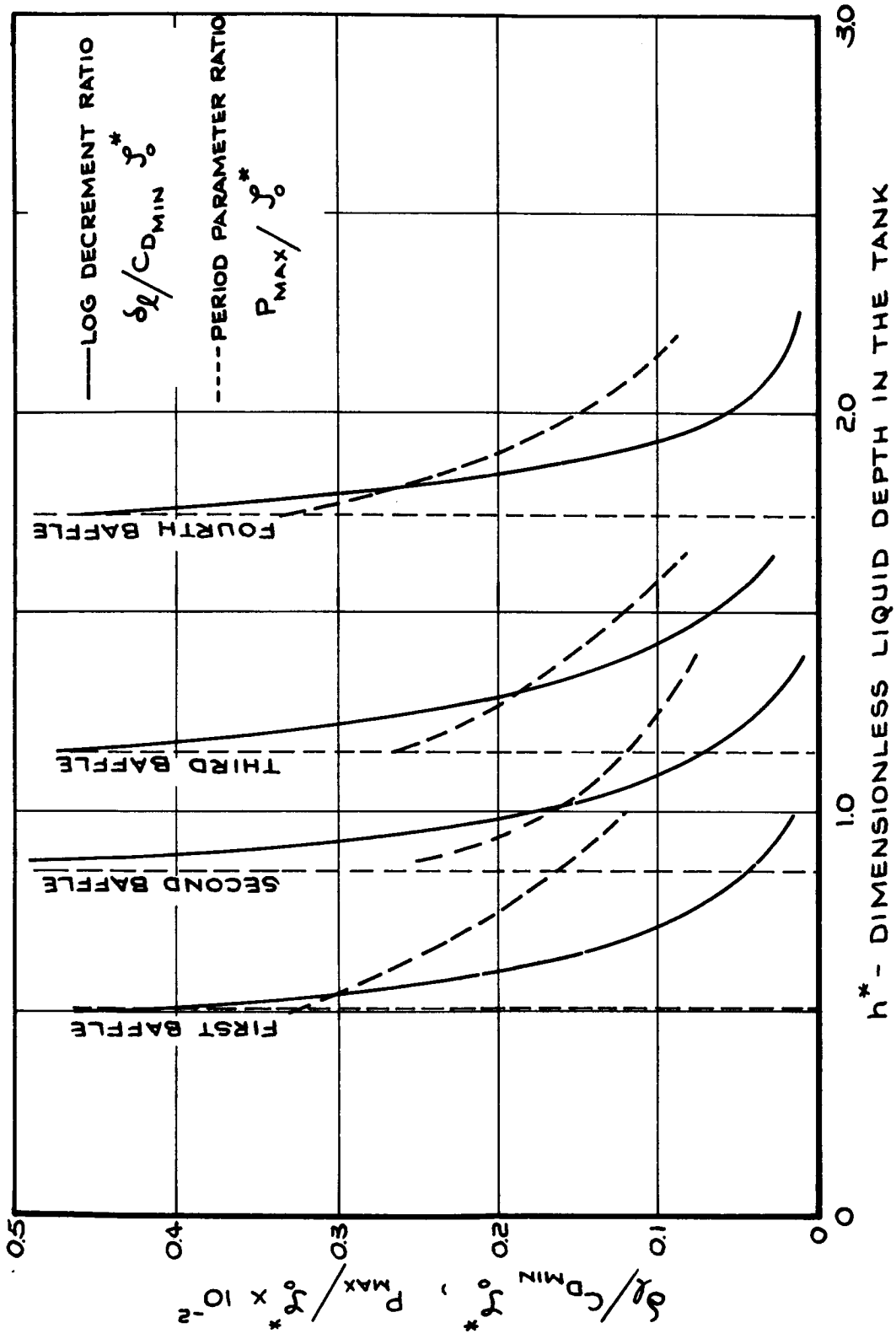

Slosh Damping in the LM Descent Tanks

Figure 2-28

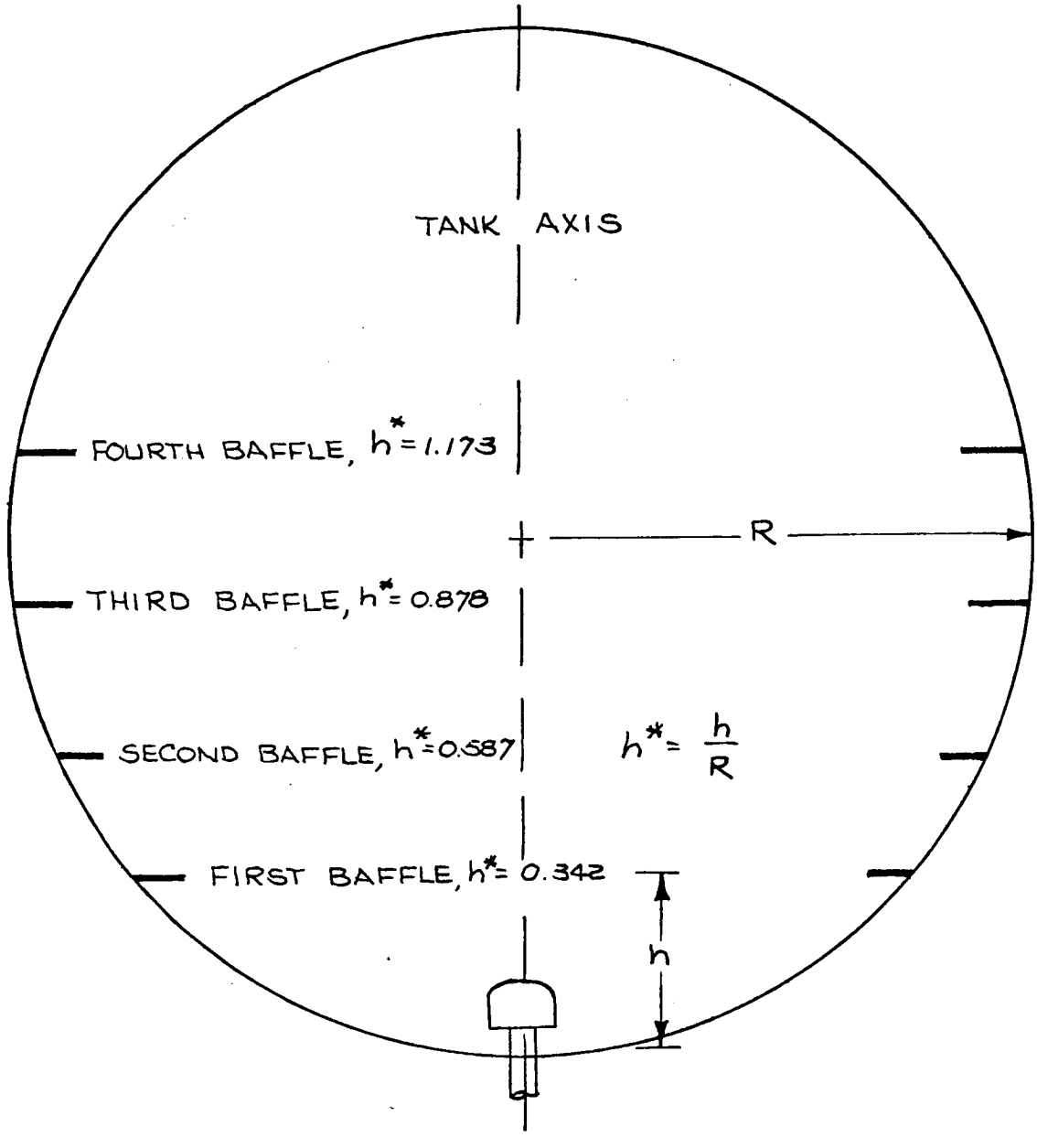

LM Ascent Tanks With Proposed Ring Baffles

Figure 2-29

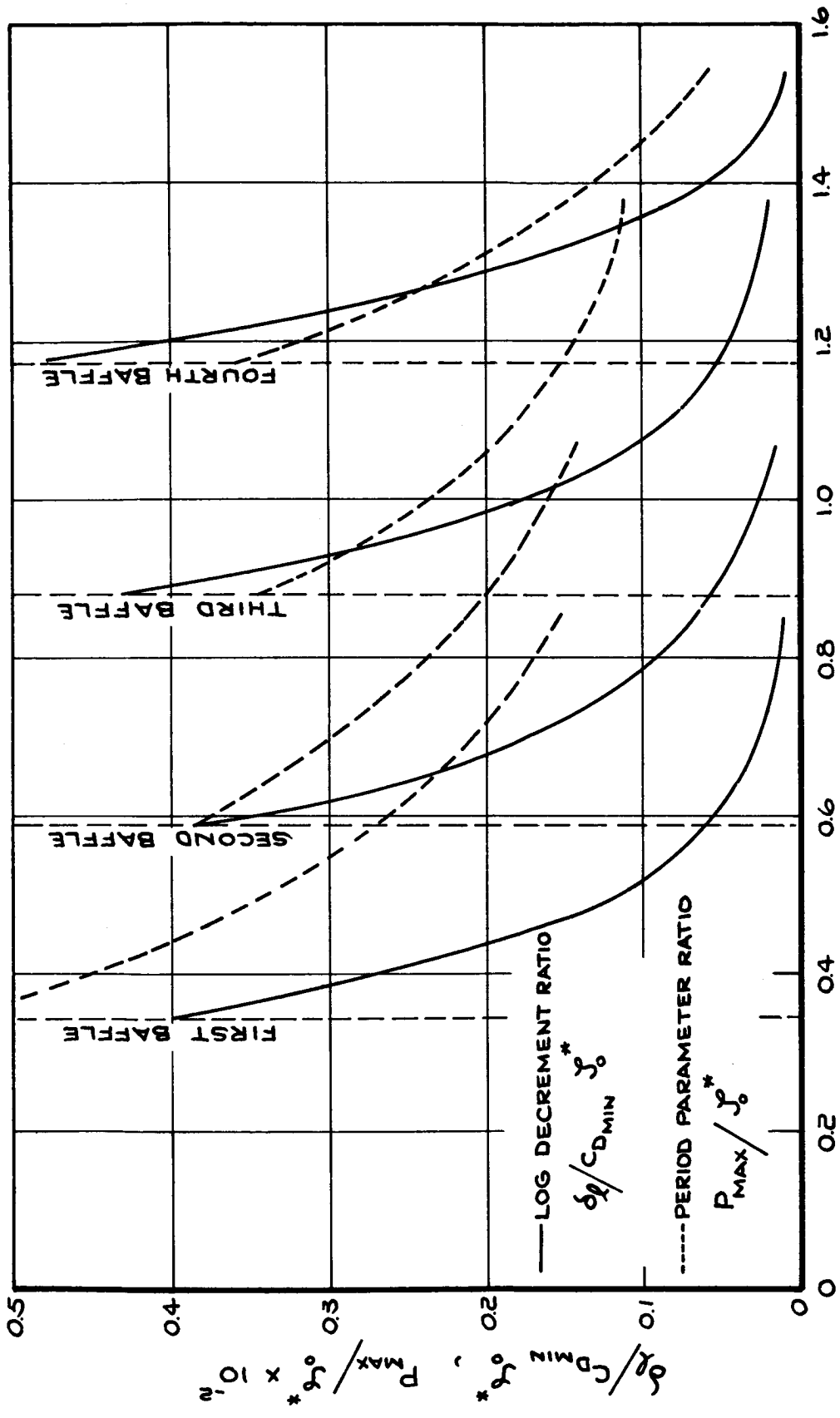

Slosh Damping in the IM Ascent Tanks

Figure 2-30

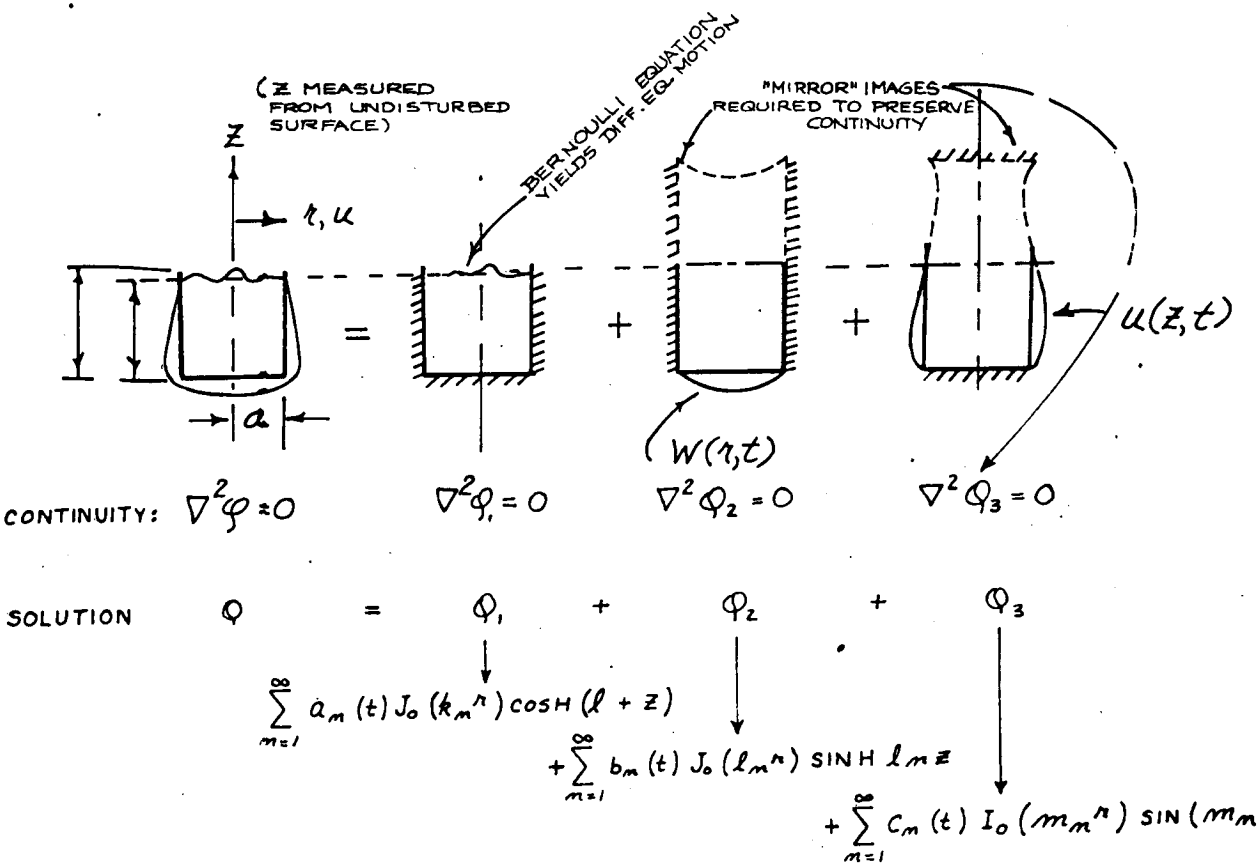

Formulation of Series Solution

Figure 2-31

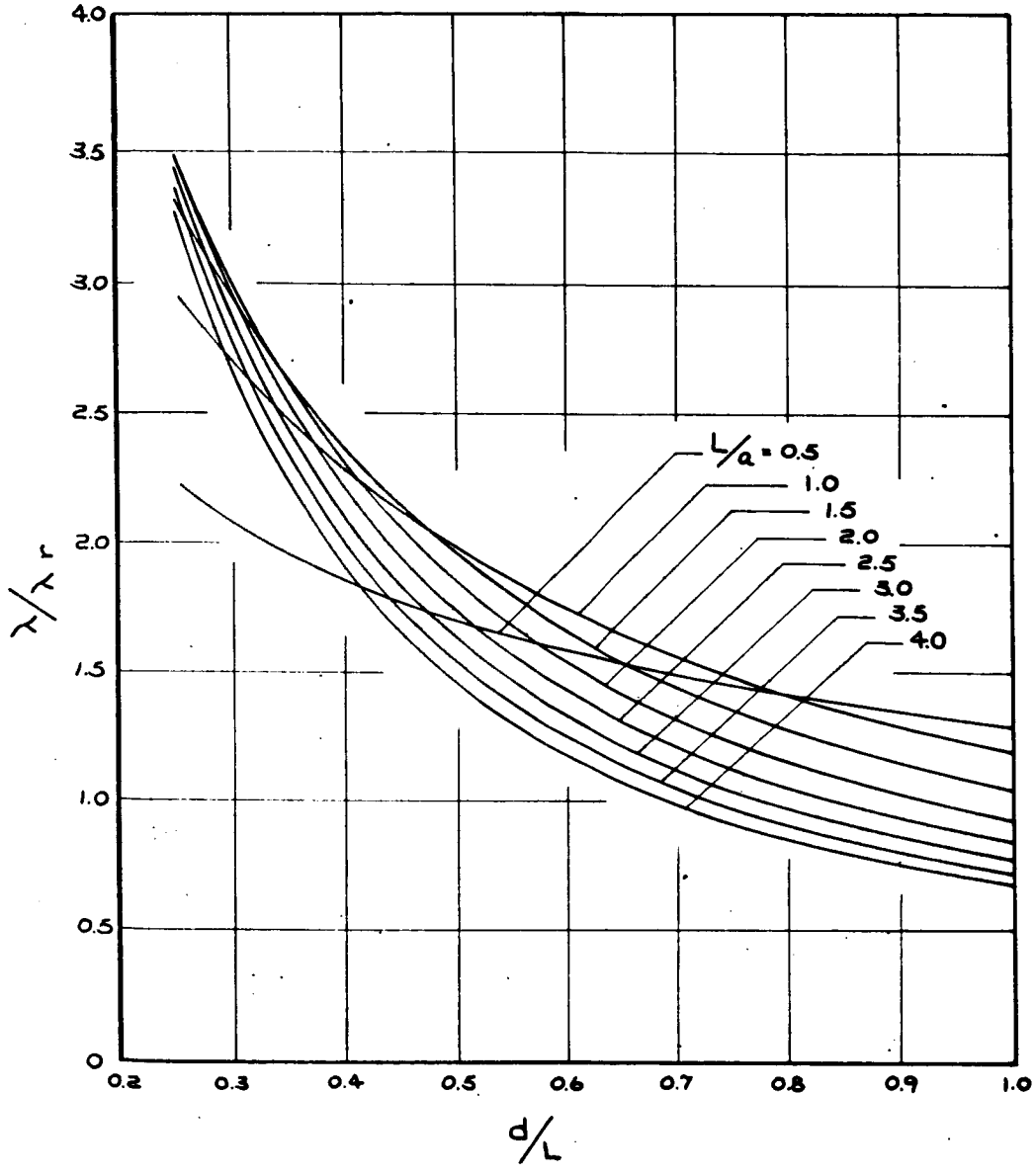

Tank Frequency Ratio vs. Depth-to-Length Ratio

Figure 2-32

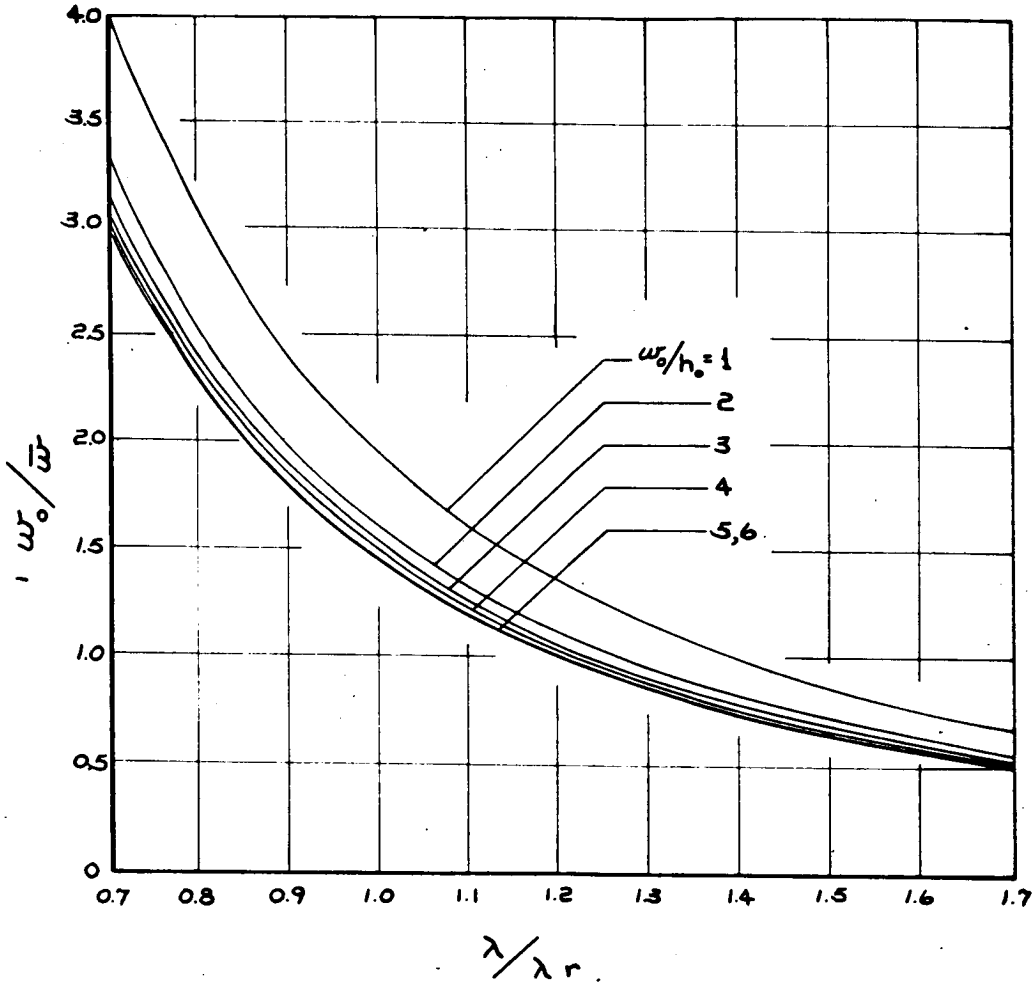

Bottom Deflection Ratio for Matching

Bottom Frequency with Wall Frequency

Figure 2-33

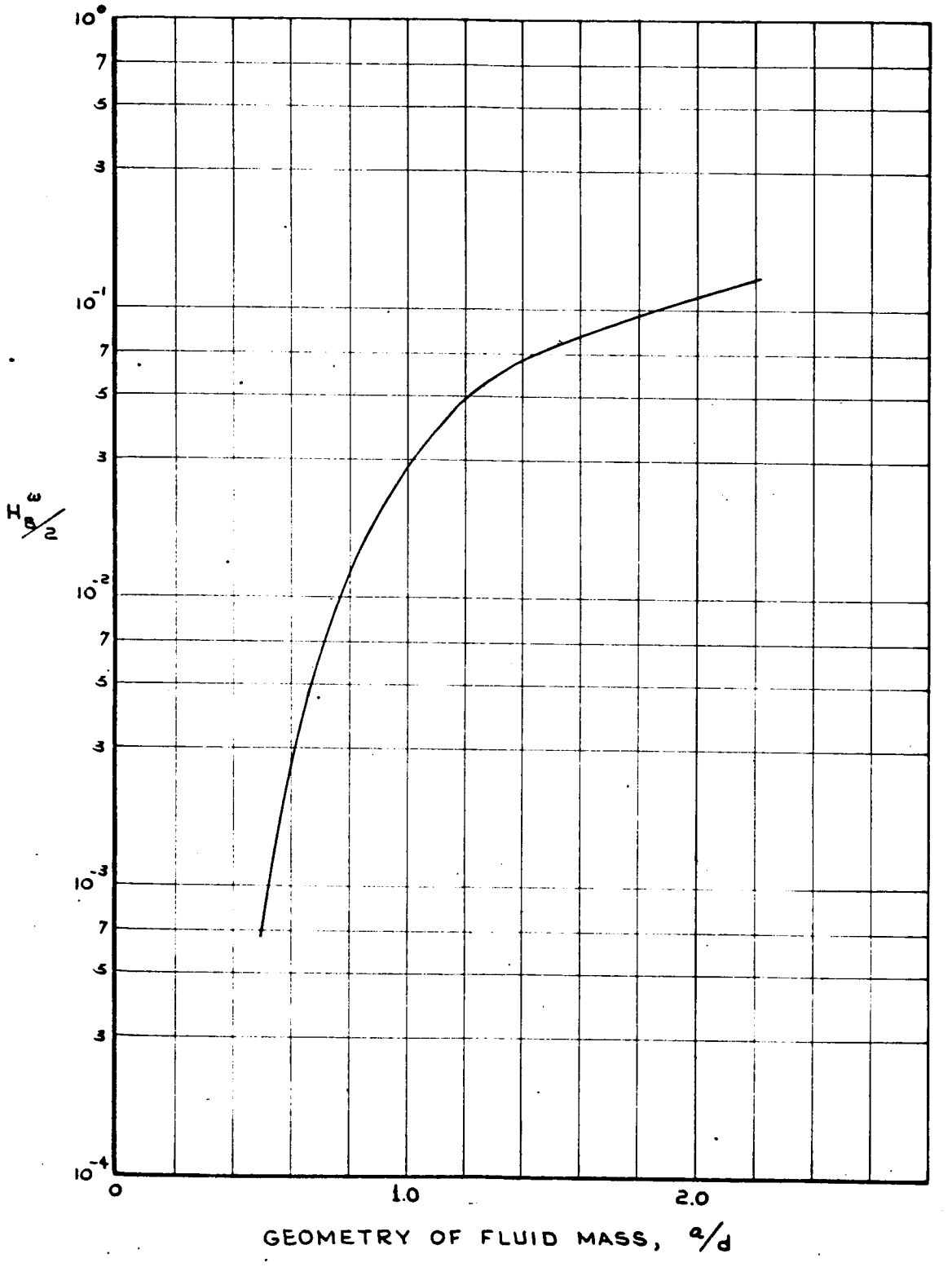

Contribution of Tank Bottom Motion to Surface Function

Figure 2-34

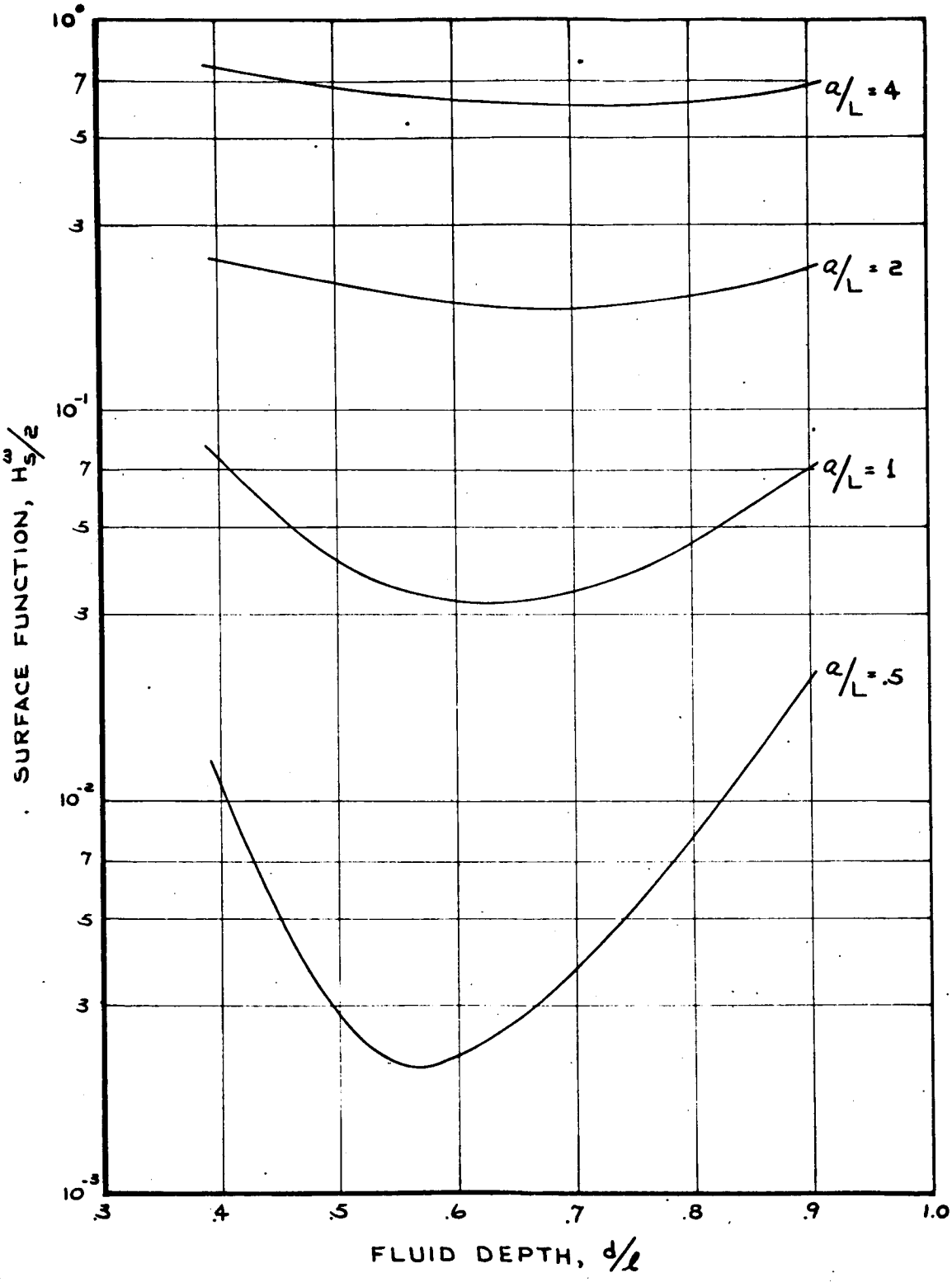

Contribution of Sidewall Motion to Surface Function

Figure 2-35

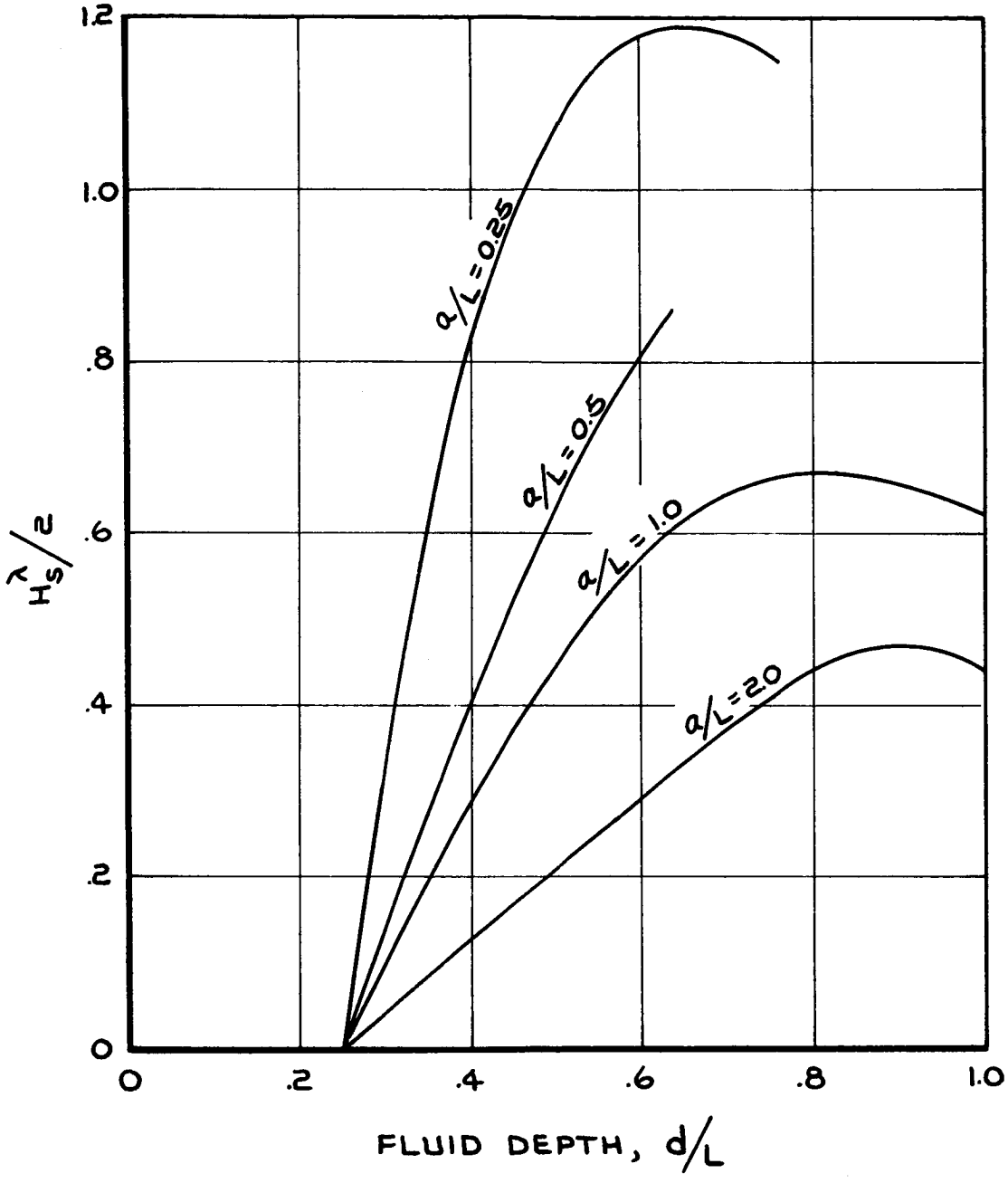

Contribution of Sidewall Motion to Surface Function

Figure 2-36

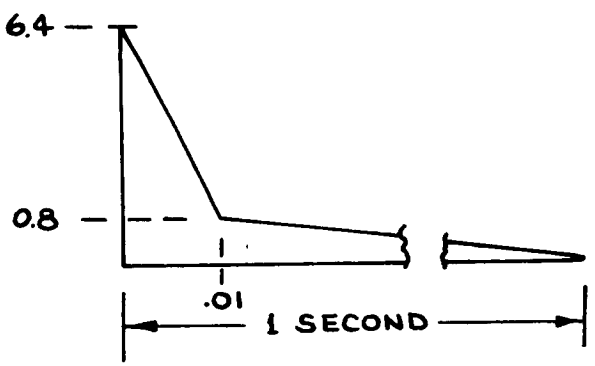

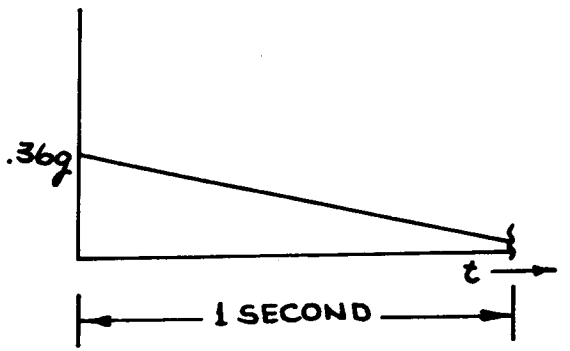

OTHER VEHICLES

SATURN: S I C; $t_o \sim .50$ SEC.

S II; $t_o \sim .25$ SEC.

S IV B; $t_o \sim .10$ SEC.

Idealized Thrust Decay Curves

Figure 2-37

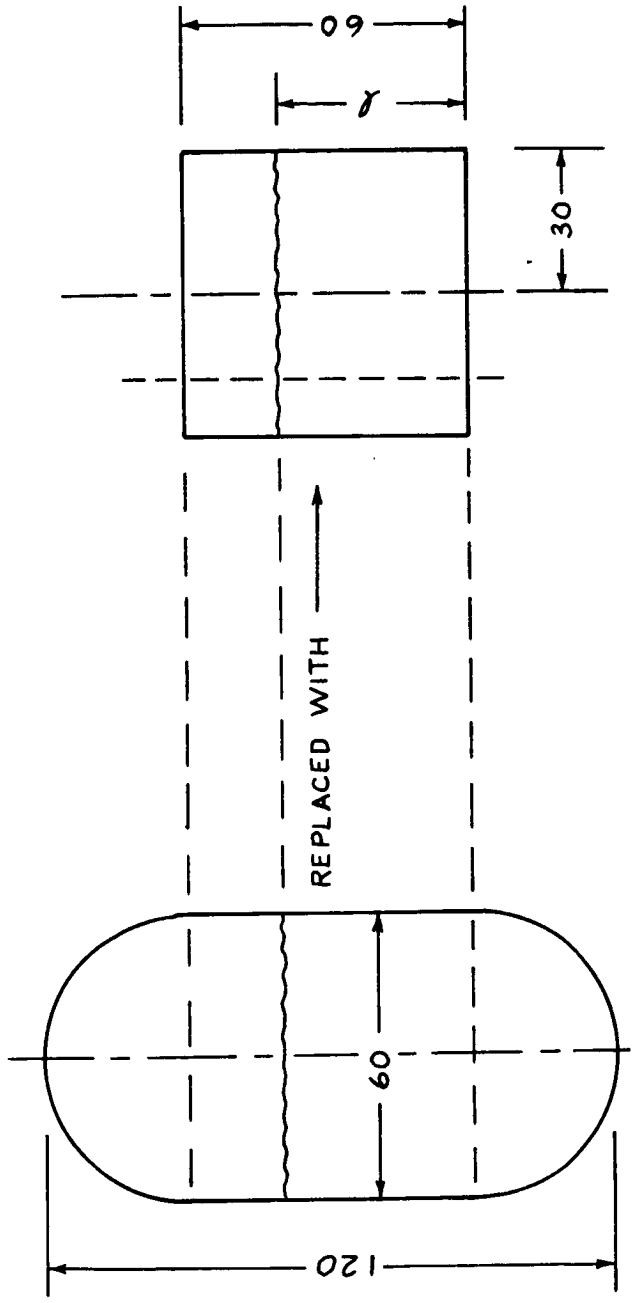

ALL DIMENSIONS IN INCHES

σ = SURFACE TENSION OF OXIDIZER (IRFNA)

ρ = DENSITY OF OXIDIZER

σ/ρ = 26.2 $cm^3/sec.^2$

WALL THICKNESS: 0.070

MATERIAL: ALUMINUM; $E = 10 \times 10^6$ PSI

Idealized Agena Oxidizer Tank

Figure 2-38

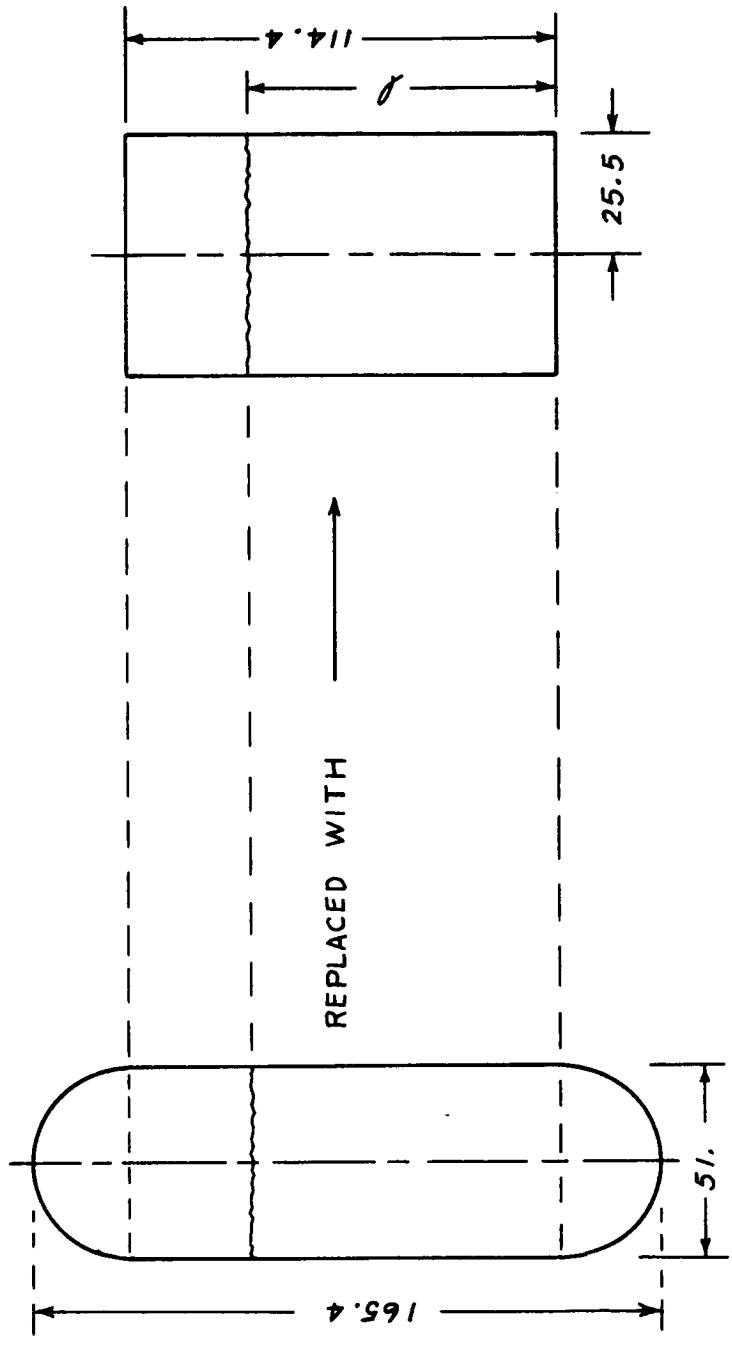

ALL DIMENSIONS IN INCHES

SURFACE TENSION OF OXIDIZER (N_2O_4) = 26.4 DYNES/CM
SPECIFIC GRAVITY : 1.45
WALL THICKNESS : 0.040 IN.
MATERIAL : TITANIUM, E = 16×10^6 PSI

Idealized Apollo Service Module Oxidizer Tank

Figure 2-39

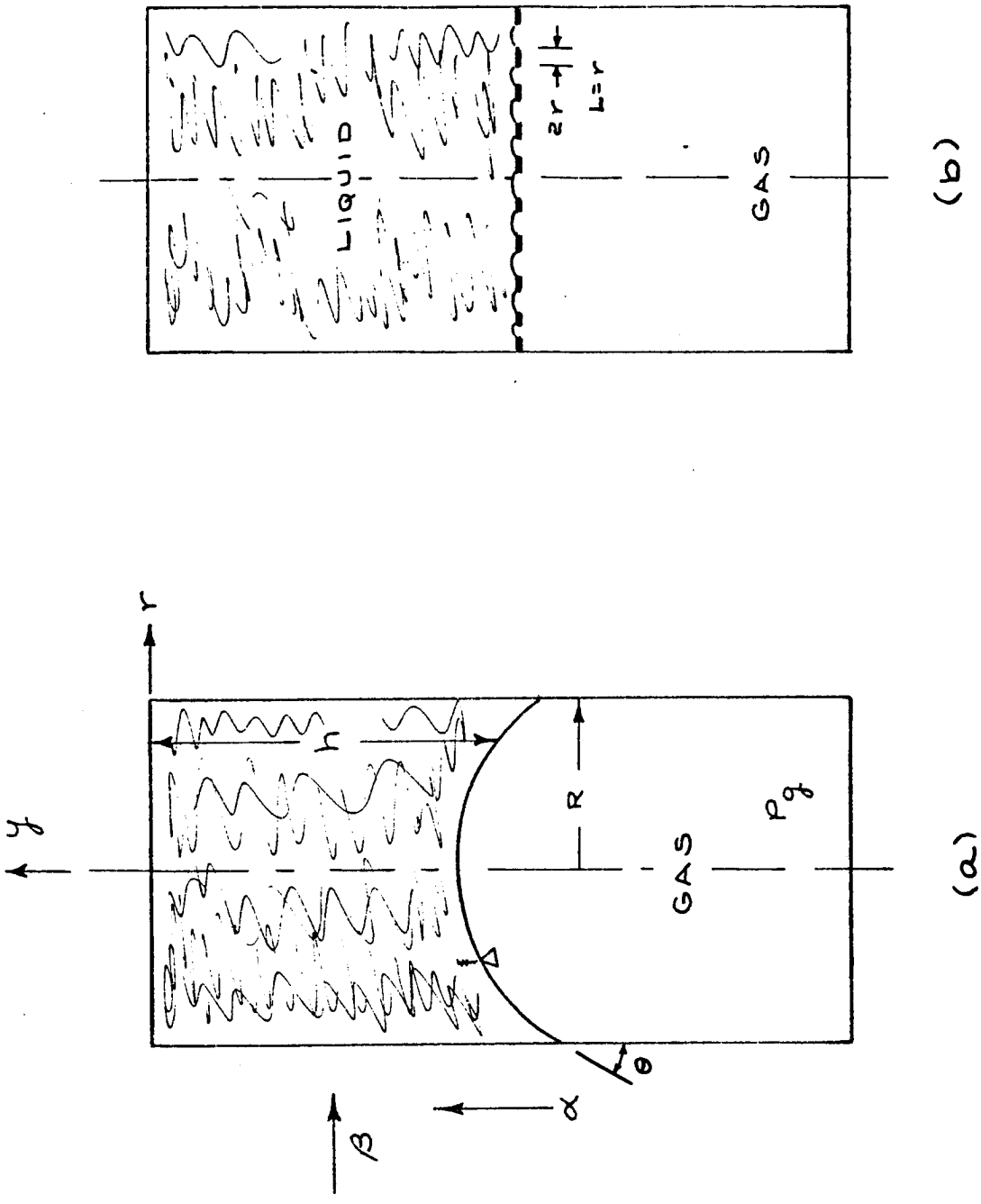

Liquid Propellant Locational Stability

Figure 2-40

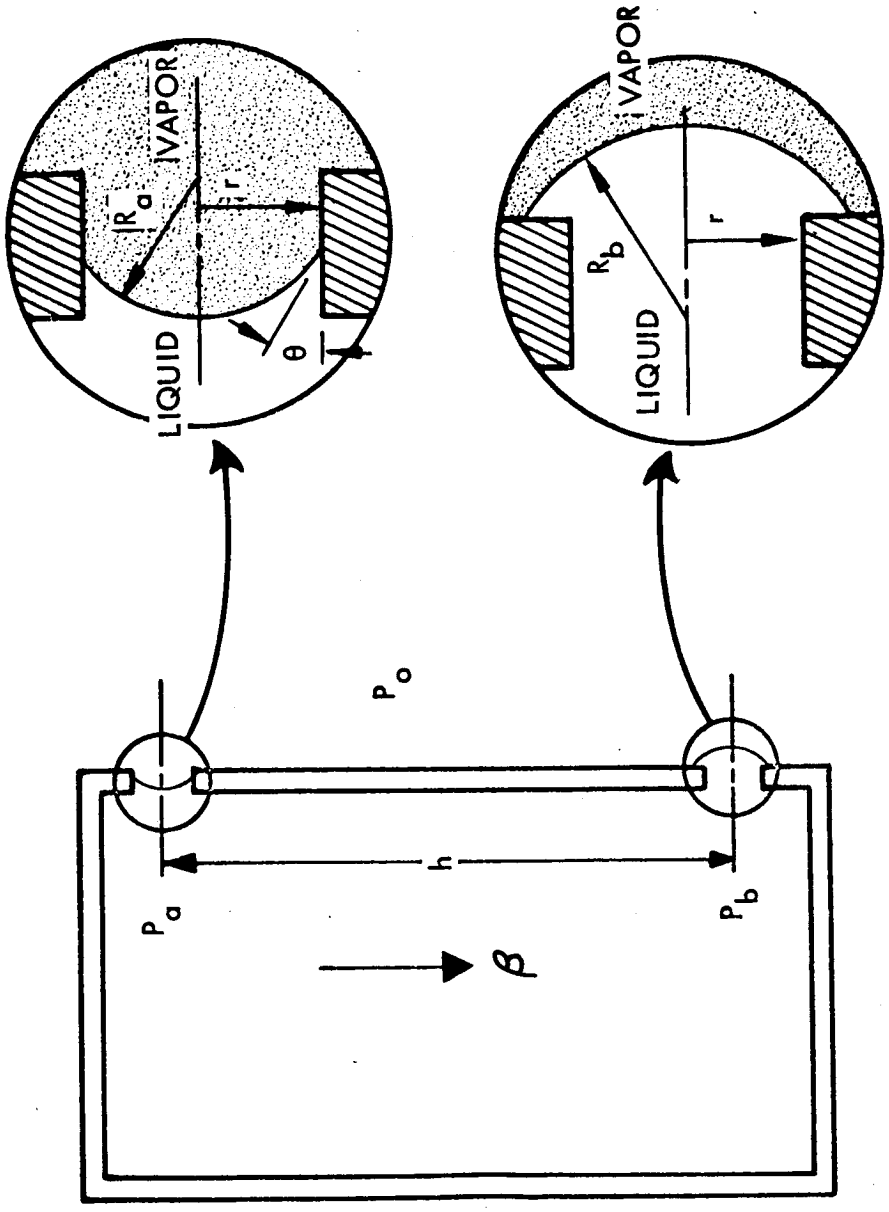

Capillary Supported Containment

Figure 2-41

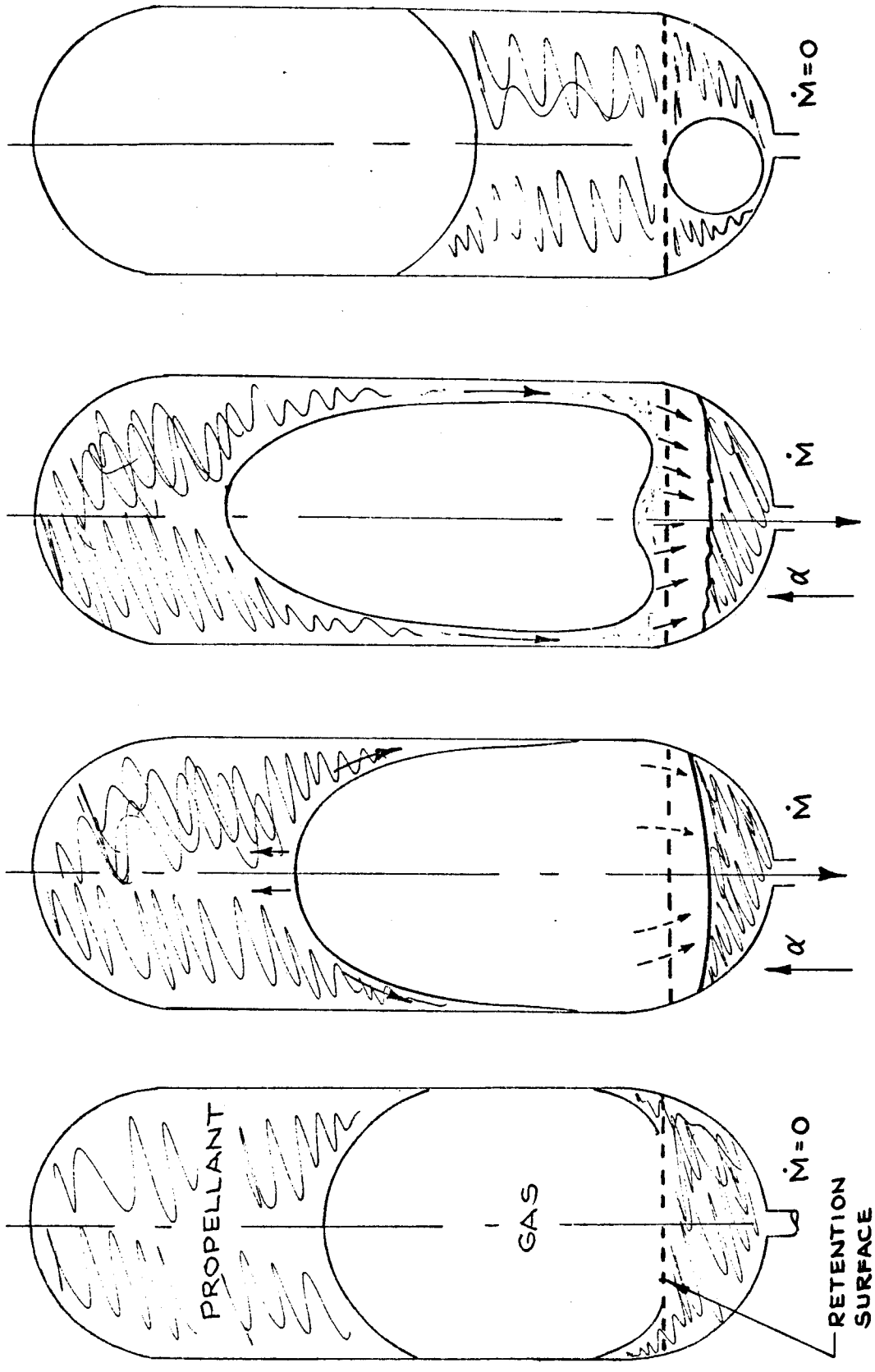

Ullage Gas Entrapment During Engine Restart

Figure 2-42

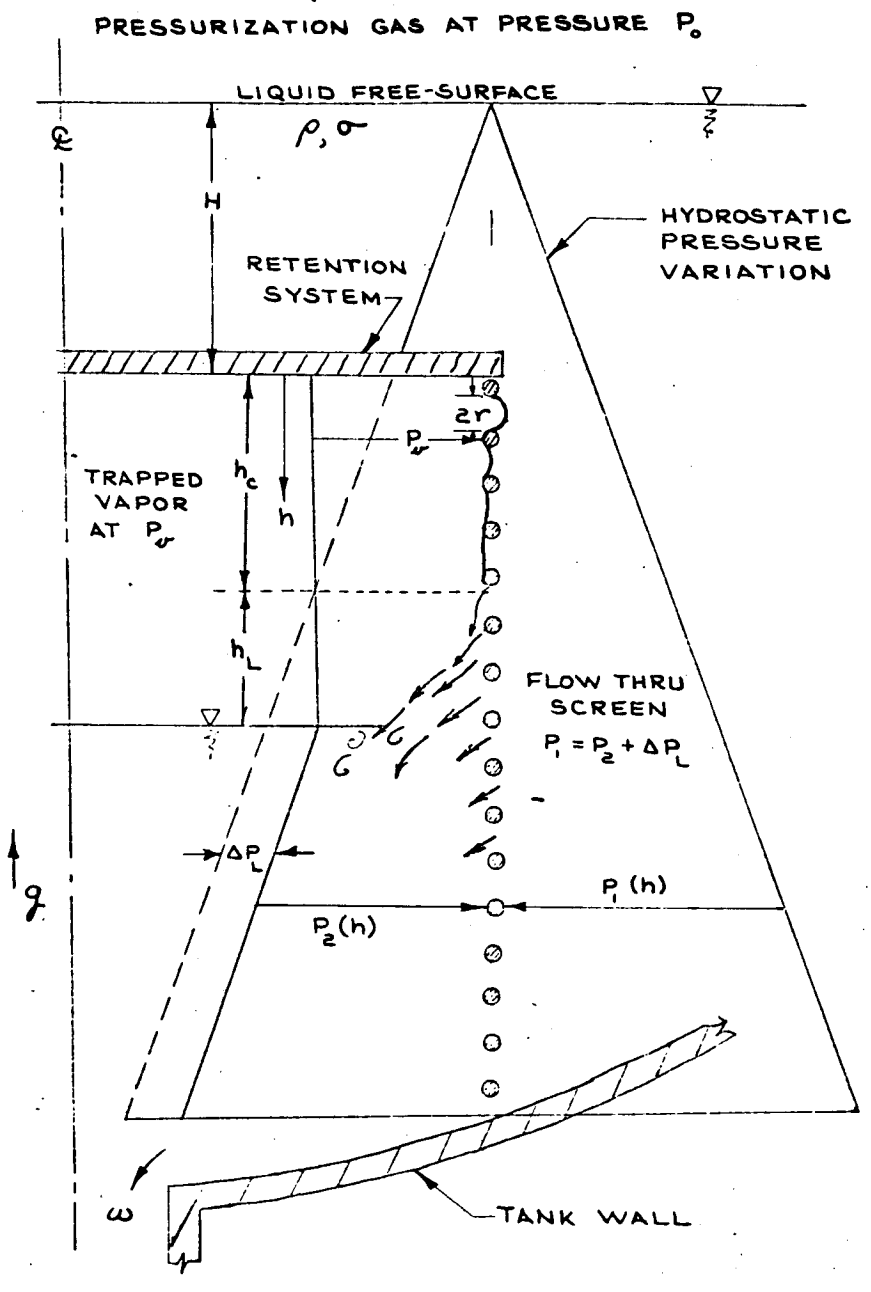

Incomplete Refill of Retention System During Engine Operation

Figure 2-43

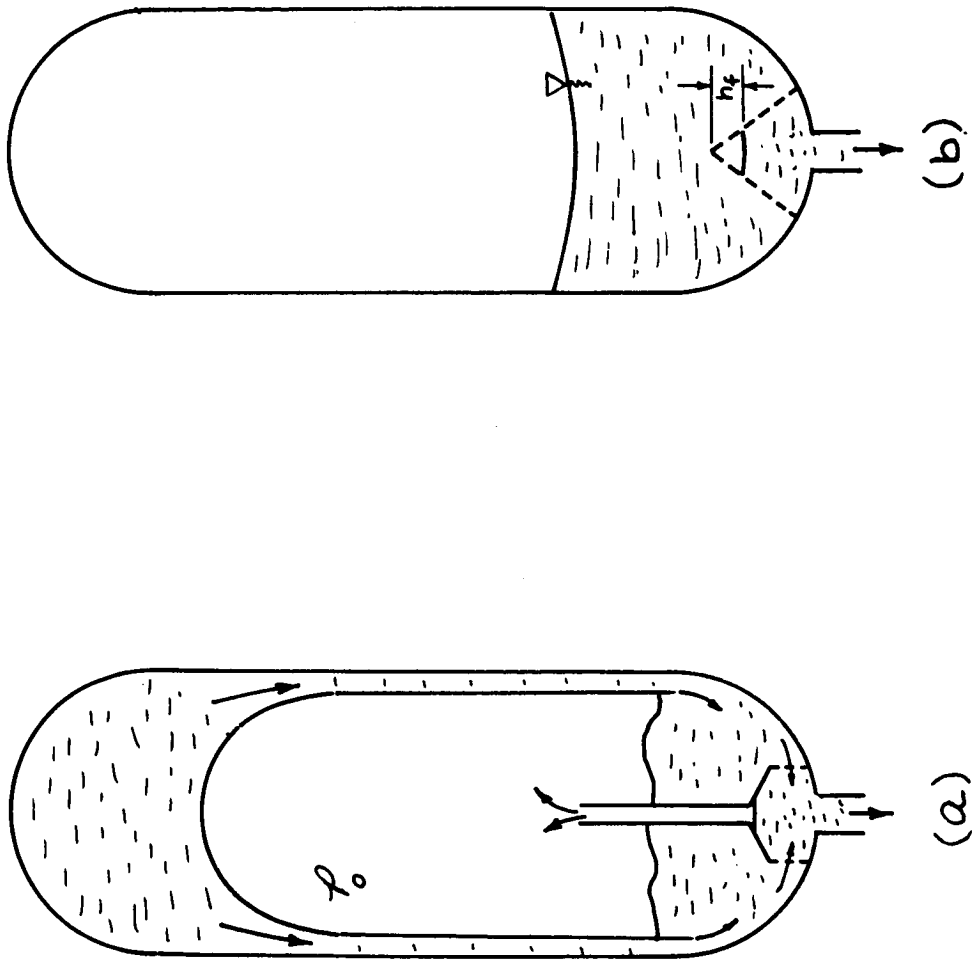

Reduction of Entrapped Ullage Gas in Retention System

Figure 2-44

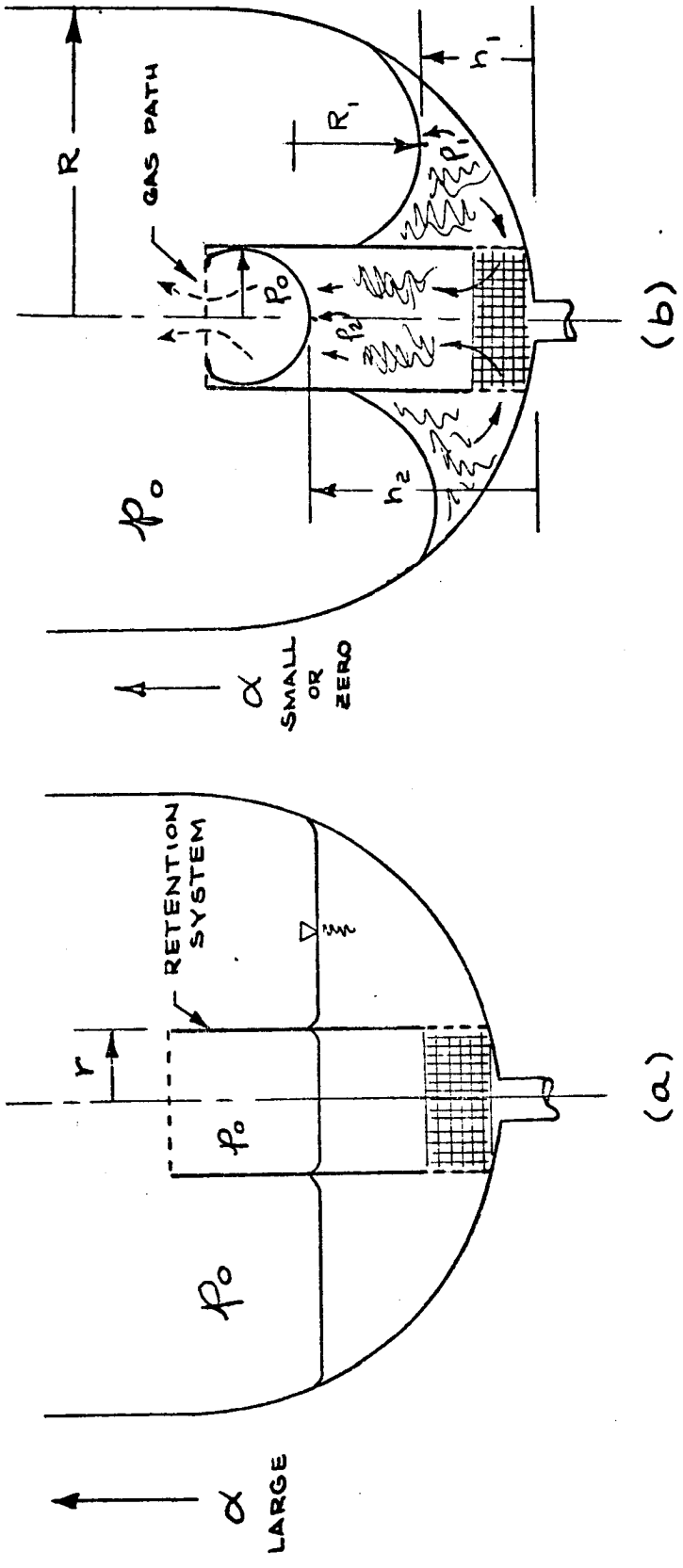

Capillary Refill

Figure 2-45

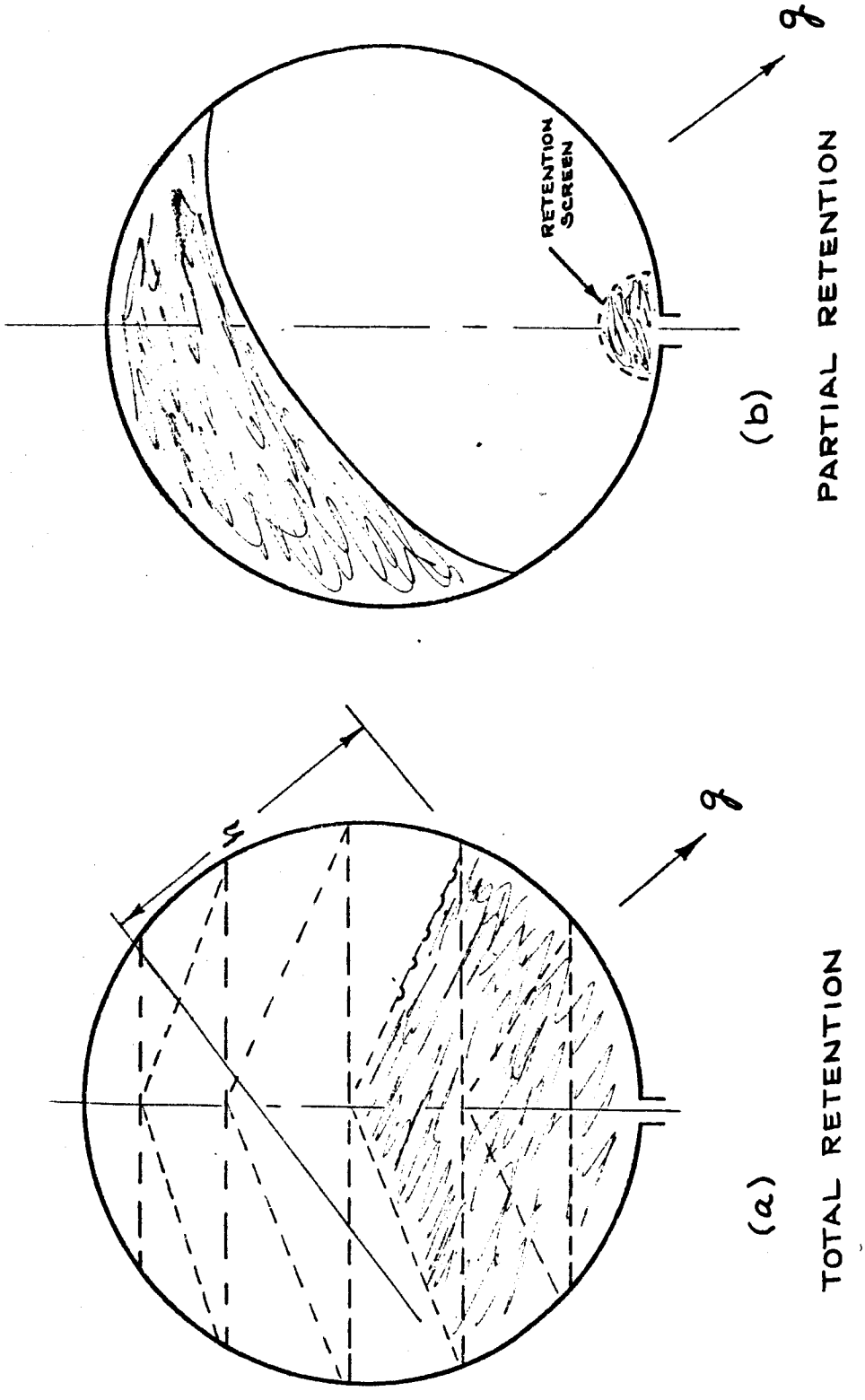

Basic Propellant Retention Approaches

Figure 2-46

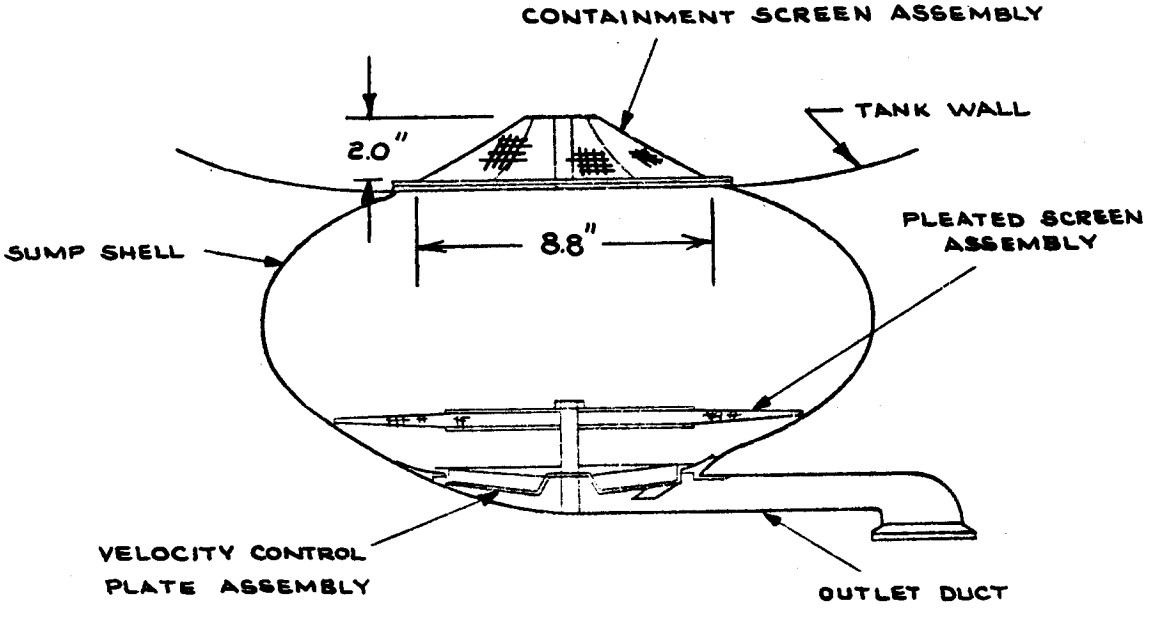

Agena Oxidizer Sump Assembly

Figure 2-47

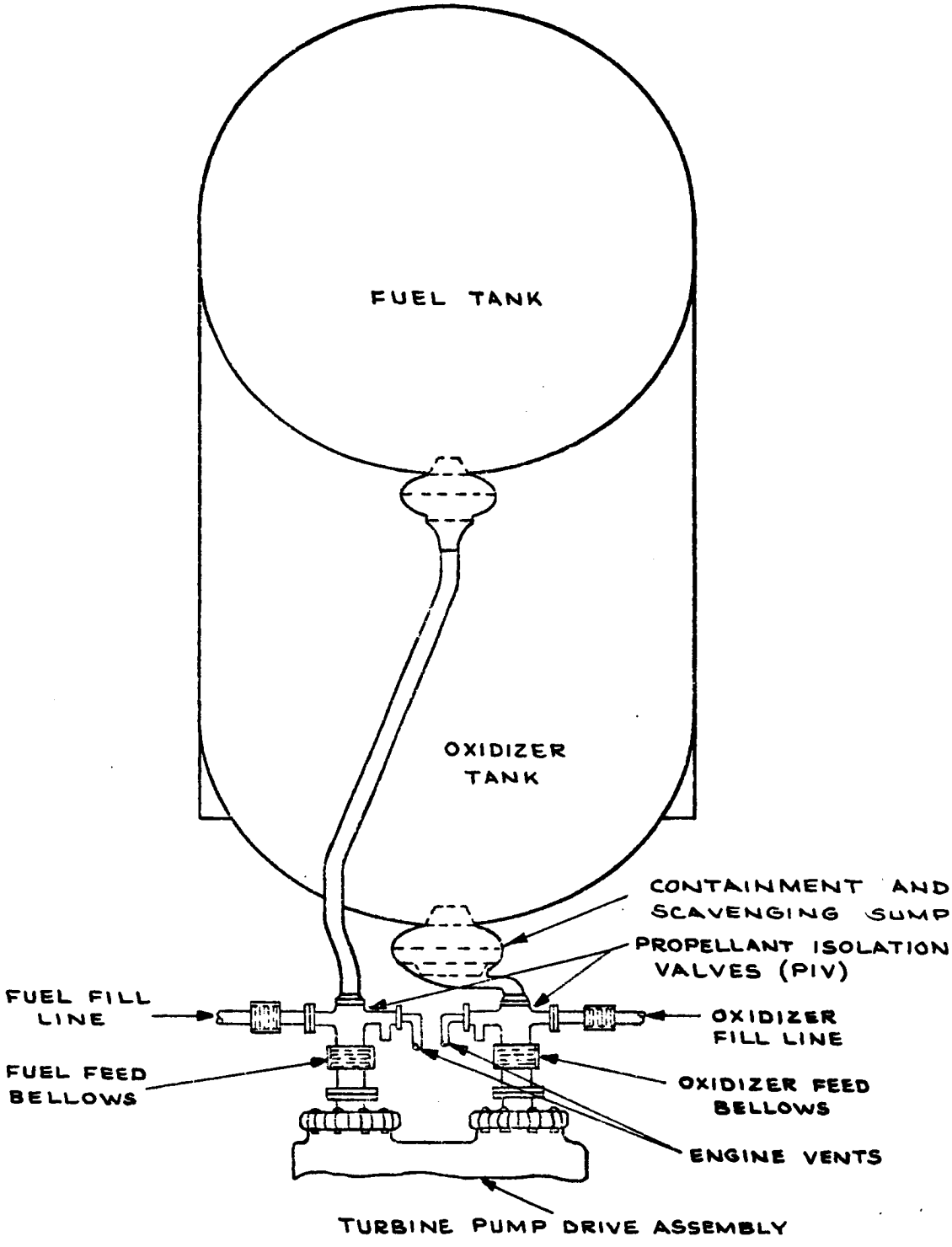

Agena Propellant System

Figure 2-48

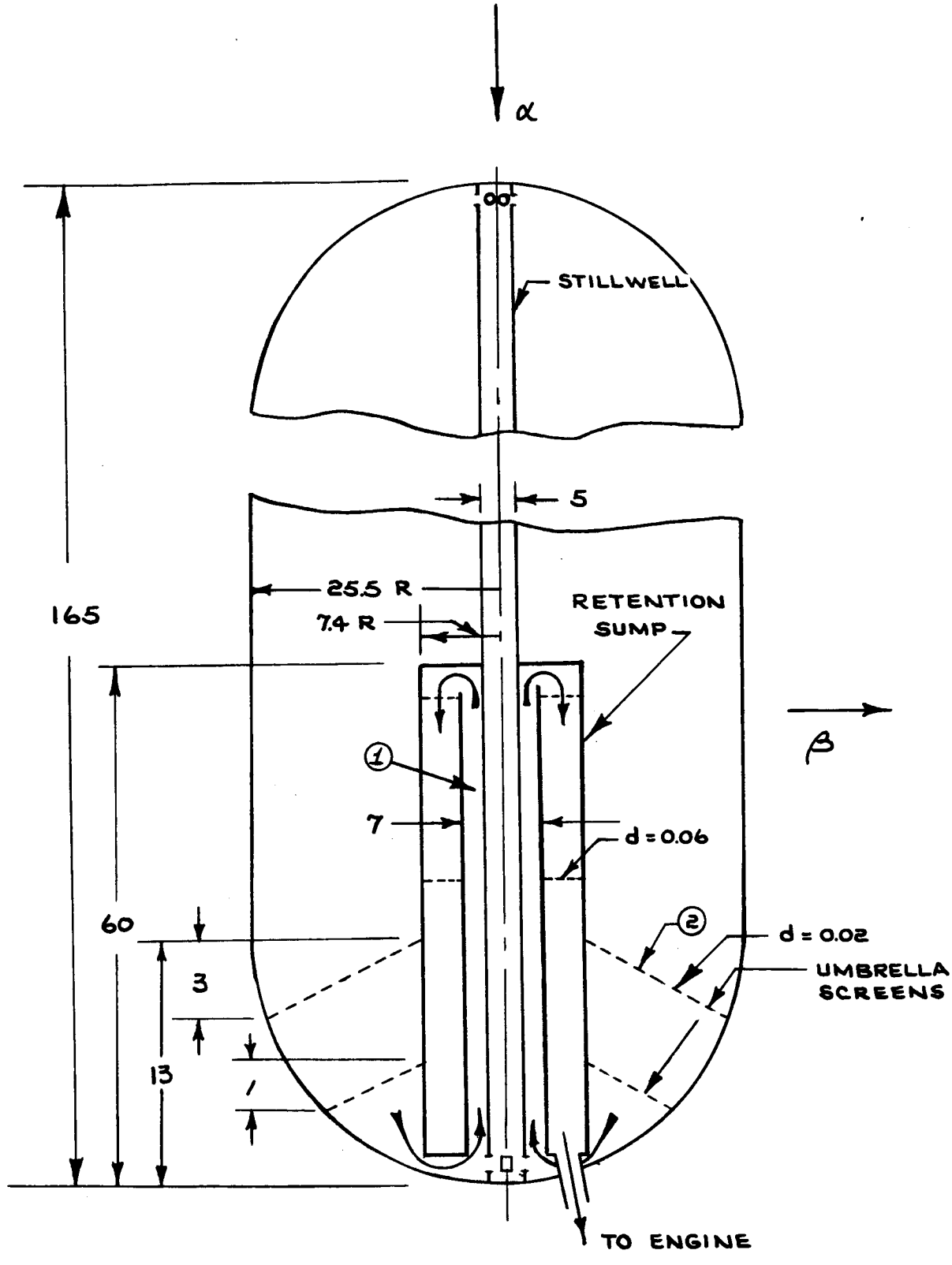

Apollo SPS Retention Sump
(Oxidizer Tank)

Figure 2-49

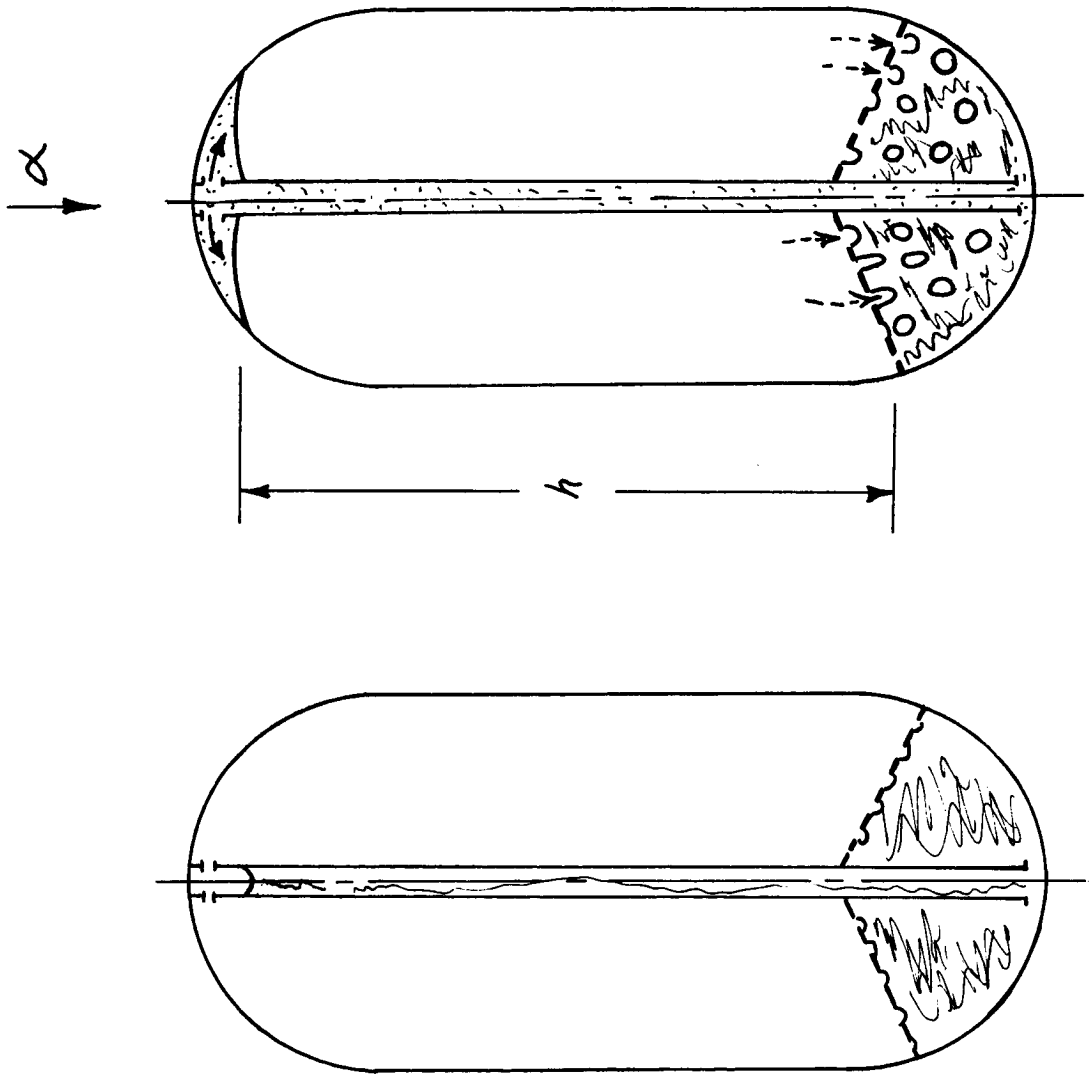

Breakdown of Capillary Stability Due to Presence of Standpipe

Figure 2-50

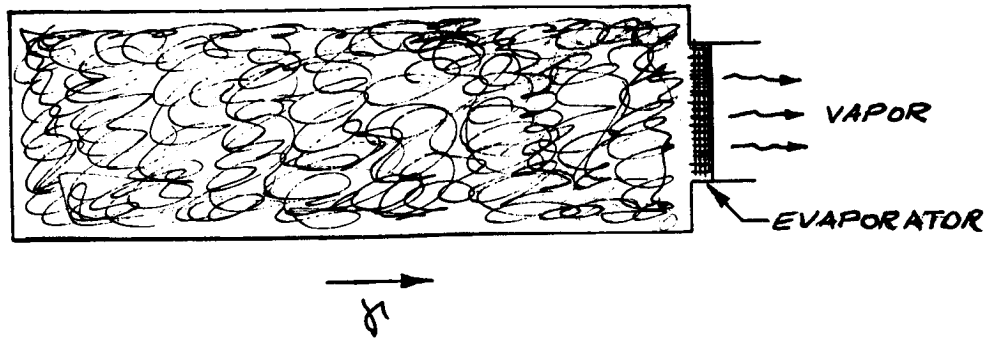

(a)

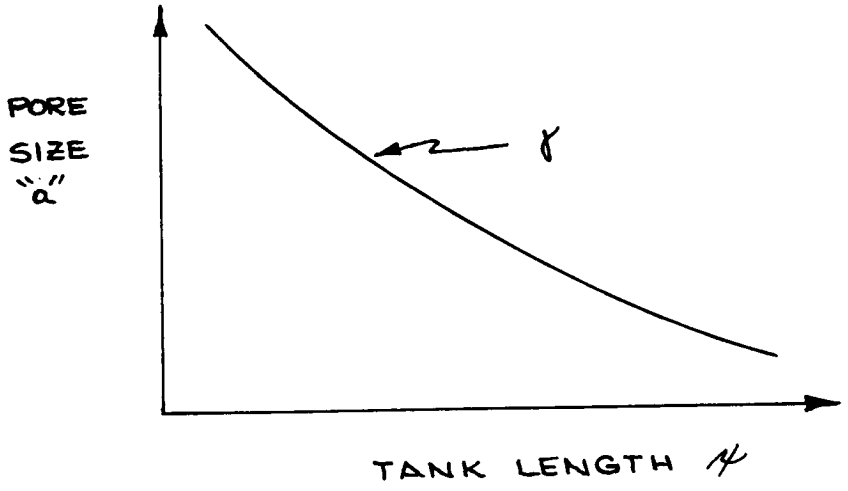

(b)

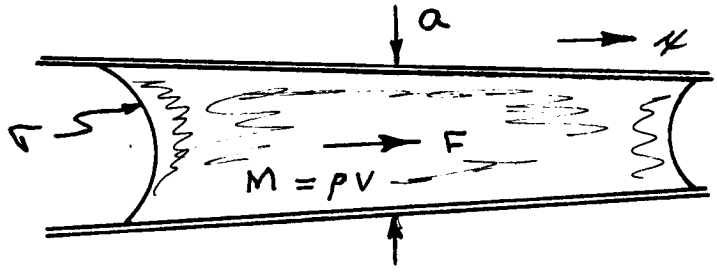

(c)

$$\gamma = F/m \cong \frac{4\sigma}{a^2 \rho g_o} \frac{da}{dx}$$

Capillary Propellant Feed System

Figure 2-51

TABLE 2-I

Agena Mission Acceleration Environment

Cause	Direction	g/g_o	Comments
Pitch & Yaw		8.2×10^{-4}	C.G. = Sta. 300, 3°/sec rate
Roll		3.2×10^{-5}	3°/sec rate
Pitch & Yaw Control (Acceleration)		8.9×10^{-3}	C.G. = Sta. 300, Angular Accel. $-0.0325/sec^2$
Earth Orientation Tumble Limit Cycle		1×10^{-6}	C.G. = Sta. 300
Drag		7.3×10^{-6}	4000 lb. vehicle, 0.029 lb. drag, 95 nm.
SPS, 1 Unit II		5×10^{-2}	4000 lb. vehicle, off-axis thrust
SPS, 2 Unit II's		1×10^{-1}	4000 lb. vehicle
Docking		2.3×10^{-1}	Short duration acceleration

Section 3
EXPERIMENTAL STUDY OF LIQUID BEHAVIOR IN PROPELLANT TANKS

This section presents the results of tests performed in support of the project. The test reports are grouped or ordered in this section according to their applicability to axisymmetric motions (e,g. reorientation) or asymmetric motions (e.g. transverse slosh). The complexity of some of the phenomena considered resulted in sophisticated test apparatus and technique in certain cases. A great deal of information was developed in these experiments. As often happens, however, some of these experiments exposed related issues which could not be resolved within the scope of work and schedule of the study.

The broad range of propellant behavior in tanks under various gravitational conditions covered in this study included many flow phenomena not capable of being described through the strict use of analytic techniques alone, or at least only with great difficulty. In some instances the flow is dissipative in nature. In others the liquid motions are highly non-linear. Still others had been postulated in broad terms but never observed or verified, in particular as they apply to spacecraft propellant tanks. For these cases, experimental investigations provided the information to form the basis for predictive techniques.

Certain aspects of propellant behavior within the scope of this project lent themselves to analysis in a more or less complete fashion. In these instances experimentation supplemented the analysis by providing insight to guide the analyses and correlation with the analytical results.

The experimental investigations reported below were basically divided into two classes from the standpoint of test technique. The first of these dealt with fluid behavior in a zero or low gravity environment. With the exception of one investigation, these tests were carried out in the low gravity environment provided by the LMSC drop test facility. Included in this group are the Axisymmetric Reorientation Test, Low-Gravity Impulsive Slosh Test, and the High Energy Residual Slosh Test. The one low gravity test not performed in the drop tower was the Low Gravity Slosh with Submerged Baffles. In this test equidensity immiscible liquids were employed to obtain the low gravity interface condition.

The other group of tests was concerned with the propellant behavior under essentially gravity dominated conditions and hence were performed at standard gravity in the laboratory. These tests are Rebound, Ullage Entrainment, and the Lunar Module RCS Feedline Gas Ingestion Test.

LMSC Drop Test Facility - The following brief description of the LMSC drop test facility will provide some general background information for those test series performed in the facility. The drop tower, shown in Figure 3-1 is located at the LMSC Santa Cruz Test Base. A test module encapsulated in a drag shield provides the basic zero gravity environment during free fall through

the drop height. Table 3-I lists the various capabilities of the facility. Figure 3-2 is a schematic of the test module which contains the pressure regulated cold gas thrust system, motion picture camera, batteries, back-lighting arrangement, and electrical circuitry for test function sequencing. By proper setting of the delay timers in the electrical circuit such events as thrust-on, thrust-off, drag shield and test module release, and certain particular test conditions can be sequenced during a drop test.

The cold gas thrust system provides accelerations on the test module as listed in Table 3-I. The acceleration values are determined during thrust calibration tests for various combinations of pressure regulator settings and nozzle geometries. This behavior is generally verified during a test by the readout of chamber pressure displayed on the test film. The uncertainty interval in this measurement is placed at $\pm 10\%$ based on test experience.

TABLE 3-I

Tower Height	186 ft
Drop Test Height	144 ft
Zero-g Test Time	2.9 sec
Drag Shield Length (overall)	19 ft 3 in
Drag Shield Diameter	54 in
Drag Shield Mass	1300 lb
Test Module Dimensions	38 in D by 44 in L
Test Module Mass	300 lb
Acceleration Range (in both directions parallel to the drop axis)	0.3 g_o to 10^{-2} g_o
Instrumentation	High speed motion pictures 400 frame/sec
Power	On board batteries and umbilical cable prior to release
Release Mechanism	Jaw and tang - pneumatic operated

AXISYMMETRIC REORIENTATION

Certain features associated with reorientation flow in clean tanks require further investigation. Included are the effect of large reorientation Bond number, increased tank length and increased reorientation times.

Spacecraft docking maneuvers, flight crew movements, etc., create impulsive accelerations that may have adverse effects on the liquid-vapor interface in the propellant tank. There is a need to understand the movement or flow of liquid resulting from a small impulse perturbation along the axis of the tank. The magnitude and time of duration of the impulse acceleration can provide a variety of liquid reactions.

The use of baffles in propellant tanks to damp sloshing action and retention surfaces to retain liquid propellant over the tank drain during disorientation will effect the flow of the liquid during reorientation. The investigations of transport of liquid past the anti-slosh and retention surfaces during the reorientation have not been reported in detail nor treated analytically.

The tests reported below were conducted in three phases; axisymmetric reorientation in clean tanks, axisymmetric reorientation under impulsive accelerations, and reorientation with ring baffles and a retention screen.

Test Objectives - In general, the objectives of the experiment were:

1) Extend range of knowledge regarding liquid reorientation to unexplored ranges of reorientation Bond number and liquid fill ratios of hemispherically ended cylindrical tanks.

2) Determine axisymmetric motions induced by axial impulses.

3) Determine, in part, the influence of anti-slosh baffles and liquid retention members on the mode of liquid reorientation and on the time required for collection.

Specifically, the information determined is:

1) Capillary response times associated with the change from a high-g to a zero-g equilibrium surface shape.

2) Wall wave trajectories over a range of reorientation Bond numbers

3) Central flow pattern in zero gravity and during a range of reorientation conditions.

4) Effect of a ring baffle configuration at two different axial tank locations and one retention system location on 1), 2) and 3) above.

5) Determine magnitude and stability of reorientation motion caused by impulsive accelerations over a range of Bond numbers B_R and Weber numbers, We.

A sketch of test tank and definition of nomenclature is given in Figure 3-3.

Correlating and Test Parameters - In order to provide the desired hemispherical interface shape as an initial condition ($B_I = 0$) all tests were preceded by a period in zero gravity following the release of the drop test module. The duration of this period was calculated from the capillary response time relation reported by Masica et al*. This relation predicts the time required for the wall wave to pass initially through its zero-g equilibrium position after the high-g condition vanishes.

To provide time for the slosh motions to decay to the zero gravity equilibrium shape, this initial response time was multiplied by a factor of four. The resulting relation for the zero gravity period is

$$\tau_o = 0.584\sqrt{\frac{D^3}{\beta}} \qquad (3.1)$$

*Masica, W.J., and Salzman, J.A., "An Experimental Investigation of the Dynamic Behavior of the Liquid-Vapor Interface Under Adverse Low-Gravitational Conditions", Symposium on Fluid Mechanics and Heat Transfer Under Low-Gravitational Conditions, Lockheed Missiles & Space Company, Palo Alto, Calif., June 24-25, 1965.

where D = test tank diameter

$\beta = \sigma/\rho$, kinematic surface tension of the test liquid

The remainder of the available drop test time was employed in conducting the various tests at the appropriate acceleration level.

The primary effect of an impulsive axial acceleration is to distort the liquid-vapor interface and impart kinetic energy to the liquid. The degree of distortion and magnitude of the velocity field in the liquid depends on the magnitude of the total impulse. The period of interest occurs upon termination of thrust. At this time the degree of surface distortion and magnitude of liquid velocity will determine the behavior of the propellant. In accordance with the above line of thought, a parameter to correlate the various flow regimes should be the Weber number. If Weber number is based on tank radius, we have

$$W_e = \frac{V^2 r}{\beta}$$

where V = a characteristic velocity at termination of thrust, cm/sec.

r = tank radius, cm.

Using free fall relations, we can relate We to the impulse since

$$\Delta V = a \, \Delta t$$

(where a is impulsive acceleration and t is time) and the impulse is

$$I = F \, \Delta t = M a \, \Delta t$$

$$W_e = \frac{I^2 r}{M \beta}$$

(where F is impulsive force on propellant mass M).

Thus, varying the impulse varies the Weber number. The impulse periods varied depending on the Weber and Bond number. For instance,

$$\frac{\text{Weber number}}{\text{Bond number}} = \frac{V^2 r/\beta}{a r^2/\beta} = \text{Froude number}$$

This relation can be reduced to

$$\Delta t = \sqrt{\frac{We}{B_r} \cdot \frac{r}{a}}$$

which is the time period in seconds of the imposed impulse.

Experimental Apparatus - The test placed in the test module (Figure 3-4) consisted of an aluminum double plate clamp, duplicate tank models contained in a single package between the clamp plates, threaded rods (for bolting), and four installation brackets. The test tanks were rectangular lucite blocks, each having an internal cylindrical surface with a hemispherical bottom that was machined and polished for optical clarity. The duplication of tank size for each test permitted the examination of different liquid fill levels under the same reorientation conditions.

For the tests with anti-slosh baffles and a retention surface, a test setup with three tanks was used. An annular ring was installed within the cylindrical surface of two of the tanks with each installation having a different axial position. A circular screen disk was positioned in the third tank. These devices were held against the cylindrical surfaces by stressing a split-oversized ring within the smaller diameter of the tank. Figure 3-5a

shows the installation of an annular ring baffle within a test tank. Figure 3-5b shows the two annular baffles and the screen disk used in the testing and the installation tool.

Four different tank radii were selected to accommodate the test requirements, 1.30, 1.84, 3.48, and 4.12 cm. The length of each cylindrical tank was eight times the radius. The rectangular lucite tank blocks were made with cross-sections of 2.5 by 2.5 inches for the two smaller tank radii and 4.0 by 4.0 inches for the two larger tank radii.

In the reorientation tests with antislosh baffles and a retention surface, two rings having an annular width of .11 tank radius and a thickness of .017 tank radius and a circular screen disk of 70% porosity were used, respectively (see Figure 3-5b).

Two tanks had single baffles installed at H/r = 1.57 and 3.34, respectively, and the third tank had the screen positioned at H/r = 3.34 where H is the position of the baffle measured above the tank bottom.

The impulsive acceleration tests were conducted with the 1.30 cm radius tanks. These tanks, having the smallest radii, provided the longest period of time for observing the effects of the impulse on liquid reorientation and stability behavior owing to the short period of time required to achieve a zero-g initial condition.

Experimental Technique - Several tanks of the same radius, having different liquid fill levels were tested simultaneously in the drop tower test module.

Two test liquids, carbon tetrachloride and isopropyl alcohol, were used in the series of 15 test runs. Table 3-II summarizes the tests conducted.

Impulsive Weber number levels ranging from 3 to 100 have been investigated for the impulsive reorientation tests. The impulsive variations were made, holding acceleration constant and varying the impulsive time duration, and at constant time duration varying the acceleration level. Using the four tanks of 1.30 cm radius, different fill levels, ℓ/r = .275, .400, 1.0, 1.67, of carbon tetrachloride liquid, were tested simultaneously. The impulse settings desired were obtained by pulsing the cold gas thrust system on the test module at preset pulse durations and thrust levels. Eleven test runs were made at various combinations of Weber and Bond number. The test points obtained are shown in Figure 3-6.

The two test drops made for examining the effects of antislosh baffles and the retention surface on the reorientation of liquids in the test tanks were conducted at reorientation Bond numbers of 30 and 62 at fixed liquid fill levels of ℓ/r = 1.67. Since only one tank radius, 3.48 cm, and one test liquid, carbon tetrachloride, was used for the tests, only variations of acceleration levels were required to change the reorientation Bond numbers.

The events of the test were preset and automatically activated during the test. The initiation of an event was signaled by a flash bulb which was connected into the circuitry controlling the particular test event. Thus the first flash indicates release and the start of the drop. The second flash signals the initiation of thrusting on the test module or the reorientation event. For the impulsive acceleration tests a third flash bulb signalled

TABLE 3-II

Axisymmetric Reorientation Test Run Data

Test Liquid		Carbon Tetrachloride σ/ρ = 16.9														
Tank Radius (cm)		1.3			1.84			3.48			3.48			4.12		
a/g*	ℓ/r**															
								REORIENTATION BOND NUMBERS								
0.01	.275	1			2											
"	.400	1	RUN (1)		2	RUN (4)										
"	1.000	1			2											
"	1.670	1			2											
0.10	.275	10			20											
"	.400	10	RUN (2)		20	RUN (5)										
"	1.000	10			20											
"	1.670	10			20											
0.26	.275	26			50			184			117	***		259		
"	.400	26	RUN (3)		50	RUN (6)		184	RUN (8)		117	RUN(10)		259	RUN (12)	
"	1.000	26			50			184			117			259		
"	1.670	26			50			184	RUN (9)		117	***		259	RUN (13)	
"	2.33	26	RUN (7)		50			184			117	RUN(11)		259		
0	.275	0									0			0		
"	.400	0									0	RUN(14)		0	RUN (15)	
"	1.0	0									0			0		
"	2.33	0									0			0		
	*	Test Acceleration									*** Test liquid for these runs					
	**	Fill Level									was isopropyl alcohol					
											= 27.6 cm^3/sec^2					

thrust termination.

With the multiple tank arrangement either four or three tank fill levels could be investigated simultaneously. As indicated by Table 3-II each tank diameter group was tested at various acceleration levels before changing over to the next diameter. In this manner test changeover time was minimized.

Data Reduction - Test liquid behavior in response to the axial accelerations was recorded on high speed (200 or 400 frames/sec) motion picture film. On this film record timing marks at 0.01 second intervals were placed. These together with the flash bulb action provided time reference for the various events. Liquid displacement information in x-y coordinates was obtained with precision film data reading machine.

Accelerations imposed on the test tank were measured by reading the chamber pressure of the cold gas jet thruster from the pressure gage shown in the movie film. However, when the thrust action was of short duration, as in the impulsive reorientation tests, the drift rate of a ball in an evacuated tube (also shown in the film) was used to determine the velocity increment generated by the impulse thrust action.

Results - Reorientation flow characteristics were studied primarily in terms of the motion of the leading edge of the liquid on the tank wall and the motion of the liquid-vapor interface along the centerline axis of the tank. Figure 3-7 shows reorientation wave profiles traced directly from the film records for two fill levels. A comparison of the two yields an indication of how flow characteristics are changed when tank fill level is reduced. In

both cases, the tank dimensions, test liquid, and induced axial accelerations are the same. The difference caused by a reduction in fill level is exhibited in the distance the liquid moves along the tank wall and the thickness of the sheet of liquid along the wall.

It must be mentioned at the outset that although the thickness of the liquid film along the tank wall is of concern in a detailed analysis of the wall wave, quantitative measurement of film thickness was generally impractical due to inadequate photographic resolution.

Capillary Response Time - Capillary response times for the reorientation of the interface to the zero-g interface shape was examined in terms of the paraxial distance between the center vertex and the leading edge of the wall wave (see Figure 3-8). Measurements have been correlated by normalizing distances with tank radius and time with $2r\sqrt{2r\rho/\sigma}$. As seen in Figure 3-8, correlation of data exists for most of the initial period in which the liquid surface is expanding, with a greater expansion rate for fill levels greater than $\ell/r = 1$. Following the first half period of oscillation, however, dissimilarity results and surface oscillations develop which are different for each case. For the drop test, the time allowed for reaching the zero gravity configuration was taken from the empirical formula of Siegert, et al*, and adding additional time for a one cycle overshoot. Due to the difference in surface oscillations, however, the liquid configuration was not always the same at that time. Thus, in some of the drop tests, a good approximation to a zero gravity configuration was not achieved.

*Siegert, C.E., Petrash, D.A., and Otto, E.W., "Time Response of Liquid Vapor Interface After Entering Weightlessness", NASA Technical Note D-2458, August 1964.

The test liquid in Figure 3-8 was carbon tetrachloride which, when in equilibrium with the material of the tanks, normally has a small contact angle, with an equilibrium zero gravity liquid configuration such that s equals r. During the initial period of liquid surface expansion, the liquid configuration may therefore be assumed closest to the equilibrium configuration when s/r = 1. From Figure 3-8 the time required to initially reach this configuration is

$$t = 0.165 \quad D^{3/2} \left(\rho/\sigma\right)^{1/2} \tag{3.2}$$

which is in agreement with Siegert (op. cit.).

The data plotted in Figure 3-8 for fill levels of $\ell/r = 0.4$ shows that a configuration in which s/r = 1 is never achieved. Instead, s/r stabilized at a value between 0.4 and 0.3 at equilibrium. This corresponds to a constant curvature equilibrium configuration with a liquid tank contact angle of between 20° and 25° indicating that the contact angle for this liquid solid combination is not zero.

Analysis of the data from this series of tests shows that the center vertex passes through its theoretical equilibrium position before the wall wave passes through its corresponding position. Thus, at the time at which s = r, the liquid vapor interface has a transient shape with slightly greater surface curvature in the center than near the wall.

For the experiments discussed in this report, $B_I = 0$. Therefore, it was expected that no central flow would occur regardless of the magnitude of B_R and that the flow would be entirely along the tank wall. In two tests at high B_R, when the initial zero gravity time was excessive, the spherical cap interface flattened and approached a low gravity interface. At the initiation of the reorientation acceleration, the forming of a central drop was noted, but immediately subsided. The flattened interface simulated a condition comparable to a small B_I condition that would not sustain a central drop.

Reorientation

Interface Trajectories - Figures 3-9 to 3-13 are liquid-vapor interface trajectories for five different fill levels. In the first three of these figures, the upper half shows the motion of the leading edge of the liquid on the tank wall, and the lower half shows the motion of the liquid along the centerline axis of the tank. The last two Figures, 3-12 and 3-13, are for the lowest fill levels and in these cases there was inadequate photographic resolution to obtain reliable data on the motion of the liquid in the center of the tank. Therefore, only the wall wave trajectories are shown for these fill levels.

In order to correlate the data and interpret any trend in behavior, time and distance measurements were non-dimensionalized. Displacement measurements were normalized with respect to tank radius, r. Time was normalized with respect to "free fall" under the applied acceleration. Thus, denoting dimen-

sionless terms by an asterisk (*),

$$S^* = S/r \tag{3.3}$$

and

$$t^* = \frac{t}{\sqrt{\frac{2r}{a}}} \tag{3.4}$$

In these terms the equation for "free fall" is

$$S^* = (t^*)^2 \tag{3.5}$$

The motion of the liquid-vapor interface in the center of the tank is characterized by an initial increase in velocity up to a steady value u. Measurement of the steady value reached in each case yields the following relation:

$$u = 0.48 \sqrt{ar} \tag{3.6}$$

This relation for velocity is in good agreement with the well established Taylor bubble velocity, for the rise of single air bubbles through liquids in tubes.

As the liquid-vapor interface approaches the hemispherical end of the tank, it begins to slow, and approach the bottom of the tank asymptotically. Hollister and Satterlee derived an equation for the depth of the liquid in the tank, H^*, as a function of non-dimensionalized time, as the depth approaches zero. In Figure 3-14, data from several tests is compared with this equation graphically. In plotting this data, an additive constant was used to adjust the time scales with theory. Agreement is good and within the accuracy of the measurements.

Trajectories of the leading edge of the wall wave are initially parabolic in form. This is illustrated in Figure 3-15 where position of the wall wave is

plotted as a function of non-dimensionalized time squared. Plotted in this way, the trajectory is nearly a straight line with a slope equal to the acceleration of the wall wave divided by the induced acceleration, a. These slopes are found to vary at random between 0.64 and 0.72 for different tests. This variation in wave front acceleration was not traceable to any aspect of reorientation. The random nature suggests that the value used for the test acceleration was inaccurate. The variation is within the uncertainty interval of ±10% for the actual test acceleration values.

At low fill levels, the liquid velocity at the wall starts decreasing, usually at some time after the velocity at the center of the tank decreases. This slowing of the wall wave is the result of the wall wave becoming so thin that viscous effects dominate. In this regime of flow, the wall wave often becomes asymmetrical and flows further in some parts of the tank than in others. In some cases the wall sheet degenerated into rivulets which proceeded farther than the wall wave.

Viscosity effects have been correlated with wave wall height in gross terms by use of a reorientation Reynolds number agreement. Assuming a wall wave velocity, v, proportional to free fall velocity and wall wave thickness, θ, proportional to the ratio of liquid volume and tank area covered by the liquid, we cast a Reynolds number in the following form.

$$R_e = \frac{\rho v \theta}{\mu} \equiv \frac{\rho}{\mu} \frac{V^*}{H^*} (a S^* r^3)^{1/2}$$

where r = tank radius

h = height of wall wave above B_I position

$S^* = S/r$

H = height of wall wave above hemispherical end of tank

$H^* = H/r$

v = wall wave velocity ($\propto \sqrt{ah}$)

V^* is volumetric fill ratio normalized on one hemispherical volume.

Since the data on wave front position was obtained in terms of h^*, rather than H^*, values for H^* in the above equation had to be approximated as follows:

For $V^* \geq 1$ $H^* = \frac{\ell}{r} + 0.66 + S^*$

For $V^* \approx 0.2$ $H^* = 0.62 + S^*$

For $V^* = 0.1$ $H^* = 0.40 + S^*$

The constants in the above relations for H^* are based on the theoretical eqilibrium configuration just before acceleration is applied.

Figure 3-16 is a plot of Re and the height of the wall wave from a number of different tests at a time:

$$t^* = t\sqrt{\frac{a}{2r}} = 2.75$$

At this time the wall wave is beginning to slow in some cases, and to appear as if viscous drag is predominating. From Figure 3-16, it is seen that this effect is important when Re as calculated above is less than 200.

Reorientation Under Impulsive Accelerations - Because of the viscous effects previously discussed and the limited applicability of such data in full scale

practice only those tanks having fill levels of h/r = 1.0 and h/r = 1.67 were observed for the effect of impulsive accelerations.

The behavior of the test liquid in response to an acceleration of short duration is characterized and presented in terms of the wave front trajectories and displacements along the tank wall. This behavior, is correlated in terms of the forces acting on the liquid following the impulse or thrust termination. As discussed earlier one parameter used to characterize the liquid behavior is an impulse Weber number,

$$We = \frac{v^2 r}{\beta}$$

Where v is the velocity increment given to the test tank by the impulse, r the tank radius and β the liquid kinematic surface tension. In addition to surface tension as a force on the liquid, viscous forces act to retard the wall flow and become important once the acceleration induced body forces are removed. A reorientation Reynolds number based on the tank velocity increment can be formulated based on tank radius to characterize this effect thus

$$R_{e_r} = \frac{vs}{\nu}$$

where s is the wall wave displacement. Forming a ratio of these two effects and taking for the characteristic velocity $v \approx 2s/t$ the following dimensionless time parameter can be obtained.

$$\frac{R_{e_r}}{W_{e_r}} = \frac{t\beta}{2\nu r}$$

A total of 11 tests were performed employing impulsive accelerations over a range of Weber numbers from 3 to 100 and a reorientation Bond number range

of 2 to 30. The test points obtained are shown on Figure 3-17 plotted in terms of the reorientation Bond number and Froude number based on the velocity increment given the test tank during the impulse period.

Figure 3-17 is a dimensionless plot of the wall wave behavior in response to the impulse. Measurements in time, t, and displacement, s, are taken from the initiation of the impulse. It can be seen that the liquid behavior is characterized by the impulse Weber number. Three general liquid configurations were observed for the range of parameters obtained. Figures 3-18, 3-19 and 3-20 are wave profiles illustrating each of these patterns. These patterns have been grouped in terms of the impulse Weber number range in which they occurred. This is not to imply a distinct flow regime boundary defined by these parameters. One flow pattern may overlap or pass gradually into the next. The scope of the test in this case was not sufficient to completely determine any distinct flow regime limits.

For the lowest Weber number of 3.5 and all test points from Weber number of 2.3 to 3.5, the wave shape variation returned to a stable interface configuration at the tank bottom within the test period as shown in Figure 3-18. Figure 3-19 exhibits the wave shape variation for a Weber number of 22 and all test points from Weber number 9 to 22. The wave moving up the wall pinched off into a sizeable annular volume of liquid held by surface tension forces along the wall in a metastable state. The remainder of the liquid was contained at the bottom of the tank returning to a zero gravity equilibrium state. For the duration of the test, the suspended liquid failed to recombine with the liquid at the bottom of the tank or collect at the top of the tank.

The wall wave configuration of the relatively high Weber number of 55 and for the test point at Weber number of 93 resulted in the wall wave reaching the top of the tank with liquid collecting at both ends of the tank. Some liquid remained on the wall in what appeared to be a pinched off state for the Weber number of 55. At this condition more liquid appeared to collect at the bottom of the tank for the lower Bond number. Figure 3-20 presents the wall wave configurations before contact with top of tank. At the Weber number of 93 with a Bond number of 4.3 and an impulse time of .81 sec., a considerable amount of liquid collected at the top of the tank. There appeared to be communication between the liquid at the top and bottom of the tank through a wall film which did not pinch off before the end of the test.

The liquid behavior of impulsive axisymmetric reorientation is best predicted by the magnitude of the ratio of the impulse inertia to the surface tension forces (Weber number). The relative displacement of the liquid along a tank wall versus the dimensionless time Re/We provides an indication of the liquid movement in prototype tanks following the impulse termination.

It can be concluded from the above results that impulsive axial accelerations at impulse Weber numbers

$$We_r < 4$$

will not produce permanent distortion or reorientation of the liquid gas interface even if the axial Bond number stability limit is exceeded. Axial impulses above this level produce a flow pattern which has characteristics dependent upon the impulse level or Weber number and the degree of viscous effects present. Once the Weber number stability limit has been exceeded a

more complex flow situation occurs. The scaling of the results of this test in this area should be qualified. Although the flow regimes observed may in fact occur in a prototype the influence of viscosity and the correlation of the flow in terms of surface tension and viscosity should be verified by a more thorough analysis and testing.

The Effect of Baffles on Reorientation Flow - Propellant reorientation tests in tanks with ring baffles and a simulated retention surface were performed at reorientation Bond numbers of 30 and 62. Two ring baffle positions were employed, one submerged and the other uncovered, a distance one tank radius above the zero-g liquid initial position at the wall. Figure 3-21 is a picture taken from the test film 0.56 seconds following initiation of the reorientation at a Bond number of 62. As can be seen the submerged baffle produced no effect on the wave front trajectory. In addition, the baffle did not become uncovered throughout the test as the flow velocity into the baffle increased.

The initially uncovered baffle deflected the wall flow toward the tank central axis where impingement occurred. The leading portion of the gas bubble above the baffle was thus cut off from the remainder of the gas in the tank. As a result of the impingement also two centrally located liquid flows were generated. One was a geyser-like reverse flow penetrating the entrapped gas and flowing back toward the top of the tank. The other flow proceeded in the direction of reorientation along the tank center. Both of these flows exhibited very little loss in that the reverse flow impinged on the tank top and began a recirculation. The reorientation flow after accelerating to its

original velocity following impingement proceeded toward the tank bottom arriving slightly ahead of the wall flow for the adjacent submerged baffle tank.

Deflection of the wall flow toward the tank center was also produced by the retention surface as shown. However, no central impingement of the deflective flow occurred. The retainer ring having a much smaller height than the ring baffles produced a smaller angle of deflection. In addition, the grids of the retention surface acted to redirect the flow in an axial direction offset from but parallel to the tank walls.

Except for the case with an initially submerged baffle the flow configuration was altered considerably by the presence of the internal hardware employed. In addition the central flow produced by the initially unsubmerged baffle accelerated at a rate higher than that for the wall sheet and arrived at the tank top in advance of the attached wall flow.

PROPELLANT REBOUND

The phenomenon of propellant rebound or geysering is the result of reorientation or settling of the liquid propellant in a partially filled storage container under the action of settling rockets. Settling produces a change in kinetic energy in the propellant. It is well established that in general the reorientation flow pattern under the action of an axially directed tank acceleration is as shown in Figure 3-22a (See 1, 2, 3 below). Shown here is the propellant flowing axially in an annular wall sheet with the ullage gas rising in a centrally located bubble. In this manner the propellant and ullage gas exchange positions. For manned spacecraft this settling generally occurs at a high reorientation Bond number (B_R) condition. For example two 100# rockets settling propellants in a 20,000 lb. spacecraft produce an axial acceleration of approximately 10^{-2} g_o. For propellant tanks 30 cm in radius containing a common propellant with a kinematic surface tension (σ/ρ) of 30 cm^3/sec^2 the resulting B_R is 300.

Most propellant tank ends are hemispheres or spheroidal in shape so that the annular wall wave front and flow entering the drain end is directed in rather organized way radially inward to impact upon itself, stagnate at the tank axis, and produce an axial flow along the tank centerline. This flow is referrred to as a geyser or rebound flow and is shown in Figure 3-22b. This

---

1. Hollister, M.P., and H. M. Satterlee, "Low Gravity Liquid Reorientation", USAF, Office of Scientific Research and Lockheed Missiles & Space Co., Symposium on Fluid Mechanics and Heat Transfer Under Low Gravitational Conditions, Palo Alto, Calif., June 24, 25, 1965.
2. Bowman, T.E., "Liquid Settling in Large Tanks", USAF Office of Scientific Research and Lockheed Missiles & Space Co., Symposium on Fluid Mechanics and Heat Transfer Under Low Gravitational Conditions, Palo Alto, Calif., June 24, 25, 1965.
3. See pp 3-5 to 3-23 of this report.

is the start of a cyclic interchange between kinetic energy and potential energy (or slosh) in the vehicle tank acceleration environment. If this interchange were "lossless" it would be expected that the interchange would continue indefinitely. Intuition indicates, however, that this exchange should be highly dissipative. One might expect an amount of ullage gas to be entrained during this geyser formation as well as a high degree of turbulence.

It is of interest to the vehicle designer to know the degree of slosh motion damping that could be expected, the quantity of propellant remaining at the drain end of the tank, and the extent of ullage gas entrainment. This information can be of aid in answering questions pertaining to the total impulse necessary for a complete settling maneuver, main engine start times and quality of propellant in the main engine feed line following engine start up.

Salzman et al* present the results of testing during which rebound or geysering was observed at relatively low acceleration levels, $B_r < 200$. A detailed analytic treatment of the geyser formation and behavior would be very difficult. The phenomena is highly nonlinear and dissipative in nature. Thus, except for some gross features of the flow that can be obtained from analytic considerations, experimentation must be used to obtain information and insight into this flow behavior.

*Salzman, J. A., and Masica, W. J., "Experimental Investigation of Liquid Propellant Reorientation" NASA TN D-3789, 1967.

Objectives

A. Investigate the extent of geysering following reorientation under high acceleration conditions (Large B_R)

1) Measure the geyser height

2) Determine the time history of geysering

3) Measure the quantity of reorientation propellants involved in the geyser.

B. Determine the effect of a ring baffle on the reorientation flow and geyser formation.

Test Parameters - Referring to Figure 3-23 the following are parameters considered to be of importance in characterizing this rebound phenomena.

Characteristic velocity: $v \propto \sqrt{g\ell}$

Reorientation time: $\tau \propto \sqrt{2\ell/g}$

Slosh frequency: $\omega \propto \sqrt{g/\ell}$

Reorientation Reynolds number: $Re_r = \frac{g^{1/2}\ell^{3/2}}{\nu}$

Reorientation Bond number: $B_r = \frac{gr^2}{\sigma/\rho}$

Reorientation Weber number: $We_r = \frac{v^2 r}{\sigma/\rho} = \frac{g\ell r}{\sigma/\rho}$

$= B_r \cdot \frac{\ell}{r}$

$h^* = \frac{h}{\ell}$ dimensionless rebound height

$t^* = \frac{t}{\tau}$ dimensionless time

Pages 3-27 and 3-28 are missing from
original document

to the scaling law:

$$g_{r_{PROT.}} = g_{r_{MOD}} \left(\frac{\ell_{MOD.}}{\ell_{PROT.}} \right)$$

Referring to the prototype postulated as an example where

$$\ell_{PROT} = 400 \text{ cm}$$

A test of reasonable size (say $r_{MODEL} = 15$ cm) according to this scaling law yields the following prototype reorientation acceleration and Bond number condition.

$$\ell_{MOD} = 100 \text{ cm}$$

$$g/g_c\Big|_{PROT} = 0.256$$

$$\beta_{PROT} = 30 \text{ cm}^3/\text{sec}^2$$

$$B_{R\ PROT} = 41{,}000$$

Consideration of the above parameters indicates that a test under standard gravitational conditions with ordinary list liquids and reasonably sized models will provide dynamic similitude for highly inertia dominated reorientation and geysering conditions.

Experimental Apparatus - The rebound tests were conducted under standard ($1g_o$) gravity conditions in a cylindrical lucite tank having a nominal 11.5 in (29.4 cm) inner diameter. The cylindrical portion of the tank was composed of one foot and two foot nominal length sections that were bolted together at flange joints to provide a desired overall length and free fall distance, "ℓ". A hemisphere formed the tank bottom and contained a drain outlet 0.75 in. in diameter.

A reservoir designed to generate the desired annular wall flow was attached to the top of the cylinder. This reservoir, shown in Figure 3-24, is a cylinder 11.5 inches in diameter by 8 inches long. The reservoir bottom is a screen mesh 150x150 wires per inch with 30% free flow area. A 3 inch diameter vent hole was cut into the flat top of the reservoir. The hole was closed off by a metal disk faced with a rubber seal and which was raised by a pair of spring loaded tension rods. A flow deflection disk 4.92 in. in radius was attached to the bottom of the reservoir to provide the desired annular pattern for the flow out of the reservoir. The disk diameter was sized so as to provide the annular wall sheet thickness equal to that surrounding and downstream of the rising gas in a typical reorientation flow. The calculations for sizing this disk are contained in Appendix A. The inlet region of the disk was given a 0.75" radius round to insure full unseparated flow in the annulus with the desired thickness specified above. A scaffold structure supported the reservoir and lucite test tank assembly in a vertical orientation as well as providing support for a hoist used to raise and lower the reservoir during a fill operation. Figure 3-25 is a schematic of the test apparatus.

The artificial manner in which the annular reorientation flow is generated with this scheme does not permit an exchange of liquid and gas across the original equilibrium interface position as is the case in an actual reorientation flow. The flow of liquid into the test tank results in an increase in the gas pressure. This increase in gas pressure is a "back pressure" on the reservoir that reduces the liquid outflow rate below the desired "free fall" conditions. The result is a decrease in liquid velocity exiting the

reservoir. To avoid this difficulty the gas in the test tank was vented to atmosphere through the liquid wall wave by a pair of vent slits diametrically placed in the tank wall a short distance down stream of the reservoir bottom. The effect of the protrusion through the wall wave was minimized by placing the vent in a low velocity region and employing sharp edged airfoil shaped vanes surrounding the slits. The effect of a ring baffle was provided by a ring that could be inserted at a flange mating joint. The ratio of the ring inner diameter to tank inner diameter was 0.9 providing a ring baffle width 0.1 of the tank radius.

High speed motion pictures taken with a HYCAM camera were used to record the liquid behavior. Framing rates were 400 or 500 frames per second depending on the particular lighting conditions. A diffuse background light was provided by back lighting sheets of polyethylene film wrapped loosely around the back of the test tank.

Since fluid properties are not important during a high-g reorientation maneuver as long as the liquid viscosity is relatively low it was possible to employ tap water as the test liquid.

Experimental Technique - The desired annular shaped wall sheet flow mode characteristic of propellant reorientation during a high g settling maneuver was obtained by use of the liquid reservoir shown in Figure 3-23. With the reservoir raised above lucite tank mating flange a basin was clamped to the reservoir bottom. The purpose of the basin was to provide a temporary bottom to the reservoir during filling. After the reservoir and basin were completely filled with tap water through the 3' diameter vent hole, the hole was sealed

off by lowering the vent cover against the compressive force of the springs. The cover is retained in this position by the tension load in the break-wire fixed at each end with set screws. With the vent sealed the liquid in the basin beneath the reservoir was drained and the basin removed leaving the liquid in the reservoir above the screen mesh supported by atmospheric pressure. The liquid-gas interface at the reservoir bottom is stabilized by the screen mesh. That is, gas is prevented from entering the reservoir past the screen by the lack of sufficient hydrostatic pressure drop across the screen mesh in the presence of the capillary pressure rise associated with forming a gas bubble in any individual screen mesh hole. The full reservoir was then centered and clamped into place at the top of the lucite test tank. Finally, the entire tank setup was aligned with the vertical using a spirit level.

Each test run was initiated by cutting the break-wire which supported the force in the compression springs allowing the spring force to lift the vent cover clear relatively instantaneously. Thus the pressure across the mass of liquid is equalized permitting the reservoir to empty by flowing through the circumferential opening formed by the flow deflection disk and tank wall.

Data reduction for each test was devoted to obtaining from the motion picture film record information about the displacement versus time of the geyser height in the tank and where possible the geyser diameter.

Results and Conclusions - During a test under standard gravity conditions with reasonably sized models it was possible to simulate the geysering and rebound phenomena in a prototype only for very large reorientation Bond numbers and Weber numbers. However, it can be shown that for common tank

geometries the reorientation and resulting rebound is generally inertia dominated. We can write the reorientation Weber number in terms of the reorientation Bond number and length; thus

$$We_r = \frac{v^2 r}{\beta} = \frac{g l r}{\beta}$$

$$= \frac{g r^2}{\beta} \cdot \frac{l}{r}$$

$$= B_r \cdot \frac{l}{r}$$

Note that l/r is proportional to the tank fill level. Haberman and Morton* show that gas bubbles rising through inviscid liquids having Weber numbers greater than 4 (where the Weber number is based on equivalent spherical radius) are inertia dominated. That is, the bubble shape is not governed or stabilized by surface tension forces.

$$\frac{\rho V^2}{2} = \frac{2\sigma}{r}$$

or

$$\frac{\rho V^2 r}{\sigma} = 4$$

Thus it is to be expected that reorientations producing Weber numbers of the order of 4 will not produce geysering; that is the ullage bubble will not be

*W. L. Haberman and R. K. Morton, "An Experimental Investigation of the Drag and Shape of Air Bubbles Rising in Various Liquids", The David W. Taylor Model Basin Report 802, September 1953.

distorted by the kinetic energy of the wall sheet flow. This result is borne out by the test observations published in reference 5 wherein it was observed that for reorientation Weber numbers less than 4 no geysering was produced. Above this value, however, some distortion of the ullage gas was produced, the extent dependent on the Weber number up to a value of approximately 10. For reorientation flows above this value inertia forces become clearly dominant and geysering with complete recirculation was observed.

Reorientation Weber numbers of 10 or greater are most generally encountered in space vehicle applications. Axial settling accelerations producing reorientation Bond numbers of 10 or greater are not uncommon and for fill levels resulting in ℓ/r values in excess of one, Weber numbers greater than 10 are generated. In all but a limited set of conditions then inertia dominated rebound behavior is to be expected.

Table 3-III lists the conditions obtained in the tests performed in this series and the corresponding reorientation parameters. Each test condition was repeated at least once.

Some general observations on the character of the geyser flow can be made from the test films. Due to the necessity of viewing the geyser through the wall flow much of the information is qualitative in nature. The surface of the liquid film flowing down the wall was rippled by turbulence and wave propagations from upstream disturbances thus reducing the clarity and contrast of the rebound shape. Nevertheless it was apparent that the column of liquid comprising the geyser was itself highly turbulent, well mixed with gas (air) and in most instances partly disintegrated. This made it addi-

TABLE 3-III

Test No,	L_{MODEL} (in)	Baffle Height h/r	τ Sec	B_R*	W_e*	Re_r*
30303	38	None	0.444	2900	19,200	2.96×10^6
30602	38	None	0.444	2900	19,200	2.96×10^6
30701	38	.158	0.444	2900	19,200	2.96×10^6
30702	38	.158	0.444	2900	19,200	2.96×10^6
30901	60	.50	.558	2900	30,200	5.86×10^6
30902	60	.50	.558	2900	30,200	5.86×10^6
30903	50	None	.509	2900	25,200	4.44×10^6
30904	50	None	.509	2900	25,200	4.44×10^6
31401	60	None	.558	2900	30,200	5.86×10^6
31402	60	None	.558	2900	30,200	5.86×10^6

* $g = 980\ cm/sec^2$ $\beta = 72\ cm^3/sec^2$ $\nu = 10^{-2} cm^2/sec$

tionally difficult to fix interfaces and wave fronts for the purpose of measurement. In the absence of detailed measurements that can be used to characterize the geyser flow conditions it is necessary to rely on visual interpretation based on the motion picture film record. Much of the information reported below is of this nature.

In general the geyser rose to its full height and then began to collapse into itself producing a radial flow that spread to the tank walls further entraining gas and then collapsing in bulk to the final quiescent condition with entrained gas passing through the liquid. This behavior might be explained by the observation that the "trailing flow" following the geyser wave front is lagging in phase but has approximately an equal amount of kinetic energy, so that the entire geyser column would not "stagnate" simultaneously. Hence the trailing flow meets the leading flow which has stagnated and is falling back into the tank bottom.

Figures 3-26, 3-27 and 3-28 contain in dimensionless form the geyser wave front trajectories measured from the bottom of the test tank and starting in time from the moment of impact of the annular wall wave at the tank bottom. Shown for reference is a nondimensionalized free fall trajectory having the form

$$h^* = 2t^* - t^{*2}$$

which would be the path traveled by a particle having an initial vertical velocity of

$$\dot{h}^* = 2$$

equivalent to the ideal kinetic energy per unit mass of the reorienting liq-

uid entering the tank bottom. Also shown is the steady-state liquid level, h^*_∞, calculated from the known quantity of liquid in the reservoir.

These trajectories exhibit one common feature. As would be expected the duration of the geyser is equal to or slightly less than twice the characteristic reorientation time

$$t^*_{GEYSER} \cong 2$$

or measured from the initiation of the reorientation maneuver,

$$t^*_{SETTLING} \cong 3$$

This is true for the gross rebound motions. Moderate amplitude slosh motions followed this geyser period.

The decreased amplitude of the geysers shown in Figures 3-27 and 3-28 indicate that under the reorientation conditions tested in this case dissipative effects are not insignificant. This magnitude of dissipation was not observed in the film records of the reorientation tests discussed earlier. The maximum reorientation Reynolds number in these tests was of the order of $3x10^4$ a factor 10^2 less than the testing under this test. Similarly the tests conducted by Salzman et al (op.cit) with a maximum reorientation Reynolds number of the order of $1x10^3$ reported no such loss effect. Although the above seems to indicate that the level of dissipation and attenuation of the geyser could be characterized by the Reynolds number such an argument has not been well established within the scope of this test. The flow along the wall is a form of rapid flow encountered in open channel flow and characterized by Froude numbers based on the sheet thickness of 1 or greater. A high

degree of dissipation occurs for this type of flow in the form of hydraulic jumps which are analagous to shock waves in compressible flow. It is probable that some form of such a "shock" loss occurs along the tank bottom. The information obtained in these tests is not sufficient to fully explain the dissipation of the reorientation energy beyond the statement that reorientation under the conditions of $We > 20{,}000$ and $Re_r > 3 \times 10^6$ geyser attenuation will occur.

The diameter of the geyser was measured as it left the hemispherical bottom. For all runs the geyser diameter was approximately 0.3D to 0.4D where D is the tank diameter. In addition until break up occurred this diameter was fairly constant along the geyser length for the period $0 < t^* < 1$. After $t^* = 1$ the geyser collapse mentioned earlier resulted in an expansion of the diameter.

The effect of a ring baffle having a width to tank radius ratio of 0.1 was investigated for two baffle positions as shown in Table 3-III. Figure 3-26 shows the effect in terms of amplitude on geysering of a baffle located one radius above the tank bottom. The geyser period remains the same; however, the amplitude is attenuated. The geyser surface was hemispherical and retained this shape during its growth to the amplitude of one tank radius shown in Figure 3-26. A considerable amount of entrained gas was observed.

A ring baffle located above the tank bottom a distance of 4.5 radii was also observed during a reorientation flow. The effect produced on the flow was similar to that discussed in Section 2 (see page 2-25). The wall flow was deflected into the tank axis. A reverse flow or geyser was produced at the

plane of the baffle. The remainder of the flow proceeded into the tank bottom along the center line and settled with no extensive rebound action.

From an overall standpoint the ring baffles employed in this test do serve to attenuate the geyser action by disorganizing the kinetic energy and thus increasing the turbulence of the settled propellants. This benefit may have mixed blessings, however. Converting the reorientation kinetic energy to smaller scale turbulence tends to increase the quantity of gas entrained and the clearing rate in the neighborhood of the chain. Unfortunately the tests conducted here were not set up to examine this aspect. The data and observation indicate a trend in the direction of extended gas clearing rates for a baffled tank, however.

APPENDIX A

APPROXIMATING A REORIENTATION FLOW WITH A "CIRCULAR HORIZONTAL SLUICE GATE"

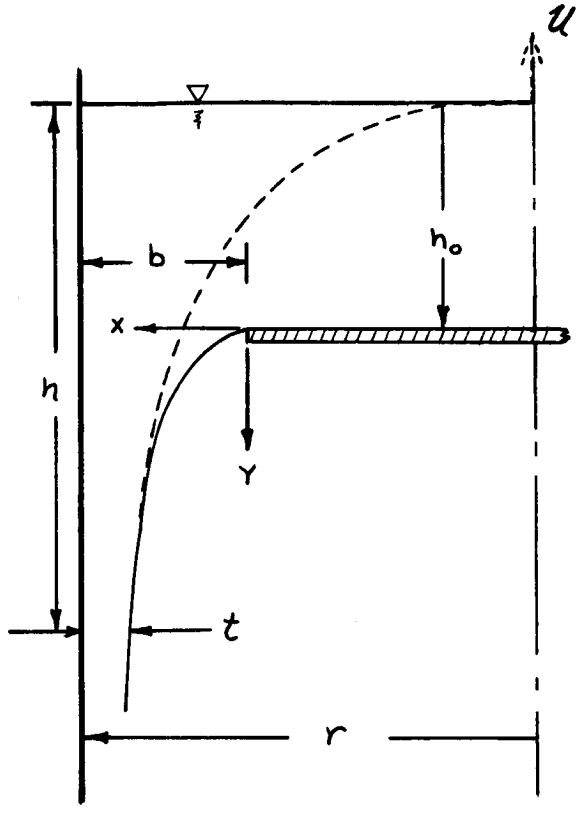

We wish to approximate the wall sheet geometry of a falling liquid film associated with the passage of a large gas bubble into a cylinder filled with a liquid such as occurs during reorientation. This is indicated by the dotted line. The flow will be approximated by that issuing from an annular slit (solid line). We wish to size b so that the flow becomes tangent to that for the rising gas bubble at some point h

For the steady state draining of a tube closed at the top we have via continuity considerations for the thickness of the liquid film, t, a distance h below the bubble vertex

$$t = \frac{\beta r}{2\sqrt{2}} \sqrt{\frac{r}{h}}$$

where $h \geq /65\ r$ and $\beta = \frac{u}{\sqrt{gr}}$

u being the bubble rise felocity. Values for β have been obtained by measurement in small scale experiments at correspondingly low Reynolds numbers, N_R.

$$N_R = \frac{u R \rho}{\mu} = \frac{0.46 \sqrt{g R^3}}{\nu}$$

These results are listed below

N_R	β	
20 - 44°	0.93	(Goldsmith & Mason*)
12,000	0.64	(Taylor & Davies**)

The trend is in the direction of $\beta \rightarrow 0.46$ the theoretical inviscid value as $N_R \longrightarrow \infty$ so it will be assumed that the discrepancy in β is due to boundary layer effects, that for a prototype tank this effect would be negligible, and that the momentum flux of the liquid past the gas is essentially free of boundary layer effects. This assumption will be carried over to the test apparatus in that boundary layer effects on the water existing from the reservoir tank will be neglected.

Setting $\beta = 0.48$

* Goldsmith, H.L., and S. G. Mason, +The Movement of Single Large Bubbles in Closed Vertical Tubes" J. Fluid Mech., Vol. 14, 1962, pp 43-58

**Davies, R.M. and G. Taylor, "The Mechanics of Large Bubbles Rising Through Extended Liquids and Through Liquids in Tubes" Prog. Roy. Soc., Vol 200A, 1949 pp 375-390.

we have

$$t = \frac{\beta r}{2\sqrt{2}} \sqrt{\frac{r}{h}}$$

$$= 0.17 \sqrt{\frac{r}{h}}\ r$$

Noting that the initial free surface liquid height h_o in the reservoir is 8" we have

$$\frac{r}{h_o} = \frac{5.75"}{8"} = 0.718$$

and t = 0.83"

This requires a deflection disk radius of 4.92".

LOW G LOW LIQUID LEVEL SLOSHING

Test Objectives and Parameters

A. The objectives of this experiment were:

1. Investigate and determine the influence of liquid depth on the fundamental sloshing frequency in a cylindrical-hemispherical ended tank under zero and low gravity conditions.
2. Measure and correlate the amplitude of the slosh based on transverse impulse and the initial wave displacement from the interface equilibrium position.
3. Gain a physical insight into the low level slosh behavior under the environmental conditions imposed.

B. The tank parameters which govern the liquid behavior are

1. Tank size.
2. Liquid (kinematic surface tension, viscosity and contact angle properties).
3. Liquid fill level.
4. Transverse impulsive acceleration.
5. Axial acceleration.

Theoretical Background - To demonstrate how the above parameters influence the experiment, the method of scaling from available analytical information and the selection of test dimensions, magnitudes and material is necessary.

To measure the frequency at the small liquid depths for a zero gravity environment, the selection of a test tank size and a test liquid was restricted by the test time duration. In the LMSC drop tower just under 3 seconds is allowed for the experiment. Test time is divided into the period

required to attain zero or low gravity free surface equilibrium and the period remaining for a number of cycles of capillary sloshing.

Thus $$t_e + t_s = 3$$

where t_e = equilibrium time, seconds

t_s = slosh time, seconds.

The time required for the liquid-vapor interface to reach its zero or low gravity shape from the high gravity shape in a flat bottomed cylinder can be estimated with the aid of the following relation reported by Siegert, et al*.

$$t_e = 0.15\, D^{3/2}\, (\sigma/\rho)^{-1/2} \qquad (3.7)$$

where D = diameter of test tank, cm

σ/ρ = kinematic surface tension, cm^3/sec^2.

The sloshing frequency of a small amount of liquid in a flat bottomed cylindrical container can be estimated with the use of the following relation reported by Reynolds, et al**.

$$\frac{D^3\omega^2}{8\sigma/\rho} = (6.26 + 1.84\, B_\alpha - 4.76 \cos\theta) \tanh\left(\frac{3.86\,\ell}{D}\right) \qquad (3.8)$$

where ω = circular sloshing frequency, rad/sec

ℓ = depth of liquid from vertex of equilibrium free surface to cylinder bottom

*Siegert, C.E., Petrash, D.A., and Otto, E.W., "Time Response of Liquid Vapor Interface After Entering Weightlessness", NASA Technical Notes D-2458, Aug. 1964.

**Reynolds, W.D., M. A. Saad, and Satterlee, H.M., "Capillary Hydrostatics and Hydrodynamics at Low g," Stanford Univ. Dept. of Mech. Engr. Rept. No. LG-3, Stanford, Calif., Sept. 1, 1964.

B_α = axial Bond number = $\frac{gD^2}{4\sigma/\rho}$

Θ = contact angle

Equation 3.8 can be put into the form of Equation 3.7 by assuming a worst case depth of liquid since it is evident that sloshing frequency is reduced for small depths.

Since the slosh period is

$$t = 2\pi/\omega$$

the total period allotted for sloshing during the test is

$$t_s = 2N\pi/\omega$$

where N is number of slosh cycles during this period. Letting $B_\alpha = 0$, $\Theta = 0$ and $\ell/D = .05$ as a worst case, Equation (3.8) becomes

$$t_s = 4.23\ ND^{3/2}(\sigma/\rho)^{-1/2} \qquad (3.9)$$

Assuming that it takes four times the period indicated in Equation 3.7 for the liquid vapor interface to reach the equilibrium shape and combining Equations (3.7) and (3.9), the following relation is obtained

$$(0.60 + 4.23\ ND^{3/2})\ (\sigma/\rho)^{-1/2} = T \qquad (3.10)$$

Where T = 3 seconds the available test time

This relation was used to determine the number of cycles which may be observed as a function of the container diameter and liquid properties to size the experiment.

The desirability of using water (in a glass tank) is obvious, but because of the contact angle hysteresis problem, a lower kinematic surface tension liquid,

isopropyl alcohol, was chosen having a value for σ/ρ of 27.6 cm^3/sec^2. This liquid also has the necessary characteristic of not reacting with the lucite or leaching like carbon tetrachloride.

In order to obtain an order of magnitude estimate of the liquid response to impulsive accelerations for the purpose of sizing the test conditions, the relation below for sloshing behavior was employed. When a 90° contact angle is assumed, it may be shown that the wall rise height resulting from a transverse impulse is given by

$$\left| h_{WALL,MAX} \right| = \frac{B_\tau}{1+B_\alpha} \sum_{m=1}^{\infty} \frac{b_m k_m}{\omega_m} J_1'(k_m) \tanh k_m L$$

where with m = 1

k_m = 1.841, separation constant defined by $J_1'(k_m) = 0$ and m = 1

k_m^3 = 6.255

b_m = 1.488 constant at m = 1

$J_m(k_m)$ = 0.581

and the nomenclature

h = slosh amplitude measured from the equilibrium surface, normalized on tank radius

h_{WALL} = slosh amplitude measured at the tank wall

B_τ = transverse Bond number = $\rho \tau r_o^2/\sigma$

τ = transverse acceleration

l/r_o = liquid fill level, dimensionless = L

ω_1 = free surface fundamental slosh frequency, dimensionless.

Considering only the fundamental slosh mode

$$\left|h_{WALL,MAX}\right| \approx \frac{1.592}{(1+B_\alpha)} \frac{B_\tau}{\omega_1} \tanh\left(\frac{1.841\,\ell}{r_o}\right) \tag{3.11}$$

First, it is noted that the transverse Bond number can be cast in a slightly different form, thus.

$$B_\tau = \Delta v \sqrt{\rho r_o/\sigma}$$

where Δv = the velocity increment impacted by the impusle or, as will be explained later, the impact velocity that establishes the sloshing. Thus,

$$\Delta v \sqrt{\rho r_o/\sigma} = \frac{\left|h_{WALL,MAX}\right| (1+B_\alpha)\,\omega_1}{1.592 \tanh(1.841\,\ell/r_o)}$$

and thus

$$\frac{h_{MAX}/r_o}{\frac{\Delta v}{\bar{\omega}_1 r_o}} = \frac{1.592 \tanh(1.841\,\ell/r_o)}{\sqrt{1+B_\alpha}} \tag{3.12}$$

This equation implies that the ratio of slosh amplitude times the slosh frequency to the impulsive velocity increment is a function of tank fill level and axial Bond number condition. The ratio for the test results will be established by plotting h_{MAX}/r_o versus $\Delta v/\bar{\omega}_1 r_o$ to obtain the linear constant.

The oscillation or sloshing of the liquid-vapor interface can be simulated to a degree by an equivalent spring-mass system influenced by viscous forces. The differential equation for such a dynamic system in free vibration is a force

balance between the inertia, viscous and restoration forces (see Jacobsen ch. 5)*.

$$\frac{d^2\bar{x}}{dt^2} + \frac{c}{m}\frac{d\bar{x}}{dt} + \frac{k}{m}\bar{x} = 0 \qquad (3.13)$$

where $\bar{x}$ = the displacement of an equivalent mass

c = a damping factor

m = the mass

k = the spring constant

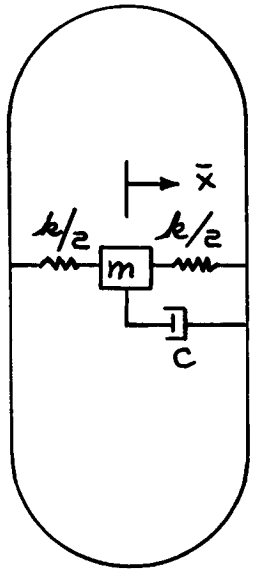

The sloshing performed in the experiments ranges from a condition at high fill level (ℓ/r_o = 1.0) where the inertia and restoration forces prevail to a condition at low fill level (ℓ/r_o = .275) where the viscous forces begin to dominate the slosh motion. In developing the analogy between the experiment and the spring-mass, the former condition will be considered where

$$c < 2\sqrt{km}$$

*Jacobsen, L.S. and Ayre, R.S., "Engineering Vibrations", McGraw-Hill Book Co., Inc., 1958

At the critical condition, where

$$C_{cr} = 2\sqrt{km}$$

the spring-mass system does not oscillate about equilibrium but goes directly from its initial displacement to the equilibrium position over some time interval. For the condition which simulates the motion of the interface about its equilibrium position,

$$C/C_{cr} < 1.0$$

this ratio is designated ν , the damping ratio.

A general solution to the differential Equation (3.13) for $\nu < 1.0$ is

$$\bar{x} = e^{-\nu\bar{\omega}_1\bar{t}}\left[\bar{x}_o^2 + \left(\frac{\Delta v + \nu\bar{\omega}_1\bar{x}_o}{\bar{\omega}_1\sqrt{1-\nu^2}}\right)^2\right]^{1/2}\cos\left(\bar{\omega}_1\sqrt{1-\nu^2}\,\bar{t} - \varphi\right)$$

where $\bar{\omega}_1 = \frac{k}{m}$, the frequency

$\bar{X}_o$ = initial displacement

$\bar{t}$ = time from impulse

Δv = initial velocity (impulse velocity)

φ = phase angle between the initial displacement and the equilibrium position

Since the second term under the square root is much larger than the first term for the experiments performed, the first term may be dropped. At the maximum displacement the cosine term becomes equal to 1.0. The displace-

ment equation becomes

$$\bar{x}_{MAX} \approx e^{-\nu \bar{\omega}_1 \bar{t}_{MAX}} \left(\frac{\Delta v + \nu \bar{\omega}_1 \bar{x}_o}{\bar{\omega}_1 \sqrt{1-\nu^2}} \right)$$

Dividing by X_o and taking the logarithm of both sides of the equation

$$\nu \approx \frac{1}{\bar{\omega}_1 \bar{t}_{MAX}} \ln \frac{\frac{\Delta v}{\bar{\omega}_1 \bar{x}_o} + \nu}{\bar{x}_{MAX}/\bar{x}_o \sqrt{1-\nu^2}} \qquad (3.14)$$

By trial and error, the damping ratio may be determined for the experimental test points using the measured quantities indicated in the equation and substituting measured wave wall amplitude (h) in place of $\bar{x}$. A simpler solution for the damping ratio called the logarithmic decrement can be used.

$$\nu \approx \ln \frac{\bar{h}_{MAX}\left[at \ \bar{t}_{MAX}\right]}{\bar{h}_{MAX}\left[at \ \bar{t}_{MAX} + \frac{2\pi}{\bar{\omega}_1}\right]}$$

when the displacements for at least 1-1/4 cycles plus a fraction of a cycle due to the initial displacement from equilibrium is discernible from the test data. However, the displacement of the liquid wall wave beyond a time ($\bar{t}_{max}$+ $\pi/2\bar{\omega}$) was difficult to measure because of the decreased magnitude of the displacement and the large liquid film left on the wall by the earlier wave displacements.

Experimental Apparatus - The basic philosophy which established the guidelines for designing the experiment was that impulsive excitation of the liquid in the test tank was required and that the result is easier to view when

the tank is motionless than when it is in motion across the camera field of view. As a result, the test arrangement was designed to slowly accelerate the model tank to a predetermined velocity and bring it to rest impulsively over a small distance. The impulse magnitude is the same as that resulting from the slower acceleration of the tank mass over a longer time before the impact (except for the effects of friction).

Based on the above considerations, a transversing platform test rig was designed and incorporated within the structure of the drop tower test capsule. The test rig consisted mainly of

1. 1.3 cm radius test tank, machined into a lucite block 2.5x2.5x2.5 cm.
2. Traversing platform: two parallel aluminum plates assembled in a rigid structure at a fixed distance apart with a set of aligned ball bushings attached to both top and bottom surfaces.
3. Two parallel rod tracks for the opposing ball bushing sets of the platform to ride on.
4. Negator spring motor for applying constant pull force on platform.

The platform tracks extended horizontally across the diameter of the test capsule. The traversing platform could be started from rest anywhere along the tracks and be pulled by the spring motor at constant acceleration up to the desired impact velocity. The lucite test tank was held between the top and bottom plates of the traversing platform. In the simulation of a slosh test point, the platform was started from rest at some position along the tracks to achieve a required velocity at impact at the end of track. A stop

terminated the movement and prevented rebound of the platform. The test tank (as well as the platform) decelerates in an impulsive manner, thus imposing the impulsive slosh mode on the test liquid.

The small positive or zero gravitational acceleration in the test tank axial direction was imposed at release of the capsule within the drop tower drag shield. This action was initiated before the traversing platform terminates its travel in order to reach the equilibrium position of the liquid-vapor interface prior to impulsive slosh. The small axial acceleration was transmitted to the capsule by an air jet thruster located on its lower side. The thruster was activated before the capsule release. Figure 3-29 is a photograph of the actual test rig.

Experimental Technique - A typical test condition is established by determining the transverse Bond number required to displace the liquid-vapor interface from its equilibrium to a desired wall height $\left|h_{wall,\ max}\right|$. The transverse Bond number, as noted for the cylindrical flat bottom tank-flat interface theory, is a function of the axial Bond number, the liquid fill depth, the fundamental slosh frequency of the liquid as well as the displacement wall height of the slosh wave. Since the slosh frequency as determined from Equation (3.8) is dependent on axial Bond number and liquid fill depth, the transverse Bond number becomes dependent only on the axial Bond number and fill depth once the liquid, radius of the tank and required wall height is fixed.

The experiments were limited to two axial Bond numbers and three liquid fill

depths. Six test points were defined for a maximum wall wave displacement as,

Test Run No.	B_α	ℓ/r_o
1	0	1.0
2	0	0.5
3	0	0.275
4	1	1.0
5	1	0.5
6	1	0.275

For these conditions the transverse Bond number range predicted from Equation (3.12) was

$$1.6 > B_\tau > 0.48$$

Knowing B_τ, from

$$B_\tau = \Delta v \sqrt{\rho r_o/\sigma}$$

the impact velocity, Δv, can be found which will give the required impulsive deceleration to the contained liquid. Once the impact velocities were established, the distances for releasing the traversing platform from the impact point were determined from the near constant acceleration imposed by the spring motor on the platform.

A series of timing sequences was required to set the order of events to satisfy the objectives of the experiments. Approximately 0.48 seconds of time was set for the liquid-vapor interface to reach its equilibrium position in the zero and low gravity environment. This sets the capsule release 0.48

seconds before the traversing platform terminates its movement to achieve a stable liquid-vapor interface before the impulsive slosh. The impact velocity requirement established whether or not the platform was released from rest before or after the capsule release. For the low axial acceleration (B_{α} = 1.0) the air jet thruster was turned on prior to the capsule release. The movie camera was activated before all other events requiring film coverage.

The movie film coverage of the test provided a means of determining the magnitude and timing of the test conditions which generate the impulsive slosh in the test liquid. The acceleration of the traversing platform and the resulting impact velocity were checked by noting the movement of the platform relative to a fixed point in the film. The timing marks on the film provided time reference. A check was made on the preset test conditions of acceleration and impact velocity. Flash bulb markers on the film indicated the beginning of an event, such as start of platform movement, thrust on, and capsule release.

The liquid interface sloshing was extracted from the film with a precision film data analyzer. Because the camera was placed relatively close to the test tank in order to provide maximum magnification, corrections to the displacement for refraction and parallax were applied to the readings. All readings were increased by 17% to account for these effects.

The fundamental slosh frequency was determined by observing the time required for the liquid slosh wave to pass through the zero or the low gravity equi-

librium position of the liquid vapor interface twice, or one-half cycle. It was difficult in subsequent half-cycle oscillations of the interface to determine the period because of the rapid damping of the slosh mode. However, measurements that could be made indicate no change in the slosh period. Another difficulty appeared in determining the wall wave position because of the liquid film left on the tank wall in the wake of a descending wave. The wave often times blended in with the film although the wave was actually receding. To correct for this in the measurements, the tank wall was assumed to be at the inside surface of the film.

RESULTS AND CONCLUSIONS - The six test points of this task gave slosh frequencies which were of the order of 25% higher than predicted by the theory. Comparison was made with predicted fundamental frequencies obtained for a contact angle of 5°. Two phenomena were clearly noted in the test behavior that can account for this; contact angle hysteresis and variation of the contact angle under dynamic conditions. Both of these aspects of behavior of a moving three phase boundary have been previously reported in the literature (see Bikerman, Chapter V, pp. 348-354)* although efforts to analyze this behavior have been unsuccessful. Advancing contact angles greater than the static value were observed on the slosh wave moving up the tank wall. Also, a hysteresis effect was noted wherever the three phase boundary remained motionless, or was "stuck", while the contact angle increased as the slosh wave moved into the tank wall.

*Bikerman, J. J., "Surface Chemistry", Academic Press Inc., 1958.

In addition to the above, viscosity by creating a boundary layer at the wall decreases the effective tank radius as far as sloshing is concerned. A 5% decrease in tank radius in this manner results in an 8% increase in sloshing frequency.

The data for the slosh frequencies is presented in Figure 3-30. The square of the dimensionless frequency is plotted versus the centerline distance between the interface (at equilibrium) and the tank bottom normalized on the radius of the tank. The theoretical variation of frequency at the 5° contact angle is presented for comparison. Based on an error analysis the uncertainty interval for the frequency was ±20%.

The slosh wave amplitude at the tank wall versus the parameter $\Delta v/\bar{\omega}, r_o$ have been plotted in Figures 3-31 and 3-32. A comparison can be made between the test data and the displacements predicted by the simplified theory for cylindrical-flat bottomed tank with liquid at 90° contact angle with the wall. It may be noted that the liquid response in terms of slosh amplitude is less than predicted from the linear theory (see Equation 3.12). The smaller slope or lower liquid wave displacement, may be attributed to

1. Hemispherical tank bottom versus the theoretical flat bottom tank.
2. Low contact angle test condition as compared to 90° flat interface theoretical calculations.
3. Liquid stuck at the initial position until contact angle reaches a critical value (hysteresis effect).
4. Viscous force opposing the slosh mode.
5. Departure of the test condition from the linear assumptions (i.e., $h_{MAX}/r_o \leq 0.2$) upon which the theory is based.

For all fill levels, ℓ/r_o, and B_α = 1.0 (Figure 3-32) the wall displacements from the test results are larger than for B_α = 0 (Figure 3-31) which is contrary to that predicted by the simple theory used to design the experiment. An error analysis indicates that a ±17% uncertainty in the parameter $\Delta v/\bar{\omega}, r_o$ is possible for the test data. Taking the opposite extremes of the error spread for the test data displacement slopes of B_α = 0 and 1.0 (Figure 3-31 and 3-32), a trend substantiating the flat-bottom, flat-interface theory of decreasing displacement with increasing B_α appears possible for the fill levels of ℓ/r_o = 1.0 and .275 but not for ℓ/r_o = .5. An examination of the first mode equivalent sloshing mass presented by Concus et al* indicates that this mass can actually increase with decreasing depth at low axial Bond numbers. The trends indicated by these experiments are reasonably consistent with the results of the referenced analytical work.

The analogy between the interface slosh behavior to that of an oscillating spring-mass under the influence of viscous damping was previously discussed. Equation (3.14) provides a means of calculating the damping ratio of the viscous forces acting on the liquid motion. The damping ratios determined for the test points indicate a rather strong effect, especially at the low fill levels. At ℓ/r_o = .275 the slosh mode is almost critically damped, that is, no oscillation about the equilibrium position of the interface. The variation of the damping ratio with liquid fill level is shown in Figure 3-33.

*Concus, P., Crane, G.E., and Satterlee, H.M., "Small Amplitude Lateral Sloshing in a Cylindrical Tank with a Hemispherical Bottom Under Low Gravitational Conditions". NASA CR-54700 prepared by Lockheed Missiles and Space Company, January 20, 1967, p 108.

The conclusions drawn from this experiment are

1. Qualitative verification of first mode slosh frequencies was obtained. The fact that test results are generally higher than theory indicates may be attributed to an apparent dynamic contact angle variation and to the importance of boundary layer thickness in the small models used.
2. Qualitative agreement with theory was reached showing that much lower response to lateral impulses may be expected in round bottom tanks compared to flat bottom tanks.

RESIDUAL SLOSHING EXPERIMENT

It was the general purpose of this experiment to examine high amplitude residual sloshing in a test tank under controlled conditions of acceleration forces and liquid properties. To this end a special apparatus, described below, was designed, constructed, and installed in the test module of the LMSC drop tower.

Considerable effort has been expended describing sloshing in boost vehicles (e.g. Bauer*,** and Stephens, et al/) and good analytical models have been developed and experimentally verified for most first mode sloshing conditions in boosters. General objectives of this study were to indicate the departure of liquid motion from its small-amplitude behavior following a reduction in the local acceleration.

Test Objectives - The specific objectives of this study were to:

1. Determine the slosh wave amplification.
2. Examine the slosh wave forces on the container.
3. Qualitatively study the effect of a baffle.
4. Qualitatively study the turnover phenomena.

* Bauer, Helmet F., "Fluid Oscillations in a Circular Cylindrical Tank," Technical Report No. DA-TR-1-58, Army Ballistic Missile Agency, Redstone, Alabama, 18 April 1958.

**Bauer, Helmet F., "Fluid Oscillations in a Cylindrical Tank With Damping," Report DA-54-4-58, Army Ballistic Missile Agency, Redstone Arsenal, Alabama, Development Operations Div., Aeroballistics Lab., 23 April 1958.

/Stephens, David G., and Leonard, H. Wayne, "The Coupled Dynamic Response of a Tank Partially Filled With a Liquid and Undergoing Free and Forced Planar Oscillations", NASA TN-D-1945, August 1963.

The primary test variables were the slosh wave kinetic energy and the axial acceleration.

Experimental Apparatus and Technique - The essential design features of the slosh test fixture are shown in Figure 3-34. The 4.12 cm radius test tank, 26.8 cm long, dome to dome, shown in Figure 3-35, was mounted on a platform hung from two cantilevered leaf springs which were driven off center by a D.C. motor driven eccentric. Excitation was stopped at or near the wave's maximum potential energy point by pulling a connecting rod latch with a solenoid. Delatching, occurring at or near the spring's minimum deflection point, was accomplished by activation of a photo sensitive resistor at the proper mechanical position. The test vessel did not move after delatching due to small spring response to wave motion. Drop timing was started with the delatching signal, permitting a drop at the maximum kinetic energy point a quarter cycle later.

Maximum amplification of the slosh wave occurs if low-g is achieved at the instant the wave is at maximum kinetic energy. Drag shield length limited test drop time with upward thrust applied to the capsule. The basic strategy was to establish a fairly large amplitude 1-g_o lateral slosh wave in the test tank by operating the motor driven shaker for a short time (this time was limited to small values because of the relatively rapid onset of rotary sloshing or swirl). The experiment was then dropped into a zero or partial g environment for data acquisition, the drop being effected as closely as possible to the instant the kinetic energy of the sloshing liquid was a maximum.

For a given test gravity level (g/g_o), fill level, and baffle geometry, the wave height was adjusted by presetting the excitation frequency and/or spin-up time of the gear-motor. A time delay provided for camera spinup and lighting stabilization prior to drop. Another time delay permitted excitation speed stabilization and maximum wave height prior to enabling the photo sensitive switch to activate at a preset mechanical position, starting the drop. The mechanical lead position of the photo switch was set ahead of the true mechanical zero position by about 30 milliseconds, permitting actuation of the relays and solenoids in series. A single mechanical lead position for all three excitation frequencies caused a variation of only ±6 milliseconds in the 30 milliseconds lead desired.

Data Reduction and Analysis - The maximum pre-drop and post-drop wave heights were measured to determine the slosh wave kinetic energy available in the low g environment. The fluid height was measured at its peak for the maximum h/R in low g. Acceleration levels were obtained from measurement of the trajectory of a ball bearing in the field of view during the first portion of the test with an estimated accuracy of 5%.*

The tests conducted and their most significant data are listed in Table 3-IV. Bond numbers ($\rho g R^2/\sigma$ where ρ is the liquid density, σ the surface tension g the acceleration and R the tank radius) varied from 1 or 2 to 65 and Froude numbers (v^2/gR where v is the wave velocity at entry into reduced g level)

*Using a root-sum-square error analysis technique and a 95% confidence level for uncertainty estimates. Kline, S.K., and McClintock, "Describing Uncertainties in Single-Sample Experiments", Trans. ASME, Jan. 1953

based on the pre-drop excitation velocity varied from 0.3 to 28. The kinetic energy levels were high enough to cause turnover in the zero-g drops and to cause the wave to progress about half-way through the upper dome on test No. 29 with $\alpha = .03$ (α being the gravity level, g/g_o). Fill levels were at 2 and 4 hemispherical volumes. Further, a baffle was inserted on Test no. 35 to study briefly its effect.

As was indicated previously a great deal of information about small amplitude sloshing exists. Some of the more useful relations are collected below. These were used in part to design the experiment and also to aid in analysis of experimental data obtained in this study.

The wave height, h, response to translational sinusoidal excitation, x at a rate ω, neglecting damping, was derived by Bauer (op. cit.) as;

$$\frac{h}{x} = 2 \sum \frac{k_1 \tanh(k_1 \ell/R)}{(k_1^2 - 1)} \quad \frac{(\omega/\omega_1)^2}{\left[1 - (\omega/\omega_1)^2\right]}$$

where $k_1 = 1.841$, ℓ is the liquid depth, ω the impressed circular frequency, and ω_1 the 1st natural circular frequency. The natural frequency (ω_1) of a freely sloshing wave has been determined* as

$$\omega^2 = \frac{\sigma}{\rho R^3} (2.80 + k_1 B) \text{ for } \ell/R > 2$$

because depths (ℓ) greater than two radii (2R) are essentially equivalent to an infinite depth of fluid.

This information facilitated computing wave kinetic energy levels at the start of a low g environment. The kinetic energy in a sloshing system at

*Concus, et al (op.cit.)

boost termination can be converted to potential energy. The maximum kinetic energy (T) of a sloshing wave can be expressed as (see Bauer*)

$$T = \frac{\pi R^2}{4} \rho g \left[1 - \frac{1}{(k,g)^2}\right] h_o^2$$

The wave height in low g cannot be determined directly with this equation because of interface nonlinearity, however, it will serve as a first approximation for comparison with data. Ideally, then, the wave height along the wall, h/R, would be increased by $\frac{go}{g}^{1/2}$. There should similarly be a shift in the liquid center of mass in a finite but reduced gravity field. The excursions of the liquid center of mass undergoing small amplitude sloshing expressed as (Bauer/)

$$\bar{Y}_o = \frac{h_1^2 - 1}{4 k_1^2 \ell} h_o^2$$

$$\bar{R} = \frac{R}{\ell k_1^2} h_o$$

$$h_o = h_{o_{MAX}} \sin \omega t$$

where h_o is the wave height at the wall and subscript max indicates the maximum value.

---

*Bauer, op. cit.

/Bauer, Helmet, F., "Nonlinear Mechanical Model for the Description of Propellant Sloshing," AIAA Journal, Vol 4, No. 9, pp 1662-1668, Sept 1966

The vertical change in the liquid center of mass ($\bar{Y}_\alpha / \bar{Y}_o$) will be different from or equal to $(g_o/g_\alpha)^{1/2}$ depending on the departure from linear behavior.

The damping factor for normal sloshing can be computed following Stephens, et al*.

$$\delta = 4.96\, \nu^{1/2}\, R^{-3/4}\, g^{-1/4}$$

where ν is the liquid kinematic viscosity.

The force which nonlinear liquid motion exerts on the tank wall must be inferred from the motion of the center of mass of the liquid. The lateral acceleration $\ddot{x}$ of the liquid center of mass is related to the force exerted by the tank wall by Newton's second law of motion

$$m\, \ddot{x} = F(t)$$

where m is the liquid mass and F(t) is the force as a function of time. Rather than double-differentiate estimates of the trajectory of the center of mass, it is far better to infer the force through examination of the double integral of the foregoing expression.

$$x = \bar{x}_o t + \frac{1}{m} \int_o^t \int_o^t F(t)\, dt\, dt$$

Experimentally, the motion of the liquid center of mass can be determined.It is then possible to approximate the trajectory by an analytical function having the proper form. Double differentiation of this function (rather than "noisy" data)will lead to the force history.

---

*Stephens, et al, op. cit.

Results - Determination of the interface position and/or liquid center of mass (C.G.) shift is desired as a function of the kinetic energy present at boost termination.

Test no. 37 was selected as a typical run for more thorough analysis. The C.G. shift was computed for approximately the first quarter cycle with the results shown on Figure 3-36. The axial C.G. shift amplification resulting from g-level reduction was computed to be about 7.05, slightly greater than the factor $\sqrt{1/\alpha}$ = 6.41 for that case. The lateral C.G. shift amplification was computed to be 2.8 by comparison. (The lateral C.G. shift is very small for low amplitude sloshing.)

The C.G. shift computation was performed for run 37. This computation proved to have a large percentage uncertainty. Interpretation of the best average position of the interface contributed the largest portion of this uncertainty. A ribbon type interface was assumed in which the liquid free-surface is curved only in the sloshing direction, remaining uncurved in the direction perpendicular to the sloshing. Straight line chord segments were then used to approximate the plane curve describing the interface, as pictured in Figure 3-38, and volumes and centroids were then found for each segment. The total volume was found by adding the segment volumes. The centroid of the liquid was obtained by dividing the sum of the moments of the segments about a datum point by the total volume.

The trajectory of the lateral center of mass (as a function of time) was used to infer an analytical expression for the lateral force exerted on the tank gy liquid sloshing up one side of a very long cylindrical tank. The result-

ing expression is

$$r = R\left[\frac{e^{-\beta t}}{2}(\beta t + 2) - 1\right]$$

where β is a constant requiring evaluation. This can be accomplished by matching the lateral velocity $\dot{r}$ to the lateral velocity of the liquid center of mass just at the instant of release into low-g. When this is done the lateral force is given by

$$F(t) = \frac{4 m \dot{x}_o^3 t}{R^2} e^{\frac{-2\dot{x}_o t}{R}}$$

and the maximum value of the lateral force by

$$F_{max} = \frac{4 m \dot{x}_o^2}{2 e R}$$

which occurs at time

$$t = \frac{R}{2\dot{x}_o}$$

In these relations m is the total liquid mass, and $\dot{x}_o$ the initial lateral velocity of the liquid center of mass.

The pre-drop kinetic energy was expressed as an equivalent wave height $(h/r)_o$ in Table 3-IV and the ratio found between pre- and post drop wave heights. A ratio was then taken of the measured wave amplification (h_α/h_o) to the idealized wave amplification $1/\sqrt{\alpha}$, α being the ratio of post-drop to pre-drop g-levels.

Figure 3-37 shows the succeeding slosh wave profiles for test No. 37. Certain noteworthy features of the liquid behavior are described as follows. A wall sheet was formed during the first slosh (Figures 3-36, 3-37a), which subsequently drained slowly back into the bulk (Figure 3-37b) while the bulk of fluid continued oscillating. The wave rose freely on the right wall (Figure 3-37a) but was damped and perturbed by the draining wall sheet on the second rise up the left wall (Figure 3-37b). The succeeding oscillations (Figure 3-37c) were relatively unaffected by the wall sheet.

The natural frequency computed was 3.44 rad/sec while the highest measured frequency was somewhat less (3.1 rad/sec). This may be attributed in part to the departure of large amplitude wave behavior from that of small amplitude waves and possibly, in part, to damping.

The damping factor was calculated for this test to be 0.024 without wall sheet draining compared to the measured value of 0,06 with interference from wall fluid draining. The test duration allowed 1-1/2 cycles of oscillation for measurement of the damping.

The amplification data of the wall slosh waves are shown on Table 3-IV . The $(g/g_o)^{1/2}$ term was divided into the observed amplification h_α/h_o to give an indication of the system's non-linearity.

The effect of changing from 2 to 4 hemispheres volume fill levels (Figure 3-35) was not appreciable in these tests.

Complete turnover, or fluid circulation up one tank wall and over the upper dome, was obtained on Test nos. 30, 31, and 33, these being zero g tests. The

TABLE 3-IV

TESTS & TEST DATA

Test No.	Equivalent $(h/r)_o$	$\alpha = g/g_o$	h_α/h_o	$\frac{1}{\sqrt{\alpha}}$	$\frac{h/h_o}{1/\sqrt{\alpha}}$	Bond Number $\frac{\rho g R^2}{\sigma}$	Froude Number $\frac{v^2}{Rg}$
*37	0.202	0.024	17.12	6.41	2.69	14.7	4.14
27	0.126	0.028	31.9	6.10	5.23	16.8	1.04
28	0.086	0.028	26.6	6.02	4.42	16.6	0.49
*38	0.063	0.027	7.8	6.12	1.27	16.1	0.27
26	0.040	0.026	45.8	6.18	7.42	15.8	0.11
29	0.336	0.030	over	5.75	over	17.5	6.94
*39	0.267	0.0159	10.38	7.92	1.31	9.6	8.26
32	0.182	0.0139	17.93	8.46	2.12	8.4	4.38
36	0.054	0.0173	4.63	7.6	0.61	10.4	0.31
33	0.305	0	over	---	over	---	---
31	0.213	0.003	over	17.4	over	1.8	27.9
30	0.165	0	over	---	over	---	---
*40	0.178	0.102	4.83	3.04	1.59	64.9	0.57
*41	0.082	0.062	5.21	4.02	1.30	37.2	0.20
**35	0.406	0.0113	4.34	9.4	0.46	6.8	26.8

* Fill volume was 4 hemispheres. All others 2 hemispheres; see Figure 3-40.
** Baffle Test; see Figure 3-35.

motion is pictured in Figure 3-39. Qualitatively, the wall sheet descending from the dome into the bulk of liquid did not cause gas entrainment, although waves were excited ahead of the wall sheet fluid. The small arrows show the direction of free-surface motion.

A baffle of 0.1 R width was installed one radius above the equilibrium fluid surface for Test no, 35. The fluid rise along the wall was only 4.34, compared to a similar test (no. 29) in which fluid half filled the upper dome. Further, the baffle did divert a significant amount of fluid toward the opposite tank wall as shown in Figure 3-40.

THE EFFECT OF BAFFLES ON LOW-GRAVITY SLOSH

Introduction - The purpose of the investigation described below is to examine the motion of liquids contained in a baffled cylindrical tank under low gravity conditions through the use of a liquid-liquid analog. Such an analog makes use of two relatively immiscible liquids of nearly equal density.

These liquids are contained in a tank so that the upper liquid occupies a volume equivalent to that normally occupied by the tank ullage gas. The lower liquid, simulating the propellant, should have wetting properties similar to that of the actual propellants of interest; concurrently, the upper liquid must not wet the container walls. By virtue of their equal densities, the interface between the two liquids will assume a shape closely approximating that which would occur under low-gravity capillary dominated conditions.

The technique of using a liquid-liquid analog to investigate the dynamics of liquid motion under low-g conditions has been proposed elsewhere (see, for example, Reynolds et al*). Reports of details of the experimental use of such a device are, however, unavailable.

The current investigation is directed toward a liquid-liquid model of the sloshing behavior of liquids contained in a cylindrical tank. Such a simulation provides a very useful tool for experimentally evaluating the effect of tank configuration, baffle design, etc., on the motion of liquids in

*Reynolds, W.C., Saad, M.A., and Satterlee, H.M., "Capillary Hydrostatics and Hydrodynamics at Low g," Stanford Univ. Dept. Mech. Engr. Rept. No. LG-3, Stanford, Calif., Sept. 1, 1964.

spacecraft propellant tanks. Drop tower testing, commonly employed in low gravity investigations, produce test durations too short to observe and measure slosh damping effects.

Test Objectives - The basic objective of the tests described here was to use the liquid-liquid analog technique to simulate the asymmetric sloshing of liquids in a deep cylindrical tank both with and without baffles and with the typical capillary dominated interface shape. The accomplishment of this objective depends directly on the degree of simulation obtained, the extent that the behavior observed in the test can be scaled up to a full size prototype. This is of particular concern here in that a dense viscous medium was employed in place of the pressurant gas used in the prototype. Thus the derivation of valid scaling laws is essential.

The container and baffle geometry considered is shown schematically in Figure 3-41. The experimental measurements consisted of a determination of the amplitude of the perturbed surface at the walls of the cylindrical container, $\zeta = Z(r_o)$, as a function of time. This determination was made for a "clean" tank(without a baffle) and for a tank having various baffle heights, h/r_o. From the amplitude measurements an estimate of the damping factor for the fundamental liquid mode was made. The damping factor, or logarithmic decrement, δ, is defined as

$$\delta = \frac{1}{n} \ln \frac{\zeta_o}{\zeta_n} \tag{3.15}$$

where n is the number of cycles over which the decay is measured, ζ_o is the initial amplitude, and ζ_n is the amplitude of the nth cycle. The damping of

the oscillations of a slightly viscous liquid resulting from boundary layer friction was examined by Miles*. An expression was presented for the damping of the fundamental antisymmetric mode of a liquid in a flat-bottomed right-circular cylinder having a constant liquid depth. The resultant damping factor is

$$\delta = K \left(\frac{g r_o^3}{\nu^2}\right)^{-\frac{1}{4}} \left[1 + 2\left(1 - \frac{\ell}{r_o}\right) \operatorname{csch}\left(3.68 \frac{\ell}{r_o}\right)\right] \times \left[\tanh\left(1.84 \frac{\ell}{r_o}\right)\right] \tag{3.16}$$

where ν is the kinematic viscosity of the liquid, r_o is the cylinder radius, g is the acceleration due to gravity, ℓ is the liquid depth, and K is a constant equal to 5.23. As ℓ/r_o is increased above 1.0, the bracketed terms have a negligible effect and the damping factor is invariant with further depth increases. This "deep-tank" damping factor is,

$$(\delta)\Big|_{\frac{\ell}{r_o} > 1} = 5.23 \left(\frac{g r_o^3}{\nu^2}\right)^{-1/4} \tag{3.17}$$

Stephens** also reports the above relation. In all cases the value of ℓ/r_o for the tests described below was greater than 4.0. Thus, the relation

*Miles, J.W., "On the Sloshing of Liquid in a Cylindrical Tank," Report no. AM 6-5, GM-TR-18, Guided Missile Res. Dev. The Ramo-Wooldridge Corp., Apr. 20, 1956.

**Stephens, D.G., Leonard, H.W., and Perry, T.W., Jr., "Investigation of the Damping of Liquids in Right-Circular Cylindrical Tanks, Including the Effects of a Time-Variant Liquid Depth," NASA TN D-1367, August, 1962.

given in Equation (3.17) was used to predict the theoretical damping to be expected in a clean tank.

Recent numerical solutions for the frequency of small amplitude linearized sloshing motions have given the value (see Concus et al*)

$$\omega_1 = 1.675 \sqrt{\frac{\sigma}{\rho r_o^3}} \tag{3.18}$$

for the first mode (fundamental) slosh frequency for zero axial Bond number and depth, h/r_o, greater than 3.0. This result is based on the assumption of an inviscid, incompressible fluid irrotationally performing small displacements. Equation (3.18) was used in this study to estimate the fundamental sloshing frequency to be expected in a clean tank. In addition the effect on the slosh frequency of a dense upper fluid must be acknowledged. Satterlee** considered the effect on interface slosh frequency produced by a dense upper liquid in a liquid-liquid analog. The result reported for large depth in both liquids is

$$\omega_1^2 = \frac{r_o^2 g k(\rho_2 - \rho_1) + \sigma k^3}{r_o^3(\rho_1 + \rho_2)}$$

where ρ_1 = density of upper liquid

ρ_2 = density of lower liquid

* Concus, P., Crane, G.E., and Satterlee, H.M., "Small Amplitude Lateral Sloshing in a Cylindrical Tank with a Hemispherical Bottom under Low Gravitational Conditions," NASA CR-54700, January 20, 1967.

**Satterlee, H.M., And Reynolds, W.C., "The Dynamics of the Free Liquid Surface in Cylindrical Containers Under Strong Capillary and Weak Gravity Conditions," Dept. of Mech. Eng., Tech. Rpt. LG-3, Stanford University, Stanford, Calif., May 1, 1964, pp. 141-144.

k = eigenvalue for the particular slosh mode and contact angle condition

σ = interfacial tension

g = local acceleration level

r_o = tank radius

Thus the slosh frequency for a two liquid system compared to a single liquid system under similar Bond number conditions is reduced by the square root of the sum of the liquid densities.

Experimental Apparatus - The design of the container for the analog experiments is illustrated in Figure 3-42. Because the best candidate for the lower liquid was a mixture of carbon tetrachloride and benzene, a container material was required which would withstand the solvent action of these liquids. Because of the nonuniform wetting behavior of these liquids on glass, and the propensity for water (the upper liquid) to wet clean glass, a plastic container constructed of CR-39* was used. It was not possible to obtain more than one size of CR-39 tubing. Thus a single cylinder size having an inside diameter of 0.500 inches was used.

In the sloshing tests with baffles, a single ring baffle was press-fitted into the tank. The thickness of th s baffle was 0.006 inches and the width 0.025 inches providing a baffle width of 0.1 r_o. The effective baffle height was varied by adding or removing liquid to vary the height of the interface. A photograph of the assembled apparatus is shown in Figure 3-43.

---

*Pittsburgh Plate Glass Co. trademark.

Experimental Technique - An experimental run with the apparatus described above involved partially filling the cylinder with a mixture of benzene and carbon tetrachloride through the filling hole in the cover plate of the apparatus. This mixture was adjusted beforehand so that the proportions of carbon tetrachloride and benzene provided a liquid whose density was very close to that of water. Water (the upper liquid) was then carefully added until the cylinder was filled and the filling holes capped off. A sloshing motion was imparted to the liquid-liquid interface by rocking the entire assembly back and forth. The container was then brought to rest and the subsequent decay in the oscillation recorded using a high speed motion picture camera. The camera was run long enough so that a record of the equilibrium surface profile was obtained after the sloshing motion had decayed.

The interfacial surface tension between the upper and lower liquids was determined using both a De Nouy tensiometer and the capillary rise technique. The tensiometer method gave values of the interfacial tension directly, while the capillary rise technique involved making separate measurements of the height of columns of water saturated with the hydrocarbon mixture and vice versa. The interfacial tension was then calculated using Gibb's rule:

$$\sigma_{1-2} = \sigma_{1(2)/AIR} - \sigma_{2(1)/AIR}$$

where σ_{1-2} is the interfacial tension between liquids 1 and 2 and $\sigma_{1(2)/AIR}$ is the surface tension of liquid 1 saturated with liquid 2 against air. The mean of several measurements yielded a value of σ_{1-2} = 37 dynes/cm. for the mixture tested. An additional measurement of the index of refraction of the

hydrocarbon mixture was required for the refraction correction described below. This measurement was performed on a Fisher refractometer, and yielded a value of $n_o = 1.4925$.

Data Reduction and Analysis - The motion of the free surface was determined from movies made during each run which were read on a frame-by-frame basis using a precision film reader.

An optical correction was required to account for the radial distortion of the interface profile observed on the film reader. This correction was obtained using a ray-tracing technique. The resultant correction is,

$$r = \frac{x}{n_L} \tag{3.19}$$

where r is the actual radial coordinate of the point on the liquid profile being observed, x is the measured radial distance, and n_L is the refractive index of the lower liquid. A plot of the equilibrium interface profile obtained in this manner is shown in Figure 3-44.

In order to simulate zero gravity conditions, it is necessary that the densities of the upper and lower liquids be as nearly equal as possible. The Bond number for the liquid-liquid system is

$$B = \frac{g(\rho_2 - \rho_1) r_o^2}{\sigma_{1-2}} \tag{3.20}$$

A measurement of the density difference between the two liquids can be obtained by measuring the velocity of a drop of one liquid falling within the second liquid in the Stokes flow regime. This is inherently a more accurate method of determining small density differences in this case than the more standard method employing a pycnometer and an analytic balance.

In the Stokes' flow regime, the velocity of a spherical drop is given by

$$V = \frac{4(\rho_2 - \rho_1) g D^2}{3 k \mu_1} \tag{3.21}$$

where

$$k = 8 \frac{2\mu_1 + 3\mu_2}{\mu_1 + \mu_2} \tag{3.22}$$

μ_1 = hydrocarbon mixture viscosity

μ_2 = viscosity of water

D = drop diameter (of liquid 2)

V = drop velocity

The viscosity of the hydrocarbon mixture was calculated from the known mixture ratio between benzene and carbon tetrachloride. This value plus the value of g = 980 cm/sec yields the following relation for the water hydrocarbon system:

$$\Delta\rho = 1.11 \times 10^{-4} \frac{V_2}{D} \tag{3.23}$$

The density difference was adjusted by an iterative process based on observation of the water drop drift rates in the hydrocarbon mixture. The upper limit for the density difference was

$$\Delta\rho \leq 1.24 \times 10^{-6} \text{ gm/cm}^3$$

This extremely small value is justified by the following two observations. A large number of water drops present in the hydrocarbon mixture ranging in diameter downward from 0.3 cm were not segregated by diameter over an approximately 36 hour period. Secondly the drop motions even for the largest

were random in nature indicating that thermal convection current velocities in the hydrocarbon were dominant. Measurements of this convective velocity for one of the largest drop sizes (D = 0.3 cm) were taken over a period of time. The average of these measurements was v = 0.01 cm/sec. These values were used to obtain the density difference limit stated above. This density difference corresponds to an effective Bond number, using Equation (3.20), of

$$B = \frac{980 \times 1.24 \times 10^{-6} \times (0.635)^2}{37} = 1.32 \times 10^{-5}$$

Figure 3-44 shows the measured interface shape compared to the theoretical hemispherical shape for a zero gravity interface. Although the above correspondence between the measurements and theory here is not an accurate verification of the measured Bond number, it does provide a good indication of the low contact angle obtained.

Figure 3-45 shows the measured interface profile obtained during a portion of the first oscillation in an unbaffled tank. These results show the large dynamic contact-angle hysteresis observed in similar transverse sloshing tests under reduced gravity conditions.

The data from the clean tank test and from tests with three baffle heights, h/r_o = 1.72, 1.44 and 0.52 are shown in Figures 3-46 through 3-51. The large scatter in the data points at small amplitudes is due to the difficulties involved in resolving the interface position at the tank wall for the small diameter cylinder used. Only a few cycles of data were obtained from the highly-damped baffle runs.

Results and Conclusions - Using the amplitude vs. time data the liquid amplitude was plotted logarithmically as a function of cycle number in Figures 3-52 through 3-55. From Equation (3.15), the slope of these curves is equal to the decay or damping factor of the interface oscillations. The data for each case, along with observed average sloshing frequencies, are summarized in Table 3-V.

The slosh frequencies listed in Table 3-V show an increasing trend as the baffle location approaches the surface. This is explained by the following qualitative argument. The flow field in the neighborhood of the baffle is disturbed relative to that flow which would exist with no baffle present. With the interface in close proximity to the baffle this distortion in the flow in turn distorts the capillary interface shape. The lowest sloshing frequency is that for zero contact angle with no contact angle hysteresis effects. It has been observed that any variation from this fundamental capillary slosh mode increases the slosh frequency. Thus the interface distortion caused by the flow field distortion caused an increase in slosh frequency as observed. The effect is similar to that produced by dynamic hysteresis of the contact angle. The above is illustrated on Figure 3-56.

Conclusions drawn from this data that can be extrapolated to a full scale vehicle are dependent upon the accuracy of similitude obtained in this test. Some observations concerning modeling are therefore in order. Comparing the values of the frequencies observed in the experiment with the theoretical value of 2.29 cps for zero Bond number and zero contact angle indicates that capillary dominated low contact angle sloshing was obtained and that the ef-

TABLE 3-V

Summary of Sloshing Frequencies and Damping Factors

Baffle Location h/r_o	Slosh Frequency Cycle/Sec	δ
	1.64	0.87
1.72	1.70	1.34
1.44	2.10	1.55
0.52	2.78	1.52

Theoretical sloshing frequency for zero Bond number in a liquid-liquid system:

$$f_1 = \frac{\omega_1}{2\pi} = \frac{1}{2\pi\sqrt{2}} \frac{1.675}{\sqrt{\frac{\rho}{\sigma} r_o^3}}$$

$$= 2.29 \text{ CPS}$$

fect of the upper liquid can be predicted for the deep tanks considered here, certainly within the degree of measurement accuracy obtainable in the small model. The fact that the measured frequency for large h/r is lower than that calculated must be attributed to the difficulty in obtaining an accurate measurement of frequency and interfacial tension.

It was not anticipated at the outset of this test series that dynamic similitude in terms of damping could be achieved. It is to be expected that slosh damping in a small model such as was necessary in these tests would be more influenced by viscous effects than would be the case for a full scale prototype. In addition the effect on slosh damping of the viscosity of the upper liquid in the model is not understood well enough to account for the lack of it in a prototype. A sloshing Reynolds number can cast in terms of the slosh frequency, tank radius and kinematic viscosity thus:

$$Re = \frac{\rho V L}{\mu}$$

setting

$$V \propto \omega r_o$$

where ω = slosh frequency in sec^{-1}

$$L = r_o$$

we have

$$Re_s = \frac{\omega r_o^2}{\nu} \qquad (3.24)$$

If the sloshing is gravity dominated

$$\omega = k\sqrt{g/r_o}$$

and the Reynolds number takes the form

$$Re_s = \sqrt{\frac{g r_o^3}{\nu^2}} \qquad (3.25)$$

(Note: This dimensionless group appears in the relation for the viscous damping under gravity dominated slosh conditions).

If, on the other hand, the slosh is capillary dominated then,

$$\omega \propto \sqrt{\frac{\sigma}{\rho r_o^3}}$$

and the sloshing Reynolds number becomes

$$Re_s = \sqrt{\frac{r_o \beta}{\nu^2}}$$

where $\beta = \sigma/\rho$, kinematic surface tension

Since the fluid properties of most common propellants and test liquids are approximately the same, the mismatch in Reynolds number simulation between model and prototype will be of the order of $(r_{MOD}/r_{PROT})^{1/2}$.

However, it was anticipated that the effect of a ring baffle relative to viscous damping could be observed. Such is the case as shown in Table 3-V. The logarithmic decrement δ generally increases with the decrease in baffle position, h/r. The trend is in agreement with experimental results reported for sloshing under gravity dominated conditions (see for example Abramson*). That this trend is not due to the increase in slosh frequency and viscous damping is evident if relation 3-17 for the viscous damping factor is recast in terms of the slosh frequency by noting that $(g \cdot r) \propto \omega^2$.

*Abramson, H.N., "The Dynamic Behavior of Liquids in Moving Containers," NASA SP-106 National Aeronautics and Space Administration, 1966.

Thus

$$\delta = \frac{c}{r_o}\left(\frac{\nu}{\omega}\right)^{1/2}$$

In this way it is seen that δ is inversely proportional to the slosh frequency for viscous damping. Whether or not the values obtained for the damping effect of the ring baffle are correct will depend on a comparison with the analytical results of baffle slosh damping and a proper accounting for the viscous damping present in the model.

STEADY STATE ULLAGE ENTRAINMENT EXPERIMENT

Need for this Experiment - The purpose of this experiment is to predict the conditions under which gas bubbles will be entrained in a propellant reorientation flow, to assist in determining the length and magnitude of propellant settling impulse necessary to eliminate bubbles from the reoriented liquid. This phenomenon of bubbling entrainment is extremely difficult to carry out in a transient experiment. Very little available information on the extent of entrainment has been found in the literature. One basic purpose was to extend the work of Lin and Donnelly*, which was an experimental study of gas entrainment due to impingement of a vertical laminar circular cross section liquid jet in a pool of the same liquid. This reference considers a free jet rather than the wall bound jet of interest in a propellant reorientation. The entrainment process, however, should be similar.

Test Objectives - Definition of the following information was selected as the primary test objectives:

1. The low limit of conditions resulting in gas entrainment.
2. The average size of bubbles entrained.
3. The number of bubbles entrained in a unit time.

Experimental Apparatus - The equipment with which the experiment was conducted is shown in Figures 3-57 and 3-58. It consists of a lower tank 6" x 30" x 36" high, with a second upper tank 24" square x 18" high. A 6" wide sluice gate mounted as shown controls the flow rate. The wall attached flow impinges on the liquid in the lower tank causing gas entrainment in the lower pool.

*T. J. Lin and H. G. Donnelly, "Gas Bubble Entrainment by Plunging Laminar Liquid Jets", A. I. Ch. E. Journal, Vol. 12, No. 3, May 1966, pp 563-571.

A water pump of 50 gal/min. capacity returns water to the upper tank. A control valve on the pump outlet sets the return flow rate and a rotary turbine flow meter is used to measure flow rate to within 1% accuracy. With the flow rate set by the valve the total head between the two tanks can be set to any value within the range of the apparatus by varying the sluice gate opening.

The gas entrainment phenomen n is recorded photographically, using back lighting techniques. The following cameras were used:

Camera	Frame Rate	Field	Exposure
Millikan	500 fps	4"x6"	1/18,000 sec
Hycam	2,000 fps	1x1-1/2"	1/40,000 sec

The two different cameras were necessary to record the total range of flow velocities and entrainment rates most efficiently for runs with widly varying test conditions.

Gas bubble entrainment was shown to be a function of the turbulence of the falling wall sheet during the testing. For this reason the inlet was suitably streamlined to avoid promoting turbulence.

Experimental Technique - The desired sluice gate opening was set to hold the total head required for the run. The control valve was then adjusted to maintain necessary flow rate. After steady state was achieved the gas bubble entrainment was photographed. The following information was recorded.

1. Temperature, T, °F
2. Sluice gate opening, d
3. Wall sheet fall height, h

4. Wall sheet thickness, t_e

Data Reduction - The motion picture film was viewed on a film motion analyzer, a film reader which permits motion analysis and convenient scaled measurement from the film. It is possible to count the number of bubbles entrained in an element of wall sheet width over a selected increment of time by viewing the film in slow motion. The element of wall sheet length selected varies from 1/4" to 1" depending on the rate of bubble formation and their diameters. The time increment was chosen sufficiently long to yield a valid average rate of bubble formation. Under low or incipient rates this was as long as 2 seconds, while at high rates it was as small as 0.2 seconds. In the latter case gas bubbles were entrained periodically in sheet form from the surface, later breaking into discrete bubbles. At least 4 or 5 of these sheets were allowed to pass in a time increment to insure a valid average. The bubble counting was done at a distance 4-1/2" below the liquid pool surface at the center of the wall sheet.

A wide range of bubble diameters was seen in this experiment. Under incipient or low rates the diameters covered a narrow range with few if any small diameter bubbles seen. At high entrainment rates (with periodic sheet entrainment) a wider diameter range was visible, with many smaller bubbles evident. In all runs there appeared to be an average size large bubble whose rate of formation seems predominant. This average size bubble was used as the basis for counting. A few larger bubbles than this were formed; they were counted at an integer-multiple of times to obtain volume equivalence. Smaller bubbles were grouped into what appeared to be equivalent volume.

There were significantly more smaller bubbles than larger than the characteristic size, especially in the high rate runs, where bubbles formed to a diameter of less than 1/10 of the characteristic diameter. The volume of gas entrained in these latter small bubbles was considered very small and their number unimportant. An accurate count of characteristic and near characteristic size bubbles was made and repeated 5 times. The average count n' is estimated to be accurate to ±20%. The volume rate of gas entrainment P' based upon estimated uncertainties in n' and the size is expected to have an uncertainty of about 63% maximum because of the cubic relationship of diameter to volume.

Discussion - The experimental data are presented in Table 3-VI. In considering wall-bound liquid reorientation it is possible to predict the wall sheet velocity U_e and thickness t_e as it impinges into the reoriented pool. In the work of Lin and Donnelly, mentioned earlier, it was shown that Reynolds and Weber numbers based upon the jet diameter and velocity at impingement provided good correlating parameters. To predict incipient gas entrainment Reynolds and Weber numbers based upon wall sheet velocity U_e and thickness t_e have been tabulated where

$$\text{Re} = \frac{U_e t_e \rho}{\mu} = \frac{Q'}{\nu}$$

$$\text{We} = \frac{U_e^2 t_e \rho}{\sigma} = \frac{U_e Q' \rho}{\sigma}$$

and

$$Q' = \frac{Q}{w} = U_e t_e ,$$

$$\nu = \frac{\mu}{\rho}$$

TABLE 3-VI

EXPERIMENTAL DATA AND RESULTS

Run No.		T	ν	β	h	U_o	R'	t_1	Re	U_o	U_1	U_o/U_1	n'	D	Y	P'	P'/P	Fr	D_{min}	D_{max}	E
		°F	$\frac{Ft.^2}{Sec.} \times 10^6$	$\frac{1}{°F} \times 10^3$	Ft.	$\frac{Ft.}{Sec.}$	$\frac{Ft.^3}{Sec.Ft.}$	Ft.		$\frac{Ft.}{Sec.}$			$\frac{1}{Ft.Sec.}$	Ft.	$\frac{Ft.^3}{Sec.} \times 10^6$	$\frac{Ft.^3}{Ft.Sec.} \times 10^2$			Ft.	Ft.	Ft.
1		65.	11.31	2.57	2.21	11.93	0.1620	0.01358	14100.	721.	4.70	2.57		0.00968	0.626			50.6	0.00272	0.01710	0.01016
2		63.	11.00	2.55	1.67	10.37	0.1610	0.01352	14600.	649.	4.75	2.18		0.00998	0.520			31.6	0.00338	0.01692	0.01024
3		70.5	10.71	2.50	1.23	8.90	0.1636	0.01338	15300.	569.	4.82	1.82		0.00987	0.503			11.1	0.00434	0.01656	0.01070
4		75.	10.20	2.51	0.89	7.59	0.1636	0.01358	16000.	496.	4.82	1.51	2736.	0.00975	0.485	1.333	0.00813	5.19	0.00661	0.01573	0.01116
5		71.	10.61	2.51	0.74	5.90	0.1636	0.01372	15300.	379.	4.99	1.19	1988.	0.00996	0.517	1.026	0.00627	0.164	0.01091	0.01520	0.01336
6		80.	9.70	2.53	2.31	12.24	0.1704	0.01302	16400.	769.	5.13	2.39		not used				66.1	0.00252	0.01710	0.00936
7		64.	11.12	2.57	2.23	11.88	0.1624	0.00972	9710.	495.	5.39	2.23		0.00900	0.382			77.7	0.00268	0.01332	0.00900
8		66.	11.20	2.57	1.77	10.49	0.1624	0.00979	9340.	433.	5.44	1.96		0.00932	0.424			45.5	0.00337	0.01291	0.00816
9		63.	11.00	2.57	1.33	9.26	0.1652	0.01136	9600.	390.	5.48	1.70	2322.	0.00967	0.311	0.794	0.00755	17.6	0.00436	0.01271	0.00860
10		69.	10.88	2.56	0.89	7.62	0.1662	0.01132	9710.	331.	5.49	1.37	992.	0.00912	0.397	0.354	0.00333	4.53	0.00676	0.01269	0.00972
11		72.	10.54	2.55	0.50	5.63	0.1662	0.01370	10100.	235.	5.61	1.01	536.	0.00973	0.481	0.258	0.00243	0.00406	0.01184	0.01209	0.01196
12		66.	11.20	2.57	2.27	12.00	0.0530	0.00430	4710.	210.	6.82	1.77		0.00897	0.379			98.2	0.00263	0.00824	0.00544
13		67.	11.10	2.56	1.77	10.68	0.0530	0.00496	4780.	220.	6.84	1.56	2598.	0.00840	0.309	0.800	0.01509	46.1	0.00336	0.00818	0.00577
14		68.	11.00	2.56	1.33	9.26	0.0540	0.00583	4910.	195.	6.94	1.35	978.	0.00929	0.419	0.410	0.00759	15.6	0.00446	0.00913	0.00630
15		70.	10.79	2.56	1.00	8.02	0.0540	0.00673	5010.	169.	6.94	1.15	162.9	0.00832	0.302	0.091	0.00091	2.70	0.00595	0.00797	0.00691
16		72.	10.54	2.55	0.68	6.12	0.1062	0.01736	10100.	254.	5.61	1.09	218.4	0.00929	0.419	0.0714	0.00096	0.232	0.01020	0.01211	0.01116
17		73.	10.46	2.55	0.46	5.44	0.1660	0.03062	15900.	351.	4.85	1.12	326.	0.01013	0.545	0.178	0.00107	0.177	0.01288	0.01615	0.01452
18	(1)	63.	11.52	2.58	2.21	11.93	0.1620	0.01358	14100.	710.	4.64	2.57	18180.	0.00781	0.250	4.54	0.02802	60.7	0.00271	0.01790	0.01030
19	(2)	68.	11.00	2.56	1.79	10.74	0.1628	0.01515	14800.	676.	4.73	2.27	14360.	0.00893	0.373	5.36	0.03292	37.0	0.00332	0.01710	0.01021
20	(3)	71.	10.66	2.56	1.33	9.26	0.1636	0.01767	15400.	593.	4.82	1.92	11420.	0.00856	0.329	4.40	0.02689	17.3	0.00446	0.01644	0.01045
21	(7)	65.	11.32	2.57	2.21	11.93	0.1054	0.00984	9320.	488.	5.42	2.20	13120.	0.00821	0.290	5.26	0.04991	74.5	0.00270	0.01308	0.00789
22	(8)	69.	10.88	2.56	1.77	10.68	0.1054	0.00988	9700.	447.	5.51	1.94	17860.	0.00860	0.332	5.94	0.05636	42.0	0.00336	0.01264	0.00800
23	(12)	66.	11.20	2.57	2.21	11.93	0.0556	0.00466	4970.	257.	6.72	1.78	11760.	0.00968	0.473	5.56	0.10000	90.7	0.00270	0.00866	0.00568

The term Q' is the volume rate of liquid flow per unit length of sheet width w so that $Q = U_e t_e w = Q'w$.

The wall sheet Reynolds numbers computed for these experiments ranged from 4500 to 16,500. Levich* indicates that the flow is turbulent if the Reynolds number is greater than 1500. Therefore, all the tests reported here were performed with a turbulent wall sheet. Figure 3-59 shows the Reynolds and Weber number data. These runs were made essentially in three wall sheet flow rates separating into three groups of Reynolds numbers. The highest Weber numbers in each group correspond to the highest rates of entrainment whereas the lowest Weber numbers in each group correspond to incipient entrainment. The three circled and numbered data points on Figure 3-59 were set up as the tests of incipient entrainment. These were found to be very sensitive to turbulence induced at and above the sluice gate; this vorticity turbulence was most difficult to avoid at the lowest heads. This is believed to be the reason that test 11 plots with a lower Weber number than the incipient test number 16 except for these low total head tests. It is apparent that wall sheet flow-induced turbulence is more dominant than sluice gate induced turbulence.

In Figure 3-59 the line just below incipient entrainment represents critical wall sheet flow conditions under which entrainment will occur. The equation of this line is $We_i = 0.5\ Re^{2/3}$. For a given wall sheet with $Q' = U_e t_e$ it is possible to predict incipient entrainment velocity U_i.

The criteria for determining bubble size and count have been mentioned above.

*V. E. Levich, Physiochemical Hydrodynamics, Prentice Hall, Inc., Englewood Cliffs, N. J., Second Edition, 1962, p. 452.

The bubble count expressed as the number of characteristic bubbles formed per unit length of wall sheet is tabulated in Table 3-VI. The characteristic bubble count n' is plotted in Figure 3-60 as a ratio of entrainment velocity U_e to incipient entrainment velocity U_i. A degree of correlation is seen between the bubble count and the dimensionless entrainment velocity. Small values of U_e/U_i represent conditions near incipient entrainment, with a low count of characteristic sized bubbles. Large values of U_e/U_i represent high rates and large counts. Although the uncertainty of the bubble count parameter is estimated to be $\pm 20\%$, Figure 3-60 shows a wider band. This indicates that U_e/U_i is probably a weak correlating parameter. Although other parameters were attempted none were found to correlate as well.

The size and volume of the characteristic sized bubbles was determined by measuring the diameter of (usually) 10 of the characteristic bubbles in a film run and averaging. This data is presented in Table 3-VI and plotted as a function of entrainment velocity U_e/U_i in Figure 3-61. It is seen that these average diameters show no variation with respect to dimensionless entrainment velocity of any other wall sheet flow parameters. The characteristic bubble diameter D shows a constant value over the range of tests, with an average value of D = 0.11". The data plots within a band $\pm 15\%$, indicating the estimated accuracy of $\pm 20\%$ on the diameter measurement is reasonable.

This rather constant value of characteristic bubble diameter was not expected. The work of Lin and Donnelly indicates that bubble diameter is expected to decrease with increase in the entrainment velocity. However, the data of Lin and Donnelly used average diameter rather than characteristic diameter.

The average bubble diameter in the present tests would also decrease as the entrainment velocity increased because of the larger number of smaller gas bubbles formed. The characteristic size used as the counting basis here shows no dependence of diameter on any wall sheet flow parameter over the range of flow conditions tested.

This experiment was designed primarily to determine the volume rate of gas entrainment P' per unit width of wall sheet and to correlate this data. The experimentally determined values of P' are presented in Table 3-VI. P' is nondimensionalized by forming the parameter P'/Q', where $Q' = U_e t_e$. This parameter P'/Q' gives the ratio of the volume rate of gas entrainment to the volume rate of liquid wall sheet flow.

Study of the films showed a periodic wave type motion near the impinging wall sheet. This observation suggests that a Froude number such as $U_e^2/2gt_e$ might be a correlating parameter. When P'/Q' is plotted against this parameter however a rather weak correlation was obtained. Because a minimum velocity U_i is required to initiate entrainment the velocity term U_e in the Froude number was replaced by the term (U_e-U_i). This Froude number is tabulated in Table 3-VI and plotted against P'/Q' in Figure 3-62. It represents the best correlation of the entrainment volume data obtained in this study. This presentation fixes the value of P'/Q' at zero when the Froude number equals zero because of the use of the velocity difference in the Froude number.

Because of the turbulence induced in the wall sheet due to vorticity in the flow upstream of the sluice gate at low total head, large changes in rate of

gas entrainment were seen in the low total head runs. This led to a large uncertainty in the experimental data for the gas entrainment rate. Therefore, this data was ignored in establishing correlation in Figure 3-62.

The false tank bottom shown in Figure 3-57 was set at several depths during one series of test runs in order to examine the effect of pool depth on bubble distribution in the lower pool. Still photographs of the distribution were taken. Although the data are primarily qualitative they can be summarized as follows.

The impinging wall sheet retains considerable momentum as its direction of flow is changed to horizontal in the shallow pool, thus carrying the bubbles across the tank bottom. In deeper pools only minor circulation is seen; the bubbles rise near the impinging wall sheet with little horizontal motion.

Levich presents a relationship to determine the critical (or largest) diameter, D_{CR}, of a stable bubble in a turbulent flowing liquid. The analysis consists of a balancing of surface tension forces tending to hold the bubble together against turbulence induced inertia forces tending to tear the bubble apart. The results of this analysis are:

$$D_{CR} = 2 \cdot L^{2/5} \left(\frac{\sigma}{k'_f \rho u^2} \right)^{3/5} \left(\frac{\rho}{\rho'} \right)^{1/5}$$

where L = scale of turbulence

k'_f = drag coefficient for inertial gas forces, estimated to have a value $1/2 < k'_f < 1$ by Levich.

ρ' = gas density

The scale of turbulence is unknown in the entrainment region of this experiment, and actually varies from the fluid surface down. According to Levich a bubble experiences maximum disruptive forces in a turbulent liquid flow when the scale of turbulence is equal to the bubble diameter, $L = D_{CR}$. For the drag coefficient, an intermediate value of $k'_f = 0.8$ is assumed. The velocity in the shear flow region of bubble entrainment is assumed to have an average value, $U = U_{CR}/2$. Substituting in the above equation:

$$D_{CR} = 2 \cdot D_{CR}^{2/5} \left(\frac{4\sigma}{0.8 \rho U_{CR}^2} \right)^{3/5} \left(\frac{\rho}{\rho'} \right)^{1/5}$$

The above expression, which estimates the critical diameter D_{CR} of a stable bubble being entrained by a turbulent wall sheet flow velocity U_{CR}, may be expressed nondimensionally in terms of a bubble Weber number, We_B.

$$We_B = \frac{\rho D_{CR} U_{CR}^2}{\sigma} = 15.9 \left(\frac{\rho}{\rho'} \right)^{1/3}$$

This bubble Weber number expression considers inertia forces and surface tension forces as being important in bubble breakup and formation. As these are the major forces which act to size the bubbles formed, this correlation should be applicable to any low viscosity, liquid-gas combination. Acceleration level should have no effect on this turbulent bubble breakup process occurring in the shear flow regime of gas bubble entrainment.

From the experience gained in viewing the test films, the smallest diameter bubbles were found to form near the liquid pool surface, where $U_{CR} \approx U_e$. Hence, by substituting $D_{CR} = D_{MIN}$ and $U_{CR} = U_e$ in the We_B expression developed above, the equation below results, which may be used to predict the mini-

mum bubble diameter D_{MIN} that will result from gas entrainment.

$$\frac{\rho D_{MIN} U_e^2}{\sigma} = 15.9 \left(\frac{\rho}{\rho'}\right)^{1/3}$$

This equation relates the minimum gas bubble diameter D_{MIN} formed to the liquid entrainment velocity U_e. This expression satisfies the observed condition that D_{MIN} decreases as the entrainment velocity U_e increases. The values of D_{MIN} are presented in Table 3-VI. As expected, for $U_e/U_i \approx 1$, D_{MIN} is of the same order of magnitude as the measured characteristic bubble diameter D, whereas for $U_e/U_i > 1$, the value of D is much greater than D_{MIN}.

The maximum bubble size may also be estimated. The maximum bubble diameter D_{MAX} for a given flow Q' is similar to the bubble diameter formed under the incipient entrainment velocity U_i. By substituting $D_{CR} = D_{MAX}$ and $U_{CR} = U_i$ in the We_B expression above, the equation below is obtained which may be used to predict the maximum bubble diameter, D_{MAX}.

$$\frac{\rho D_{MAX} U_i^2}{\sigma} = 15.9 \left(\frac{\rho}{\rho'}\right)^{1/3}$$

Values of D_{MAX} are presented in Table 3-VI. The measured characteristic bubble diameter D is of the same order of magnitude as the computed value of D_{MAX} for each test run. This result is expected due to the large characteristic bubble diameters chosen in the analysis of the film data.

Thus, an average or mean bubble diameter may be considered to be

$$\bar{D} = \frac{D_{MAX} + D_{MIN}}{2}$$

The data for $\bar{D}$ presented in Table 3-VI are of the same order as the data from

the experiment, showing reasonably good agreement.

Results and Conclusions - The criteria for incipient gas bubble entrainment have been established as Weber and Reynolds numbers where

$$We_i = \frac{u_e^2 t_e \rho}{\sigma} = 0.5\, Re^{2/3} = 0.5\, \frac{Q'}{\nu}$$

Q' is liquid flow rate per unit flow width. The critical Reynolds number for incipient entrainment in turbulent flow is 1500 (see Levich, ibid).

A relationship for gas volume entrained has been developed as

$$\frac{P'}{Q'} = 0.0009\, \frac{(u_e - u_i)^2}{2 g t_e}$$

This relationship is the result of a curve fit to the experimental data, Figure 3-62. The term $(U_e - U_i)^2/2gt_e$ is a modified Froude number which provides good correlation.

Minimum bubble size may be estimated from

$$\frac{\rho D_{MIN} u_e^2}{\sigma} = 15.9 \left(\frac{\rho}{\rho'}\right)^{1/3}$$

Maximum bubble size is similarly

$$\frac{\rho D_{MAX} u_i^2}{\sigma} = 15.9 \left(\frac{\rho}{\rho'}\right)^{1/3}$$

The photographs of the bubble distribution in the reoriented liquid pool, permit the following general observations of the bubble distributions. If the pool is shallow entrained bubbles are likely to be found throughout the liquid with a rather strong toroidal circulation pattern induced by the impinging wall sheet. If the pool is deep, the entrained bubbles will be forced down until the liquid momentum is dissipated and the bubbles will

then rise to the surface near the wall. No bubbles should be found at the center or the bottom of the tank and only a small circulation pattern will exist because of the large pool depth. Because of the two dimensional nature of the test tank, more detailed liquid pool conditions cannot be inferred for a three dimensional tank bottom found in spacecraft tanks.

With a prediction of bubble distribution and sizes in a reoriented propellant pool, it is possible to estimate the rise velocity of these entrained bubbles with respect to the liquid pool. A reference such as Haberman and Morton* can be used to predict the rise velocity of various sized bubbles of any gas in any liqiuid in any gravity field. The results of this gas bubble entrainment analysis might form the input to a gas bubble ingestion analysis at the tank drain or an analysis of bubble rise time from the liquid pool under reorientation accelerations.

*W. L. Haberman and R. K. Morton, "An Experimental Investigation of the Drag and Shape of Air Bubbles Rising in Various Liquids", the David W. Taylor Model Basin Report 802, September 1953.

GAS INGESTION IN LUNAR MODULE REACTION CONTROL SUBSYSTEM PROPELLANT LINES THROUGH ASCENT PROPULSION SUBSYSTEM INTERCONNECTION

When propellants are transferred from the main storage tanks in the Lunar Module to the ascent engine or reaction control subsystem (RCS) after a period of near weightlessness, there is a possibility that pressurant gas bubbles will be entrained in the propellants as they leave the storage tanks. These bubbles are entrained when the propellant has been previously reoriented away from the drain end of the tank by low gravity forces. As operational difficulties with the RCS may arise if gas bubbles are mixed with the RCS propellant, it is necessary to know the behavior of these bubbles in the section of main propellant line where the RCS propellant line is connected, and if there is any possibility of entrainment in RCS propellant flow.

Figure 3-64 is a sketch of the main propellant storage tanks and associated piping in the ascent stage of the Lunar Module. Gas entrainment in RCS propellant flow was studied by building two scale models of the sections of pipe which feed the RCS, one model for the fuel line and one for the oxidizer line.

Test Objectives - The experiment was designed to investigate the possibility of gas entering the RCS propellant lines through the interconnection with the ascent propulsion system propellant lines. Specifically the objectives of this investigation were to determine:

1. The probability that gas flowing in the ascent engine feedline will be partially ingested with an RCS feedline flow,
2. The approximate percentage of gas in the main propellant lines which enters the RCS lines as a function of liquid flow rates

and gas flow rates, and

3. The qualitative nature of gas bubble behavior in the propellant lines.

Experimental Apparatus and Experimental Procedure - In constructing a scale model of the piping and propellant flow it is necessary to duplicate the characteristics of the system which effect bubble motion. It is desirable also to use water rather than the actual propellant, and to obtain results which would be valid under the low gravity conditions incurred by the Lunar Module.

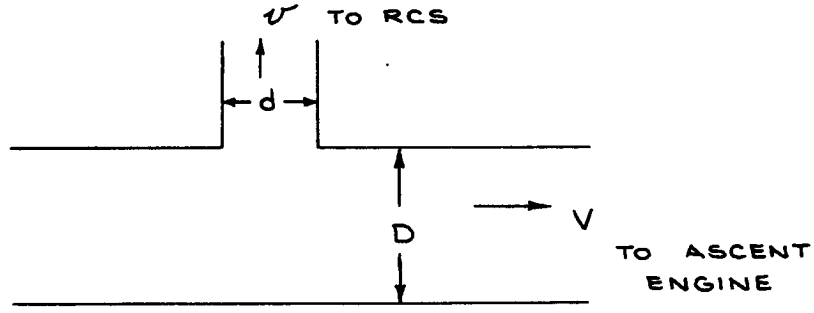

Geometric similitude requires that:

$$\frac{d_1}{D_1} = \frac{d_2}{D_2} \tag{3.26}$$

where the subscripts 1 and 2 represent prototype dimensions and model dimensions respectively.

The requirement for dynamic similitude in the flow in this case is satisfied by preserving between the model and prototype the Reynolds number and Froude

number. Use of the latter implies that the gas bubble behavior in the feed lines are not influenced by viscosity or surface tension but rather by inertial and gravitational forces. Froude number preservation insures that the ratio of inertial forces to gravitational forces in the liquid surrounding the bubbles is the same, and the same Reynolds number insures that the velocity profile and degree of turbulence are similar.

The above requirements are expressed algebraically as follows:

For Froude number similarity,

$$\frac{V_1^2}{g_1 D_1} = \frac{V_2^2}{g_2 D_2} \tag{3.27}$$

$$\frac{v_1^2}{g_1 d_1} = \frac{v_2^2}{g_2 d_2} \tag{3.28}$$

(where g is the body force per unit mass acting on the liquid)

and for Reynolds number similarity,

$$\frac{D_1 V_1}{\nu_1} = \frac{D_2 V_2}{\nu_2} \tag{3.29}$$

$$\frac{d_1 v_1}{\nu_1} = \frac{d_2 v_2}{\nu_2} \tag{3.30}$$

(where η is the kinematic viscosity of the liquids)

Rearranging terms in Equations (3.27) and (3.28) and applying equation (3.26) yields:

$$\frac{v_1}{V_1} = \frac{v_2}{V_2} \tag{3.31}$$

Thus the flow velocities must have the same ratio.

The flow rate in the model depends on the model diameter, D_2. Expressing flow rate in terms of w, volume per unit time ($w = \frac{\pi D^2 V}{4}$), Equation (3.29) can be rewritten as:

$$\omega_2 = \omega_1 \frac{D_2}{D_1} \frac{\nu_2}{\nu_1} \tag{3.32}$$

The gravity condition corresponding to a model diameter D_2 is found from Equation (3.27), which is rewritten as:

$$\frac{g_1}{g_2} = \left(\frac{\omega_1}{\omega_2}\right)^2 \left(\frac{D_2}{D_1}\right)^5 \tag{3.33}$$

Equations (3.26), (3.31), (3.32) and (3.33) were used to determine the model sizes and liquid flow rates. Equation (3.30) is redundant and automatically satisfied when the other conditions are met.

The actual size of the propellant lines in the Lunar Module was taken from the most recent drawing available, Grumman Aircraft Engineering Corporation drawing number LTM280-25503, dated 4-16-65. The inside diameters corresponding to D_1 and d_1 are 1.152 inches and 0.718 inches respectively. The lines used in the model were made from standard 25 mm and 15 mm glass tubing. The inside diameters corresponding to D_2 and d_2 are 0.857 inches and 0.512 inches respectively.

The propellant line configuration was taken from Grumman Aircraft Engineering Corporation drawing number LDW 280-51350 (undated). The portion of the lines represented in the models include the junction between RCS line and main pro-

pellant line, the bend in the main propellant line upstream of the RCS line junction, and the section of the pipe upstream of the bend. Figures 3-65 and 3-66 are drawings of the glass portions of the models. The bend radius in the main line is approximately 3 diameters in both models.

The flow rates on which the models are based are taken from the calculated burn rates of the engines. For fuel these are 35 gpm to the ascent engine and 0.98 gpm to one RCS engine, and for oxidizer 35 gpm and 1.13 gpm respectively. The corresponding design rates for the models are found from Equation (3.32) to be 26 gpm of fuel to the ascent engine and 0.73 gpm of fuel to the RCS engine, and 26 gpm and 0.84 gpm respectively of oxidizer. As flow rates may vary under actual conditions, depending, for instance, on operating mode of the engines, behavior trends were investigated by varying the flow rates in the models.

The gravity condition simulated by the model size is found from Equation (3.33) to be 0.41 g_o. This is considered realistic for periods in which the ascent or descent engine is operating. Since the Froude number being simulated for the main propellant line is 91.1, which indicates that flow in the main line is inertia dominated, the results are not likely to be greatly influenced by gravity. Conclusions, however, cannot be drawn from this model for the low gravity situation in which only the RCS engines are operating. Another set of models would be required which would be very small in size, and which would have to be tested under conditions simulating the small accelerations that occur while the RCS engines are operating.

Each of the models was tested separately. When properly oriented for testing the section of the fuel line model with the RCS line junction makes an angle of 84.7° with the vertical, and the upstream portion of the line makes an angle of 55.4° with the vertical. The corresponding portions of the oxidizer line model make angles of 12.2° and 67.4° with the vertical respectively.

Description of Apparatus - Figure 3-67 is a schematic diagram of the experimental apparatus. The model of the feedline was fabricated of glass to permit flow visualization. Two methods were used to measure liquid flow rates in the models. The total flow was measured with a turbine flow meter inserted in the system upstream of the gas bubble injection point. Flow rate in the RCS line was measured by collecting and weighing the water discharged over a 30 second interval. Both types of measurements of liquid flow rate are considered accurate to within ±1%.

Gas bubbles were introduced by injecting air at 100 psi through a valve in the main line. The injection point was sufficiently upstream for bubbles to become symmetrically distributed about the axis of the glass tube before reaching the first bend in the model. Bubble sizes ranged from approximately 0.01 cm to 1.5 cm.

Gas bubble flow was photographed with a HYCAM high speed movie camera using a nominal frame rate of 2000 frames per second and 1/40,000 second exposure per frame. Gas flow rates in the main line were estimated from the film by measuring bubble diameters. Some of the larger bubbles were of irregular shape and their volumes were found by visually estimating their equivalent

spherical diameter. In the RCS line it was generally more practical to collect the entrained bubbles. This could not be done, however, under the one test condition where there was no liquid flow in the RCS line, and measurements had to be made from the films. The bubble collection technique consisted of passing the discharge through an inverted flask filled with water. The bubbles moved to the top of the flask so that gas flow rate could be found by measuring the rate at which the water level was depressed.

Test Sequence - Each of the models was tested at five different fluid flow conditions with up to three gas rates for each fluid rate. The desired basic flow rate of 26 gpm could not quite be obtained due to lack of pump capacity. Having as nearly as possible the basic flow rate in the main line (25.5 gpm), however, the models were first tested with RCS flow close to the basic rate and then slightly below. This was followed by an overall reduction in flow rates, and then a test with no flow in the RCS line and the basic rate in the main line. The final test consisted of flow through the RCS line only.

Results and Conclusions - Under all test conditions it was found that gas bubbles were ingested with RCS flow. With the basic flow rates in both main line and RCS line approximately one percent of the gas in the main line was entrained in the RCS line.

The bubbles introduced in the main line quickly became axisymmetrically distributed. The smaller bubbles tended to be evenly distributed along the radius of the tube and the larger bubbles tended to move along the center line. Only the smaller bubbles, less than 1 mm in diameter, maintained spherical shape. The remainder were irregular undulating shapes indicating a lack of

dependence on fluid properties.

In the upstream section of the glass models the radial distribution of bubbles was apparently unaffected by gravity. This is expected from the high Froude number conditions. Figure 3-68 shows sketches of the bubble trajectories as they enter the bend in the main line. In the oxidizer line model, the bubbles were observed spiraling around the circumference of the tube toward the inside of the bend. As they enter the downstream section of the model, the bubbles are almost entirely on the inside of the bend. In the fuel line model, the bubbles are apparently not affected as much by the bend. Only the larger bubbles appeared to move toward the inside. As they enter the downstream section of the model they are deflected off the bottom of the tube and quickly resume an axisymmetric distribution. The difference in behavior between oxidizer line and fuel line models is due in part to the 15° greater bend angle in the oxidizer line. Some of the difference may also have been due to gravity which tends to prevent bubbles in the fuel line from being redistributed toward the insid of the bend, and tends to aid this redistribution in the oxidizer line model. Tests were carried out only in orientations modelling spacecraft design. The effect of gravity in other directions was not determined.

The liquid flowing past the RCS line connection separates at the RCS inlet and causes a vortex in the RCS line (the axis of which is perpendicular to the RCS feedline axis. This is shown in Figure 3-68. Some of the bubbles entering this vortex are recirculated back into the main line. Most, however, circulate several times around the vortex and then continue further

into the RCS line. Those which do return to the main line often coalesce just prior to reentry and enter in bunches or as one larger bubble.

When there is no net liquid flow through the RCS line, the vortex still exists and entrains bubbles. In the oxidizer line model, the bubbles coalesce and form larger bubbles which drift out of the vortex into a relatively still section of the line where they come to rest at the top of the tube. In the fuel line model, the bubbles usually leave the vortex before coalescing and collect in the highest portion of the tube.

One test was made on each model with all the liquid flowing into the RCS line, with no net liquid flow further along the main line. This test represents a condition in the Lunar Module with propellant flow into the RCS line, and the descent engine rather than ascent engine operating. In the oxidizer line model, approximately two-thirds of the gas in the main line entered the RCS line, the remainder under the buoyant force continuing up into the main feedline. In the fuel line model nearly all the bubbles moved along the top of the main tube under the action of gravity and up into the RCS line.

The quantitative data obtained from these tests is listed in Tables 3-VIIand 3-VIII. The gas flow rates tabulated cannot be considered precisely applicable to the Lunar Module. The gas entrained in the model RCS lines was essentially contained in the smaller bubbles, and the relative densities of small and large bubbles which could be expected in the Lunar Module is unknown. In addition, gas flow rate measurements are only accurate to within about $\pm 50\%$. They serve only to indicate that there is gas ingested in the

RCS feedline under the conditions tested, and the flow rate order of magnitude.

Figures 3-69 and 3-70 are plots of gas flow rates (from Tables 3-VII and 3-VIII) which occur with the high liquid flow rate in the main line. Both plots are similar in that they show about 1% of the gas in the main line being entrained in the RCS flow. The circles on the graph represent a higher liquid flow rate in the RCS line than triangles. The reason these curves cross is not understood. The trend upward, however, is due to the larger bubble size entrained in the RCS flow at the higher gas flow rates.

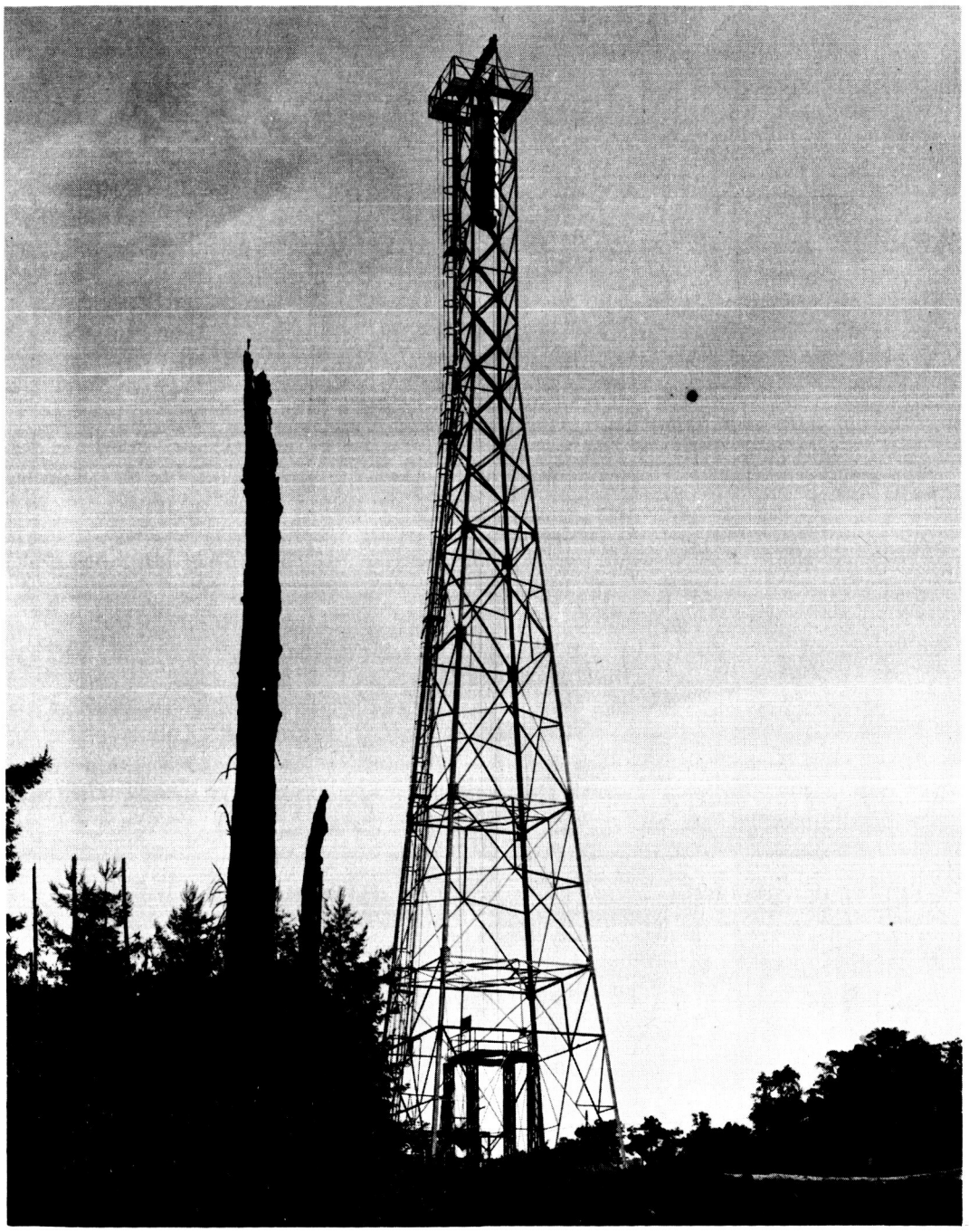

LMSC DROP TOWER

Figure 3-1

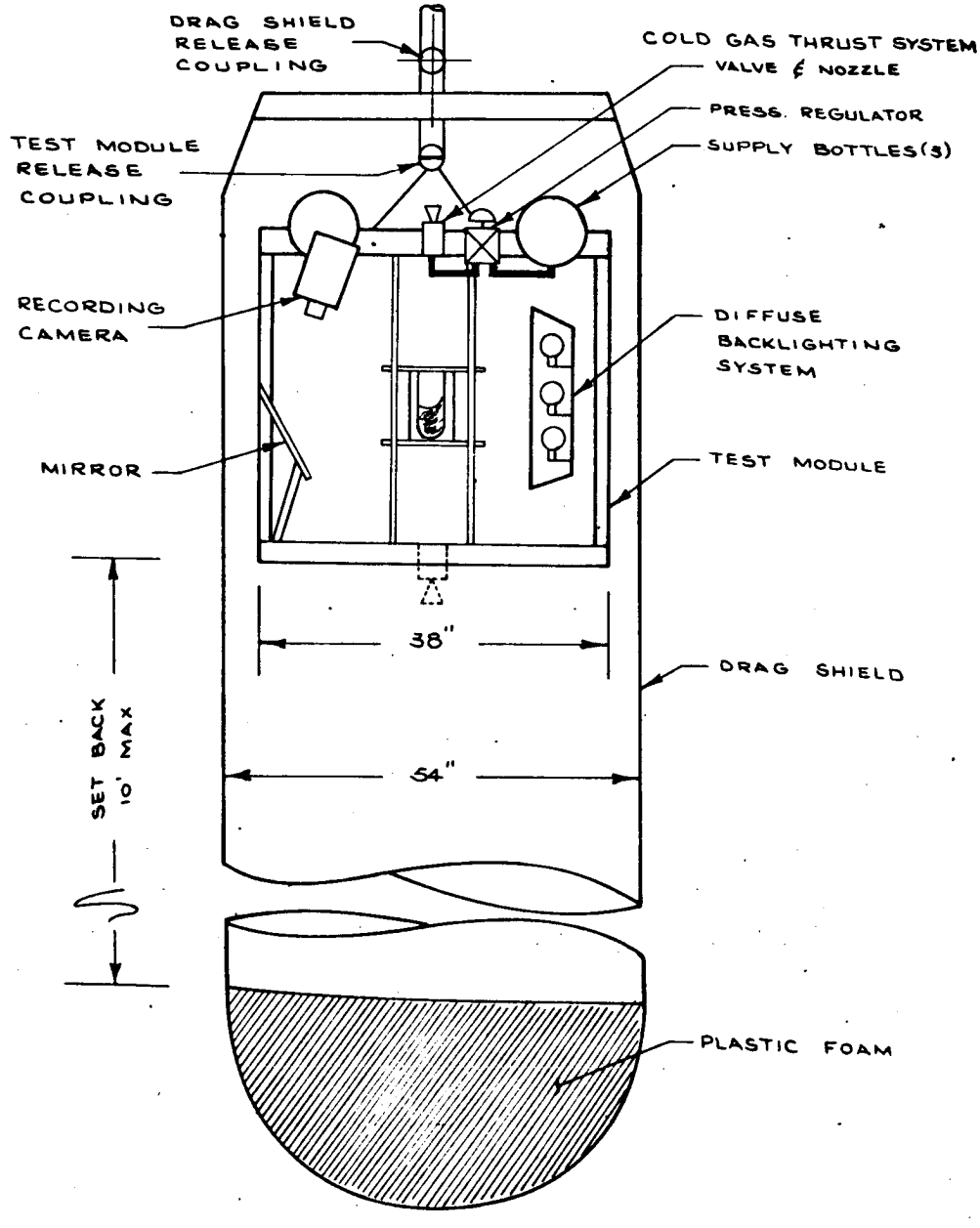

Drag Shield and Test Module Schematic

Figure 3-2

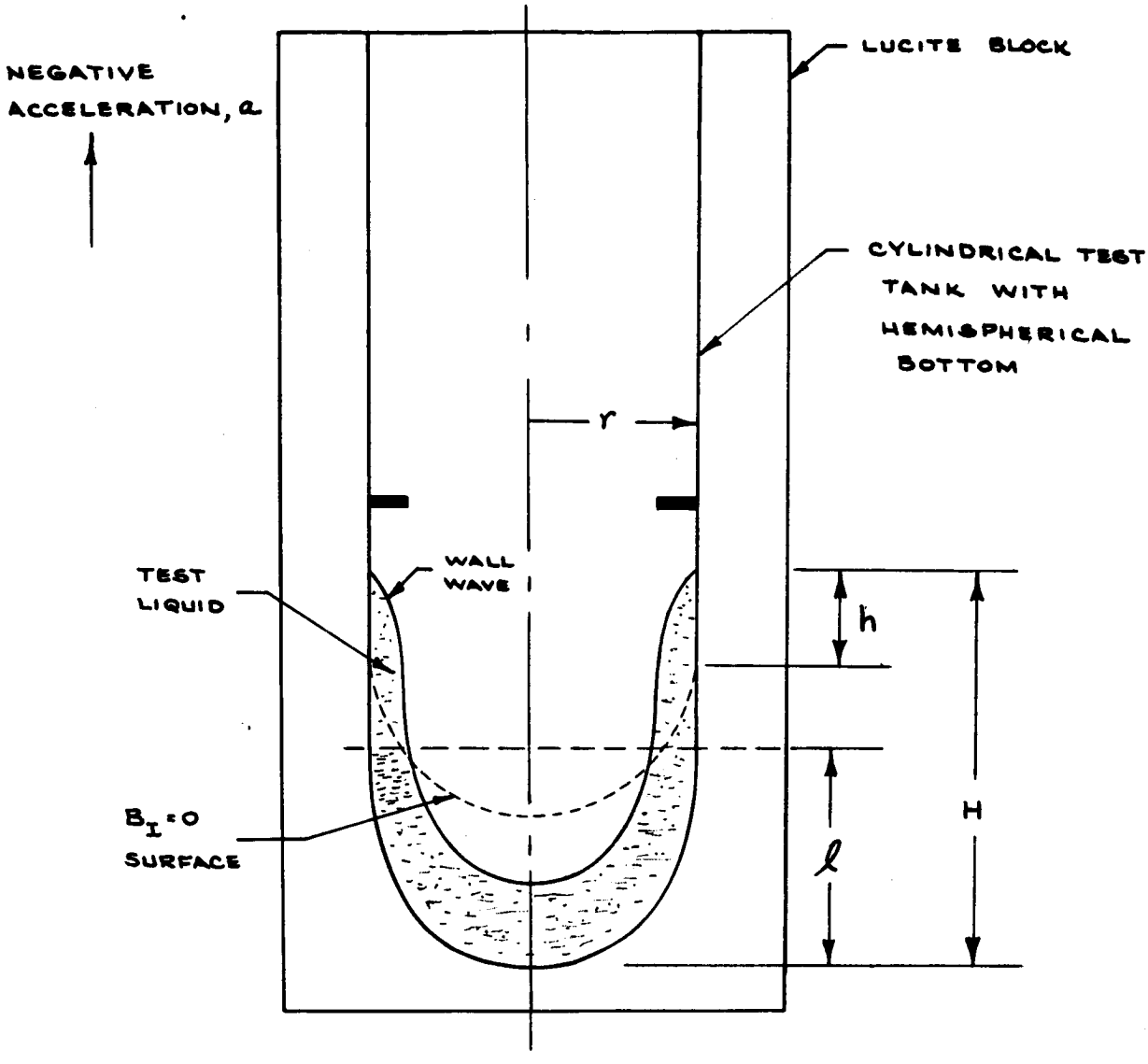

h = DISPLACEMENT PARALLEL TO TANK AXIS

ℓ = LIQUID SURFACE HEIGHT AT ^1g_o

ρ = TEST LIQUID DENSITY

σ = TEST LIQUID SURFACE TENSION

V = LIQUID VOLUME

Test Tank and Definition of Nomenclature

Figure 3-3

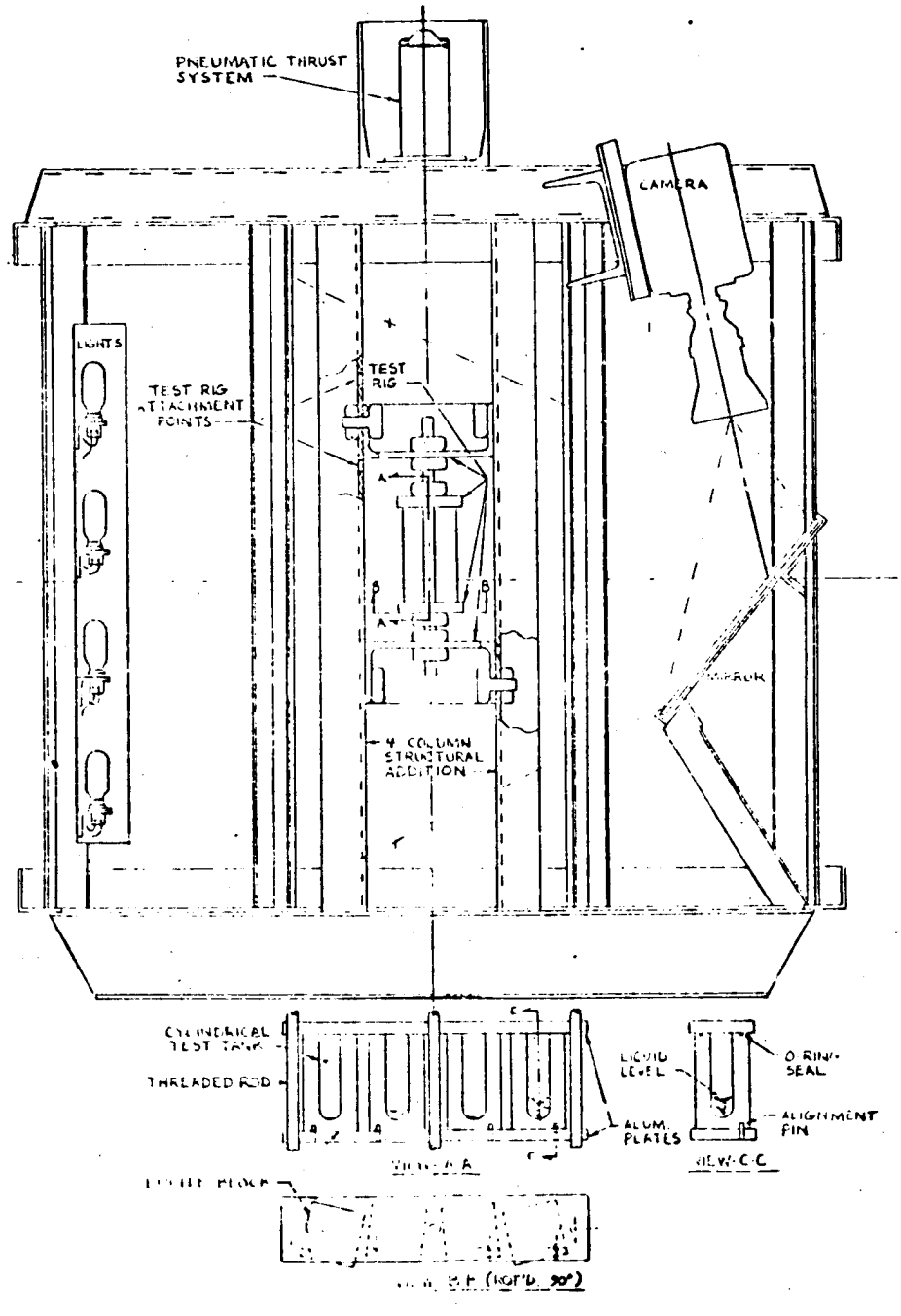

Reorientation Test Installed in Test Module

Figure 3-4

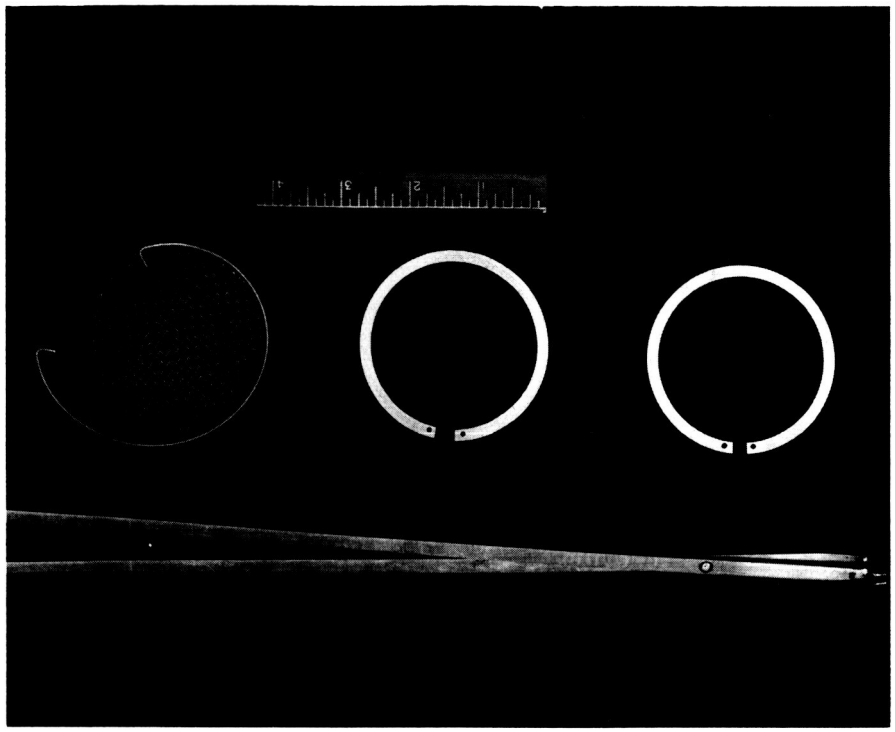

(b) BAFFLES AND RETENTION SURFACE

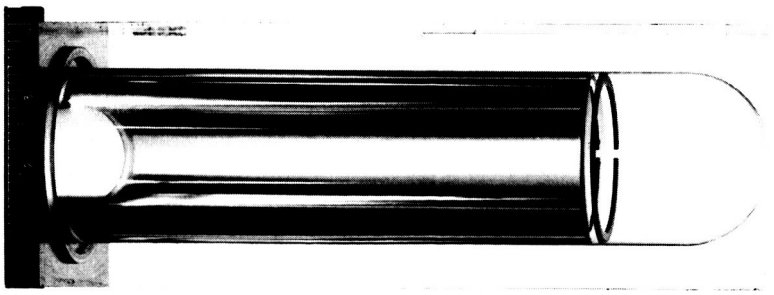

(a) REORIENTATION TEST TANK

Figure 3-5

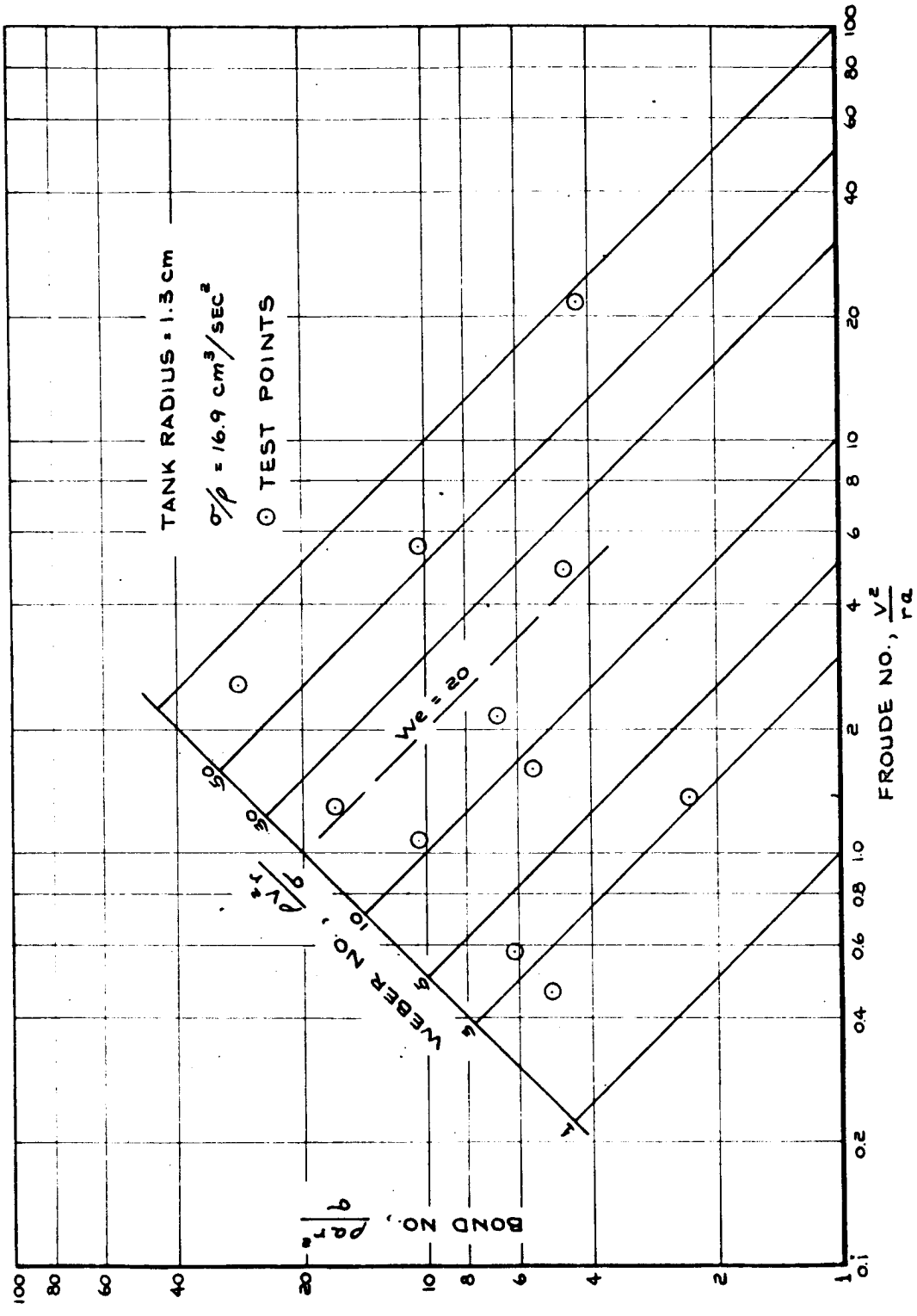

Test Points Obtained During Axisymmetric Impulsive Reorientation

Figure 3-6

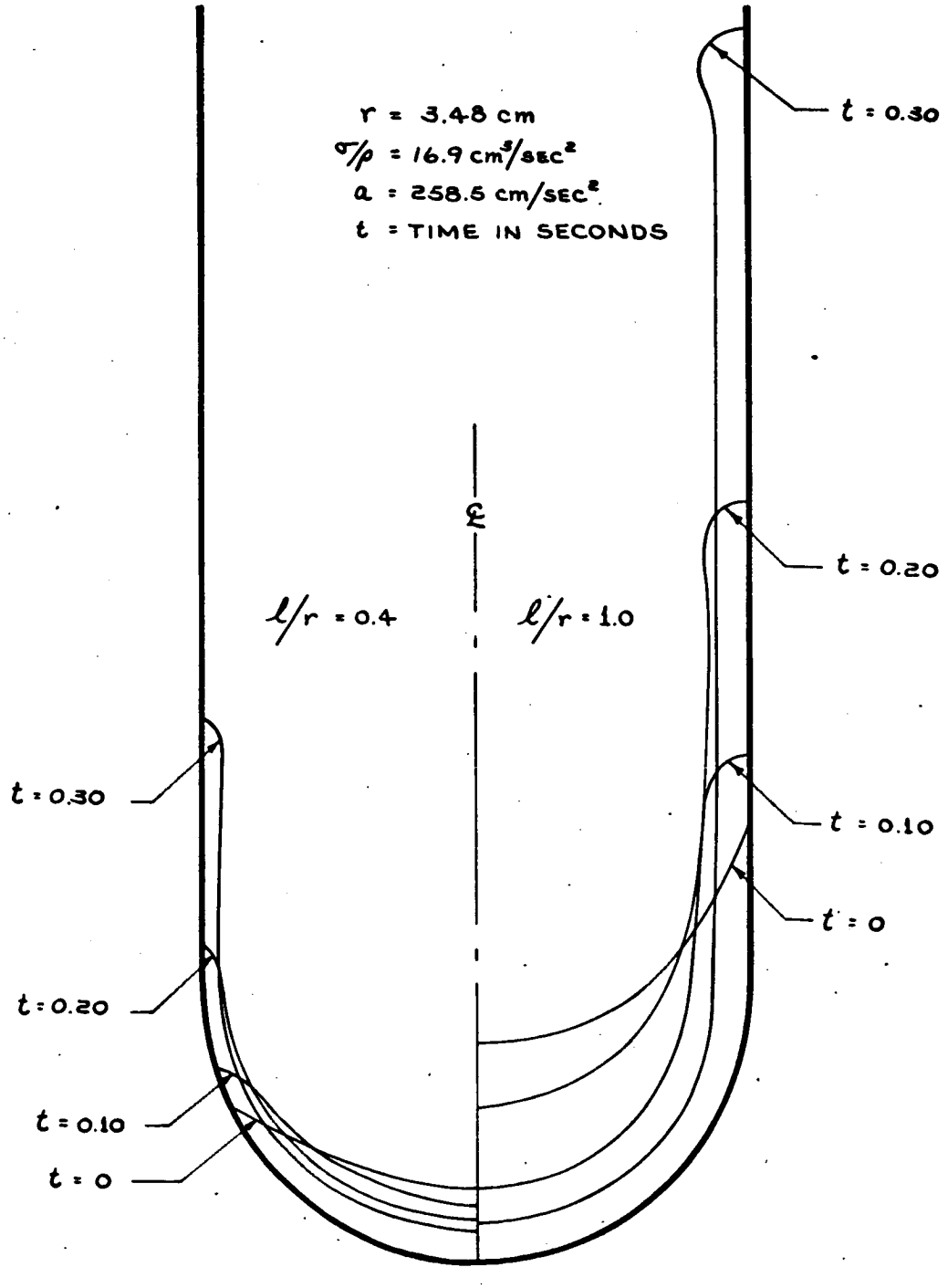

Wave Profiles

Figure 3-7

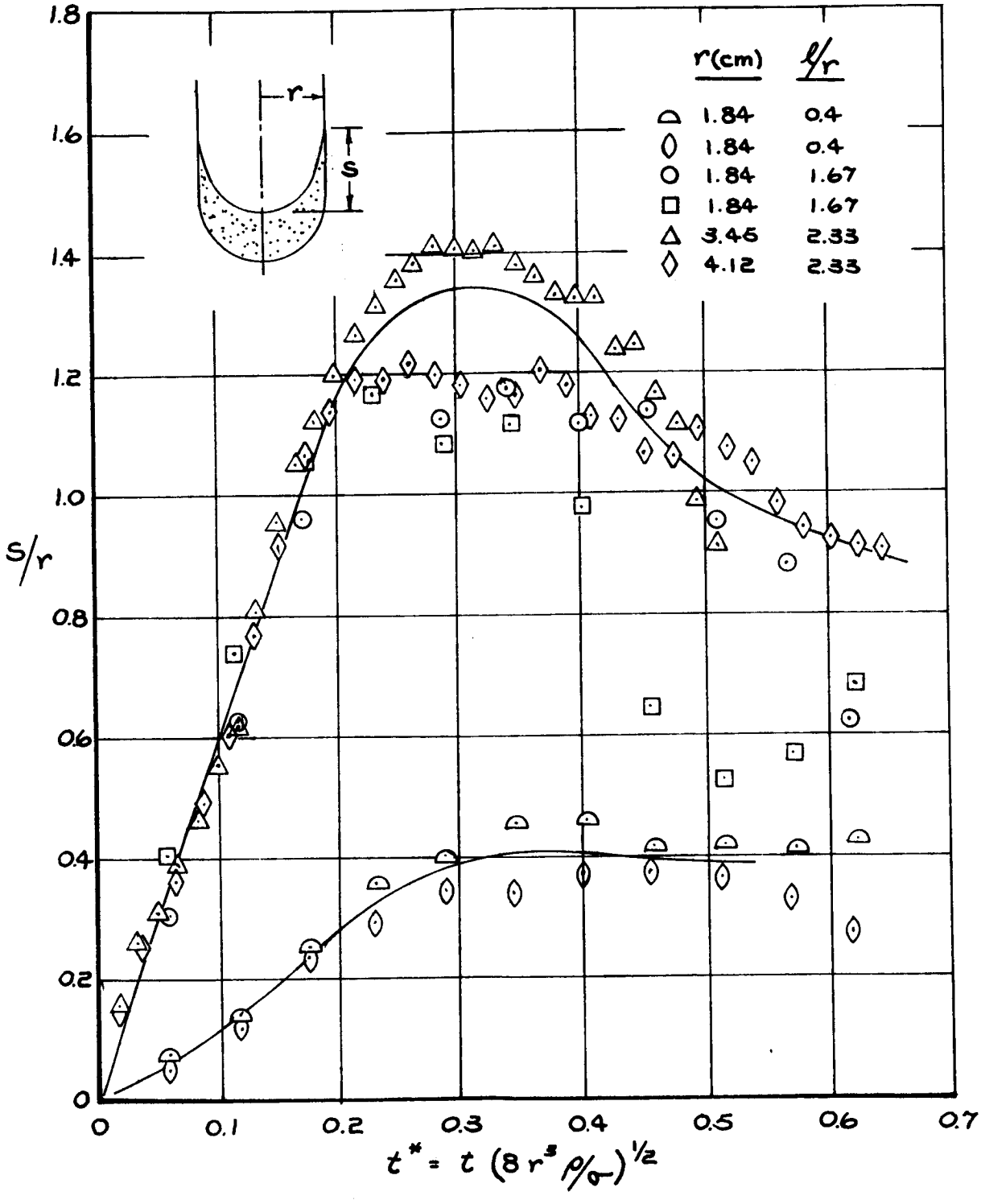

Zero Gravity Response

Figure 3-8

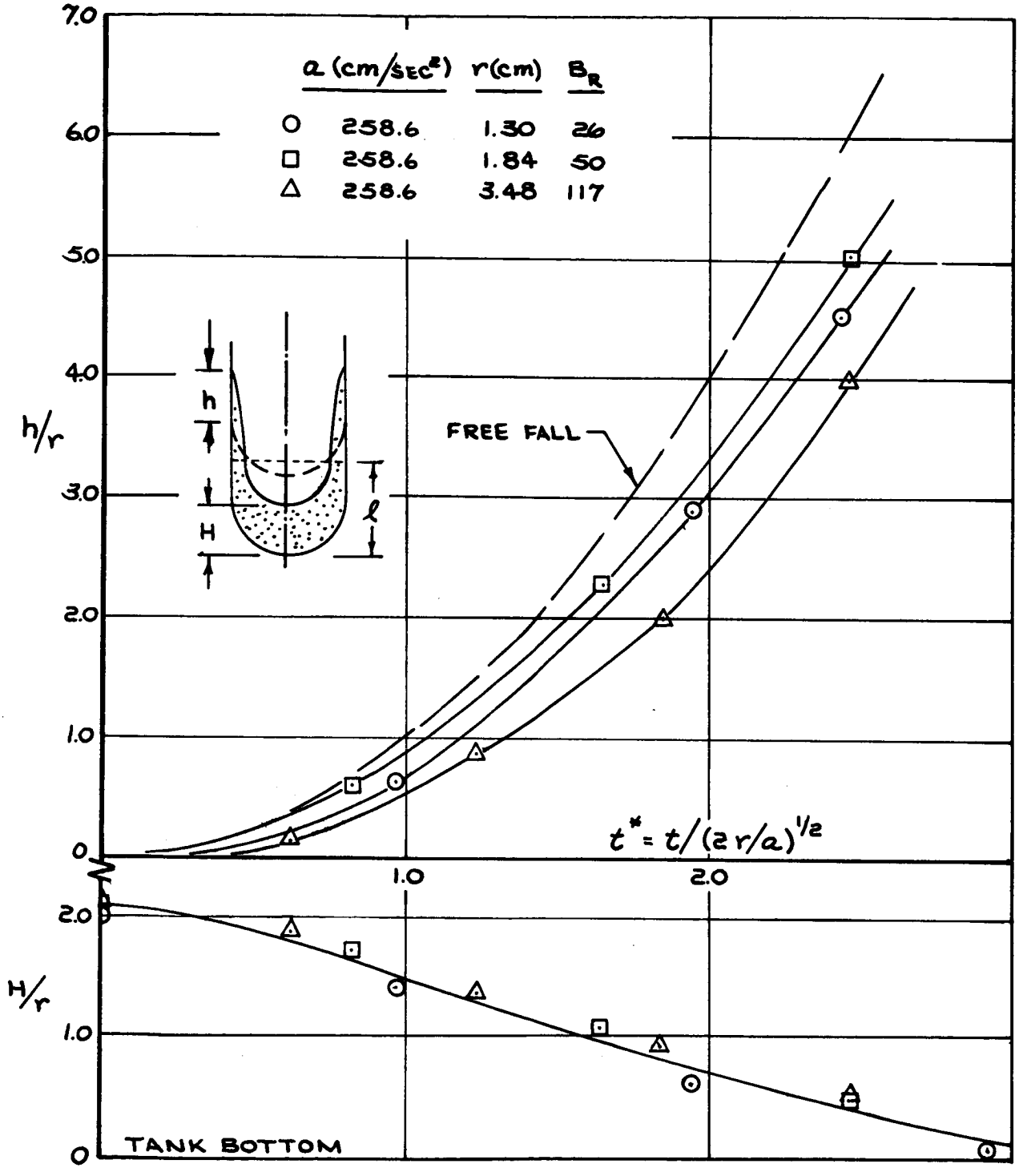

Liquid-Gas Interface Trajectories
(1/r = 2.33)

Figure 3-9

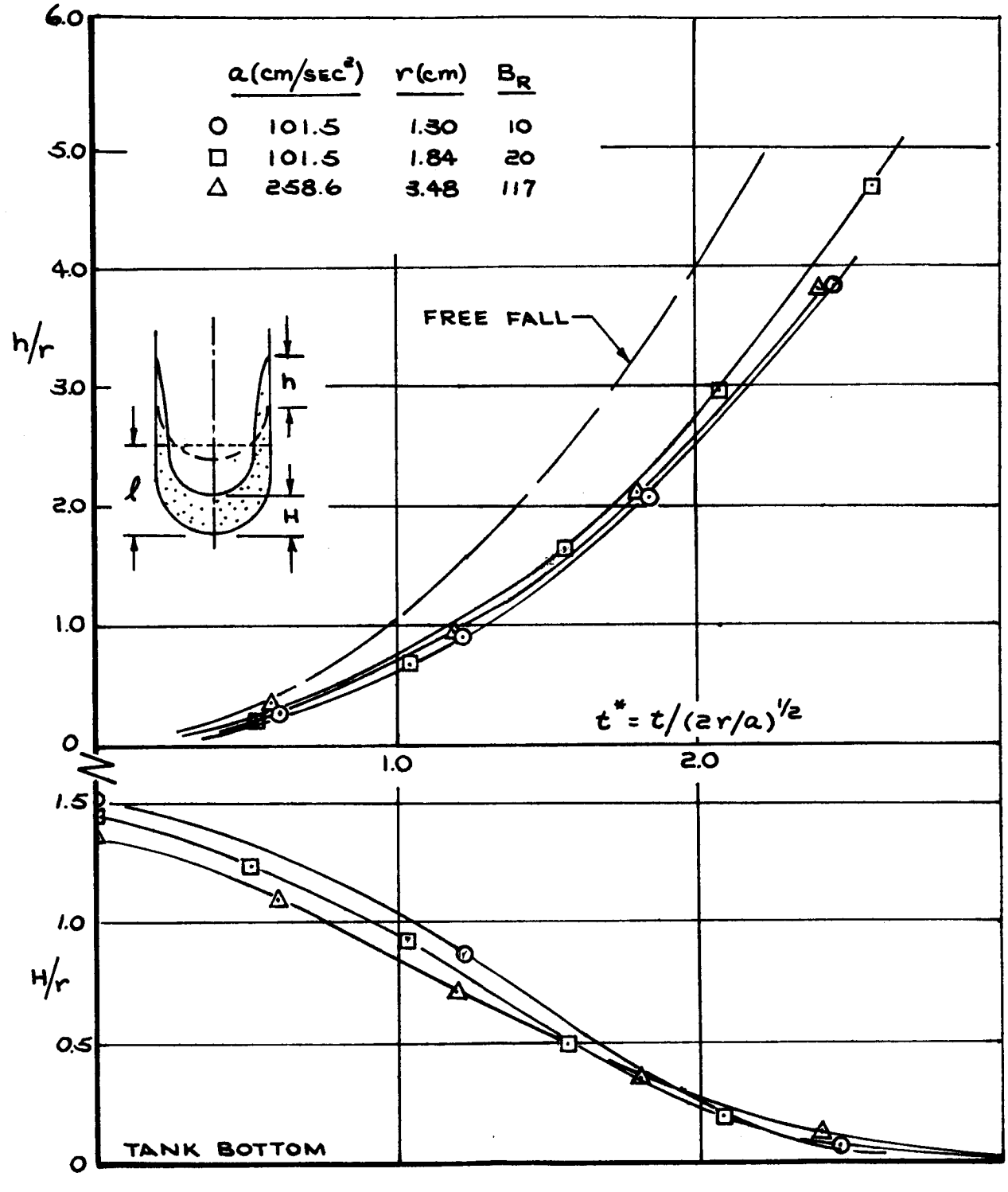

Liquid-Gas Interface Trajectories
(1/r = 1.67)

Figure 3-10

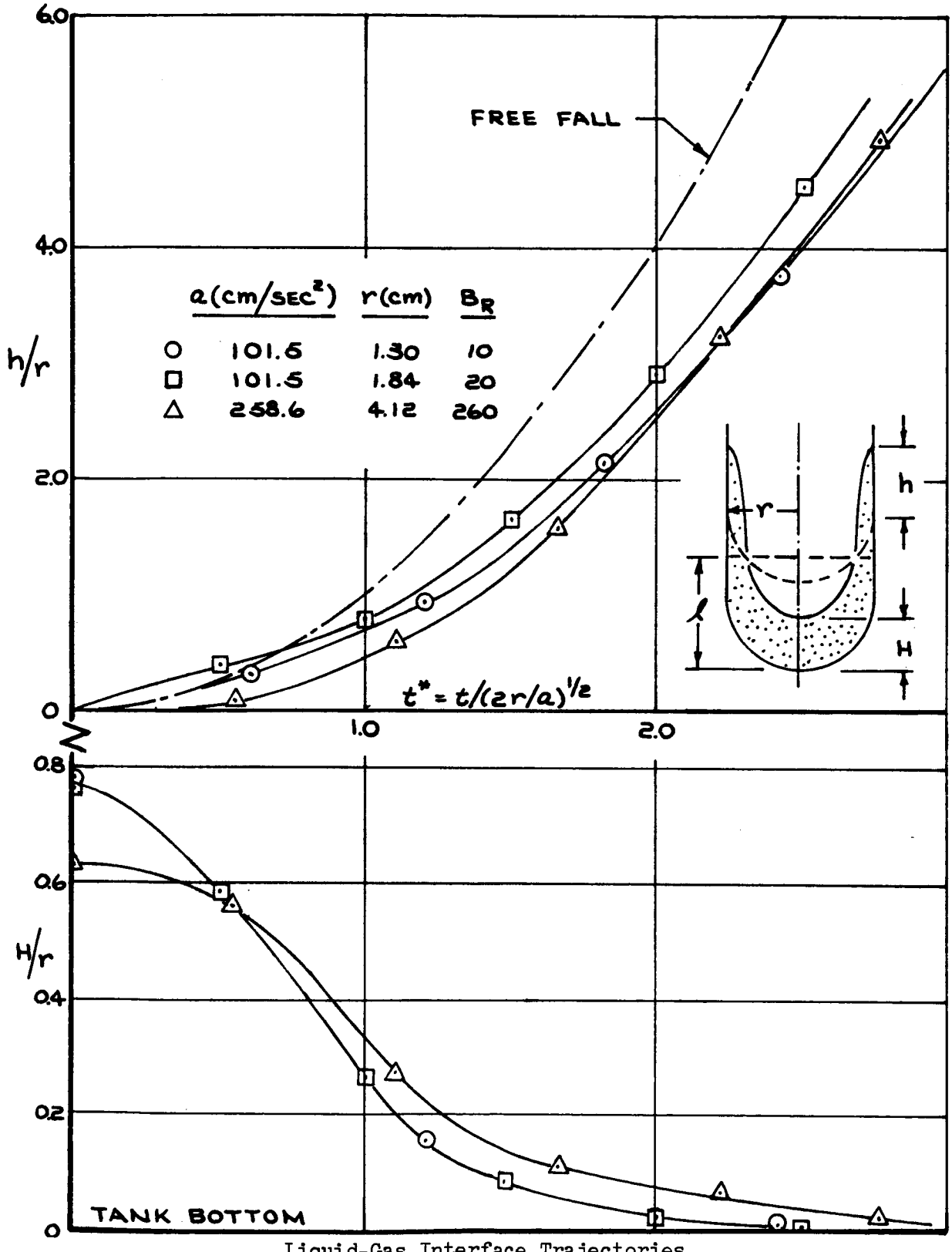

Liquid-Gas Interface Trajectories
(1/r = 1.0)

Figure 3-11

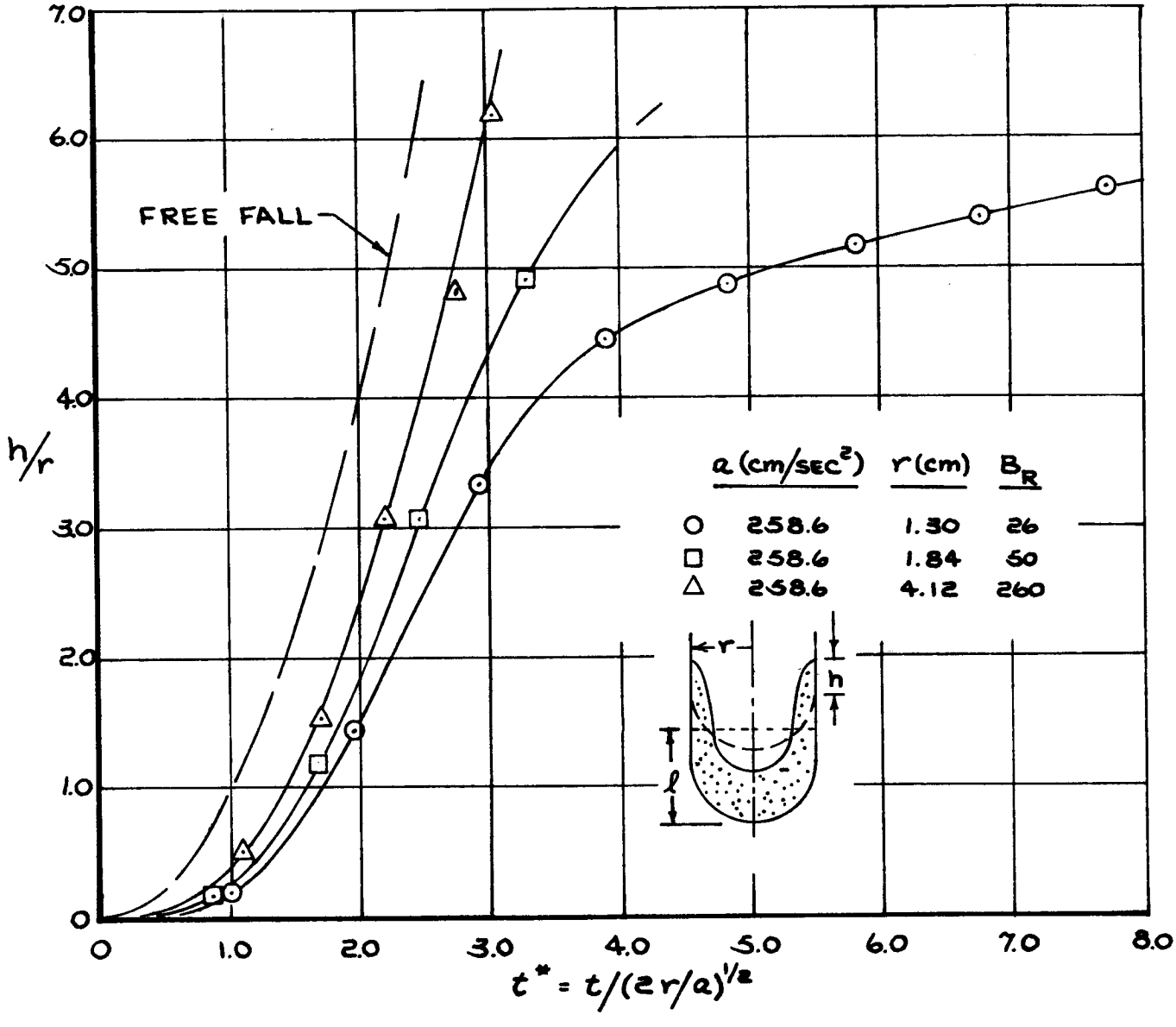

Liquid-Gas Interface Trajectories
(1/r = 0.4)

Figure 3-12

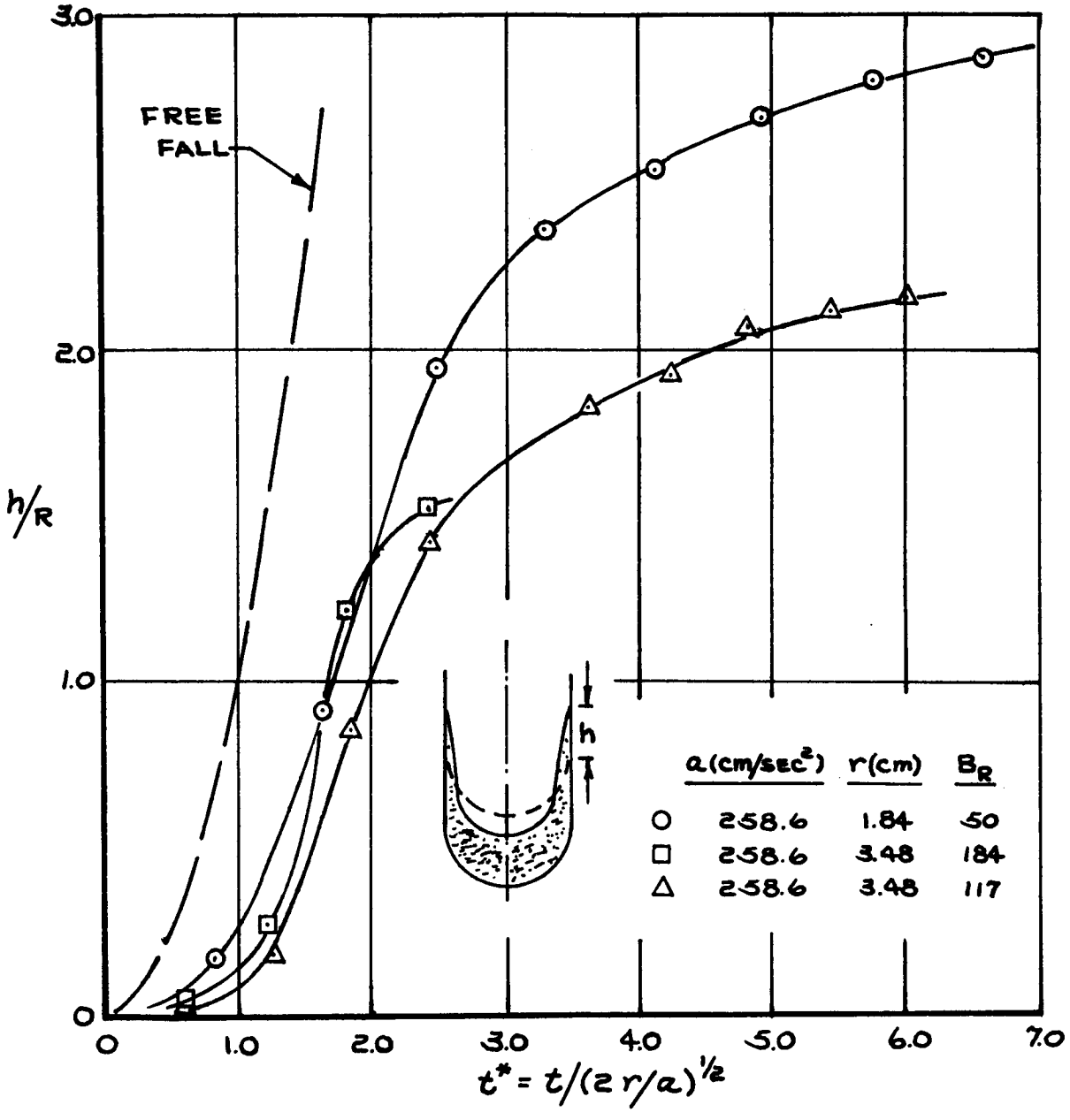

Liquid-Gas Interface Trajectories
(1/r = 0.275)

Figure 3-13

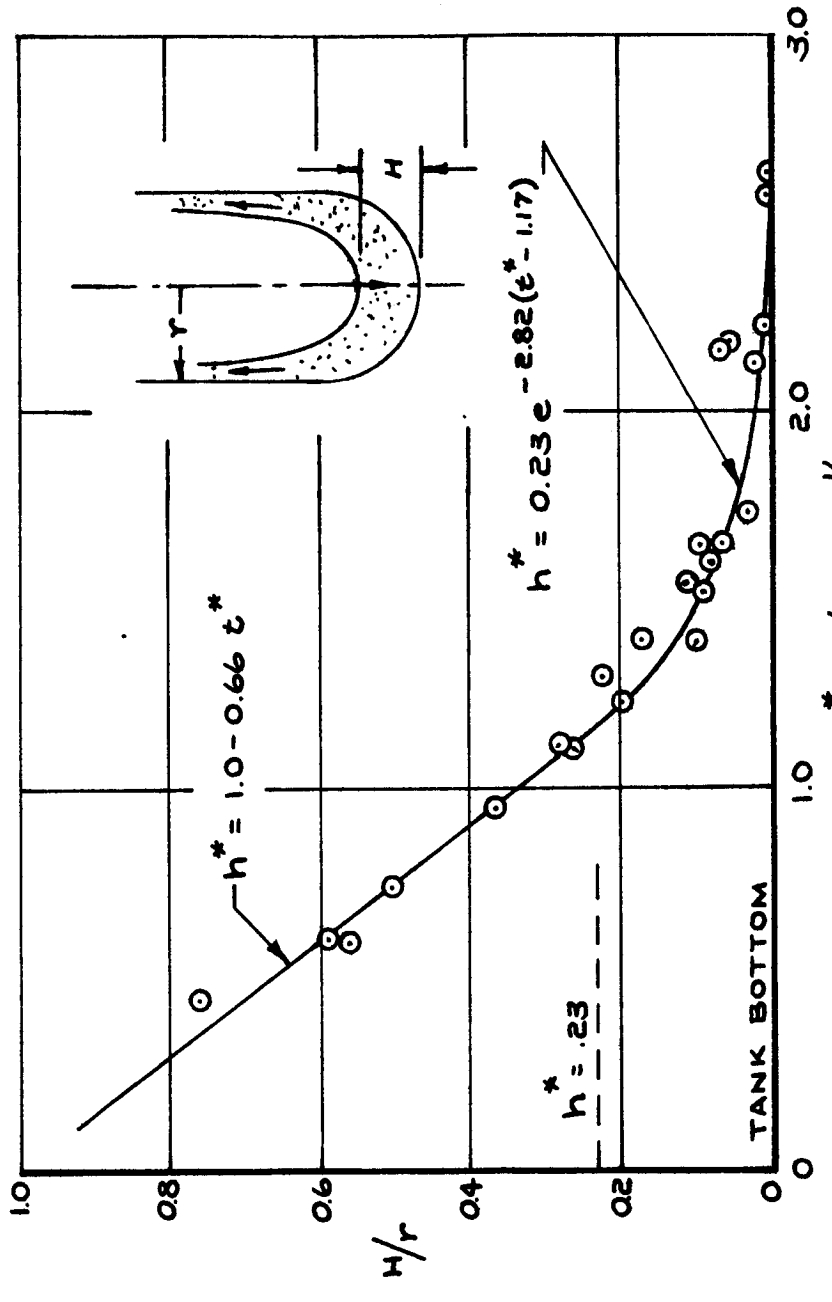

Liquid Depth Approaching Tank End

Figure 3-14

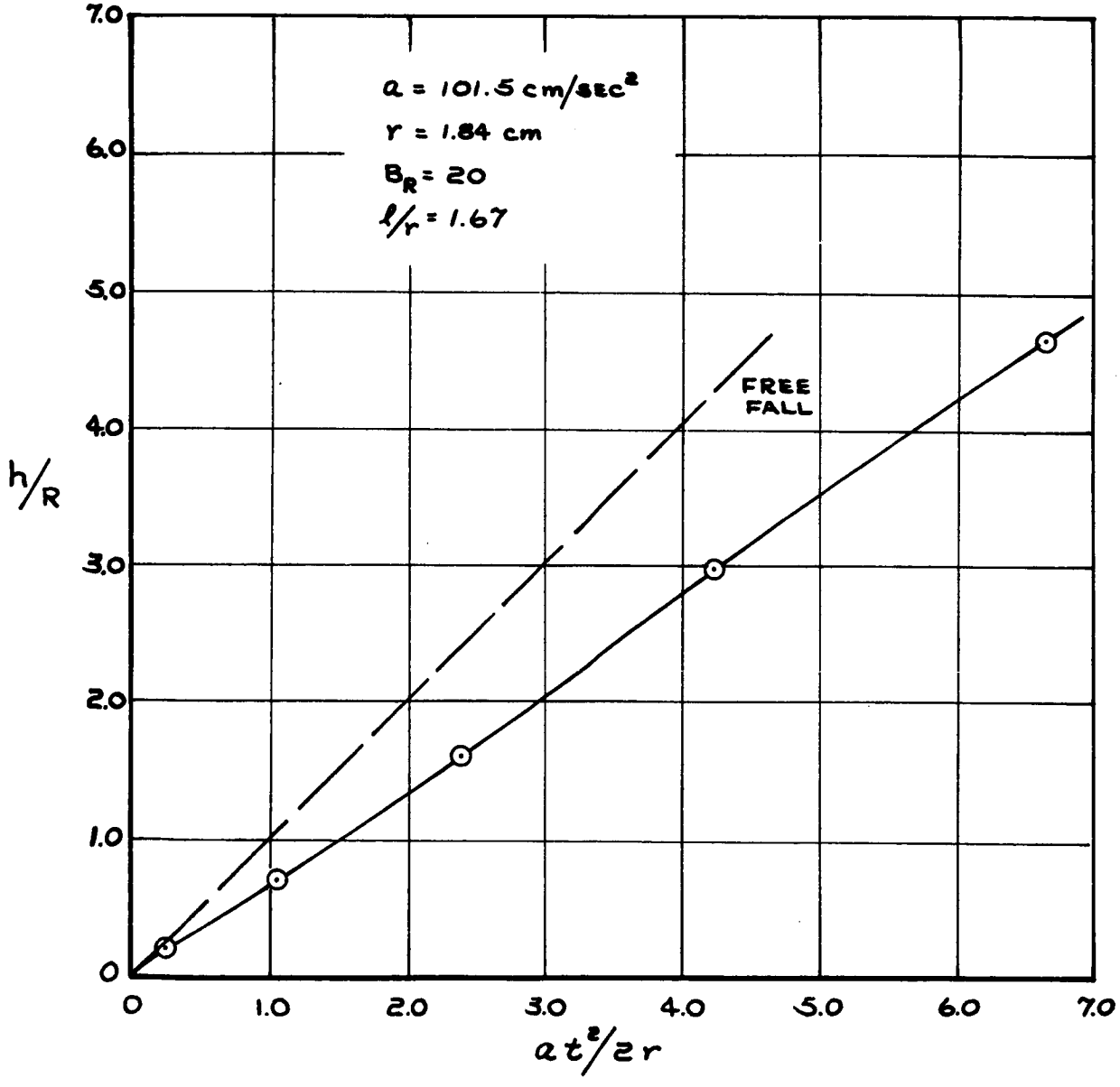

Wall Wave Trajectory

Figure 3-15

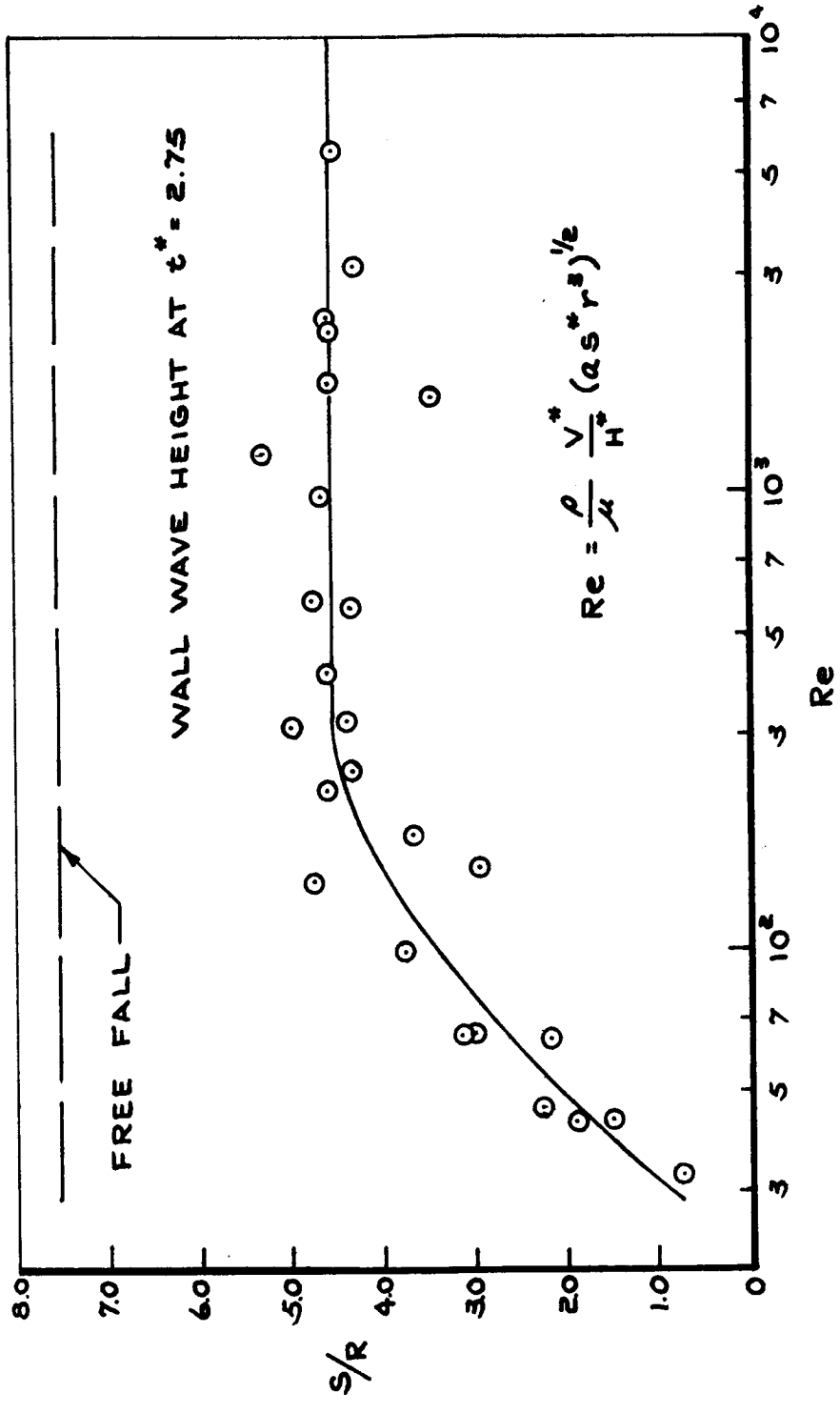

Reynolds Number Effect During Reorientation

Figure 3-16

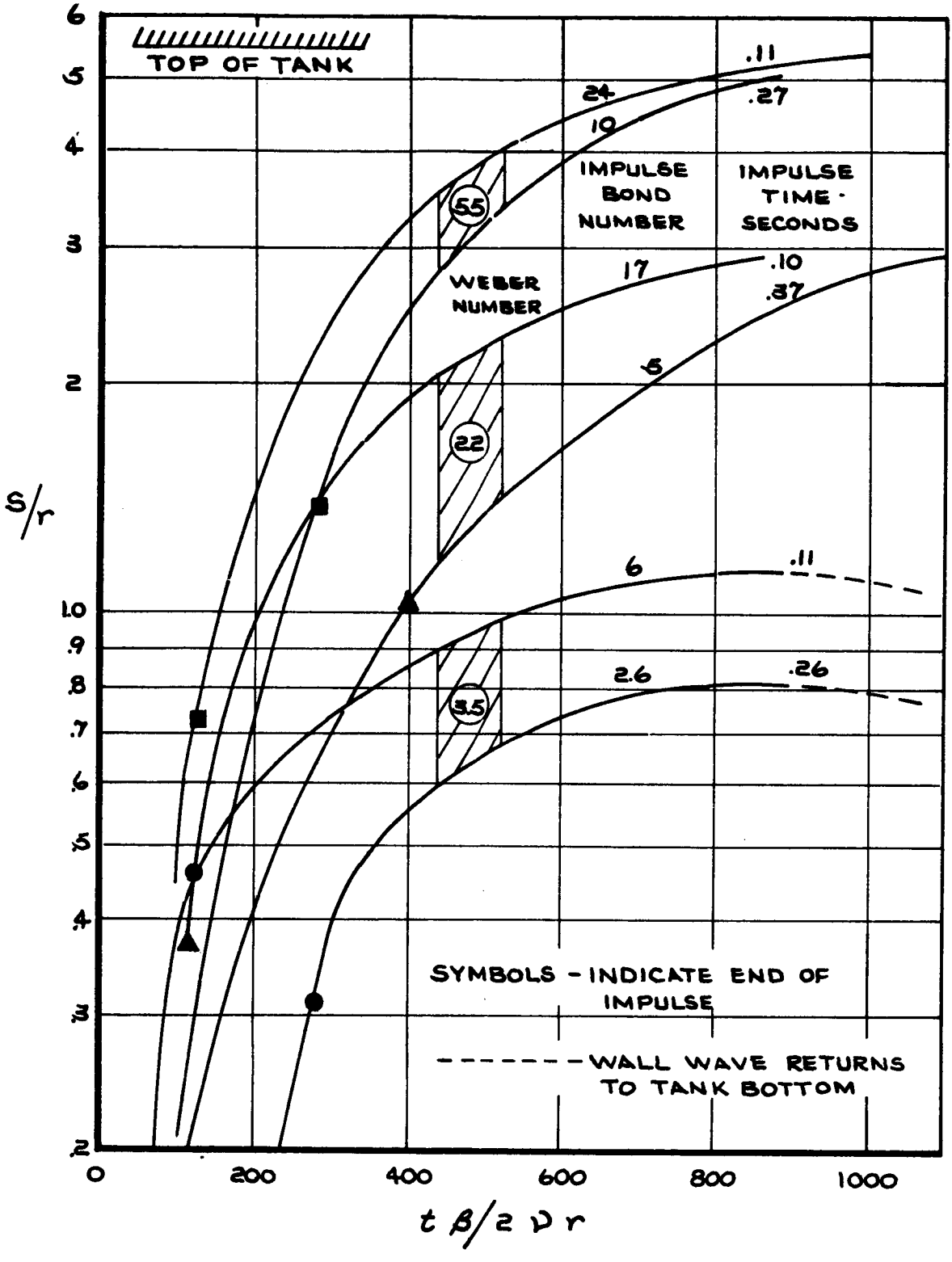

Impulsive Axisymmetric Reorientation

Wall Wave Displacement from Interface Equilibrium Position

Figure 3-17

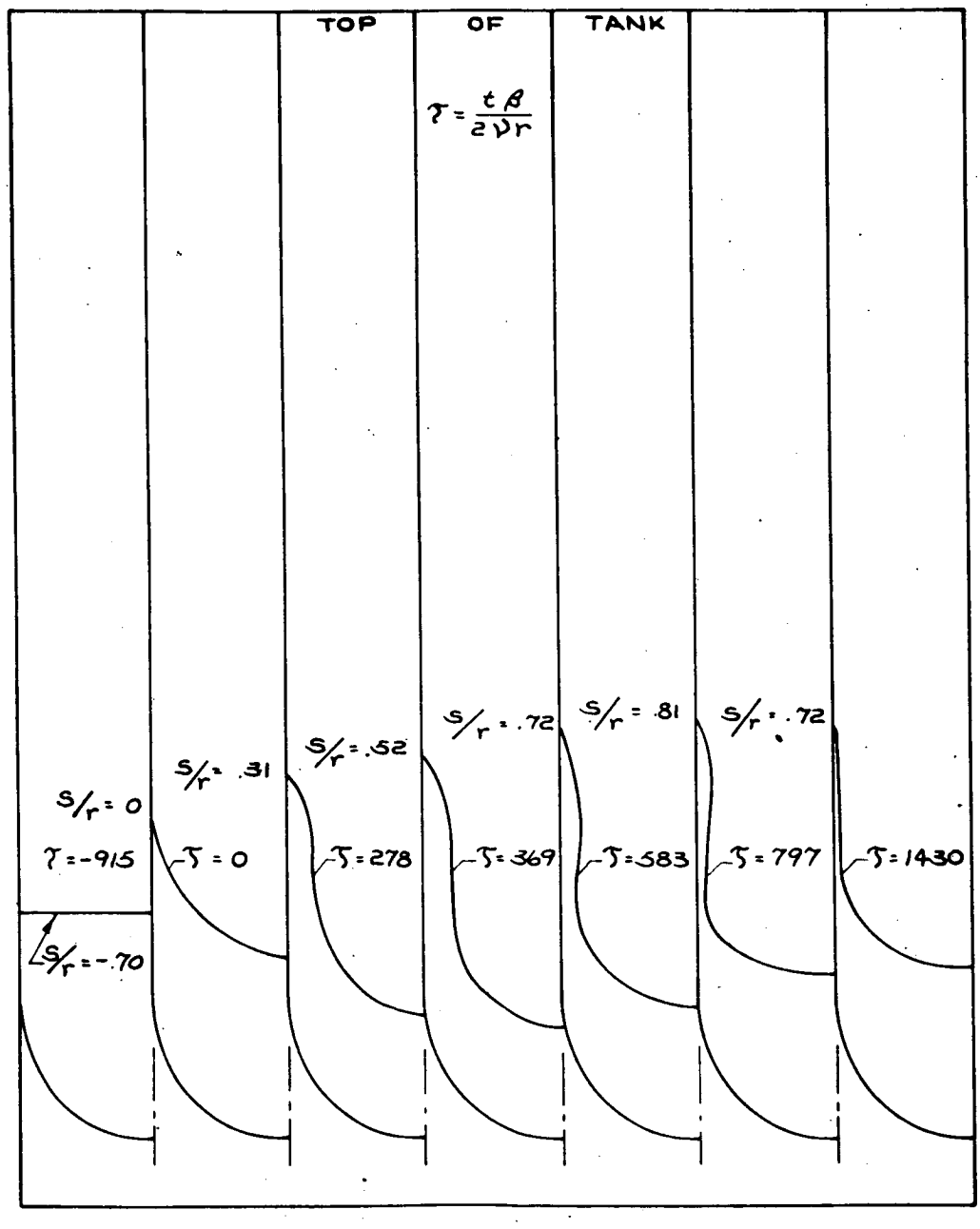

Impulsive Axisymmetric Reorientation Wall Wave Shapes

Figure 3-18

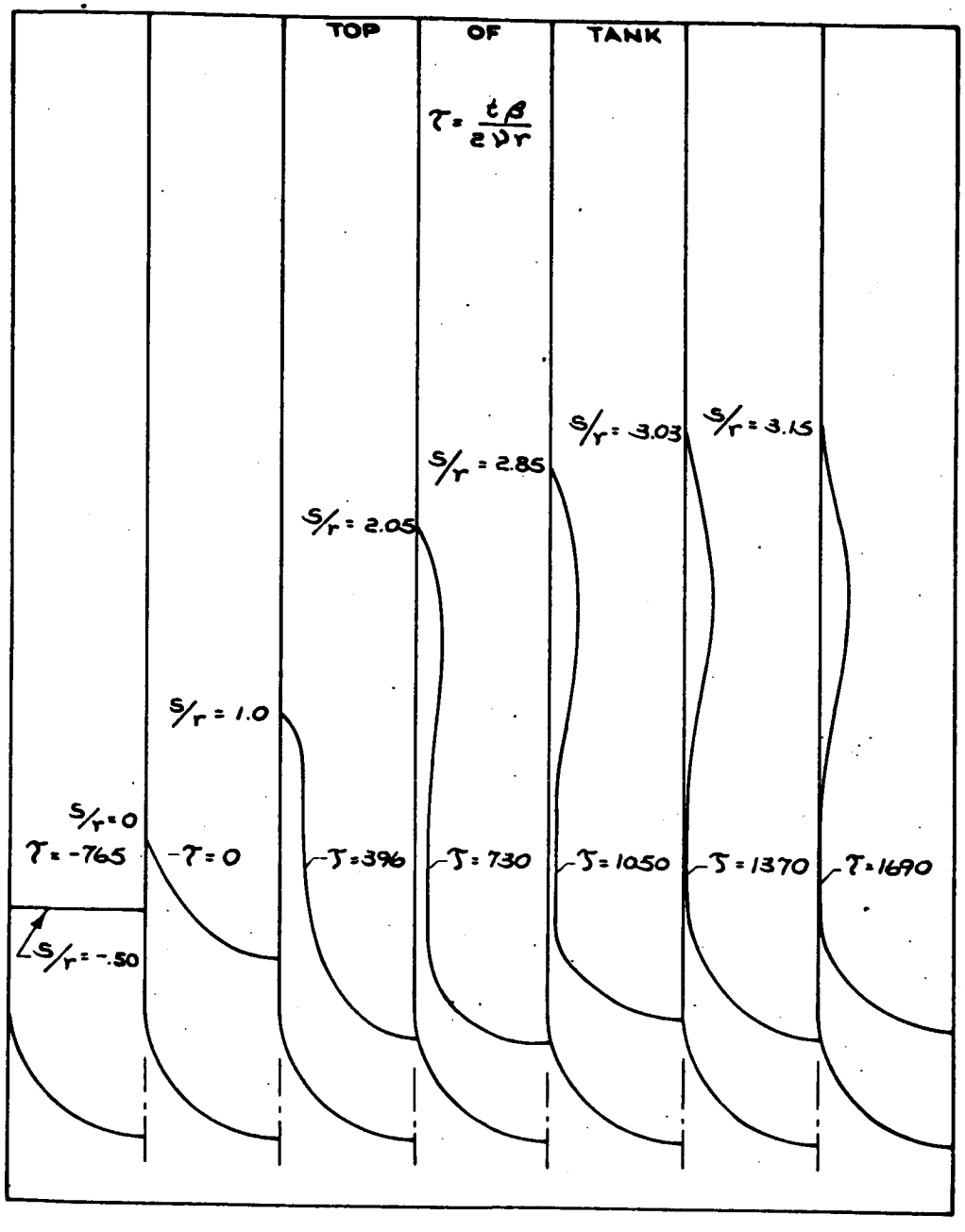

Impulsive Axisymmetric Reorientation Wall Wave Shapes

Figure 3-19

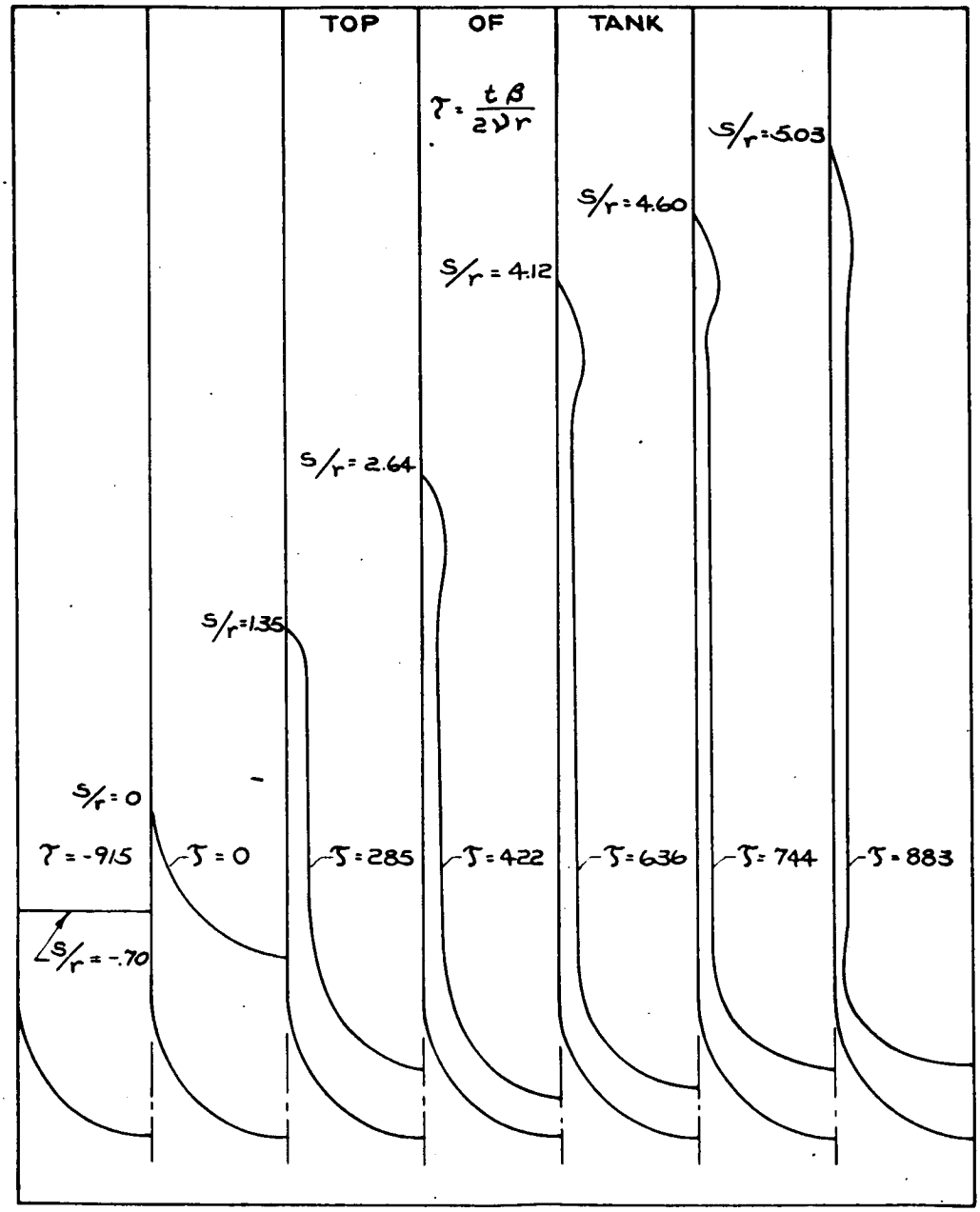

Impulsive Axisymmetric Reorientation Wall Wave Shapes

Figure 3-20

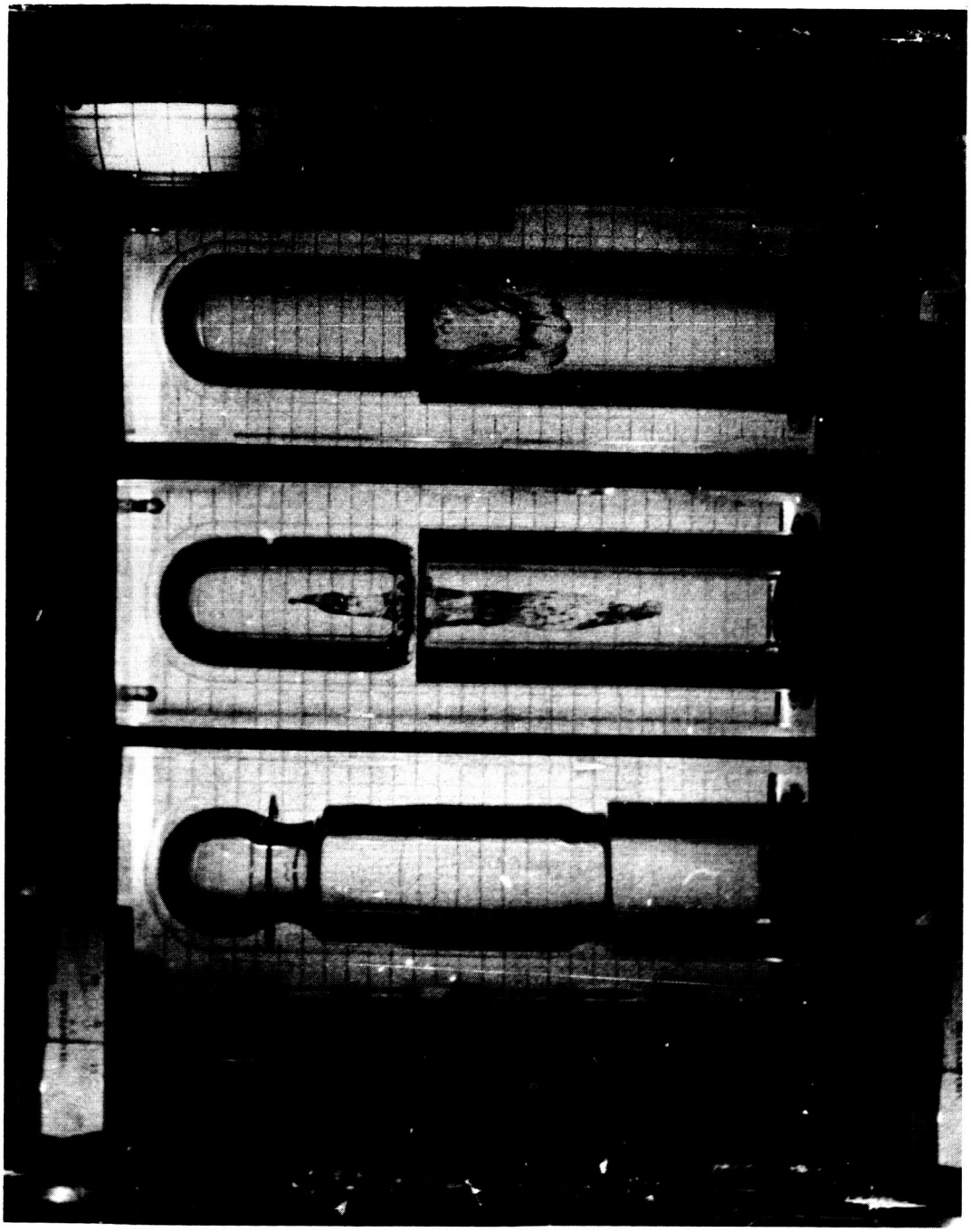

REORIENTATION IN TANKS WITH BAFFLES

Figure 3-21

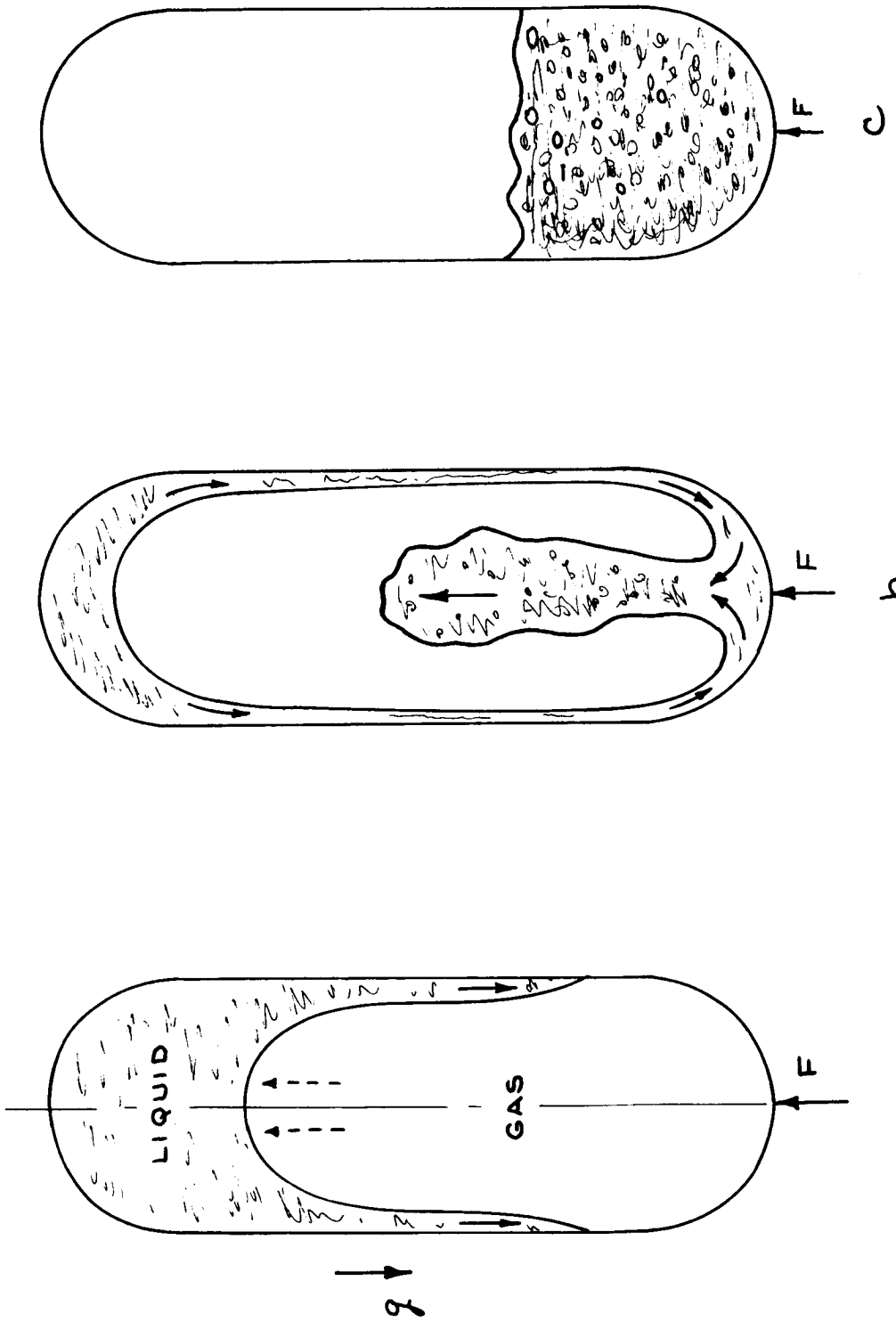

Axial Reorientation Flow Pattern

Figure 3-22

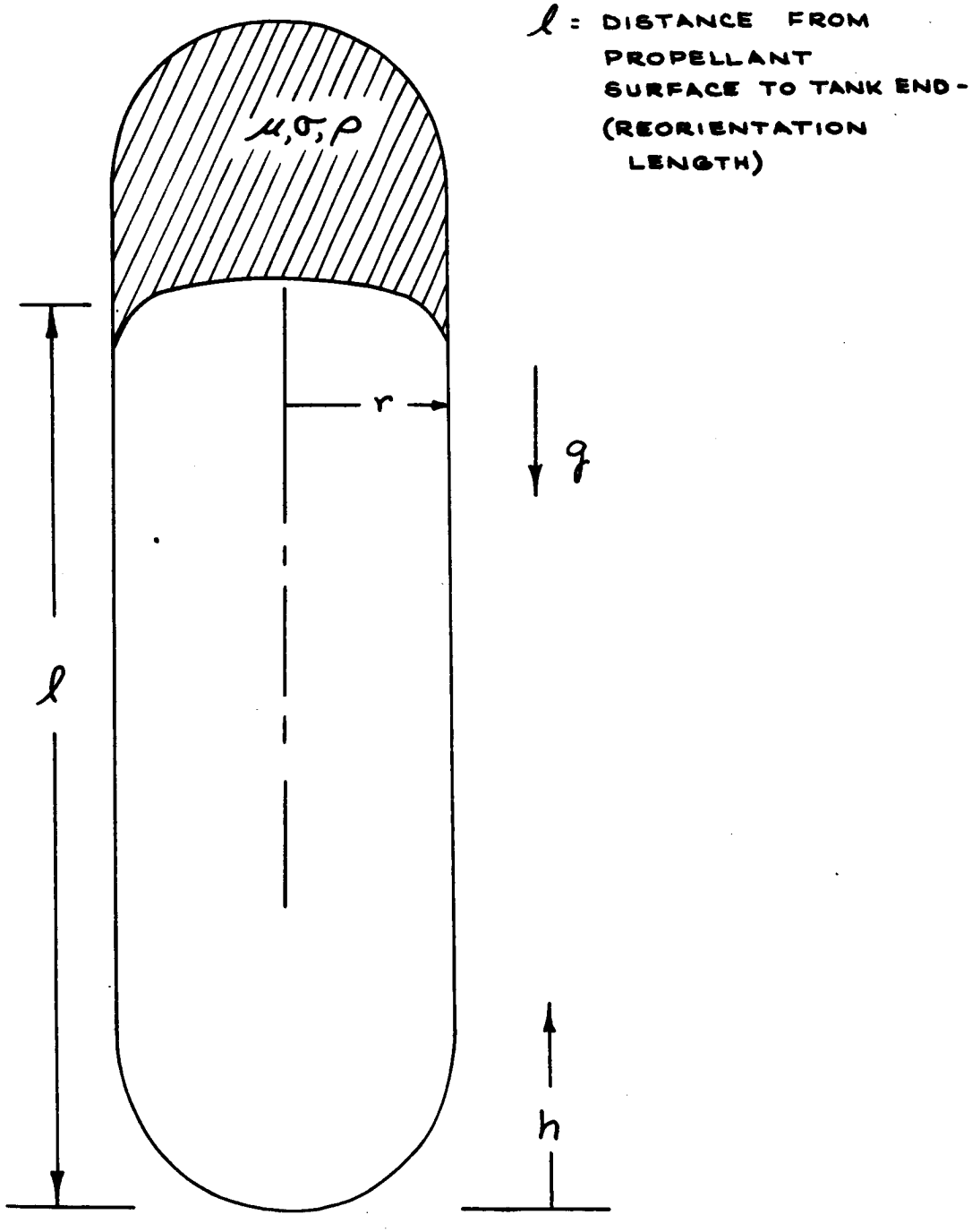

Rebound Experiment Parameters

Figure 3-23

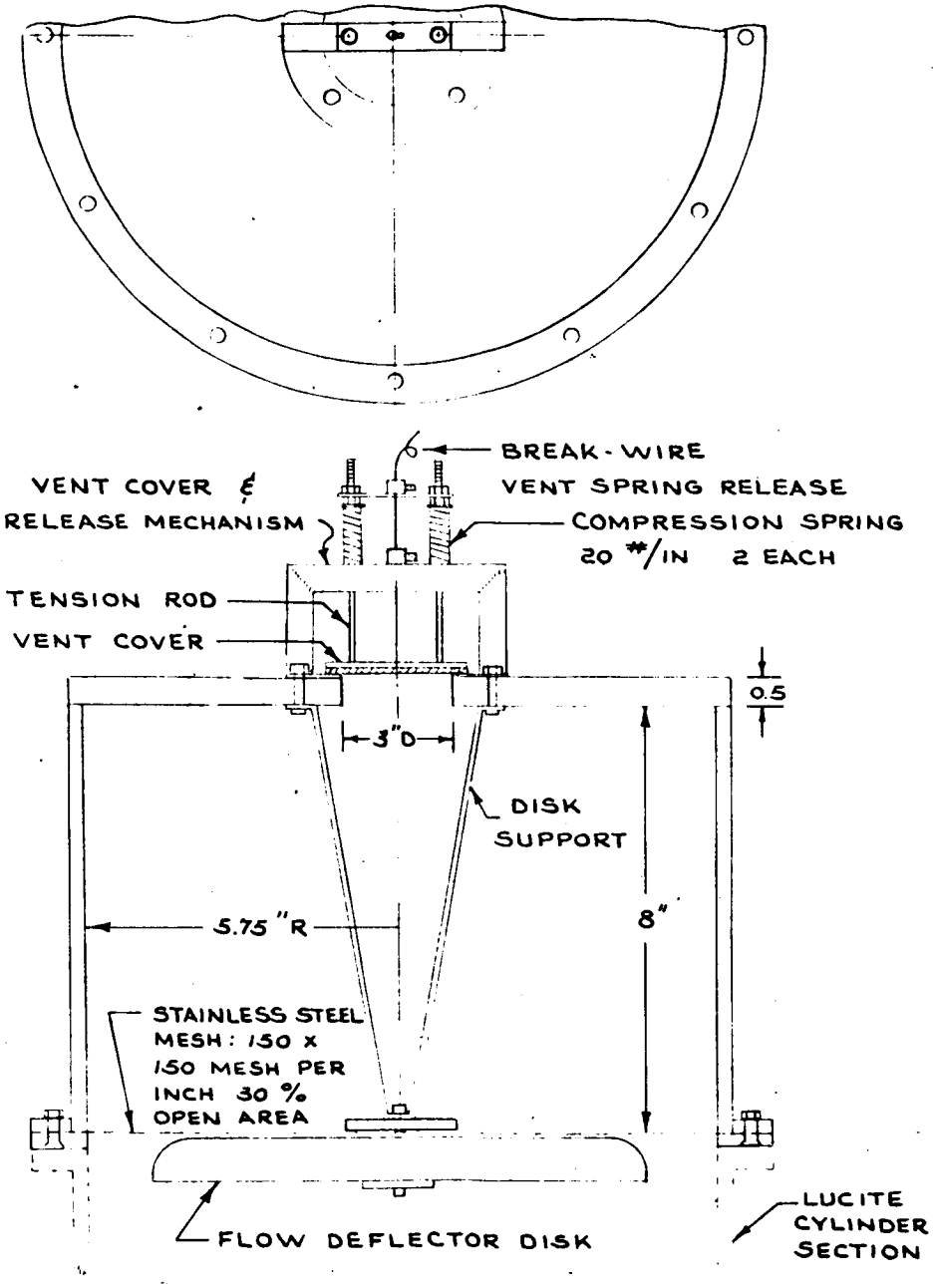

Reservoir and Liquid Release Mechanism

Figure 3-24

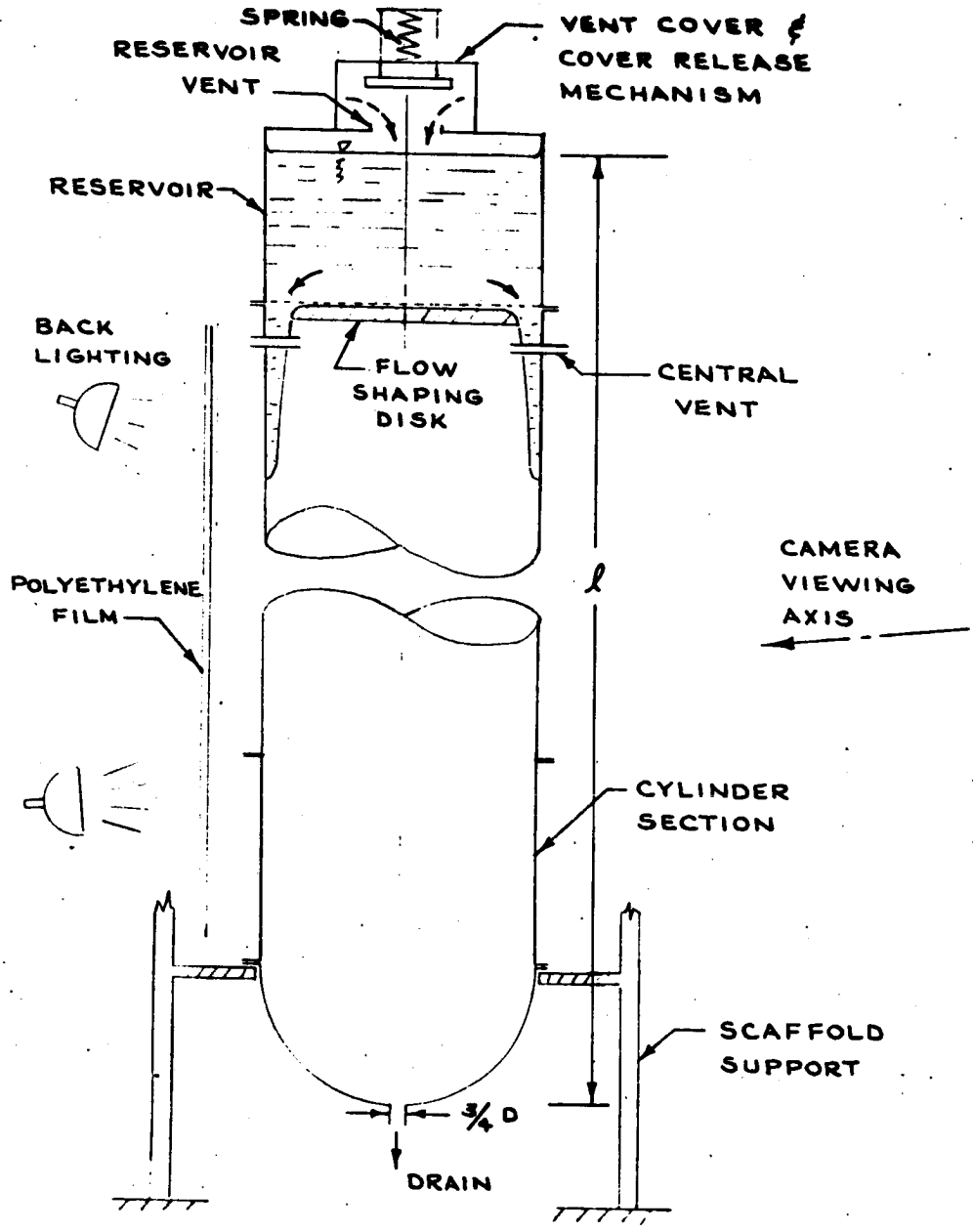

Rebound Test Apparatus

Figure 3-25

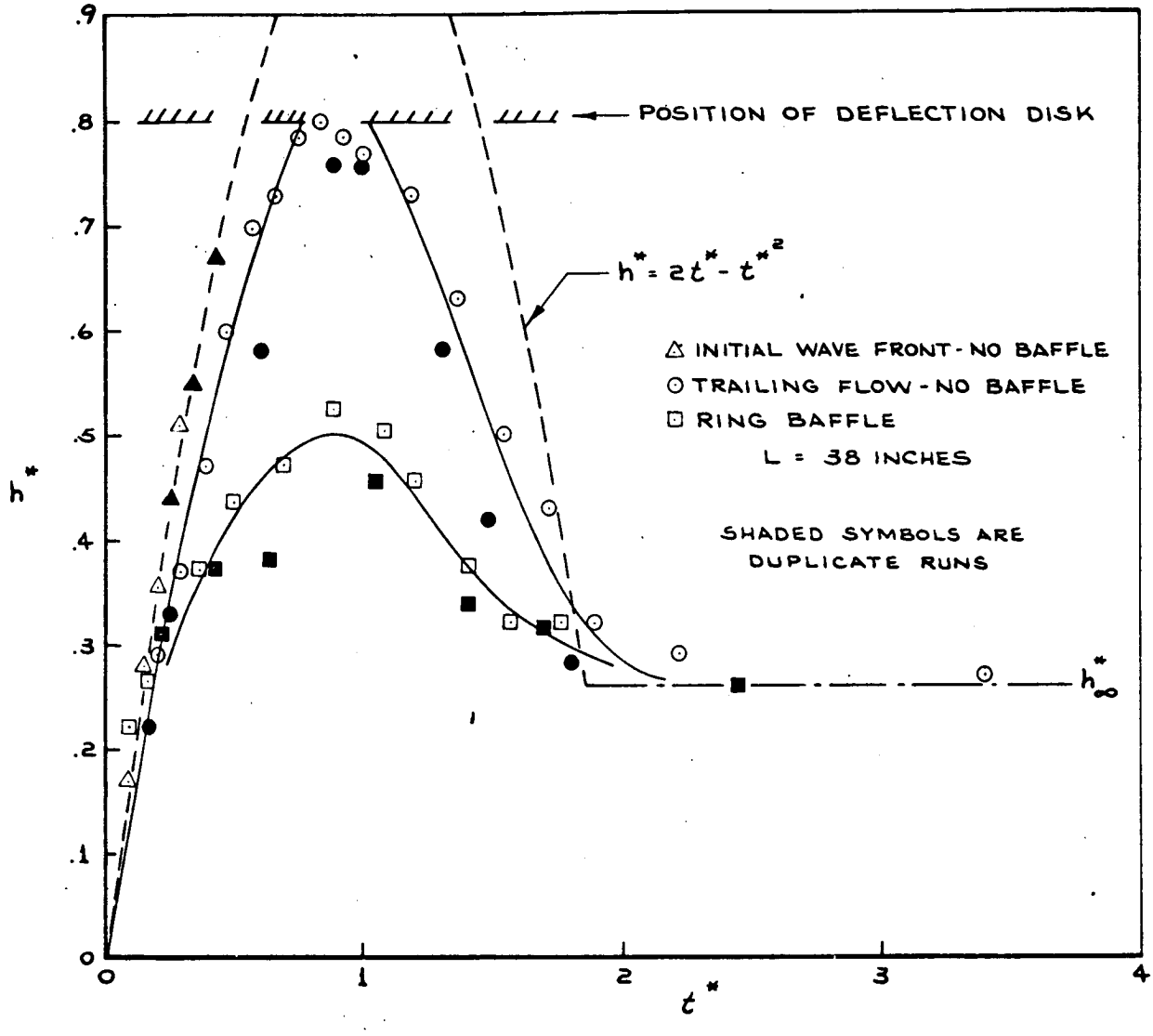

Geyser Trajectory
(L = 38 in)

Figure 3-26

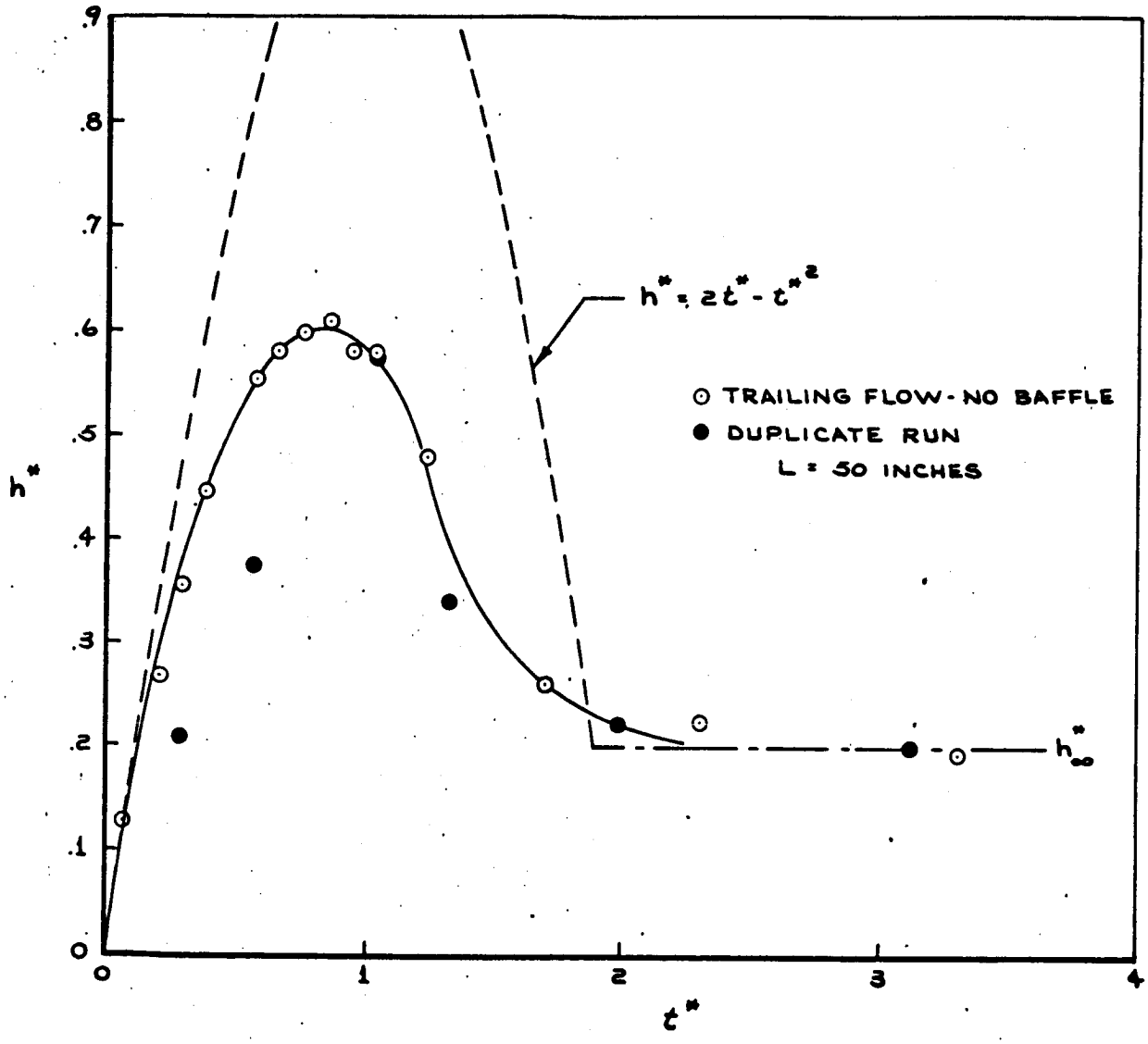

Geyser Trajectory
(L = 50 in)

Figure 3-27

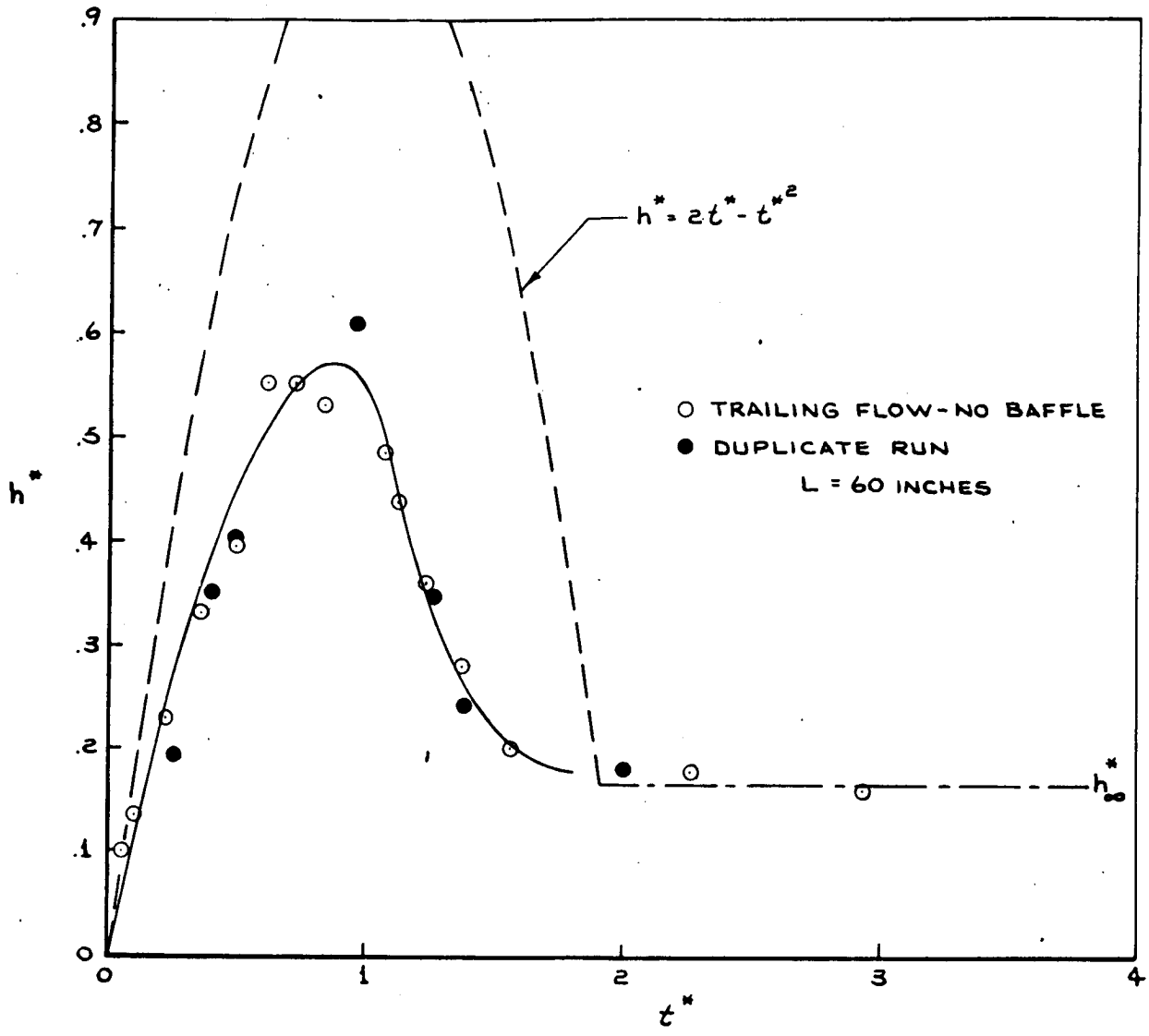

Geyser Trajectory
(L = 60 in)

Figure 3-28

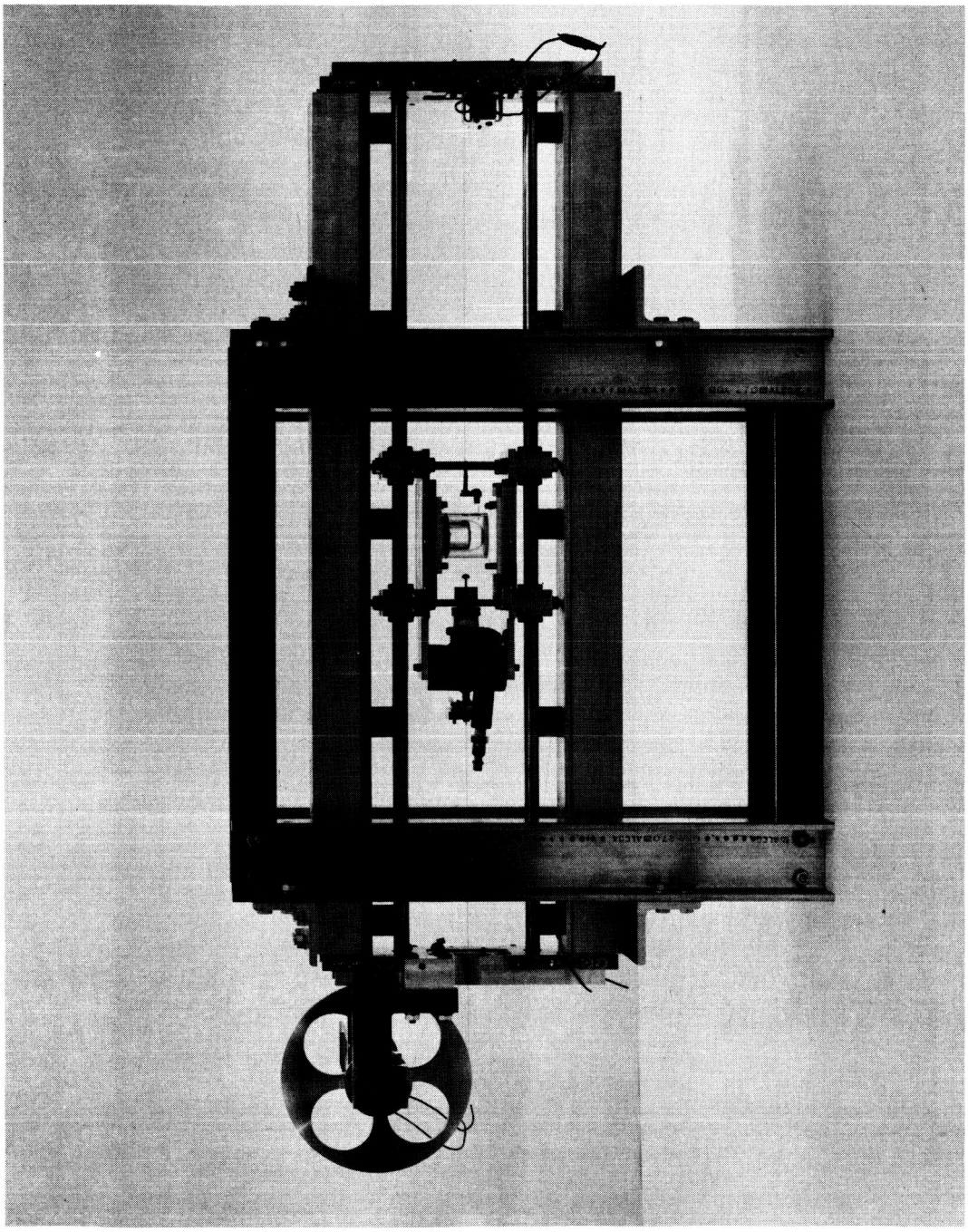

LOW-G IMPULSIVE SLOSH TEST APPARATUS

Figure 3-29

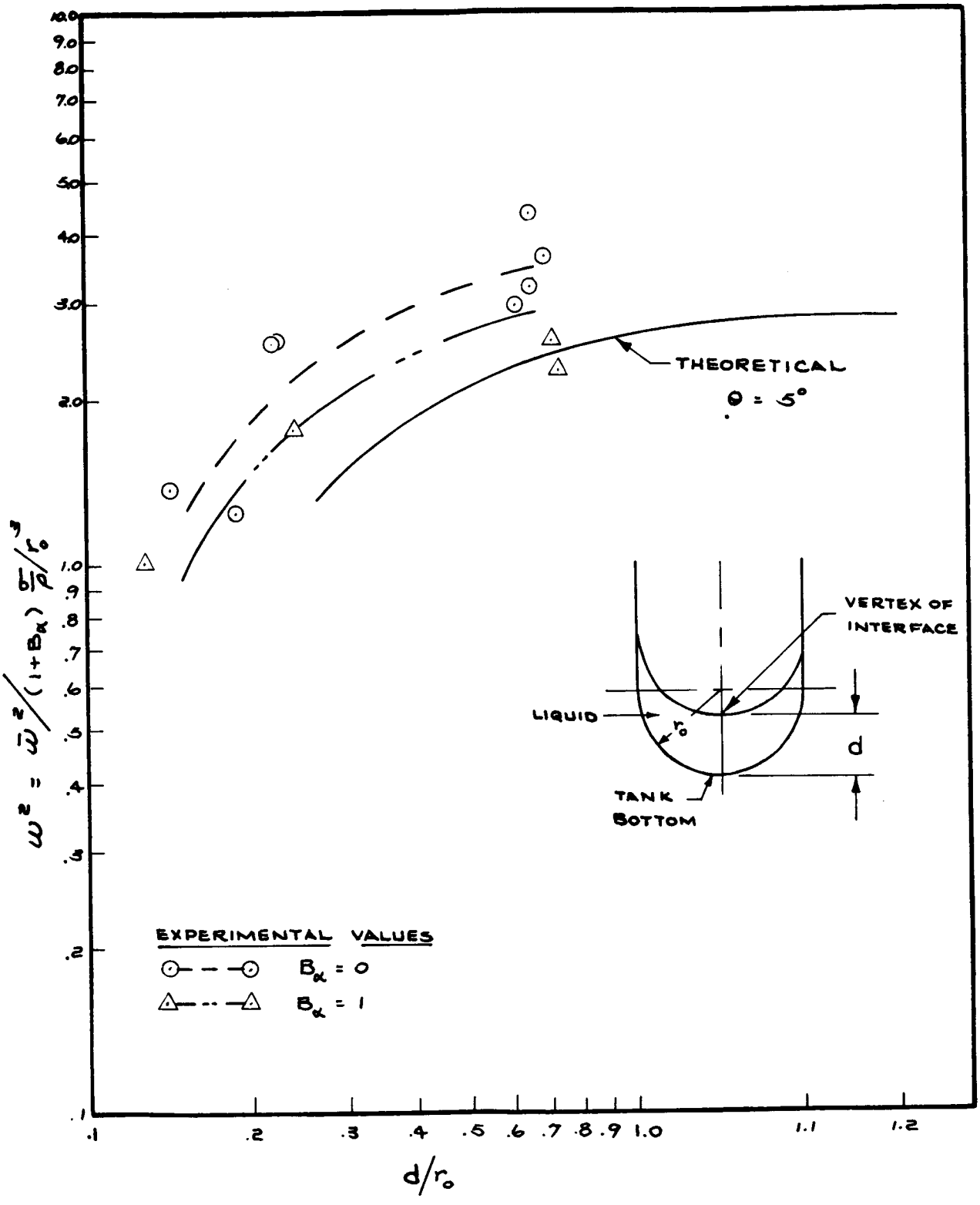

Comparison of Sloshing Frequency Between Test Results and Prediction

Figure 3-30

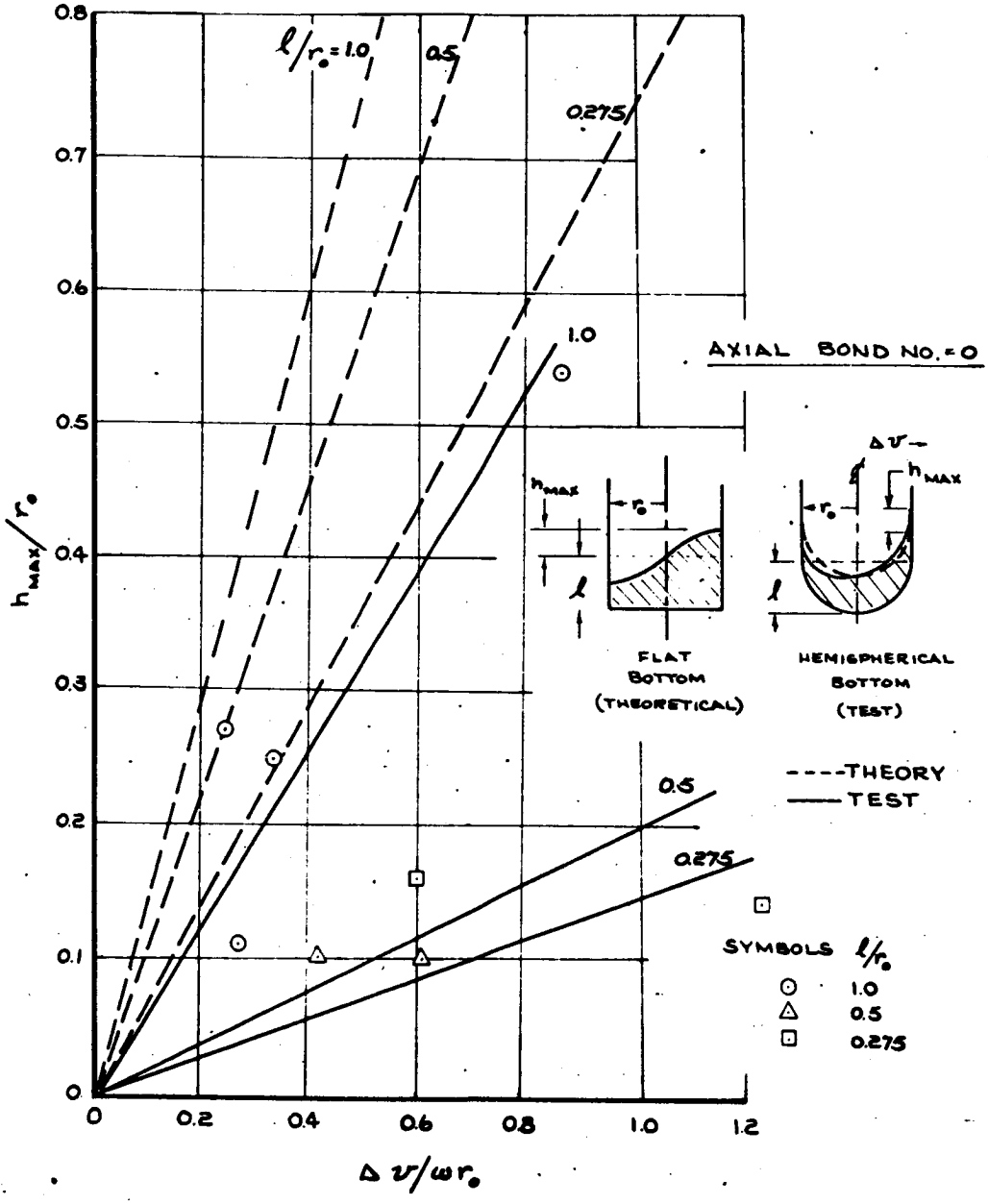

Lateral Slosh Response

to a Transverse Impulse Axial Bond Number - 0

Figure 3-31

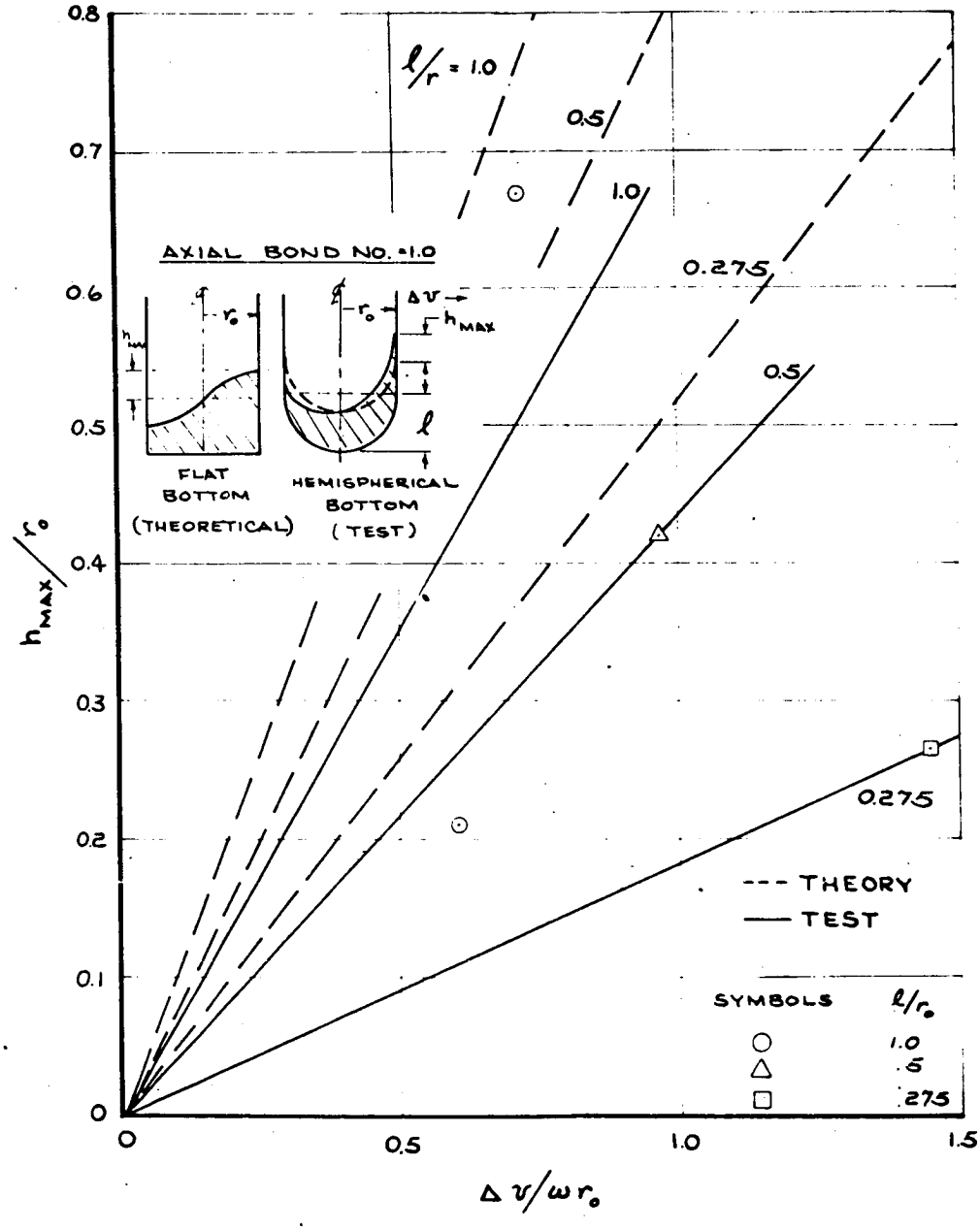

Lateral Slosh Response

to a Transverse Impulse Axial Bond Number - 1

Figure 3-32

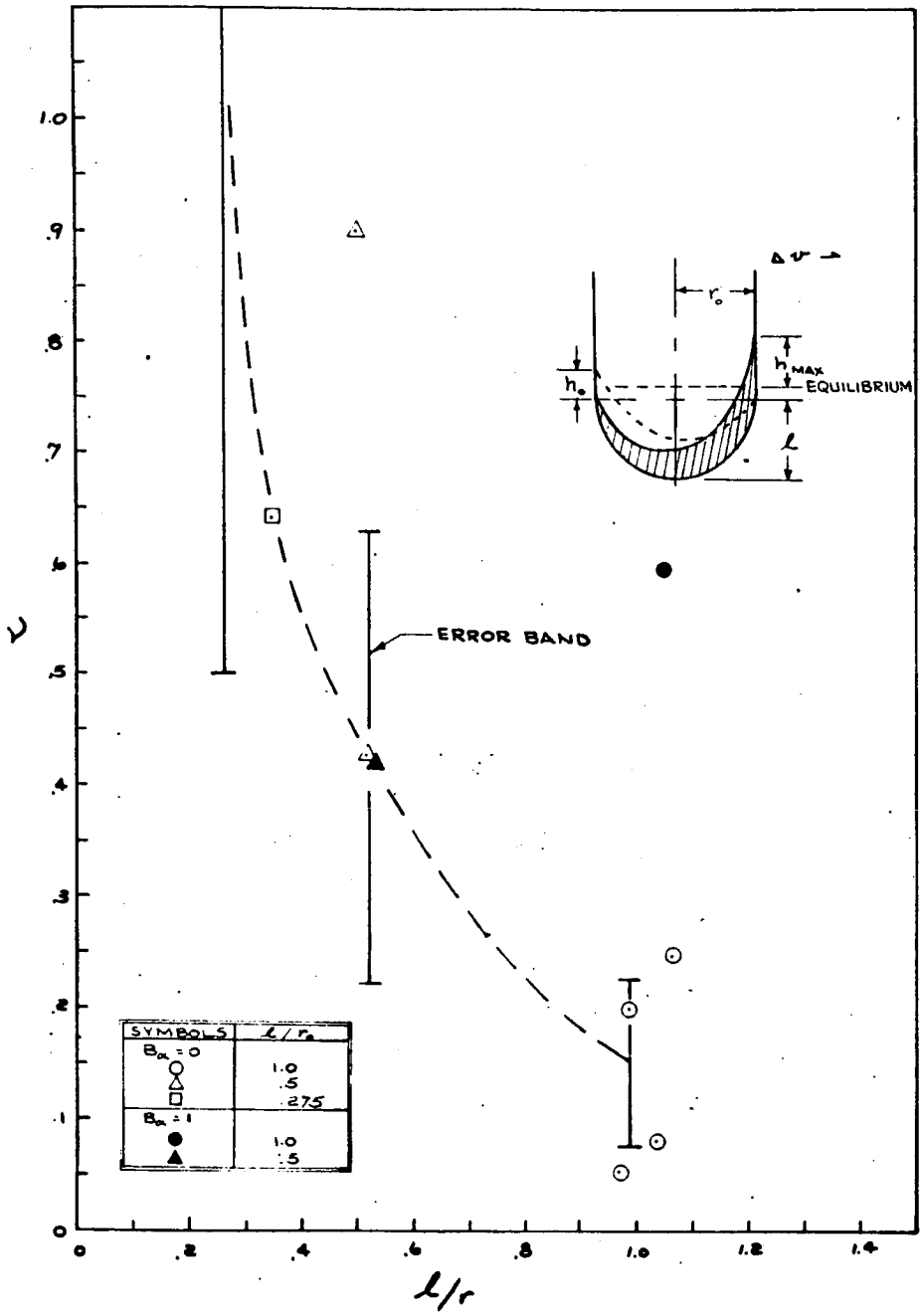

Variation of Damping Ratio with Liquid Fill Level

Figure 3-33

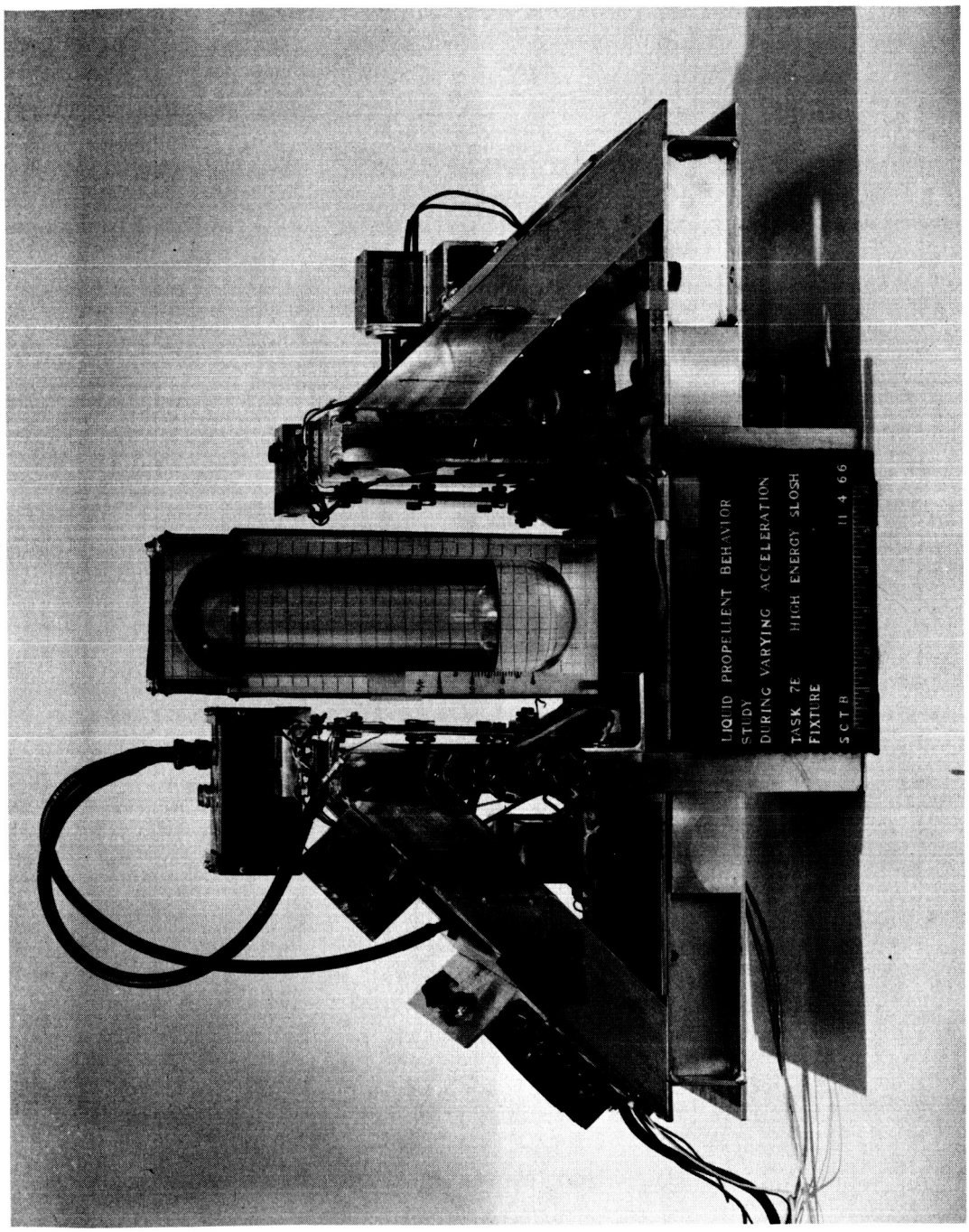

RESIDUAL SLOSH TEST APPARATUS

Figure 3-34

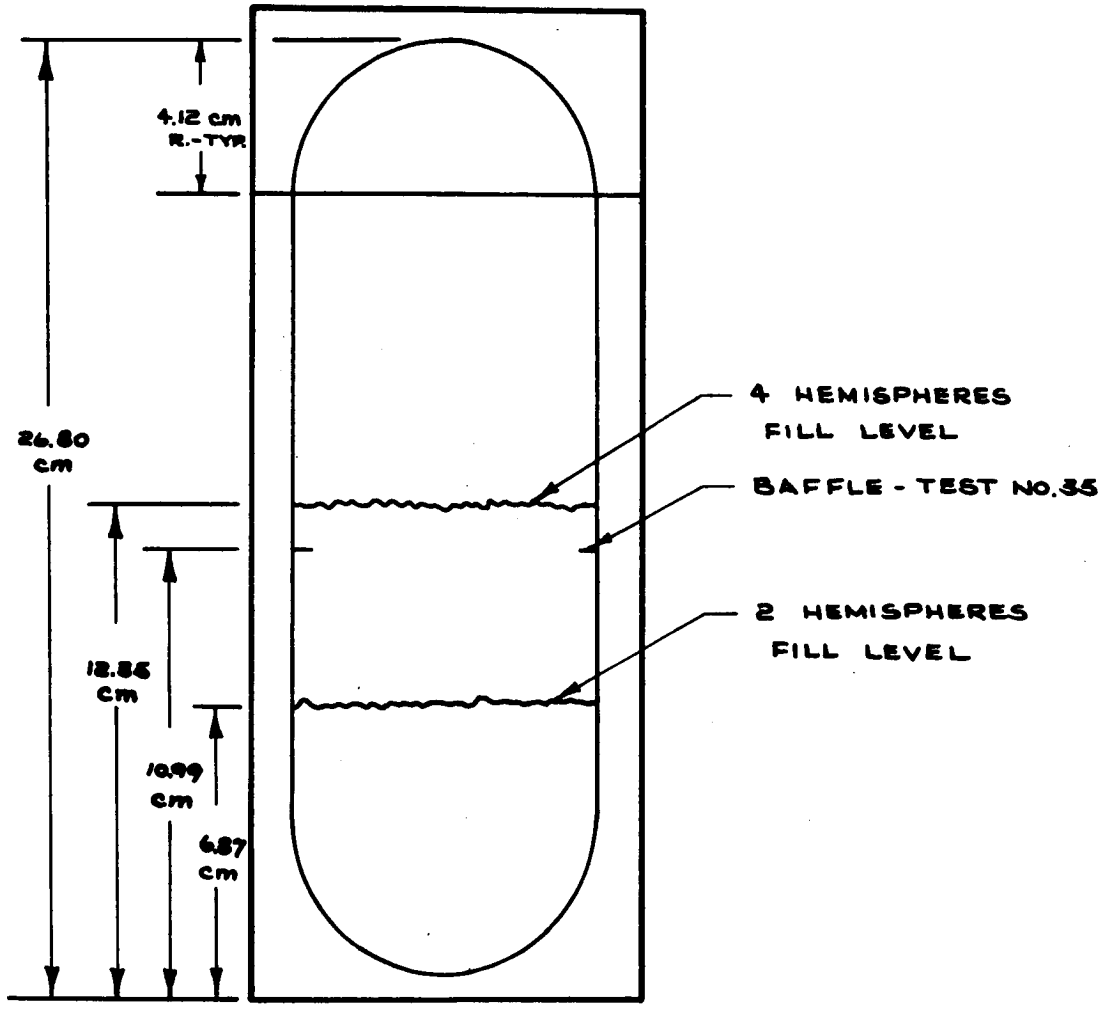

Residual Slosh Test Tank Geometry

Figure 3-35

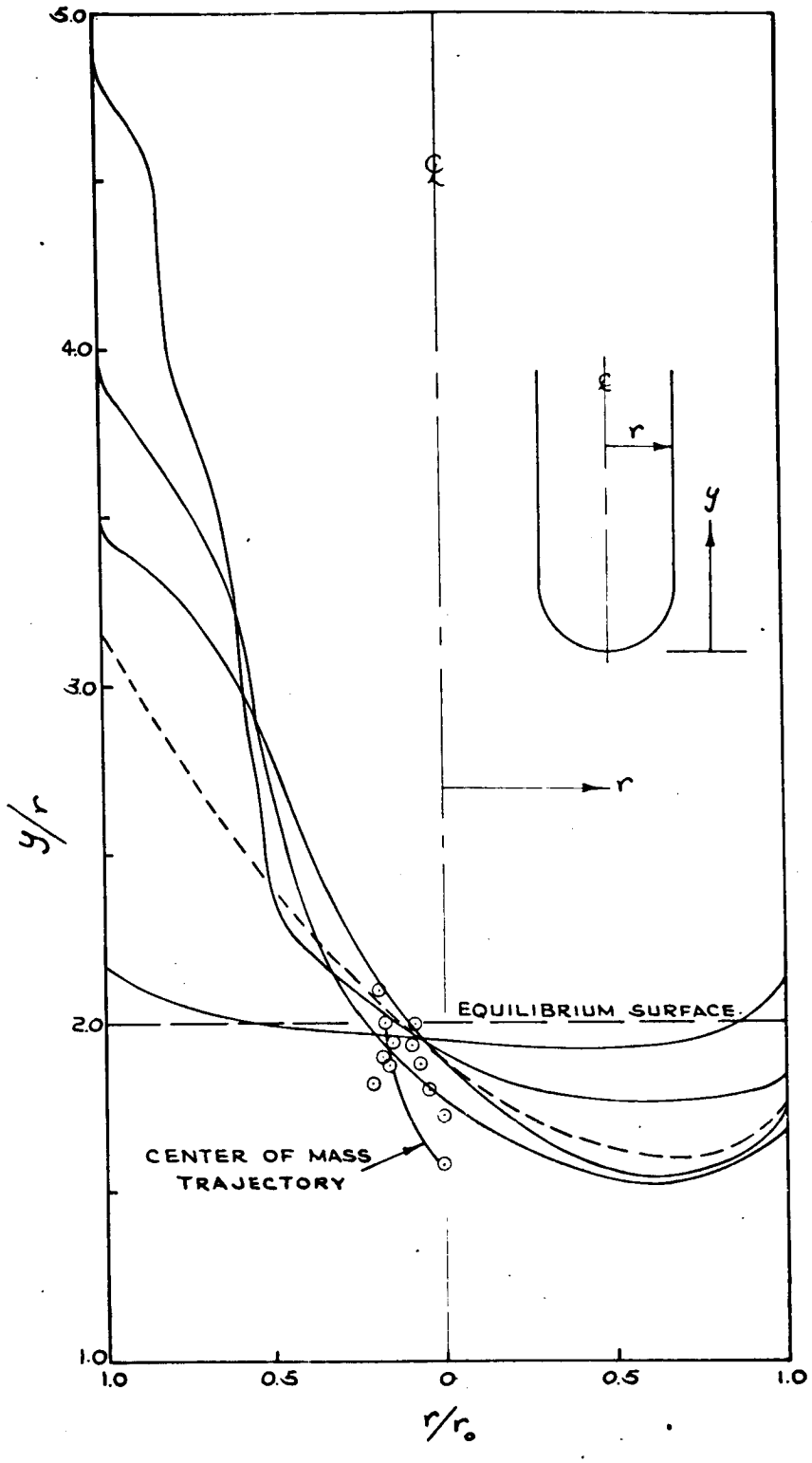

C. G. Shift and Wave Profiles

Figure 3-36

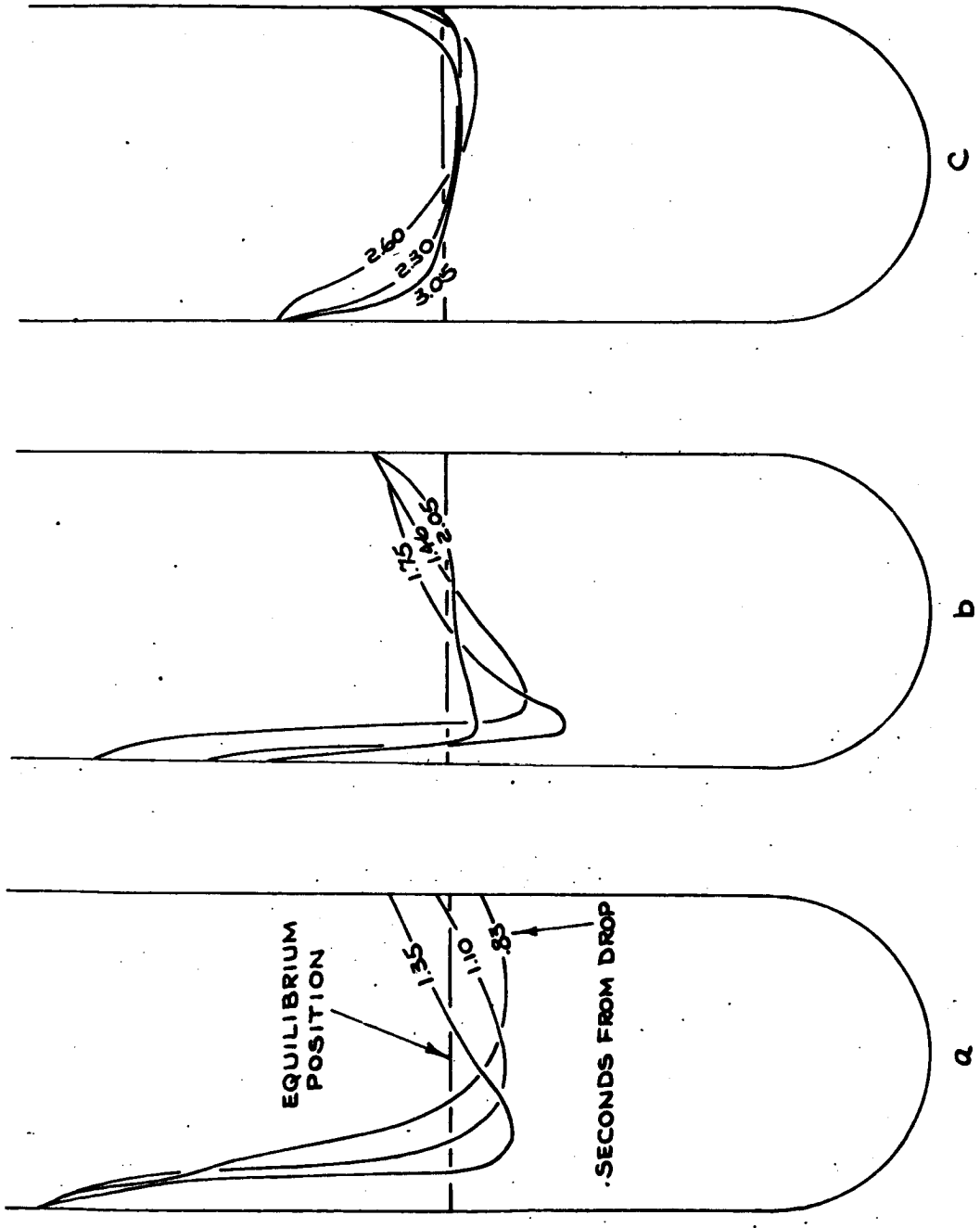

Interface Motion

Figure 3-37

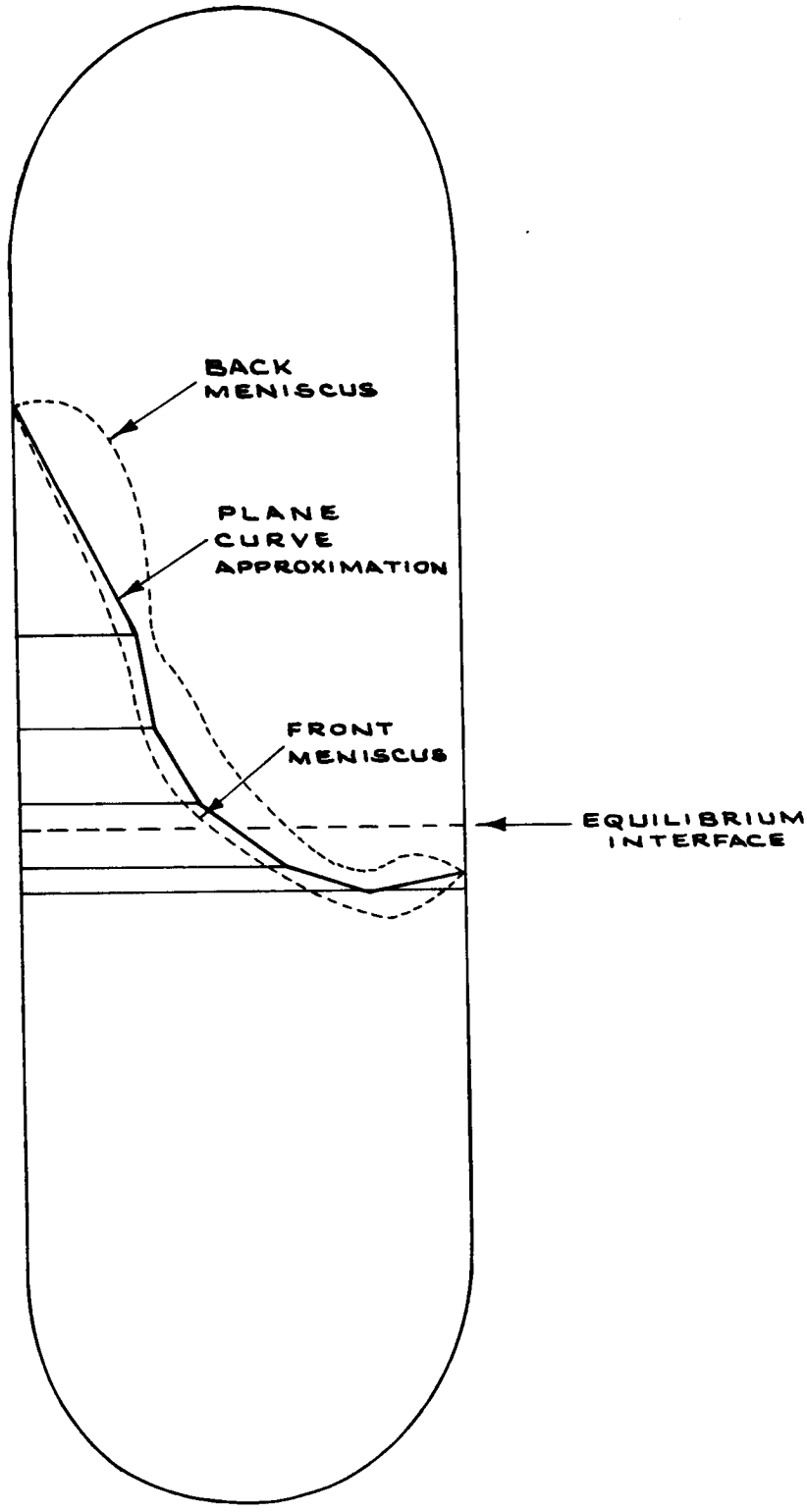

Plane Curve and Chord Segment

Idealizations of Large Amplitude Wave

Figure 3-38

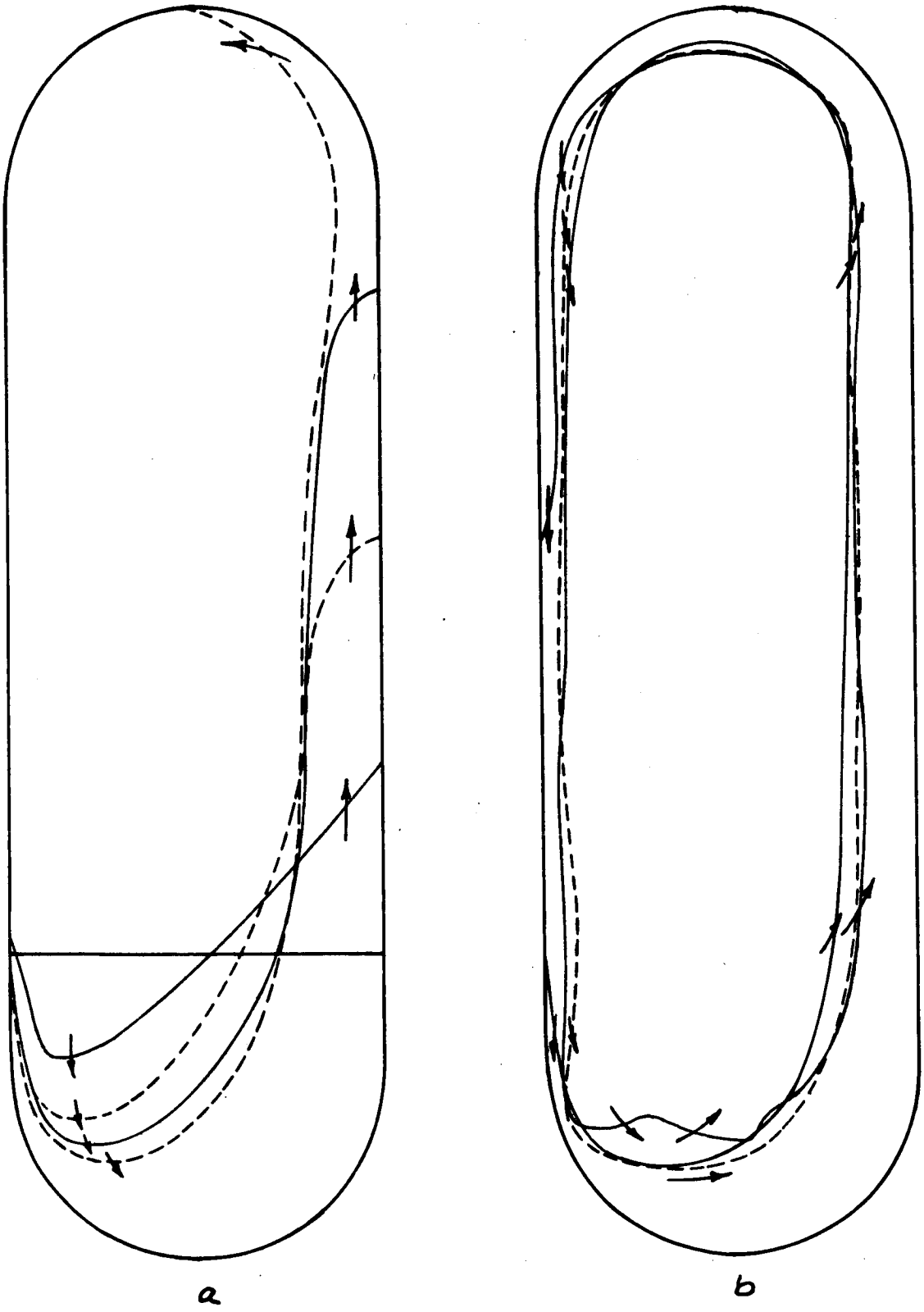

Residual Slosh Wave Profiles

Figure 3-39

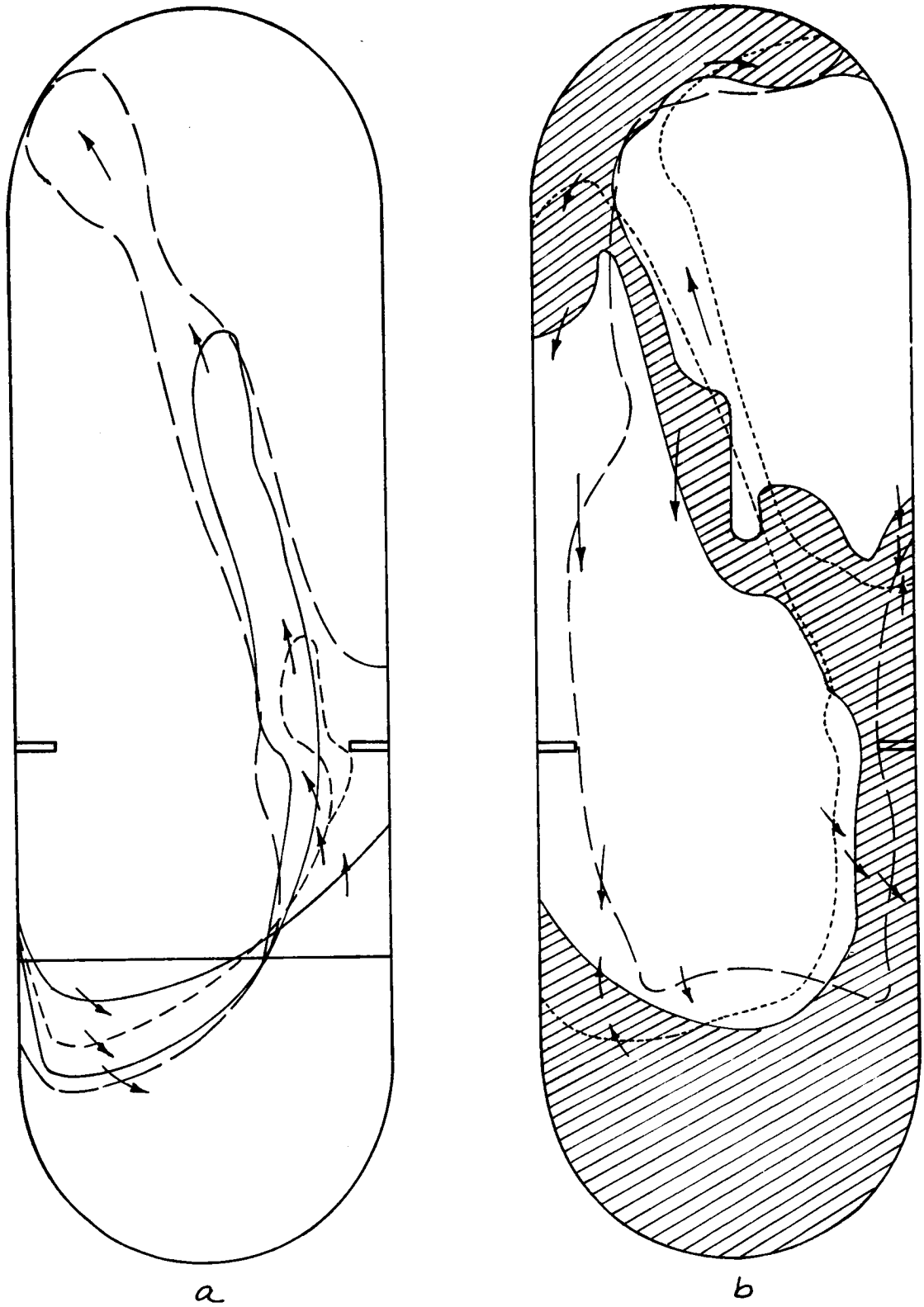

Residual Slosh Wave Profiles in Tank With Ring Baffle

Figure 3-40

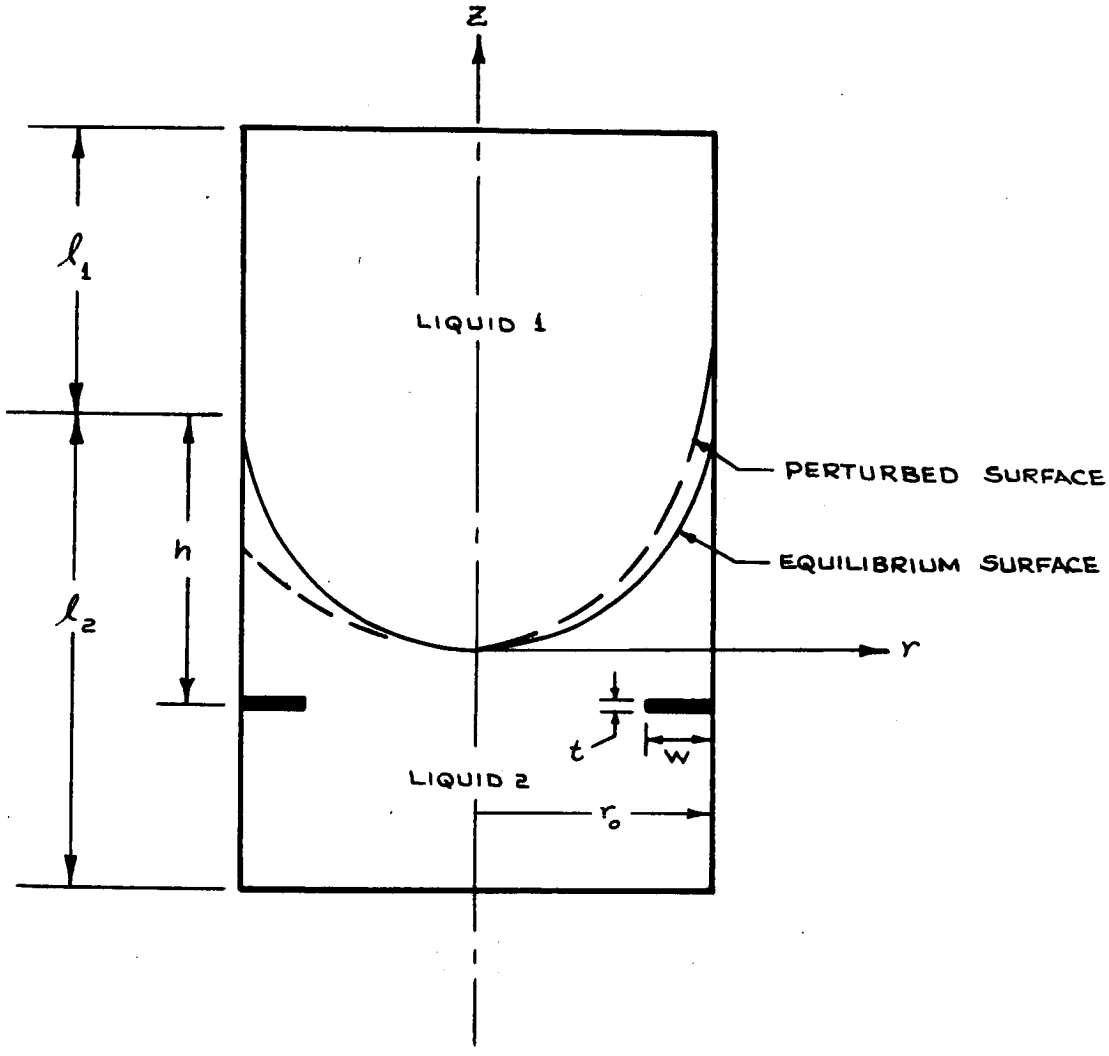

Container and Baffle Geometry for Liquid-Liquid Analog

Figure 3-41

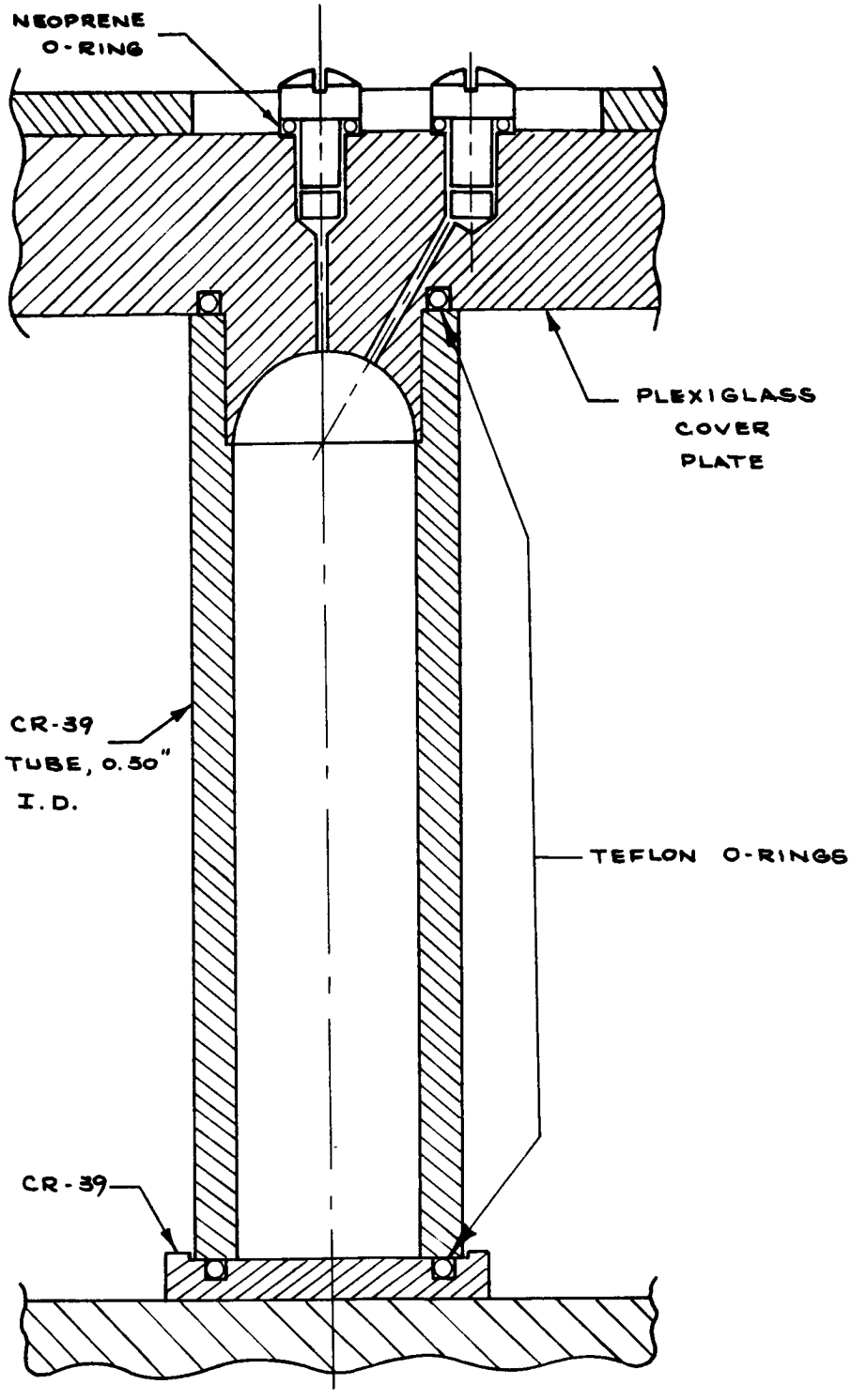

Analog Test Apparatus

Figure 3-42

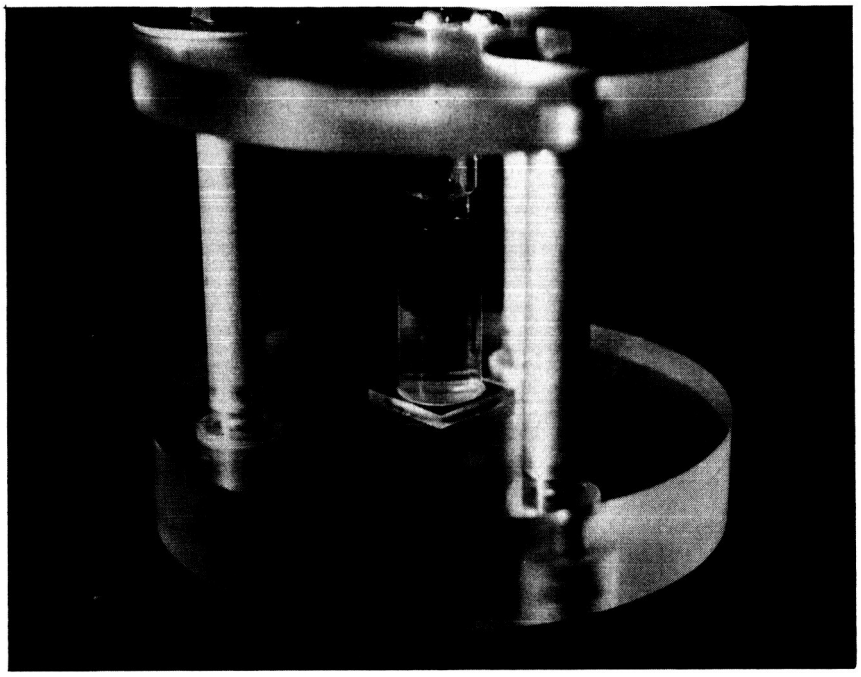

PHOTOGRAPH OF TEST APPARATUS WITH BAFFLE INSTALLED

Figure 3-43

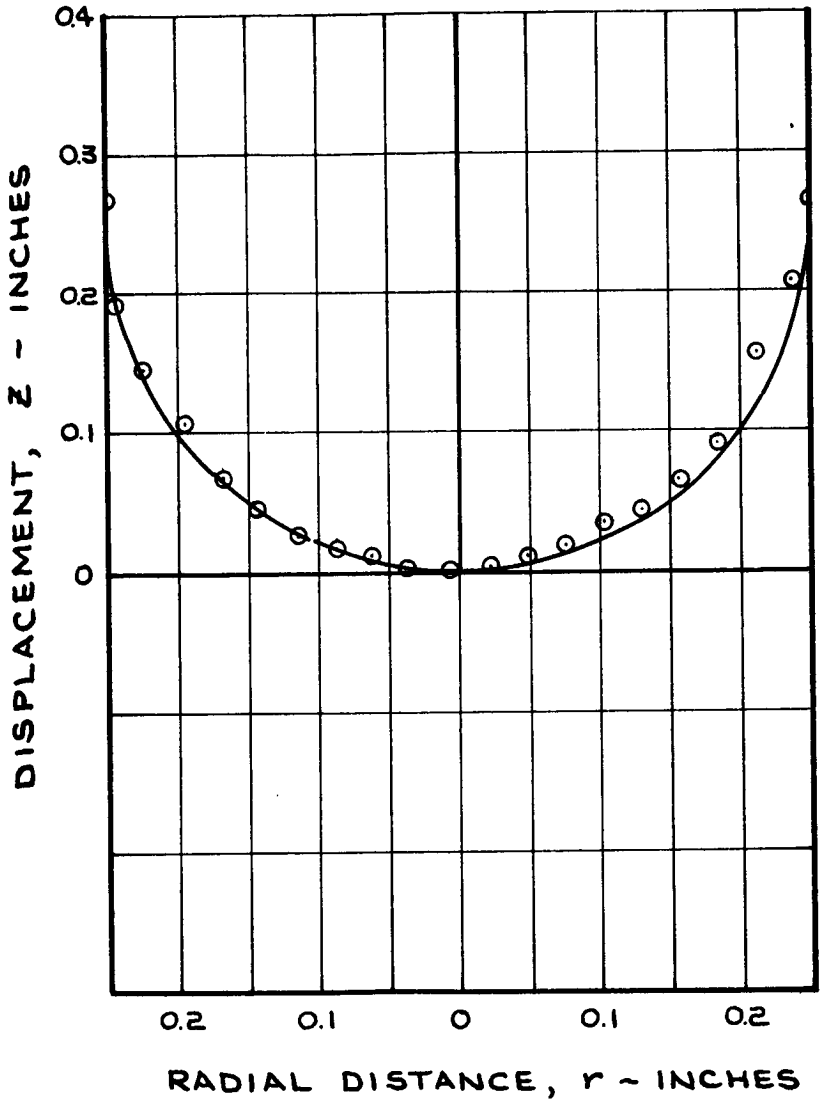

Equilibrium Interface Profile

Figure 3-44

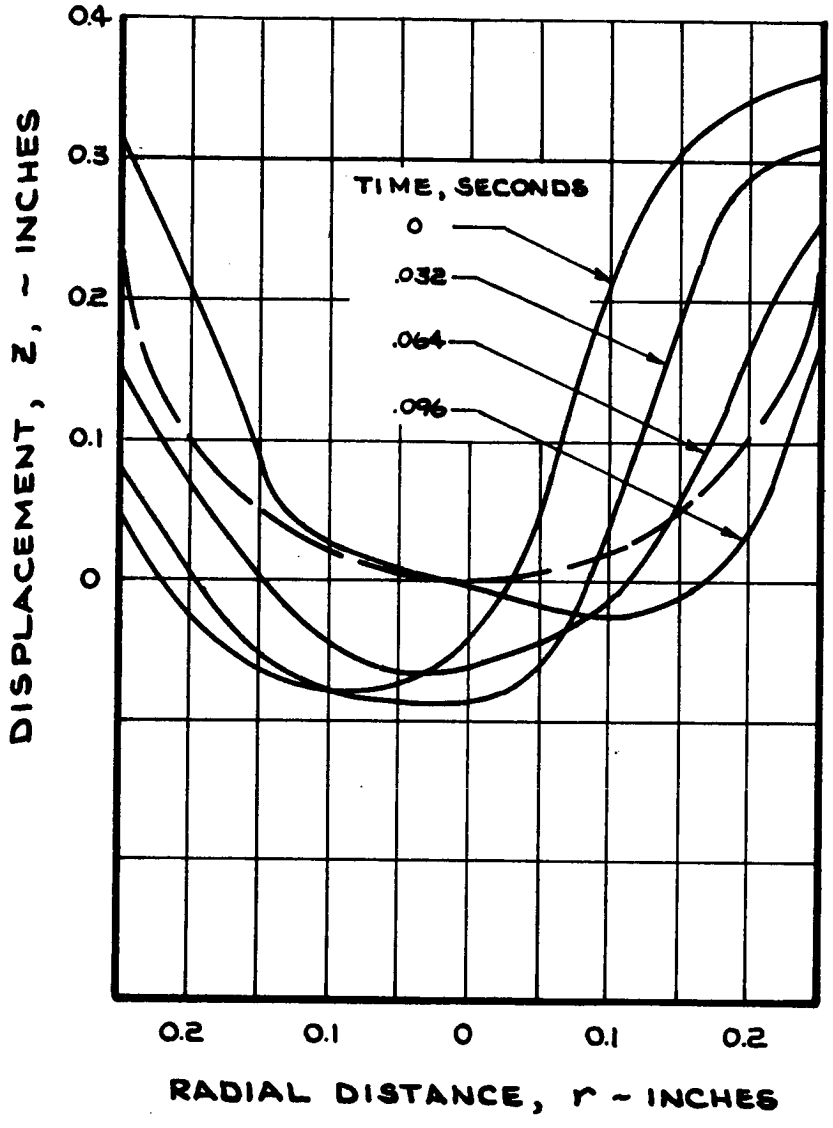

Interface Sloshing Profiles Subsequent to Slosh Initiation in Unbaffled Tank

Figure 3-45

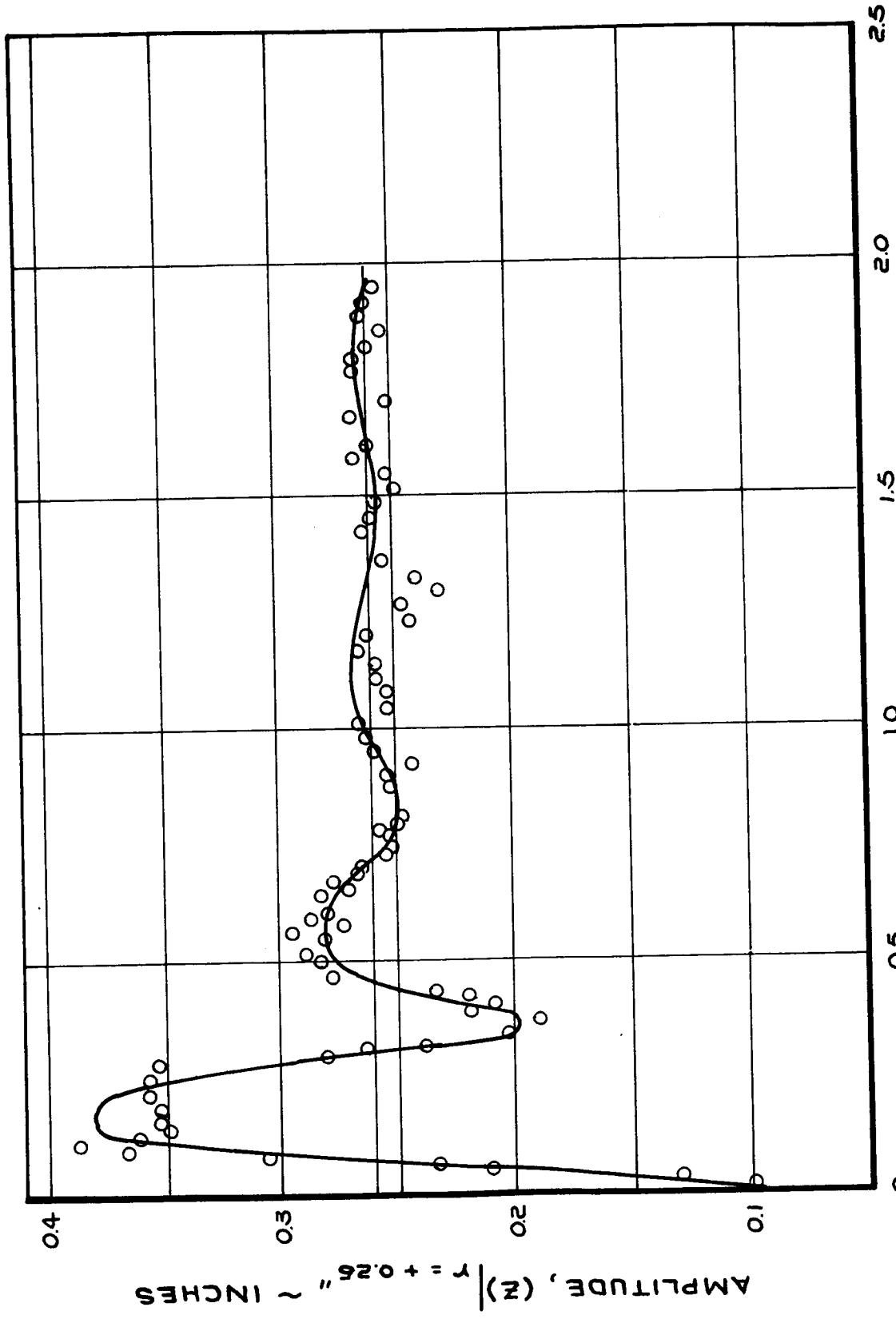

Wall Wave Amplitude vs. Time for Clean Tank

Figure 3-46

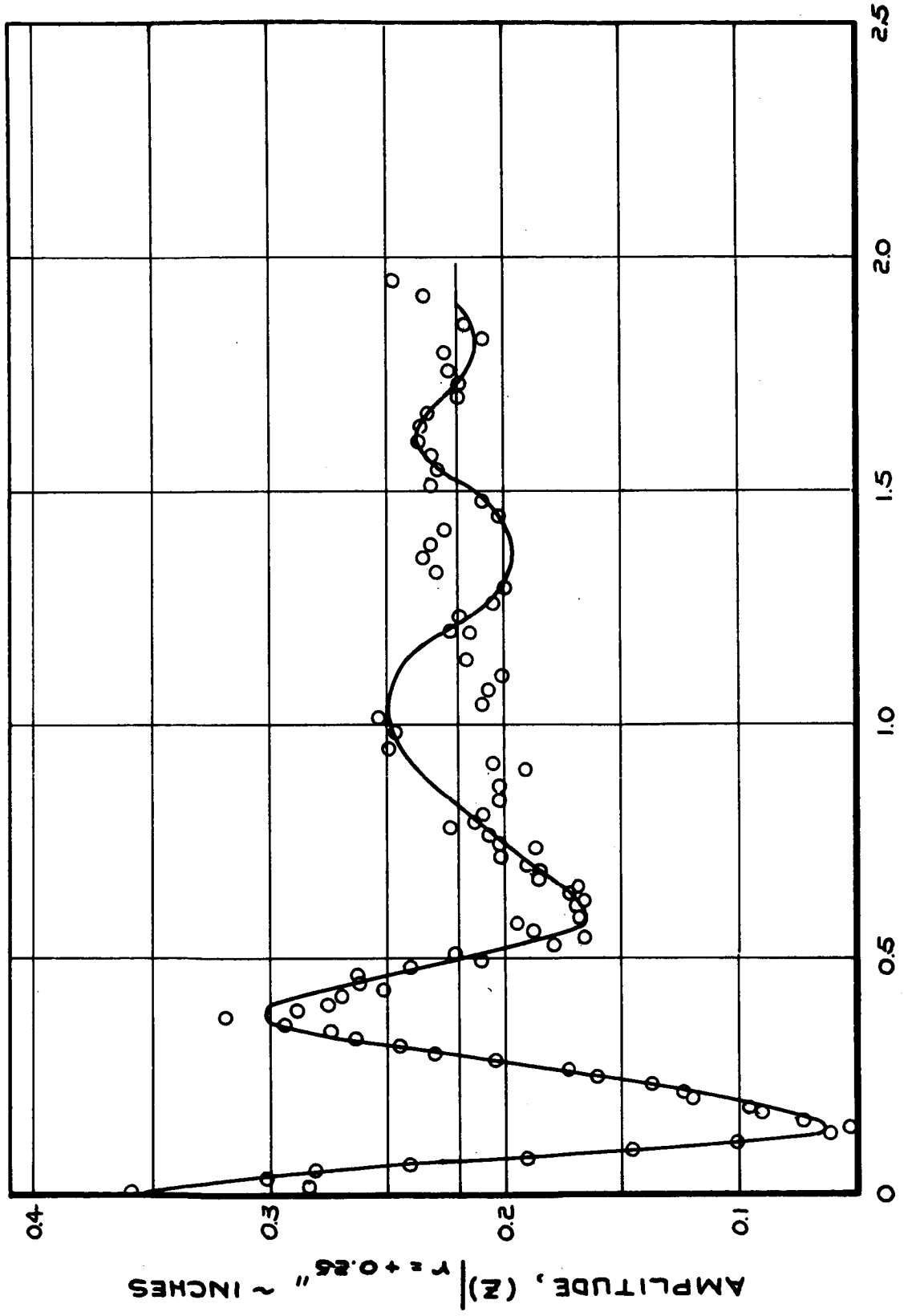

Wall Wave Amplitude vs. Time for Clean Tanks

Figure 3-47

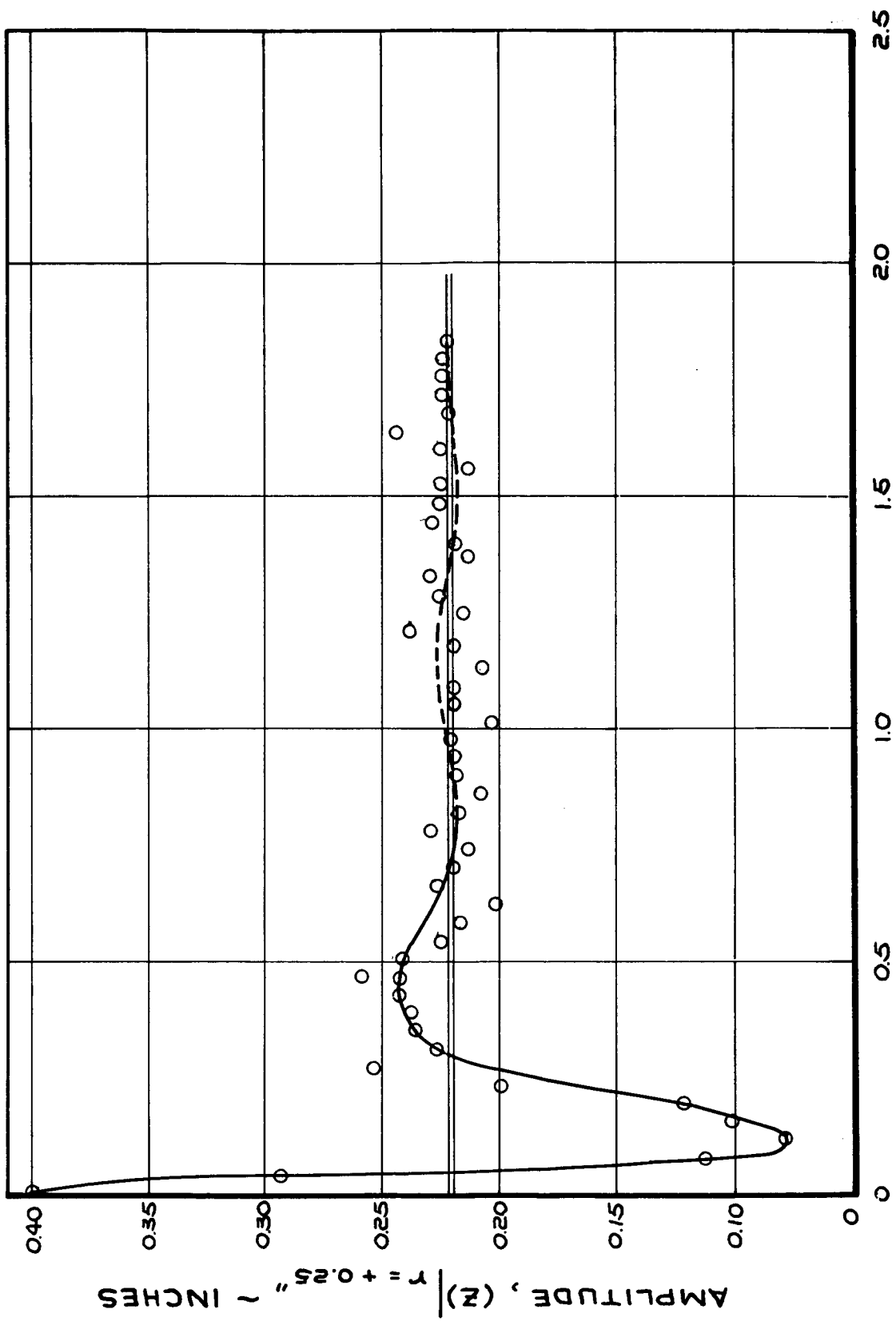

Wall Wave Amplitude vs. Time, Baffle $h/r_o = 1.72$

Figure 3-48

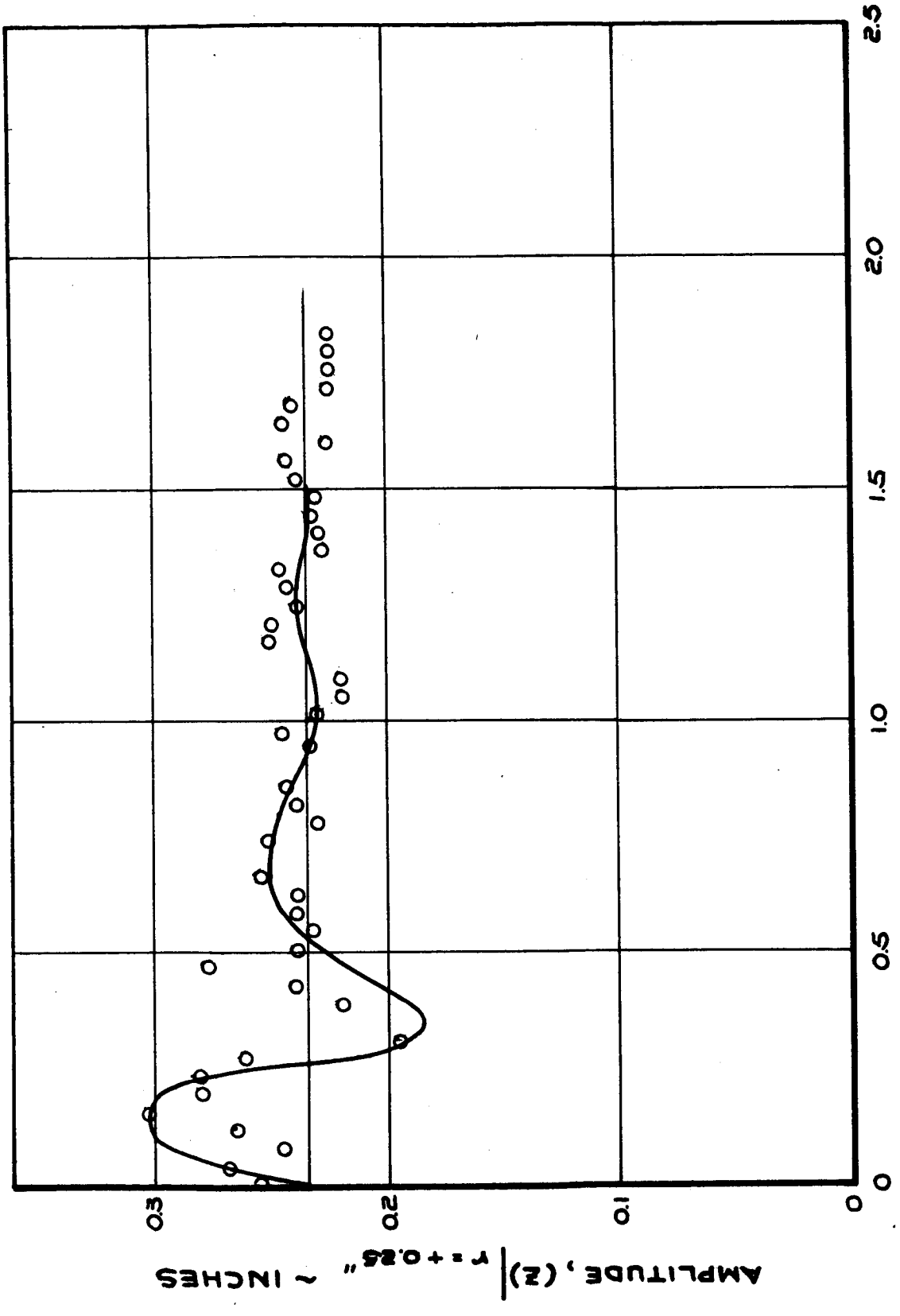

Wall Wave Amplitude vs. Time, Baffle $h/r_o = 1.72$

Figure 3-49

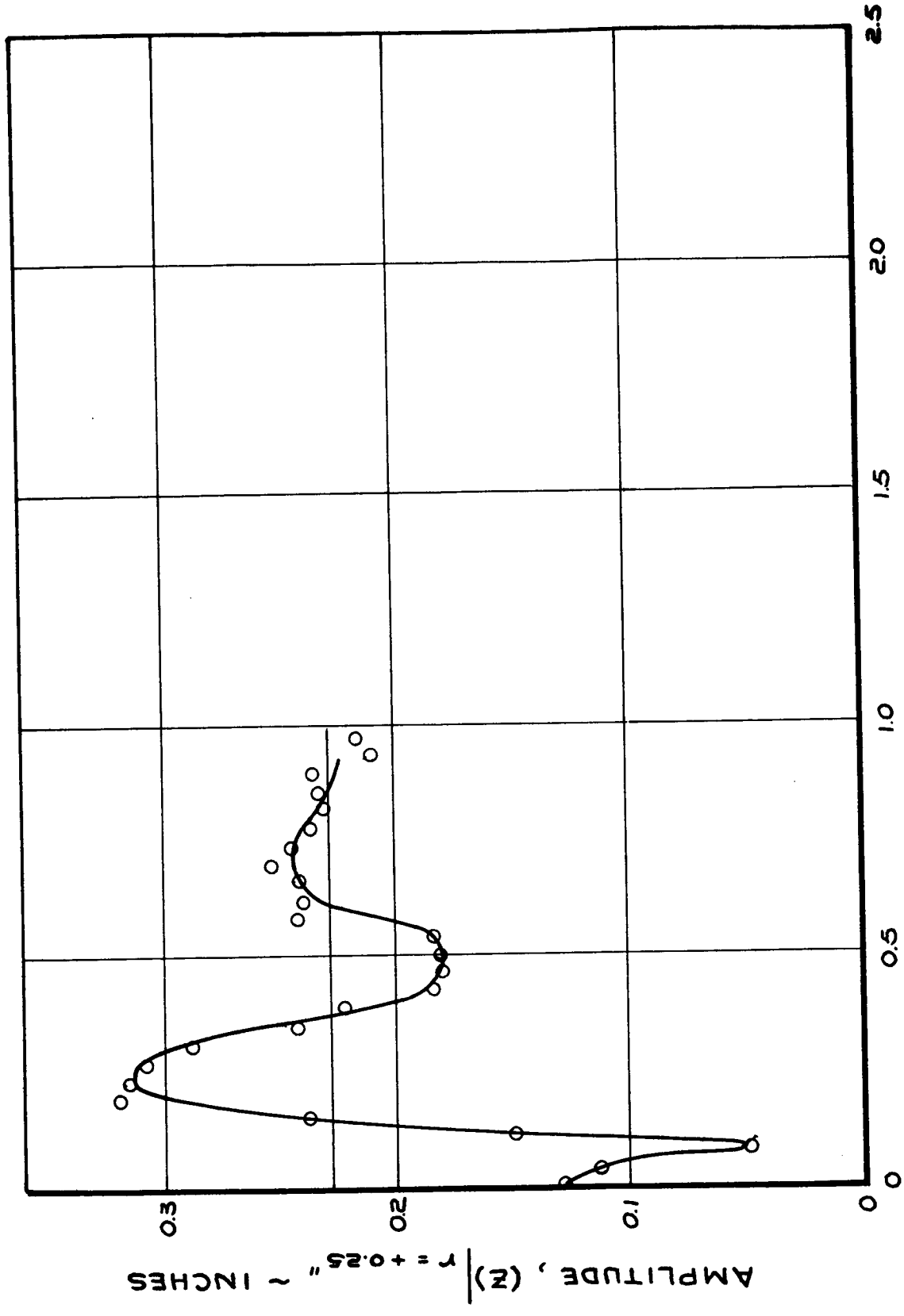

Wall Wave Amplitude vs. Time, Baffle $h/r_o = 1.44$

Figure 3-50

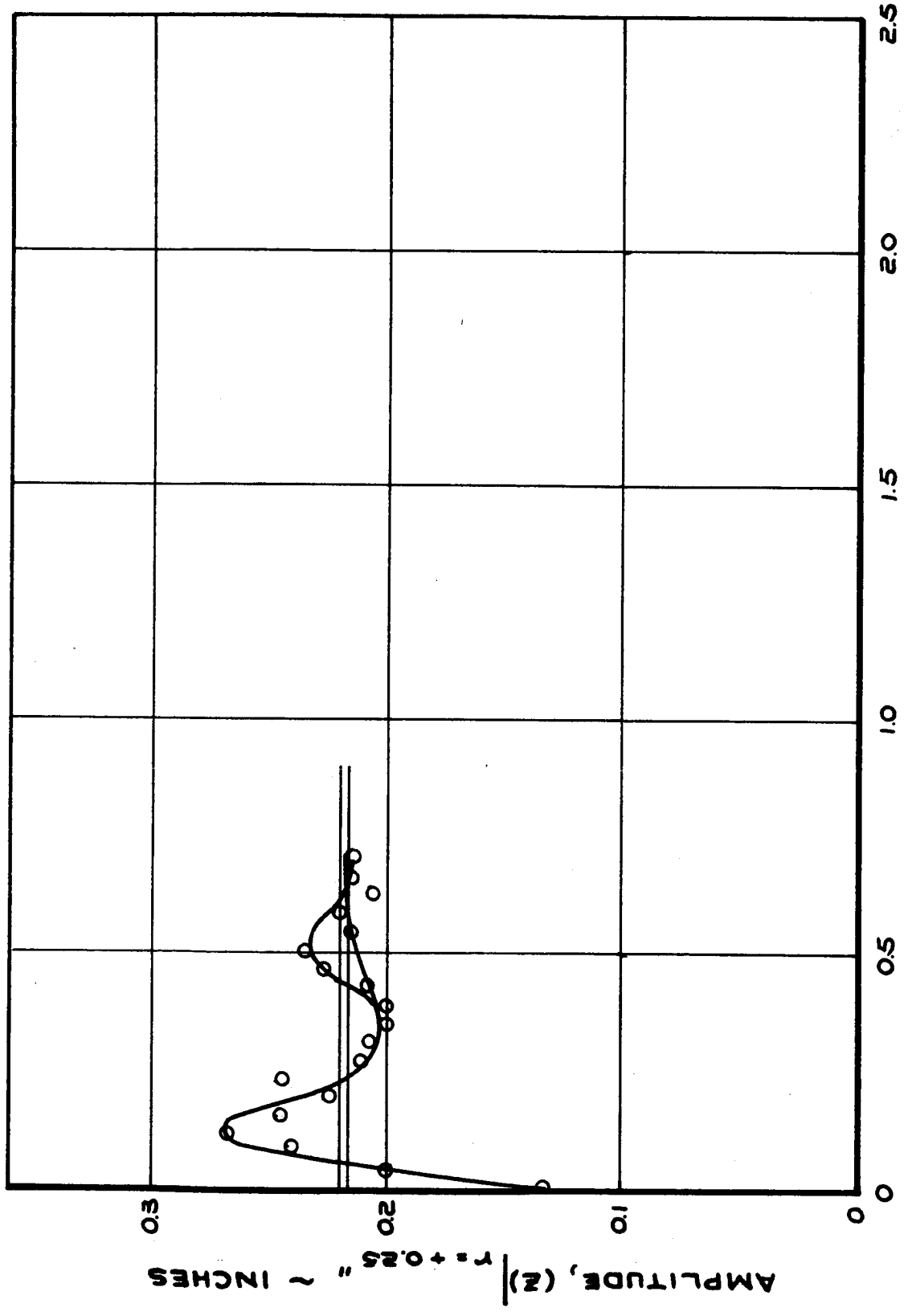

Wall Wave Amplitude vs. Time, Baffle $h/r_o = 0.52$

Figure 3-51

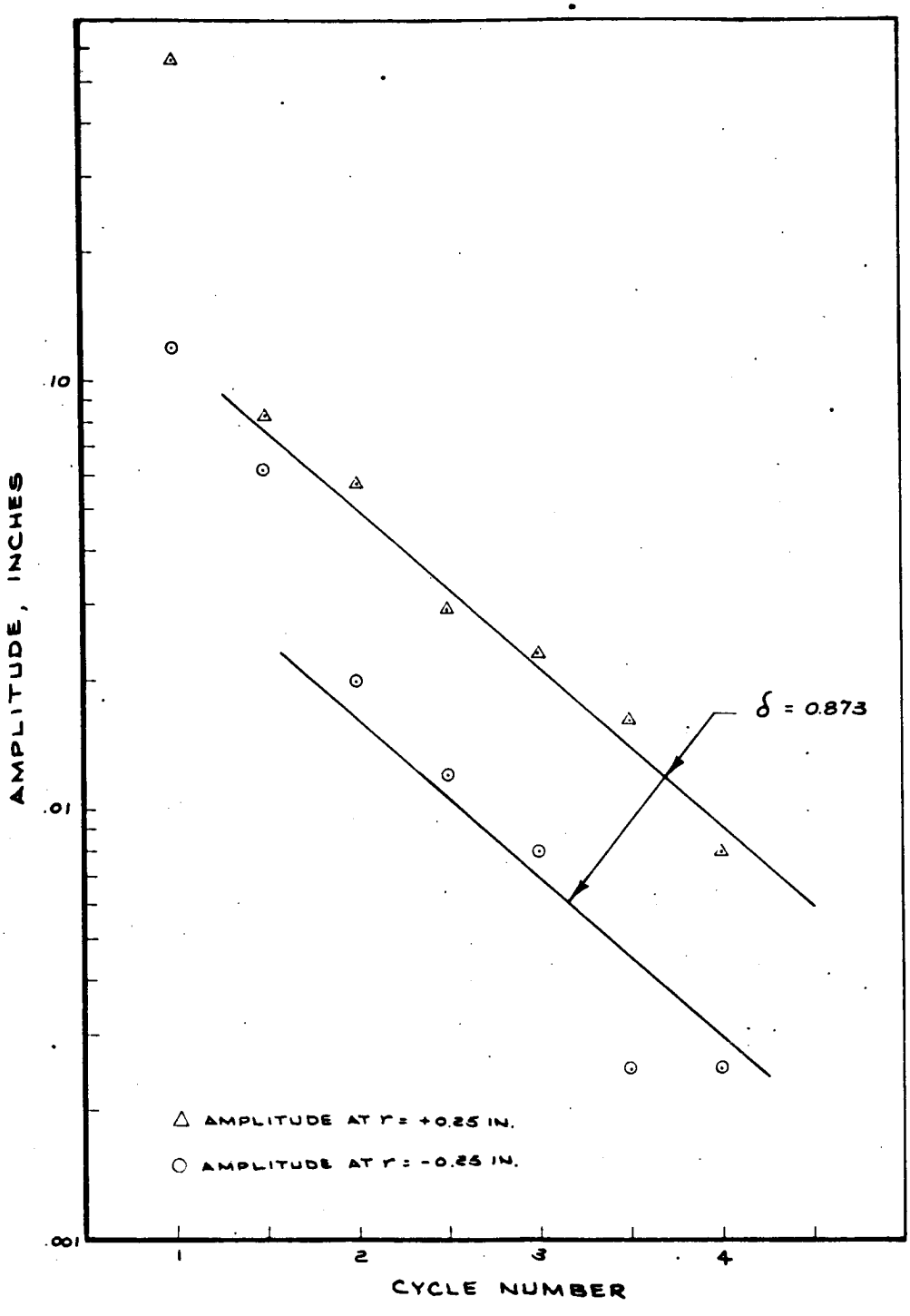

Damping of Interface Oscillations in Clean Tank

Figure 3-52

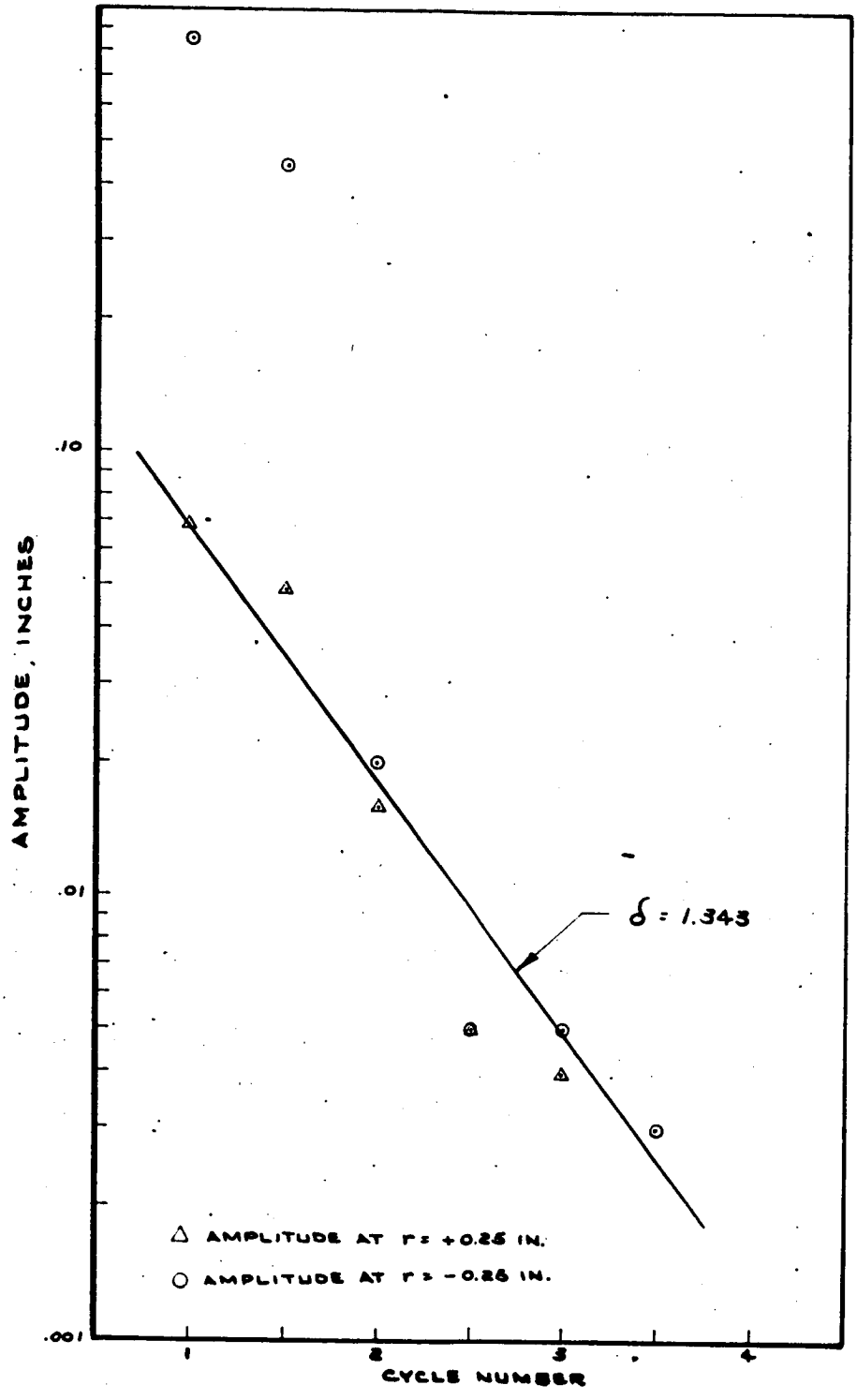

Damping of Interface Oscillations in Baffled Tank

Figure 3-53

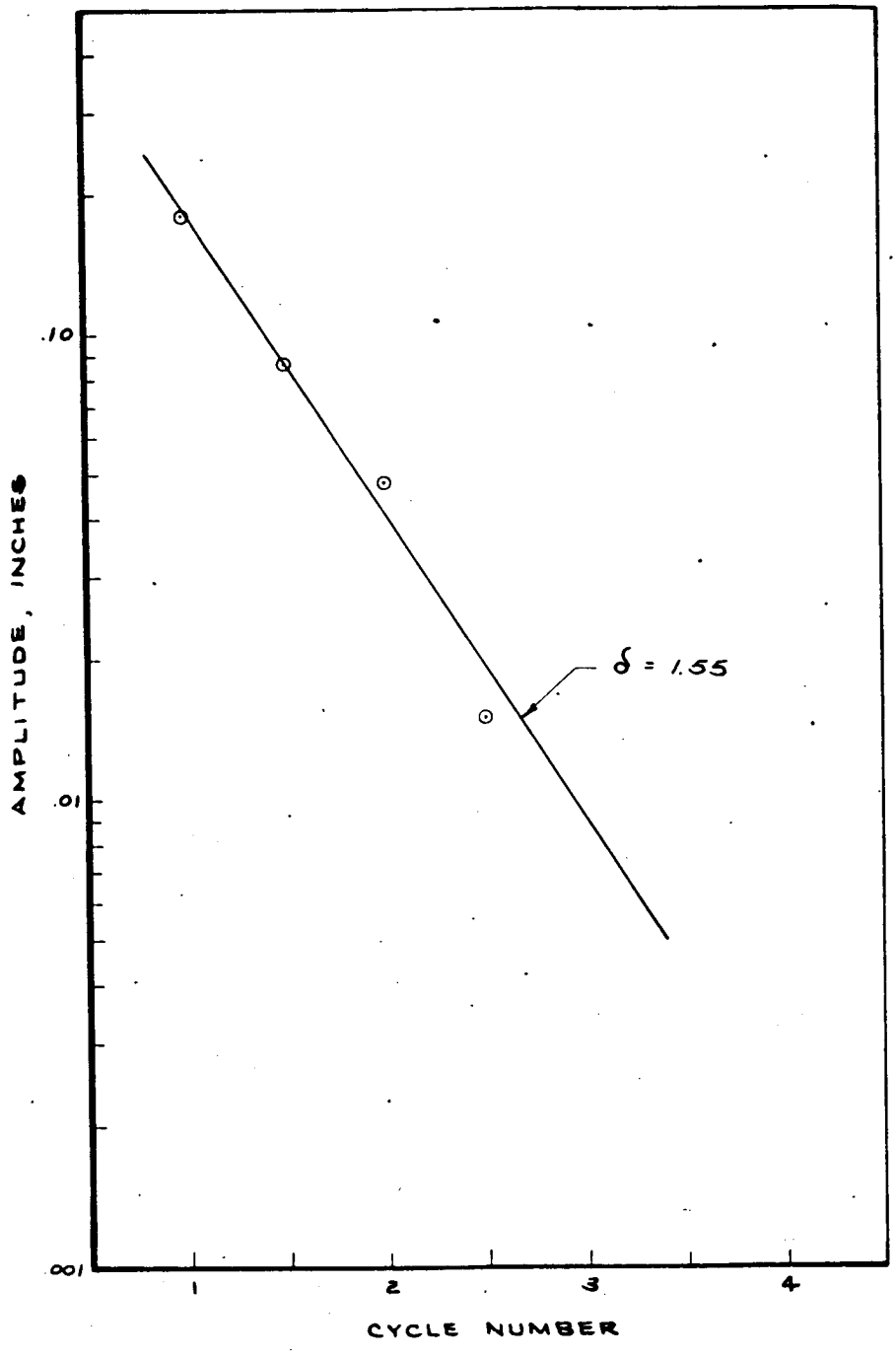

Damping of Interface Oscillations in Tank With Baffle

Figure 3-54

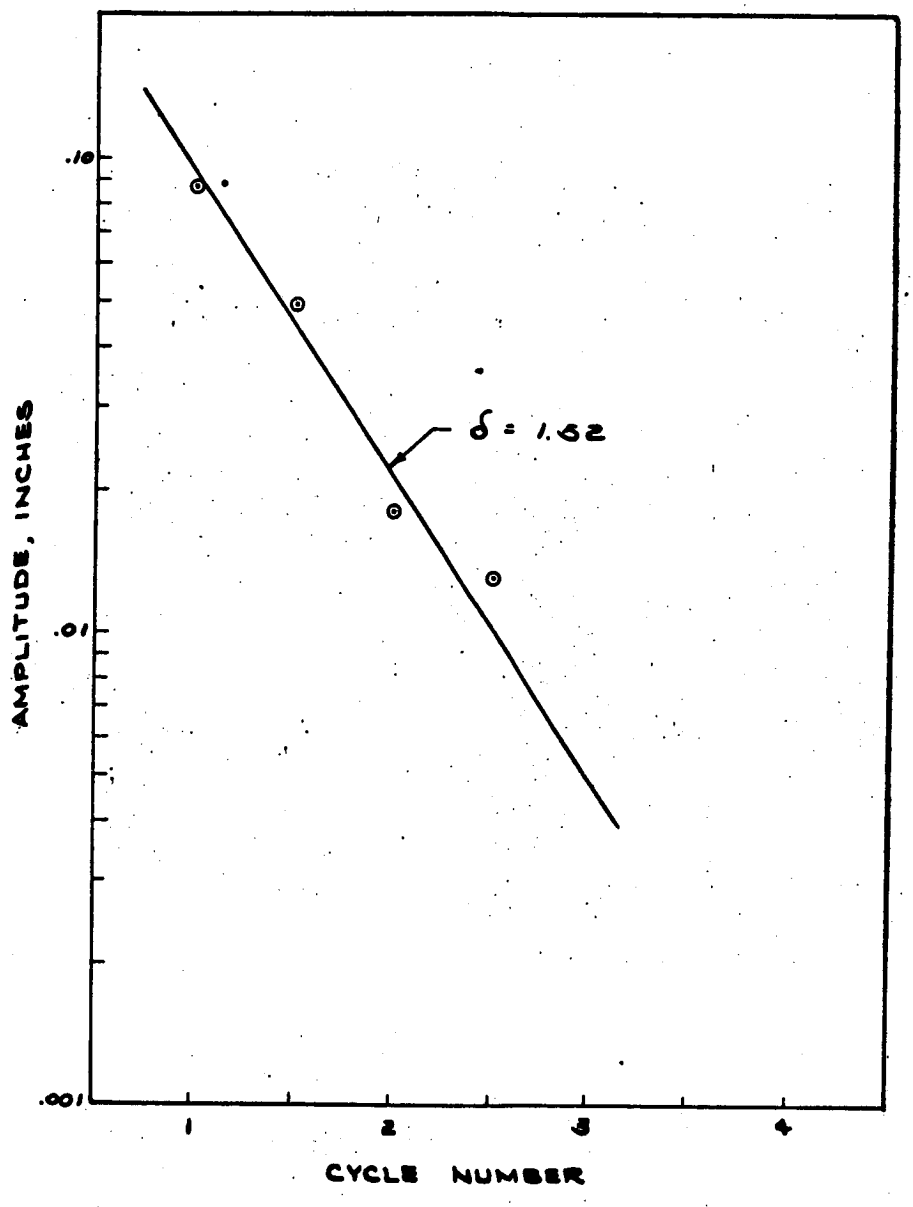

Damping of Interface Oscillations in Tank With Baffle

Figure 3-55

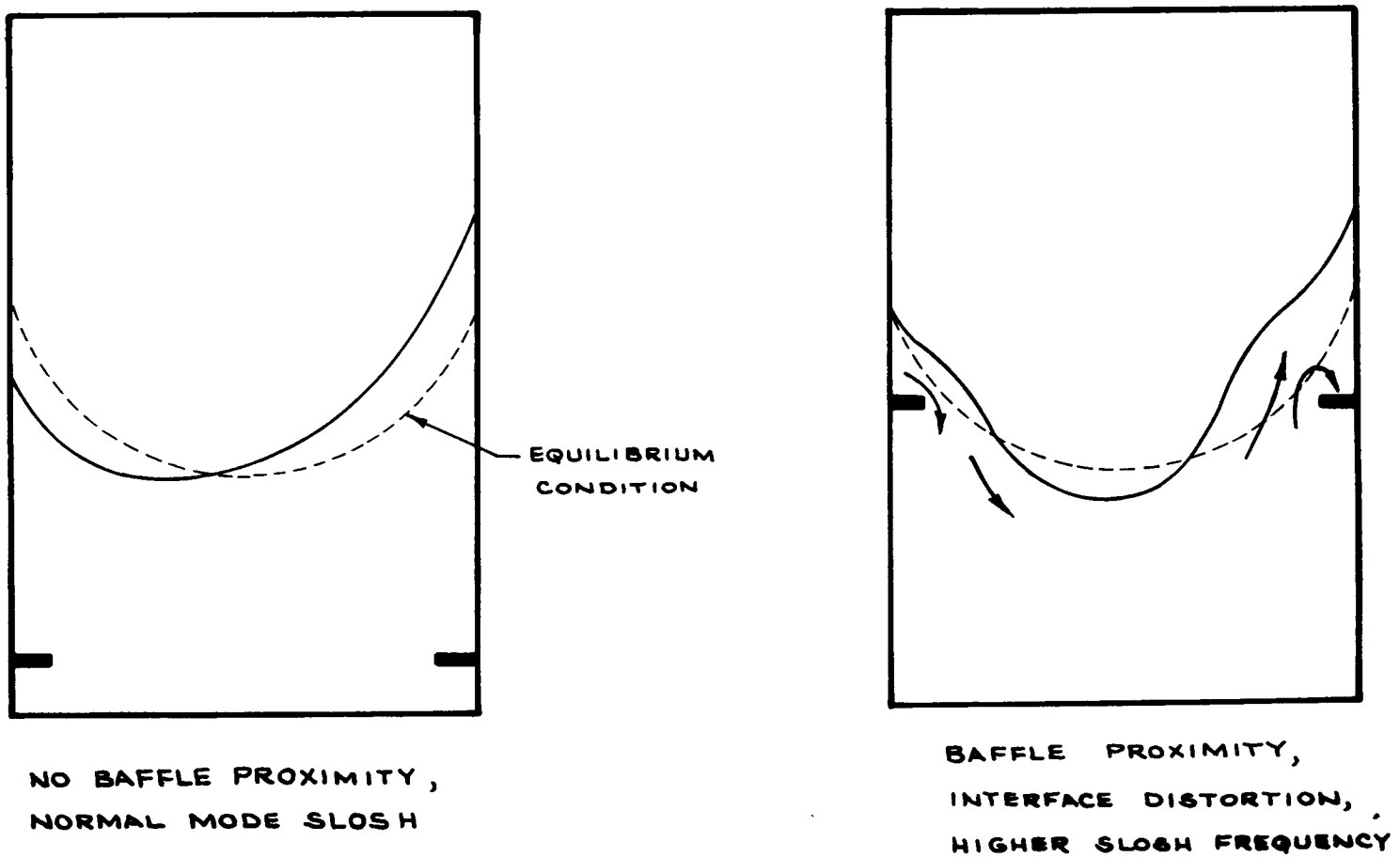

Effect of Baffle Proximity

Figure 3-56

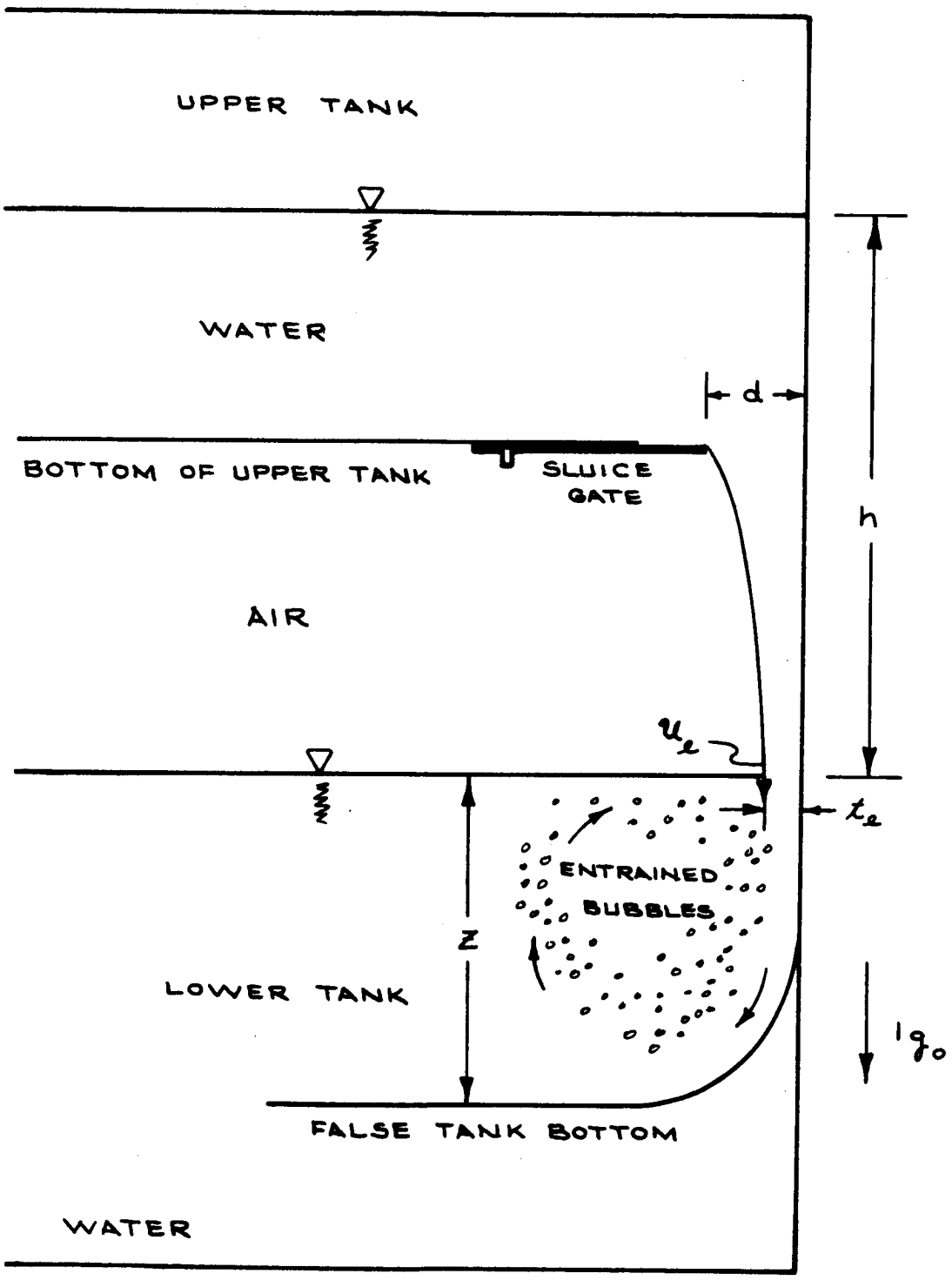

Test Apparatus Flow Geometry

Figure 3-57

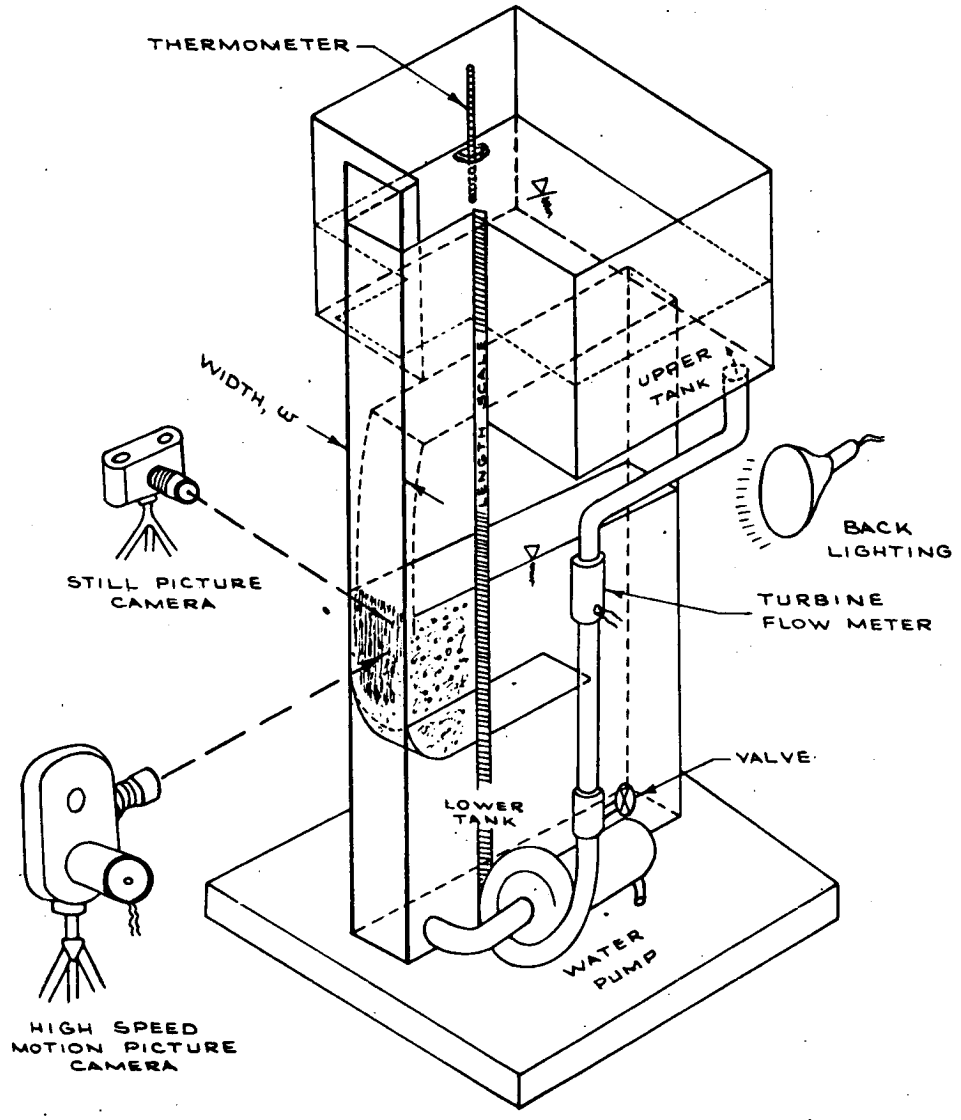

Isometric Drawing of Experimental Apparatus

Figure 3-58

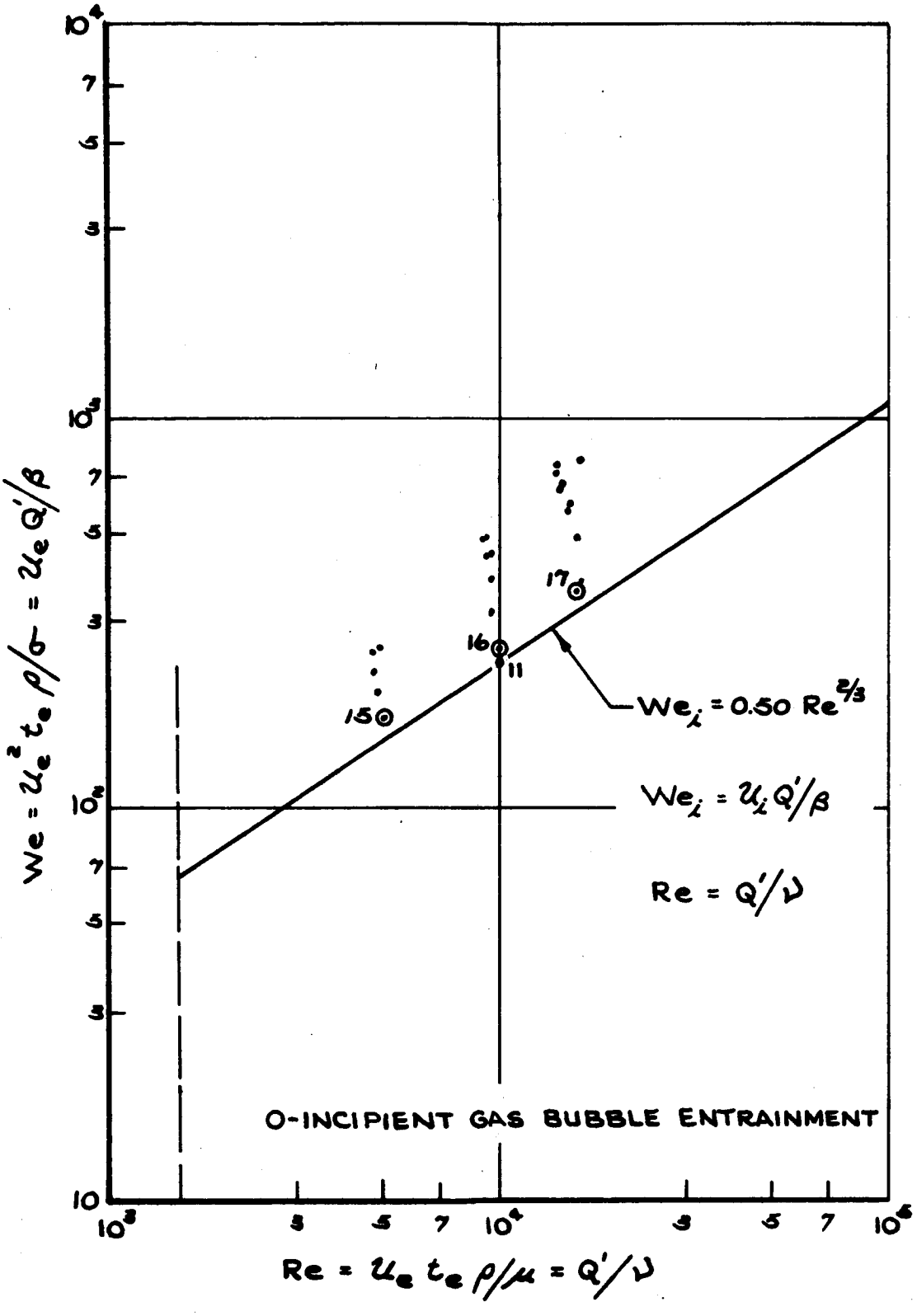

Weber Number Versus Reynolds Number

For Gas Bubble Entrainment Tests, Acceleration = 1g

Figure 3-59

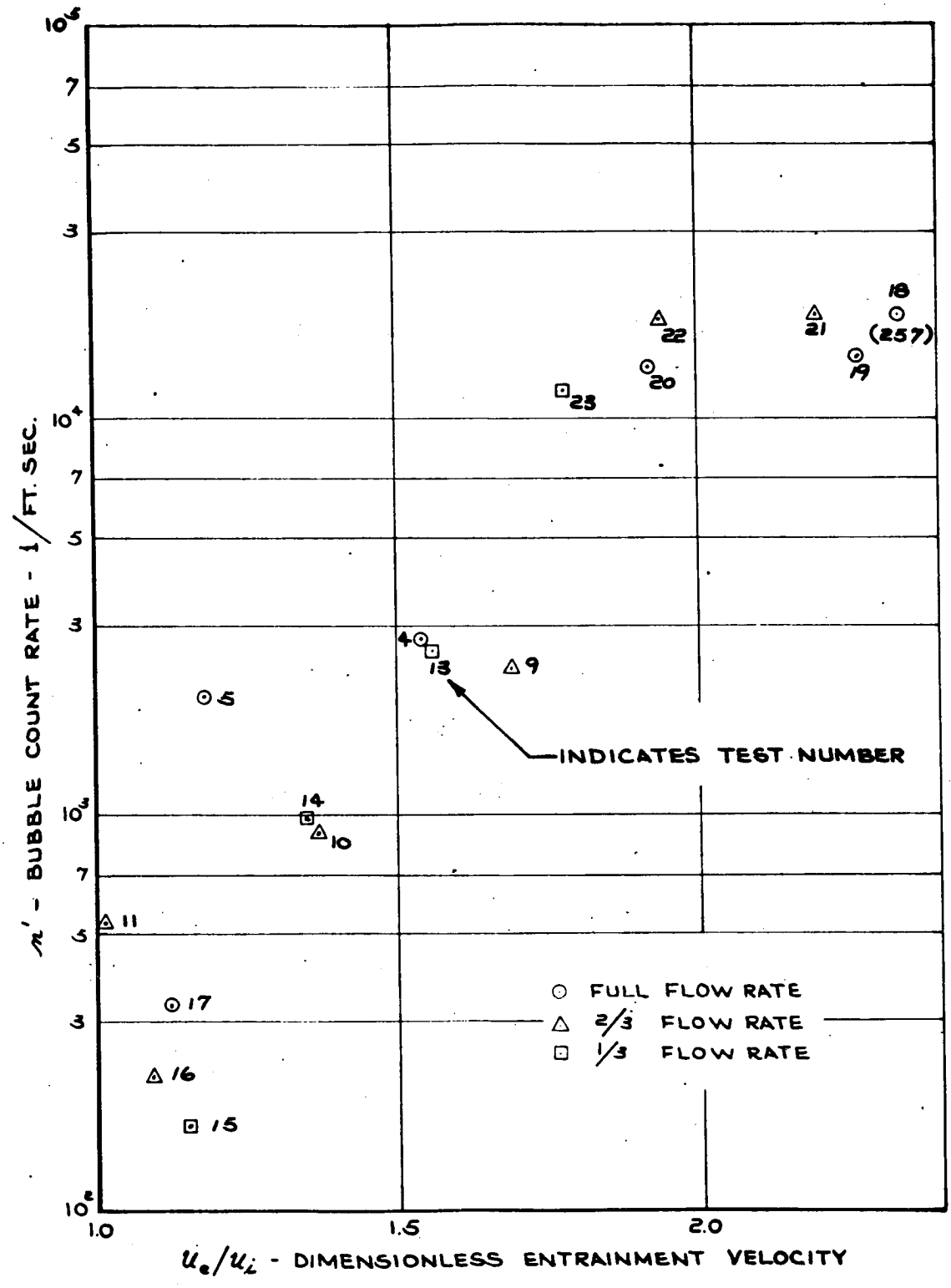

Characteristic Bubble Count Versus Dimensionless Entrainment Velocity

Figure 3-60

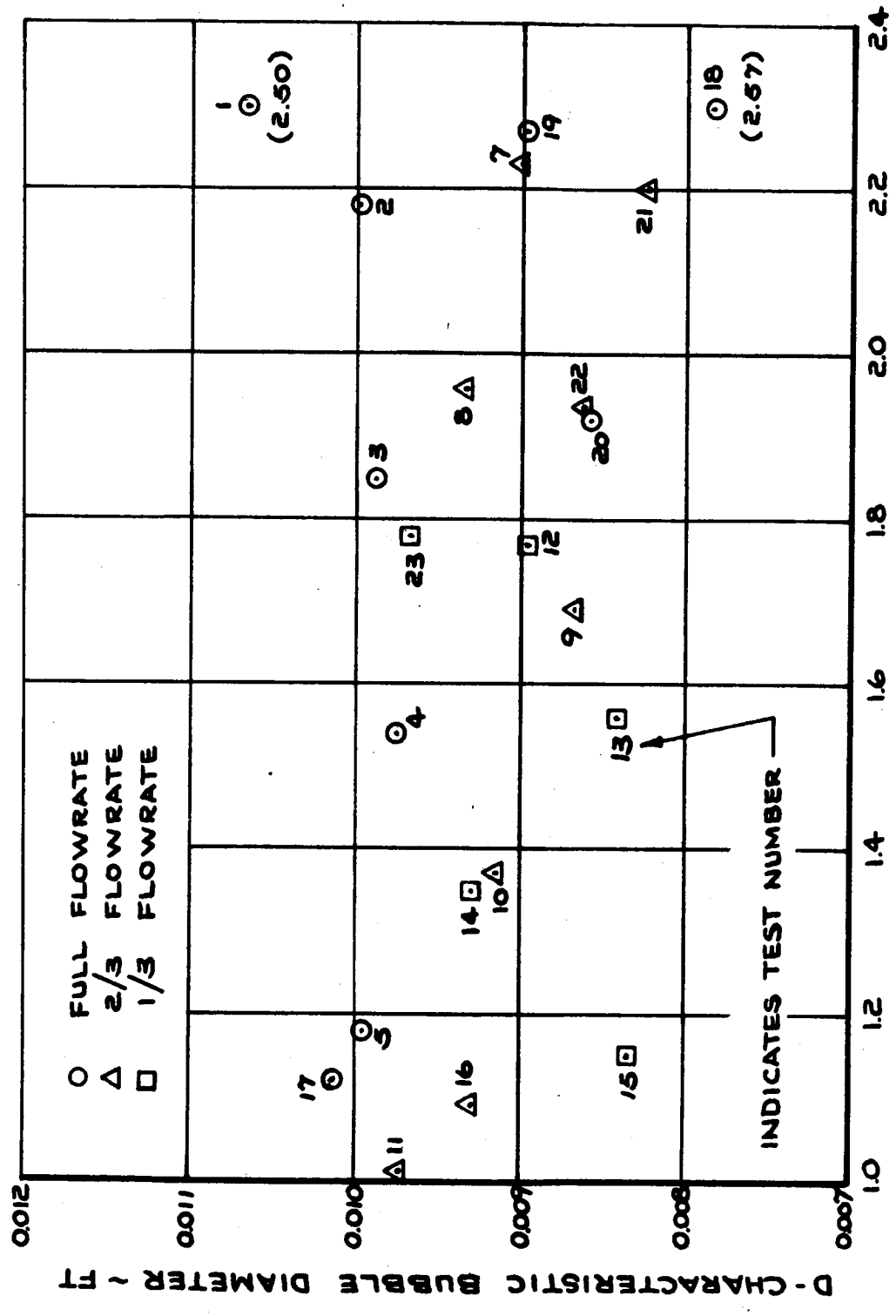

Characteristic Bubble Diameter Versus Dimensionless Entrainment Velocity

Figure 3-61

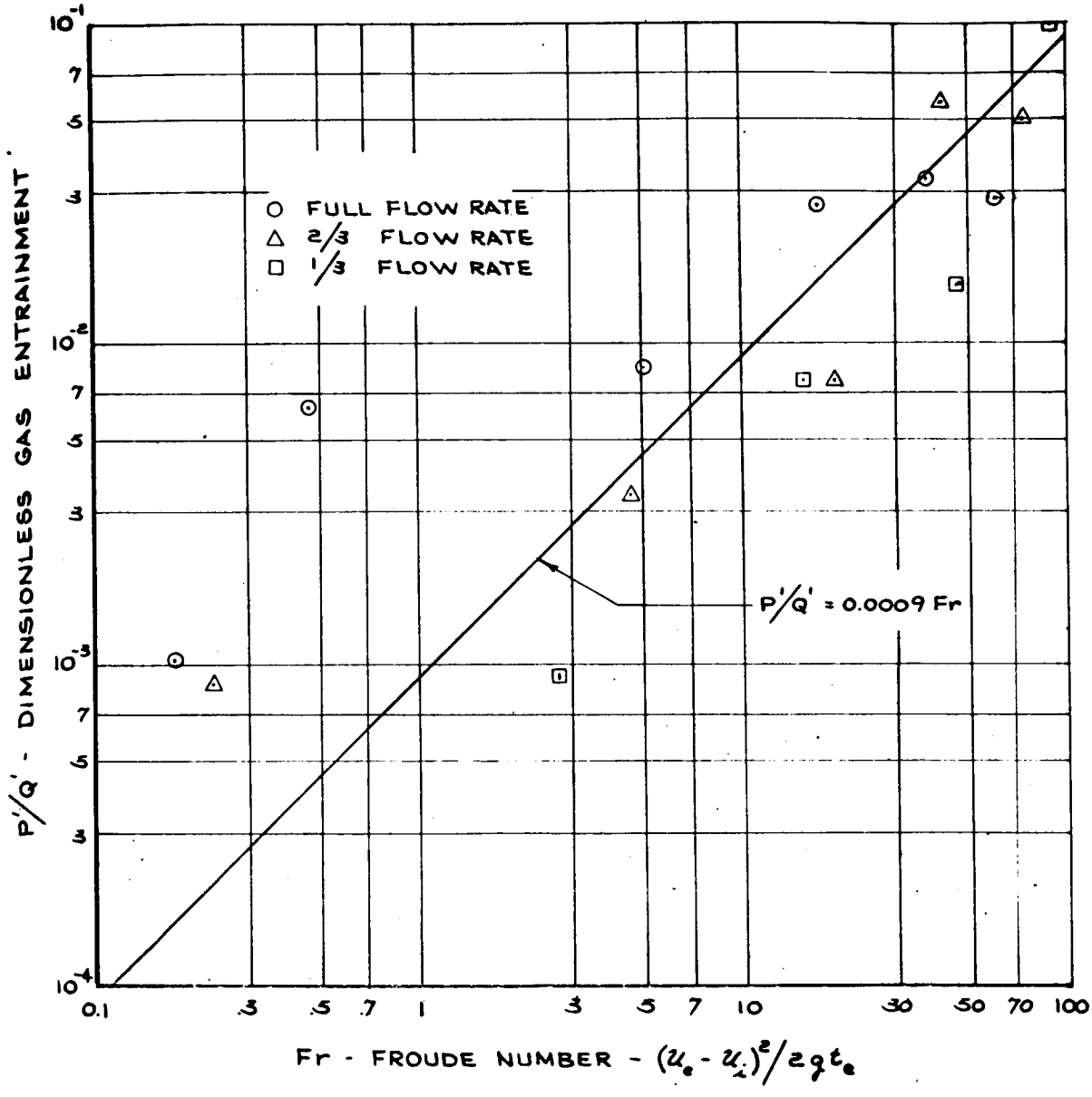

Dimensionless Gas Entrainment Versus Froude Number

Figure 3-62

ENTRAINED GAS BUBBLE DISTRIBUTION FOR LOWEST POOL DEPTH
OF Z = 8 INCHES

Figure 3-63a

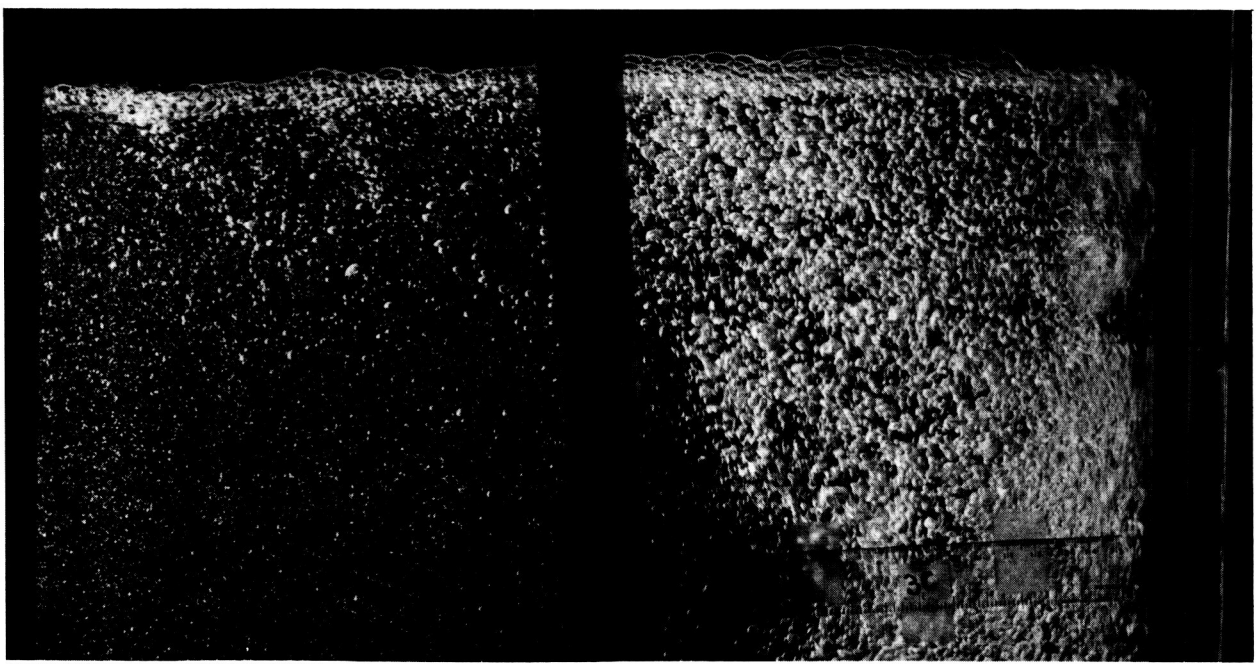

ENTRAINED GAS BUBBLE DISTRIBUTION FOR GREATEST POOL DEPTH
OF Z = 20 INCHES

Figure 3-63b

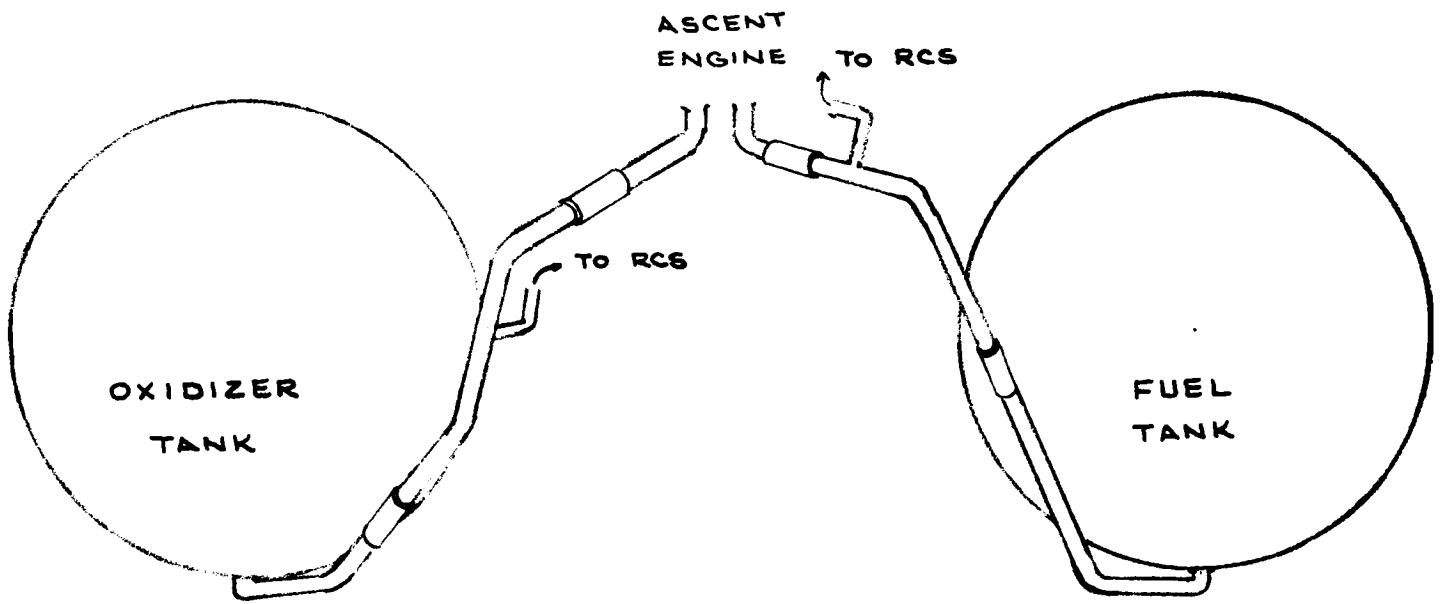

Ascent Stage Propellant System

Figure 3-64

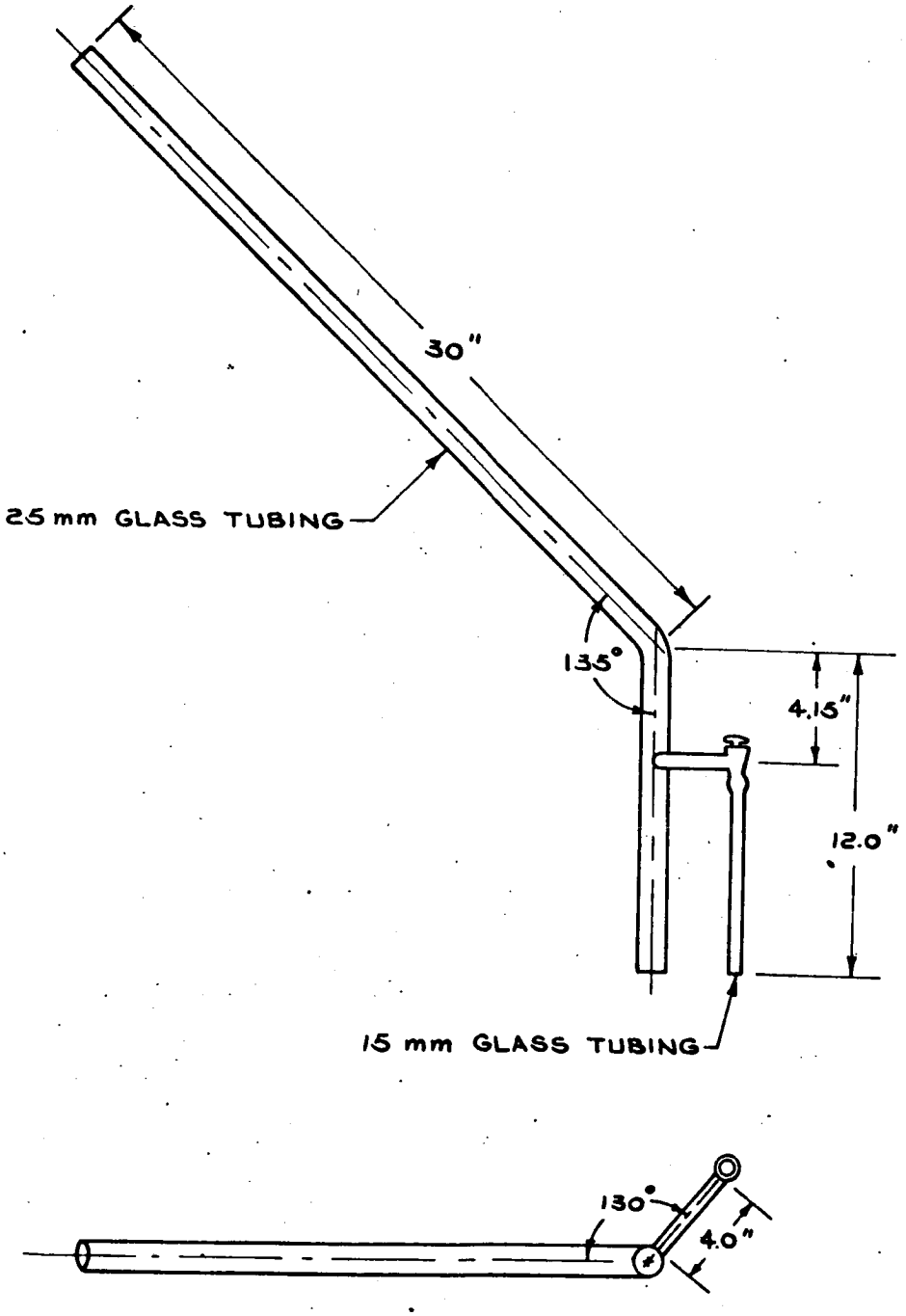

Fuel Line Model

Figure 3-65

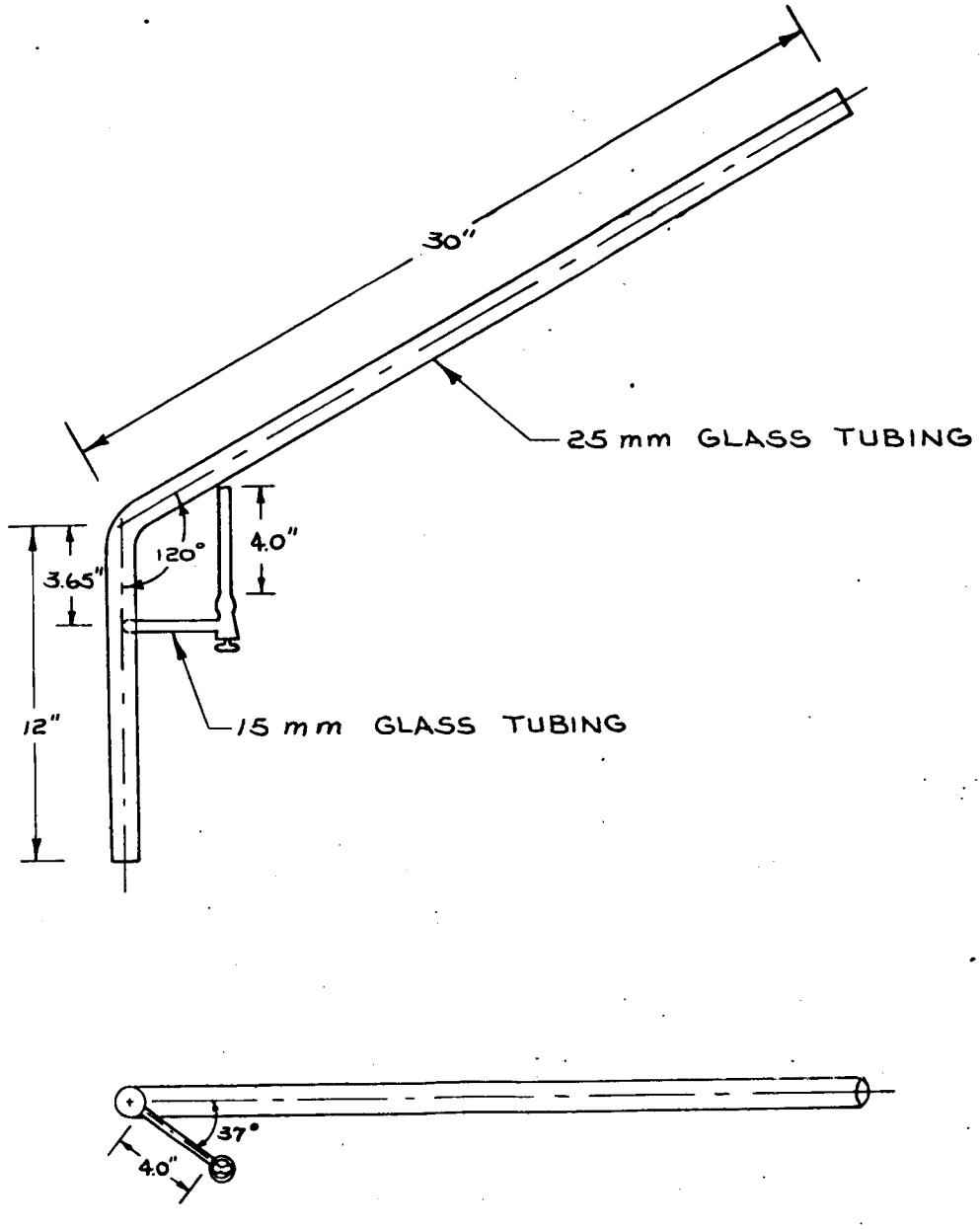

Oxidizer Line Model

Figure 3-66

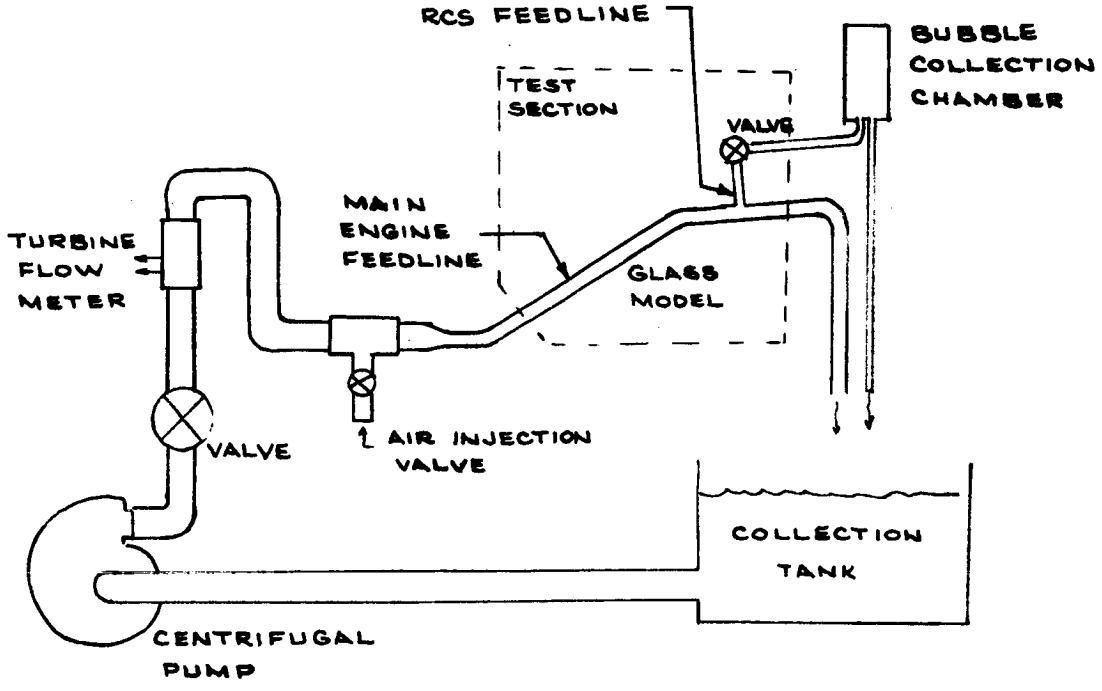

Diagram of Experimental Apparatus

Figure 3-67

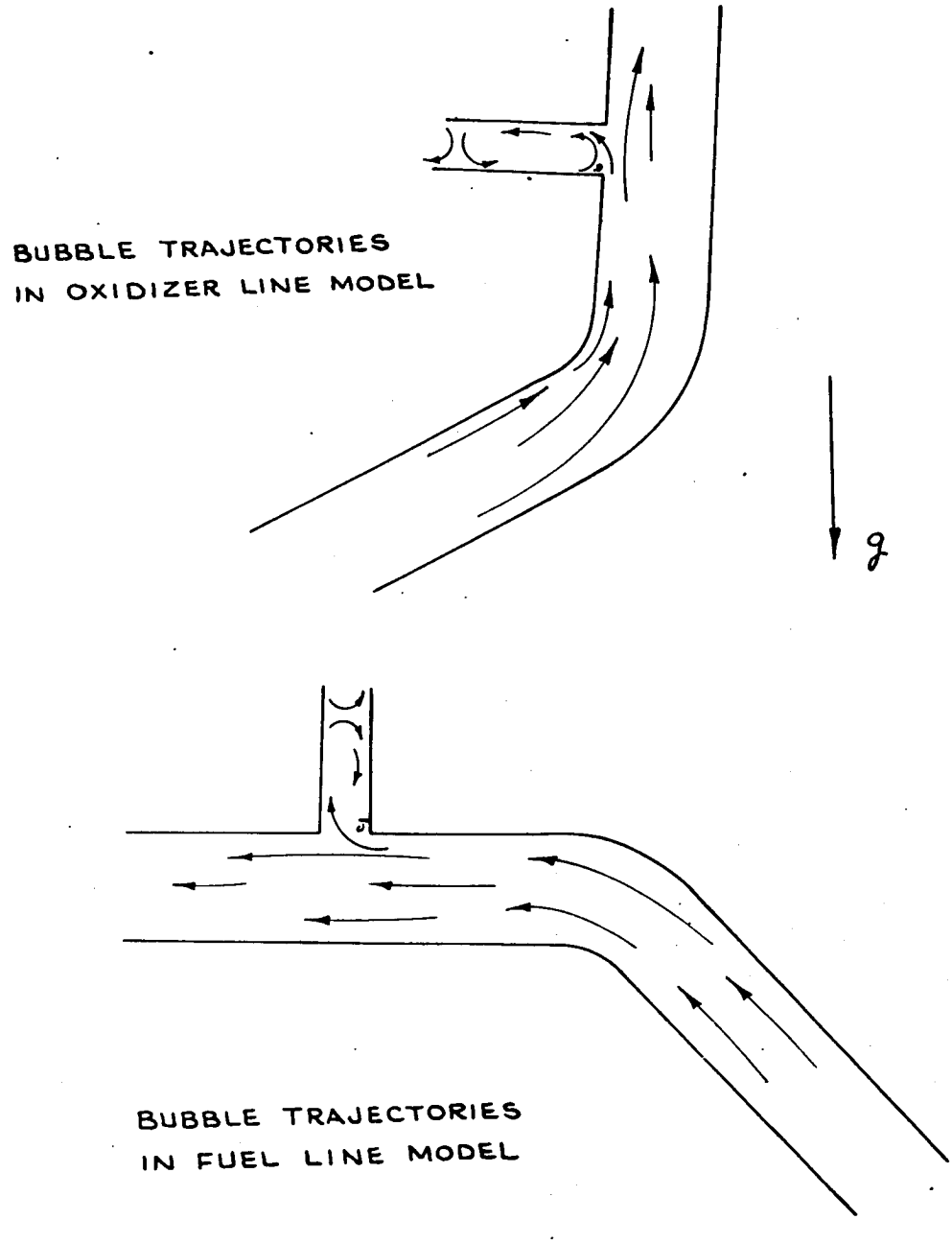

Bubble Trajectories in Fuel Line Model

Figure 3-68

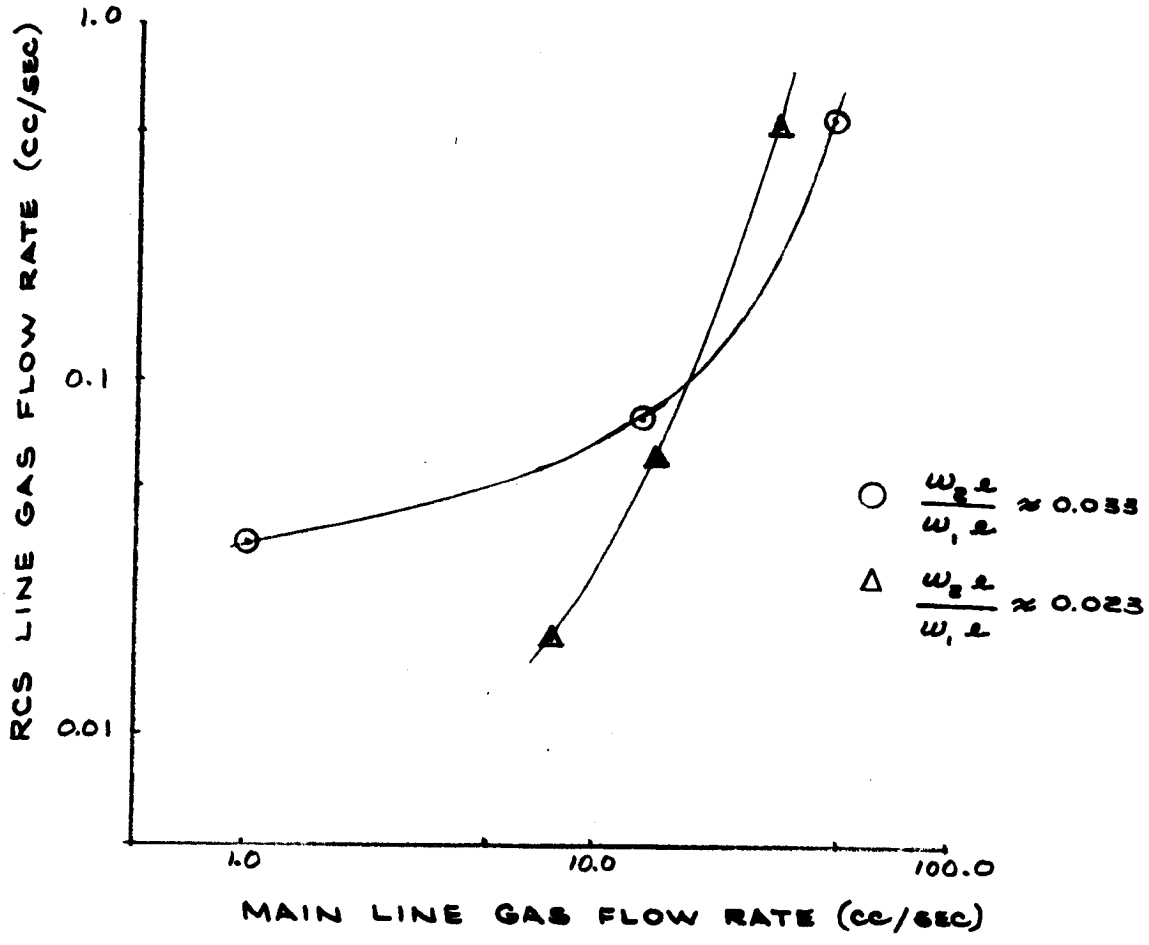

Gas Flow Rates in Fuel Line Model

Figure 3-69

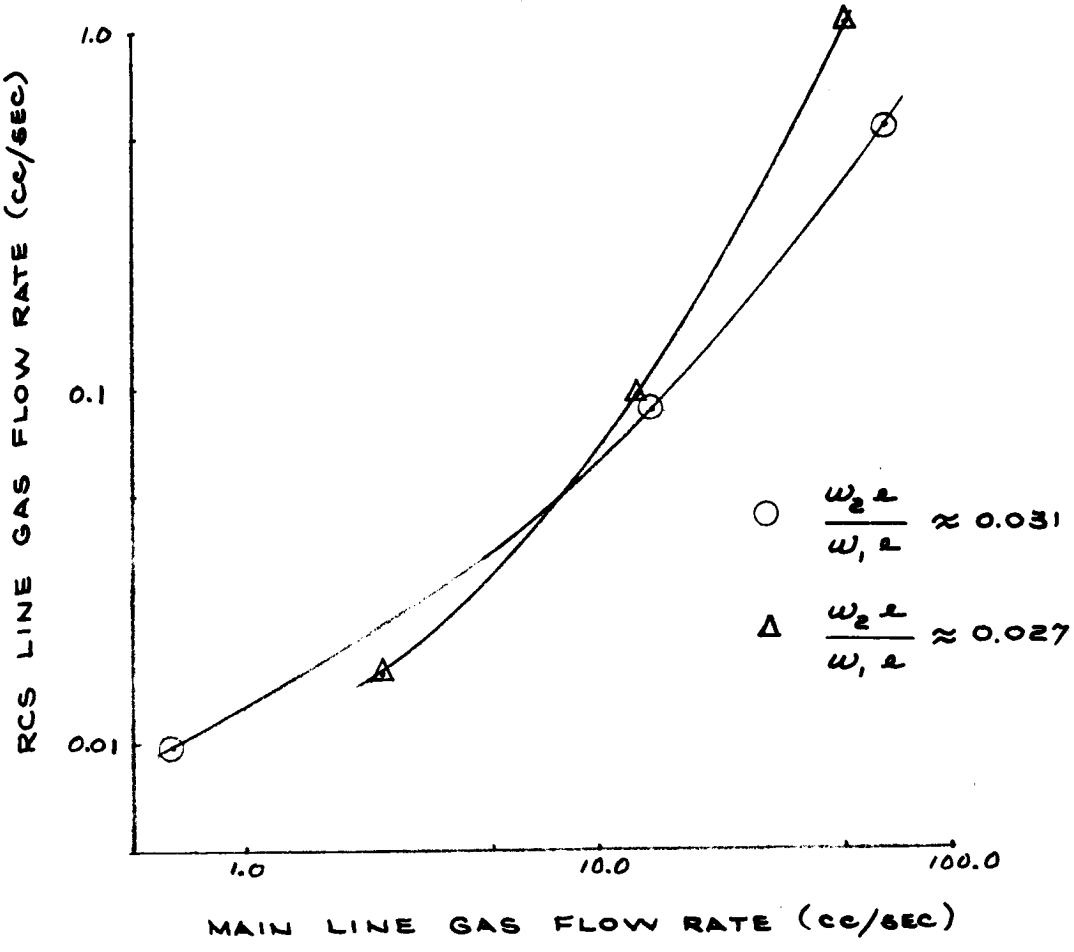

Gas Flow Rates in Oxidizer Line Model

Figure 3-70

Table 3-VIII

OXIDIZER LINE DATA

W = Flow Rates in cc Per Second

Subscripts

0 - Total Flow
1 - Flow to Ascent Engine
2 - Flow to RCS
ℓ - Liquid
q - Gas

Prototype Parameters

$R_e = \frac{D_1 V_1}{\eta_1} = 98{,}700$

$F_r = \frac{V_1^2}{g_1 D_1} = 91.1$

$\frac{W_{2\ell}}{W_{1\ell}} = 0.0323$

$Re = \frac{D_2 V_2}{\eta_2}$	$Fr = \frac{V_2^2}{g_2 D_2}$	$W_{o\ell}$	$W_{2\ell}$	$W_{1\ell}$	$\frac{W_{2\ell}}{W_{1\ell}}$	W_{oq}	W2g
87,800	76.3	1547	45.9	1501	0.0306	0.655	0.00952
87,000	74.8	1533	45.9	1487	0.0309	14.51	0.085
86,300	73.6	1522	46.7	1475	0.0316	67.7	0.533
87,600	75.9	1537	39.1	1498	0.0261	2.50	0.0157
87,300	75.4	1533	39.9	1493	0.0267	13.26	0.0928
86,000	73.2	1513	41.6	1471	0.0283	52,9	1.035
48,000	22.8	841	20.4	821	0.0249	0.839	0.00017
47,900	22.7	841	21.7	819	0.0265	66.4	0.0532
47,700	22.5	838	22.2	816	0.0272	82.1	0.563
89,100	78.5	1523	0	1523	0	29.6	0.00018*

*This is net gas flow rate into RCS feed line before the feed line is saturated with gas

Table 3-VII

FUEL LINE DATA

W = Flow Rates in cc Per Second

Subscripts

0 - Total Flow
1 - Flow to Ascent Engine
2 - Flow to RCS
ℓ - Liquid
g - Gas

Prototype Parameters

$$Re = \frac{D_1 V_1}{\eta_1} = 92{,}500$$

$$Fr = \frac{V_1^2}{g_1 D_1} = 91.1$$

$$\frac{W_{2\ell}}{W_{1\ell}} = 0.0280$$

$Re = \frac{D_2 V_2}{\eta_2}$	$Fr = \frac{V_2^2}{g_2 D_2}$	$W_{o\ell}$	$W_{2\ell}$	$W_{1\ell}$	$\frac{W_{2\ell}}{W_{1\ell}}$	W_{og}	W_{2g}
93,300	86.1	1647	52.4	1595	0.0329	1.05	0.0350
93,400	86.2	1649	52.8	1596	0.0331	13.95	0.0787
93,500	86.5	1652	53.3	1599	0.0333	47.8	0.553
93,800	87.1	1642	38.1	1604	0.0237	7.61	0.0190
101,000	100.8	1764	37.9	1726	0.0220	14.90	0.0610
93,100	85.8	1630	37.9	1592	0.0238	33.6	0.528
68,200	46.0	1195	29.1	1166	0.0250	0.745	0.0329
95,000	89.3	1624	0	1624	0	1.840	0.0078*
94,900	89.0	1622	0	1622	0	37.7	0.00953*

* These are net gas flow rates into RCS feed line before the feed line is saturated with gas.

Section 4
RESULTS OF THE STUDY

In this section of the report the results of analysis and experiments made in the course of the study will be brought together.

Most of the liquid motions investigated during the study can be divided into two general classes: axisymmetric and asymmetric. Axisymmetric motions are involved in liquid settling maneuvers. Additionally, the motions caused by relaxation of structural strain energy during engine shut-down transients is axisymmetric. All of the sloshing motions experienced in the operation of a space vehicle are asymmetric. These two categories provide a convenient way of discussing the results of the study.

Lateral Liquid Motion - Asymmetric liquid motions were the subject of seven distinct investigations performed in the course of the study:

a) Small amplitude lateral sloshing - the quasi-steady state analytical treatment of sloshing.

b) Large amplitude lateral motions - an analysis of such motions as an initial/boundary value problem.

c) Transient lateral motions following engine shutdown - an analysis related to the one just preceding.

d) Damping provided by ring and screen type baffles - an analysis to extend the results of earlier work to tank geometries of practical interest.

e) An experiment to verify sloshing frequencies for small amounts of liquid in a hemispherically bottomed cylindrical tank and to verify calculated response to impulsive perturbations.

f) An experiment to determine the response of laterally sloshing liquid to the sudden reduction in body forces as when engine cutoff occurs.

g) An experiment to determine the effect of interface curvature (as when the axial Bond number is low) on the damping afforded by ring baffles.

The analysis of lateral sloshing motions can, for convenience, be divided into two categories. The more conventional analysis of small-amplitude sloshing permits the convenient study of normal-mode sloshing as well as the response to periodic and some nonperiodic lateral perturbing accelerations. By contrast, the analysis of large amplitude motions is, by virtue of the much greater mathematical difficulties arising from nonlinearities of the problem, restricted to initial value problems. The following is an attempt to draw together all analysis and experiments of lateral liquid motions.

Consider first, the behavior of liquids undergoing small amplitude motions. The analysis of a) above and the experiment of c) were the core of work in this area in the study. This was supplemented by the analysis of d) and the experiment of g). Normal mode sloshing of liquids in hemispherically bottomed cylindrical tanks under low-g conditions was the subject of the analysis carried out under contract NAS 3-7119 for the Lewis Research Center. Experiments and further analysis carried out under this study were designed to verify and extend the results of this work which is reported in detail in NASA report number CR-54700. From an applications viewpoint, the major results of this study were the determination of normal mode sloshing frequencies in tanks of the geometry described and the development of equivalent mechanical analog parameters to aid analysis of the dynamic interaction of space vehicle tanks and liquids contained therein. First mode natural fre-

quencies are plotted in Figure 4-1. Results are limited to a contact angle of 5 degrees representative of the low contact angles which liquid propellants normally make with tank materials. Figure 4-2 gives the relationship between liquid depth measured along the tank axis and liquid volume required to make practical use of Figure 4-1. Experiments in this study developed the first mode natural frequency information shown in Figure 4-3. Agreement is marginal at best, all of the experimental results being high. Two reasons have been developed to qualitatively explain the apparent difference between theory and experiment.

(1) The boundary layer occurring next to the tank wall is estimated to be about 0.05 radius thick. This causes effectively a reduction of the characteristic length of the problem. An increase in the first mode sloshing frequency on the order of 10% can be explained by this effect.

(2) A further action of liquid viscosity is to cause an increase in the apparent contact angle during the movement of the studying slosh wave up the tank wall.

The experiments of Satterlee and Reynolds* indicate that the additional 15% increase in natural frequency parameter $\omega_1^2 = \bar{\omega}_1^2 \left[(1+B_N)\frac{\sigma}{\rho r_0^3}\right]^{-1}$ can be explained by a dynamic contact angle variation as small as 7°. Variations of this size and larger were observed. Table 4-I lists the first five eigenvalues or natural frequency parameters

$$\omega_k^2 = \bar{\omega}_k^2 \left[(1+B_N)\frac{\sigma}{\rho r_0^3}\right]^{-1}$$

*Satterlee, H.M. and Reynolds, W.C., "The Dynamics of the Free Liquid Surface in Cylindrical Containers Under Strong Capillary and Weak Gravity Conditions", Stanford Univ. Dept. Mech. Engr. rpt. no. LG-2, Stanford, Calif., April 1964.

where in these two expressions $\bar{\omega}_k$ is the natural frequency, B_α the axial Bond number, r_o the tank radius, and σ/ρ the ratio of liquid surface tension to density.

Mechanical analog parameters have also been computed and are presented in Figures 4-4 and 4-5. The geometry for their use is given in Figure 2-22 in Section 2. With the aid of these figures a mechanical analog for first mode lateral sloshing may be constructed. The use of this artifice is satisfactory as long as imposed periodic lateral perturbations do not have frequencies near the eigenvalues in Table 4-I.

The experimental response to impulsive lateral sloshing has been plotted in Figures 4-6 and 4-7. The first of these is limited to test conditions of $B_\alpha = 0$ and the second to $B_\alpha = 1$. The results on both plots have been normalized using the prediction from 1st mode response to a lateral perturbing impulse for the case of liquid with a 90 degree contact angle in a flat-bottomed cylinder. It is noticed that the normalized response for two shallow depths for $B_\alpha = 1$ are greater than the corresponding cases for $B_\alpha = 0$. Reference is invited to Figure 4-5 which gives the mass of the equivalent mechanical analog. The mass for $B_\alpha = 0$ is seen to be greater than for $B_\alpha = 1$ under any circumstance and especially at shallow depths where it appears to increase greatly. The response of an oscillator with a mass value obtained from Figure 4-5 would have a response of greater amplitude for $B_\alpha = 1$ than for $B_\alpha = 0$. This is at variance with the theory for the 90 degree contact angle, flat-bottomed cylinder case. Thus the results plotted in Figures 4-6 and 4-7 agree reasonably with the trends ob-

served from the theoretical calculations for tanks of the same geometry.

The slosh damping analysis and experiment of d) and g) were designed to supplement the work just summarized. The analysis was restricted to cases wherein the equilibrium free-surface is a horizontal plane. This restriction enabled extension of previous analysis to consideration of tank geometries of practical interest without the great amount of work required by consideration of the effects of the highly curved equilibrium free-surface, characteristic of low Bond number (low-g) conditions. The logarithmic decrement for full circular screen or perforated baffles in the cylindrical section of the tank perpendicular to the tank wall is plotted in normalized form as a function of baffle depth in Figure 4-8. Figure 4-9 presents a correction factor which gives the influence of baffle departure angle from being perpendicular to the tank wall. This together with Figure 4-8 enables evaluation of the damping coefficient for a full screen baffle at any reasonable angle to the cylindrical wall at any position in the cylindrical portion of the tank. Similar results are presented for ring baffles in Figures 4-10, 4-11 and 4-12. Figure 4-10 gives the logarithmic decrement as a function of baffle depth and depth of liquid in the cylindrical section of the tank. Figure 4-11 presents selected results which give the effect of ring baffle width. Figure 4-12 gives the effect of baffle tilt with respect to the horizontal.

The most important finding of this particular investigation has been the fact that the damping factor is not a function of Bond number. Consider for example the case of ring baffles. The drag coefficient is determined from the

so-called period parameter $P = U_m T/D$ (U_m being the maximum liquid velocity in the region of the baffle, T the period of oscillation, and D the baffle width). The effect of reducing the Bond number is to reduce the natural frequency of the sloshing motion. This reduces U_m and increases T; thus the effect of either cancels that of the other.

The experiment g) above was performed to determine the effect of free-surface curvature on the effectiveness of baffles, and in particular, ring baffles since these are most often used in propellant tank design. Success was achieved in adjusting the liquid density difference to very low values. This provided good simulation of the very highly curved free-surface shapes characteristic of very low axial Bond numbers. Other experimental difficulties, though, prevented observing clearly the effect of interface curvature per se. However, there appeared to be an important side effect of the baffle which after the fact is quite reasonable. The baffle apparently distorts the flow sufficiently to create a distortion of the free-surface. The effect of this is similar to that of dynamic contact angle variation, namely, the sloshing frequency is increased. This effect is plotted in Figure 4-13. It appears, then that the major influence on damping afforded by ring baffles is simply to reduce the time required to damp the motion from that which would be predicted on the basis of Miles' approach used in the analysis just described. The mechanism is not the increase of damping coefficient per se, but merely to increase the frequency. What takes place simply requires less time to happen.

Considerable effort was devoted throughout the study to develop an adequate numerical method for calculating large amplitude, nonlinear, motions which

can occur in liquid rocket propellant tanks, particularly as transients. The success as far as lateral motions are concerned is somewhat limited. Figure 4-14 presents a comparison of the results of analysis and of experiments. There is reasonable qualitative agreement, but the comparison presented is of a relatively early instant in a large amplitude lateral motion. Even here, though, the analytical results are the results of extrapolating calculations from an earlier stage. Otherwise, the numerical scheme used in performing the calculations would have shown an instability at a much earlier stage. The extrapolation for lateral sloshing analysis is not nearly as credible as when applied to axial liquid motions since there are unfortunately no independent results to use as a guide. (This will be expanded presently in the discussion of axial motions).

Much more reliance must be placed on experimental results in the case of large amplitude lateral liquid motions. A single experiment, f) above, was performed in order to gain more insight into this phase of liquid behavior. One of the major purposes of this experiment was to obtain information about the forces which a liquid exerts on its tank while undergoing large amplitude sloshing. With this in mind the trajectory of the center of mass of the liquid was obtained by a graphical examination of the liquid free-surface during a high amplitude slosh. From this a model was established to describe the lateral force imposed by the liquid on the side of the tank for the case in which the length of cylindrical tank above the free surface is of infinite length.

Axisymmetric Motions - Axisymmetric liquid motions and related liquid behavior in spacecraft propellant tanks were the subject of five investigations in this study. They were,

a) Large amplitude axisymmetric slosh and analysis of liquid motions in response to axial accelerations.

b) An analysis of the liquid response to axisymmetric structural vibrations of a propellant tank.

c) An experimental investigation of the reorientation flow or response to an axial acceleration in clean tanks and in a baffled tank. This investigation also included an examination of the effect of an impulsive acceleration.

d) An experiment to examine the geysering or rebound that results from a reorientation flow.

e) An experimental investigation of ullage gas entrainment resulting from a reorientation flow.

Broadly speaking the motions considered here are sloshing motions (both stable and unstable)that are the result of accelerations directed parallel to the longitudinal axis of the tank or to the axis of symmetry of the liquid-gas interface. From the standpoint of propellant behavior in spacecraft tanks, however, the results of the above studies (except b) are related to and concurred with the reorientation and settling of propellants away from or into the tank drain in response to an acceleration imposed on the tank.

The reorientation or settling maneuver itself was described analytically in a), above. The problem is an initial value boundary value problem. Expansion of the non steady state velocity potential in a Fourier series was used to obtain an analytic description of the free surface in spatial and time coordinates. A velocity extrapolation technique allowed the computations to continue beyond the point in time where previous calculations had

produced numerically unstable behavior.

To complement and verify if possible the results of the analysis performed the reorientation tests of c) above were performed for a range of reorientation Bond numbers, B_R, and fill levels.

Figure 4-15 shows a comparison between the behavior predicted by the computational routine and that observed in the low gravity testing for the same reorientation Bond number and contact angle condition. Figure 4-14 is a plot showing the theoretical liquid interface velocities at the wall and tank center. In both the theory and the test as for all the testing the free surface initial condition was the equilibrium zero gravity hemispherical interface shape. The agreement in Figure 4-13 is quite good.

Comparison of the wall wave trajectories shows that the wave front predicted is falling at a greater rate than that for the experiment. As can be seen in Figure 4-16 the theoretical wave front at the wall has a parabolic trajectory with acceleration equal to the tank acceleration whereas the experimental values obtained for the wall wave front acceleration were less than that applied to the tank. In dimensionless form the wave front trajectory is:

$$S^* = t^{*2} \quad \text{theoretical}$$

$$S^* = kt^{*2} \quad \text{experimental}$$

where $0.64 \leq K \leq 0.72$

$S^* = s/r$

$t^* = t\sqrt{g/2r}$

where s is the distance travelled by the wavefront.

Viscous effects in the real fluid, not included in the theory, and manifest

in the small test models, are considered to account for the difference in behavior, although the manner by which viscosity retards the wall flow is not thoroughly understood. Furthermore, the variation in K noted above was not traceable to the effect of viscosity in terms of model size. Thus no strong conclusion is available concerning the validity of extrapolating the results of the analysis and test to a full scale vehicle. However, conservation and the absence of experience to the contrary indicate that the wall wave front acceleration should be taken as 0.7 the tank acceleration.

The other aspect characterizing a settling flow is the trajectory of the ullage or pressurization gas in the tank center. Figure 4-15 shows fairly good agreement here. The theoretical wave front leads that for the test. This effect is also exhibited in Figure 4-16 where the velocity goes beyond the well established asymptote of 0.46 for a Taylor bubble as measured in the tests. Observation of the computational routine behavior indicated that the interface velocity was tending to approach this asymptote without the aid of the velocity extrapolations. In this case apparently the extrapolation technique was not necessary.

The testing showed that as the central ullage bubble approaches the tank hemispherical end its velocity decreases from the steady value, $\dot{H}^* = 0.46$, exponentially beginning when the liquid depth, H, is 0.23 of the tank radius such that the liquid-gas interface distance from the tank end is given by

$$H^* = 0.23e^{-2.82\ t^*}$$

where $H^* = H/r_o$

and $t^* = 0$ is taken at the time when $H^* = 0.23$ (here r_o is tank radius).

This was in agreement with the theory developed by Satterlee and Hollister*.

In the experimental investigations into reorientation flow the effect of tank fill level was examined. In this respect an effect of propellant viscosity was discernable. The low fill levels produced correspondingly thin wall sheets and a retardation of the wave front below that indicated above. This effect was exhibited in terms of a reorientation Reynolds number based on tank fill level and reorientation distance. No effect of tank fill level and propellant viscosity was observable for Re > 200 where (see Section 3, p.3-18)

$$Re = \frac{(ar^3)^{1/2}}{\nu} V^* \frac{h^*}{H^*}$$

Propellant behavior in response to axial accelerations of an impulsive nature were also examined in the tests under c) above. In this case the parameter of concern is the impulsive Weber number

$$We = \frac{V^2 r}{\beta}$$

where v is taken as the velocity increment given to the tank or vehicle by the impulse. As might be expected it was shown that impulsive maneuvers (at reorientation Bond numbers in excess of the stability limit) resulting in Weber numbers less than 4 do not cause a permanent distortion of the propellant interface and reorientation of the propellant. Above this limit partial propellant reorientation takes place the degree depending on the magnitude of the impulsive Weber number.

*Satterlee and Hollister op. cit.

Ring baffles, circumferential stiffeners, and retention surfaces can have a marked influence on the reorientation flow pattern when they are initially unsubmerged. This was demonstrated in reorientation tests with such hardware items present in the tank models. Basically, the reorientation flow is deflected into the tank center. In the case of a ring baffle the deflected flow eventually spans the tank cross-section, dividing the ullage volume in two and setting up to opposite axial flows at the tank center one into the drain and the other back toward the tank top. This also sets up a new interface condition at the baffle location which must fail to allow passage of the remaining ullage gas.

In the experiment listed under d) the geyser or rebound effect produced by the undeflected wall flow impinging on itself at the tank bottom was examined under high simulated reorientation Bond number conditions. It was observed that the geyser amplitude was attenuated with the flow returning to less than its original height. After the initial rebound motion the geyser motion dissipated quickly into turbulence. The period of rebound motion was equal to twice the time required to reorient the propellants. Ring baffles near the tank bottom attenuate the geyser action but do not eliminate it completely. Ring baffles higher on the tank wall produce the same effect described above and in this manner prolong the total settling time for the propellant.

The analysis of the effect on the propellant surface resulting from tank structural strain relaxation at main engine cutoff indicated that large amplitude propellant motions do not occur. Sufficient strain energy is present in the tank structure to overcome normal stabilizing effect or surface ten-

sion. But, very small axial thrusts are sufficient to limit the free surface excursions. Propellant tank structures even partially loaded with liquid have vibrational frequencies of the order of 100 sec^{-1}. Further, rocket engine cutoff is not a step change to zero thrust (and zero gravity level) but has a tailoff character. Thrust decay times in the analysis were of the order of 1 second for the Agena and Apollo Service Module. Thus the liquid surface oscillations generated by tank vibrations at cutoff are stabilized by the low but non-zero vehicle acceleration associated with thrust decay. These oscillations are then damped out by the end of engine thrust tailoff.

Propellant reorienting in an undeflected wall flow pattern entering the tank bottom will initially undergo the geysering or rebound discussed above. The geyser decays and forms a pool of settled propellant and entrained pressurization gas. Wall sheet flow entering the pool of settled propellant will continue to entrain more gas. In the experimental investigation listed as e) above the mechanism of this entrainment was studied in a series of steady state one-dimensional flow tests. A series of flow conditions characterized by wall sheet velocity, U_e, and thickness, t_e, were observed and the resulting gas entrainment correlated. The results apply only to high Reynolds number (turbulent) flow such that the Reynolds number, $Re > 1500$ where $Re = U_e t_e \rho/\mu$ with ρ and μ being the propellant density and viscosity respectively.

The test conditions covered the Reynolds number range $5000 < R_e < 20{,}000$. It was determined that the condition for initiation of gas entrainment or incipient bubbling can be described in terms of the Reynolds number above and a wall sheet Weber number. The relation for incipient gas entrainment

$$We_i = 0.50\, R_e^{2/3} \qquad 4.2$$

where $We_i = \dfrac{U_i^2\, t_e\, \rho}{\sigma}$

U_i is the wall velocity for incipient bubble entrainment and σ the propellant surface tension

The volume rate of gas entrained is a function of wall sheet Froude number and can be obtained by the following relation

$$P'/Q' = 0.0009\, F_r$$

where P' is the volume rate of gas bubble entrainment,

and Q' is the volume rate of flow for the wall sheet,

(both per unit wall sheet width) and

$$Fr = \frac{(U_e - U_i)^2}{2 g t_e}$$

with g the local acceleration level and the other terms as defined above.

This correlation should be valid for the Froude number range $0 < Fr < 500$. The Froude number range of the investigation was $5 < Fr < 100$.

Finally of interest is the characteristic entrained gas bubble size. Of course the gas bubbles entrained are not of one size but cover a range. For any re-

orientation condition described in terms of U_e and t_e the upper and lower limits of the gas bubble size range can be determined from the following relations

$$\frac{D_{MIN}\, U_e^2}{\sigma/\rho} = 15.9\left(\frac{\rho}{\rho_l}\right)^{1/3}$$

$$\frac{D_{MAX}\, U_i^2}{\sigma/\rho} = 15.9\left(\frac{\rho}{\rho_l}\right)^{1/3}$$

The value for U_i in the last equation is obtained from the equation for incipient bubble entrainment as a function of wall sheet Weber number.

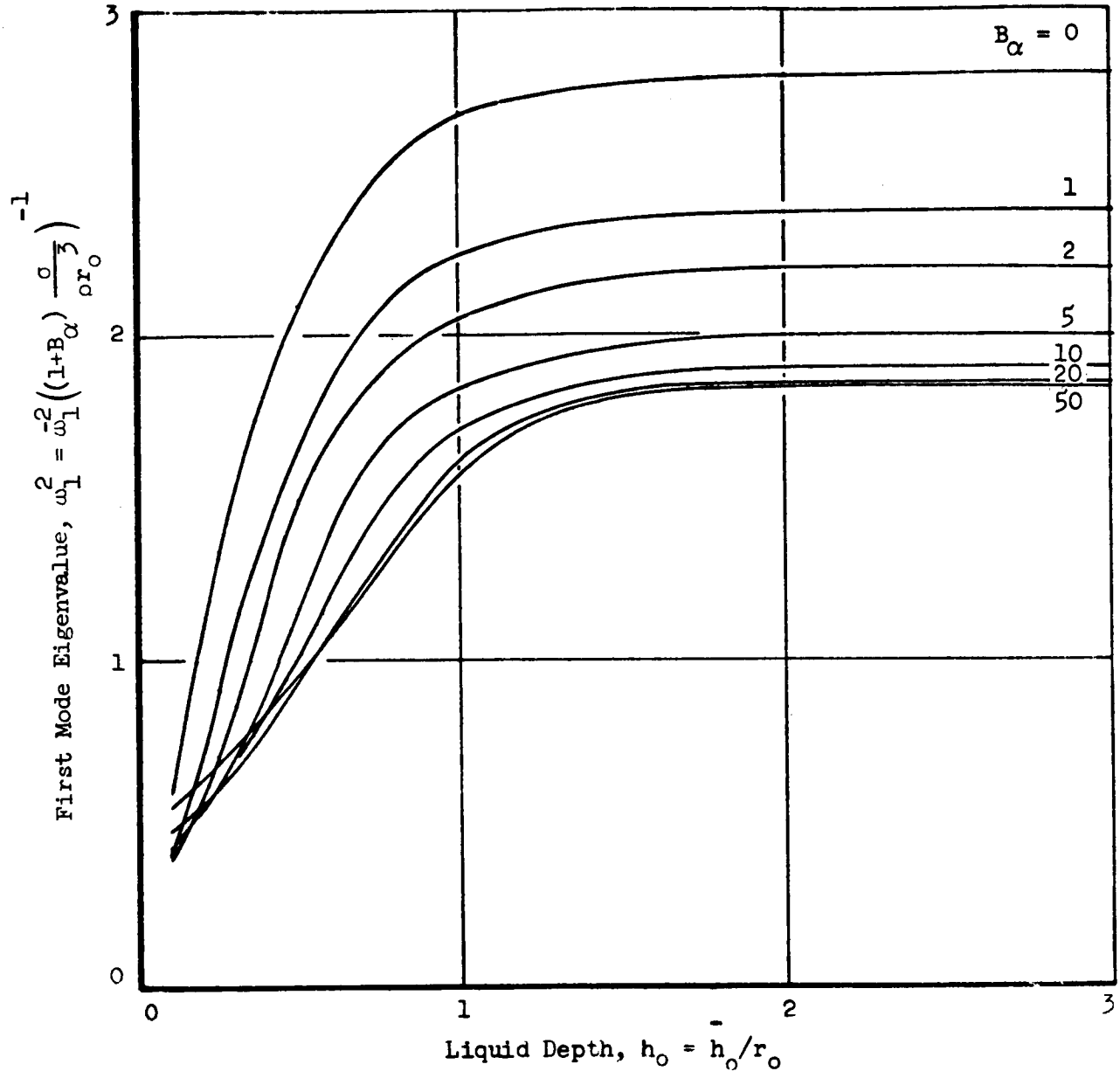

First Mode Eigenvalue for Lateral Sloshing in a Cylindrical Tank with Hemispherical Bottom

θ = 5 degrees

Figure 4-1

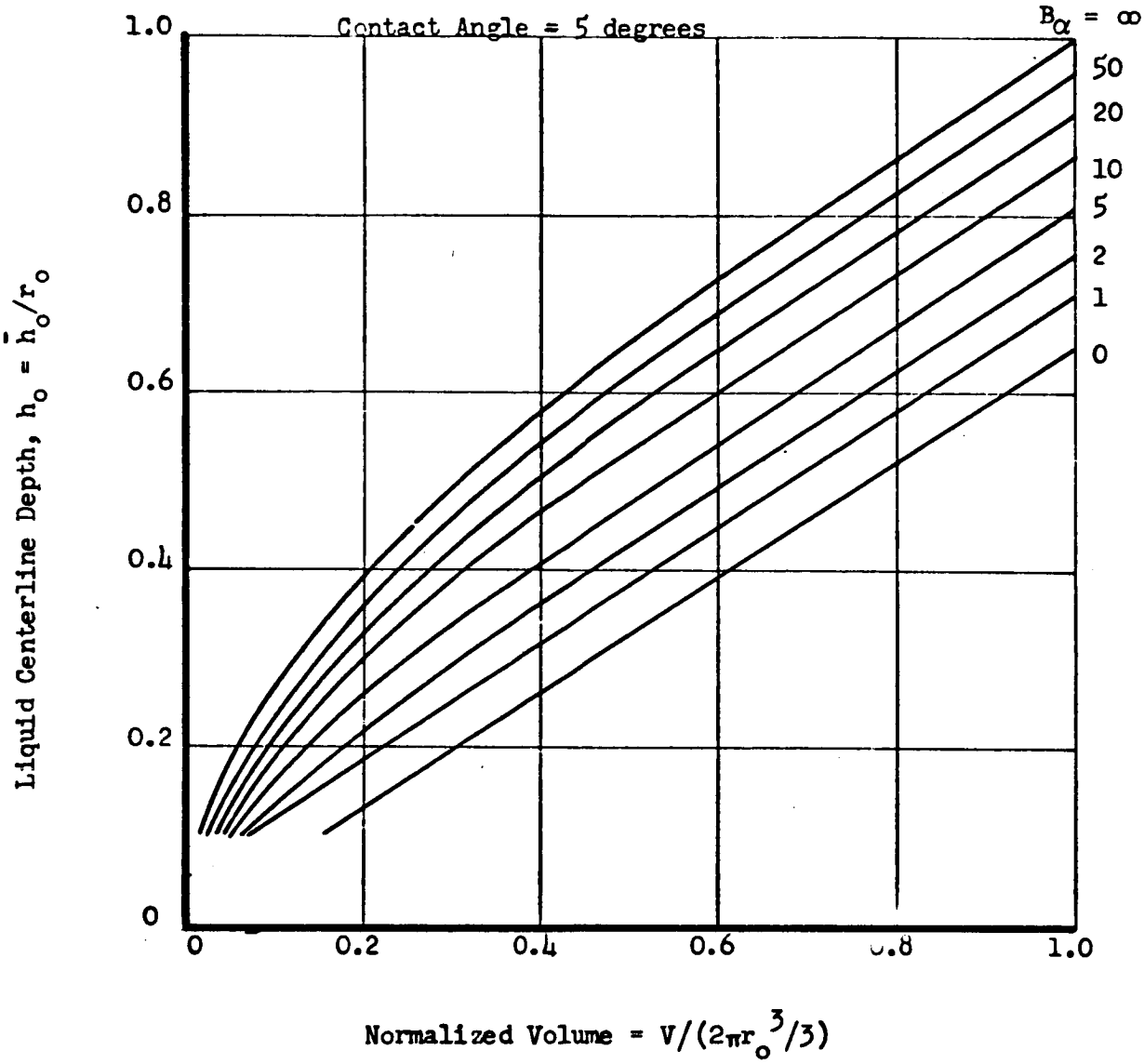

Liquid Centerline Depth - Tank Volume Relationship

Figure 4-2

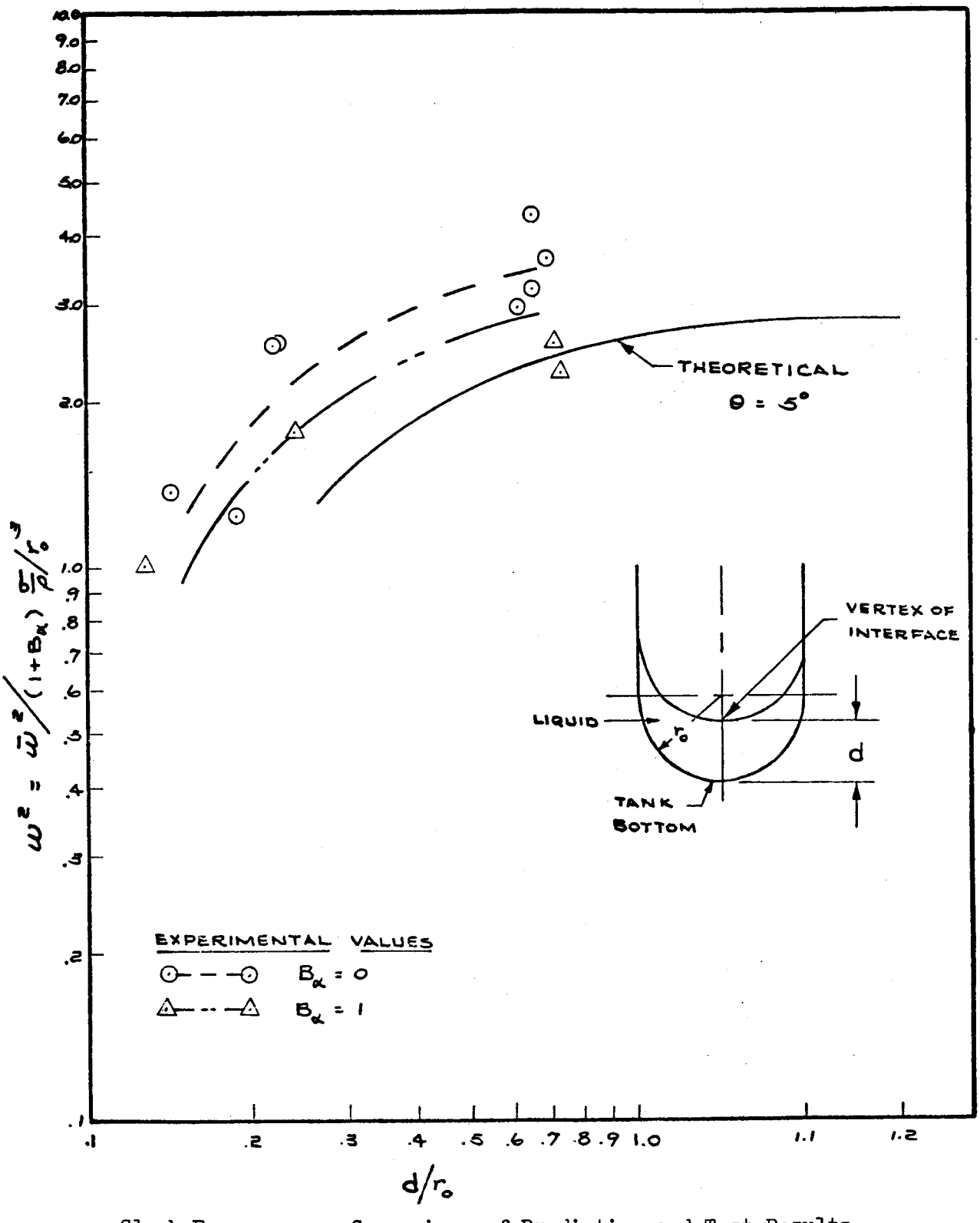

Slosh Frequency -- Comparison of Prediction and Test Results

Figure 4-3

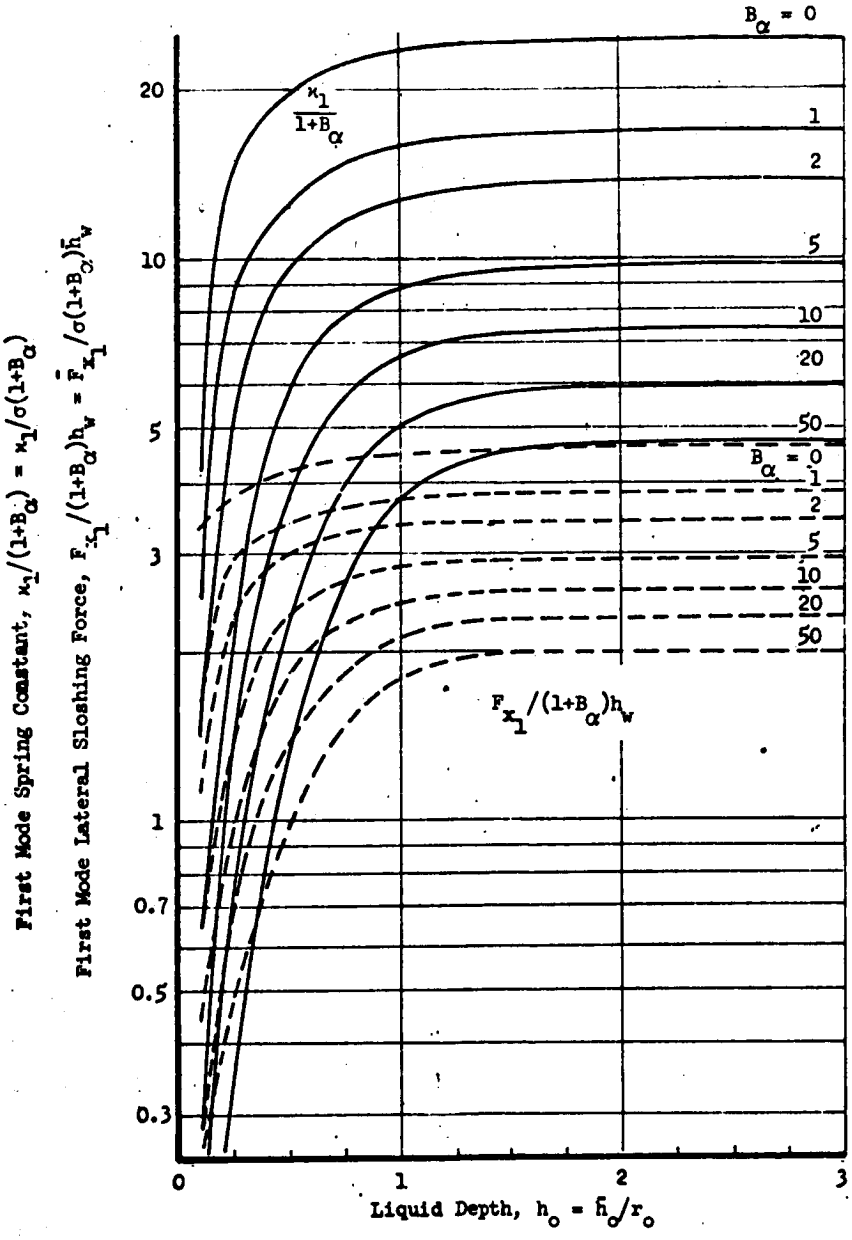

First Mode Mechanical Analog Spring Constant and Lateral Force
Cylindrical Tank With a Hemispherical Bottom

θ = 5 degrees

Figure 4-4

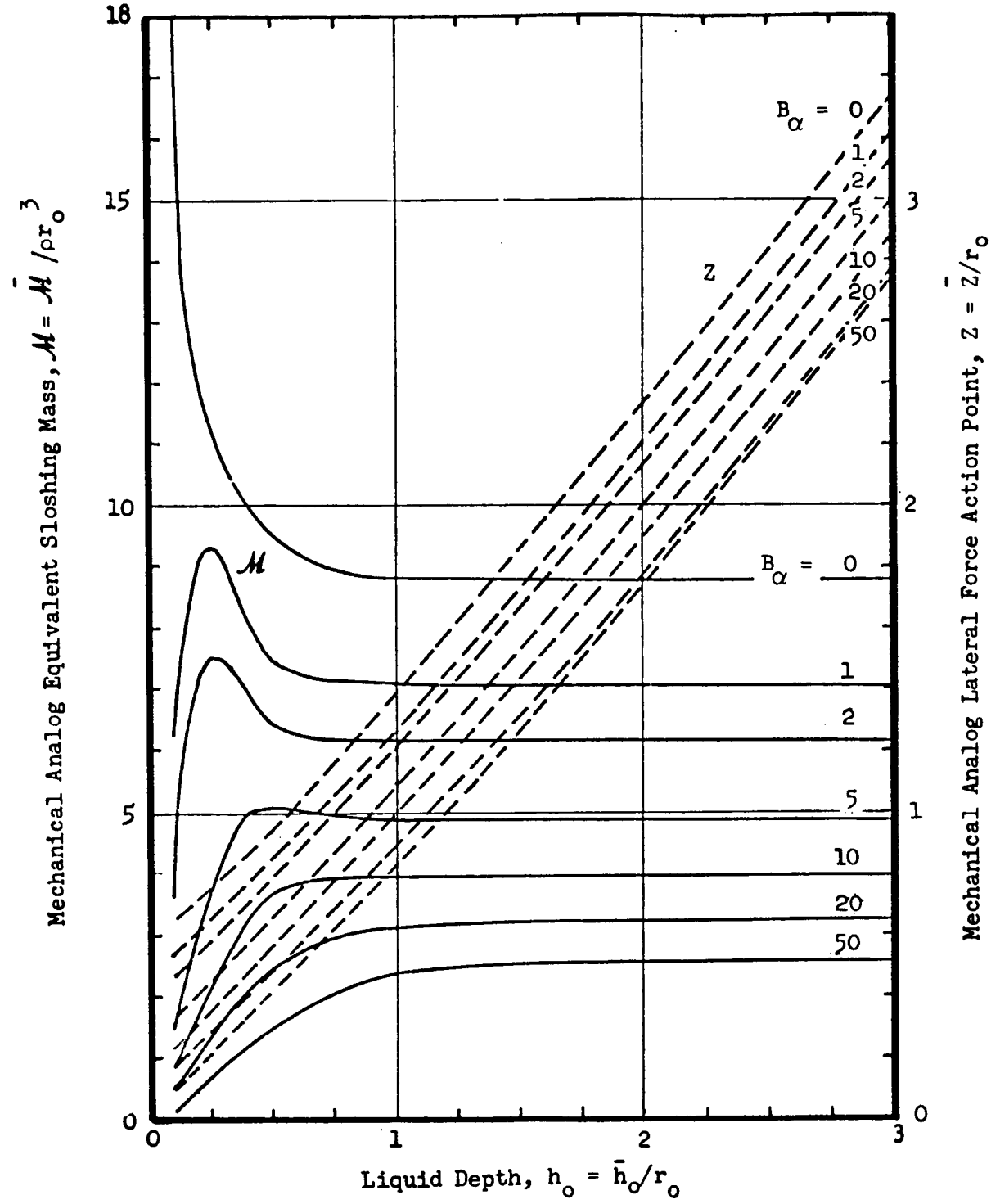

First Mode Mechanical Analog Sloshing Mass and Lateral Force Action Point for Lateral Sloshing in a Cylindrical Tank With a Hemispherical Bottom θ = 5 degrees

Figure 4-5

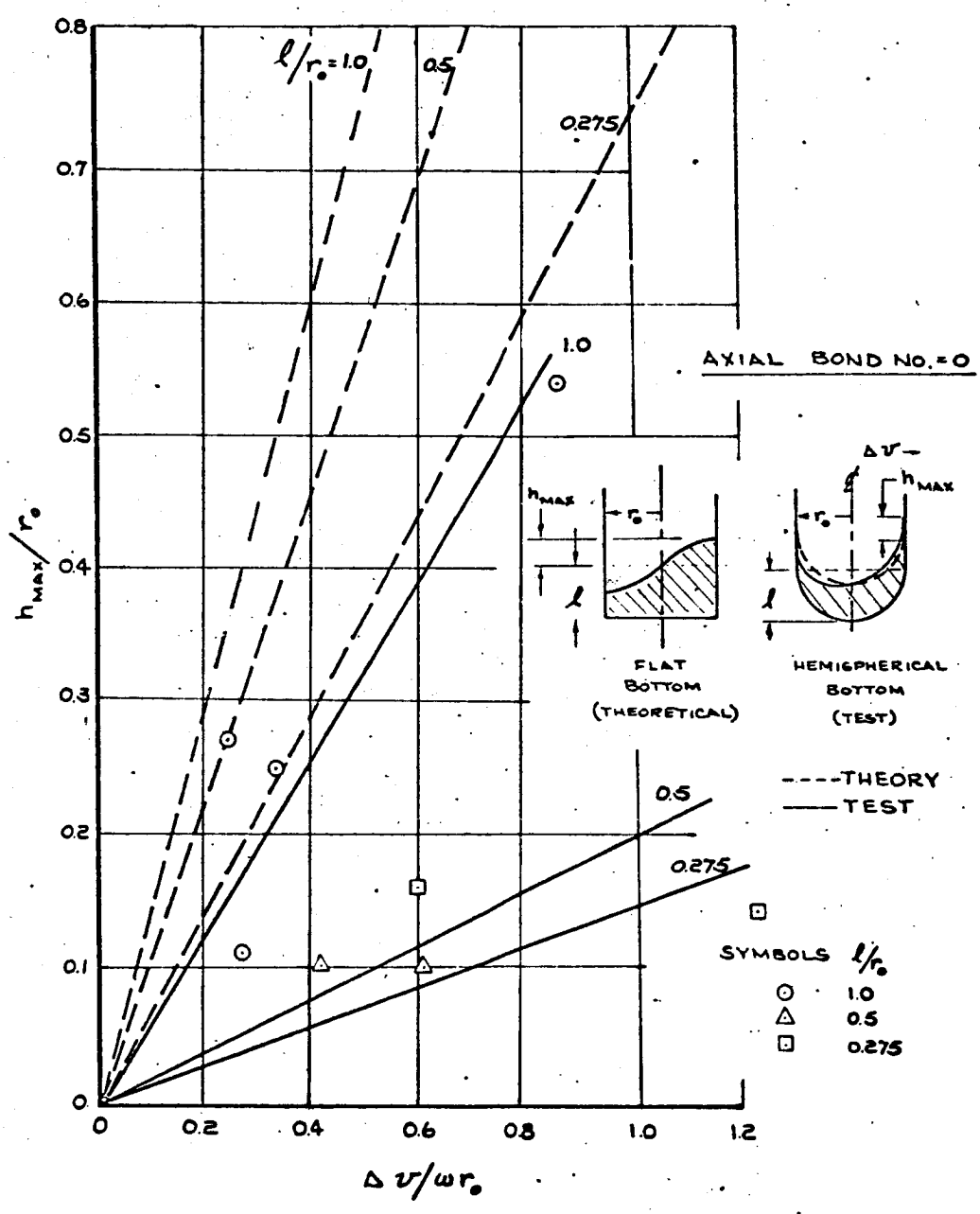

Lateral Slosh Response

to a Transverse Impulse Axial Bond Number - 0

Figure 4-6

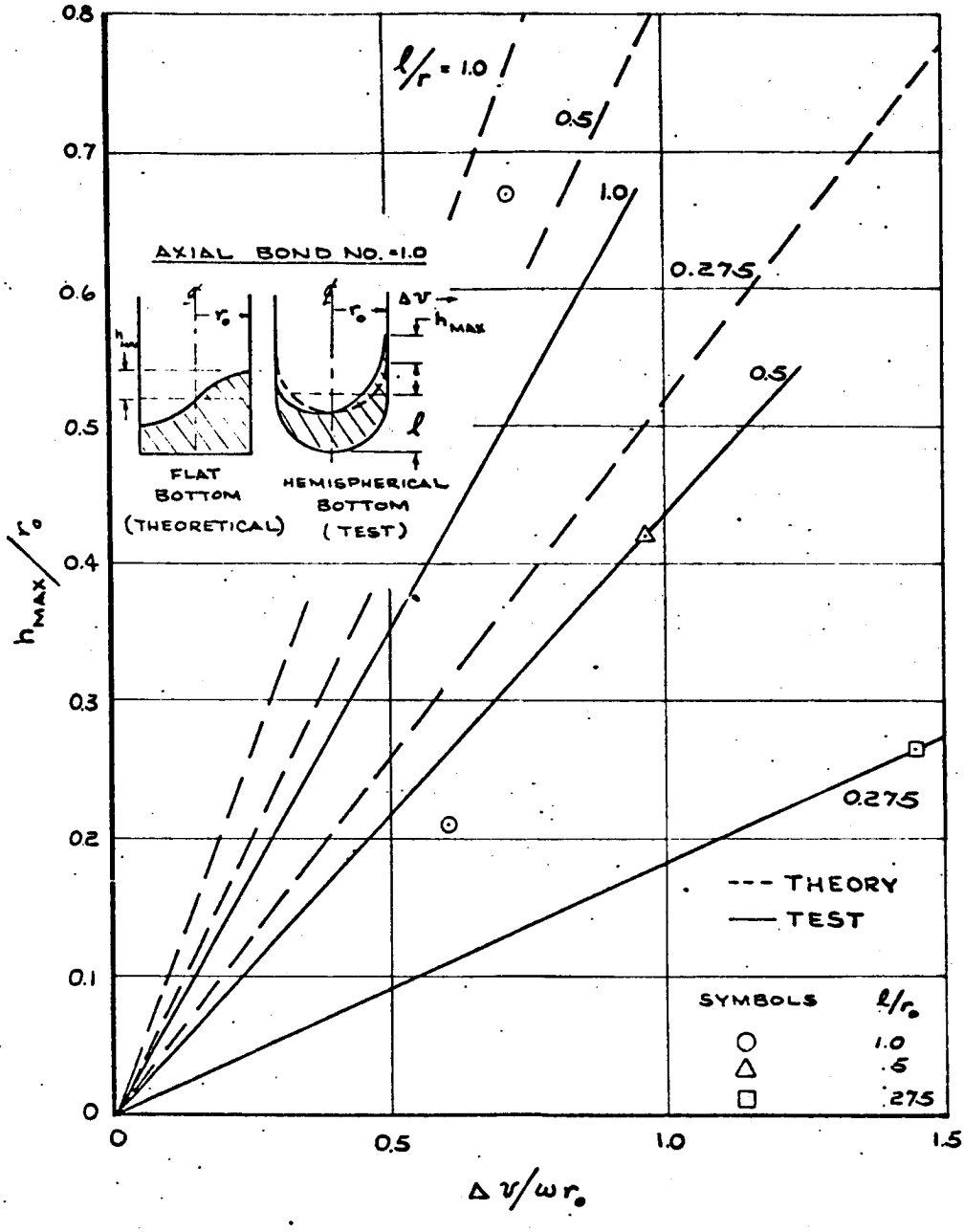

Lateral Slosh Response

to a Transverse Impulse Axial Bond Number - 1

Figure 4-7

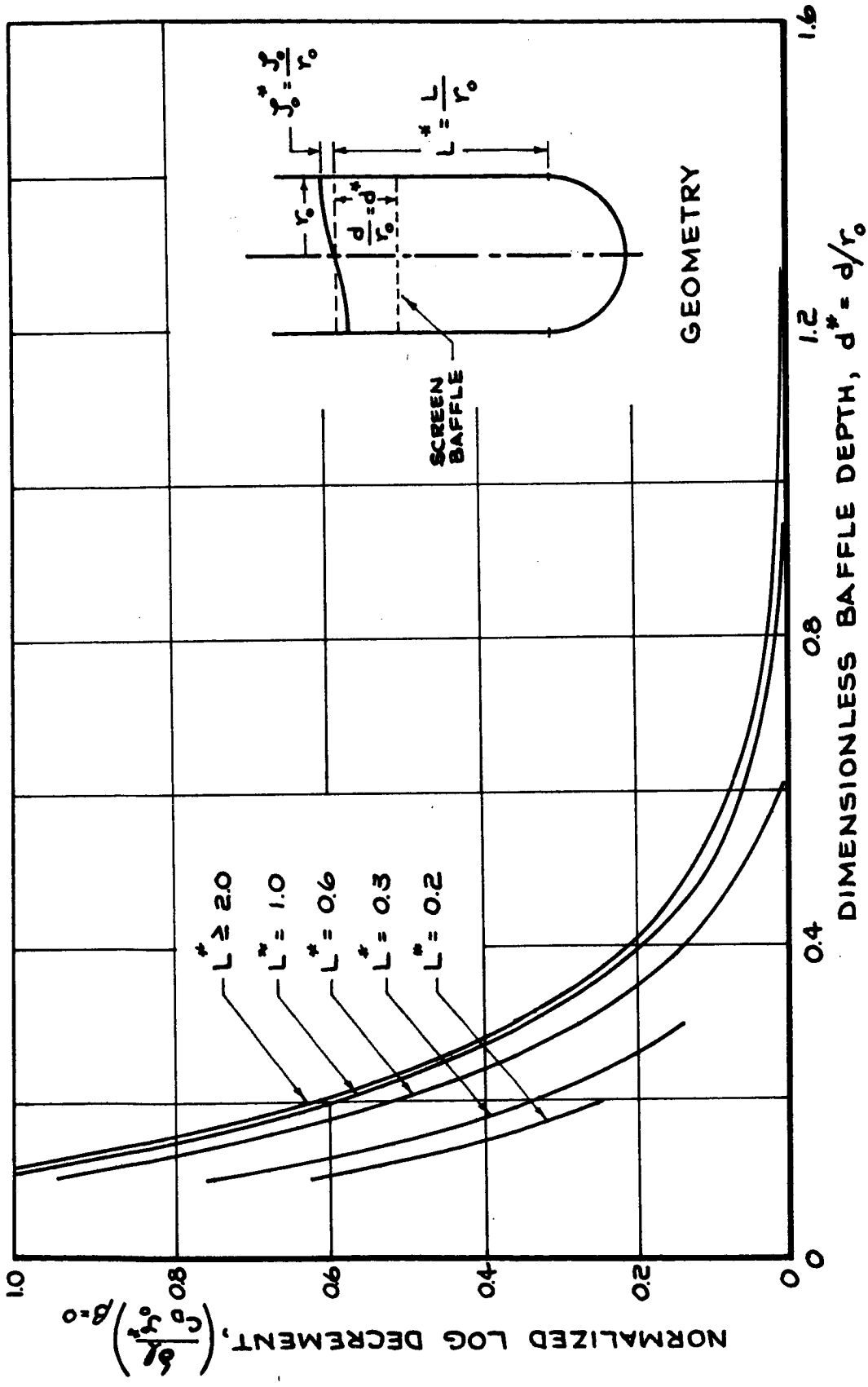

Effect of Baffle Depth on Log Decrement

Figure 4-8

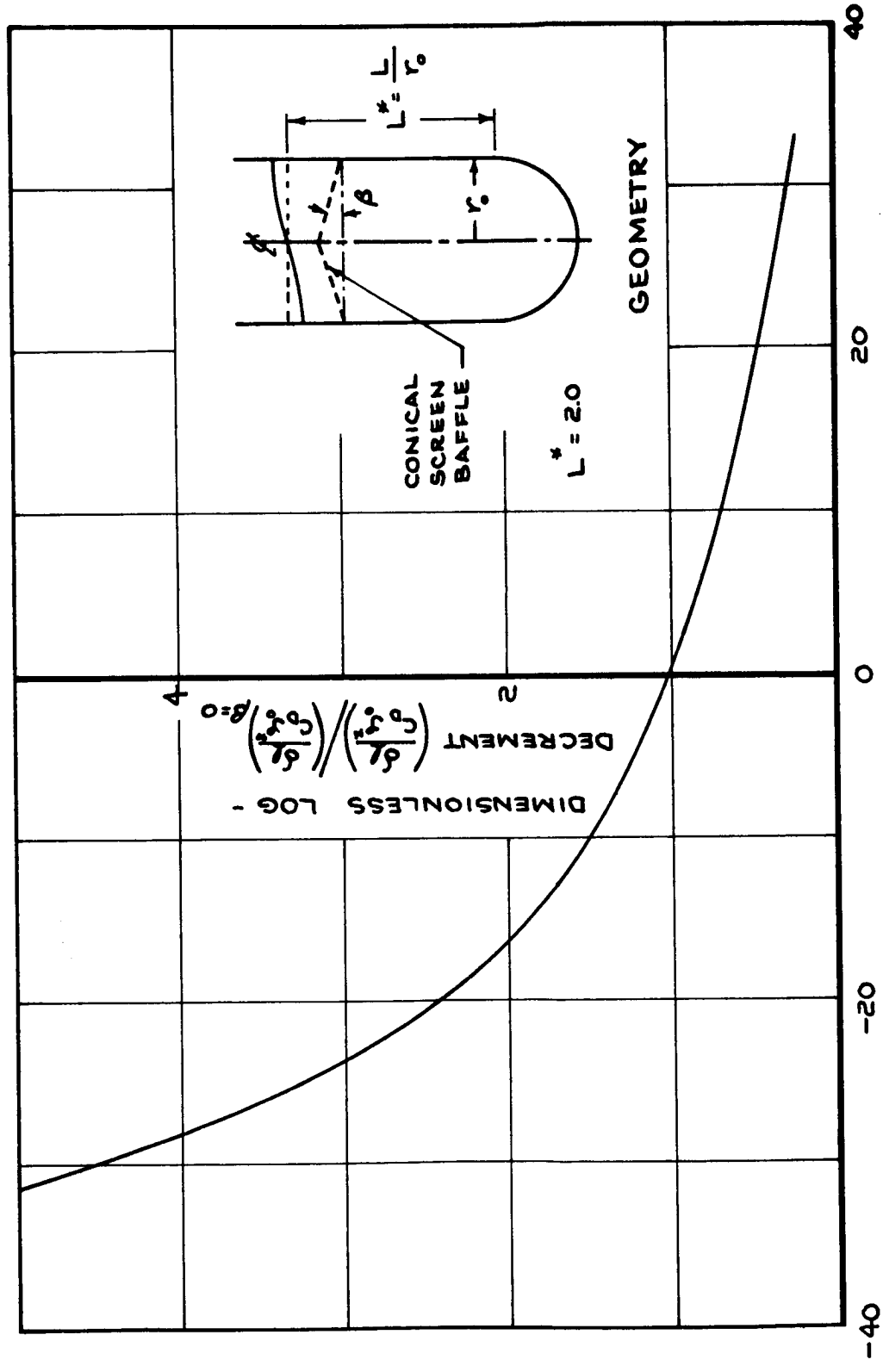

Effect of Baffle Angle on Log Decrement

Figure 4-9

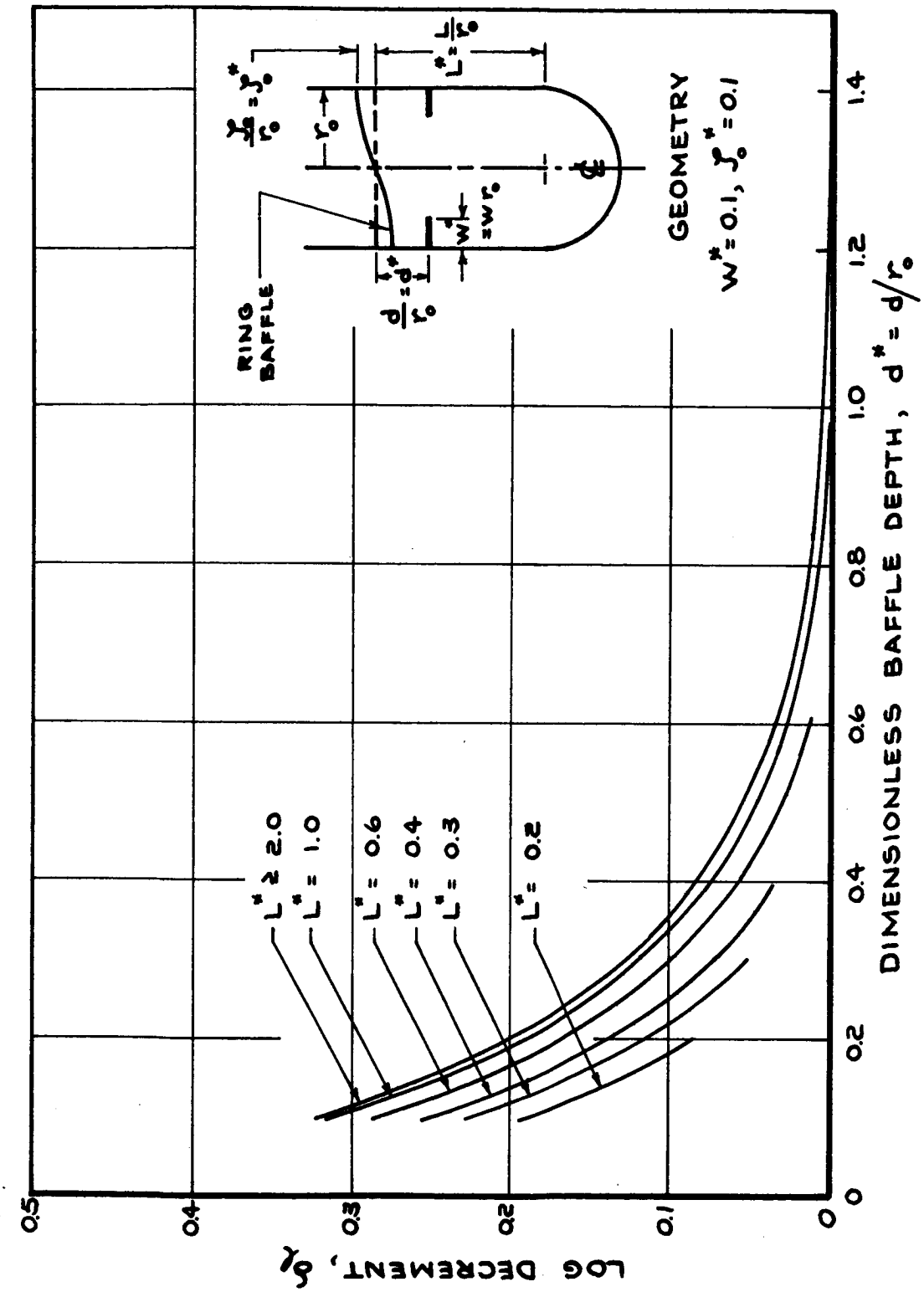

Effect of Baffle Depth on Log Decrement

Figure 4-10

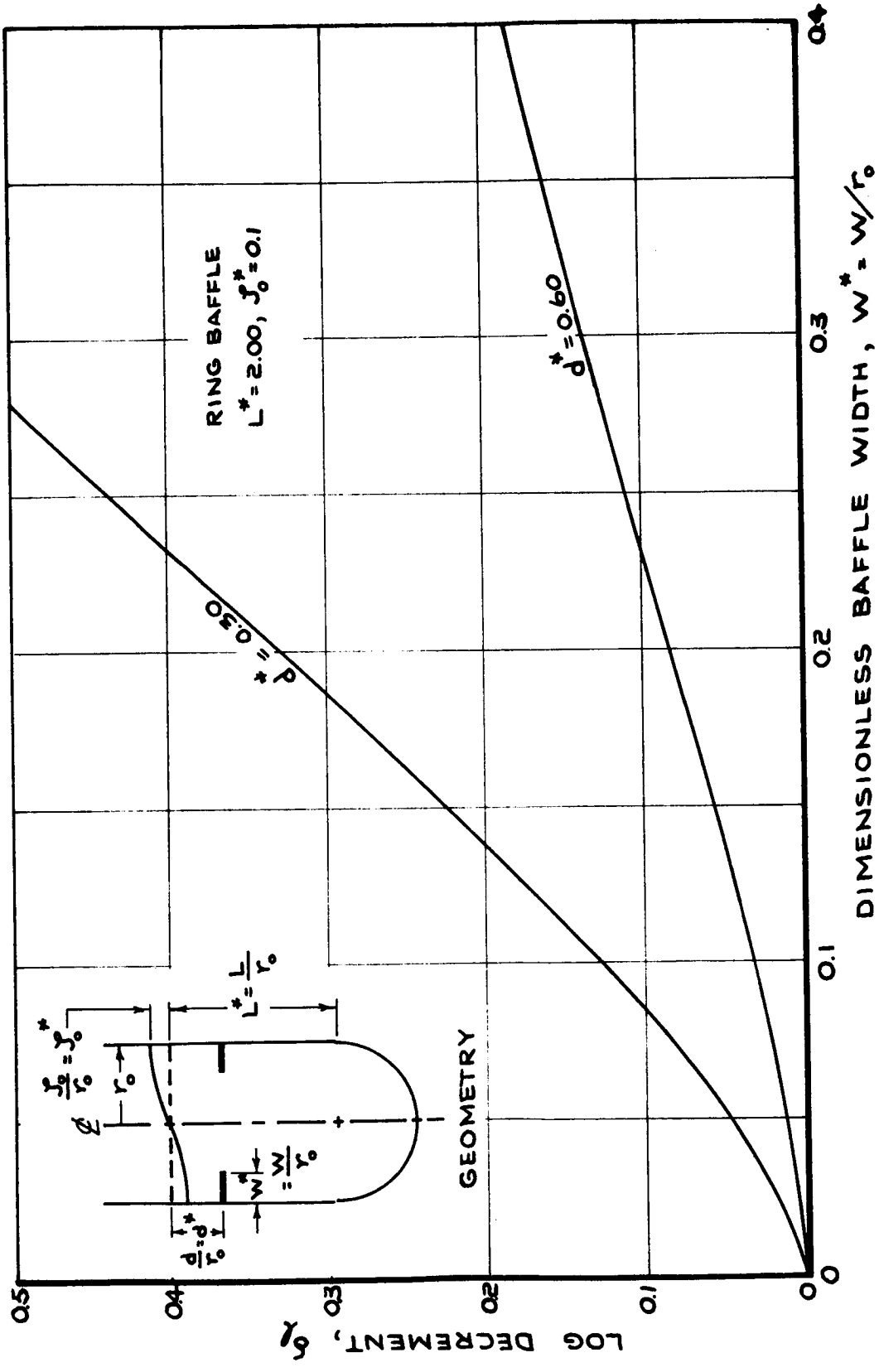

Effect of Baffle Width on Log Decrement

Figure 4-11

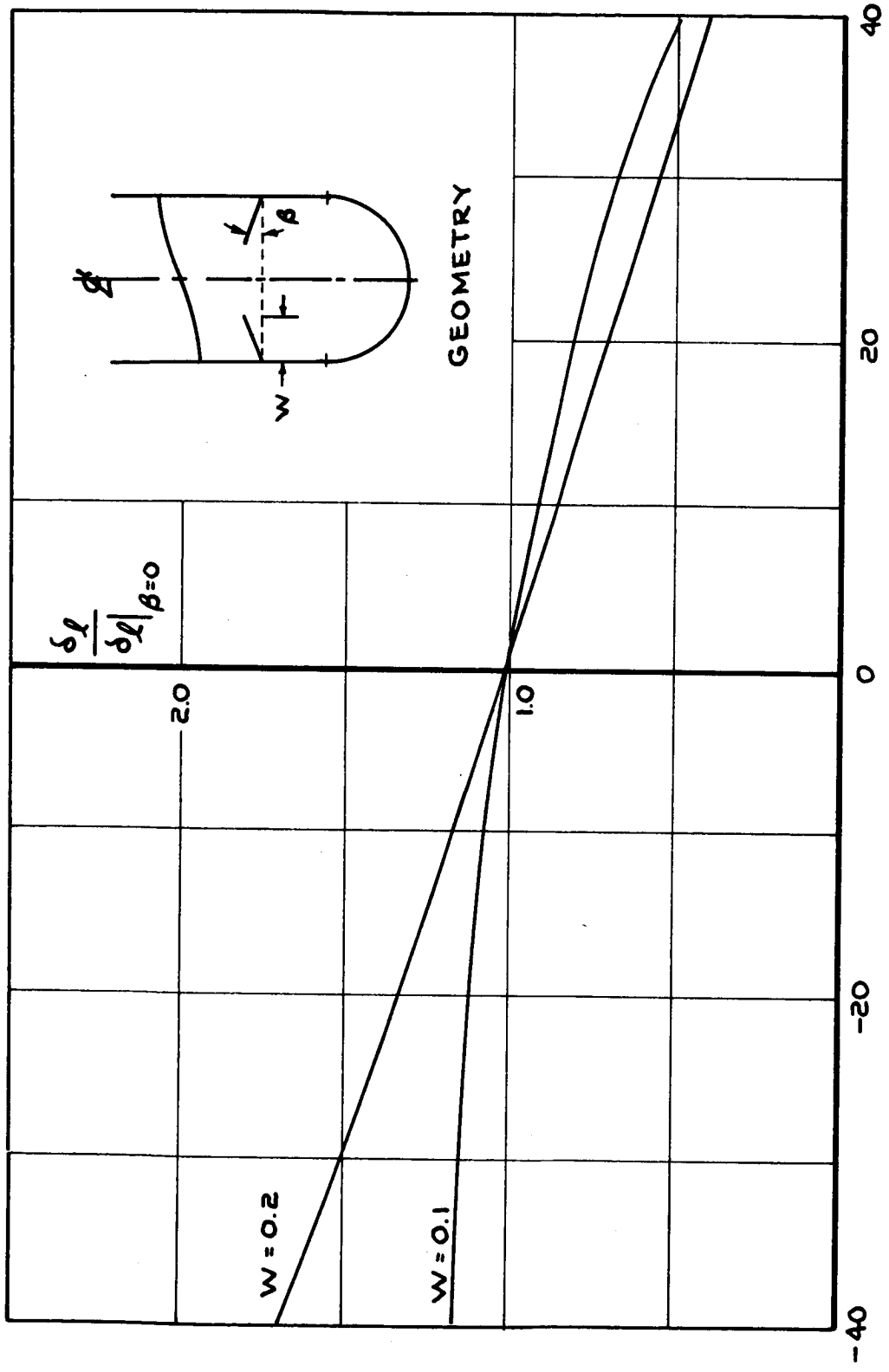

Logarithmic Decrement of a Tilted Ring Baffle

Figure 4-12

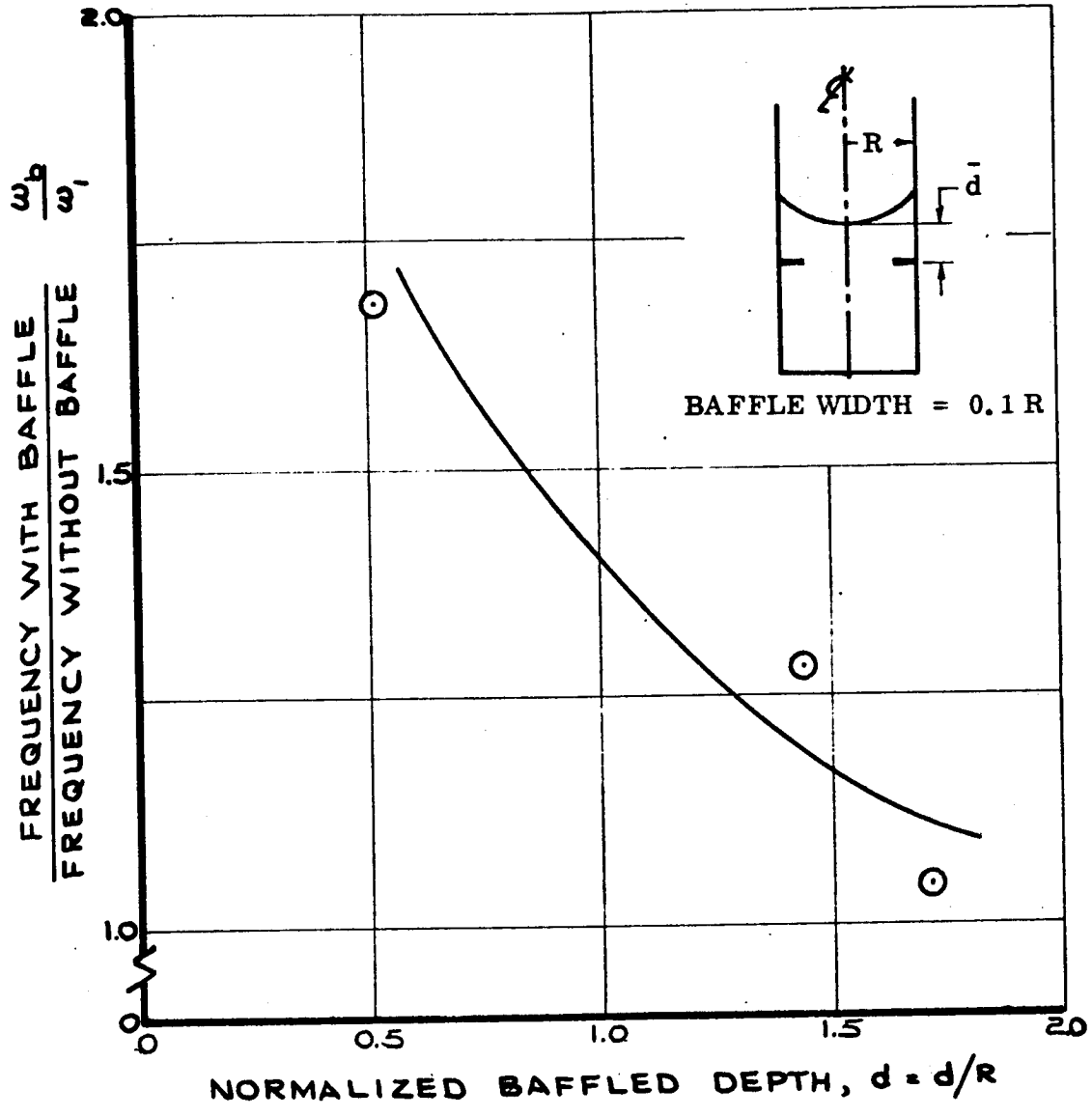

Effect of Ring Baffle Location on Zero-g Sloshing Frequency

Figure 4-13

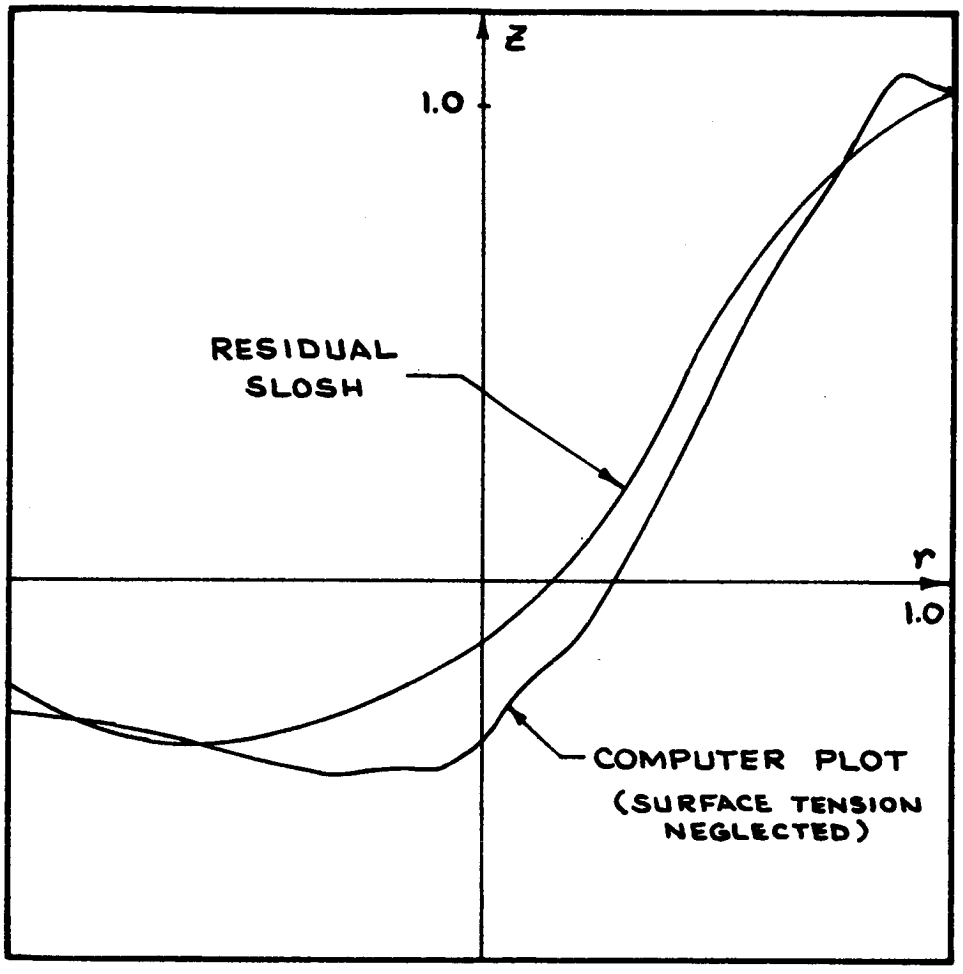

Qualitative Comparison

of

Analytic Prediction and

Measurement of Residual Slosh Profile

Figure 4-14

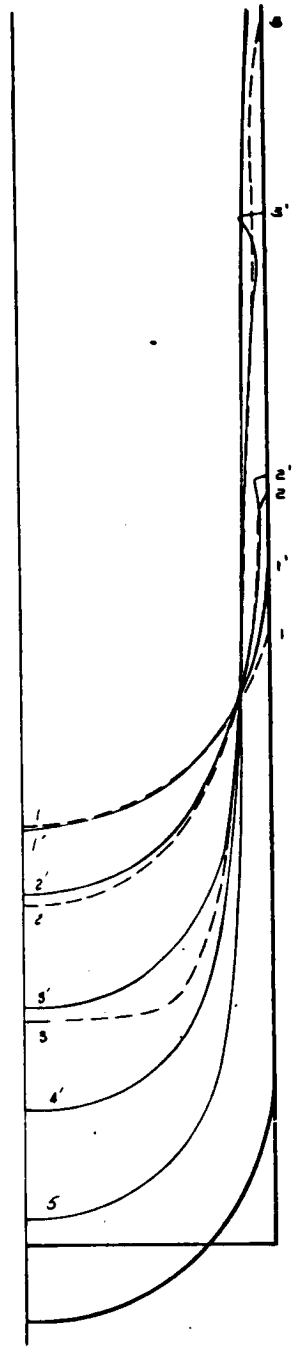

——— Experimental, contact angle = 0°
Hemispherical Bottom
Fill Level = 2.33, B = 260

- - - - - Analytical, contact angle = 15°
Flat Bottom
H = 2.0, B = 260

The analytical and experimental results are shown at the same times in this case.

Approximate Quantitative Agreement of Experimental and Analytical Results

Figure 4-15

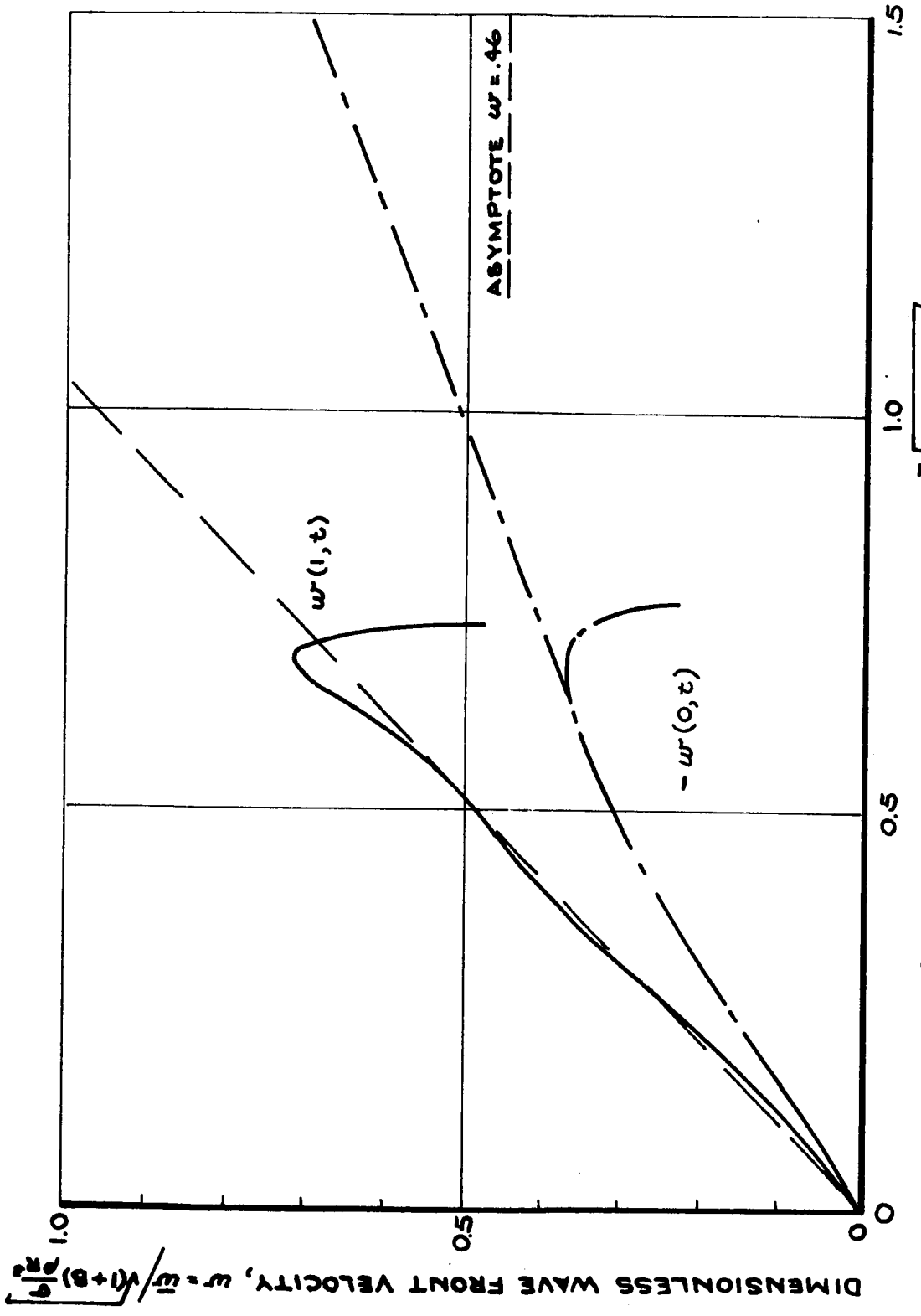

Wave Front Trajectories During Reorientation

Figure 4-16

TABLE 4-I

Lateral Sloshing Eigenvalues
For Cylindrical Tank With Hemispherical Bottom
Θ = 5 degrees

Bond No. $B_\alpha = \rho g_\alpha r_o^2/\sigma$	Depth $h_o = \bar{h}_o/r_o$	Eigenvalues $\omega_k^2 = \bar{\omega}_k^2[(1+B_\alpha)\sigma/\rho r_o^3]^{-1}$				
		k = 1	2	3	4	5
0	3	2.81	34.6	137	353	723
	2	2.80	34.6	137	353	723
	1	2.69	34.0	136	353	723
	1/2	2.11	31.5	131	349	721
	1/4	1.33	24.8	113	314	675
	1/10	0.596	12.5	63.6	197	465
1	3	2.38	26.2	95.8	239	480
	2	2.38	26.2	95.8	239	480
	1	2.25	25.8	95.7	239	480
	1/2	1.65	23.6	92.0	235	477
	1/4	0.981	16.7	74.1	203	432
	1/10	0.403	12.5	73.0	239	578
2	3	2.21	22.4	78.3	191	380
	2	2.20	22.4	78.3	191	380
	1	2.07	22.1	78.3	191	381
	1/2	1.49	20.2	75.6	188	378
	1/4	0.717	11.8	54.2	154	338
	1/10	0.397	12.7	74.2	240	not produced
5	3	2.00	17.0	55.4	131	255
	1	1.85	16.8	55.3	131	255
	1/2	1.17	14.1	50.8	124	245
	1/4	0.615	9.93	45.7	129	279
	1/10	0.408	11.8	67.3	214	502
10	3	1.90	13.3	40.4	92.1	176
	2	1.90	13.3	40.4	92.2	177
	1	1.72	13.2	40.3	92.1	177
	1/2	1.02	10.4	35.1	83.5	164
	1/4	0.604	8.74	38.3	104.1	219
	1/10	0.434	10.6	58.2	180.5	417
20	3	1.85	10.2	28.6	62.5	117
	1	1.62	10.1	28.5	62.3	117
	1/2	0.941	8.11	25.5	58.9	114
	1/4	0.629	7.62	30.8	80.1	165
	1/10	0.475	9.34	48.1	144	325
50	3	1.84	7.54	18.2	36.7	65.2
	2	1.83	7.55	18.3	36.8	65.5
	1	1.58	7.48	18.2	36.6	65.1
	1/2	0.939	6.40	17.5	37.3	68.7
	1/4	0.701	6.41	22.1	52.7	103
	1/10	0.549	7.77	35.7	101	218

Section 5

APPLICATION TO PREDICTION OF APOLLO MISSION LIQUID BEHAVIOR

INTRODUCTION

The basic reason underlying the engineering study of liquid behavior in rocket propellant tanks is, of course, to enable prediction of liquid behavior and minimize the possibility of operational difficulties arising from unforeseen liquid behavior. Major concerns are the possibility that liquid will not be properly located to support engine firings, that dynamic liquid behavior will unfavorably interact with spacecraft control systems, and that tank drains may be unported by sloshing, vortexing and so-called propellant blow through.

The material in this section of the report is divided into three parts. The first treats the liquid behavior in the Service Propulsion System (SPS), the second presents analysis of liquid behavior in the Lunar Module (LM) Descent and Ascent Propulsion Systems, and the last discusses all the possible failure modes of the SPS propellant retention system and then specializes this discussion to an analysis of the behavior of this system in the Apollo AS503A earth orbital mission in which the Service Propulsion System is propelled backwards by the Lunar Module.

APOLLO SERVICE PROPULSION SYSTEM LIQUID BEHAVIOR ANALYSIS

Propellant response and reaction during the various Apollo maneuvers planned is important to effective mission planning. Propellant must be available at the tank drains for Service Propulsion System firing and the effect on the control system of propellant motion resulting from various maneuvers determined. These two factors primarily affect the amount of RCS propellants required to insure mission success. Knowledge of fluid reaction to an attitude control pulse is required since the subsequent reacting force for a given situation varies with the wave height.

Objectives. The objectives are to make a general review of the Apollo mission propellant behavior for potential problem areas. Specifically:

1. Define propellant reaction to maneuvers
2. Define the effect of propellant reactions on the system.

Analysis Assumptions and Methods. The complexity of the Apollo mission in general and the uncertainty in sequencing of crew performed maneuvers in particular, requires that simplifying assumptions be made. A set of simplified reference conditions are listed which will provide representative propellant behavior.

A typical mission profile was extracted from the available data* and abbreviated for this analysis as shown on Table 5-1. Acceleration changes have a predominant effect on fluid behavior in this environment; so four

*"Project Apollo, AS-504A Preliminary Spacecraft Reference Trajectory, Vol. I" (Conf., unclassified title), by Mission Analysis Branch, Mission Planning and Analysis Division, NASA, MSC Internal Note No. 66-FM-70, 1 July 1966, Houston, Texas.

simplified configurations have been assumed between those events which significantly affect vehicle weight. The pertinent geometrical characteristics of these four configurations are listed in Table 5-II. The portion of mission where each applies is listed in Table 5-I. Pitch and yaw accelerations have been averaged to permit using a single value for each configuration. With this assumption, a set of eight reference maneuvers common to each configuration was considered. These maneuvers are described briefly as follows:

Navigation - A typical navigation maneuver for star sighting is assumed to involve pitch, yaw, and roll maneuvers. Turns of 180° are assumed for pitch or yaw and roll. This latter assumption amounts to a worst case condition. Maneuver sequence would include combined pitch or yaw and roll during acceleration and at velocity.

IMU/Alignment - Pitch, yaw, and roll through a full revolution on each axis would be performed in two sets of 180° maneuvers, but no combined pitch-yaw and roll maneuvers. A similar maneuver is specified to IMU alignment in the Lunar Module.

Orientation - Orientation maneuvers possible will involve the same attitude changes as those on IMU alignment except combined pitch, yaw, and roll will be possible.

Ullage - Axial thrusting only with the RCS (Reaction Control System) to position the ullage for SPS ignition.

SPS Firing - Main CSM (Command Service Module) engine firing with RCS operation for attitude control.

Roll Control and Damping - This is a post SPS firing maneuver for correcting attitude, possibly due to high energy slosh waves. A series of pitch, yaw, and roll RCS firings will be utilized to counteract these motions.

Thermal Control - Rotation in roll is assumed, about the longitudinal axis, at 2 rev/hr and 5 rev/hr, with no pitch-yaw corrections added.

Attitude Control - A thruster pulse width of .020 sec is assumed together with reported guidance system dead bands of $.05^{o}$ in roll and $.5^{o}$ in pitch and yaw.

Propellant response to maximum vehicle accelerations are determined about the pitch-yaw, roll, and longitudinal axes separately. Slosh wave frequencies, amplitude, damping, and forces are computed. Ullaging times are estimated for all four configurations. These propellant characteristics are then applied to the four configurations of the reference mission. The reference maneuvers within each mission segment are then analyzed and potential problem areas noted. All of the reference maneuvers have characteristics in common, which permits further simplification of the analysis.

Combined pitch-roll maneuvers do not have a straight-forward analysis available. A rotating slosh mode would be generated which is assumed to create more complex but lower slosh forces on the vehicle than the pure transverse accelerations assumed.

Analysis - Vehicle Characteristics. The pitch-and-yaw moments of inertia averaged to a single value give about $\pm 10\%$ variation in vehicle moment of inertia. Moments of inertia used in computing the maximum accelerations in Table 5-II were calculated with bottomed propellants as a reference

condition. The c.g. (center of gravity) locations for all configurations are shown on Figure 5-1, with other pertinent dimensions used in this analysis. Figure 5-2 illustrates the axis definitions and nomenclature used.

Fluid Behavior. The results of this project have been used for predicting low-g liquid behavior; high-g behavior was analyzed using the information collected in NASA SP-106*.

The square of first mode slosh frequency can be shown to be** for moderate to high axial Bond number ($B_o > 50$)

$$\omega_1^2 = \left[\left(\frac{k_1}{r_o}\right)^3 \frac{\sigma}{\rho} \tanh(k, h_o) + \frac{k_1}{r_o}\, g \tanh(k, h_o)\right]$$

where r_o is the tank radius, or possibly a length in a transverse maneuver, σ is the liquid surface tension, ρ the density, h_o the liquid depth, g the local acceleration, and $k_1 = 1.84$. This equation reduces (for application throughout this analysis because of the relatively great liquid depth) to

$$\omega_1^2 = \frac{k_1 g}{r_o}$$

---

* The Dynamic Behavior of Liquids in Moving Containers, NASA SP-106, H. Norman Abramson, Editor, NASA Contract No. NAS 4-94(07), Southwest Research Institute, 1966, U. S. Government Printing Office, Washington, D. C.

** Reynolds, W. C., Saad, M. A., and Satterlee, H. M., "Capillary Hydrostatics and Hydrodynamics at Low-g," Tech. Rpt. No. LG-3, Dept. of Mech. Engr., Stanford Univ., Sept. 7, 1964.

Forces caused by lateral sloshing can be computed by use of a spring-mass mechanical analog, as shown in Figure 5-2. Parameters for this artifice were obtained from NASA CR-54700*. The parameters appropriate to this study are listed below.

		$B_\alpha = 0$	$B_\alpha \geq 100$
Equivalent spring constant	$\frac{\bar{\kappa}}{(1+B_\alpha)\sigma}$	24.9	3.86
Lateral force	$\frac{\bar{F}_x}{\sigma(1+B_\alpha)\bar{h}_w}$	4.62	1.80
Equivalent mass	$\frac{\bar{m}}{\rho r_o^3}$	8.8	1.43
Lateral force action point	$\frac{\bar{z}}{r_o}$	(See Table 5-IV)	

Where $\bar{\kappa}$ is the equivalent spring constant, $\bar{F}_x$ is the lateral force produced by a slosh wave of amplitude $\bar{h}_w$, $\bar{M}$ is the equivalent sloshing mass, and $\bar{Z}$ is the calculated location for the analog measured from the tank bottom.

This artifice has been used in this study to compute liquid forces and responses resulting from application of pulse control thrusts by the RCS. The excursion of the analog $\bar{X}$ is first computed

$$\bar{X} = \frac{g_T \bar{t}_1}{\bar{\omega}}$$

where g_T is the transverse acceleration, $\bar{t}_1$ is its duration, and $\bar{\omega}$ the natural frequency of the resulting wave also determined from NASA CR-54700 for zero-g conditions as

$$\bar{\omega}_1^2 = \omega^2 \frac{\sigma}{\rho r_o^3}$$

*Prepared by Lockheed Missiles and Space Co. for the NASA Lewis Research Center, Jan. 20, 1967.

(The frequency at Bond numbers between zero and 50-100 and greater were not required in this analysis.) The forced produced by the analog (and the wave) is determined from

$$\bar{F}_x = \bar{K}\,\bar{x}$$

and the liquid free surface response from the values in the preceding table in the text.

Slosh Damping was determined by use of Equation 4.10b) for the logarithmic decrement in NASA SP 106* modified so that the slosh frequency is a parameter.

$$\delta = 6.10\sqrt{\frac{\nu}{r_o^2\bar{\omega}}}$$

where ν is the kinematic viscosity of the liquid. The time t_1 to damp to 1/e times an original wave height was computed using

$$t_1 = \frac{2\pi}{\delta}$$

Vehicle rotations or control system operation will cause a transition in propellant behavior from a zero g capillary dominated system to a gravity dominated system. The duration and magnitude of large amplitude slosh forces during these transitions are required. Other investigations carried out during this study provide information with which to estimate these quantities. The greatest transients are possible when engine thrusts are terminated and residual slosh motion is present. The effect of this

---

* The Dynamic Behavior of Liquids in Moving Containers, NASA SP-106, H. Norman Abramson, Editor, NASA Contract No. NAS 4-94(07), Southwest Research Institute, 1966, U. S. Government Printing Office, Washington, D. C., P. 111

residual slosh can be interpreted in terms of the transverse motion of the mass center of the liquid, $x(t)$, in response to transverse force on the liquid by the tank. This is expressed by

$$\ddot{\bar{x}} = \frac{\bar{F}_x(\bar{t})}{\bar{m}}$$

where $\bar{F}_x(\bar{t})$ is the lateral force produced by motion of the entire liquid mass $\bar{M}$. Integration of this twice with respect to time with initial conditions $\bar{x}(0) = \dot{\bar{x}}_o$ (reflecting the worst case assumption that liquid kinetic energy is maximum and displacement from equilibrium is zero) yields:

$$\bar{x} = \dot{\bar{x}}_o \bar{t} + \frac{1}{\bar{m}} \int_0^{\bar{t}} \int_0^{\bar{t}} \bar{F}_x(\bar{t})\, d\bar{t}\, d\bar{t}$$

Consider transient carry-over of the liquid wave into a tank of infinite length. Drawing on test experience,* the lateral translation of the c.g. is approximated by

$$\bar{x} = \bar{r}_o \left[\frac{e^{-\beta \bar{t}}}{2} (\beta t + 2) - 1 \right]$$

with β a constant requiring evaluation. This approximation can be substituted into the preceding integral equation and the result differentiated twice to obtain the time variation of the lateral force. Thus,

$$\bar{F}_x(\bar{t}) = \bar{m}\, \bar{r}_o\, \beta^3\, \frac{\bar{t} e^{-\beta \bar{t}}}{2}$$

The constant β can be evaluated from the initial velocity of the c.g.

$$\beta = 2 \frac{\dot{\bar{x}}_o}{\bar{r}_o}$$

*See Residual Sloshing Experiment, in Section 3 of this report

Thus

$$\bar{F}_x(\bar{t}) = \frac{4\bar{m}\dot{\bar{x}}_o^3 \bar{t} e^{-\frac{2\dot{\bar{x}}_o \bar{t}}{\bar{r}_o}}}{\bar{r}_o^2}$$

The maximum force is

$$\bar{F}_x(\bar{t})_{MAX} = \frac{4\bar{m}\dot{\bar{x}}_o^2}{2e\bar{r}_o}$$

The reaction force exerted by the liquid on its tank is the negative of this.

Results. Calculations of the liquid behavior in the Apollo Spacecraft Propulsion System made in the course of this analysis are summarized in Tables 5-III and 5-IV. Table 5-III lists the acceleration environment for the four configurations discussed in this analysis.

General liquid behavior is presented in Table 5-IV.

The mechanical analog locations are given on lines 1 and 2 (see also Figure 5-2).

Natural sloshing frequencies are given on lines 3, 4, and 5.

Zero-g slosh wave responses to an assumed 0.020 second minimum RCS impulse are listed on lines 6, 7 and 8.

Slosh wave responses during axial thrusting of the RCS were computed but shown to be always less than 1 inch. In a similar vein, lateral forces produced by sloshing during axial RCS operation were computed, the largest being about 0.26 lbf. The forces produced by zero-g slosh waves were also computed and turned out to be always less than 0.04 lbf. Slosh wave response and lateral forces occurring during SPS firing were not

computed since they obviously should be within the capability of the spacecraft control system as long as the natural frequencies listed on line 4 are avoided. It seems apparent that sloshing would persist for considerable periods of time in the SPS tanks in zero-g -- principally because of the low zero-g slosh frequencies.

Transient forces produced by high energy, large amplitude waves were calculated using the technique outlined previously. The maximum possible forces and the force estimated when the liquid wave reaches the tank top were calculated for configuration IV in which the highest SPS acceleration occurs. The maximum possible lateral force was estimated to be 89 lbf. The moment produced by this force about the vehicle c.g. was estimated to be 195 lbf-ft. This compares with a maximum corrective moment capability of about 1300 lbf-ft. No precise way is known to calculate damping for such a situation, but an estimate of 20 seconds is offered. This is triple the time required for the wave to reach the tank top at its initial velocity. (This velocity should be relatively undiminished because of the very high energy of the wave relative to capillary restoring forces, i.e., high Weber number.)

These calculations are based on assumptions that thrust cutoff occurs at maximum kinetic energy and that the prior wave height is 0.1 tank radius and that the correct arm for estimating liquid produced moments is L_{P-Y} = 42 inches (for configuration IV).

The model developed for analysis of lateral forces produced by high energy waves indicates that the maximum force is proportional to the

square of the wave amplitude during the preceding high-g situation. The following pages provide some discussion of other liquid behavior in the four phases of the mission.

Translunar I: CSM/Lunar Module (LM)-SIV B Transposition* and Docking: High vehicle weight and propellant fill level minimize the propellant sloshing forces to be counteracted by the RCS. No venting or SPS firing is planned so ullaging is not required.

A typical sequence of maneuvers might include separation, a 180° pitch-yaw, an aligning roll, closure, fine adjustments in attitude and closure, and docking. Probable ullage reaction to these maneuvers is shown on Figure 5-3 and discussed below. Pitching could be performed in two minutes with $\ddot{\theta} = 0.003$ rad/sec^2 acceleration for 10 seconds to 0.03 rad/sec. The bottomed propellant interface 2 feet from the CSM c.g. would "see" 10^{-3} g at this velocity, giving a Bond number of 85 reorienting the ullage toward the vehicle c.g. The ullage bubble would reach the vicinity of the CSM centroid during this 2 minute pitch-yaw maneuver. A roll maneuver after the pitch-yaw would tend to align the ullage against the inner tank walls. Docking closure acceleration with the RCS will initiate proper ullaging for about 1/3 the tank length (Table 5-III). Fine attitude control and closure decelerations will perturb the ullage bubble but not cause serious problems. A retention screen failure is possible if the ullage bubble is on the screen at docking deceleration although it is unlikely that an

---

* Transposition in this sense refers to the inverting maneuver performed by the CSM prior to extraction of the LM from the spacecraft LM adapter.

ullage bubble would be in this position.

The navigational star sightings will induce numerous excursions of the ullage but are not considered in detail since no adverse acceleration is applied and ullage volume is low.

IMU alignment and midcourse orientation require consideration due to their proximity to the first midcourse SPS burn. No ullaging maneuver is specified at this point, presumably because of low ullage volume. This appears feasible but certain precautions should be considered. Almost any pitch-yaw maneuver such as an IMU alignment will provide favorable ullaging. Since no adverse accelerations are foreseen, the only precautions advisable are to minimize roll maneuvers in both rate and duration and to follow a roll with a prolonged pitch-yaw.

The thermal control rolling maneuver at either 2 or 5 revolutions per hour will position the ullage inboard, causing a portion of the containment screens to be dry but not failing. Failure should not occur in this configuration but a low margin of safety exists in the trans-earth configuration IV.

RCS checkout, IMU alignment, lunar injection orientation, and lunar injection are all maneuvers similar to those just discussed and similar arguments apply. From this point forward in the mission, propellant depletion permits high slosh waves and increases the possibility of retention screen failure because more screen area can become exposed.

Lunar Orbit CSM/LM-II: After this time in the mission, reorientation must be considered and slosh waves can become important with regard to

control. However, analysis shows the maneuvers create potential problem areas which will vary only in time and magnitude for the succeeding configurations. The centripetal acceleration due to a pitch-yaw maneuver with RCS only will favorably position the ullage away from the containment screens and against the upper dome, after the lunar orbit propellant depletion. Angular acceleration (τ_{P-Y}) will initially control the surface behavior but pitch-yaw maneuvers uniformly accelerated to angular velocities greater than or equal to .01 rad/sec will provide $B_o \geq 10$ and tend to favorably position the ullage. Sloshing will have been induced by acceleration to this angular velocity and centripetal acceleration level but will damp fairly soon. Since the pitch-yaw maneuver favorably affects ullage position, RCS propellants could be conserved by ullaging with a pitch or yaw only. That is, a 4 minute 360° pitch could be initiated and stopped with 20 seconds of RCS giving 4 minutes bottoming time, whereas 27 seconds of only axial RCS thrust would be required for bottoming, exclusive of screen clearing, and still give no safety factor.

Since the RCS maximum capability in configuration II cannot cause excessive wave forces, or adverse ullage positioning in any mode except for an unlikely RCS roll-adverse axial thrust combination, attitude control and orientation maneuvers prior to lunar orbit separation should cause no additional difficulties.

Lunar Orbit - Separated III: The LM separation is preceded by a yaw orientation which will tend to favorably position the ullage. The only detrimental combination of maneuvers appears to be a roll maneuver just prior to separation which would cause the screens to be dry and subject

to failure under adverse separation accelerations.

Configuration III in Lunar Orbit will be station keeping with attitude control, experiencing no additional problems. If the propellants are not subjected to significant accelerations, the ullage bubble may be expected to cling to the central standpipe, free of all tank ends due to capillary pumping along the standpipe. Capillary forces (minimum energy interface) will not permit the ullage to enter the region below the containment can and into the screens, nor will capillary pumping occur from the sump tank to storage tank.

Ullaging is required to permit a CSM plane change with the SPS, preparatory to LM rendezvous. Ullaging time and RCS propellant required will depend on the technique employed, as previously discussed. Since the plane change is preceded by IMU alignment, pitch-yaw maneuvers will have bottomed the ullage without further RCS firing, if the roll maneuvers are not last.

Transearth - IV: The LM/CSM docking and separation maneuvers (during configuration IV) can lead to a deorientation of the propellants in the sump tank and subsequent failure of the retention system umbrella screens with relatively low liquid depths indicated in Table 5-II. Consider the LM docking event in lunar orbit with propellants covering the screens. A docking impulse producing a velocity increment of 10 cm/sec produces an impulsive Weber number in the oxidizer tank of

$$We = \frac{(\Delta V)^2 R}{\beta_{N_2O_4}} = \frac{100 \times 25.5 \times 2.54}{19} = 342$$

Based on the results of the study of reorientation under impulsive

accelerations, an impulsive Weber number of this magnitude could result in complete draining of the propellant above the retention screens and recollection at the top of the sump tank exposing the umbrella screen to pressurization gas. Since the stability limit of these screens in the presence of the full stillwell is of the order of 2×10^{-3} g_o (see Passive Retention System Analysis Section 2) an adverse acceleration of 8×10^{-3} g_o such as that produced by the RCS system during separation of the CSM and LM (see Table 5-III) would cause failure of the screens over those areas exposed to pressurization gas. The quantity of pressurization gas forced past the screens is dependent on the duration of the RCS acceleration period during the separation maneuver.

Conclusions. A roll maneuver should not be followed by an adverse acceleration such as docking, if retention screen failure is to be avoided.

The RCS may not be capable of counteracting the maximum forces of a high energy slosh wave generated in SPS firing, but such a perturbation would probably be of short duration.

RCS propellants for ullaging could be conserved by ullaging over a longer time pitch or yaw instead of with axial accelerations only.

Operation of the Service Module RCS can cause retention system failure. The extent of the failure, i.e., how much liquid is displaced, depends on the duration of the thrust.

Table 5-I

APOLLO SERVICE MODULE MANEUVERS SIGNIFICANT TO PROPELLANTS

*Maneuvers After Injection	*Acceleration Systems & Axis	Configuration
Docking CSM/LM-S IVB	RCS	
Star Sighting	RCS,P-Y,R	Translunar
IMU Alignment	RCS,P-Y,R	
Midcourse Orientation	RCS,P-Y,R	
Midcourse	SPS	
Roll Control & Damping	rcs,P-Y,R	
Thermal Control	RCS,R	
RCS Check Out	RCS,P-Y,R	
IMU Alignment	RCS,P-Y,R	
Lunar Inject Orientation	RCS,P-Y,R	
Lunar Injection	SPS	Translunar
Roll Control & Damping	RCS P-Y,R	Lunar Orbit-Mated
Orientation	RCS,Y	
LM Separation		Lunar Orbit-Separated
Lunar Orbit-Attitude Control	RCS,P-Y,R	
IMU Alignment	RCS,P-Y,R	
Ullage	RCS-A	
Plane Change	SPS	
Roll Control & Damping	RCS-P-Y,R	
LM-Orientation, Tracking, Hold	RCS-P-Y,A	
LM/CSM Docking	RCS-P-Y,R,A	
LM Jettison & Damping	RCS-P-Y,R,A	
Roll Control & Damping	RCS -P-Y,R	
IMU Alignment	RCS-P-Y,R	Lunar-Orbit Separated
Star Sighting	RCS-P-Y,R	
Orientation	RCS-P-Y,R	
Ullage	RCS-A	
Transearth Injection	SPS,RCS,P-Y	

(continued)

Table 5-I (continued)

*Maneuvers after Injection	*Acceleration Systems & Axis	Configuration
Roll Control & Damping	RCS-P-Y,R	Transearth
Thermal Control	RCS-R	↓
IMU Alignment	RCS-P-Y,R	
Orientation	RCS-P-Y,R	
Ullage	RCS-P-Y,R	
Midcourse	SPS-RCS P Y	

*Note: CSM is Command Service Module
LM is Lunar Module
RCS is Reaction Control System
SPS is Spacecraft Propulsion System
P is Pitch
Y is Yaw
R is Roll
A is Axial
P-Y denotes the average of pitch and yaw.

Table 5-II

GEOMETRICAL CHARACTERISTICS

	I Trans-lunar mated	II Lunar Orbit mated	III Lunar Orbit-(separated)	IV Trans-Earth (separated)
1. Ullage Volume, %	10	68	75	85
2. Average propellant depth $(\bar{h}/\bar{r})_o = h_o$	6.58	4.88	4.40	3.78
3. Average Ullage Depth $(\bar{h}/\bar{r})_u = h_u$	0.82	2.52	3.00	3.62
4. Free surface to pitch-yaw axis, L_{P-Y}	47	88	27	42
5. Side oriented liquid depth $(\bar{h}/\bar{r})_s = h_s$	1.96	1.25	1.15	1.02
6. Free-surface to vehicle roll axis, L_R - ft.	2.56	3.98	4.18	4.45

Note: See Figure 5-2 for definition of terms.

Table 5-III

ACCELERATION ENVIRONMENT

Item	Configurations I	II	III	IV
Axial Accelerations				
1. SPS acceleration, g/g_o	0.233	0.322	0.668	0.829
2. Bond Number B_α (SPS)*	34,500	47,700	99,000	123,000
3. RCS acceleration, g/g_o	0.0023	0.0032	0.0067	0.0083
4. Bond Number B_α (RCS)*	345	477	990	1230
Pitch-Yaw Accelerations				
5. Angular Acceleration, $\ddot{\theta}_{P-Y}$, rad/sec^2	0.00322	0.00352	0.0172	0.0184
6. Resulting transverse acceleration, τ_{P-Y}/g_o	$.387 \times 10^{-3}$	$.802 \times 10^{-3}$	1.2×10^{3}	2.0×10^{-3}
7. Bond number, $B_{\tau,P-Y}$ **	58	80	167	207
Roll Accelerations				
8. Angular accelerations $\ddot{\theta}_R$, rad/sec^2	0.0197	0.0490	0.0720	0.0775
9. Resulting transverse acceleration, τ_R/g_o	3.87×10^{-3}	7.49×10^{-3}	10.6×10^{-3}	10.7×10^{-3}
10. Bond Number, $B_{\tau,R}$ ***	580	803	1670	2070
Translation Acceleration				
11. RCS acceleration τ_{TRANS}/g_o	0.0021	0.0029	0.0061	0.0075
12. Bond number, $B_{\tau,TRANS}$	3.5	436	905	1130

* $B_\alpha = \rho g r_o^2/\sigma$

** $B_{\tau,P-Y} = \rho \tau_{P-Y} r_o^2/\sigma$

*** $B_{\tau,R} = \rho \tau_R r_o^2/\sigma$

Table 5-IV

LIQUID BEHAVIOR SUMMARY

Item	Configurations			
	I	II	III	IV
Mechanical analog location $\bar{Z}/r_o$				
1. for $B_\alpha = 0$	6.62	5.50	4.86	4.20
2. for $B_\alpha = \infty$ (1)	6.06	4.36	3.76	3.50
Natural Frequencies (2), rad/sec				
3. for zero-g (3)	0.0175			
4. for SPS operation	2.60	3.06	4.38	4.90
5. for RCS operation	0.260	0.306	0.438	0.490
Zero-g slosh response (4), ft				
6. to pitch-yaw pulse	0.075	0.16	0.24	0.39
7. to roll pulse	0.75	1.6	2.4	3.9
8. to translation pulse	0.41	0.57	1.20	1.50
Slosh damping ratio, δ				
9. for zero-g	0.060			
10. for SPS operation	0.0049	0.0045	0.0038	0.0036
11. for RCS operation	0.015	0.014	0.012	0.011
Slosh damping times, sec.				
12. for zero-g	6000			
13. for SPS operation	530	460	380	360
14. for RCS operation	1610	1460	1200	1160

(1) Effectively $B_\alpha > 100$.

(2) For axial acceleration or zero g.

(3) Based on $\sigma/\rho = 26.4$ Cm^3/sec^2 and $r_o = 49$ in (the average of fuel and oxidizer properties and dimensions)

(4) Computed based on minimum pulse width 0.02 sec for 2 RCS units for $B_\alpha = 0$.

ANALYSIS OF APOLLO LUNAR MODULE PROPELLANT BEHAVIOR DURING LUNAR DESCENT AND ASCENT

The purpose of this analysis is to predict the behavior of the propellants in the Lunar Module (LM) tanks due to flight disturbances encountered in the LM lunar descent and ascent missions. The source of information regarding the lunar mission used in this study was NASA/MSC Internal Note No. 66-FM-70 (Confidential).

Objectives. The major objectives of this study are:

1. To predict the location of the ullage gas volume in the propellant tanks during the descent and ascent phases of the mission to determine whether drain unporting can occur.
2. To examine the sloshing situations which occur to estimate the sloshing magnitudes, forces, and rates of decay.
3. To predict ullage orientation after settling maneuvers.
4. To evaluate liquid propellant interaction with LM Reaction Control System (RCS) operation.
5. To estimate forces resulting from liquid impacts occurring during LM APS/CSM (Command/Service Module) docking.

Mission Profile. The mission profile for the LM ascent and descent flights is described below, with emphasis on the main engine thrusts. The studies outlined above are in chronological order with respect to the mission flight plant. The three propellant behavior studies occur from CSM/LM separation and LM descent to LM ascent and CSM/LM docking where applicable.

After CSM/LM separation in or it around the moon, the LM/DPS coasts for 30 minutes before performing a Hohmann transfer burn for approximately 33 seconds, which uses three thrust levels and alters the orbit for descent to the lunar surface. After a coast of approximately 1 hour, the LM/DPS is put into a main descent thrust which lasts for approximately 10 minutes, with throttling of the descent engine, and results in a lunar landing.

After a lunar stay of approximately 1 day, the ascent phase is started, according to plan. Leaving the descent stage on the moon, the LM/APS main engine burns for approximately 7 minutes at one thrust level, putting the LM into a coplanar orbit with the CSM. After this single ascent thrust, many orbital adjustments are made with the LM/RCS to provide the near zero relative velocity required for docking. The final CMS/LM docking maneuver is performed with a closing velocity of approximately 1 ft/sec provided by the LM/RCS.

Liquid Behavior Analysis Ullage Reorientations Prior to Main Engine Thrusts. During the LM descent phase, two ullage reorientations are performed, one before the Hohmann transfer main engine thrust and the other before the main descent firing of the LM/DPS. Both the LM descent and ascent propellant tanks, shown respectively in Figures 5-4 and 5-5, have a high fraction of propellant fill during these ullage firings, in the range of 0.90 to 1.00. These relatively small ullage volumes, with an equivalent spherical diameter D_e much less than the tank diameter D, will rise as spherical capped bubbles under the ullage acceleration. From Haberman and Morton* the rise

*W. L. Haberman and R. K. Morton, "An Experimental Investigation of the Drag and Shape of Air Bubbles Rising in Various Liquids," The David W. Taylor Model Basin Report 802, Sept. 1953.

velocity U_∞ of this bubble in a liquid of infinite extent may be predicted from the constant drag coefficient, $C_D = 2.6$. The ratio of ullage bubble diameter to tank diameter D_e/D may then be computed, and the rise velocity U_∞ in the tank of diameter D may then be estimated from Figure 4 of Harmathy*. The distance S that the bubble rises in the time of the ullage thrust t may be estimated from the bubble rise velocity U_∞ and this distance S may be compared to the total length of the descent tanks, $L = 5.84$ ft. These computations are shown below in tabular form for the descent tanks that supply the LM/DPS.

Quantity	1st Ullage Hohmann Transfer	2nd Ullage Main Descent
Acceleration, g	$0.00615g_o = 0.198$ ft/sec^2	$0.00622g_o = 0.200$ ft/sec^2
Fraction Fill, descent tank	0.949	0.930
Equiv. diameter, D_e	1.83 ft	2.03 ft
$U_\infty = 0.716\sqrt{gD_e}$	0.431 ft/sec	0.456 ft/sec
Tank diameter, D	4.25 ft	4.25 ft
D_e/D	0.431	0.478
U/U_∞	0.75	0.70
Rise Velocity, U	0.323 ft/sec	0.320 ft/sec
Thrust time, t	11.20 sec	11.20 sec
$S = Ut$	3.62 ft	3.58 ft

For the two ullage reorientations shown above in the descent tanks, the total distance of ullage bubble rise, $S \approx 3.6$ ft, is 60% of the total tank length $L = 5.84$ ft. Then, even with the ullage gas volume initially at the drain end of the tank, it would rise into the upper 40% of the

* T. Z. Harmathy, "Velocity of Large Drops and Bubbles in Media of Infinite or Restricted Extent," A.I.Ch.E. Journal, Volume 6, Number 2, June 1960, pp. 281-288.

propellant tank volume due to the ullage thrust. Hence, following these ullage maneuvers, the ullage gas volume would be located in the upper 40% of the descent tank volume, far enough from the propellant tank drain to allow no gas ingestion in the LM/DPS main engine start-up for both the Hohmann Transfer and Main Descent.

The above analysis assumes that the ullage volume moves as a single gas bubble, and that it is not fractionated before or during the ullage thrust. Experiments with propellant reorientation in model tankage have shown that the ullage volume will remain as a single volume. Also, without violent maneuvers prior to the ullage thrust, the ullage gas will be in the form of a single volume from the last main engine thrust on the vehicle.

For the LM Ascent stage, only one main engine thrust is used to place the spacecraft in orbit about the moon. The ullage volume is initially located at the top of the ascent propellant tanks with the LM landed on the moon, so that no ullage maneuver is required at the start of the main engine ascent phase. Further control of the LM/APS required for docking with the CSM is accomplished through the RCS thrusters, and no attempt was made to consider propellant orientations in the nearly empty LM ascent tanks because these propellants will never be drawn from the ascent tanks.

Propellant Sloshing During Main Engine Thrusts: The first descent main engine firing is the Hohmann transfer following the RCS ullage thrust. Since this ullage process may result in the ullage volume located anywhere (conservatively) in the upper 40% of the descent tanks, this ullage volume may be located in an antisymmetric position with respect to the tank axis. In fact, the pitch, roll and yaw maneuver contemplated prior to the first

ullaging will very likely result in an off-axis location for the ullage bubble. Upon start of the descent engine, this antisymmetrically located ullage bubble will rise to the surface and create an antisymmetric slosh mode at the liquid free surface. With the small fractional ullage volume of 0.051 at its most disadvantageous antisymmetric location, it is estimated that the largest amplitude first mode slosh would be approximately 0.20 of the tank radius, $\mathcal{J}_{o_{MAX}}^{*} = \mathcal{J}_o/R = 0.20$. Depending on the ullage volume location at the descent engine start, the induced first mode dimensionless slosh amplitude may be anywhere in the range $0 < \mathcal{J}_o^{*} < 0.20$, with an equilibrium liquid level of $h^{*} = 2.40$.

During the Hohmann transfer thrust, which lasts a period of 32.77 seconds, and involves three main engine thrust levels, the slosh damping caused by the upper ring baffle was estimated using the methods and procedures developed in Section 2 of this report. In the analysis of this damping, caused by the upper ring baffle during the Hohmann transfer thrust, the dimensionless depth d^{*} of the upper ring baffle varied from $0.65 > d^{*} > 0.60$. Three initial dimensionless sloshing amplitudes $\mathcal{J}_{o_i}^{*}$ caused by an antisymmetric ullage volume location at Hohmann start-up were assumed, and the sloshing amplitude at the end of the Hohmann transfer cutoff $\mathcal{J}_{o_f}^{*}$ were computed and are presented below.

Hohmann Transfer Slosh Damping

Initial Sloshing amplitude, $\mathcal{J}_{o_i}^{*}$ (assumed)	0.050	0.100	0.200
Final sloshing amplitude, $\mathcal{J}_{o_f}^{*}$	0.047	0.091	0.173

As seen from the above tabulation, the upper ring baffle of the descent tank, at $h^{*} = 1.74$, provided very little damping for the assumed propellant

sloshing with the equilibrium liquid level at $2.34 < h^* < 2.40$. With the baffle at a dimensionless depth $d^* = \frac{d}{R} \approx 0.60$, the ring baffle is very ineffective in providing slosh damping during the 32.77 seconds of Hohmann transfer thrust. Therefore, the sloshing magnitude induced at Hohmann start-up would be only slightly damped during the Hohmann transfer thrust. The logarithmic decrement δ_ℓ of this assumed slosh damping was found to be in the range $0.010 < \delta_\ell < 0.024$ for this ring baffle damping.

The viscous damping associated with sloshing in the upper hemispherical region of the descent tank was estimated based upon work in NASA SP 106*. The viscous slosh damping was estimated from

$$\delta_\ell = C_3 \left(5.23\, \upsilon^{1/2}/R^{3/4} g^{1/4}\right),$$

where $C_3 \approx 2.0$ for this fill level. The logarithmic decrement based upon viscous damping was found to range from $0.005 < \delta_\ell < 0.017$, for the Hohmann transfer thrust phase. As these viscous damping factors are approximately 1/2 of those due to the upper ring baffle, their effect on slosh damping would be small compared to the already small values computed for the ring baffle. Because of the small effects of viscous damping in both the LM ascent and descent tanks, viscous slosh damping will not be considered in the low amplitude sloshing encountered above.

The main descent thrusts will begin with an ullage gas fill fraction of

---

*H. N. Abramson, editor, "The Dynamic Behavior of Liquids in Moving Containers," National Aeronautics and Space Administration, NASA SP-106, 1966.

0.070 at an equilibrium liquid fill level of $h^* = 2.34$ and will occur over approximately 10 minutes time with a number of thrust levels resulting from the throttleable LM descent engine. At the end of this time, at lunar landing, the LM descent tanks have a liquid fraction fill of 0.083, and a dimensionless fill level of $h^* = 0.40$. Hence, during the main descent phase, the LM descent tanks go from a virtually full to a virtually empty propellant configuration, and the equilibrium liquid level passes each of the four baffles shown on Figure 5-4.

As in the previous Hohmann transfer phase, the main descent phase starts with a small ullage volume fill fraction of virtually the same conditions following the RCS ullage maneuver. Depending on the antisymmetric location of this ullage bubble, sloshing modes may be developed at the start of the LM descent engine. At this time the upper baffle is at a dimensionless depth $d^* \approx 0.60$, and during the next two minutes of firing time the liquid level will drop past the upper baffle. At baffle depths of less than $d^* = 0.50$, the ring baffles are most efficient at slosh damping, so that propellant sloshing should be drastically reduced as the liquid level approaches the baffle from above.

Assuming dimensionless slosh amplitudes $\mathcal{L}_{oi}^*$ of 0.05, 0.10, and 0.20 induced at LM main descent thrust initiation, a slosh damping analysis was made as the liquid level passed the baffle. The final dimensionless sloshing amplitudes $\mathcal{L}_{of}^* = \mathcal{L}_{of}/R$ were found to vary from 0.0005 to 0.002, which means that virtually all sloshing of the propellant is damped out as the liquid fill level passes in the baffle depth range $0.5 > d^* > 0$.

Based upon this calculation, it can be said that any sloshing induced in the

liquid propellants at a level above a baffle will be virtually damped out as the liquid level drops past the baffle under main engine thrust in either the LM descent or ascent tanks. The logarithmic decrement δ_ℓ of damping reaches values in the range 0.1 to 1.0 as the liquid surface approaches the baffle depth.

During the main descent phase sloshing may occur due to roll, pitch, or yaw programmed into the spacecraft flight path down to the hover phase. From the Grumman report* on the LM/RCS maneuvers during main descent, estimates of transverse accelerations were made on the descent tanks due to roll, pitch, and yaw about the center of gravity. Transverse accelerations were estimated to range as high as 0.01 g_o during the LM descent phase due to radial accelerations induced by a constant roll, pitch or yaw rate of as much as 10°/sec about the axis of rotation, and tangential accelerations due to the acceleration or decelerations of roll, pitch, or yaw rates in a plane perpendicular to the axis of rotation. Then these induced transverse accelerations, a_T, in the range $0 < a_T < 0.01\ g_o$, are compared to the main thrust axial accelerations, a_A, in the range $0.20\ g_o < a_A < 0.65\ g_o$, the transverse accelerations are at maximum 1/20 of the axial accelerations. Transverse thrust of this level could not induce slosh amplitudes ζ_o greater than 0.10 of the tank radius R, so that, except for conditions near 1st sloshing mode resonance, dimensionless slosh amplitudes in the range $0 < \zeta_o^* < 0.10$ will result from these roll, pitch, or yaw motions during LM descent thrust. Sloshing frequencies in the range $0.15 \text{ cps} < f < 0.27 \text{ cps}$ have been calculated for this study. As long as control system frequency is adjusted

*R. Peerce, "RCS Thrusters Duty Cycle for the Design Weight LEM (U)," Grumman Aircraft Engineering Corporation, LEM Engineering Memorandum, LMO-310-256, 11 October 1965, (Confidential).

to be $f_c < 0.1\ f$ or $f_c > 1.5\ f$, the foregoing result will hold.

If these sloshing motions were to occur with the liquid propellant surface at a dimensionless depth $d^* = \frac{d}{R} > 0.5$ above the nearest baffle, then this sloshing would be only slightly damped and would persist for minutes. However, if this sloshing surface moves within the dimensionless depth $d^* < 0.5$, then considerable damping will be obtained from the ring baffle, and this transverse acceleration induced sloshing due to roll, pitch, or yaw motions will be damped out within approximately 30 seconds.

The sloshing induced by possible lateral translations of the LM descent stage while in the lunar hovering mode searching for a lunar landing spot is of major interest in this study. Just before lunar touchdown, the LM descent tanks are only 0.083 full of liquid propellants, with a dimensionless fill level $h^* = \frac{h}{R} = 0.40$, which is below the lowest ring baffle. Under these low fill levels, sloshing induced by lateral accelerations while searching for a landing point may possibly uncover the LM descent tank drain, and allow ullage gas ingestion to the LM descent engine. The following discussion is pointed at determining the likelihood of this unfortunate occurrence. In the hovering mode, the lateral or transverse accelerations are induced by the RCS thrusters which fire for a 5 second time period and impart a transverse acceleration of $a_T = 0.0125\ g_o$ on the LM/DPS. This compares to an axial acceleration in the hovering mode of $a_A \approx 1/6\ g_o$ which acts continually until let down.

The sloshing amplitudes and forces which result from these intermittent transverse accelerations may be computed by means of a mechanical oscillating model of the sloshing liquid in the tank bottom. Using the modeling

methods of Rattayya* the amplitude of the induced sloshing mode may be estimated. With a minimum liquid depth of h = 0.40 R at the hemispherical bottom, the time required for a first mode sloshing cycle under the axial acceleration a_A is approximately 3.68 seconds. Since the transverse acceleration A_T occurs for 5 seconds, which is greater than 1/4 of the slosh cycle, the maximum slosh energy will be imparted to the slosh mode. Here, again, thrust reversals during the hover mode must be accomplished so as to avoid resonance with the liquid. The control system frequency range of $0.14 \text{ cyc/sec} < f_c < 0.36 \text{ cyc/sec}$ should be avoided. This assures that amplification of the 1st mode wave will not cause drain unporting. The maximum dimensionless slosh amplitude is calculated to be $\zeta_o^* = \zeta_o/R = 0.10$. This results in a maximum lateral slosh force of approximately 8 pounds on each of the oxidizer tanks and approximately 5 pounds on the fuel tanks.

The general character of this transverse induced slosh wave is shown in Figure 5-6, which shows the maximum possible slosh wave amplitude superimposed on the propellant's equilibrium position. This figure shows that the resulting slosh wave does not pose a threat to uncovering the LM descent tank drain. The vortex suppression device at the tank drain is always covered with liquid to a depth of approximately 0.40 of the tank radius.

---

*J. V. Rattayya, "Sloshing of Liquids in Axisymmetric Ellipsoidal Tanks," AIAA Second Aerospace Sciences Meeting, AIAA Paper No. 65-114, January 25-27, 1965.

It may be concluded that lateral sloshing modes induced during the hovering maneuver prior to LM/DPS lunar landing do not appear to pose a threat to ullage gas ingestion in the LM descent engine. The lateral slosh forces which result are also quite small, on the order of 10 pounds per tank.

During the LM ascent phase, which results from a single, one-thrust-level burn of the LM ascent engine, requiring approximately 7 minute's time, the axial acceleration varies from $0.36\ g_o < a_A < 0.65\ g_o$. Since the propellants are bottomed and the liquid surface is horizontal at lift-off, no sloshing can be induced by an antisymmetric location of the ullage gas as in the descent stage. During the main ascent, a pitch and yaw motion are made with the RCS thrusters at a rate of about 10°/sec, which is similar to the pitch rates used in the descent phase. Because of similar distances from the vehicle center of gravity for the ascent and descent tanks, the radial accelerations due to pitch and yaw will be comparable. However, due to the lighter mass of the LM/APS stage, greater angular accelerations will result from RCS induced angular momentum changes to the start and stop of pitch rates. This will result in a higher tangential acceleration perpendicular to the radius vector about the center of gravity. It is estimated that these radial and tangential accelerations could result in a transverse acceleration a_T on the LM ascent tanks in the range $0 < a_T < 0.018\ g_o$. Because this is at most 1/20 of the main thrust axial acceleration, then the maximum slosh amplitude that could result from these pitch and yaw

motions is 0.10 of the tank radius. Hence, dimensionless slosh amplitudes, $\ell_o^* = \ell_o/R$, in the range $0 < \ell_o^* < 0.10$ will result from the proposed pitch and yaw motions during LM/APS main thrust.

If the LM ascent tanks are baffled as shown in Figure 5-5, then these motions should be damped rapidly, because this tank is well baffled except for fill levels near the top, and a depth $d^* > 0.5$ is unlikely compared to the liquid surface. If the ascent tank does not have the ring baffles shown in Figure 5-5, then the slosh damping due to viscous damping will be minimal, and these induced slosh amplitudes will persist and diminish over several minutes of thrust time. The calculated log decrement here is about 0.01 or less. The maximum possible amplitudes, $\ell_o^* \approx 0.10$, of these pitch and yaw induced slosh modes do not pose a threat of gas ingestion at LM/APS shut-down, as these occur midway in the ascent engine thrusting time. Here, again, control system frequency must avoid 0.35 cyc/sec $< f_c <$ 0.95 cyc/sec to avoid resonance with 1st mode sloshing.

Propellant Reorientation After Main Engine Thrust: Following a LM main engine thrust in orbit around the moon, the liquid propellant will reorient from a high Bond number, high gravity configuration, to a low Bond number, low gravity configuration. The reorientation times and sloshing frequencies that result from surface tension and inertia forces which are dominant during zero thrust flight may be estimated using the suggestion of Reynolds, et. al.* This analysis will be applicable to the LM descent

*W. C. Reynolds, M. A. Saad, and H.M. Satterlee, "Capillary Hydrostatics and Hydrodynamics at Low-g," Mechanical Engineering Department, Stanford University, Stanford, California, Technical Report Number LG-3, September 1, 1964.

tanks following Hohmann transfer thrust, and to the LM ascent tanks following main ascent thrust and RCS thrusts prior to CSM/LM docking. The main LM descent thrust, , resulting in lunar landing, will not involve this type of propellant reorientation due to the previously bottomed tanks during hovering and the lunar gravity. The time required for liquid to reorient from the high g, flat interface to the zero g, curved interface of diameter of curvature D is

$$\Delta t = k\sqrt{\rho D^3/\sigma}$$

where $k = 0.16$* for cylindrical or spherical tanks. Then, $\Delta t = 0.16\sqrt{D^3/\beta}$. With the LM spacecraft in orbital flight and no external thrusts being applied, tank Bond numbers on the order of 0.02 have been computed for the small orbital accelerations that exist on the LM ascent and descent tanks. The liquids in these tanks subjected to a Bond number much lower than unity will behave largely as if they were in a zero gravity environment.

For the LM descent stage at the end of the Hohmann transfer thrust, the ullage volume tank fraction is 0.070 and the equivalent spherical diameter of the ullage volume is 2.03 ft. Substituting this diameter in the reorientation time expression above yields approximately 15 seconds for both the oxidizer and fuel tanks. As this reorientation time represents 1/4 of the slosh motion time, this small ullage volume will oscillate about its zero gravity equilibrium position at about 1 cyc/min. It is doubtful that the baffles will provide much slosh damping for this small volume vapor cavity, so equilibrium will be obtained by viscous damping over a long period of time. RCS thrusts that occur during this coast phase before main descent thrust will also create the same frequency oscillations about the

*Reynolds et al, op. cit.

zero gravity equilibrium shape in a new location in the descent tanks following RCS thrust.

For the LM ascent stage following main ascent thrust, the spherical tanks are only filled to a fraction 0.027 of the tanks volume. With the ascent tanks mostly filled with ullage gas at this time, the diameter of curvature of the liquid gas interface will be approximately equal to the tank diameter, D = 4.08 ft. Substituting this diameter into the zero g reorientation time expression yields a Δt of approximately 45 seconds. Hence, the axial sloshing period resulting from this motion would be on the order of 3 minutes. Similar motions would result from liquid reorientation following the many axial or nonaxial RCS thrust adjustments made before CSM/LM docking. The small amount of liquid would be transported to new locations in the tanks during each RCS thrust acceleration on the tanks.

CSM/LM Docking: The last maneuver prior to hard docking of the LM APS is a 7.70 second thrust of the RCS to engage the probe in the droque preparatory to hard docking. This accelerations of 0.039 g_o will result in a LM velocity of approximately 1 ft/sec that will bottom the approximately 1 ft^3 of propellants remaining in each of the LM tanks. When the hard docking is accomplished, the docking deceleration will force this liquid to run to the upper end of the ascent tanks. If ring baffles are located in the ascent tank, this liquid will fall through the tank center and impinge on the bottom, with little or no rebound. If the ascent tanks do not have ring baffles, then a wall bound reorientation will occur from the bottom to the top of the ascent tanks, possibly resulting in a liquid rebound jet at the tank top and flow back along the center toward the bottom. It

will be assumed that the hard docking implies an almost instantaneous stop of the LM when meeting the CSM, or at most over a few tenths of seconds of time.

For both the baffled and unbaffled tanks, consider that after hard docking the liquid travels toward the tank bottom at a mean velocity of 1 ft/sec, requiring 4 seconds to traverse the LM tank diameter. Assuming that the liquid will impinge at the top of the tank over a one second time period, the average deceleration on the liquid propellants is 1 ft/sec^2 from 4 to 5 seconds after the hard dock. The force created by this one cubic foot of liquid impinging on the tank top can now be estimated using Newton's second law. For the oxidizer tank, this will result in mean force per one second impingement time of 3 pounds; for the fuel tank, approximately 2 pounds. If the impingement time is assumed to be only 0.1 second at the tops of the tanks, then the forces exerted on the oxidizer and fuel tanks would be 30 and 20 pounds, respectively. The above force estimates would best apply to the baffled tank. In the unbaffled tank, where an unimpeded rebound phenomena would develop down the tank center, forces approximately double those given above should be estimated for impingement at the tank top. The forces appear very small compared to spacecraft docking weights. No serious difficulties can be envisioned resulting from the effect of the docking impact on liquid behavior in the tanks.

Conclusions. The studies of propellant reorientations and sloshings made before, during, and after main engine thrusts of the LM ascent and descent stages when separated from the CSM in the vicinity of the moon are

presented in this report. After ullaging prior to main engine start, no ullage gas should be entrained in the LM/DPS stage at the start of either the Hohmann transfer or main descent. Since these small ullage volumes may be antisymmetrically located with respect to the tank axis, slosh amplitudes as high as 0.2 of the tank radius may occur at descent engine starts.

When considering sloshing with main engine firing for both the LM/DPS and LM/APS, slosh amplitudes less than 0.1 of the tank radius can be expected from the roll, pitch, and yaw perturbations programmed into the flight. For ring baffled tanks, this sloshing will be well damped as the liquid level approaches a baffle. If the tanks are not baffled, then a sloshing mode will persist for minutes of time, and will only be slowly damped due to viscous and geometry interactions with the tank walls. The time for one sloshing cycle ranges from 1.3 to 6.5 seconds during main engine thrust in this study.

The sloshing caused by later perturbations of the LM/DPS while searching for a lunar landing point were found to induce slosh amplitudes of 0.10 the tank radius. Since the minimum fill level in the descent tanks is 0.40 of the tank radius, this magnitude of sloshing will not even come close to uncovering a tank drain, and no ullage gas ingestion should result in the descent engine during the hovering maneuver.

Estimates of propellant reorientation and oscillation times were made for the propellants after main engine shutdown in a low Bond number, near zero gravity environment. Also, during the LM/CSM docking, a rough estimate of the forces induced by the propellants on the tops of the LM ascent tanks was made. These forces might be as high as 60 pounds for the oxidizer

tank and 40 pounds for the fuel tank on the LM/APS.

It appears that baffles are not actually required in the LM descent or ascent stage tanks as long as control system frequency f_c is chosen outside the range 0.10 cyc/sec $< f_c <$ 0.95 cyc/sec. The expected forces produced by lateral sloshing are small enough to be ignored. With the above restriction, drain unporting will not occur.

FLUID STABILITY ANALYSIS OF THE PROPELLANT RETENTION SYSTEM OF THE APOLLO SERVICE MODULE

The analysis considerations discussed in Section 2 of this report regarding passive propellant retention have been applied to a detailed analysis of the Apollo Service Module retention system and possible modes of failure. A specific requirement for this analysis was to determine possible failure modes of the retention system during certain maneuvers planned on the earth orbital mission AS503A in the Apollo program. The results of this analysis are presented here.

The first portion is a general analysis of the stability characteristics of the Apollo SPS retention system. This is followed by analysis with particular reference to the AS503A mission.

The system of interest is sketched schematically on Figure 5-7. The dimensions of the fuel and oxidizer tanks are, for the purpose here, not significantly different and will, therefore, not be considered separately. Approximate dimensions (scaled from North American drawings V17-480241 and V17-947030) are shown on Figure 5-7. The size of the openings in the retention screens shown were obtained from conversations with NASA personnel.

During engine operation liquid enters the sump through the inner annulus and is collected in the outer annulus of the cylindrical sump can which is ducted to the engine. An additional quantity of propellant is retained at the sump inlet by the screens external to the outer annulus. The central standpipe provides communication between the liquid in the sump and the liquid at the opposite end of the tank.

The analysis presented here is concerned with the behavior of the liquid sump can when body forces on the liquid, which result from vehicle accelerations, are directed downward and from side to side on Figure 5-7.

While the tank is filled, the gravitational body force is directed as shown on Figure 5-8. Liquid rising in the sump traps a quantity of gas in what is then the upper end of the sump. The pressure during filling is one atmosphere, whereas the operating pressure is 180 psia. Therefore, the volume of the gas bubble is reduced to 15/180 of its original size.† During operation in a low-g environment in which the acceleration is in the direction shown on Figure 5-9, the liquid gas interfaces will look generally as shown. Gas bubbles will protrude through the perforated screens as indicated. There will be an interface between the liquid in the sump and the trapped gas approximately as shown. The stability limit of a liquid-gas interface in an annular container in an adverse gravitational field as is the case here has been calculated by Seebold et. al.* and observed in drop tower experiments conducted at LMSC. The stability limit is correlated on the basis of a critical Bond number $B = \rho g r^2/\sigma$ where ρ is the liquid density, g is the local acceleration, r the tank radius, and σ the propellant surface tension. This is a function of the radius ratio of the annulus. For the large annulus this critical Bond number is estimated to be in the range of 0.5 to 1.5 and for the small annulus 0.5 to 1.0. Using 33.1 and 18.3 cm^3/sec^2 for the kinematic surface tension of the fuel and oxidizer,

*"Capillary Hydrostatics in Annular Tanks", by Seebold, Hollister and Satterlee, J. Spacecraft, Vol. 4, No. 1, Jan. 1967.

† See note on page 5-55

respectively, gives the acceleration stability limits shown below where g_o is standard gravity.

Annulus	Fluid	g/g_o min.	g/g_o max.
inner	fuel	2.1×10^{-4}	4.3×10^{-4}
	oxidizer	1.2×10^{-4}	2.4×10^{-4}
outer	fuel	$.49 \times 10^{-4}$	1.5×10^{-4}
	oxidizer	$.27 \times 10^{-4}$	$.81 \times 10^{-4}$

For accelerations greater than the above, the gas will move upward in two bubbles, the larger lodging against the "lower"screen in the outer annulus and a smaller one coming to rest at the "top" of the can. The liquid column supported by the screen in the outer annulus represents a case of pressure supported stability where the capillary forces serve to stabilize the meniscus. The stability limit will occur at a Bond number of unity or greater. The diameter of the circular openings in these screens is 0.06 inch. In order to achieve a Bond number of unity with the oxidizer and this screen, an acceleration of 3.2 g_o is required (5.8 g_o for the fuel). This acceleration is considerably greater than any to be considered here.

In order for the gas to flow through the umbrella screens external to the sump, a pressure difference must exist across the screen which exceeds the maximum bubble pressure $\phi\sigma/r$ where r is the screen hole radius. For the ideal case, with perfect wetting and cylindrical holes, the value of ϕ is 2. However, only about 50% of this maximum bubble pressure is obtained in

practice.* The pressure in the liquid adjacent to the screen differs from the gas pressure, P_g, by the hydrostatic head $\rho g h$, where h_1 is the vertical distance between the free surface and the screen opening as shown in Figure 5-10a. At the stability limit, this difference is just equal to the bubble pressure, $\phi \sigma / r$. Equating these and solving for the critical acceleration yields

$$g_{cr} = \frac{\phi \sigma}{\rho r h_1} \qquad 5.1$$

In order to find the minimum value of the critical acceleration, the maximum value of h_1 is used, which is approximately 155 inches. For a hole diameter of 0.020 inch and with $\phi = 1.0$, equation 5.1 yields 3.4×10^{-3} g_o for the minimum value of the critical acceleration for the fuel and 1.9×10^{-3} g_o for the oxidizer. The gas which passes the "lower" screen will collect below the upper screen as shown in Figure 5-10a. If the pressure difference P_1-P_2 exceeds the bubble pressure $\phi \sigma / r$, there will be a gas flow through the upper screen, where P_1 and P_2 are the pressures existing on either side of the "upper" screen as shown in Figure 5-10a. Expressing the pressure difference P_1-P_2 in terms of the hydrostatic head difference leads to the following criteria for flow through the "upper" screen:

$$g/g_o = \frac{\phi \sigma}{\rho r (h_3 - h_2)} \qquad 5.2$$

*"Propellant Containment Utilizing Screen Mesh and Perforated Plate Surfaces", by M. P. Hollister, LMSC Report A665481, 29 Dec. 1964

and since $h_1 > h_3 - h_2$, the acceleration required for gas flow through the "upper" screen when it is partially wet on the lower side is greater than that for gas flow through the "lower" screen.*

*In order for the gas volume below the upper screen to expand, liquid must be displaced up over the end of the central standpipe. This requirement may be expressed by the following inequality

$$P_1 > \rho g (h_4 - h_2)$$

also

$$P_1 = P_g - \rho g h_2$$

so that

$$P_g > \rho g h_4 \qquad \text{(a)}$$

The last inequality (a) will certainly be satisfied at all times, therefore, it may be concluded that if the acceleration is sufficiently high for gas to pass through the lower screen but is less than that given by Equation 5.2, the gas volume is free to expand.

If the liquid level falls below the "lowest" point of the upper screen as shown in Figure 5-10b, the criteria for gas flow through the "upper" screen is reduced to the requirement of Equation 5.1 with $h = h_5$.

The gas, after passing the "upper" screen, will collect in a bubble at the "top" of the tank. As the bubble grows it will eventually cover the openings at the "upper" end of the gaging system. When this happens, the liquid communication between the ends of the tank will be broken and the liquid in the gaging system will seek a new level such that pressure equilibrium is attained. This situation is pictured in Figure 5-11. Pressure equilibrium is achieved when $h_7 = h_8$. The stability of the liquid above the "lower" screen is now a case of pressure supported stability (where the surface tension serves to stabilize the interface) with respect to the head h_7 and capillary supported stability with respect to the head h_6. The criterion to be satisfied for the pressure to support the liquid column is that the Bond number be less than about unity. This is the same criterion stated above for the stability of the screens within the outer annulus of the sump. It was pointed out that the interface at the screens in the outer annulus would always be stable and, therefore, since the hole size in the umbrella screens is smaller than those in the outer annulus screens, it may be inferred that the Bond number criteria will always be satisfied at the umbrella screens as well. The bubble pressure, $\phi \sigma / r$, will resist the head difference, $\rho g h_6$, which exists across the "lower" of the two umbrella screens. Therefore, the capillary stability limit is given by Equation 5.1 with h corresponding to h_6 in Figure 5-11. Using a value of h_6 of 3 inches and ϕ of unity yields a critical acceleration of 0.096 g_o for the limit at which the oxidizer will remain capillary supported and 0.174 g_o for the fuel.

Lateral Accelerations. A sump tank with two different partial fill levels is pictured with a lateral acceleration in Figure 5-12a and b. Two different stability cases are represented here. Where the liquid level is "above" the central standpipe (quantity sensing probe), as in Figure 5-12a, the tendency for the phases to stratify horizontally as a result of the imposed acceleration is opposed by the capillary forces at the "upper" portion of the screen. The pressure difference from gas to liquid required for gas flow across the screen ($\phi\sigma/r$) is obtained with the acceleration given by Equation 5.1 with h measured as shown in Figure 5-12a. The required pressure difference will, of course, be achieved first at the "uppermost" openings. Therefore, the maximum value of h_9 should be used.

Once the stability limit is exceeded, the liquid in volume (1) will reorient completely before the liquid in volume (2) will begin to reorient. It would, in fact, be possible to reduce the acceleration after reorientation in volume (1) begins such that volume (2) would remain completely full of liquid after reorientation was complete in volume (1).

With the fill level "below" the central standpipe, as pictured on Figure 5-12b, the stability of the liquid in volume (2) is governed now by the stability limit of the liquid-gas interface at the 3/8 inch diameter circular holes located around the circumference of the standpipe near the opposite end from the sump inlet. This stability limit is given by Equation 5.1 with h measured as shown on Figure 5-12b. If the critical acceleration is exceeded, the liquid in volume (2) and the inner annulus of the sump can will reorient first, leaving liquid standing in volume (1).

This situation is shown in Figure 5-12c. The stability criteria for volume (1) remains unchanged

Following the above reorientation, the liquid in the outer annulus of the sump can becomes capillary supported with respect to the head h_{11} shown on Figure 5-12c. The stability limits calculated from Equation 5.1 for the configuration of Figures 5-11b, 5-12a and 5-12b are summarized below for the fuel and oxidizer.

Figure	Fluid	Radius Inch	Head	(g_{cr}/g_o) h inch	(g_{cr}/g_o) min. (g_{cr}/g_o) h/h_{max}.
5-11b	fuel	0.01	h_1	.289	.0064
	oxidizer			.524	.012
5-12a	fuel	0.188	h_2	.0965	.0036
	oxidizer			.175	.0065
5-12b	fuel	0.06	h_3	.0154	.00143
	oxidizer			.0278	.00258

The last column of the above table tabulates the minimum value of the critical acceleration (corresponding to the maximum value of h) for each of the configurations.

Reorientation Rates. The rate of liquid flow from or into the sump is, in general, limited by the restriction either at the umbrella screens or at the openings to the quantity sensing probe at the opposite end of the tank. Considering first the situation pictured on Figure 5-9, for accelerations very slightly in excess of the critical, the gas will begin to penetrate "uppermost" screen openings. Bubbles will form and detach in a periodic fashion. The reorientation rate in this case is limited by the bubble formation rate. As the acceleration is increased, more of the sites will

become active and, eventually, when the acceleration reaches the level where the head difference is large relative to the bubble pressure, $\phi\,\sigma/r$, the periodic bubble formation will be replaced by gas jets. An upper limit on this flow rate is obtained by caluclating with Bernoulli's equation the flow rate across the various screens, assuming that the gas pressure drop across the screen ($1/2\rho u_g^2$) is equal to the full liquid head difference $\rho g\, h_1$. There is thus obtained

$$u_g = C\sqrt{2 h_1 g \rho_L/\rho_g} \qquad 5.3$$

where U_g = gas flow velocity through the screen holes

C = an orifice coefficient

h_1 is measured as on Figure 5-10a

As the gas flows into the sump, an equal volume of liquid must flow out through the holes in the gaging system at the "bottom" of the tank. From Bernoulli's equation, the liquid velocity through these holes is given by, u_L,

$$u_L \approx C\sqrt{2 g h_4} \qquad 5.4$$

neglecting flow losses in the screens which, for this case, are small. Comparison of Equations 5.3 and 5.4 indicates that $u_g >> u_L$ and, further, since the area for gas flow through the umbrella screens is much larger than the area of the holes in the gaging system, it is apparent that the reorientation rate is limited by the flow rate of liquid out of the gaging system.

Once the gas bubble which forms at the "top" of the tank becomes sufficiently large to envelope the "upper" end of the gaging system, the height of liquid in the gage tube will begin to fall and a variable h must be considered. If S is the cross sectional area of liquid in the gaging system and A the flow area of the holes in the gaging system, the following differential equation results when the flow rate out of the gaging system is equated to the change in liquid volume in the gaging system

$$S\,dh = -u\,A\,dt \qquad 5.5$$

where S is the flow area in the tank.

Using Equation 5.4 for U, separating variables and integrating from h_i ($= h_4$) to h_f and from 0 to t yields

$$t = \frac{S\sqrt{2}}{CA}\,\frac{\sqrt{h_i} - \sqrt{h_f}}{\sqrt{g}} \qquad 5.6$$

the value of dimensionless constant $\sqrt{2}\,S/CA$ is approximately 70. The value of h_f is approximately one foot in order to balance the liquid head above the screen. For example, consider a nearly empty tank so that $h_i \approx$ 13 ft. Then Equation 5.6 becomes

$$t = \frac{180}{\sqrt{g}}$$

If, for example, $g = .1\ g_o$, then t = 100 seconds.

The laterally accelerated tank is shown in Figure 5-13 during reorientation. Initially, the flow area for the displacing gas is small relative to the area

available for liquid flow across the lower portion of the umbrella screen. During this initial period the reorientation rate will be limited by the gas flow velocity given by Equation 5.13. The volume of gas which flows through the screen in time dt is

$$dV = u(h)\, A(h)\, dt \qquad 5.7$$

where u and A (flow area) are functions of h as noted. If the area of the falling free surface is denoted by S(h), then

$$dh = \frac{dV}{S(h)} \qquad 5.7$$

so that

$$dh = \frac{u(h)\, A(h)}{S(h)}\, dt \qquad 5.9$$

Combining (5.2) and (a), separating variables and integrating yields

$$\int_{h_i}^{h} \frac{S(h)}{A(h)} \frac{dh}{\sqrt{h}} = \sqrt{2c^2 g \rho_L/\rho_g} \int_0^t dt \qquad 5.10$$

Once the geometrical relations S(h) and A(h) are defined, Equation (5.10) may be integrated to yield h as a function of time. This relation is provided to aid analysis not envisioned in this study. Its use was not required in the retention system performance analysis to follow. As h decreases, the

area for gas flow will increase so that eventually the restriction for gas flow may no longer predominate.

Refilling of Sump. Should the sump become emptied of liquid during a re-orientation maneuver, refilling will occur when the acceleration vector is reversed. Initially, when there is communication between the two ends of the tank via the central standpipe, the screens offer no resistance to liquid flow. However, when a sufficient amount of liquid has collected around the sump inlet to seal off the end of the standpipe as on Figure 14a, the displaced gas will attempt to penetrate the screens. When this occurs, the screens become stable for accelerations less than that given by Equation 5.1 with h measured as indicated on Figure 14a. When this limit is exceeded, liquid will flow through both screens. When the liquid level in the "bottom" of the tank rises to the point such that a portion of the "underside" of the upper screen is wetted, as shown on Figure 14b, the value of h becomes variable as indicated on Figure 14b.

Liquid will not rise up the inner annulus because to do so would require compressing the trapped gas in the sump which could occur only at gravity levels well beyond the capability of the vehicle.

Rotations. Angular vehicle rotations and accelerations will result in accelerations normal to the tank axis. Such accelerations will affect the liquid in the sump region in essentially the same manner as the lateral accelerations treated above. The centripetal acceleration, a_c, resulting from an angular velocity ω and tangential acceleration, a_t, resulting from an angular acceleration α, are broken into components normal and

parallel to the tank axis on Figure 15a. The lateral acceleration components $a_{c\ell}$ and $a_{t\ell}$ are shown on a vehicle end view on Figure 15b. These accelerations add to give a_ℓ as shown on Figure 15b. These lateral accelerations actually vary across the tank but, for simplicity, an average value corresponding to the value at the center of the tank is considered.

In terms of the geometry of Figure 15, the lateral acceleration components are:

$$a_{t\ell} = a_t \frac{z}{\sqrt{z^2 + e^2}}$$

and

$$a_{c\ell} = a_c \frac{f}{\sqrt{z^2 + e^2}}$$

where $e = R \cos(\xi - 90)$

and $f = R \sin \gamma$

The centripetal and tangential accelerations a_c and a_t are given by

$$a_c = r\omega^2$$

$$a_t = r\alpha$$

where

$$r = \sqrt{R^2 + z^2}$$

One the total lateral acceleration component, a_ℓ, is obtained, the stability limit of the interface at the umbrella screens may be calculated from Equation 5.1 with h measured as indicated on Figure 15.

Note that the total lateral accelerations may be different for each tank. Furthermore, depending on the values of γ and ξ, the total lateral acceleration may be less than the components a_{cl} and a_{tl} and may, in fact, be zero while a_{cl} and a_{tl} are finite.

Examples

Case I $\alpha = 0, \quad \gamma = 90^{\circ}$

$Z = 200$ inch

$R = 50$ inch

$$\frac{f}{\sqrt{z^2+f^2}} = 0.243$$

$r = 206$ inch $= 17.2$ ft.

so that

$$a_{cl} = (0.243)(17.2)\omega^2 = 4.2\,\omega^2$$

equating to Equation (1) yields

$$a_{cl} = 4.2\,\omega^2 = \frac{\phi\sigma}{\rho r h}$$

Solving for ω with $h = 40$ inches yields

fuel $\quad \omega_{cr} = 0.32$ rad/sec.

oxidizer $\quad \omega_{cr} = 0.24$ rad/sec.

Case II $\omega = 0, \quad \xi = 90^{\circ}$

Since $\xi = 90^{\circ}, \quad l = g$

and $$\frac{z}{\sqrt{z^2+l^2}} = 0.97$$

so that

$$a_{tl} = 0.97\,(17.2)\,\alpha = 16.7\,\alpha$$

equating $a_{t\ell}$ to equation (1) as was done with $a_{c\ell}$ in Case I, yields

fuel $\alpha_{cr} = .025$ rad/sec^2

oxidizer $\alpha_{cr} = .014$ rad/sec^2

EARTH ORBITAL FLIGHT. Twice during the earth orbital mission, AS-503A, there will exist accelerations which are directed along the tank axis in a direction which will tend to cause the liquid to reorient from the sump region to the opposite end of the tank (see reference below*). These are events 7 and 11 wherein the LM descent engine is employed while the LM and Service Module are mated. These two events are described as follows:

Event	V	Duration
7	30 ft/sec	32 seconds
11	778 ft/sec	165 seconds

Assuming the acceleration constant over each period yields 0.0291 g_o and 0.147 g_o for the accelerations during events 7 and 11, respectively.

The fuel remaining is 95% and 15% of the initial loading during events 7 and 11, respectively. It is assumed that the storage tanks will not be used for this mission and that the sump tanks will be initially filled in the range of 75% to 95% of capacity. On this basis, then, the height of the large umbrella screen "above" the free surface (corresponding to h_1 on Figure 5-10a will be in the range of 14 to 44 inches for event 7 and approximately 140 inches for event 11.

*Project Apollo, Preliminary Mission Profile for AS-503A, MSC Internal Note No. 65-FM-160, Nov. 165. (Unclassified)

The critical acceleration above which the screens will allow passage of gas, computed from Equation 5.1, using the above values of h, is tabulated below for events 7 and 11.

Event	inch	fluid	gcr/go
7	14	oxidizer	0.021
	44	oxidizer	.0066
11	140	oxidizer	.0021
7	14	fuel	0.037
	44	fuel	.012
11	140	fuel	.0037

For these calculations, a value of unity for ϕ was used. The interface at the umbrella screens is clearly unstable for event 11 and certainly for the 44 inch head during event 7. With the 14 inch head in the oxidizer tank during event 7,the situation is not so clear since a ϕ of 1.4 (which is entirely possible) would cause the interface to be stable. The 14 inch head in the fuel tank should be stable.

The size of the bubble which will vapor lock the stillwell is approximately 50 in^3. Using Equation 5.4 and an area of 0.662 in^2 corresponding to the six 3/8 diameter holes in the gaging system, the time required to flow 50 cubic inches of liquid from the sump during the events 7 and 11 is calculated and tabulated below.

Event	Initial Fill Level	Height of Liquid in Gaging System (inch)	Time to Flow 50 in^3 of Liquid
7	95%	23	4.3 sec.
	75%	53	2.4 sec.
11	75%-95%	144	1 sec.

At the above times, then, the gaging system will become vapor locked and the height of liquid in the gaging system will begin to fall. The final height reached during event 7 and 11 may be calculated using equation (9). The final height calculated is tabulated below.

Event	Fill Level at Launch %	Height of Liquid in Gaging System Initial-Inch	Final-Inch
7	75	23	12
	95	53	35
11	75-95	149	12

Note that for event 7 with the lesser fill level and for event 11 the asymptotic value of the liquid height is reached. With the higher fill level, there is insufficient time during event 7 to reach the asymptote.

The liquid volume above the lower umbrella screen as pictured in Figure is clearly stable for event 7 but a ϕ of 1.5 is required to support the head h_1 in the oxidizer tank during event 11 so that in this latter case, the situation is not well defined and the liquid may remain within the confines of the umbrella screens or may begin to reorient through the gaging system to the opposite end of the tank. This configuration is probably stable in the fuel tank during event 11 since a ϕ of 0.85 is calculated for stability.

Note: Since this analysis was completed it has been made known that the Apollo SPS tanks are filled at 50 psig. The compression of the bubble inside the retention system indicated on page 5-45 will reduce the gas volume inside the retention system to about 65/180 = 0.36 times its original volume compared to the 91.7% reduction previously calculated. (The gas ullage volume outside the retention system, of course, remains constant during pressurization.) The difference is not great and will not change conclusions drawn in the analysis.

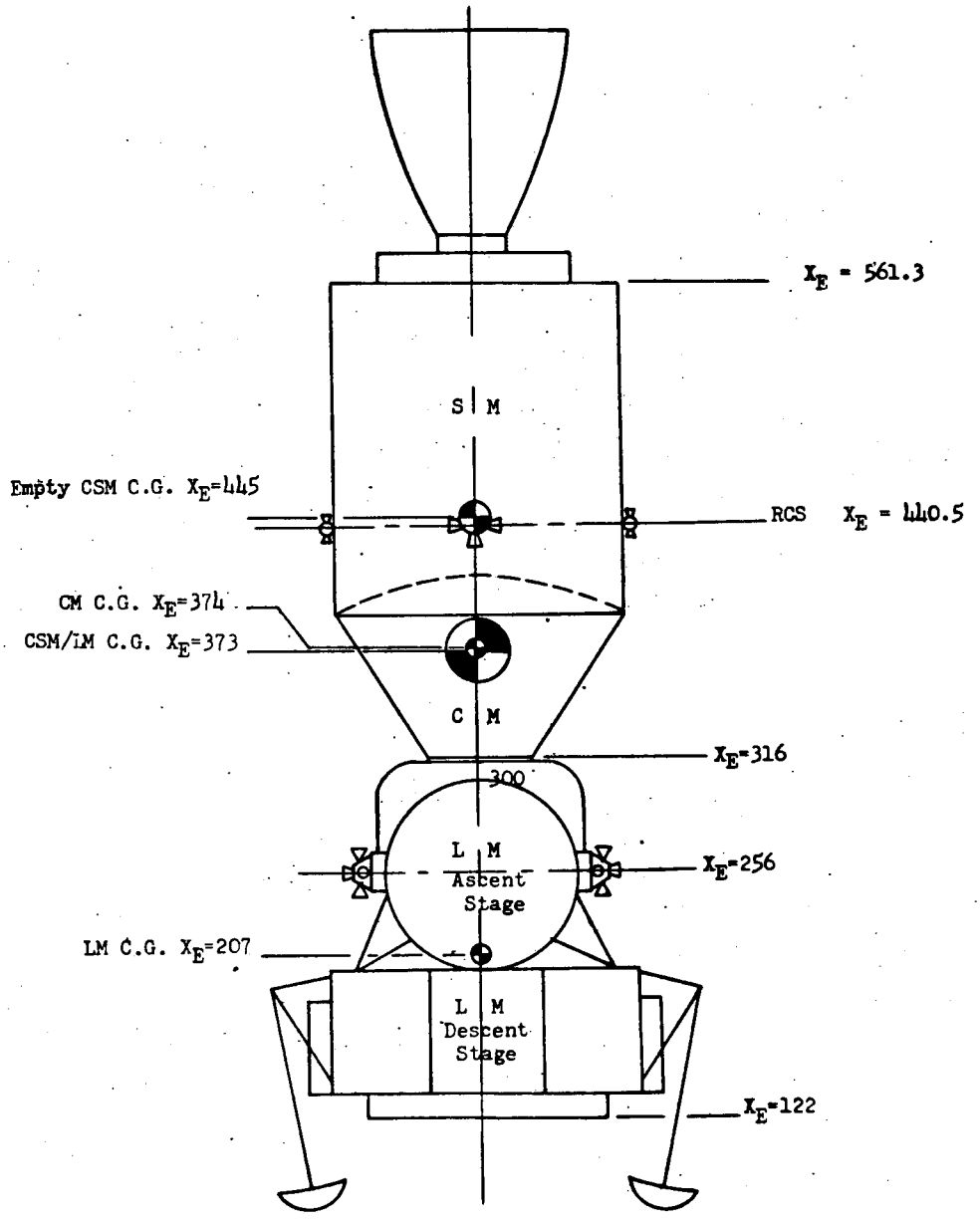

NOTE: X_E indicates distances in the LM coordinate system (Reference I)

CSM/LM Configuration

Figure 5-1

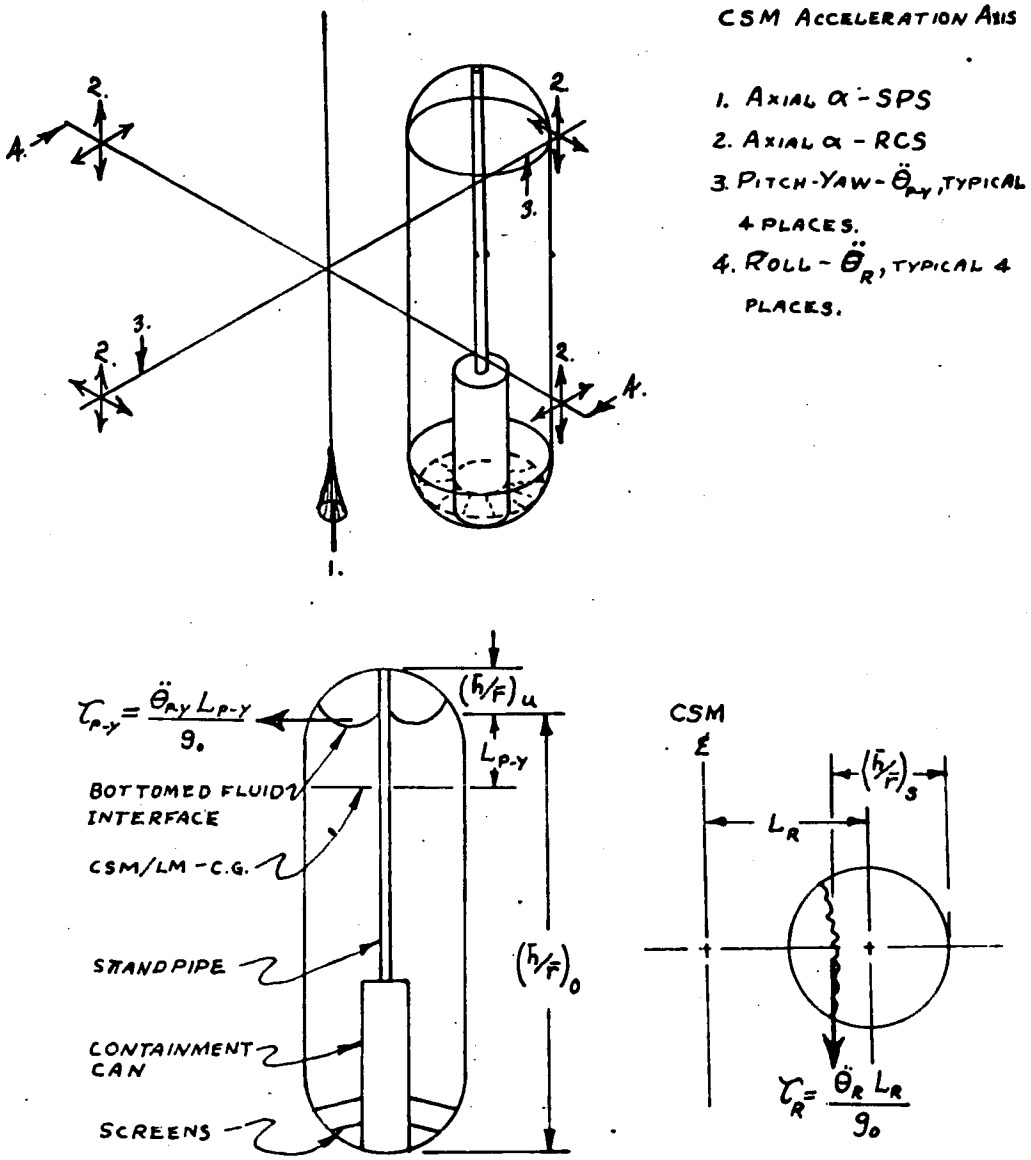

Tank Geometry Nomenclature

Figure 5-2

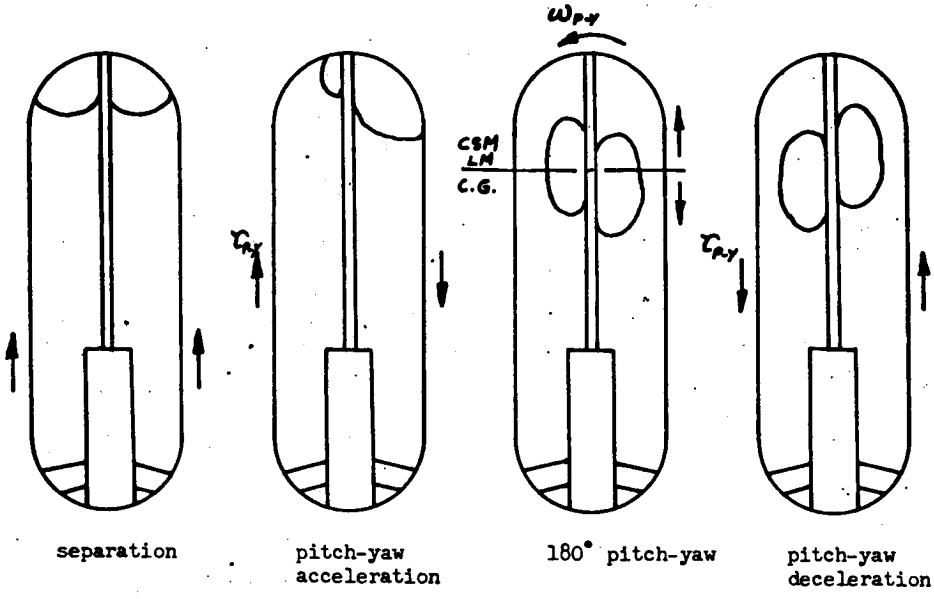

Note: Arrows indicate direction of acceleration applied.

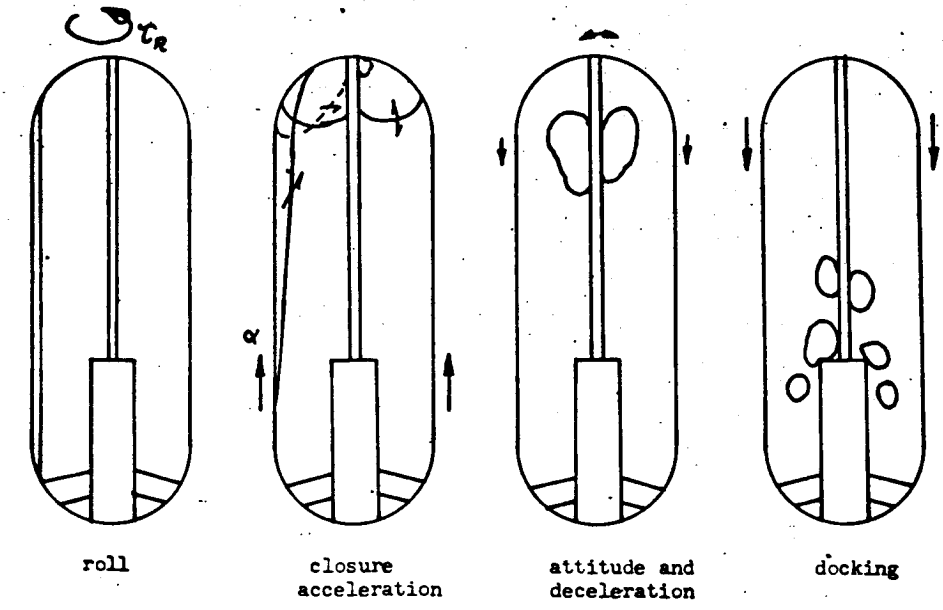

Probable Ullage Positions During Transposition and Docking

Figure 5-3

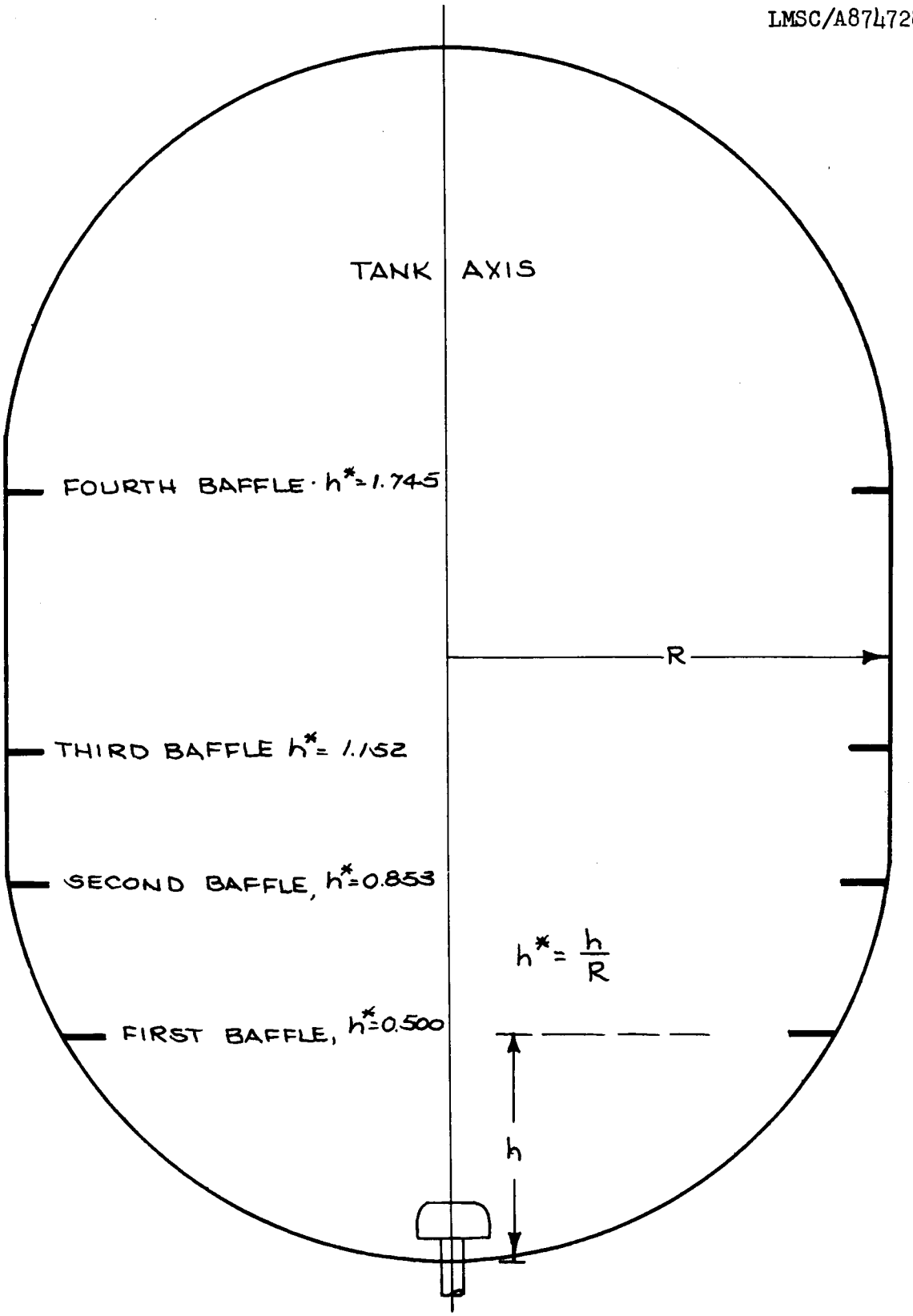

LM Descent Tanks with Proposed Ring Baffles

Figure 5-4

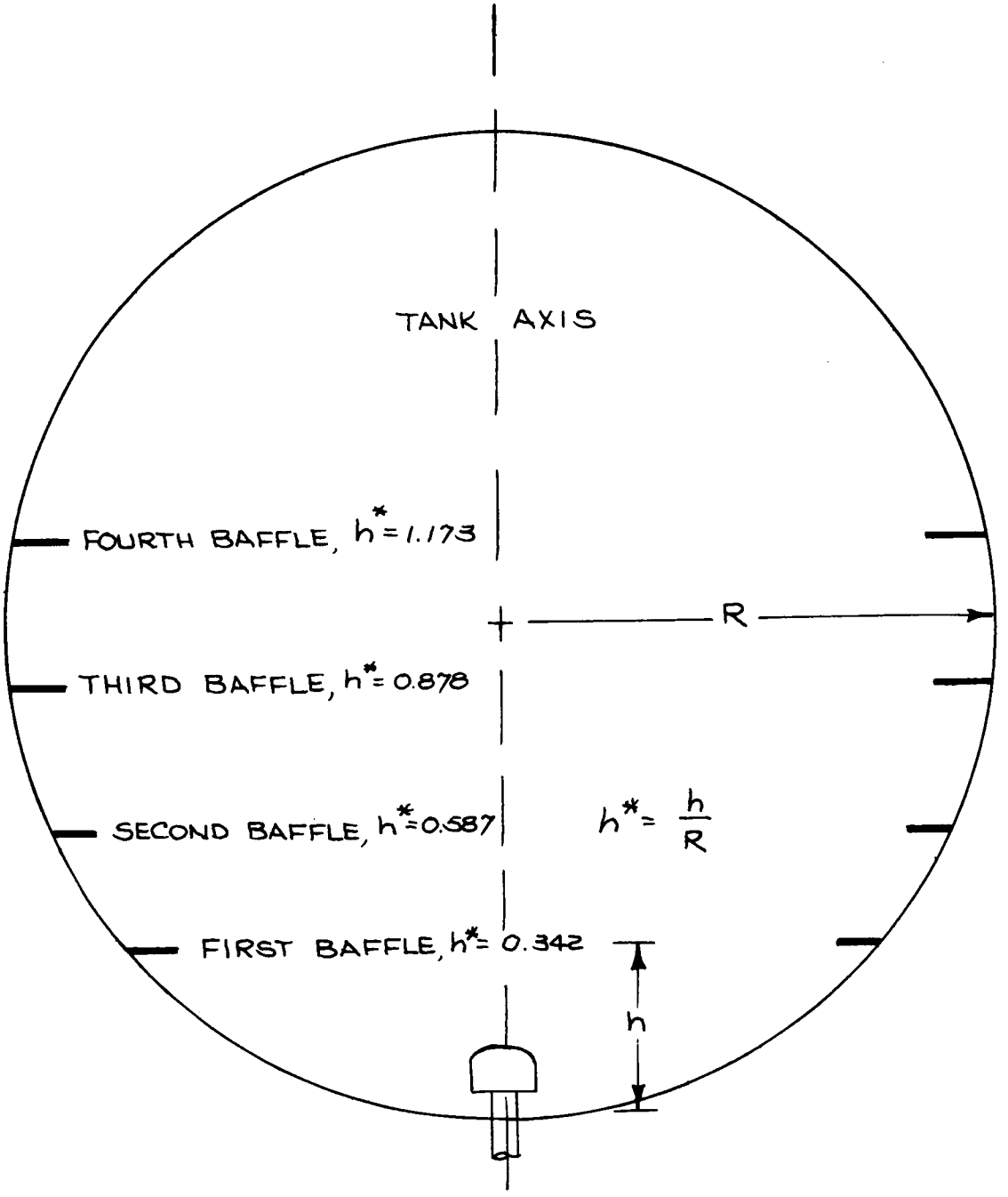

LM Ascent Tanks With Proposed Ring Baffles

Figure 5-5

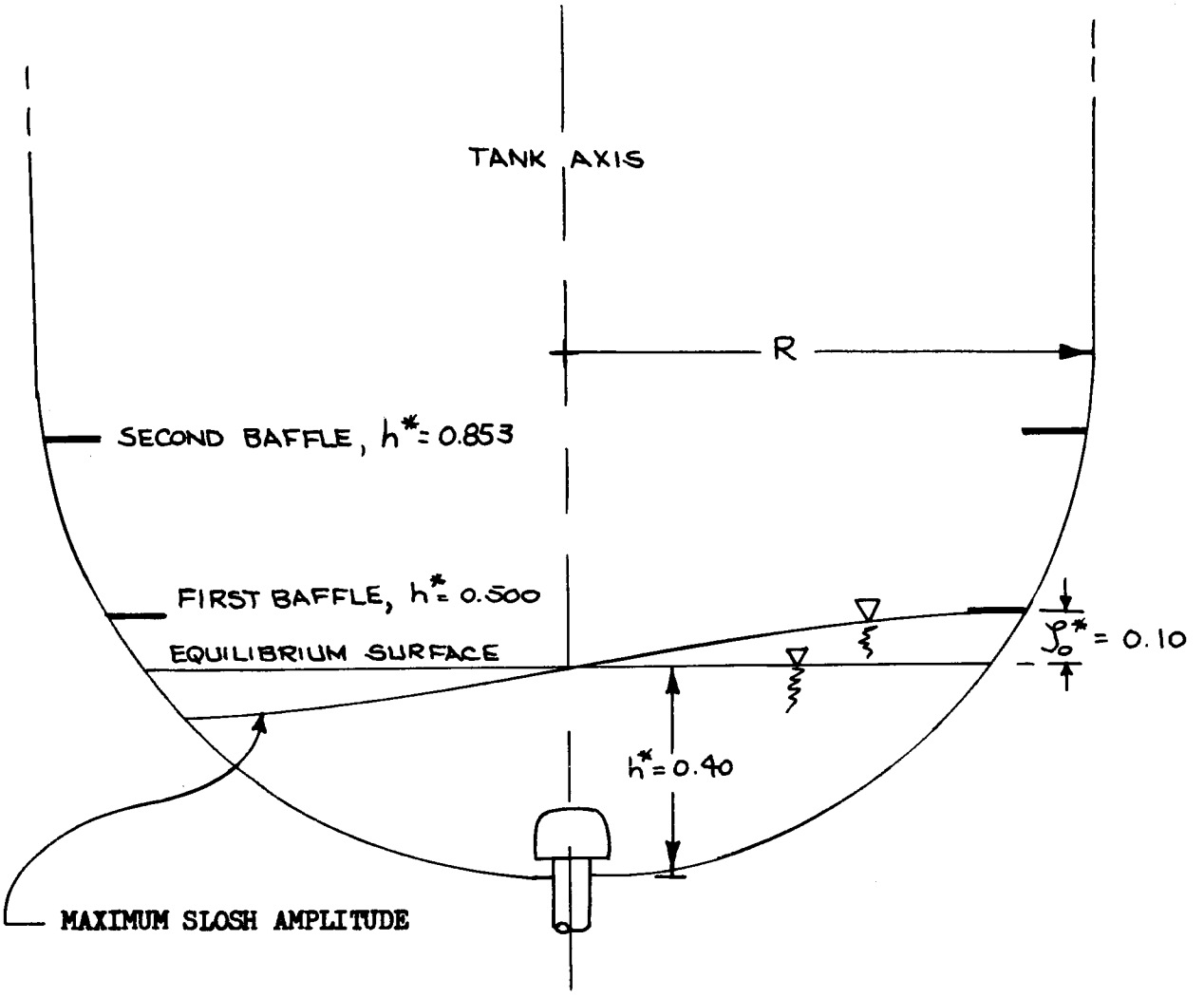

Sketch of Maximum Slosh Amplitude Induced by Transverse Accelerations at End of LM/DPS Hover

Figure 5-6

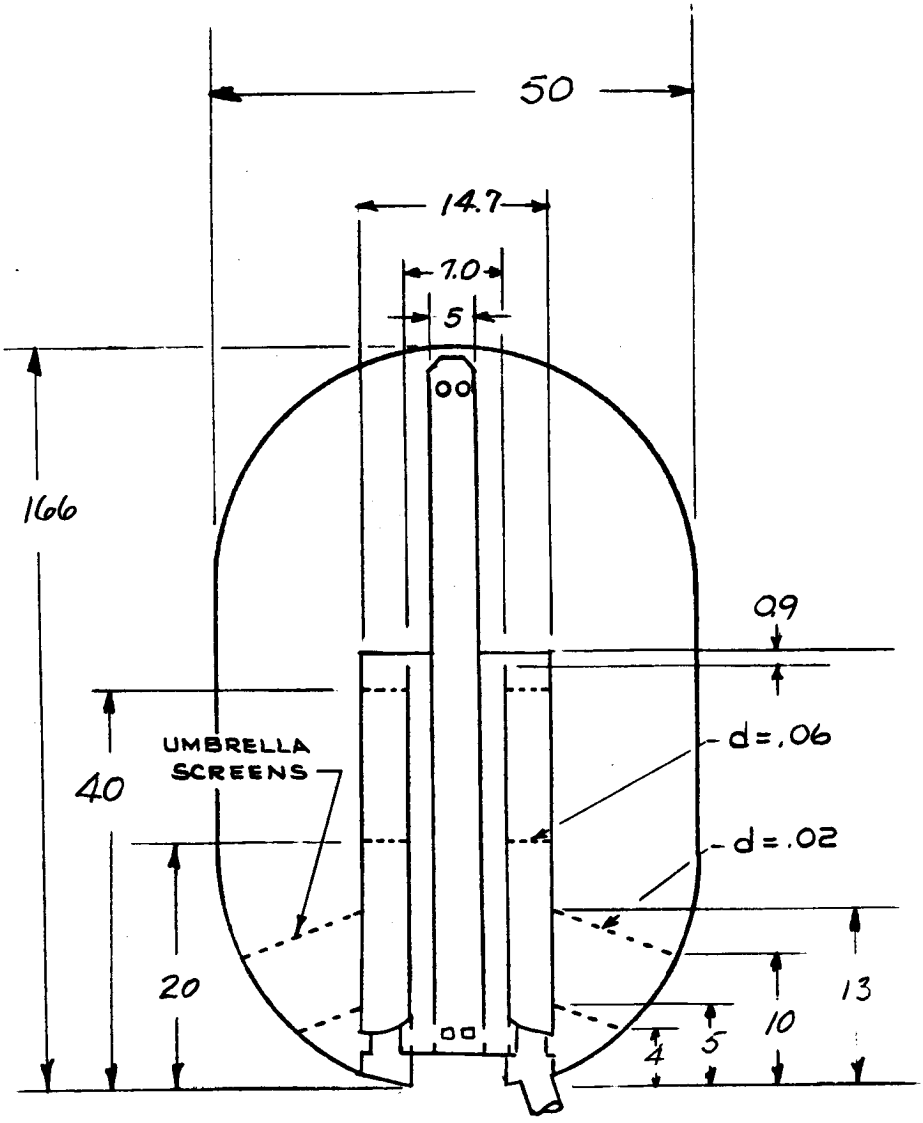

Approximate Dimensions of Apollo Sump Tanks

Figure 5-7

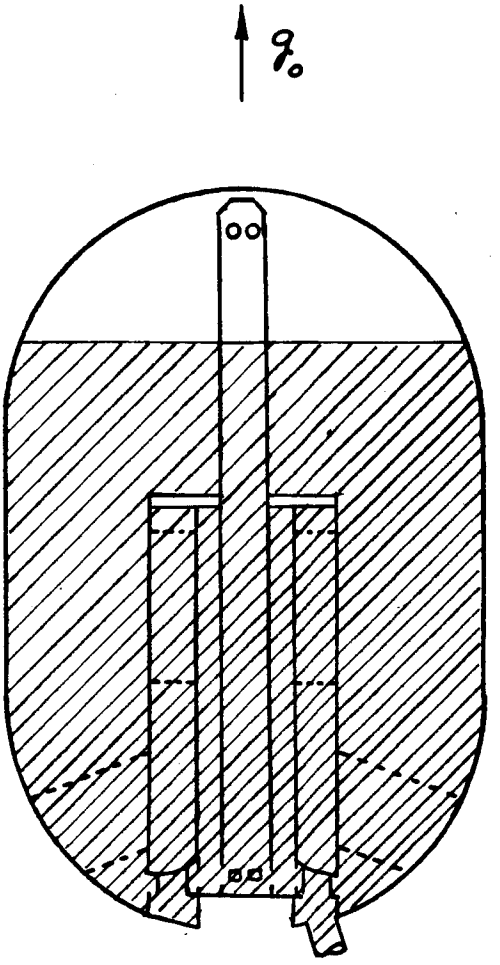

Propellant Orientation Before Launch

Figure 5-8

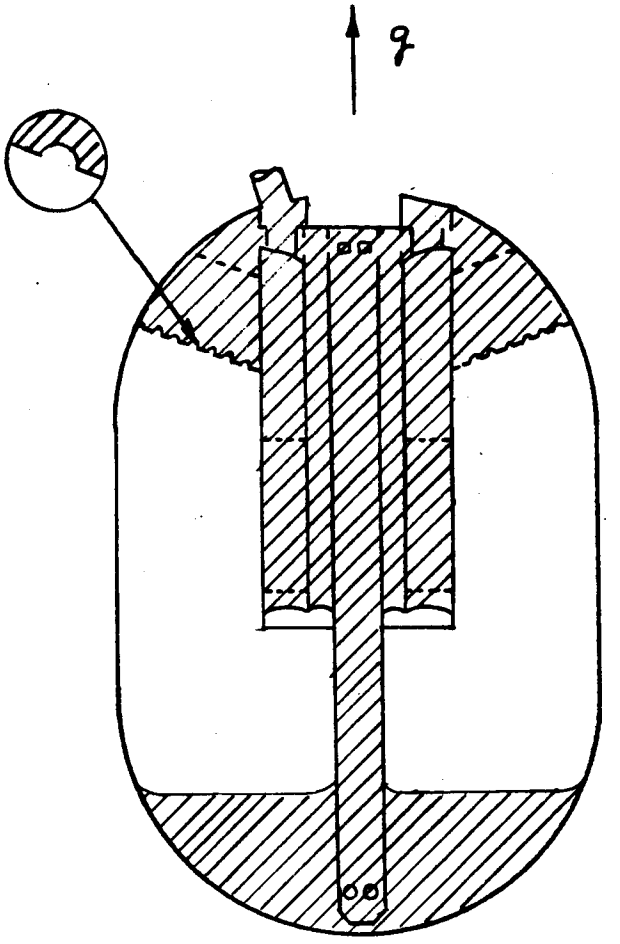

Propellant Orientation With a Small Adverse Acceleration

Figure 5-9

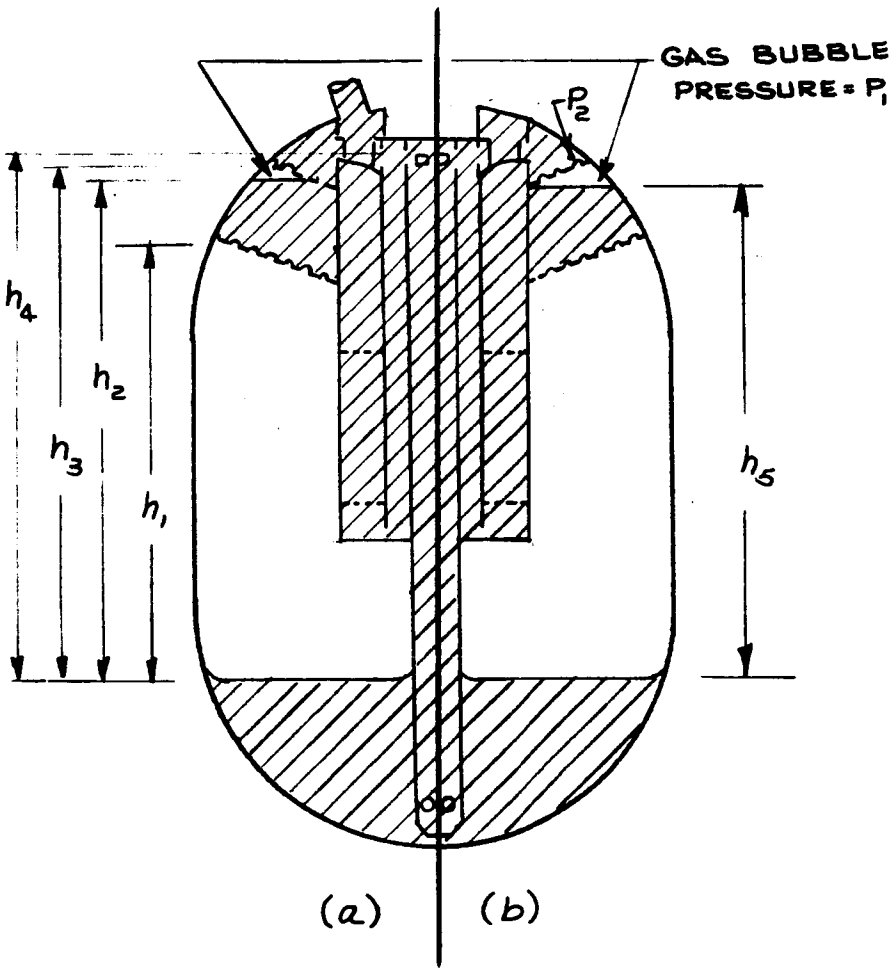

Interface Locations During Reorientation

Figure 5-10

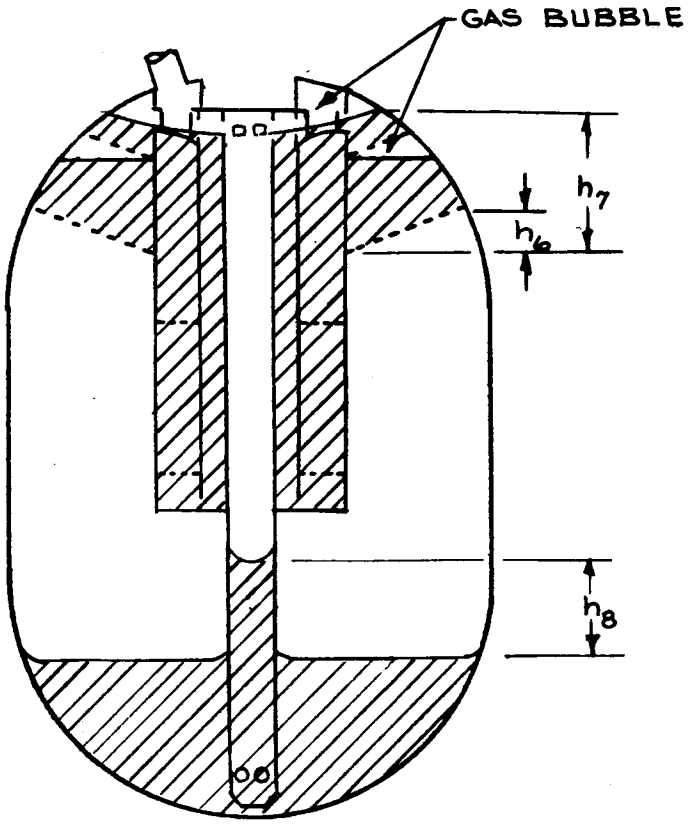

Interface Locations When Liquid Communication Between Ends of Tank is Broken

Figure 5-11

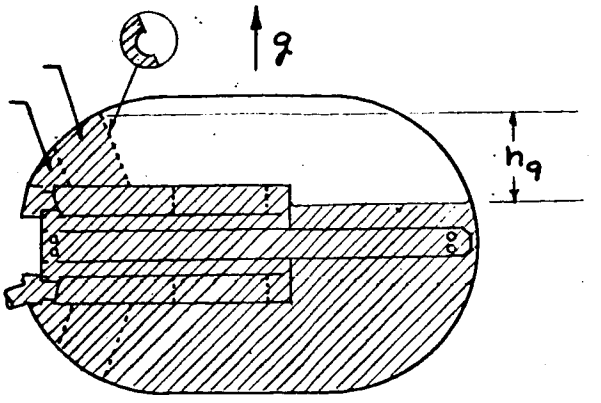

a) Laterally Accelerated Tank-Liquid Above Level Sensing Probe

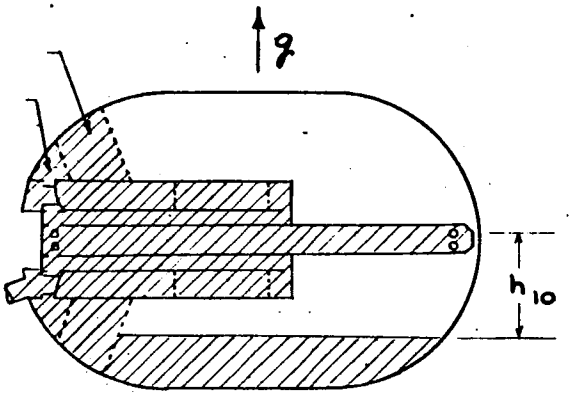

b) Laterally Accelerated Tank-Liquid Below Level Sensing Probe

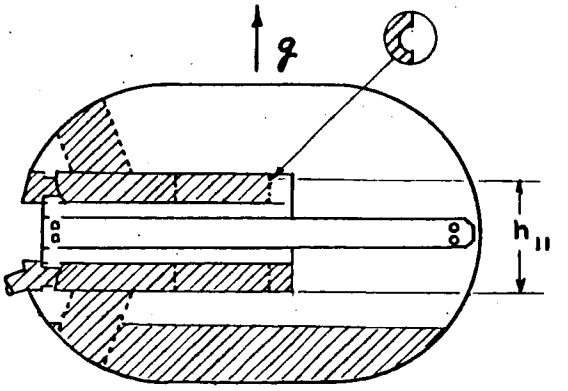

c) Propellant Level Following Reorientation from Volume 2

Figure 5-12

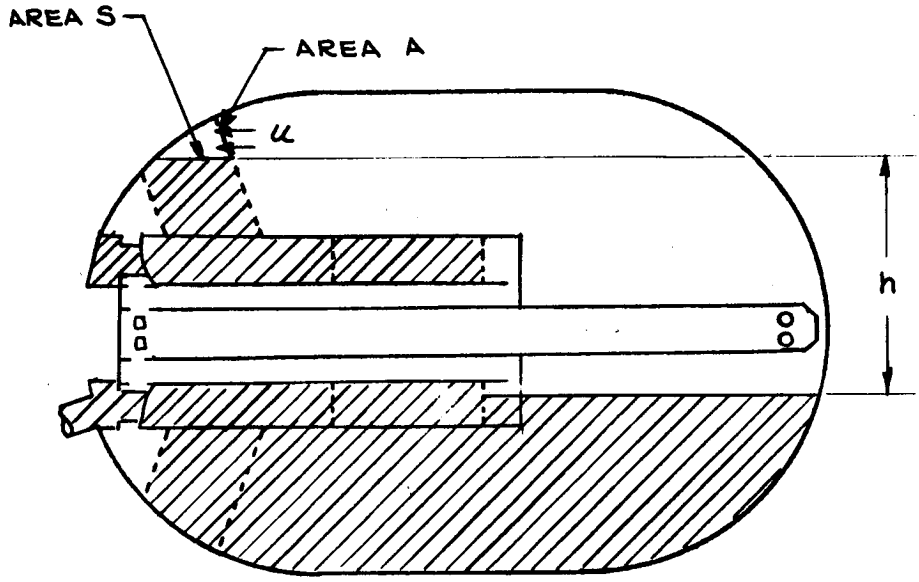

Reorientation Process in the Laterally Accelerated Tank

Figure 5-13

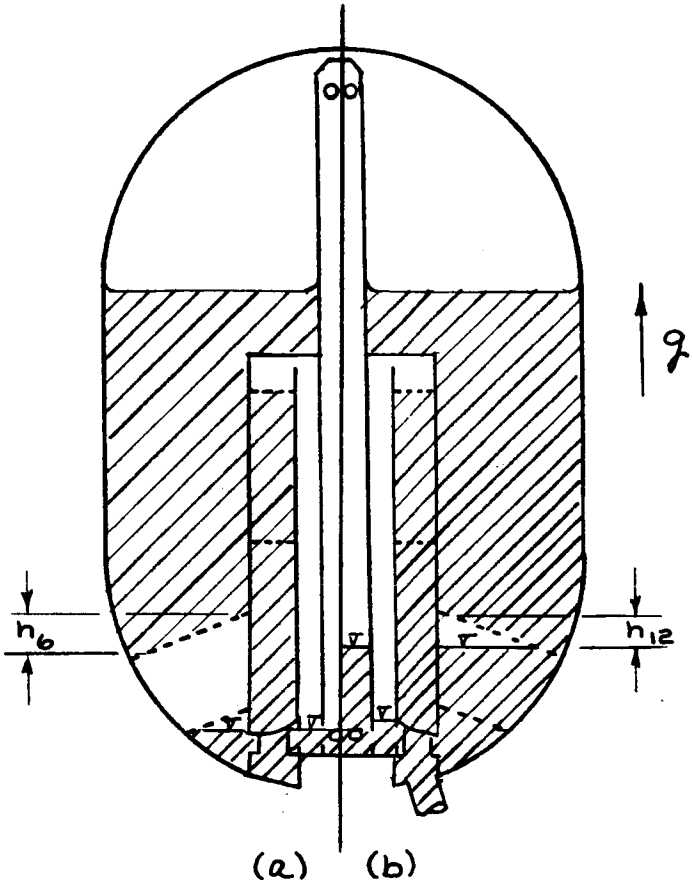

Refilling of Sump

Figure 5-14

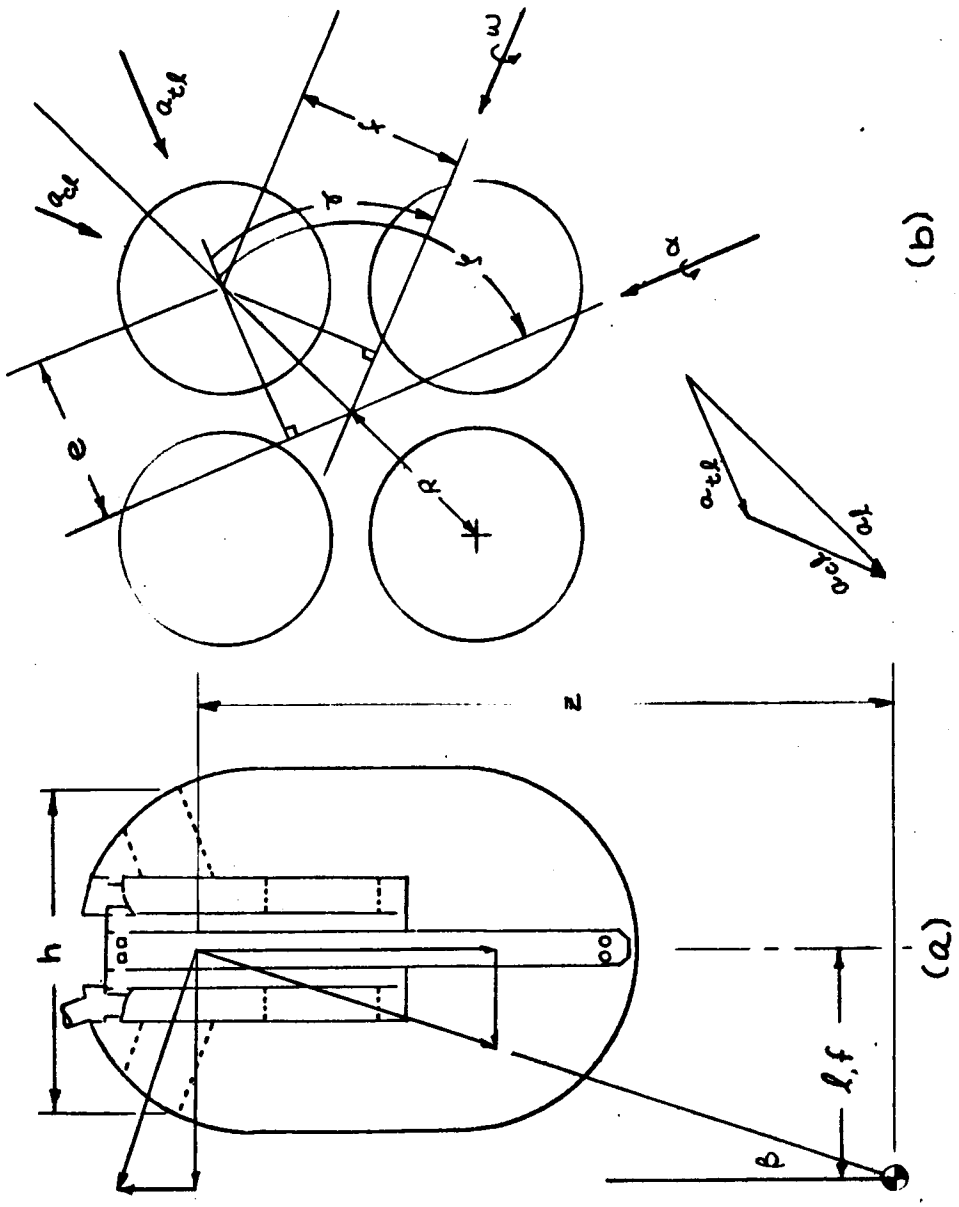

Accelerations Resulting From Angular Rotations

Figure 5-15

APPENDIX I

LIQUID BEHAVIOR EXPERIMENTS ABOARD A GEMINI SPACECRAFT

During the period approximately encompassed by June 1 and September 15, 1966, part of the work of this project involved preparation of test plans for a series of experiments to be performed aboard the Gemini XI spacecraft. The report to follow was submitted in support of this effort. Later, Lockheed personnel provided on-the-spot assistence with the performance of the experiment. Unfortunately, flight conditions prevented the designated astronaut from recovering the movie film record of the experiment. The following report was submitted to the NASA Manned Space Flight Center on July 21, 1966, and is appended to the Final Report for record purposes.

Operation of the propulsion system or application of other forces to a liquid-fueled orbital vehicle can cause an adverse interaction between the contained liquid and guidance and control systems. More information on fluid response to such forces is required for best vehicle design. Much of the uncertainty about the design of liquid propellant tank and feed systems stems from the lack of a long-term low-g test environment. Performing liquid behavior experiments aboard a Gemini spacecraft will increase the available test time over that available in drop towers or aircraft and significantly extend and complement existing information. Such information is needed to assure success of the Apollo mission.

The test equipment to be used in the proposed orbital experiments consists primarily of:

a) A sheet metal structural light box. This is attached to the Blast Shield Door at the interface between the Equipment Adapter and the Retro Adapter.

b) A lucite test tank.

c) Lighting - provided by approximately 12 small incandescent light bulbs (type GE 8081F).

d) Cameras - 2 each - 6 frames per second, electrically operated and mounted in a cam-operated, quick release holding fixture.

e) A black face Accutron clock with a sweep second hand.

The test tank to be used in the programmed experiments is a 1/8 scale model of one of the Apollo Service Module (SPS) tanks. The test fluid is an inert fluorinated hydrocarbon heat transfer fluid called FC-43 by its manufacturer, Minnesota Mining and Manufacturing Company. Its density is 1.88 gms/cc and its surface tension is about 16 dynes/cm; consequently, its ratio of surface tension to density is 8.52 cm^3/sec^2. It appears to be completely inert and has very low solubility with most fluids and gases except for nitrogen. The fluid has been tinted a very light blue to permit better discrimination of the interface and entrained bubbles in the top and side view movies being taken.

The experiments planned are listed in Table I in their order of preference. Mission plans and expediency in sequencing of the maneuvers dictates a variation from this order of preference in the nominal experiment plan.

Table I

EXPERIMENT PRIORITIES AND SEQUENCIES

Priority	Test	Sequence
1	High Energy Slosh - A	3
2	High Energy Slosh - B	4
3	Low Energy Slosh - A	5
4	Low Energy Slosh - B	6
5	Settling, Desettling & Retention	2
6	Docking	8
7	Longitudinal Slosh	7
8	Agena PPS	1

Each of these experiments' objectives and simulation techniques are discussed below.

High Energy Slosh. Spacecraft orbital maneuvers can develop considerable momentum in contained liquids. At sudden termination of the orbital maneuver, this momentum has to be dissipated in the liquid essentially without body forces. Sloshing periods are long, and wave amplitudes may be large, depending on the amount of residual momentum. The amount of momentum carried over into low gravity liquid motion depends on the impulse induced by the orbital maneuver. If termination is instantaneous all the momentum is carried over. Generally, it is necessary to terminate the orbital maneuvers as quickly as possible. Large residual momentum effects may be expected.

In this test, sloshing motion will be induced with pitch momentum. A

pitch rate change will be employed sufficient to cause a slosh wave to carry over the top of the test tank. This will permit observation of the wave amplification effect due to an acceleration reduction, gas entrainment, and subsequent low-g sloshing and slosh decay. The objectives of the test are the following:

1. Obtain a time-indexed photographic record of sloshing motion following rapid termination of constant-rate pitch.

2. From photographic records determine

   a) Time history of slosh wave leading edge motion at tank wall.

   b) Damping factors for large-amplitude slosh wave decay in low-g.

   c) Frequency vs. amplitude data for large amplitude, low-g sloshing.

   d) Estimate time history of liquid center of mass motion.

3. From 2d, estimate forces and moments exerted on spacecraft by liquid motion.

4. Attempt correlation on one experiment of force and moment maximum, and maximum wall wave heights in the event carryover does not occur.

Low Energy Slosh. A natural extension of the High Energy Slosh experiment is a small-amplitude or Low Energy Slosh experiment in a low-gravity environment. This would provide a long duration experimental check on low-gravity sloshing theory which has heretofore been checked only in short duration experiments in drop towers. In addition, the effect of a central standpipe in possibly altering the low-gravity, small amplitude sloshing frequency will be observed.

In this test, small amplitude sloshing will be induced by means of a small

pitch rate change. The objectives are:

1. Obtain time-indexed photographic record of low-g, small amplitude sloshing motion.

2. From 1, determine low-g sloshing frequency vs. amplitude.

3. Check low-g, small amplitude sloshing theory.

Little frequency shift is to be expected due to amplitude decay during this part of the experiment. Small amplitude sloshing could be defined as that amplitude below which slosh amplitude has a negligible effect on slosh frequency.

Settling, Desettling, and Retention. Orbital maneuvers can impose adverse axial accelerations strong enough to destabilize the liquid contained in one end of a propellant tank. Reorientation of liquid starting from low-g conditions proceeds with a transient flow of liquid down the tank wall and the attendant formation of a central rising bubble. The reorientation flow is not greatly different in a tank with a relatively thin central standpipe. When the wall sheet converges at the tank bottom it produces a central jet flow or geyser along the axis. The subsequent flow of interest is either recirculation or a very large amplitude axial sloshing motion. Limiting Bond numbers for stability are of the order of unity, but efficient propellant settling generally requires reorientation Bond numbers in excess of 100. Thus, fairly large axial thrust is usually required in model tests, since the model tanks are generally smaller than the prototype.

In the Settling experiment, backward pointing thrusters will provide the necessary adverse acceleration. The objectives of the test are as follows:

1. Obtain time-indexed photographic record of reorientation flow and subsequent liquid motions.

2. From 1, obtain damping factors for the geysering flow and large amplitude axial slosh that result after reorientation.

3. Frequency vs. amplitude for axial sloshing.

Capillary devices such as screens or perforated plates are capable of retaining liquids under certain adverse acceleration conditions. The acceleration level beyond which effective retention is no longer possible is determined by the geometry of the capillary device and the orientation of the destabilizing acceleration. Here, the effectiveness of the perforated plate retention system will be determined under lateral and axial accelerations.

Docking. The behavior of fluid subjected to a series of adverse maneuvers is of interest because of the uncertainties involved in describing surface motions resulting from varying forces and accelerations. A typical maneuver such as an actual docking will provide an indication of the time, duration, and effect of varying forces.

The objectives of the test are to obtain photographic data of fluid surface behavior which can be related to spacecraft accelerometer data.

Approximations of center of mass movement during docking, force levels applied, their sequence, and damping effects of out of phase accelerations will be made.

Longitudinal Slosh. Roll maneuvers tend to centrifuge contained liquids

outward, particularly when the container centerline is displaced from the roll axis. The Apollo flight plan contains just such a maneuver during the spin temperature stabilization period of its flight. Liquid thus displaced to the outer portion of a cylindrical tank wall will exhibit high-g longitudinal sloshing, because the roll rate will generally provide a transverse Bond number well in excess of unity. Initially the slosh amplitude will be large if the liquid was located elsewhere prior to initiation of the roll maneuver. Large amplitude sloshing cannot persist, however, because the liquid motion is stabilized by the relatively large radial body force produced by the centrifugal acceleration. At lower roll rates the liquid would exhibit the characteristics of lower-g sloshing about an equilibrium surface which is curved along the cylindrical tank wall with an interface displaced, but not destabilized, by transverse acceleration. Thus there are two important sloshing regimes associated with the roll maneuver; one in which the effective transverse acceleration in an off-axis cylindrical tank is sufficient to destabilize the interface and position the liquid on the outer part of the tank wall, one in which transverse acceleration is only sufficient to distort the equilibrium interface. Sloshing characteristics in these two regimes can be expected to be entirely different. While the steady roll rate will determine the orientation of the equilibrium interface about which sloshing will occur, the angular acceleration rate required to achieve the steady roll rate will determine the amplitude of the initial slosh wave. Thus low angular acceleration to a given roll rate will result in little more than a gradual shift of the equilibrium interface position, while high acceleration will result in a

substantial overshoot of the same equilibrium interface position.

The Slosh During Spin Temperature Stabilization experiment will therefore be conducted at three roll rates.

1. Obtain time-indexed photographic record of liquid motion during spin temperature stabilization maneuver.
2. From 1, obtain time history of transition wave motion at high and low points on tank wall.
3. From 1, obtain slosh damping factor.
4. From 1, obtain frequency vs. amplitude history.
5. If possible, correlate over/under shoot with acceleration rate and roll rate.

Agena Primary Propulsion System. The Agena PPS minimum burn provides 1-3 seconds of about 1-g_o acceleration against the retaining screens. This maneuver will provide enough acceleration to insure complete refilling. An objective then will be to obtain a photographic record of the screen fluid retention failure. In addition, the dynamic fluid response to a high acceleration and subsequent deceleration is of interest. The best data will be obtained if the test fluid has previously been oriented and allowed to become quiescent.

The data required is a photographic record of the fluid behavior just before, during, and after the PPS minimum burn. This data will be related to spacecraft accelerometer records.

The timelines developed for the proposed experiments are listed later in

the text under Test Timelines. They were developed primarily on the basis of calculations made using the relations collected in a section entitled "Experiment Criteria." The timelines listed can be used in the docked (i.e., Gemini spacecraft and Agena mated) or the undocked mode of operation. Use of identical timelines has obvious training and emergency or contingency advantages. The required rates and impulse propellant usage will be different. These differences are noted. The order of the experiments planned was evolved considering higher priority tests and efficient maneuver sequencing. The docked and undocked configuration capabilities used in test planning are shown on Table II. The tentative timelines for data acquisition for the tests are also included, as is an estimate of OAMS propellant usage for the docked and undocked operation modes.

Alternatives or contingencies considered are:

1. If the Attitude Control and Maneuver Electronics (ACME) packages are inoperative or power limits the experiment duration so accelerometer readings are not available, useful fluid behavior data would still be obtained if thruster time duration data is available.

2. This experiment's primary objectives can be met in either the docked or undocked modes but will probably be crew limited by pitching rates for one of the High Energy Slosh tests in the undocked mode.

3. If propellant usage or elapsed time becomes a limitation, delete experiments from the lowest order of preference first.

4. Light bus voltages below 21 volts will not provide enough light for good pictures.

Experiment Criteria

The basis for the particular time lines specified in Appendix A are discussed in the following paragraphs.

Settling Times . Reference 1 gives the rate of penetration of the pressurization gas into the low-viscosity fluid at high Bond numbers (> 12) as:

$$v_o = 0.48\sqrt{\alpha r}$$ where r is the radius of gas bubble

If the depth of fluid is L the time for complete penetration can be determined to be:

$$t = \frac{L}{0.48\sqrt{\alpha r}}$$

t = time seconds

L = length cm

α = acceleration-cm/sec^2

r = radius - cm

A factor of about two was applied to the settling times obtained from this relation with the data of Table II. This gave a nominal settling burn time of 10 seconds which includes a time pad for both the docked and undocked configurations.

Screen Retention. The fluid retention capability of screens or perforated plates in an adverse gravity field has been studied and reported in Ref. 2. A dimensionless expression for the condition of failure was found to be:

$$\phi = \frac{grh}{\sigma/\rho} > 2$$

where

g = prevailing acceleration - cm/sec^2

r = hole dimension - cm

h = head or height of screen parallel to the acceleration - cm

σ/ρ = a ratio of surface tension to density - cm^3/sec^2

Slosh Frequencies. The slosh frequency was used to determine the time span required for several cycles to occur. The number of slosh cycles to be recorded or permitted to occur for damping of the interface motion was selected by judgment.

Ref. 3 gives the following for the frequency of first mode sloshing under low gravity conditions:

$$\omega_1^2 = \left(\frac{k_1}{r}\right)\frac{\sigma}{\rho}\tanh\left(k_1\frac{\ell}{r}\right) + \frac{k_1}{r}\alpha\tanh\left(k_1\frac{\ell}{r}\right)$$

where

ω = first mode circular frequency - radians/sec

k_1 = first zero of $J_1'(x) = 1.841$

r = tank radius - cm

σ/ρ = ratio of surface tension to density cm^3/sec^2

$\tan(k_1 \ell/r) = 1$ for the fill level (ℓ) in this geometry

α = acceleration perpendicular to the equilibrium surface - cm/sec^2

The geometry and test fluid of the test system substituted into this relation gives a 20 second/cycle period. An upper bound considering real fluid effects such as contact angle hysteresis, large contact angle, and

non linearities will not cause the period to exceed 60 seconds/cycle (Ref. 3). Therefore, the 300 second period provided in portions of the time line will permit 5 to 15 cycles to occur to damp out extraneous motions.

A prediction for wave heights at the tank wall resulting from fluid response to a transverse acceleration at low axial accelerations is presented in Ref. 4 to be:

$$\left(\frac{h}{r}\right)_{WALL} = 0.67\ Bo_{\gamma} = 0.67\ \gamma\ t\ \sqrt{\frac{r}{\sigma/\rho}}$$

where γ is the transverse acceleration and the other terms are as previously defined. For this configuration:

$$\left(\frac{h}{r}\right)_{WALL} = 0.659\ \gamma\ t$$

A wall wave height extending to the dome apex was assumed (h/r = 15) and the necessary deceleration times were obtained using the spacecraft capabilities listed in Table II. The deceleration rates were high enough to keep the time duration of the impulse less than the time for a quarter of a wave cycle so the impulse will be effectively transmitted to fluid momentum.

There is a possibility that following the rapid termination of the pitch motion a low pitch rate will remain. Accordingly, a maximum residual pitch rate value was determined as an acceptable condition. Attempts to reduce the pitch rate to zero by use of an attitude control system and roll conditions after the rapid depitching maneuver are much less desirable than some low but non-zero residual pitch rates. The acceptable maximum value

for this rate is 0.9°/sec in the docked mode and 1.9°/sec in the undocked mode. If these tolerances cannot be met with proper timing of the thrusters specified, it is likely that the resulting test conditions will be unacceptable.

Side Tank Sloshing. The sloshing frequency of liquid in the side of a cylindrical tank can be estimated through the use of shallow-water theory. The natural frequency is given by

$$\frac{b\omega^2 L^4}{A(\sigma/\rho)} = \pi^4 + \pi^2 \frac{g\rho L^2}{\sigma}$$

where

ω = natural frequency, rad/sec

b = width of equilibrium free surface

L = length of tank

A = cross-section of volume occupied by liquid

σ = liquid surface tension

ρ = liquid density

g = local acceleration (centrifugal acceleration in the case of interest).

Assumptions used in developing the relation just given include:

a) flat equilibrium interface. This approximately so for transverse Bond number $B_{Trans} = \frac{\rho g r^2}{\sigma}$ greater than 10 where r_o is the tank radius.

b) Square tank ends, not hemispherical as in the test tank. The length used for calculation can be suitably adjusted to account

for this.

c) Small amplitude of slosh wave.

d) Mean depth small compared to tank length

Use of this relation yields a sloshing period, $T = 2\pi/\omega$, of about 7.9 seconds for a transverse Bond number of 10. This is achieved when the spacecraft roll rate is 11.5 degrees/second.

References

1. Fluid Mechanics and Heat Transfer Under Low Gravity Symposium Proceedings, Sponsored by USAF Office of Scientific Research and Lockheed Missiles and Space Co., 24-25 June 1965, Palo Alto, Calif., pp 2-1 to 2-17.

2. Hollister, M. P., "Propellant Containment Utilizing Screen Mesh and Perforated Plate Surfaces," LMSC Report, R&D Division, 24 March 1964, Sunnyvale, Calif.

3. W. C. Reynolds, M. A. Saad, and H. M. Satterlee, "Capillary Hydrostatics and Hydrodynamics at Low-g," Stanford University, Dept. of Mech. Engrg., Rpt. No. LG-3, Sept. 1964.

4. LMSC/A765989, 3rd Progress Rpt. on NAS 3-7119, Interface Dynamics, dated 1 October 1965.

Table II

CONFIGURATION CAPABILITIES

Maneuver	OAMS TCS No.	*Accelerations		Moment Arm To Free Surface	Propellant Usage lbm-sec
		Rate Command	Max. °/sec		
DOCKED					
Settling-Fwd	9 & 10	12.96 cm/sec^2	N/A	N/A	0.727
Settling-Aft	11 & 12	9.97 cm/sec^2	N/A	N/A	0.618
Pitch	1 & 2 Up 5 & 6 Down	0.0164 rad/sec^2	0.941	368 cm	0.1818
	15 Up 16 Down	0.354 rad/sec^2	2.03	368 cm	0.364
	1,2,15 Up 5,6,16 Down	0.525 rad/sec^2	3.01	368 cm	0.545
Roll	2,6,4,8 Left 1,5,3,7 Right	0.1814 rad/sec^2 (0.0453 ea.)	10.4	31.4 cm	0.364 (0.091 ea)
UNDOCKED					
Settling-Fwd	9 & 10	24.85 cm/sec^2	N/A	N/A	0.727
Settling-Aft	11 & 12	19.1 cm/sec^2	N/A	N/A	0.618
Pitch	1 & 2 Up 5 & 6 Down	0.0737 rad/sec^2	4.22	90.3 cm	0.1818
Radial Transl'n	13 Right 14 Left	12.51 cm/sec^2	N/A	N/A	0.364
Roll	2,6,4,8 Left 1,5,3,7 Right	0.229 rad/sec^2 (0.0573 ea.)	13.12	31.4 cm	0.364 (0.091 ea)

*Agena weight after injection burn

TEST TIMELINES

Agena PPI Liquid Test No. 8

(Docked only)

Test Time Sec	Maneuver	Film Time Sec.	Gemini Prop. Req'd, Lbs
	Tumbling, orient vehicle parallel to orbit path, reduce rate to minimum values.		
0	Power up. Camera on. Settle using Nos. 9, 10.		
10	Nos. 9, 10 off		7.3
30	Camera off.	30	
1830	Agena SPS 16 lb_f thrusters (2 each) on.		
1840	Camera on.		
1900	Agena PPS on (Agena SPS off).		
1903	Agena PPS off.		
1930	Camera off.	90	___
1930	Sub-totals	120	7.3

TEST TIMELINES (continued)

High and Low Energy Slosh, Desettling, Axial Retention, Settling

Test Nos. 1, 2, and 5

Test Time Sec	Maneuver	Film Time Sec	Gemini Prop. Rqd-lbs Docked	Undocked
	Tumbling.			
	Power up.			
0	Orient vehicle transverse to orbit. Reduce rates to minimum values.			
300	Camera on to observe equilibrium surface and Desettling Test #5			
305	Nos. 11, 12 on.			
315	Nos. 11, 12 off.		6.2	6.2
	Camera off.	15		
815	Camera on to observe equilibrium surface and for Settle and Retention Test No. 5.			
820	Nos. 9, 10 on			
830	Nos. 9, 10 off.		7.3	7.3
850	Camera off.	35		
1130	Pitch with Nos. 5, 6, and 16 to 3.55°/sec (17.0°/sec undocked with Nos. 5 and 6).		6.4	0.87
1228	Camera on for High Energy Slosh-A, Test No. 1			
1230	Arrest pitch with Nos. 1, 2, and 15 (Nos. 1 and 2 undocked).		6.4	0.87
1245	Camera off.	17		
1290	Camera on.			
1300	Camera off.	10		
1345	Camera on.			
1355	Camera off.	10		
1400	Camera on.			
1410	Camera off.	10		
1500	Pitch to 1.5°/sec using Nos. 5, 6, and 16. (8.5°/sec with Nos. 5 and 6 undocked).		3.2	0.37

High and Low Energy Slosh, Desettling, Axial Retention, Settling, Tests Nos. 1, 2, and 5 (Continued)

Test Time Sec	Maneuver	Film Time Sec	Gemini Prop.Rqd-lbs Docked	Undocked
1658	Camera on for High Energy Slosh-B, Test No. 2.			
1660	Arrest pitch rate with 1, 2, and 15 (Nos. 1, 2 only, undocked).		3.2	0.37
1675	Camera off.	17		
1720	Camera on.			
1730	Camera off.	10		
1775	Camera on.			
1785	Camera off.	10		
1830	Camera on.			
1840	Camera off.	10		
2150	Settle with Nos. 9,10 on.			
2160	Nos. 9, 10 off.		7.3	7.3
	Pitch to ω = 0.24°/sec using Nos. 5, 6 (0.098°/sec undocked).		0.02	0.01
2468	Camera on for Low Energy Slosh Test-A, Test No. 3.			
2470	Arrest pitch rate with Nos. 1,2		0.02	0.01
2500	Camera off.	32		
2545	Camera on.			
2555	Camera off.	10		
2595	Camera on.			
2605	Camera off.	10		
2650	Camera on.			
2660	Camera off.	10		
2700	Pitch to ω = 0.12°/sec using Nos. 5, 6, (to 0.05°/sec undocked).		0.01	0.003
2998	Camera on for Low Energy Slosh-B Test No. 4		0.01	0.003
3000	Arrest Pitch rate with Nos. 1,2.			
3030	Camera off.	32		
3075	Camera on.			

High and Low Energy Slosh, Desettling, Axial Retention, Settling, Tests Nos. 1, 2, and 5 (continued)

Test Time Sec	Maneuver	Film Time Sec	Gemini Prop.Rqd-lbs Docked	Undocked
3085	Camera off.	10		
3130	Camera on.			
3140	Camera off.	10		
3185	Camera on.			
3195	Camera off.	10		
3195	Sub-totals	268	40.06	23.31

TEST TIMELINES (continued)

Side Tank Sloshing Test

No. 7

Test Time Sec	Maneuver	Film Time Sec	Gemini Prop. Rqd-lbs Docked	Undocked
	Power up.			
0	Orient vehicle parallel to orbit path. Reduce rates to minimum values.			
300	Camera on to observe equilibrium surface and start of experiment.			
305	Roll accelerate to ω = 1.545°/sec using Nos. 2, 4, 6, and 8.		0.054	0.043
315	Thrust using Nos. 9, 10 to increase velocity by 0.1 ft/sec		0.171	0.089
330	Camera off.	30		
350	Roll accelerate to ω = 3.86°/sec using Nos. 2, 4, 6, and 8. Camera on.		0.054	0.043
355	Thrust using Nos. 11, 12 to decrease velocity by 0.1 ft/sec.		0.171	0.089
370	Camera off.	20		
390	Roll accelerate to ω = 11.5°/sec using Nos. 2, 4, 6 and 8. Camera on.		0.266	0.211
395	Thrust using Nos. 9, 10 to increase velocity by 0.1 ft/sec		0.171	0.089
410	Arrest roll rate.		0.402	0.309
440	Camera off.	50		
440	Subtotals	100	1.289	0.873

TEST TIMELINES (continued)

Screen Retention with Transverse Acceleration Test No. 5

(Undocked only)

Test Time Sec	Maneuver	Film Time Sec	Gemini Prop. Req'd - lbs
	Power up.		
	Orient vehicle along orbit path, reduce rates to minimum values.		
0	Camera on.		
5	No. 13 on.		
15	No. 13 off (Approx. 4 fps transverse of orbit).		3.6
30	No. 14 on.		
40	No. 14 off.		3.6
60	Camera off.	60	
60	Subtotals	60	7.2

TEST TIMELINES (continued)

Docking and Undocking Test

No. 6

Test Time Sec	Maneuver	Film Time Sec	Gemini Prop. Req'd - lbs
	Power up.		
0	Camera on for Docking Test No. 6		
5	Undock and accelerate BEF using Nos. 11, 12		
15	Nos. 11, 12 off.		6.2
25	Camera off.	25	
35	Camera on. Using Nos. 9, 10 move up to the vehicle and redock.		12.0
95	Camera off or until depleted	60+	
95	Sub-totals	85	18.2

Experiment Cost Summary

Sequence No.	Experiment	Film Time Sec	Gemini Propellant Usage - lbs Docked	Undocked	Elapsed Time, sec
1	Agena PPS	120	7.3	N/A	1930
2	Settling, Desettling and Retention	50	13.5	13.50	850
3	High Energy Slosh A	47	12.8	1.74	560
4	High Energy Slosh B	47	6.4	0.74	430
5	Low Energy Slosh A	62	7.34	7.32	820
6	Low Energy Slosh B	62	0.02	0.006	535
7	Longitudinal Slosh	100	1.289	0.873	440
contingency	Translation Retention	60	N/A	7.20	60
8	Docking	85	18.2	N/A	95
	Totals	633	66.849	31.379	5700